Fractography of Ceramic and Metal Failures

Mecholsky/Powell, editors

ASTM **STP 827**

FRACTOGRAPHY OF CERAMIC AND METAL FAILURES

A symposium
sponsored by ASTM
Committee E-24 on Fracture Testing
Philadelphia, Pa., 29-30 April 1982

ASTM SPECIAL TECHNICAL PUBLICATION 827
J. J. Mecholsky, Jr., Sandia National Laboratories, and S. R. Powell, Jr., Bell Helicopter Company, editors

ASTM Publication Code Number (PCN)
04-827000-30

1916 Race Street, Philadelphia, Pa. 19103

Library of Congress Catalog Card Number: 83-71813

NOTE

The Society is not responsible, as a body,
for the statements and opinions
advanced in this publication.

Printed in Baltimore, Md. (b)
March 1984

Foreword

The Symposium on Fractography in Failure Analysis of Ceramics and Metals, sponsored by ASTM Committee E-24 on Fracture Testing, was held at ASTM Headquarters, Philadelphia, Pennsylvania, on 29-30 April 1982. J. J. Mecholsky, Jr., Sandia National Laboratories, and S. R. Powell, Jr., Bell Helicopter Company, served as symposium chairmen. This volume, *Fractography of Ceramic and Metal Failures*, has been edited by Messrs. Mecholsky and Powell.

Related ASTM Publications

Fracture Mechanics: Fifteenth Symposium, STP 833 (1984), 04-833000-30

Fatigue Mechanisms: Advances in Quantitative Measurement of Physical Damage, STP 811 (1983), 04-811000-30

Elastic-Plastic Fracture: Second Symposium, Volume 1—Inelastic Crack Analysis, STP 803 (1983), 04-803001-30

Elastic-Plastic Fracture: Second Symposium, Volume 2—Fracture Resistance Curves and Engineering Applications, STP 803 (1983), 04-803002-30

Corrosion Fatigue: Mechanics, Metallurgy, Electrochemistry, and Engineering, STP 801 (1983), 04-801000-30

Probabilistic Fracture Mechanics and Fatigue Methods: Applications for Structural Design and Maintenance, STP 798 (1983), 04-798000-30

Fracture Mechanics: Fourteenth Symposium—Volume I: Theory and Analysis, STP 791 (1983), 04-791001-30

Fracture Mechanics: Fourteenth Symposium—Volume II: Testing and Applications, STP 791 (1983), 04-791002-30

Residual Stress Effects in Fatigue, STP 776 (1982), 04-776000-30

Low-Cycle Fatigue and Life Prediction, STP 770 (1982), 04-770000-30

A Note of Appreciation to Reviewers

The quality of the papers that appear in this publication reflects not only the obvious efforts of the authors but also the unheralded, though essential, work of the reviewers. On behalf of ASTM we acknowledge with appreciation their dedication to high professional standards and their sacrifice of time and effort.

ASTM Committee on Publications

ASTM Editorial Staff

Janet R. Schroeder
Kathleen A. Greene
Rosemary Horstman
Helen M. Hoersch
Helen P. Mahy
Allan S. Kleinberg

Contents

METALS

Failure Analysis Techniques

Applied Fractography

PANEL REPORTS

Introduction

This volume, a result of the ASTM Symposium on the Fractography in Failure Analysis of Ceramics and Metals, is a reference text on the fractography of ceramics and the state-of-the-art techniques for failure analysis of both ceramics and metals. Previous volumes on fractography have been predominately oriented towards metal fractography. It is our hope, however, that the two communities share innovative techniques and approaches so that both will benefit. It was apparent at the symposium that fractographic principles can be applied to many materials and that more interaction between metallurgists and ceramists will be mutually beneficial. It is in this spirit of cooperation that this book is published.

The symposium and this volume were organized in the two broad areas of ceramics and metals. Ceramics are discussed in three sections: Fracture Analysis Techniques, Surface Analysis Techniques, and Applied Fractography. The two fundamental technique sections are an excellent state-of-the-art reference to the fractography of brittle materials, while the third section presents examples of fractography in research and forensics. Metals are covered in two sections: Failure Analysis Techniques and Applied Fractography. The former presents the most recent approaches to fractography, the latter reviews case histories. Thus we have a descriptive atlas of failures.

We believe this volume is a benchmark in the attempt to unite the field of fractography. This collection of papers demonstrates the similarities in approach to failure analysis for metals and ceramics while emphasizing the common and unique fracture features in these analyses. The field of fractography is expanding in scope and knowledge. This volume provides the latest in topics and techniques.

J. J. Mecholsky, Jr.

Sandia National Laboratories, Albuquerque, New Mexico; symposium chairman and editor

S. R. Powell, Jr.

Bell Helicopter Company, Ft. Worth, Texas; symposium chairman and editor

Ceramics

Fracture Analysis Techniques

Roy W. Rice[1]

Ceramic Fracture Features, Observations, Mechanisms, and Uses

REFERENCE: Rice, R. W., **"Ceramic Fracture Features, Observations, Mechanisms, and Uses,"** *Fractography of Ceramic and Metal Failures, ASTM STP 827*, J. J. Mecholsky, Jr., and S. R. Powell, Jr., Eds., American Society for Testing and Materials, 1984, pp. 5-103.

ABSTRACT: The character and occurrence of mist, hackle, and crack-branching features on ceramic fractures are reviewed and possible mechanisms for causing these features are discussed. Besides glass and polycrystalline fractures, substantial attention is paid to fractures of ceramic crystals, for which new data are presented and similarities shown to fractures of brittle metal crystals. Distinct geometrical effects exhibited by crystal fracture features are illustrated and discussed, as are the variable distances from fracture origin to the onset of features such as mist.

Crack branching of ceramics, which is suggested to be the merging of hackle, is shown to follow the same type of relations as for the onset of mist and hackle. If there is rebranching, it tends to occur at multiples of the original branching distance. Substantial data (again much of it new) show that branch angles are similar for a wide variety of ceramics as well as for brittle fracture of metals. Branch directions are shown to depend on the nature of the test specimen (or crystal directions), and biaxial testing is shown to increase branch angles over those for uniaxial flexure of tension testing. Observations, mechanisms, and effects of intergranular versus transgranular fracture are discussed. The determination and character of flaws causing fracture are summarized, and questions concerning their behavior are raised (for example, effects of complex flaws and of mixed-mode failure).

KEY WORDS: fracture, fractography, ceramics, fracture mode, fracture origins, fracture mechanism, fracture surfaces

Crack propagation in any material is determined by the nature of the material and the stress conditions. Generally the overall conditions (those applicable on the scale or greater than that) of the crack itself as well as the local conditions (those applicable on the microstructural scale) determine the crack path. The combinations of these conditions vary in such a fashion as to lead to

[1]Head, Ceramics and Glass Branch, Naval Research Laboratory, Washington, D.C. 20375.

a significant range of crack path character, making the resultant fracture topography a record of the integration of the material and mechanical factors determining the crack path. Thus fractography, the study of fracture topography and its relation to crack propagation, is basically an attempt to deconvolute these patterns into the material and mechanics factors. Such deconvolution is important both for scientific understanding and for practical applications.

This paper reviews the most pronounced and most common fracture features, which are also usually the most important ones for mechanical understanding and applications. Three broad classes of fracture features in ceramics are discussed. In order of decreasing emphasis these are (1) the classical mirror-mist-hackle-crack-branching patterns, (2) the interaction of a crack with microstructure, and (3) failure-causing flaws. Glasses, single crystals, and polycrystalline materials are addressed, with the extent of discussion approximately increasing in the order listed. Further, while this paper is focused on ceramic materials, some basic similarities with brittle fracture of metals, especially in single crystals, will be noted. In many cases, fractography examples have been purposely chosen from somewhat different materials to help in illustrating the diversity of materials over which similar features occur.

The aforementioned three classes of fracture features resulting from uniaxial flexural loading are addressed first, along with some secondary discussion of effects of biaxial flexure and uniaxial tension. Next, the effects of other stress conditions in terms of the nature of the stress as well as the rate, spatial extent, and time of load application are addressed. The focus is on lower temperature (mainly room temperature) fractures where materials are typically quite brittle, but some examples and discussion of higher temperature fractures will be given.[2] Finally, the mechanisms causing the various fracture features, some of the important applications of fractography to ceramics, and research needs are discussed.

Mirror, Mist, Hackle, and Crack Branching on Glass and Polycrystalline Fractures

General Behavior

The basic mirror-mist-hackle-crack-branching features, described and discussed in detail elsewhere [*1–4*], are addressed here as a basis of more detailed subsequent discussion. Under typical tensile or flexural loading, mechanical failure of many glasses and polycrystalline bodies with limited or no porosity occurs due to the propagation of a single crack. Resultant fracture typically shows a relatively flat, smooth region, most or all of which is approximately perpendicular to the tensile axis around the initial flaw from which failure

[2]Fractures and data from higher temperature or different tests will be specifically noted. All other fractures and data are for room-temperature tests.

proceeded. This flat, smooth region is called the *mirror*, since on glasses (where it was first observed) as well as on single crystals and some polycrystals discussed later, it is sufficiently flat and relatively smooth that it provides a high degree of mirror-like reflectivity. The mirror is typically bounded by *mist*, small ridges oriented in a direction parallel to that of crack propagation (Figs. 1 to 3). Mist typically merges into the next set of features, similar larger ridges called *hackle*, and these merge into macroscopic *crack branching* as the crack propagates outward (provided the specimen is large enough relative to the fracture stress; see Eq 1). These features are usually quite distinct on dense silicate glasses, where they were first and most extensively studied, but they have also been shown to occur on fractures of a variety of other materials including nonsilicate glasses, some porous silicate glasses, and glass-like materials (for example, glassy carbon).

Shand [5] was apparently the first to specifically identify and discuss these features in a polycrystalline ceramic, namely a highly crystallized glass. Kirchner [6] and Rice and colleagues [2,3,7] were among the first to extensively study these features in a variety of polycrystalline bodies. While there is overall general similarity between the features on glass and polycrystalline fractures, there are a number of important differences. Most of these arise from effects of increasing pore and especially grain sizes on the crack path. With increasing transgranular fracture, often accompanying increasing grain size, mist ridges cease to be larger than the grain, ultimately becoming individual fracture or cleavage steps on grain fracture surfaces. This change often leaves fracture mirrors reasonably identifiable (Figs. 4 and 5). However, de-

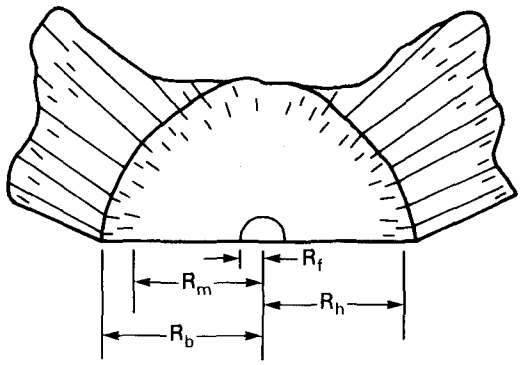

FIG. 1—*Schematic of fracture mirror and related features. Idealized features and their radii are the failure-initiating flaw* (R_f); *fracture mirror* (R_m)—*the mist boundary (average onset of mist, shown as small radial lines); hackle boundary* (R_h)—*the average onset of hackle (shown as longer radial lines); and crack-branching boundary* (R_b)—*the average beginning of macroscopic branching shown as two sections of an arc. The top portion of some of the crack branching (and also some of the hackle) is missing, as is often the case due to stress gradients such as those in flexure testing (see Figs. 2, 7, 8, and 14). Some mist continues into the hackle region and both in turn continue into the crack-branching region.*

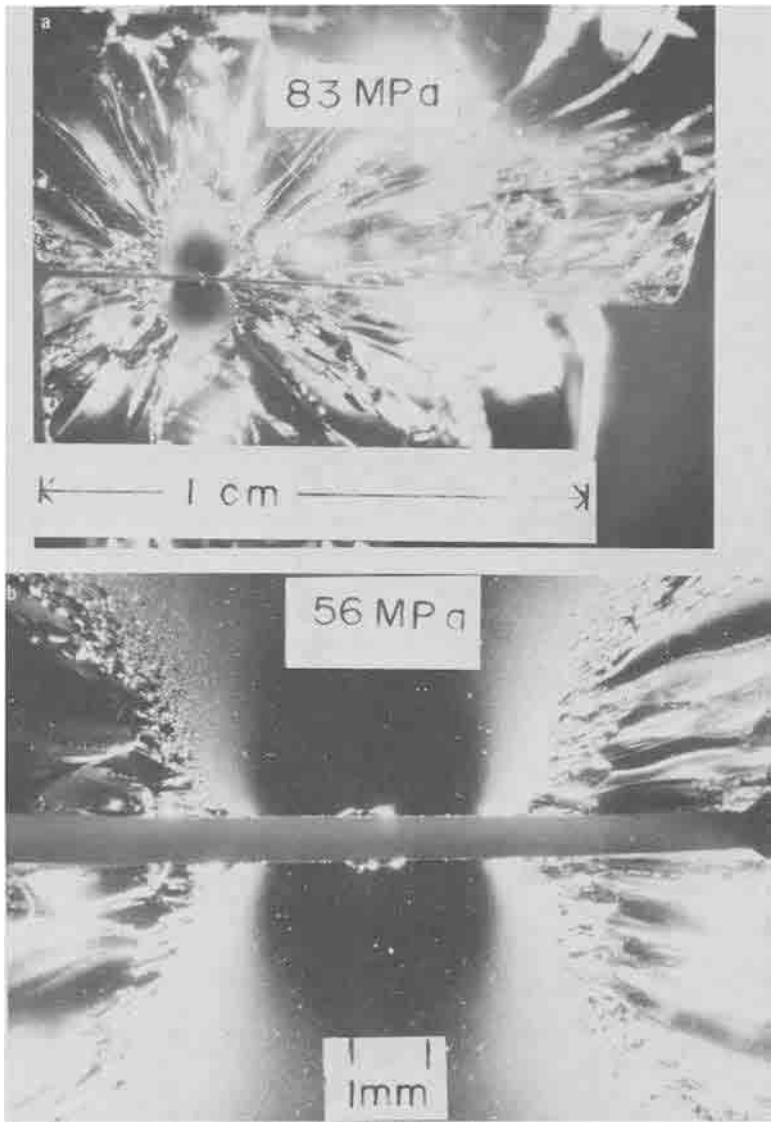

FIG. 2—*Examples of glass fracture mirrors. Portions of matching fracture halves of two silicate glass specimens with room-temperature flexure strengths of* (a) *83 MPa (12.1 × 10³ psi) and* (b) *56 MPa (8.1 × 10³ psi). Note some elongation of the small mirror in* (a) *towards the neutral axis, and only a limited amount of mist and no hackle between the mirror and the neutral axis in* (b). *Note also some towing in of the mirrors at the fracture surface; this indicates earlier onset of mist and hackle.*

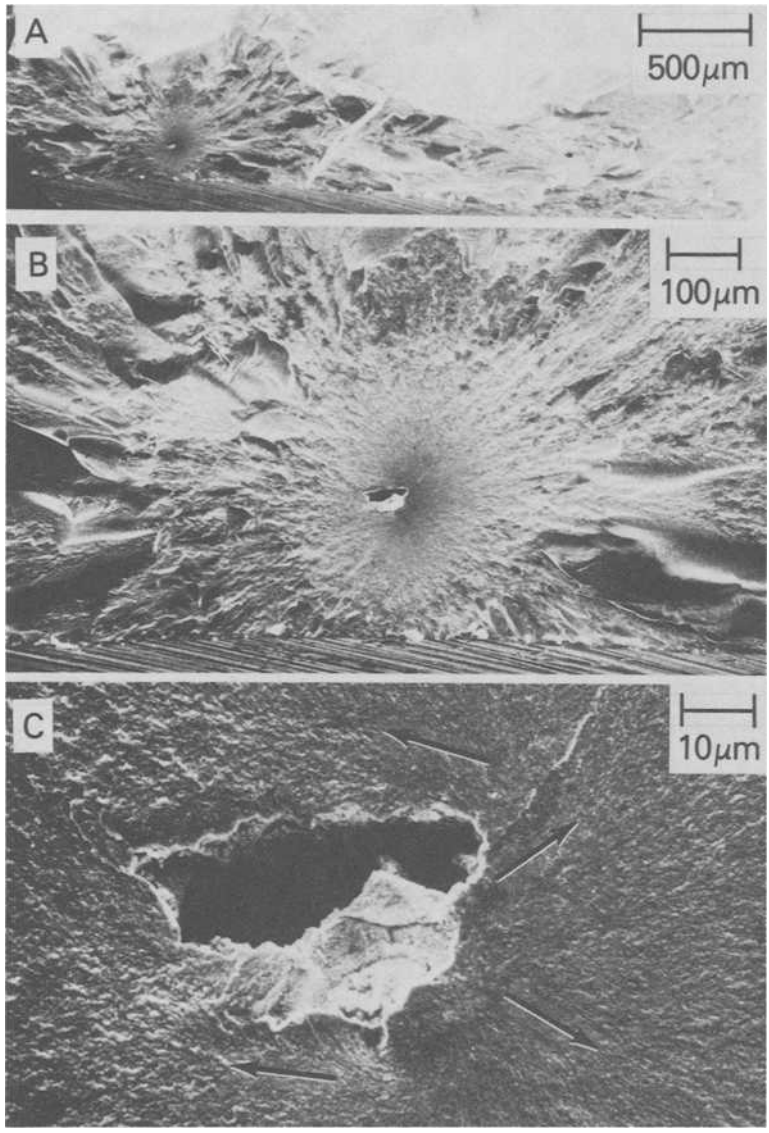

FIG. 3—*Fracture mirror and related features in a very fine (submicron) grain tungsten-carbon alloy. Failure in room-temperature flexure testing is from an internal irregular large pore. Note the relatively smooth character of the fracture mirror and the gradual increase in roughness, some irregularity of the mirror, and some limited increase in the dimensions of the mirror towards the neutral axis. The fracture started on the right side of the pore, sweeping around it to the left (arrows), leaving the mirror larger on the right and shorter on the left, especially where the two halves of the crack met at the upper left-hand corner of the pore towards the top side of the mirror. Fracture stresses were 1430 and 930 MPa (203 and* $\sim 135 \times 10^3$ *psi) respectively at the tensile surface and at the pore. This is representative of the general character of mirrors for internal origins.*

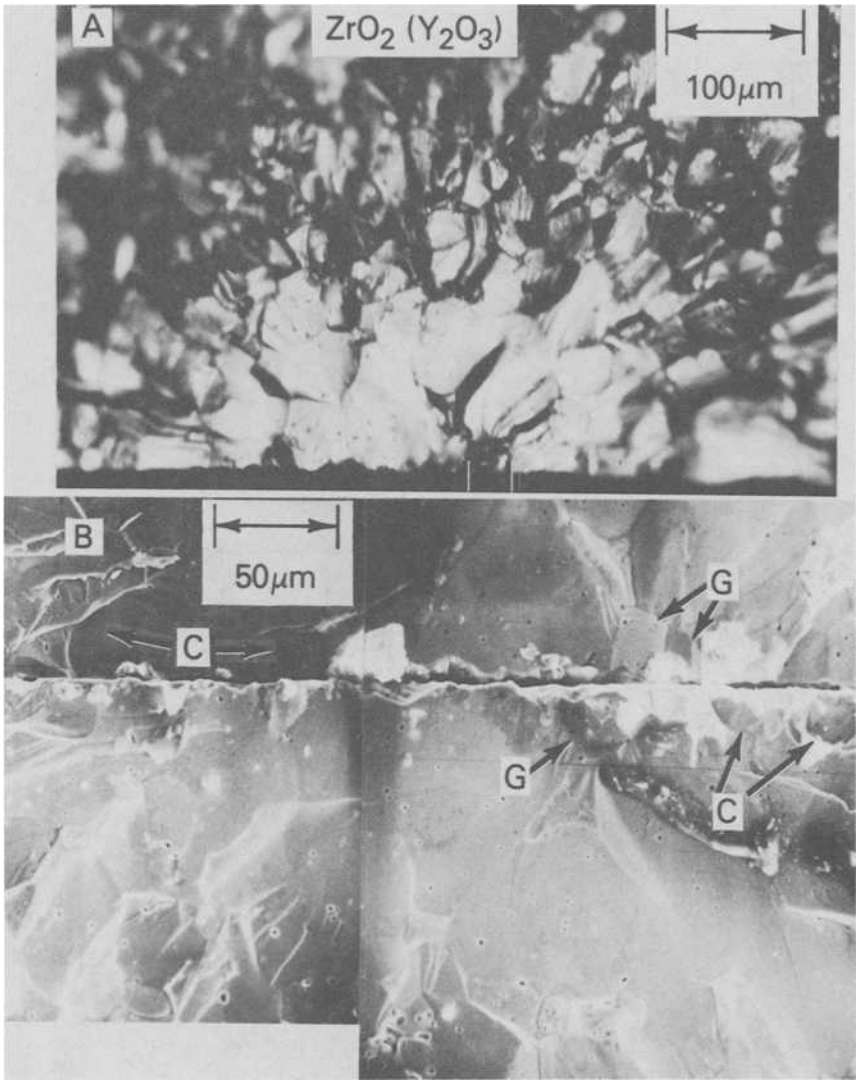

FIG. 4—*Fracture mirror in a large-grain ZrO_2 specimen fully stabilized with 11 wt% Y_2O_3.* (a) *is an optical photo of one fracture surface primarily in the fracture mirror area, showing an unusually clear and flat (hence bright) mirror area for such a large grain body.* (b) *is an SEM micrograph of parts of the matching fracture halves of the same fracture. While better contrast could be achieved with more care and especially with more modern SEMs, the difference between this and* (a) *shows the much greater contrast that can be achieved optically. The higher magnification of the SEM also indicates that there are possible flake-like chips* (C) *of material missing from even within the fracture mirror, suggesting some possible crack branching possibly due to interacting with pre-existing cracks. (Note that the bright white patches may be debris from such chips, the white character being caused by charging.) This figure illustrates one of the important needs for further study, the comparison of detailed matching fracture surfaces. Failure at 290 MPa (42.1 × 10^3 psi) apparently initiated from the grain boundary surface* (G).

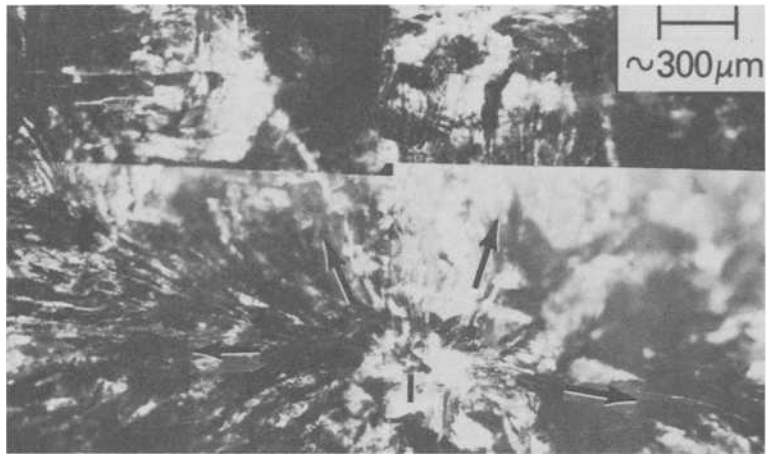

FIG. 5—*Fracture of large-grain CaO. This composite photomicrograph of a recrystallized crystal fractured in flexure at 1315°C (2400°F) shows the overall hackle-type ridges (arrows) and the origin (vertical mark; the origin is shown at higher magnification in Fig. 45c). Often such optical examination more clearly shows the overall pattern of these features than SEM.*

creasing strengths with increasing grain and pore sizes (and total porosity) reduce the density and often the clarity of fracture features. This effect, combined with increased roughness with larger grain and pore sizes, typically makes the mirror (Fig. 6), mist (Figs. 4 to 6), and even some hackle less discernable, in the extreme case obliterating all normally observed fracture features (Fig. 7). Increased roughness of intergranular fracture accentuates these trends and can substantially change the character of the fracture features, especially at larger grain sizes (Fig. 8). The only fracture feature that may be clearly observed (if the specimen is sufficiently large relative to the strength of the sample) is macroscopic crack branching; see Figs. 10 to 13, discussed later for examples of such branching. On the other hand, where a reasonable amount (25% or more transgranular failure) occurs, one can commonly identify the mirror, mist, and hackle of polycrystalline features. Other heterogeneities (for example, microcracking and second phases) can sufficiently perturb the crack front so as to make these features difficult, or impossible, to detect on polycrystalline fractures. Even in such cases, however, if the specimen is sufficiently large for its strength—that is, larger than R_h, as discussed below—macroscopic crack branching should again commonly occur and be observable.

It has long been established that the product of the failure stress (σ_f) and the square root of the distance (R_i) from the center of the fracture origin to the appearance of each of these sets of features forming essentially a boundary—

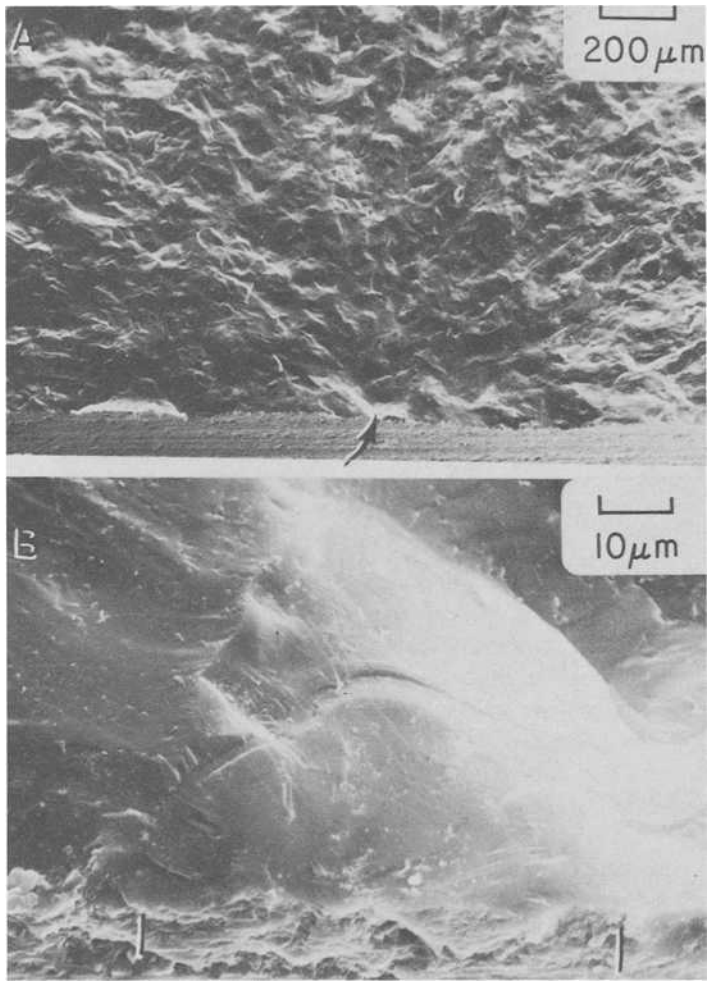

FIG. 6—*Fracture of large-grain B_4C. Although at lower magnifications overall features corresponding to hackle can be discerned, they are not much greater than the scale of the perturbation of the fracture due to the grain size. Specific mist features are not readily detected because of the roughness due to the grain size.* (b) *is a high magnification of the fracture origin (between vertical marks; see also the arrow in* a). *Fracture stress was 217 MPa (31.7 × 10^3 psi).*

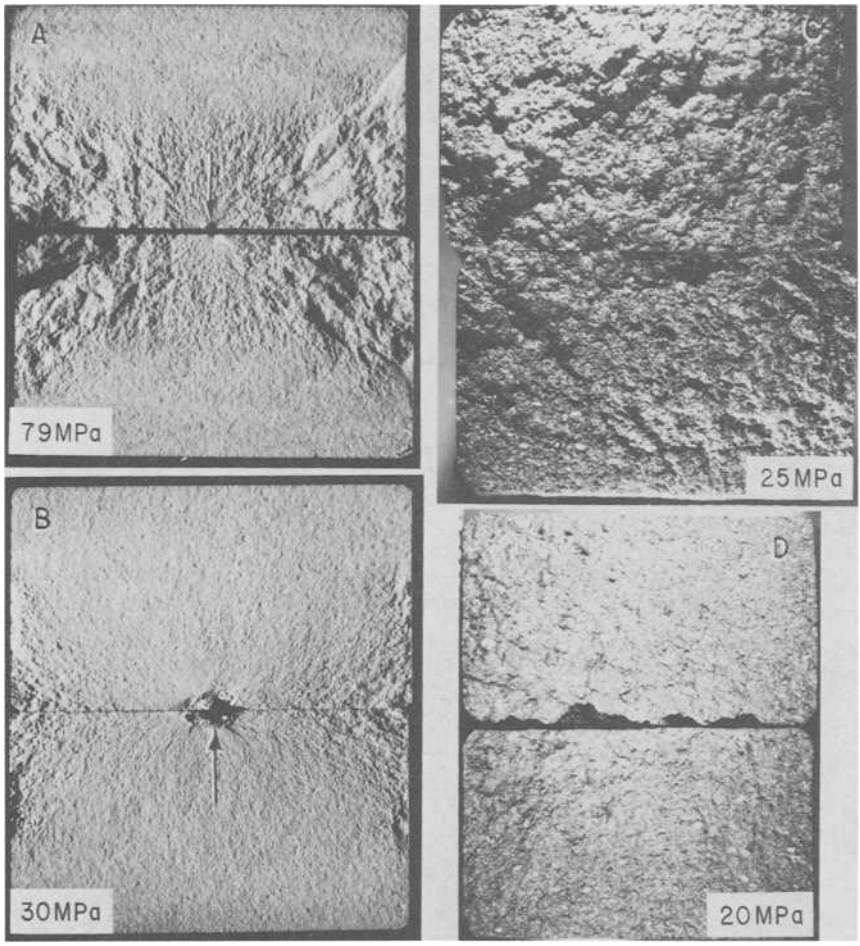

FIG. 7—*Fracture features of two graphite materials. Large bars 1.3 by 2.5 cm (0.5 by 1 in.) of two commercial graphites having typical (~25%) porosity were used to assure seeing their fracture features.* (a) *and* (b) *show matching flexure fracture halves of POCO graphite having a fine (~2 μm) grain size and fine (~2 μm) pore size.* (a) *failed at 79 MPa (11.5 × 10^3 psi) from a flaw (arrow) introduced by a 100-kg Vickers indent.* (b) *failed at 30 MPa (4.3 × 10^3 psi) from a flaw introduced by a small chisel. In* (a) *only mist and small hackle occur between the mirror and the neutral axis while none appears in* (b), *and in* (b) *the mirror is much larger with a lower failure stress. (Higher strength POCO failing from natural flaws shows complete mirrors.)* (c) *and* (d) *are matching fractures of a reactor-grade graphite having ~40 μm grain size and pore sizes to ~100 μm. These specimens failed from natural flaws at respectively 25 MPa (3.6 × 10^3 psi) and 20 MPa (2.9 × 10^3 psi). No mirror and related features can be distinguished on these fractures because of the roughness of the fracture topography on the microscale due to the larger grain and pore size.*

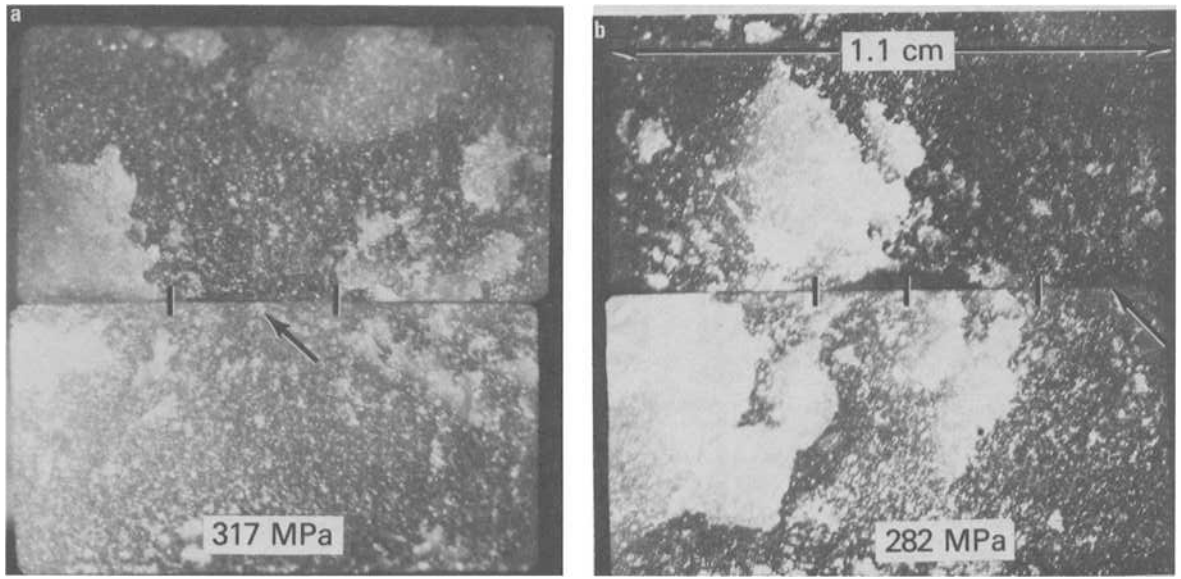

FIG. 8—*Fracture of large-grain Al_2O_3. Optical photos of matching fracture halves of two larger than normal Lucalox flexure bars are shown for failure stresses respectively of* (a) *317 MPa (46 × 10^3 psi) and* (b) *282 MPa (41 × 10^3 psi). Mist is not clearly identified, hackle occurs as fine white-appearing flakes, and macroscopic crack branching (whose onset is marked by vertical lines) occurs as larger white flakes due to reflection of light from both the top and bottom surface of the flake. These features generally allow definition of the origin area (arrows). If smaller specimens (for example, approximately one third the size of these) had been tested at the same failure stress levels, little or none of the fracture features would have been observed because the specimens would have been too small relative to the fracture stress levels. Note the longer sequence of crack-branching features in* (b) *despite its lower failure stress because of the longer distance afforded by the fracture occurring near the right side of the specimen. Also note alternate crack branches on opposite fracture halves.*

that is, the onset of mist (R_m), hackle (R_h), and crack branching (R_b)—is a constant (B_i) for a given material:[3]

$$\sigma_f \sqrt{R_i} = B_i \tag{1}$$

Two points should be noted. Firstly, specimen size does not enter the equation. Thus wherever R_i (that is, R_m, R_h, or R_b) exceeds the distance from the origin to the specimen edge, features associated with that R_i are simply not present in that direction. Because of the inverse relation of σ_f and R_i for constant B_i, the failure stress also plays an important role in the extent to which the various features are seen within a given specimen size. Secondly, a study of several materials by Mecholsky et al [*3, 7*] showed that correction for crack shape factors brought results for a much broader range of crack shapes into agreement with those for simple (half-penny shaped) flaws. Using such flaw shape corrections (and eliminating the stress gradient factors discussed below) suggested to those authors that normalizing the behavior of a variety of materials for these factors may result in a universal constant for each set of features. This result, a direct conclusion of their work, was first explicitly stated by Bansal [*8*]. That the overall flaw shape effect, not just one dimension, must be considered for most flaws is illustrated in Fig. 9.

Comparison of Eq 1 with the Griffith/Irwin equation gives

$$\sigma_f = Y\sqrt{2E\gamma}/R_f = YK_{Ic}/\sqrt{R_f} = A/\sqrt{R_f} \tag{2}$$

where

R_f = flaw size,
E = Young's modulus,
γ = fracture energy,
K_{Ic} = fracture toughness, and
Y = a parameter dependent on flaw shape and specimen size.

This leads to the important and widely recognized relationship of mirror to flaw size (R_i/R_f) and related ratios:

$$R_i/R_f = (B_i/YK_{Ic})^2 \tag{3}$$

[3]While we speak of boundaries here, it should be noted that the density of mist and hackle generally decreases with decreasing failure stress. Also, the mist and hackle generally appear to be dependent upon some statistical aspects of nucleation such that they do not form an exact boundary. This dependency, plus some of the variations that are discussed later, cause some uncertainty in the measurement of these various boundaries. The statistical uncertainty is typically most pronounced for the mist and least pronounced for crack branching. However, there are real statistical variations in the crack-branching boundary as well as possible breaking off of the initial part of the crack-branching boundary due to its thin nature (Figs. 66 and 67).

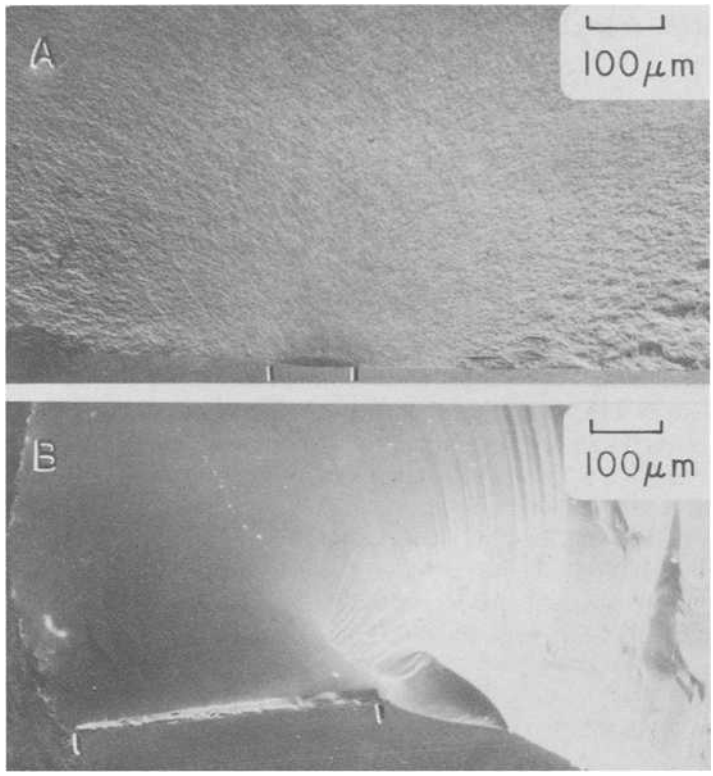

FIG. 9—*Mirrors around elongated flaws.* (a) *is a part of the fracture surface of a polished disk of MgF_2 broken in biaxial flexure (see 7 of Fig. 12) at 91.5 MPa (13.3 × 10^3 psi). Note the elongated polishing flaw at the origin (vertical line).* (b) *is a fracture origin of a spinel crystal tested in flexure with a {100} tensile surface and a ⟨100⟩ tensile axis failing at 130 MPa (18.9 × 10^3 psi). This flaw extends almost the full width of the mirror (bounded by arc segments with progressively larger amplitude leading to macroscopic crack branching at the right edge of the photo. Using the horizontal dimensions of these flaws to measure the mirror-to-flaw-size ratios gives anomalously low values (~3 and ~1 respectively), but calculating these by using the radius of the equivalent area semicircular flaw gives normal values (~11 and ~4 respectively).*

Under normal uniform tension, the mist, hackle, and branching boundaries are circular in shape. It is now well established, however, that stress gradients lead not only to the distortion of these features but can also result in some not forming over part (Figs. 1, 2*b*, and 6 to 8) or even all of the fracture surface. Johnson and Holloway [*9*] drew specific attention to these distortions in flexure, where progressively more and more of these features are missing as their size increases sufficiently to approach about half way to the neutral axis in flexure specimens. They further showed that these variations are completely consistent with Eq 1, provided σ_f is corrected at each point along any fracture boundary for any stress gradients. Thus, if the stress is not uniform in a body at the instant of failure, the mist and other features will form at different dis-

tances from the origin that for failure from a uniform stress. Since failure commonly occurs at the maximum stress, decreasing stresses away from the origin often keep Eq 1 from being satisfied within the confines of the specimen over part or all of the fracture surface; therefore more features will be missing. On the other hand, these features will form sooner if failure occurs in a region of lower stress (due to a larger flaw) and propagates into a region of higher stress. Further broad applicability of Eq 1 will be shown in later discussion.

Specific Aspects of Crack Branching

Consider some detailed aspects of crack branching and several variations of such branching. Firstly, crack branching may not always continue to the specimen edge. Besides the stress gradient effects discussed previously and those discussed later, such incomplete branching is most commonly associated with lower stresses relative to the specimen size. With increasing stress to specimen size, branching usually becomes progressively more complete; that is, the branch cracks are more likely to propagate to the boundaries of the specimen, resulting in the specimen being broken into more than two pieces (Figs. 10 to 13). As crack branching becomes more complete, the second variation, that of an increase in the number of branch cracks occurring from the boundary for the onset of crack branching, begins to occur. Thus a branching crack may divide into two cracks or alternatively may form two branches with the main crack also continuing (Figs. 12 and 13). (The continuation of the main crack may or may not be complete, depending for example on the stress level.)

Whether the main crack continues beyond the point of branching appears to depend on the material and type of test. Limited data (Table 1) suggest a strong preference for branching-only in a commercial crystallized glass material tested biaxially, while similar testing of optical-grade magnesium fluoride (MgF_2) much more commonly showed branching with continuation of the main crack (Fig. 12). The cause of this difference has not been resolved. The crystallized glass has a significantly higher fracture toughness than the MgF_2, but both have about the same Young's modulus. However, the MgF_2 was tested biaxially with a ring-on-ring test where there is horizontal constant stress levels over much of the sample, while the crystallized glass was tested by a ball-on-ring test where there is no constant stress.

The orientation of crack-branching directions can depend explicitly on the nature of the test. Specifically, rectangular bars tested in flexure that exhibit crack branching almost always do so by branching in directions normal to the loading direction, in typical flexure testing forming horizontal wedges, as shown by extensive observations of the author (Fig. 10).[4] On the other hand,

[4]Single crystals with orientation of preferred fracture planes favoring vertical crack branching may give greater occurrence of such branching in rectangular bars; this will be discussed later (see Fig. 26).

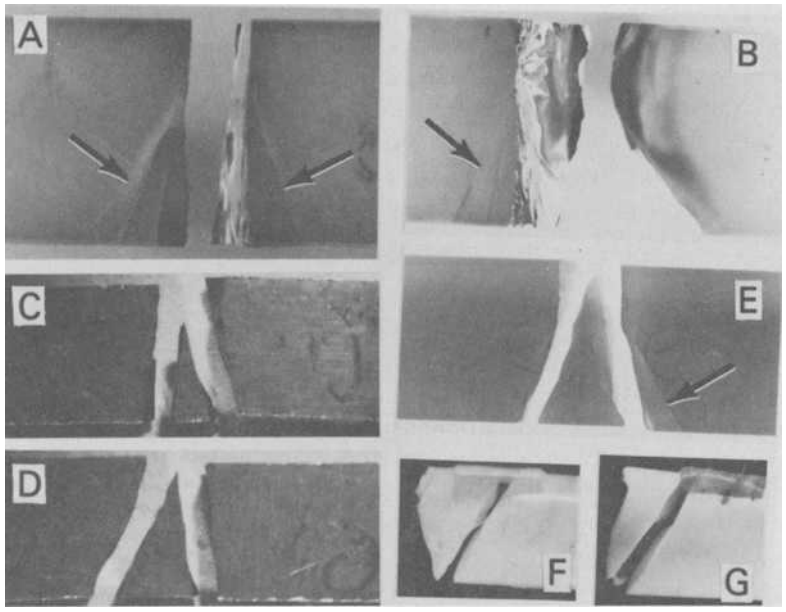

FIG. 10—*Macroscopic crack branching in various flexure-tested bars and rods.* (a) *and* (b) *are borosilicate glass specimens failing at* (a) *50 MPa (7.3 × 10³ psi) and* (b) *83 MPa (12.1 × 10³ psi). These vertical views show the complete specimen widths of ~2.5 cm (~1 in.). Note the missing section in* (b) *due to some macroscopic crack branching being completed, and several incomplete branches between the arrows.* (c) *and* (d) *are fine-grain hot-pressed B_4C specimens failing respectively at 540 MPa (78.3 × 10³ psi) and 383 MPa (58.5 × 10³ psi). Note the wedge-shaped piece formed by complete crack branching in each specimen, shown in their complete widths of 0.53 cm (~0.21 in.).* (e) *is a hot-pressed MgF_2 specimen failing at 92 MPa (13.4 × 10³ psi) shown in its complete width of 1.78 cm (0.7 in.). Note the triangular piece from complete crack branching.* (f) *and* (g) *are horizontal views of one side of the fracture and associated wedge-shaped pieces left from crack branching in rods of 0.51 cm diameter (0.2 in. diameter) failing respectively at 274 MPa (39.8 × 10³ psi) and 291 MPa (42.2 × 10³ psi). Unlike all the rectangular bars tested in flexure, which had crack branching forming a wedge horizontally, the round rods had wedges formed by crack branching in the vertical direction.*

limited testing of round rods of several materials (silicate glasses, crystallized glasses, glassy carbon, and SiC) showed them to always form branches in a direction orthogonal to that of flexure-tested rectangular bars—that is, they branched vertically (Fig. 10)—if branching occurred.[5]

With increasing failure stresses or specimen size, branch cracks as well as the continuation of the main crack after the onset of branching can branch again and any of these can in turn rebranch a number of times (Figs. 12 and 13). Note also that the branches effectively seek out and branch into uncracked

[5]In discussion of this point with the author's colleague, Dr. David Lewis, he recalled that in flexure testing of over 2000 glass rods in a college course, branching always formed vertical wedges.

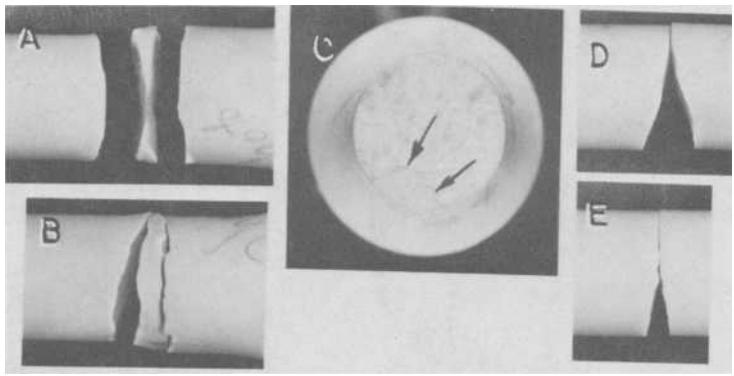

FIG. 11—*Crack branching in tension-tested Al_2O_3.* (a) *and* (b) *are two different side views showing one of two crack-branching wedges formed when the specimen failed at 229 MPa (33.2 × 10^3 psi) from a surface flaw.* (c) *shows a top view of the fracture with one of the crack-branching wedges in place (arrows indicate onset of crack branching).* (d) *and* (e) *are two specimens failing respectively from a surface origin at 172 MPa (25.0 × 10^3 psi) and from an internal origin at 162 MPa (23.5 × 10^3 psi). The tensile section of all the specimens is ~15 mm in diameter.*

material within the general constraint of the range of crack-branching angles discussed below. Thus as one goes to higher stresses for a given specimen size where more rebranching is allowed, the rebranching paths swing around from the ends of the original crack, causing cracking over a wider angle from the direction of the original crack so that at high strengths extensive shattering of the specimen occurs.

Rebranching of cracks tends to occur at multiples of the distance from the origin to the first branch (at least in the absence of large decreases in stress). Such rebranching approximately satisfies modification of Eqs 1 and 3:

$$R_{bn} \sim nR_{bi} \tag{4}$$

where n is the first, second, etc., stage of branching. There are definite variations of this. The first and most systematic is a general increase in the distances for each subsequent set of branching in a decreasing stress field. While detailed quantitative studies have not been made, this decrease appears to be consistent with the stress gradient effects discussed above and below. Secondly, there is a significant statistical variation of R_{bn} since branches of the second, third, etc., stage of branching sometimes occur sooner or later than expected or not at all. On close examination apparently missing branches may be revealed as incomplete branches, but there do appear to be truly missing branches.

Next consider the angles of branching. Some data on crack-branching angles are shown in Table 1 for original branches and rebranches (which show no differences) and for branching with or without the continuation of the

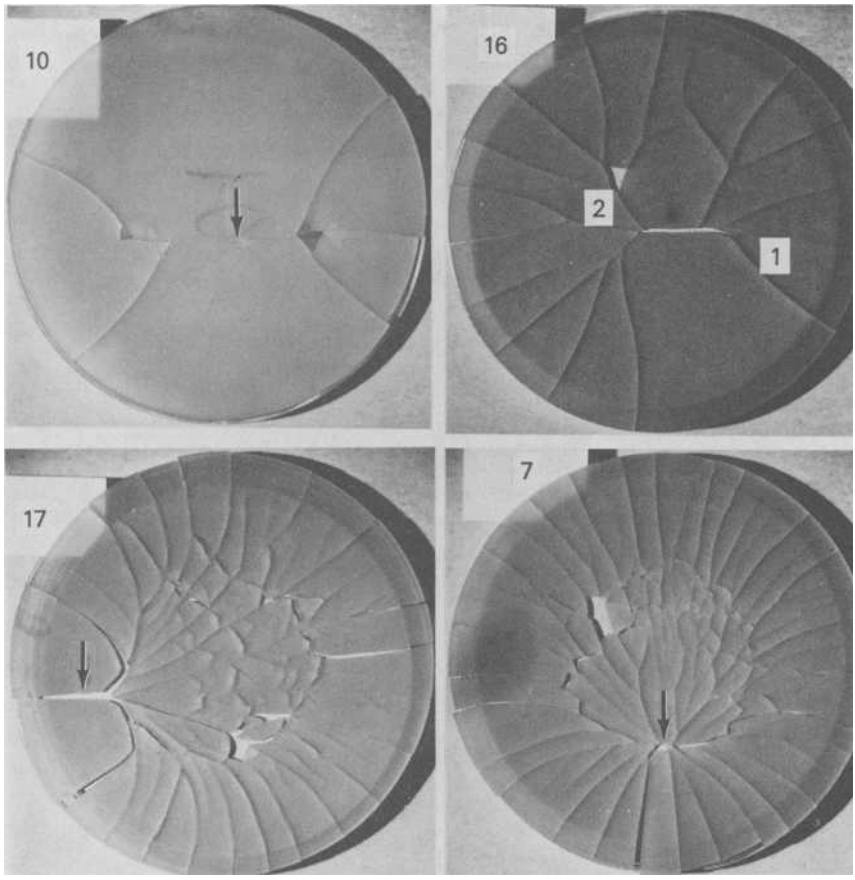

FIG. 12—*Crack branching in biaxially tested MgF_2. Disks of 8.5 cm diameter (~3.35 in. diameter) failed in a ring-on-ring-test with diameters of 7.92 and 3.83 cm (3.2 and 1.5 in.) at failure stresses of* (10) *47.0 MPa (6.83 × 10^3 psi),* (16) *60.2 MPa (8.75 × 10^3 psi),* (17) *86.9 MPa (12.6 × 10^3 psi), and* (7) *91.5 MPa (13.3 × 10^3 psi). Note the increased cracking due to progressive rebranching with higher failure stress. Origins in all cases marked by an arrow. Occasionally the crack only forms two branches and does not continue along the original direction between these two branches (the right- and left-hand set of branches in Disk 10). In some cases the crack may start to continue along the center and terminate (~1 mm into Piece 1 of Disk 16).*

main crack. Most of these data were measured on specimens tested by the author and his colleagues; however, some data from the literature [*10*] are also included. While there are basic changes in these angles with different stress conditions, there are also significant variations as shown, for example, by the standard deviations. Further, even along a given branch the angle does not necessarily stay constant.[6] For example, if a branch starts out at an un-

[6]Values in Table 1 represent the average branch angles, neglecting decreases in branching angles near the edges of specimens (biaxially tested disks).

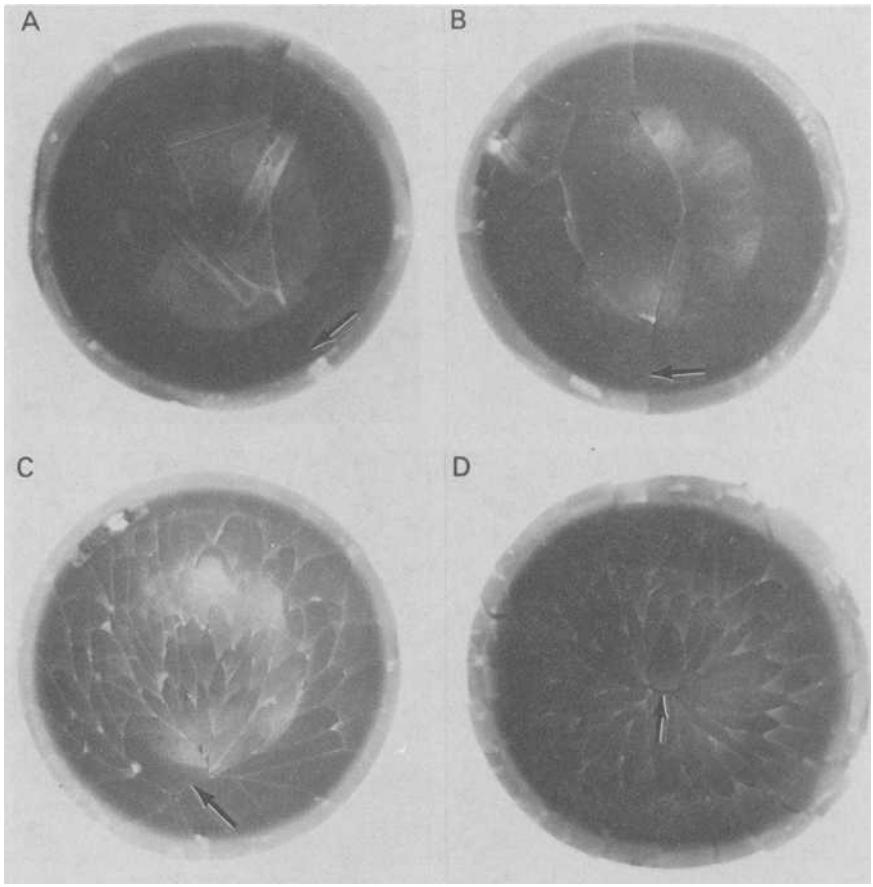

FIG. 13—*Crack branching in MgF_2 domes. These hot-pressed MgF_2 domes (sectors of spherical shells ~4 mm thick) failed in thermal shock testing, that is, by biaxial failure (arrows mark approximate fracture origins). Analysis of specimen fractures shows that these domes are presented in the order of increasing failure stress, which corresponds with increasing crack branching, consistent with the behavior of the flexure-tested specimens in Fig. 12.*

usually low angle, it usually does not follow a straight line but curves some to increase its overall angle from that of the original branch position. More commonly, with branching at about or greater than the average angle of initial branching, the crack may often curve to reduce the angle of this branch, at least in the cases of branching near the edge of the specimen where the decreasing stress gradients may be a factor (Figs. 12 and 13).

It is interesting to note that metals failing in a brittle fashion appear to show the same crack-branching behavior as ceramics. For example, measurements from Weimer's studies of explosively loaded FS-01 steel [*11,12*] give 23 ± 13 deg for the included angle between branches (10 measurements) and 21 ± 11

TABLE 1—*Crack-branching angles.*[a]

	Uniaxial Loading				Biaxial Loading			
	Flexure		Tension		Flexure		Thermal	
Material	BO	B+C	BO	B+C	BO	B+C	BO	B+C
Pyroceram (9606)	19 ± 7 (8)	...	...	...	78 ± 17 (13)	...	43 ± 22 (29)	31 ± 22 (50)
Al_2O_3	24 ± 8 (13)	19 ± 17 (2)	...	...	...	...	...	...
	...	18 ± 8 (6)	15 ± 5 (12)	10 (2)	77 ± 3 (3)	45 (2)	32 ± 29 (29)	41 ± 25 (35)
Si_3N_4 (HP-NC 132)	...	...	...	...	...	...	42 ± 24 (6)	33 ± 11 (6)
SiC (HP)	...	...	...	...	...	...	48 ± 24 (6)	30 (1)
Pyrex	...	...	...	...	...	...	21 ± 11 (3)	75 (2)
Soda lime glass	...	22 ± 6 (6)	...	...	61 ± 18 (3)	...	...	...
MgF_2	...	18 ± 13 (4)	...	...	...	47 ± 12 (7)	27 ± 6 (10)	17 ± 4 (6)
MgO	...	16 ± 5 (5)	...	...	...	...	...	...
Glassy carbon	25 (2)	18 ± 2 (2)	...	...	...	...	...	...
B_4C	25 ± 5 (5)	...	...	...	...	...	...	...

[a]In degrees. BO = branch only; that is, the crack forks into two branches without the main crack continuing (on a macroscopic scale). B+C = branching of the original plus continuation of the original crack. Number of values averaged are shown in parentheses.

deg for the average of 5 measurements for the included angles between branches and the continuation of the original crack. Thus the average angles and variations, including the difference in angles whether or not the main crack continued, were the same as for ceramics.

Specific Aspects of Mist and Hackle

Mist and hackle, like crack branching, tend to repeat if the specimen is sufficiently large relative to the failure stress; thus $R_{mn} = nR_{m1}$ and $R_{hn} = nR_{h1}$ in analogy with Eq 4. In fact, this repetition of mist and hackle seems to be more uniform than that of crack branching, though this has not been extensively studied. The present author and his colleagues, and apparently a

number of other investigators, have generally observed some aspects of this repeating mist and hackle, but probably the first specific focus on it and particularly good examples of it were by Abdel-Latif et al [*13*]. In this repetition, mist and hackle are basically mutually exclusive so far as the specific fracture areas on which they occur; that is, one does not see mist on top of hackle or *vice versa*. Repetition of mist may occur as an expansion of mist extending between hackle ridges (Fig. 14) or nucleation subsequent to the termination or "fading out" of hackle. Repetition of mist and hackle means they continue on crack-branching surfaces.

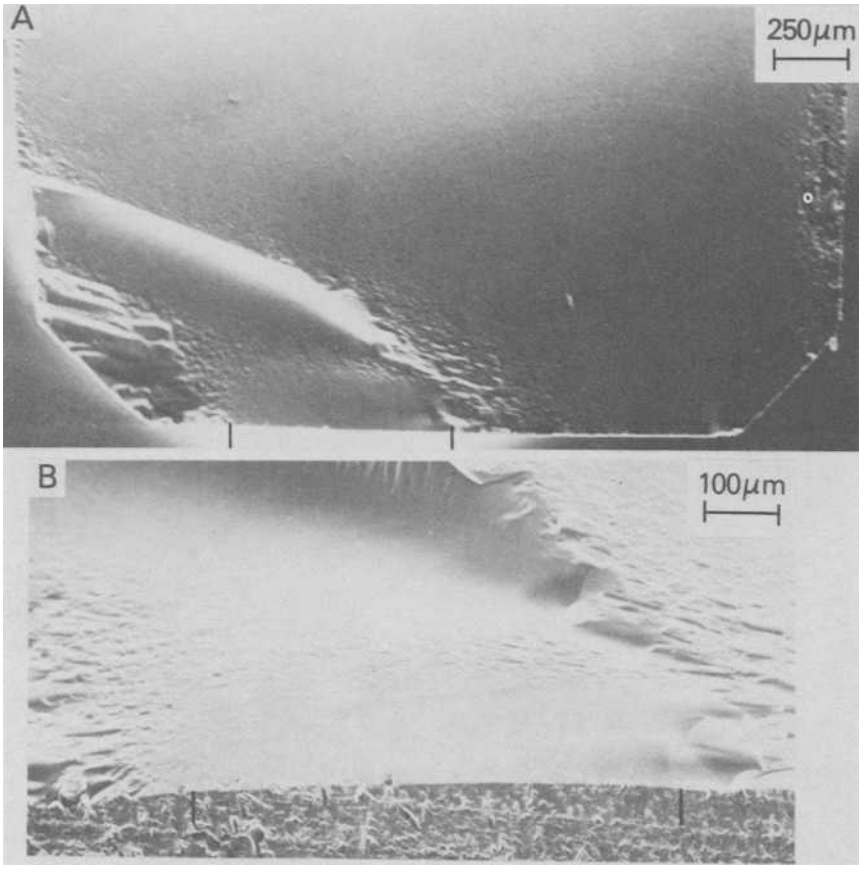

FIG. 14—*Intermixing and repeated formation of mist and hackle. This glassy carbon specimen failed at 70 MPa (10.2 × 10³ psi) from a machining flaw from the bevelled right-hand edge of the specimen in* (a). *Note the absence of the mist and hackle towards the neutral axis because of the low failure stress relative to the specimen size. Note also typical onset of mist, then hackle (vertical marks), as the crack moved to the left, continuation of mist (center area of* b), *the one major segment of hackle, and the repeated formation of added mist and hackle at the third vertical mark to the left.*

Johnson and Holloway [*14*] observed two types of mist and hackle on glass surfaces. Both involved similar branching, the difference being whether the main crack continued or not; this was also observed for the branching noted in the previous section. Beauchamp's [*15*] micrographs of glass fractures reveal detailed fracture features of mist and hackle such as lateral spreading of the secondary crack (Fig. 15).

Microstructure can significantly vary the character of mist and hackle.

FIG. 15—*Mist and hackle on glass fracture. Crack propagation left to right. Note fracture stress showing local crack fanning out in association with hackle formation (at arrows) and diminishing height of hackle (near vertical marks) associated with distinct turning of fracture steps across the hackle ridges. (Photo courtesy E. Beauchamp, Sandia National Laboratories.)*

Where mist and hackle encompass many grains, such as on fractures of fine-grained polycrystalline materials (Figs. 3, 7*a*, 16, 17, and 66), they generally have the same smooth wedge or arrow shaped ridge character as on glasses (see also Fig. 9 in Ref *2*). However, as grain size or other microstructural factors affecting crack propagation (for example, porosity or second phases) increase in size, mist and hackle begin to change in character. Thus mist and hackle often become more flakelike as grain size increases so that they encompass a few grains (Fig. 8). As grain size becomes substantially larger than the scale of the mist and hackle, they generally become less distinct. Hackle can often still be discerned, at least at lower magnification, especially with transgranular fracture (Fig. 5) where mist appears to be replaced by fracture steps on fractured grains.

Variations of Mirror Character

The hackle and especially the mist features that define the mirror vary and hence change the mirror size or shape. Of broad concern are generic effects which alter the normal application of Eqs 1 and 3. The most general of these effects is the early formation of mist in most if not all polycrystals (for example, at R_m/R_f ratios at 50 to 60% of those in glasses). As will be discussed later, this has been attributed to nucleation of mist on the scale of the grains. The same concept and limited observation suggest that hackle may begin sooner (at lower R_h/R_f ratios than in glasses) as the grain diameter approaches the width of hackle ridges.

A number of investigators have noted asymmetrical mirrors not associated with stress gradients, but they have generally neglected them. However, Freiman et al [*16*], studying mixed-mode failure in glasses, observed mirror asymmetries about an axis through the origin and perpendicular to the tensile surface and hence not caused by stress gradients. They noted that the larger portion of the mirror on one side of the (indent-induced) flaws typically had about the same mirror-to-flaw-size ratio as found for symmetrical mirrors. The present author has observed many similar extreme mirror asymmetries and variations of mirror character. Irregular flaws, and especially machining flaws not normal to the stress axes (Fig. 17), are common sources of this. Failure from inclusions and especially pores can also be important sources of significant mirror distortion or asymmetry.

Variations of flaw character, such as flaws deviating from a single plane, may lead to different ends of the flaw acting somewhat or totally independently. Such situations would appear to be particularly common among flaws having a substantial angle to the tensile axis. Limited variations in the angles at or near the flaw ends substantially change the effects of mixed-mode failure owing to the nonlinear dependence of the stress intensity on the flaw-stress angle and hence the stress response of the associated portions of the flaw. Failure may initiate from both ends of a flaw, or one end may dominate.

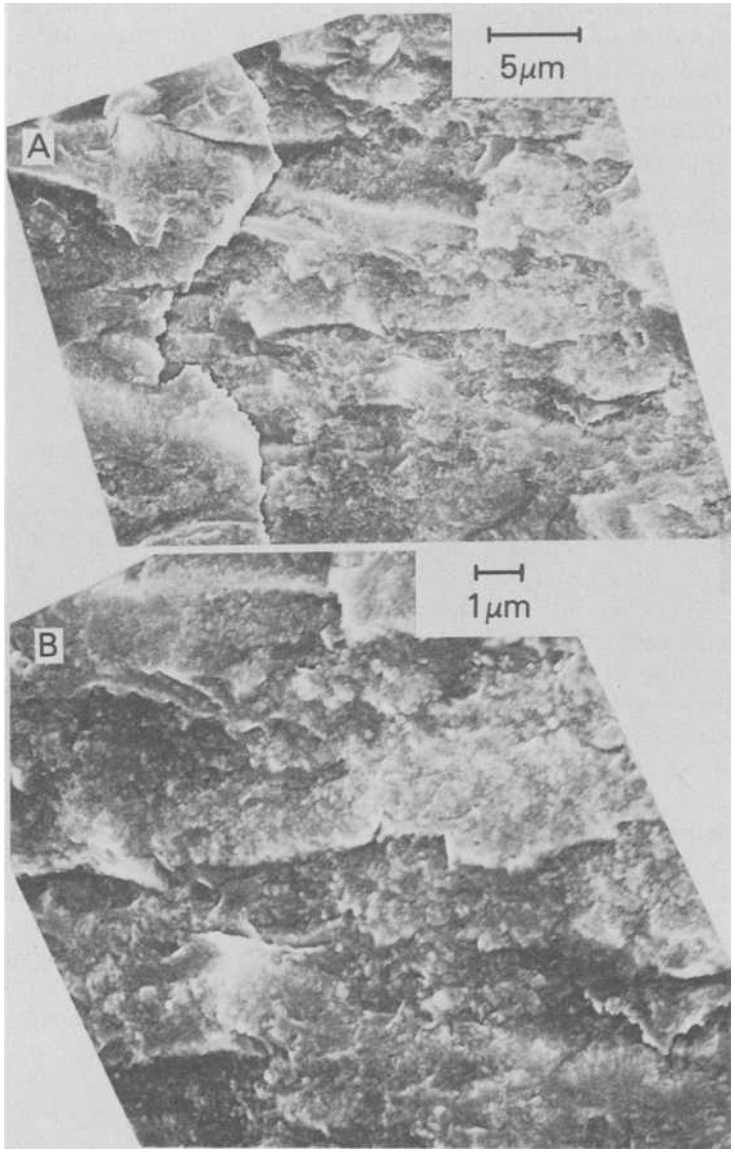

FIG. 16—*Examples of mist and hackle in fine-grain polycrystalline materials.* (a) *and* (b) *are respectively intermediate and higher magnifications of part of mist-hackle-crack branching fractures of a fine-grain CVD SiC specimen failing at 517 MPa (75 × 10³ psi). Crack was propagated right to left. Hackle shape is somewhat similar to that on glass fracture (Fig. 15), but somewhat more irregular in part due to the grain structure (~0.2 μm diameter) affecting fracture detail in* (b). *Note also the irregular path of macroscopic crack branching in* (a).

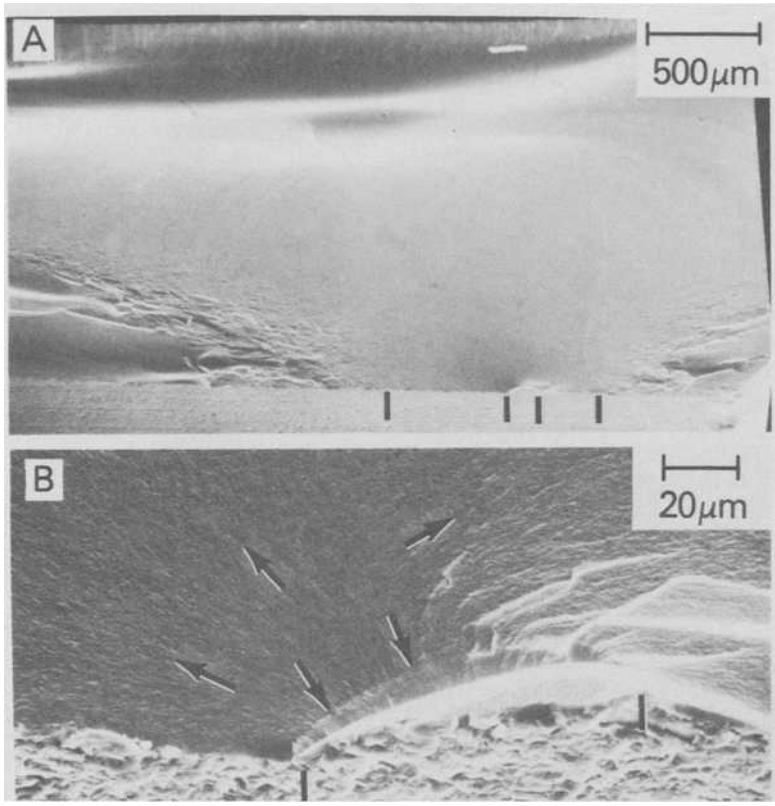

FIG. 17—*Distortion of fracture mirrors with an out-of-plane flaw.* (a) *Lower magnification of a crystallized (keatite) glass specimen failing at 117 MPa (17 × 10^3 psi) from a machining flaw (inner vertical marks) not perpendicular to the stress, and an asymmetric mirror (outer vertical marks).* (b) *Higher magnification of flaw showing the second boundary (lower two arrows) attributed to slow crack growth; this fracture started over the left half of the flaw and propagated as indicated by the upper three arrows. Such failure initiation from only part of a flaw characteristically gives asymmetric mirrors.*

The present author studied in more detail the mixed-mode data of Freiman et al [*16*]. While there is a fair amount of scatter, which apparently precluded those authors from observing that there was in fact some variation in the apparent mirror-to-flaw-size ratio as the angle of the flaw to the tensile axis decreased, plotting of their data (Fig. 18) does indeed show a systematic variation. Such a variation would be consistent with the foregoing suggestion that different parts of a nonplanar flaw or a flaw not normal to the stress can act essentially independently, leading to the flaw acting as two flaws, with each generating its own portion of a mirror. Such effects would clearly be expected to increase as the average angle of the flaw relative to the tensile axis decreases. Similarly, failure from a pore, especially a surface pore, with cracks

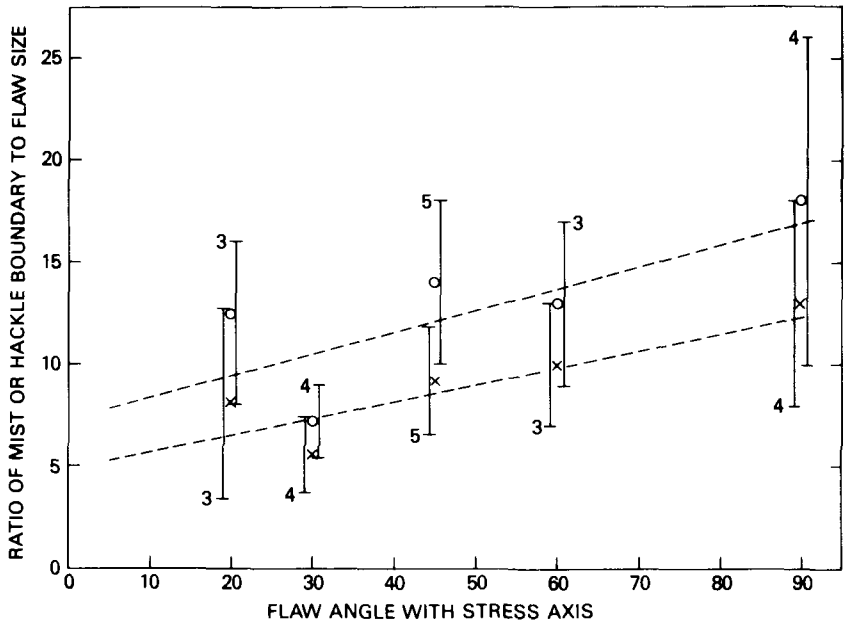

FIG. 18—*Changing mirror-to-flaw-size ratios for mixed-mode failure. Plotting data of Freiman et al* [16] *for mixed-mode failure in soda lime glass shows the ratio of the distance from the fracture origin to the mist or hackle boundary to that of the flaw size for the largest mirror dimensions as a function of the flaw angle relative to the stress axis. Circles are for hackle and X's for mist boundaries. Despite substantial scatter there is clearly a systematic decrease in these ratios as the angle of the flaw relative to the stress axis decreases.*

at different positions (for example, opposite intersections with the surface) would be expected to frequently give asymmetric mirrors, since the flaws would often be of different size, orientation, etc. (leading to different σ_p/σ_a ratios for the portions of the pore that they are associated with).

Rice (the present author) [*17*] observed that with failure of glasses from pores, the ratio of the mirror size to the pore (~ flaw) size is often much less than the normal values found for glasses failing from machining flaws (about 14 to 1). He has shown that this can be explained by recognizing that the pores are often much blunter flaws than normal sharp cracks. Several investigators, especially Baratta [*18*], have shown that a pore (radius R) plus a radial crack (L) progressively approaches the behavior of a sharp crack of size $R + L$ as L/R increases. This transition in flaw bluntness can be expressed as the changing ratio of the failure stresses from a pore plus crack (σ_p) and from a flaw of the same net size (σ_a). Recognizing that a pore plus a partial crack does not necessarily act as a sharp flaw of the same net size, while at the same time realizing that the mirror boundary (mist etc.) formation is caused by a sharp crack, Rice [*19*] showed that in Eq 3 the mirror-to-flaw-size ratio should be

modified by the "bluntness of the flaw". Thus if $\sigma_a = A/\sqrt{R_f}$, then $\sigma_p = \sigma_p/\sigma_a$ $A/\sqrt{R_f}$; and since $\sigma_p = B_i/\sqrt{R_i}$, then

$$R_i/R_f = (B_i/A)^2 (\sigma_a/\sigma_p)^2 \tag{5}$$

The mirror-to-flaw-size ratio is reduced by the "bluntness" of the flaw, that is, by $(\sigma_a/\sigma_p)^2$. Alternatively, multiplying the mirror-to-flaw-size ratio for a blunter flaw by $(\sigma_p/\sigma_a)^2$ should give the mirror-to-flaw-size ratio for failure from a normal sharp flaw.

Rice showed that Eq 5 brought the mirror-to-flaw-size ratios for failure from pores plus a crack into general agreement with normal ratios (Table 2). Exact agreement was not obtained, since the generally uncertain extent of the flaws meant that only an upper limit to σ_p/σ_a could be determined. The greatest deviations occurred when the original mirror-to-pore-size ratio was closest to the normal mirror-to-flaw-size ratio, which would tend to indicate that these are the cases where the σ_p/σ_a bounds are particularly high; that is, the associated cracks are probably larger and the σ_p/σ_a values probably are not too much greater than one.

Besides the aforementioned generic variations of mirror patterns and the normal statistical variations of mist onset noted earlier, mist (and sometimes hackle and possibly crack branching) can be initiated at shorter or longer than normal distances from the origin or distorted by defects or variations in microstructure. Other flaws can have several effects. Often flaws over which the fracture passes are propagated by the stress field ahead of the crack, generating their own mirror. These often are small enough or far enough from the main mirror to cause little distortion (Fig. 19), but occasionally they may be larger and overlap with the main mirror. At the other extreme are occasional failures seen from multiple flaws (especially in some single crystals; see Fig. 20), leading to either separate mirrors or larger mirrors than for one of the flaws alone. Occasionally overlapping mirrors are seen with failure from an irregular defect (Fig. 21), with different parts apparently acting, at least in

TABLE 2—*Examples of mirror sizes from pore fracture origins* [17].

R_m/R_f	σ_p/σ_a	$(\sigma_p/\sigma_a)^2 (R_m/R_f)$
9	<1.5	<20
7.3	<1.2	11
8.0	1.4	17
2.7	<2.1	<12
3.1	<2.6	<21
6	<2.8	<47
12	<2.1	<53
14	<1.5	<32

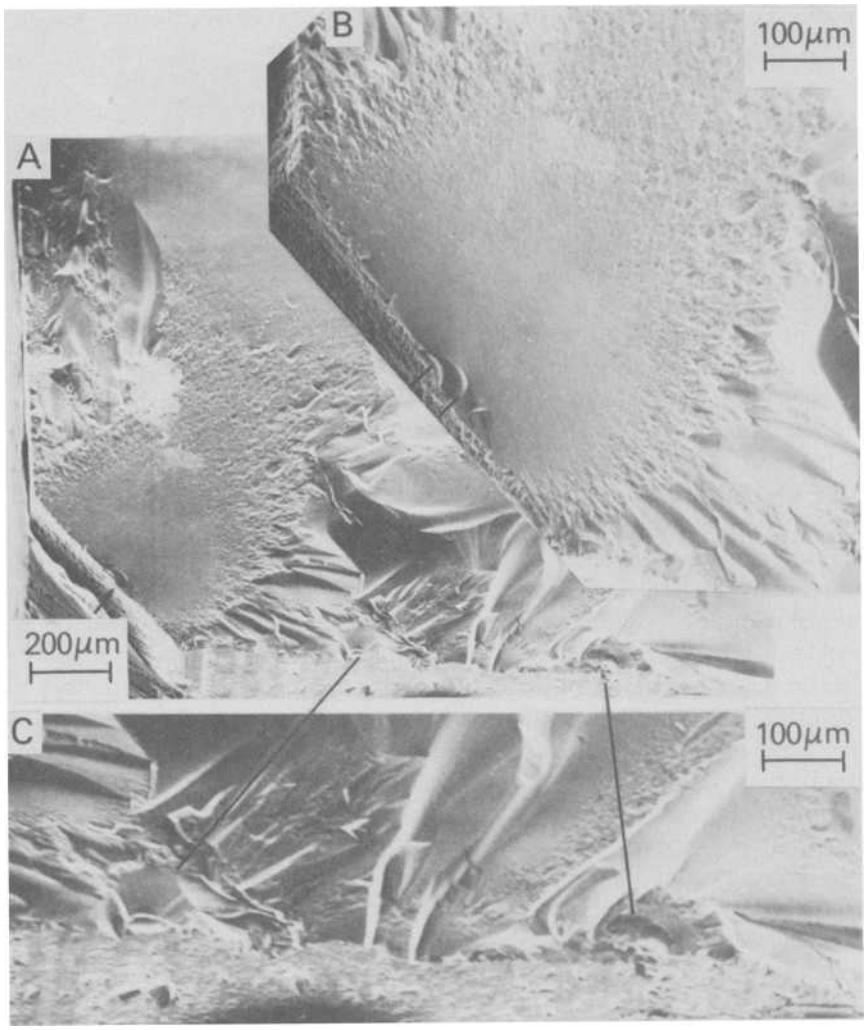

FIG. 19—*Secondary mirrors in glassy carbon.* (a) *and* (b) *Low and intermediate SEM photos of origin (arrow in* a, *lines in* b*) and mirror area.* (c) *Higher magnification of areas of* (a) (marked) *showing small mirrors around small secondary flaws activated during fracture at 102 MPa (14.8* $\times$ 10^3 *psi).*

part, as independent flaws. Between distortions due to intersecting mirror patterns and distortions due to partly independent flaws, are distortions due to the crack encountering another flaw or defect within the mirror region. Thus the intersection of the crack with another flaw within the mirror region typically leads to early onset of mist and hackle (Fig. 22*a*). This may be related to the phenomena of flaws encountered beyond the mirror. Deflection

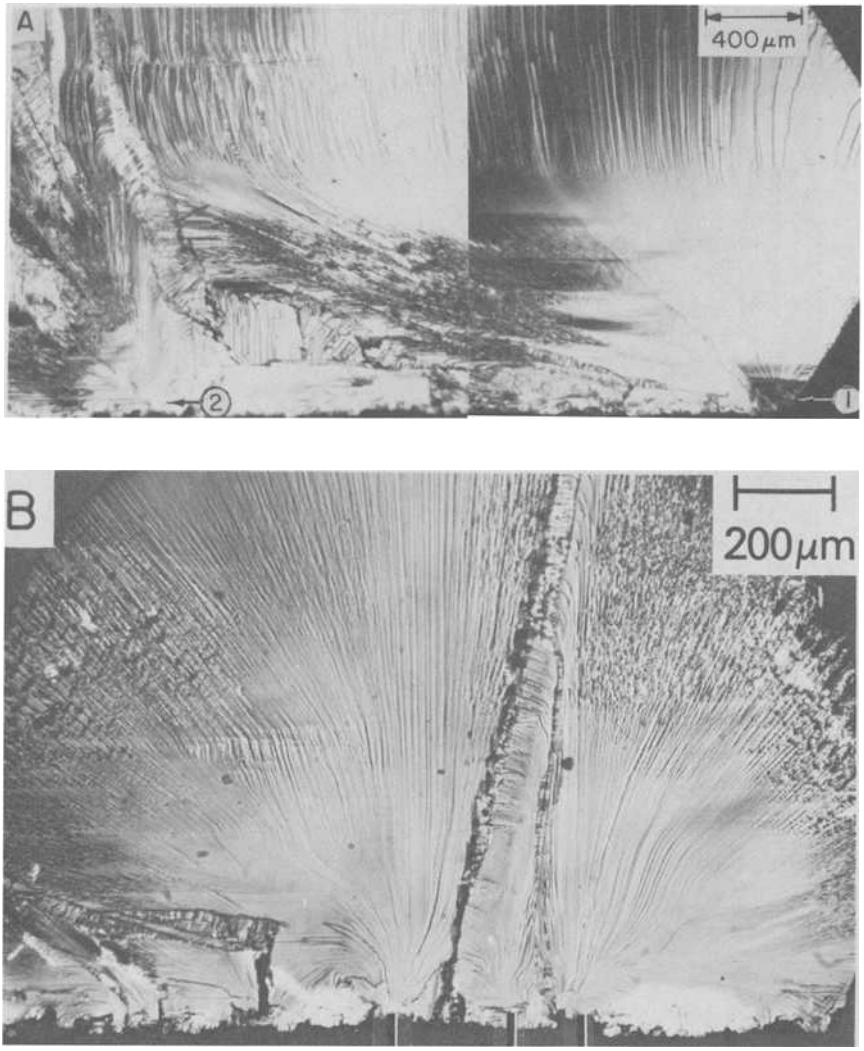

FIG. 20—*Overlapping mirrors in MgO crystals. Machined specimens with {100} tensile surface and ⟨100⟩ tensile axis failing from* (a) *a corner* (1) *with a secondary origin* (2) *and associated mirror to the left, and* (b) *origins (vertical marks) whose mirrors highly overlap, giving a single distorted mirror. Note the horizontal bands of mist and hackle due to their density being increased by slip bands (horizontal lines) in both cases.*

of a crack around a pore has also been observed to initiate mist and ultimately also perturb the hackle formation (Fig. 22*b*).

An extremely common if not universal occurrence for failure originating independently from two different sides of a pore (besides generating different size mirror portions on each side of the pore) is the forming of fracture tails

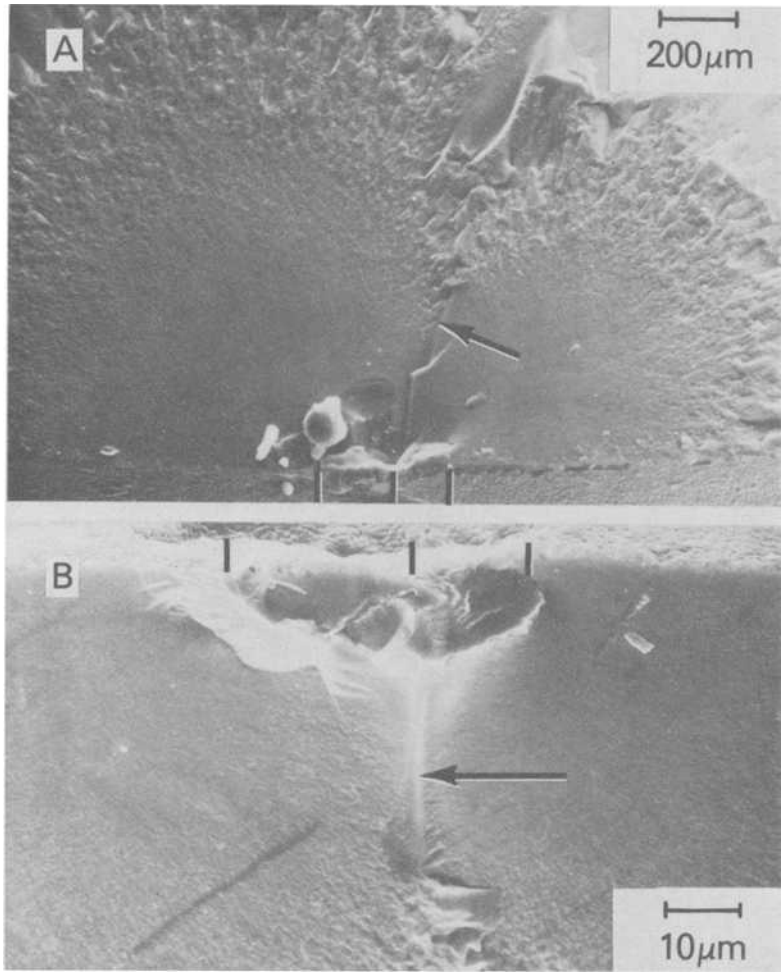

FIG. 21—*Overlapping mirrors from failure from opposite ends of an irregular defect.* (a) *Lower magnification SEM photo showing two overlapping mirrors.* (b) *Higher magnification SEM photo of the matching half. Note the Z-shape to the defect (an agglomerate or precipitate) in this extremely fine grain (CNTD) SiC body with a slightly oxidized surface. Failure stress was 717 MPa (104 × 10^3 psi). Cracks formed separately from either end of the defect leading to the distinct fracture surface step associated with the major change in orientation of the fracture surface through the defect from the resultant overlapping of the two cracks. Note that the mirror-to-flaw-size ratio of ~5:1 for each mirror side and the associated portion of the flaw is consistent with general polycrystalline values.*

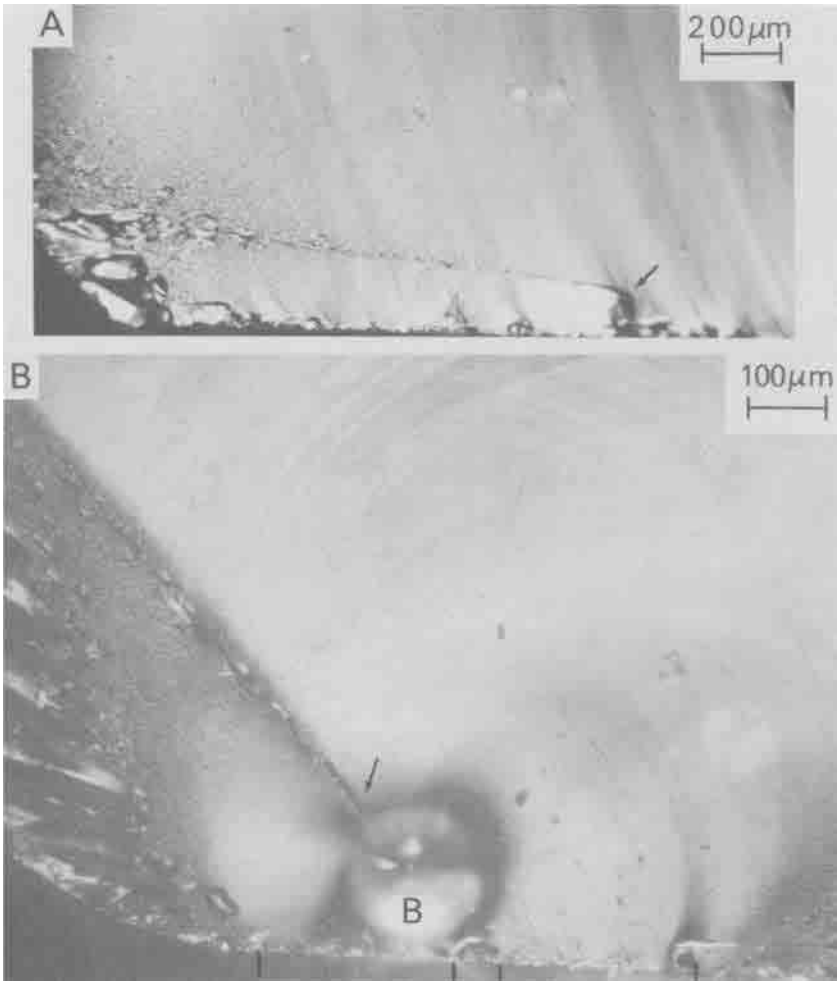

FIG. 22—*Early onset of mist and hackle associated with defects.* (a) *Fracture of a soda lime glass specimen at 65 MPa (9.4 × 10³ psi) shows the onset of mist with somewhat earlier onset of hackle from a crack (arrow) to the left of fracture origin (not shown; past right edge of the photo).* (b) *Similar early onset of mist and hackle due to the fracture running around a bubble* (b) *(revealed by additional side lighting besides the reflected light used for the optical microscopy). Specimen failed at 70 MPa (10.2 × 10³ psi) from the fracture origin marked by two center vertical lines on the tensile surface.*

where the two cracks meet and overlap. (This is identical to the formation of fracture tails when a crack encounters a pore [*20*].) Failure occurring from only one side of a pore commonly leads to asymmetric mirrors; these can be quite extreme (Fig. 23).

Microstructures of polycrystalline materials offer other opportunities for

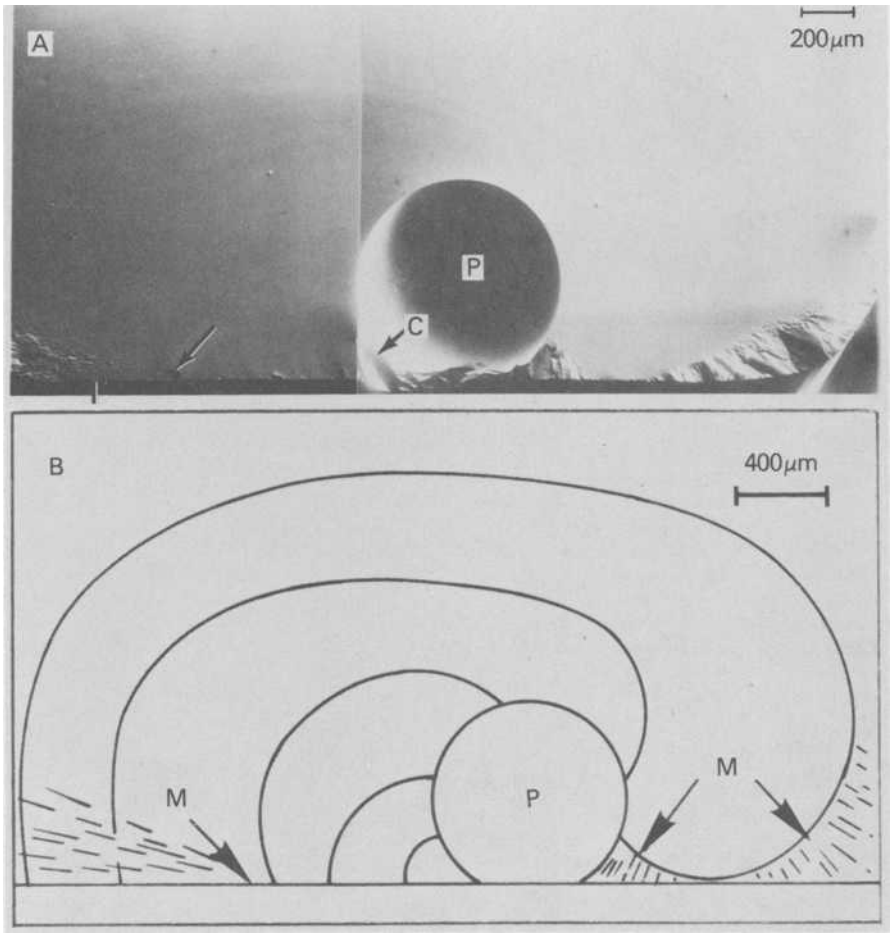

FIG. 23—*Extremely distorted mirror from failure from a pore in a silicate glass.* (a) *lower magnification SEM photograph of the fracture surface showing failure initiating from a chip* (c) *and associated crack on the left-hand side of the pore* (p) *and the mist* (m) *and hackle features to the right and left.* (b) *Schematic of the failure showing how the crack propagated around the pore, actually generating mist and hackle features on the immediate right-hand intersection of the pore and the specimen tensile surface. Fracture stress was 42 MPa (6 × 10^3 psi).*

initiating mirror deviations and variations. Polycrystalline materials with secondary (growth cone or colony) structures, such as often occur in materials made by chemical vapor deposition (CVD), can have mist or hackle initiated where the crack passes over their boundaries (Fig. 24). Such cones or colonies are often elongated and have preferred crystal orientations within them which can affect the orientation as well as the overall occurrence of mist and hackle feature. Also, portions of single-crystal fracture patterns (discussed in the

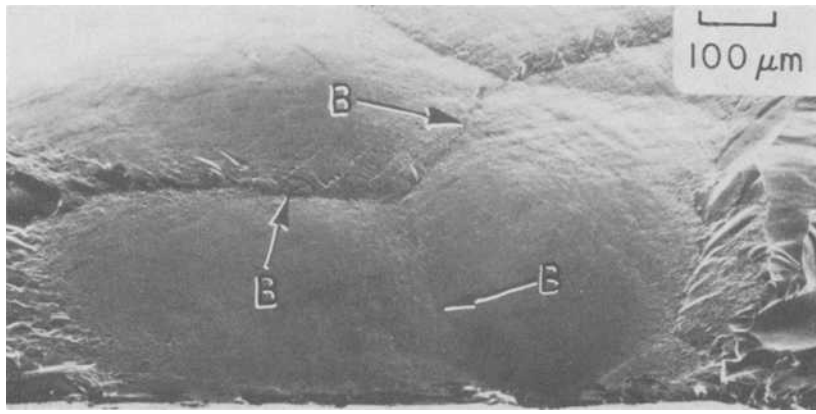

FIG. 24—*Distortion of mirror features due to microstructure. A portion of the flexure fracture surface of a CVD SiC body failing at 493 MPa (71.6 × 10^3 psi) is shown. This specimen, with substantial growth cone structure (leading to the typical botryoidal deposition surface), was tested with the tensile axis parallel with the deposition direction so that the fracture formed perpendicular to the axis of the growth cones having varying shapes. The grain-like structure observed in this photo is the cross-sectional cone structure. Note the pronounced anisotropy of the mirror shape due to the difference in shape of these cones and the early onset of mist and small hackle associated with these boundaries* (B). *Fracture of specimens with growth cones parallel with the tensile surface often gives substantial mirror distortion; fracture with the growth comes perpendicular to the tensile surface can also give some distortion but much of this is masked by stress gradient effects in flexure (× 100).*

next section) can be observed on polycrystalline fractures when at least one grain whose size is a measurable fraction of the mirror size fractures transgranularly with the proper orientation near the mist boundary (Fig. 25).

Single Crystals

Single-crystal fractures generally exhibit mirror, mist, hackle, and crack-branching features usually significantly different from those observed on glass or polycrystalline fractures. As will be discussed later, these differences appear to be related to ease of fracture on one crystal plane relative to another. Here we will focus on the description and occurrence of these features.

Consider the overall failure plane itself and possible associated crack branching. Single crystals often have significant preferences for fracture on certain planes, with these planes varying from crystal to crystal. Thus there are highly preferred {100} cleavage planes in most alkali halide structure crystals and {111} cleavage planes in most calcium fluoride (CaF_2) structure crystals. Even where definitive cleavage is not observed, one often finds substantial preference for fracture near certain planes; however, fracture of some crystals appears to be determined more by avoiding fracture on or near a

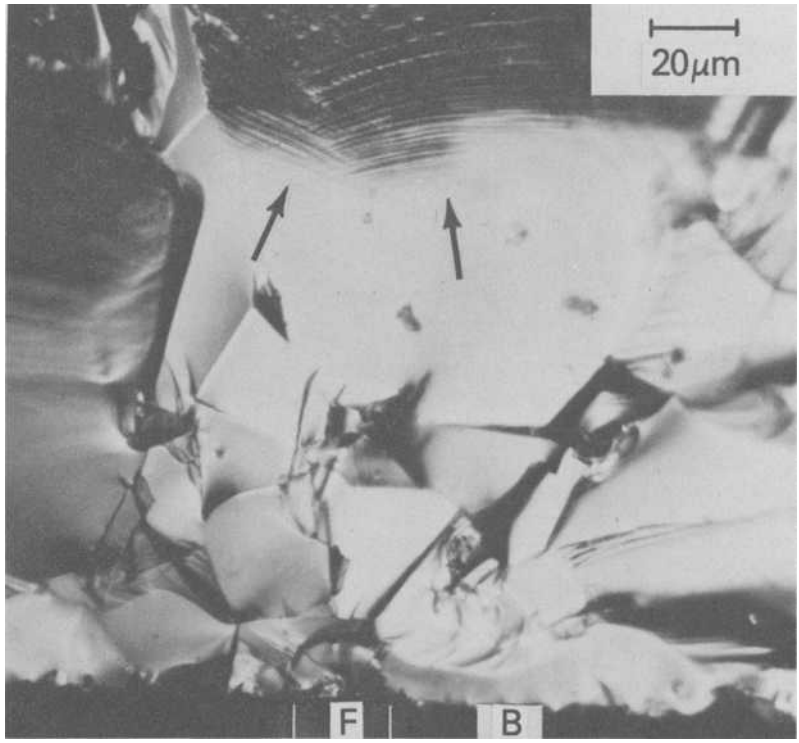

FIG. 25—*Portions of single-crystal fracture pattern seen on a large grain on a polycrystalline* $MgAl_2O_4$ *fracture. Specimen failed at 262 MPa (38* $\times$ 10^3 *psi) from a typical machining flaw* (F) *in one of its smaller grains adjacent to a grain boundary surface* (B) *at the tensile surface (bottom), but had a much larger grain sufficiently close to the fracture origin that part of the mist and hackle defining the fracture mirror showed up as an arc segment (arrows) as discussed in the text. See Figs. 28 to 31 for comparison.*

plane or set planes due apparently to high fracture energy (for example, avoidance of basal plane fracture in sapphire). Such preference for, or avoidance of, some fracture planes, which is apparently associated respectively with minima and maxima in fracture energy, in turn significantly affects crack branching. A crack propagating on a particular plane in a single crystal may or may not have another crystal plane of suitable orientation and ease of fracture to branch onto. In general, branching is less common in single crystals because of the strong preference for cracks to propagate mainly on certain planes which are often less favorably oriented for branching. When branching occurs, the orientation of allowed or preferred fracture planes, relative to the plane of crack propagation, is a major, if not the only, determinant of branching angles (Figs. 26 and 27). Equation 1 (and hence Eq 3) appears to be applicable to single crystals (but with different constants as discussed later). Also, while some branches may be partially or totally missing (Fig. 27), limited

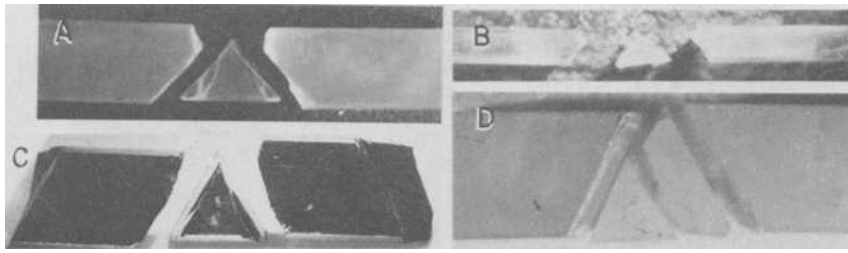

FIG. 26—*Examples of crack branching in flexural testing of single crystals.* (a) *and* (b) *are stoichiometric* $MgAl_2O_4$ *crystals tested at 1400°C but representative of behavior at room temperature.* (a) *Top view of a specimen with a* {100} *tensile surface and a* ⟨110⟩ *tensile axis failing at 222 MPa* (32.2×10^3 *psi) showing horizontal branching of the crack onto* {100} *surfaces.* (b) *Side view of a specimen with a* {110} *tensile surface and a* ⟨111⟩ *tensile axis failing at 427 MPa* (61.9×10^3 *psi) showing branching onto a* ~{100} *plane. Such vertical crack branching, although not the dominant mode of branching of single crystals, appears to be more commonly based upon the availability of crystallographically suitable fracture planes.* (c) *Fractures of a silicon crystal with a* {111} *tensile surface and a* ⟨110⟩ *tensile axis failing at 169 MPa* (24.5×10^3 *psi). Note the wedge-shaped piece due to crack branching along* ~{110} *fracture surfaces. Note also essentially the same fracture surfaces at either end of the bar due to other fracture tests.* (d) *SiC crystal fractured at room temperature at 590 MPa* (85.5×10^3 *psi). The original crystal was provided courtesy Dr. Schaeffer, Carborandum Company, who notes that the tensile surface was probably an* {0001} *surface such that the tensile axis was probably parallel to a* $\{10\bar{1}0\}$ *prism face. The ~60 deg crack-branching planes thus probably represent fracture on another* $\{10\bar{1}0\}$ *surface.*

observations indicate that Eq 4 is generally approximately applicable. Finally, as noted earlier, orientation of preferred fracture planes can lead to vertical crack branching of rectangular crystal bars tested in flexure (Fig. 26).

Next consider single-crystal mirror patterns, where there are significant changes or differences from glasses and polycrystalline materials owing to the significant crystallographic character of many features bounding fracture mirrors. Observations of a number of single-crystal fractures shown them to be made up of either arc segments (Figs. 28 to 34) or of long thin "whisker" or "lance-like" features (Figs. 35 to 41 and Table 3). While some mirrors may have specific crystallographic shape (Fig. 35), most have less obvious crystallographic dependences. Various aesthetic patterns that the author has termed *cathedral* (Figs. 28 and 29; see also Ref *20*) or gull-wing (Fig. 30) mirrors are outlined primarily or exclusively by arc segments. These arc segments stop and start, increasing in amplitude as the distance from the origin increases and often culminating in macrocrack branching or change of the fracture plane (Figs. 28, 29, 33, and 34). Excellent examples of this in quartz have been given by Ball and Payne [*21*]. Arc segments appear to occur mainly, or only, on secondary fracture or cleavage planes, since they are associated with crack branching. They thus tend to parallel the progression from mist through hackle to crack branching on glass and polycrystalline fractures.

Whisker-lance features, on the other hand, generally do not show this progression. They generally only broaden, and possibly thicken some, with dis-

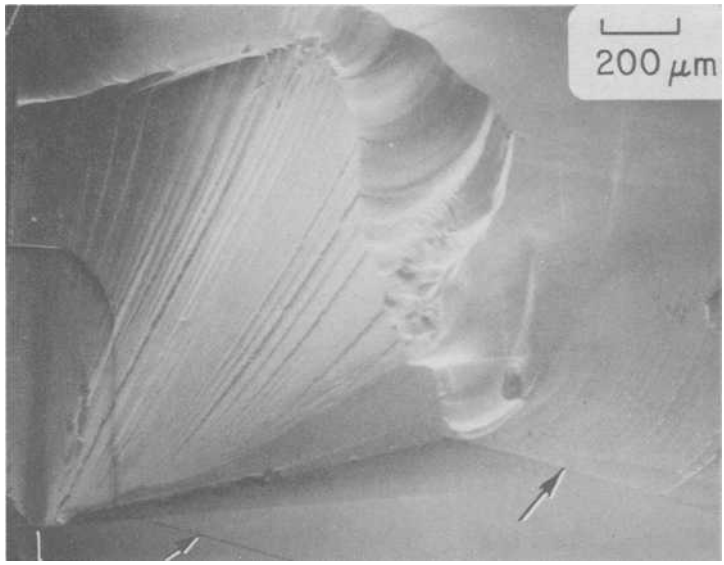

FIG. 27—*Crack branching in a $MgAl_2O_4$ crystal. This stoichiometric specimen fractured in flexure at room temperature at 356 MPa (51.7 × 10^3 psi) with a {100} tensile surface and ~⟨100⟩ tensile axis (some probable variation from this axis may be the cause of the cathedral-like mirror to the left above the vertical line). Note the macroscopic crack branching at 45 deg (onto {100} planes) and the whisker-lance mist-hackle on the {100} plane failure. Note also the "missing" crack branch between the two, that is, the branch that would have to be present to maintain branching at multiples of the first branch distance.*

tance from their onset; hence they do not generally form separate mist and hackle. Such whisker-lance mist-hackle has not been observed to be followed by crack branching, but is observed on crack branches beyond arc-outlined mirrors (Fig. 27). These observations are consistent with such whisker-lance mist-hackle occurring mainly, or exclusively, on primary cleavage or fracture planes from which branching is much more limited, but on to which branching is favored. Some complication and uncertainty in separating the two types of mist and hackle features between primary and secondary fracture planes may be caused by deviations of the fracture surface from a single plane (Fig. 33).

Whisker-lance mist-hackle on fractures of crystals of some materials occurs continuously around the origin whenever the criterion of Eq 1 is met; for example, on {111} fractures of CaF_2 (Fig. 36) and zirconium oxide (ZrO_2) (Fig. 33) and apparently on {100} fractures of titanium carbide (TiC).[7] However, crystals of other materials have segments, often substantial ones, in which mist-hackle is missing from symmetrically located sectors around the

[7]Note, however, that there may possibly be some systematic variation in the onset or density of such mist-hackle as a function of crystal direction around the origin.

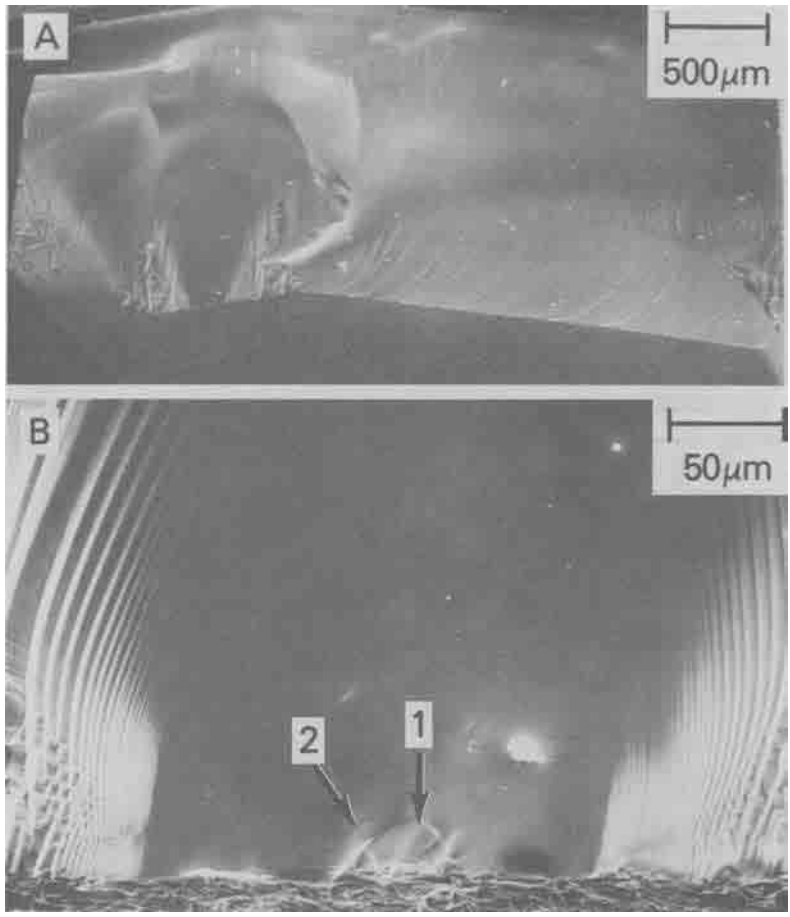

FIG. 28—*Simple cathedral fracture mirror on $MgAl_2O_4$ crystal fracture. This stoichiometric crystal fractured in flexure with a {100} tensile surface and a ⟨100⟩ tensile axis at 169 MPa (24.5 × 10^3 psi).* (a) *Low magnification photo showing the fracture mirror and the subsequent crack branching to the left and especially to the right (vertical marks).* (b) *Higher magnification photo showing details of the mirror and the associated arc mist and hackle features. Note the half-penny-shaped flaw with a second boundary to the left, which suggests possible slow crack growth due to environmental or residual stress effects (see also Fig. 64).*

origin (Figs. 37 to 39 and Table 3). Although detailed study has not been made, a number of observations, primarily of Wallner lines, suggest that there is no significant perturbation of the crack front from the regions where the whisker-lance mist-hackle has formed. Initial work on magnesium oxide (MgO) (Fig. 41) shows that whisker-lance mist-hackle does involve some overlapping cracks.

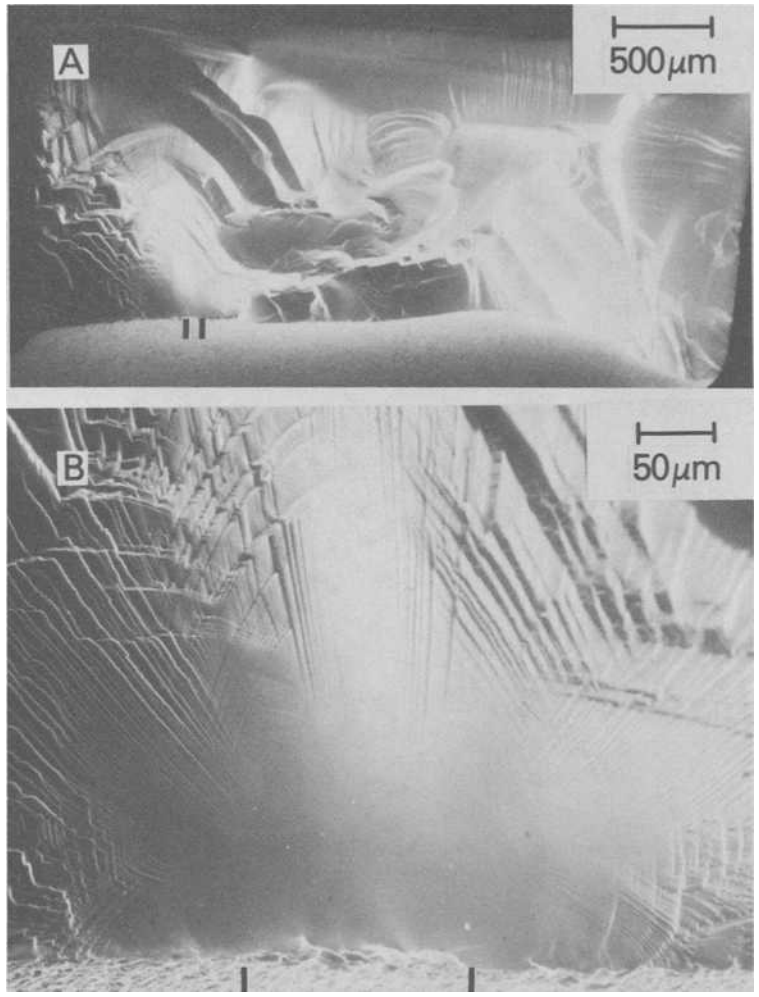

FIG. 29—*Complex cathedral mirror on $MgAl_2O_4$ crystal fracture. This stoichiometric crystal fractured in flexure at room temperature with a {110} tensile surface and a ⟨100⟩ tensile axis at 172 MPa (24.9 × 10^3 psi).* (a) *Low magnification photo showing the overall fracture and its complexity.* (b) *Higher magnification photo of the fracture mirror area and the failure-initiating flaw (between vertical lines). Note the more complex character to the arc segments as well as some intersecting segments of whisker-lance mist-hackle.*

Arc mist-hackle may also occur only over certain geometrical sectors around the origin. Commonly one set of arc segments intersects another set (Figs. 28 to 32), sometimes arc segments intersect whisker-like mist-hackle features (Fig. 29), but for a number of systems arc segments do not intersect in a given crystallographic direction (Figs. 28, 30, 34, and Table 3). In such

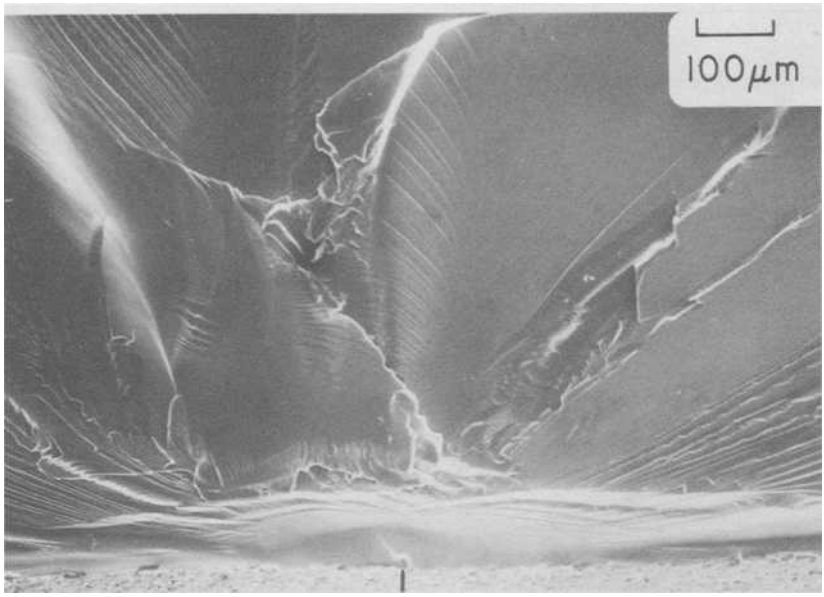

FIG. 30—*Gull wing mirror on a $MgAl_2O_4$ crystal fracture. This stoichiometric crystal fractured at room temperature in flexure with a tensile surface of {110} and a tensile axis of ⟨110⟩ at a fracture stress of 361 MPa (52.4 × 10^3 psi) giving a mirror-to-flaw-size ratio of 3 (based on vertical measurements). Note the nearly semicircular-shaped flaw (vertical line) and the associated intersecting arcs forming the mirror. Note also that these arcs do not necessarily fully touch the tensile surface; they appear to be half of two intersecting cathedral-type mirrors (×100).*

cases there is a definite continuation of mirror character beyond the boundary for initiation of mist and hackle. This mirror continuation is usually as narrow tongues and occurs in certain crystallographic directions; for example, {100} in MgO fractured on {100} planes [*2*] and ⟨100⟩ in $MgAl_2O_4$ fractured on {110} planes (Fig. 28). Note that the cathedral and gull wing mirror are thus half-plane cuts 90 deg apart through a symmetric plane figure. Because of this, the mirror size cannot be measured parallel with the tensile axis of gull wing mirrors; it has been measured normal to the tensile surface [*2*]. When mirror tongues occur, they tend to become narrower as the fracture stress increases. While there are several variations, it is important to note that mirror tongues are limited in number and that most if not all can be seen in any particular crystal system with the proper orientation. Thus there is extreme commonality of these features among many different crystals, depending upon the orientation of the fracture plane and tensile stress within the crystal structure.

There has been less extensive study of mirror-size/fracture-stress or flaw size relations in single crystals. The available data suggest that where mist-hackle occurs its onset generally obeys Eqs 1 and 3. Another important difference between single crystals and glass or polycrystalline materials is that

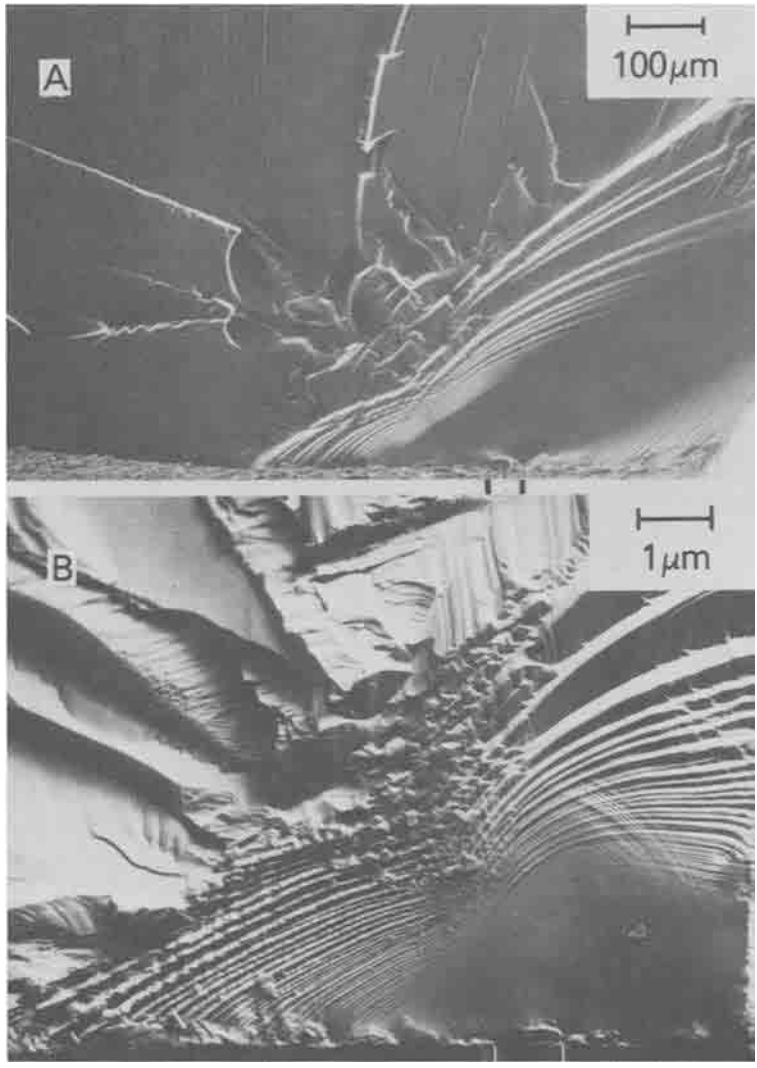

FIG. 31—*Examples of room-temperature fracture mirrors on $MgAl_2O_4$ and Al_2O_3 crystals of different orientation.* (a) *Stoichiometric $MgAl_2O_4$ crystal with a $\{111\}$ tensile surface and $\sim\langle 110\rangle$ tensile axis failing at 191 MPa (27.7×10^3 psi). Note the skewed orientation of the cathedral-type mirror and the mirror to flaw (vertical marks) size ratio of only ~5.* (b) *SEM photograph of an Al_2O_3 crystal of unknown orientation fracturing at 310 MPa (45.0×10^3 psi). Note the mirror to flaw (vertical marks) size ratio of ~5.*

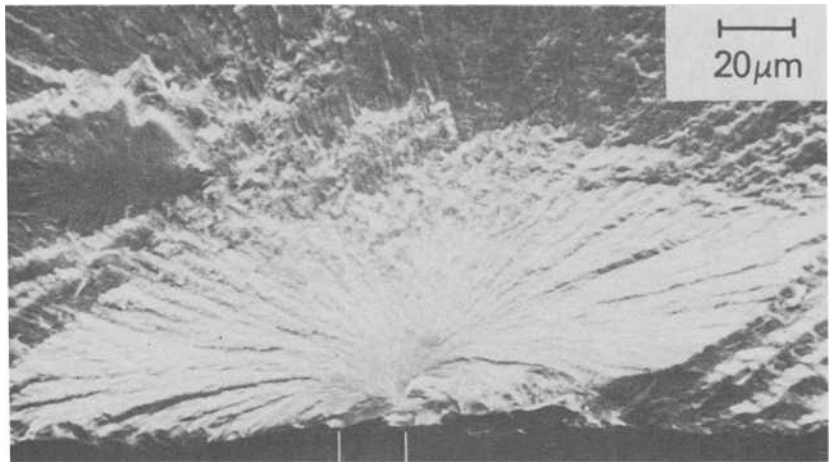

FIG. 32—*Fracture mirror in partially stabilized ZrO_2 crystal fractured at room temperature at 1034 MPa (150 × 10^3 psi). Note the characteristic machining flaw approaching a half-penny flaw (vertical marks) and the associated double-cathedral-type mirror with a nearly horizontal axis of symmetry.*

much broader variations of B_i and R_i/R_f values are seen (Table 4). There is more uncertainty in these data, because they are often more limited and because greater variation of mirror patterns and related features combined with less extensive study has resulted in little standardization of measurement criteria. For example, almost all single-crystal data have been obtained in flexure. Where sectors of the patterns are missing this often requires that measurements be made not parallel with the tensile surface, but partially along the stress gradient, for which correction has not always been made.

Nonetheless, it appears quite clear that there is a much broader range of mirror-to-flaw-size ratios in single crystals than in glasses or polycrystals. For example, the author had earlier thought that there were certain orientations and resultant fracture surfaces, primarily {100} fracture surfaces in spinel, on which no mist or hackle formed [*2*]. Yet further testing at higher temperatures where greater strengths are observed (tests courtesy of Mr. R. Ingel) has revealed that mist-hackle features are indeed formed but at a much greater than normally expected distance from the fracture origins (Figs. 37 and 38 and Table 4). Also note that crack branching in some single crystals is observed to occur without any mist or hackle formation; an example is branching after failure initiation on a {110} plane branching onto a {100} plane in MgO (see Fig. 10 and Ref *2*).

Aspects of observed slow crack growth (SCG) behavior in single crystals have important implications. Recent single crystals observations by McKinney et al [*24*] show that zig-zag slow crack growth paths similar to intergranular

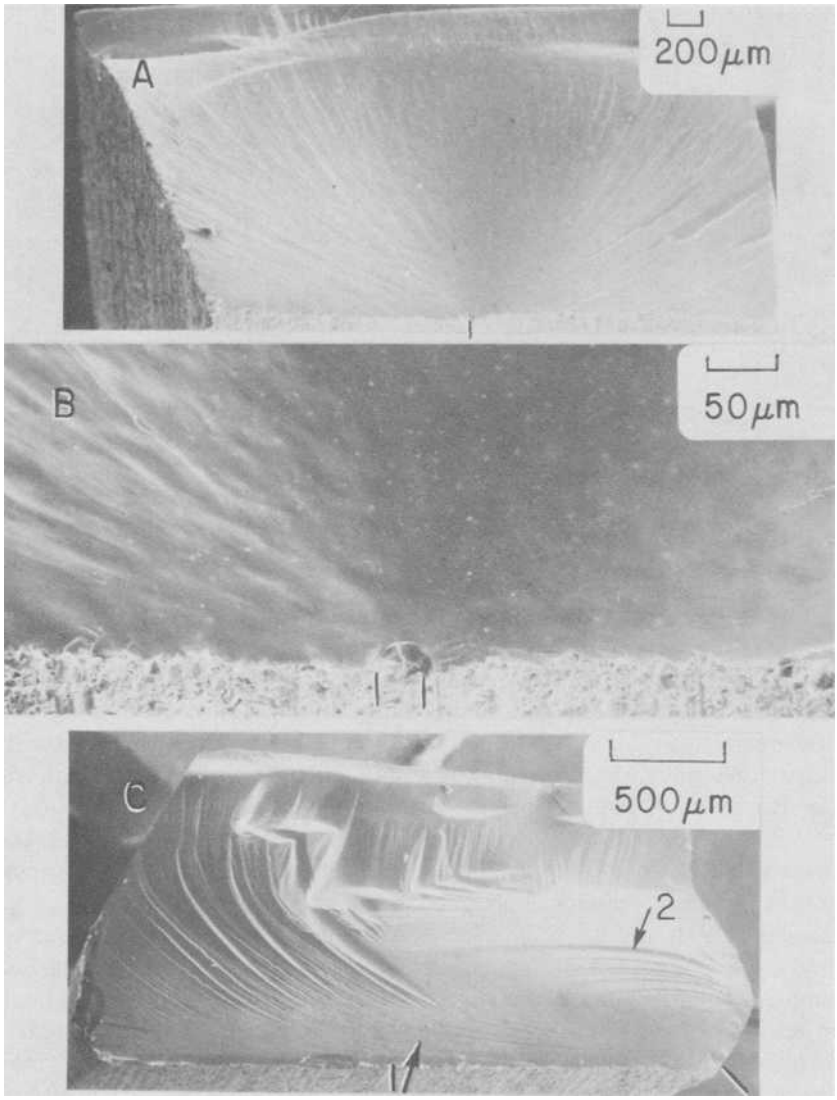

FIG. 33—*Fracture surfaces of fully stabilized ZrO_2 crystals.* (a) *and* (b) *are lower and higher magnifications of a specimen, stabilized with 4.5 wt% (9.4 mole %) CaO, failing at room temperature at 265 MPa (38.4 × 10^3 psi) from a characteristic machining flaw (vertical marks). Note the whisker-lance mist-hackle on what is believed to be a {111} fracture surface, some asymmetry of the mirror, and the variable or statistical nature of the onset of mist-hackle features.* (c) *Another crystal of the same type fractured at room temperature at 204 MPa (29.7 × 10^3 psi) from a machining flaw (mark at right-hand edge of sample). Note the complex fracture and the apparent cathedral-like mirror. The upper arcs appear to be from a true cathedral mirror associated with subsequent crack branching onto another fracture surface. However, the lower set of the mist-hackle markings near the tensile surface appears to be whisker-lance mist-hackle. The two different types of mist-hackle apparently occurred owing to the different fracture surfaces involved.*

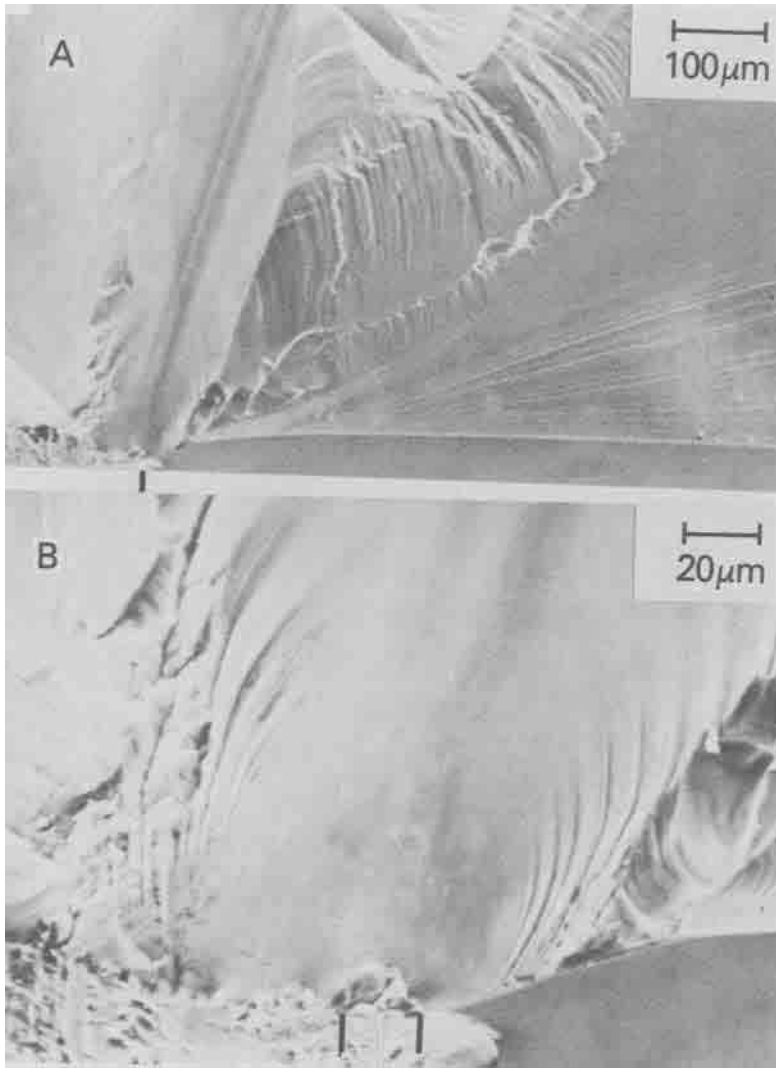

FIG. 34—*Fracture mirrors on a silicon crystal. This specimen (see also Fig. 26c) fractured at room temperature at 169 MPa (24.5 × 10^3 psi). Note the failure origin from the corner, and an associated cathedral-type mirror, but with subsequent whisker-lance mist-hackle after the crack has branched onto another, apparently more preferred, fracture surface (as indicated by the ready branching).*

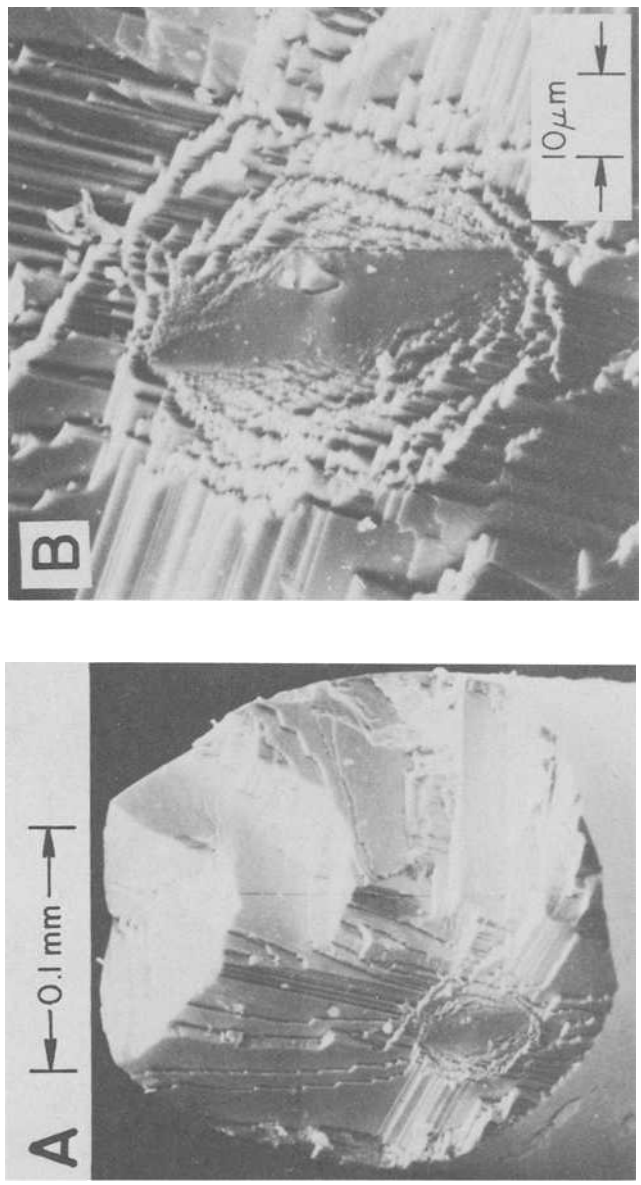

FIG. 35—*Tensile fracture of a C-axis Al_2O_3 filament at ~22°C. Note the clear diamond shape of the fracture mirror and the associated fracture steps (possibly related to occurring on or near the rhombohedral planes). Sapphire shows fracture features similar to this well beyond 1200°C, possibly to nearly 1900°C* [19]. *(Photos courtesy Dr. P. Becher from his studies at NRL.)*

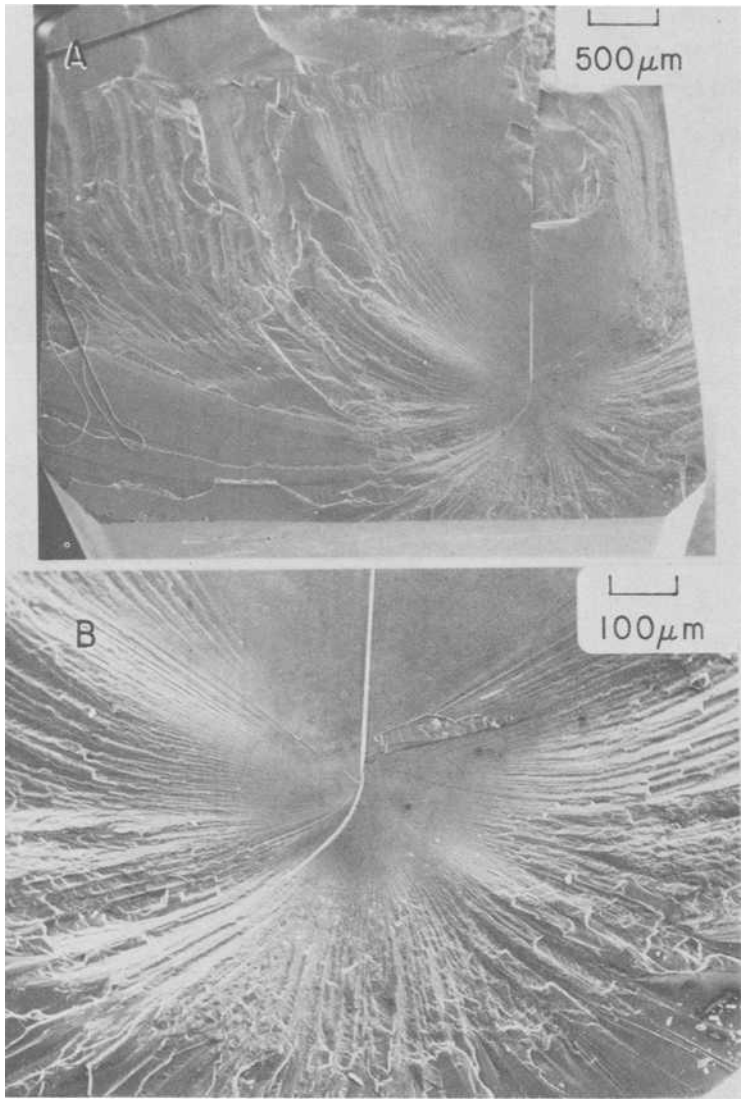

FIG. 36—*Internal fracture origin in CaF_2 crystal. This flexure specimen fractured at room temperature at 144 MPa (20.9 × 10^3 psi) from an internal crack (approximately vertical, curving to the left towards the bottom). Note the asymmetry of the mirrors associated with this irregular flaw, the absence of mist and hackle towards the neutral axis side of the failure, and the somewhat variable onset of the whisker-lance mist-hackle.*

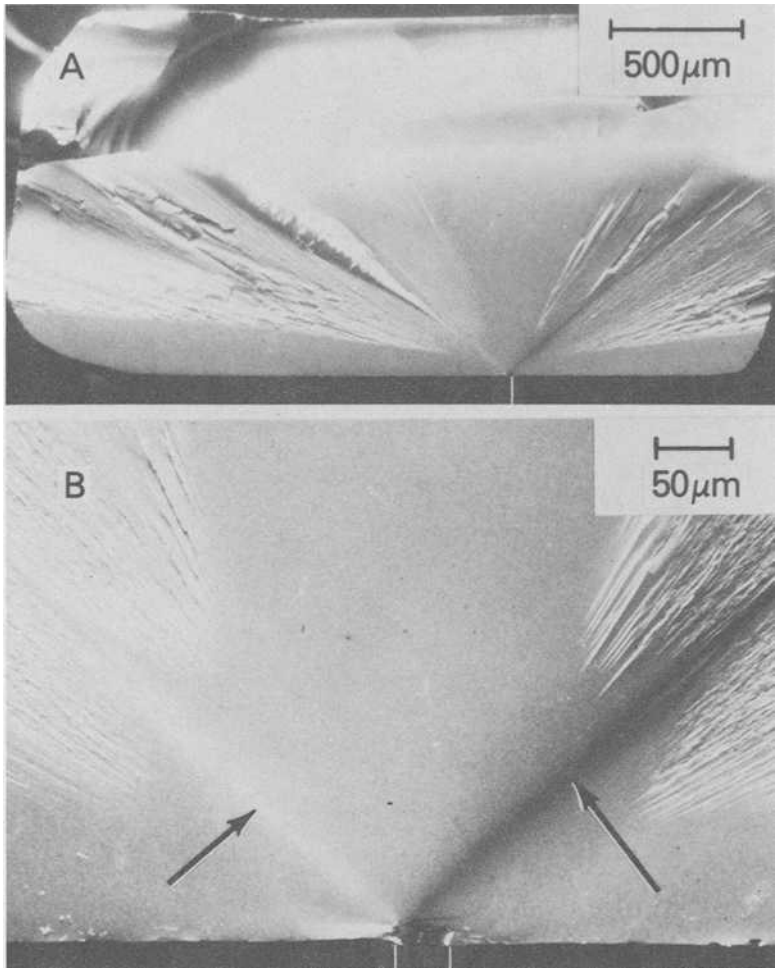

FIG. 37—*Example of whisker-lance mist-hackle on a $MgAl_2O_4$ crystal fracture. This stoichiometric crystal with a {100} tensile surface and a ⟨100⟩ tensile axis fractured at 346 MPa (50.2 × 10^3 psi) at 1400°C but is also representative of room-temperature fracture. Note the distinct whisker-lance mist-hackle, its formation only over a certain well-defined angular sector, a variation in its onset (implying a statistical aspect of nucleation), and the two rays extending out from the origin and ~⟨110⟩ directions which appear to be axes of symmetry for the mist-hackle sectors. Note also the very large mirror-to-flaw-size ratio of ≥14.*

fracture in polycrystals can be caused by intrinsic factors and do not require extrinsic factors such as impurities. This appears to have important implications for the question of whether a crack intrinsically follows a more tortuous intergranular path or whether it does so simply due to grain boundary impurities. During SCG studies of $MgAl_2O_4$ crystals, McKinney et al observed that

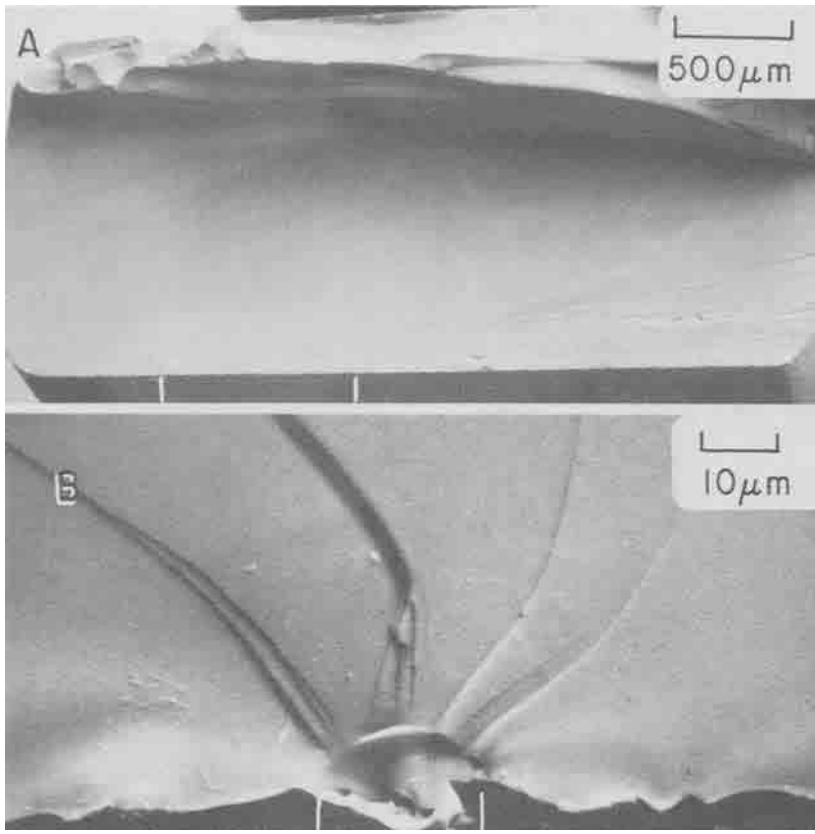

FIG. 38—*Another example of whisker-lance mist-hackle on a $MgAl_2O_4$ crystal fracture.* (a) *This stoichiometric crystal with a {110} tensile surface and a ⟨100⟩ tensile axis fractured at 116 MPa (16.8×10^3 psi) at room temperature. Note the whisker-lance mist-hackle to the right of the fracture origin (vertical arrow); this angular sector of mist-hackle has only about half the angular spread of that in Fig. 37.* (b) *Higher magnification of the fracture origin showing a typical machining flaw (vertical marks) and some resultant fracture steps which in this case are not directly related to the mist and hackle. Ratio of the mirror to original flaw size is ~83.*

specimens oriented for growth on {110} planes had growth on this plane only at high crack velocities. At low velocities the crack followed a saw-tooth path on {100} planes. An earlier observation of Becher and Freiman [*25*] showed that during SCG in CaF_2 crystals in concentrated hydrogen fluoride (HF) environments, fracture tended to deviate off {111} planes. Both of the foregoing observations appear to have implications of basic environment/solid-bond interactions.

Brittle fractures of metal crystals (chromium at room temperature [*26,27*] and iron [*28*], molybdenum [*29–32*], and tungsten [*33–36*] at lower tempera-

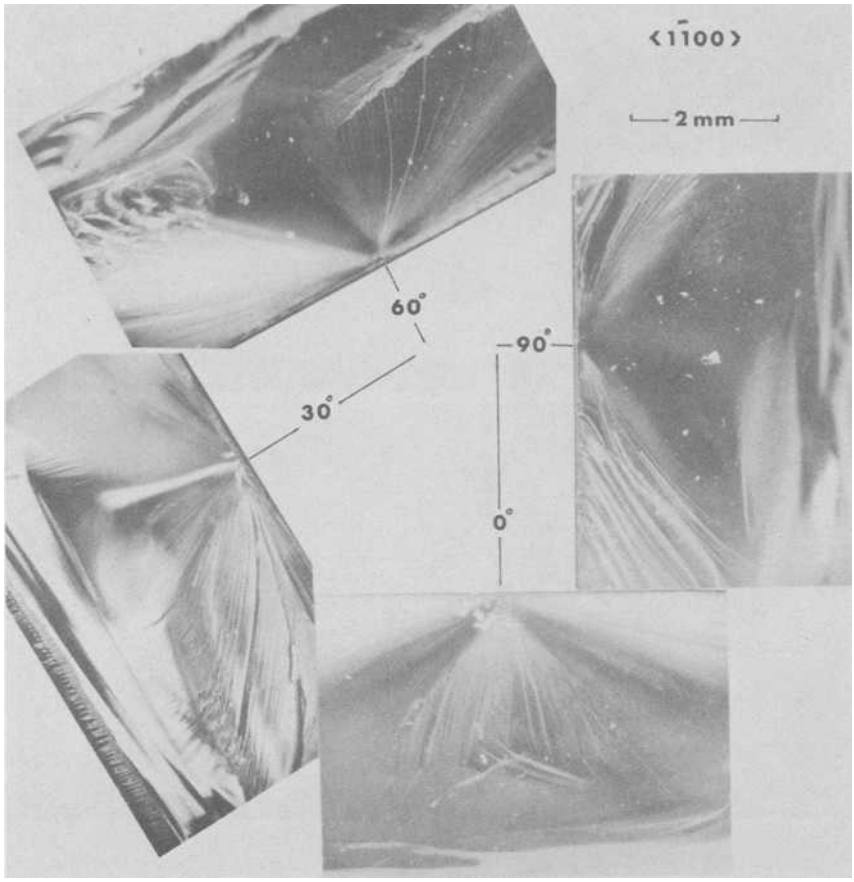

FIG. 39—*Examples of Al_2O_3 single-crystal fractures about a ⟨1010⟩ tensile axis. Note the formation of whisker-lance mist-hackle only in certain angular sectors, which from the composite set of different fractures can be seen to have a four-fold symmetry about the tensile axis. (Photo courtesy Dr. P. Becher from his work at NRL.)*

tures) have many similarities to ceramic crystal fractures (Fig. 40). Although data are limited, various boundaries on such fractures generally appear to be consistent with Eqs 1 and 3. Lance or whisker mist-hackle generally forms on primary fracture surfaces, and mirror tongues occur on such surfaces in specific directions—for example, ⟨100⟩ in iron, molybdenum, and tungsten (Fig. 40) and apparently ⟨110⟩ in chromium.

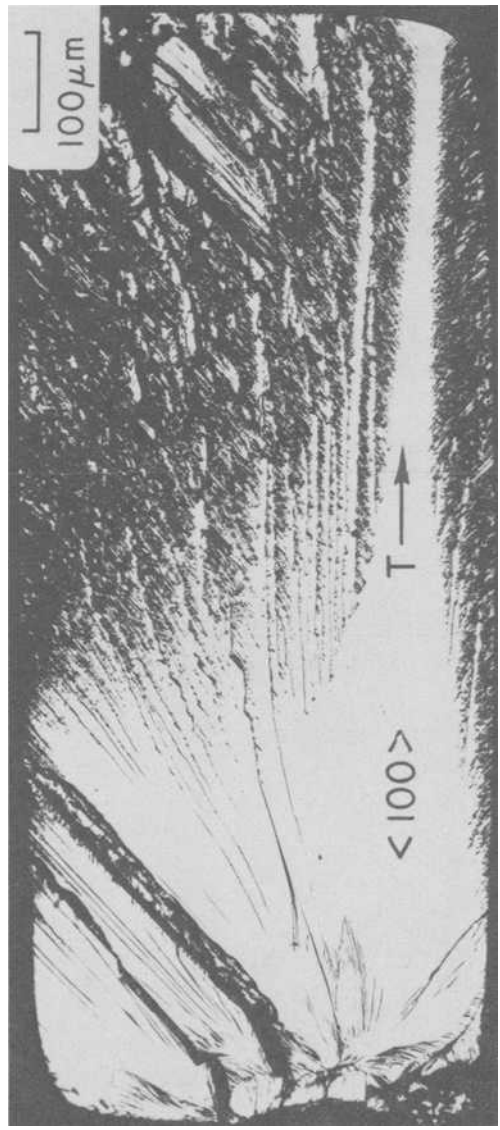

FIG. 40—*Fracture of a tungsten crystal tested at 77 K. This photo of a {100} fracture (courtesy Professor D. Hull, University of Liverpool) shows a distinct tongue* (T) *of mirror character extending in the ⟨100⟩ direction (arrow). The onset of mist-hackle has a definite whisker-lance character.*

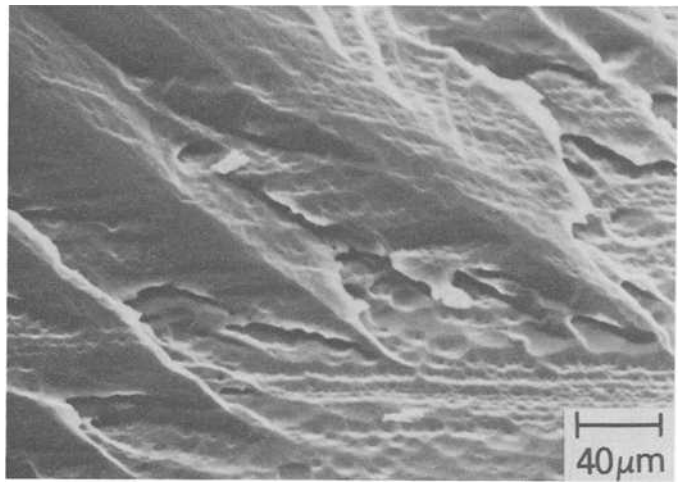

FIG. 41—*Whisker-lance mist-hackle on a MgO {100} fracture. Mist-hackle starts near the lower and right-hand photo edges and runs at ~45 deg to the horizontal at the edge of the mirror. Etching of the sample clearly shows secondary cracks under part of the mist-hackle.*

TABLE 3—*Type of mist-hackle on single-crystal fractures.*[a]

			Mist-Hackle Occurrence			
	Crystal		Arc-Rib		Whisker-Hackle	
Material	Structure	Cleavage Planes	Fracture Plane	MCD[b]	Fracture Plane	MCD
TiC	cubic (NaCl)	{100}	N.O.[c]	N.O.	{100}	none?
MgO	cubic (NaCl)	{100}	N.O.	N.O.	{100}	⟨100⟩
CuF_2	cubic (CaF_2)	{111}	N.O.	N.O.	{111}	none
ZrO_2	cubic (CaF_2)	{111}	none {111}	...	{111}	none
$MgAl_2O_4$	cubic	{110}, {100}	none {111} or {100}?	⟨100⟩	{100} or {110}	⟨100⟩
Al_2O_3	hexagonal	...	...	yes?	...	yes
TiO_2	...	...	...	yes	...	...
SiC	hexagonal	{10$\bar{1}$0}?	none {10$\bar{1}$0}?	...	{10$\bar{1}$0}?	yes?
Si	cubic (diamond)	{111}	none {111}	yes?	{111}	yes?

[a] A question mark indicates some uncertainty in the designation.

[b] MCD = missing crystallographic direction (crystal direction that is the axis for absence of features).

[c] N.O. = not observed owing to limited study or lack of fractures on other planes.

TABLE 4—*Examples of* R_m/R_a *ratios in crystals.*[a]

Crystal	Fracture Plane	R_m/R_a
Ge	111	3 to 7[b]
CaF_2	111	5 ± 1 (5)
ZrO_2	111?	11
$MgAl_2O_4$	100	71 ± 35 (8)
$MgAl_2O_4$	110	8 ± 4 (17)

[a]Number of values averaged are shown in parentheses.

[b]Based on published fractographs in Refs *22* and *23*.

Crackpath-Microstructural Interaction

Intergranular versus Transgranular Failure

The amount of transgranular versus intergranular failure is important in fractography. As noted earlier, the mirror region is normally defined by its flatness and the onset of mist. Except for fine-grain sizes, intergranular fracture does not allow the sufficient flatness of fracture that transgranular fracture does to give the characteristic mirror flatness. The roughness of intergranular fracture may even make detection of mist difficult (if it is formed). It is not clearly established that mist will occur with intergranular failure in larger grain bodies. By definition, the mirror and R_m typically require some (say, 30%) transgranular fracture in larger grain bodies.

Transgranular fracture is also important in determining fracture origins, since it allows formation of river marks, fracture tails, etc., used to guide one back to the origin [*2*], and may help define the origin by the change in mode of fracture or, more commonly, a shift in the fracture surface not allowed by the prescribed fracture path with intergranular fracture. The significance of transgranular fracture increases as grain size increases, progressively diminishing the clarity, then occurrence, of fracture steps and tails, mist, and finally hackle on a multigrain scale. At large-grain sizes with mostly intergranular fractures, fracture origin determinations are often limited to identifying obvious, isolated, processing defects located at about the center of crack-branching patterns. Thus, besides aiding in the identification of fracture features, knowledge of intergranular versus transgranular failure can improve the understanding of the mechanism or cause of failure.

Consider the overall trend of fracture in dense bodies as a function of grain size. Under normal room-temperature fracture, intergranular fracture is

more common at finer grain sizes and transgranular fracture is more common at larger grain sizes. Limited quantitative observations of intergranular versus transgranular failure as a function of grain size on a few materials [*2,37,38*] show this trend (Fig. 42). These observations appear to have been made primarily on cubic materials. Recent studies of noncubic structures—for example, aluminum oxide (Al_2O_3)—indicate that there can be considerable transgranular failure at fine and intermediate grain sizes, while transgranular failure decreases at larger grain sizes [*2,38*] (Fig. 42). Fracture does not necessarily become totally intergranular in large-grain bodies of noncubic structure: some limited transgranular failure has been observed in quite large (millimetre-size) grains in fused-cast Al_2O_3. Although some workers have believed that intergranular fracture is intrinsic at finer grain sizes, the substantial transgranular failure found in some dense fine-grain Al_2O_3, and espe-

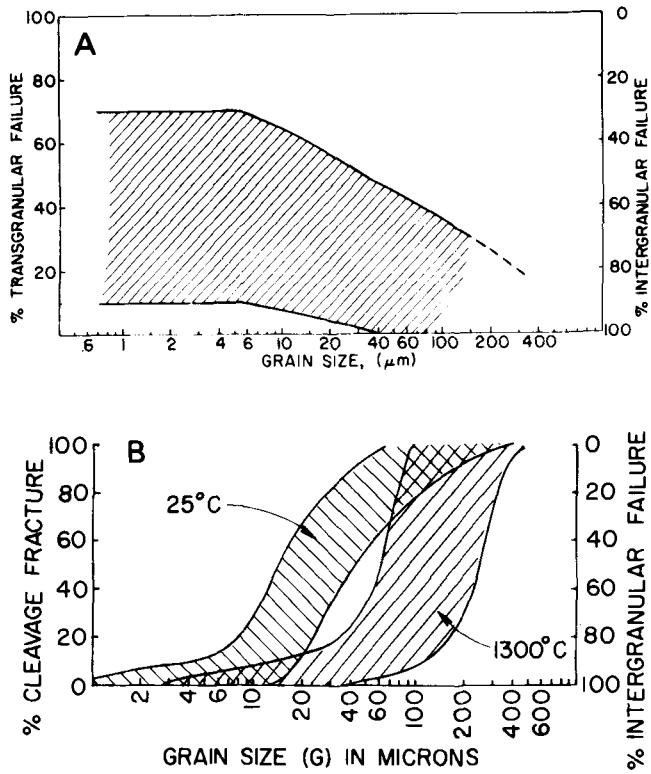

FIG. 42—*Fracture mode of Al_2O_3 and MgO as a function of grain size.* (a) *Al_2O_3 data for dense hot-pressed material tested at room temperature.* (b) *Data for dense hot-pressed MgO tested at 25 and 1300°C. In both cases most of the larger grain samples were obtained by heat treatment of the hot-pressed bodies.*

cially the nearly total transgranular failure observed in very fine (<0.5 μm) grain, high-strength, partially stabilized zirconia [*2,38*], argues against this.

It has also been believed that increasing grain boundary impurities and increasing grain boundary porosity enhance intergranular failure. Specific data are limited, but general observations support the relation between intergranular porosity and intergranular fracture. Similarly, there is some evidence for grain boundary impurities enhancing intergranular fracture. Observations by Rice et al [*39*] support the effect of intergranular phases in silicon nitride (Si_3N_4), where hot-pressed bodies with grain boundary phases showed substantial intergranular fracture (Fig. 43). This was in contrast to almost totally transgranular fracture in CVD Si_3N_4 and substantial transgranular fracture in reaction-sintered Si_3N_4 except where there is a substantial amount of finer dispersed intergranular porosity; that is, denser sections of material around larger pores typically had transgranular fracture. The issue of impurities and possibly of porosity at grain boundaries and intergranular fracture, however, is not straightforward. For example, if finer grain MgO, which has mainly intergranular fracture, is heat treated to give larger grains, it has increased transgranular fracture (Fig. 42) despite apparently increased grain boundary concentration of impurities [*40,41*].

Two experimental conditions can substantially change the amount of transgranular versus intergranular failure. The first is temperature. Intergranular failure is very frequently observed to increase with temperature (Fig. 42 provides an example of the limited quantitative data). Congleton et al [*42*] have reported intergranular fracture increasing from 55% at -196°C to ~ 70% at 600°C in a dense Al_2O_3 (Lucalox).

The second experimental condition is crack velocity or test environment. Several observations of the mode of failure in stress corrosion studies of ceramics at room temperature have indicated that slow crack growth is predominately, if not exclusively, by intergranular fracture; see the studies on MgO [*43*], ZnSe [*44*], MgF_2 [*45*] (Fig. 44), and Al_2O_3 [*46*]. However, it cannot be unequivocally determined at this time whether this is an effect caused by either crack velocity or stress corrosion. Heuer [*47*] has indicated a possible increase of intergranular failure with decreasing crack velocity in Al_2O_3. While most attention has been on H_2O at or near room temperature, other environments may also aid or result in intergranular fracture. Thus intergranular fracture, whether it was associated with grain boundary impurities or was possibly an intrinsic phenomenon, has been reported for titanium boride (TiB_2) in molten aluminum [*48*].

The occurrence of predominant, if not exclusive, intergranular failure in the fracture origin region associated with slow crack growth brings up the important issue of local variations in intergranular fracture over the fracture surface. Although data or discussion of this is limited, three general trends have been observed. The first is fracture initiation from grain boundaries (Fig. 45). In addition to the slow crack growth via intergranular fracture noted previ-

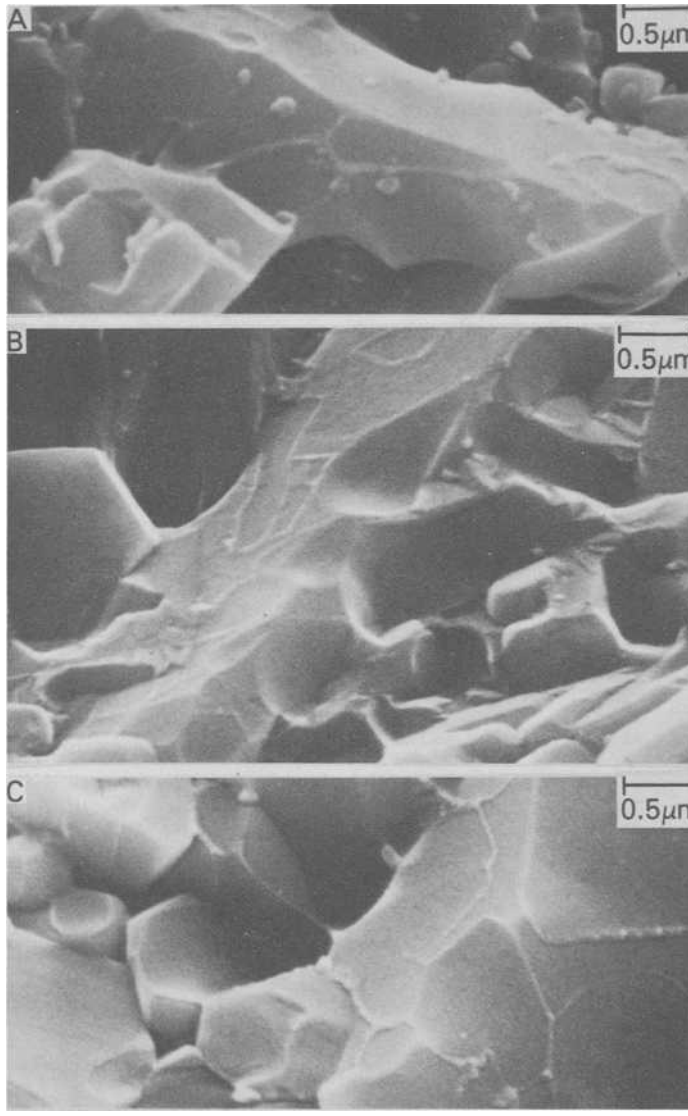

FIG. 43—*Examples of grain boundary phases on fractures of hot-pressed Si_3N_4 bodies. Room-temperature fractures reveal second phases along grain boundaries (mainly along triple lines) in Si_3N_4 hot-pressed with* (a) *5% Y_2O_3,* (b) *5% MgO, and* (c) *8% ZrO_2. Such second phases are most readily seen on larger grains as shown in these photos. (Photos courtesy B. Bender, NRL.)*

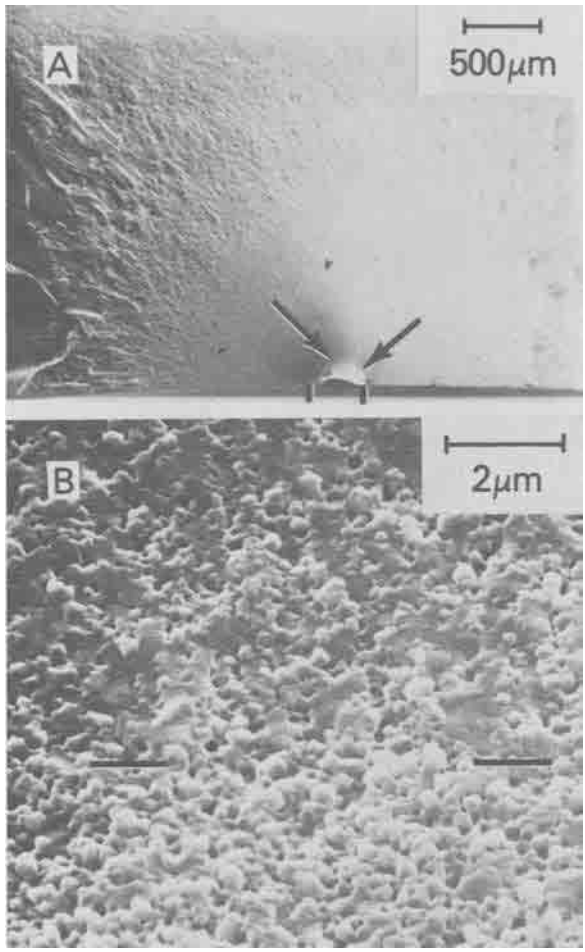

FIG. 44—*Intergranular slow crack growth in MgF_2.* (a) *Low magnification SEM photo of the fracture origin of a MgF_2 dome that failed from thermal stress. The dark feature (vertical bars) is the flaw from which failure initiated. The white region above this is attributed to slow crack growth (based on Mecholsky's studies* [44]*).* (b) *Higher magnification of the transition from slow crack growth to the mirror. Note the transition from all intergranular fracture below the horizontal markers to mixed inter- and transgranular fracture above the marks. See also Fig. 63*b.

ously, cases of fracture initiation from grain boundary surfaces in the absence of stress corrosion effects have also been observed. It has been demonstrated in some partially stabilized ZrO_2 (PSZ) that grain boundary surfaces not connected to the tensile surface and hence not expected to be subject to environmental effects have been frequent sources [*49*] of failure (Fig. 45*b*), which indicates possible effects of excessive accumulation of noncubic phases

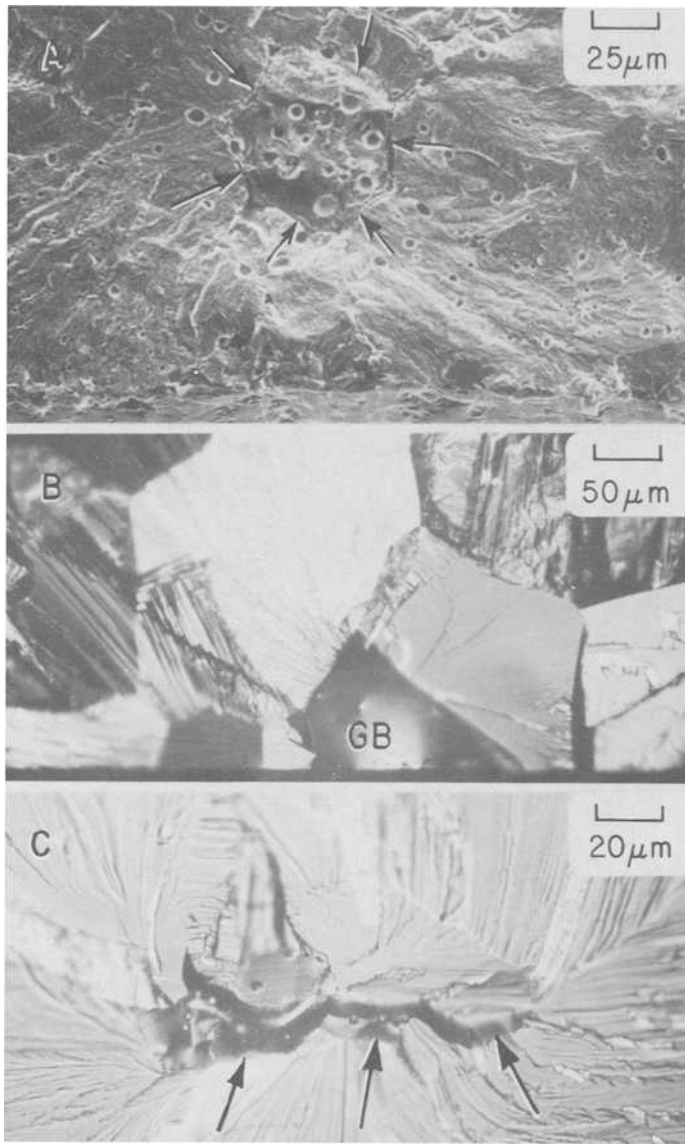

FIG. 45—*Examples of fracture initiation from grain boundary surfaces with total surrounding transgranular failure.* (a) *Commercial ZrO_2 (Zircoa 1027), partially stabilized with 2.8 wt% (8.1 mole %) MgO, failing at 350 MPa (50.8×10^3 psi) at room temperature from a grain boundary surface somewhat inside the tensile surface (arrows).* (b) *Fully dense MgO specimen failing at room temperature at 124 MPa (18.0×10^3 psi) from a grain boundary surface* (GB) *intersecting the tensile surface.* (c) *Recrystallized CaO single crystal fractured at 1315°C (2400°F) which yielded at 69 MPa (10×10^3 psi) and ultimately fractured at 141 MPa (20.5×10^3 psi); failure initiated inside the tensile surface from the intersection of three grain boundary surfaces (arrows) with resultant crack propagation totally transgranular (Fig. 5 shows lower magnification of this fracture). See Fig. 4 for another example of failure initiation from a grain boundary.*

at these boundaries. Grain boundary initiation of fracture appears to greatly increase at higher temperatures. The author has shown that failure at higher temperature in fully dense materials (obtained by recrystallizing single crystals of MgO or CaO) begins to show failure initiation from grain boundary surfaces surrounded by all transgranular failure as an intermediate step between all transgranular failure at room temperature and predominately intergranular failure at higher temperatures [*37*].

The second general trend of intergranular fracture is for it to increase at limited, but apparently characteristic, distances from the fracture origin (Fig. 46). Kirchner [*50–52*], who has been a leader in these observations, has reported such variations in various Al_2O_3 bodies, associating them with the crack reaching critical stress intensity levels. Rice [*53*] has shown increased intergranular failure being a factor in the fracture roughness in the mist and hackle regions of fracture of polycrystalline materials—for example, in a cubic ($MgAl_2O_4$) and a noncubic (B_4C) material. Finally, there has been some limited suggestion that the amount of transgranular failure may increase in flexure samples as the crack approaches the compressive surface in flexural testing [*2,37*].

Fracture in the Presence of Second Phases

Consider pores as fracture origins. Extensive demonstrations elsewhere show that pores, either singularly or collectively, can be fracture origins in glasses [*17*] and especially in polycrystalline samples [*17,54–57*] including cermets [*58,59*] (Figs. 3, 23, 46, and 47). Where pores are occasionally found in single crystals, they often serve as fracture origins. As noted earlier, failure from pores, at least in glasses, may frequently originate independently from two different portions of the pores, especially for pores exposed by machining. Independent fractures then proceed around the pore until they meet, developing a fracture tail (Fig. 47). Such fracture tails may occur on pores in a cluster [*17*] where part or all of the cluster also acts as a fracture origin. This raises important questions as to the ability of fractography to unravel the sequence of failure, namely whether the pores link together before or during failure or both. Less is known about the details of fracture initiation from collections of pores in polycrystalline samples due in part to less study as well as frequently less definition of the more subtle fracture features which can be more clearly seen on glass fractures.

Two general aspects of the interaction of a propagating crack with individual pores are well established. Firstly, as with crack initiation from a pore, a crack typically leaves a fracture tail on the opposite side of the pores from which it approached (see Fig. 4 of Ref *2*). This is the result of the crack being separated into two independent cracks when it intersects a pore and minor perturbations in the propagation of the two crack halves which almost never meet on exactly the same plane on the opposite side of the pore. The two por-

FIG. 46—*Fracture surface of a high-strength Al_2O_3 specimen tested at −196°C. Fracture at 651 MPa (94.5 × 10^3 psi) originated from the large pore within the large grain near the left-hand edge of the photo, about 60 μm in from the tensile surface. Note the relatively smooth flat fracture through and somewhat beyond the large grain, except for the fracture tails* (T) *associated with both the main* (1) *and a secondary* (2) *pore. Beyond this smoother area the fracture becomes rougher and begins to involve some intergranular failure as well as a number of features which appear to be similar to cathedral-type mirrors, or portions thereof, seen on single-crystal Al_2O_3 fracture* (a to e). *The orientation of these apparent cathedral mirrors as well as other fracture features indicate that the local direction of crack propagation was significantly different from a simple smooth semicircular flaw spreading out from the origin. (Photo courtesy Dr. H. Kirchner, Ceramic Finishing Company.)*

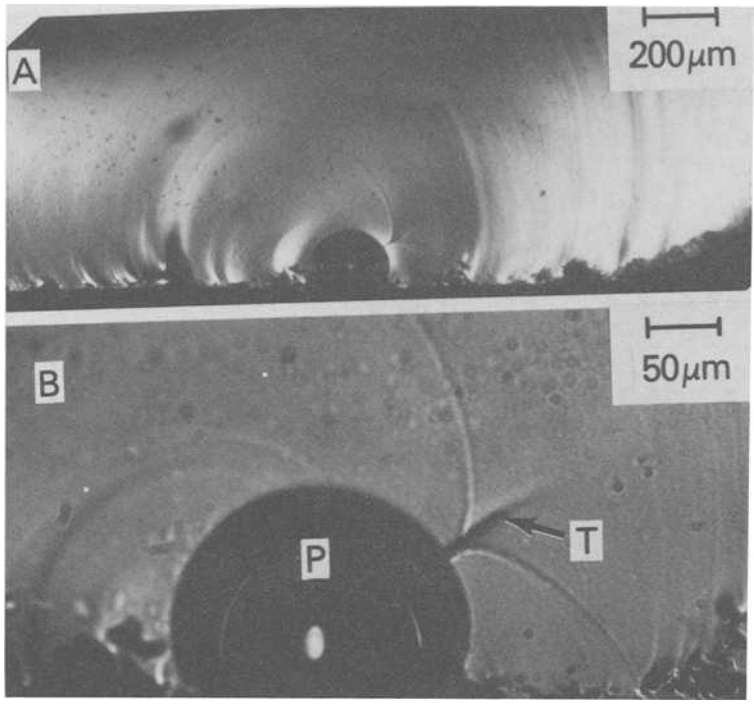

FIG. 47—*Example of fracture tails associated with a pore-initiating failure in SiO_2 glass at 81 MPa (11.7 × 10^3 psi).* (a) *Lower magnification photo showing the pore and surrounding fracture.* (b) *Higher magnification of pore and the fracture tail* (T) *due to overlapping of cracks initiating on opposite sides of the pore* (P).

tions of the rejoined crack overlap, creating a fracture step or tail until such time as the cracks again pull together onto a single plane. Another aspect of propagating cracks interacting with pores is that the crack typically is retarded as it closely approaches a pore and then accelerates as it breaks away from it. This has been very nicely shown by ultrasonic marking of crack fronts, first by Kerkhof [*60*] and more recently by Green et al [*61*].

Second-phase particles or fibers can frequently be sources of failure [*54-59, 62-63*], depending on their size, location relative to the stress field, and especially on their differences in properties with the matrix. The property usually of greatest importance is thermal expansion. While the stresses around such a particle are known in principle for simple-shaped particles, two complications commonly occur: (1) the particles are often not simple in shape, and (2) the degree of bonding and interaction between particle and matrix can significantly change events, raising questions such as whether cracks from particles occur before or during stressing (Fig. 48). Ultimately fractography may be an important tool for better understanding and resolving some of these uncertainties.

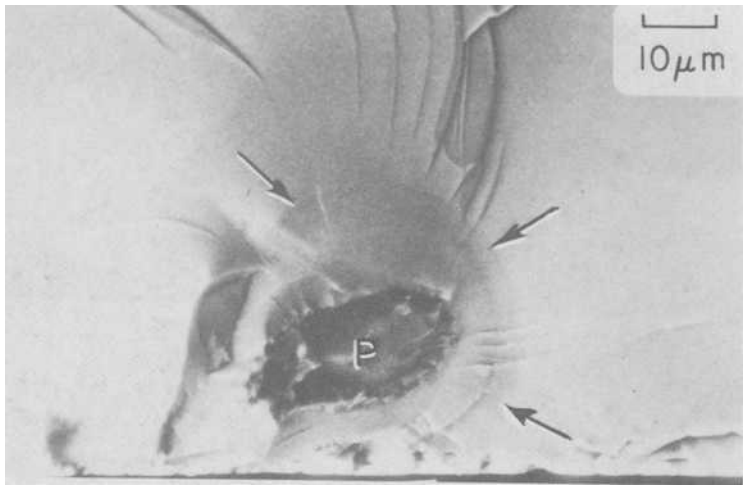

FIG. 48—*Failure of a ZrO_2 single crystal from a foreign particle. This ZrO_2 single crystal (fully stabilized with 8 wt% Y_2O_3) fractured at room temperature at 143 MPa (20.3 × 10^3 psi) from a silicate particle* (P). *The demarcation (arrows) indicates what is probably the boundary of the crack from this particle that was the ultimate source of failure. (Photo courtesy B. Bender and R. Ingel, NRL.)*

Fractography can also be a valuable tool for understanding the interaction between a propagating crack and various second-phase particles. Much remains to be understood but some important examples are available. Identified cases of second-phase particles (or grains) fracturing ahead of the crack front with their fracture propagating back towards the main crack front are rare, but cases of this and of the particle fracturing after the crack has passed have been observed (Fig. 49). Small bars of SiC deposited on a tungsten wire commonly showed the tungsten core fracturing from the opposite side of the failure initiation in SiC and propagation in the opposite direction of the SiC fracture [*64*] (Fig. 50). Again, studies using ultrasonic marking of fracture surfaces can be very useful in understanding interactions of a propagating crack with individual second-phase particles; see the glass studies of Green and Nicholson and colleagues [*65,66*].

Besides the important fractographic aspect of a crack interacting with an individual second-phase particle or fiber is their overall effect on fracture character. Current observations of the author and colleagues indicate that fine-grain ceramic bodies such as Al_2O_3 containing substantial percentages of a fine second-phase particle dispersed in it leads to a rougher texture in the normal mirror region; that is, it often appears as though the mist extends clear to the fracture origin (Fig. 51). More extreme deviations can be observed with larger volume fractions and especially larger particle sizes. In the latter case, however, much of the problem of defining mirrors and related features is

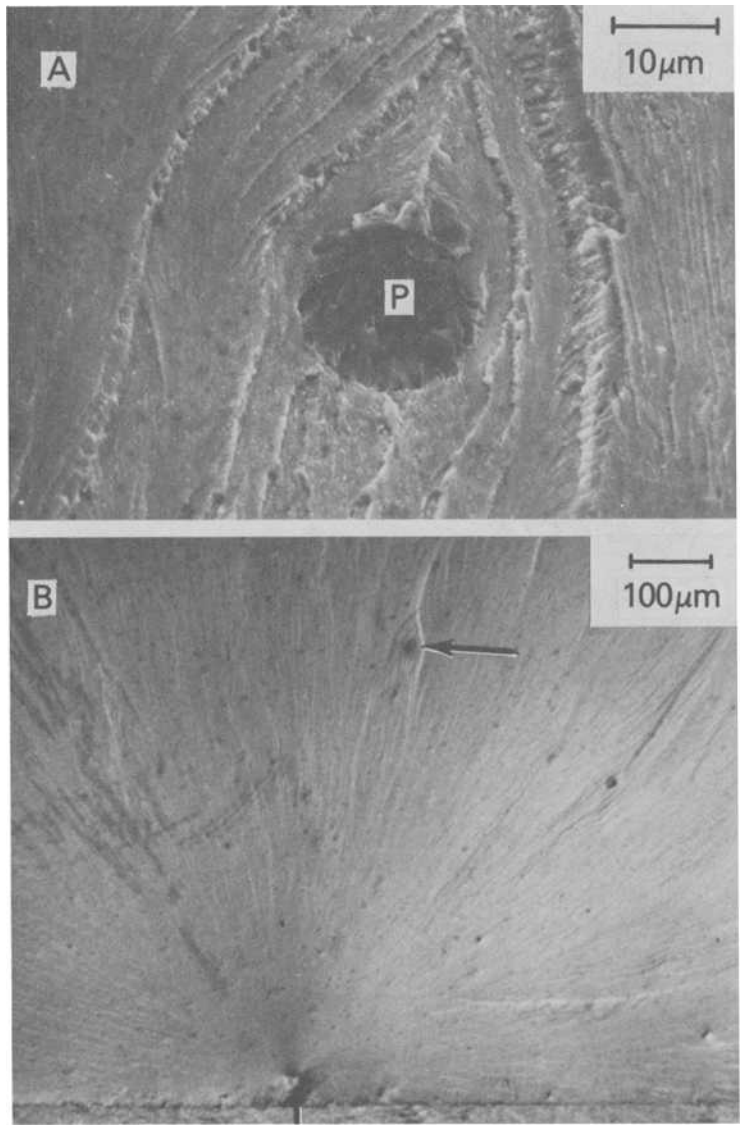

FIG. 49—*Fracture of a foreign particle in a ZrO_2 crystal.* (a) *Higher magnification photo of one of the silicate particles* (P) *through which the fracture passed.* (b) *Lower magnification photo of overall fracture surface, showing the location of this particle (arrow). Fracture markings clearly show that the crack swept part or all the way around this particle before it in turn started to fracture from the opposite side from which the crack approached it. Fracture stress was 606 MPa (88 $\times$ 10^3 psi).*

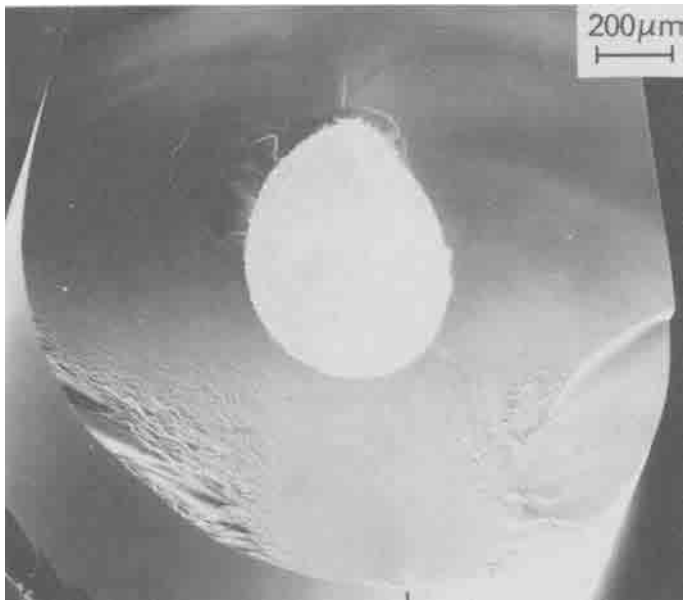

FIG. 50—*Fracture of a large inclusion in a ceramic body. This photomicrograph shows a very fine grain (CNTD) SiC specimen fractured at room temperature at 490 MPa (71.0 × 10^3 psi) from a machining flaw originating at the bottom of the specimen (vertical mark) and associated mirror. Only when the fracture had swept almost if not completely around the tungsten core (on which it was deposited) did this core in turn begin to fracture in the opposite direction from which the SiC specimen was fracturing.*

caused by reduced strengths combined with the larger perturbation of the fracture surface owing to the larger particle size. The interaction of ZrO_2 precipitates in partially stabilized ZrO_2, with the crack and their resultant exposure on the fracture surface (Fig. 52), is an important example and extension of second-phase crack interactions. Normal fractography can often be done on bodies containing some metallic phases that have some ductility, as shown by the extensive and effective fractography on cobalt-bonded tungsten-carbon bodies [*58,59,62,67*]. Larger amounts of metal reduce the distinction of the usual fractures, but may still allow useful fractography (for example, identification of fracture origins; Fig. 53) to be done. Extreme cases of two-phase bodies are ceramic fiber composites, such as carbon carbon composites, and the more recent fiber composites, in which the matrices are various ceramics such as glasses or refractory oxides [*68,69*]. Fracture of fibers in composites can also be found (Fig. 54). Such observations can be very important in ascertaining the mechanisms operative in the composites.

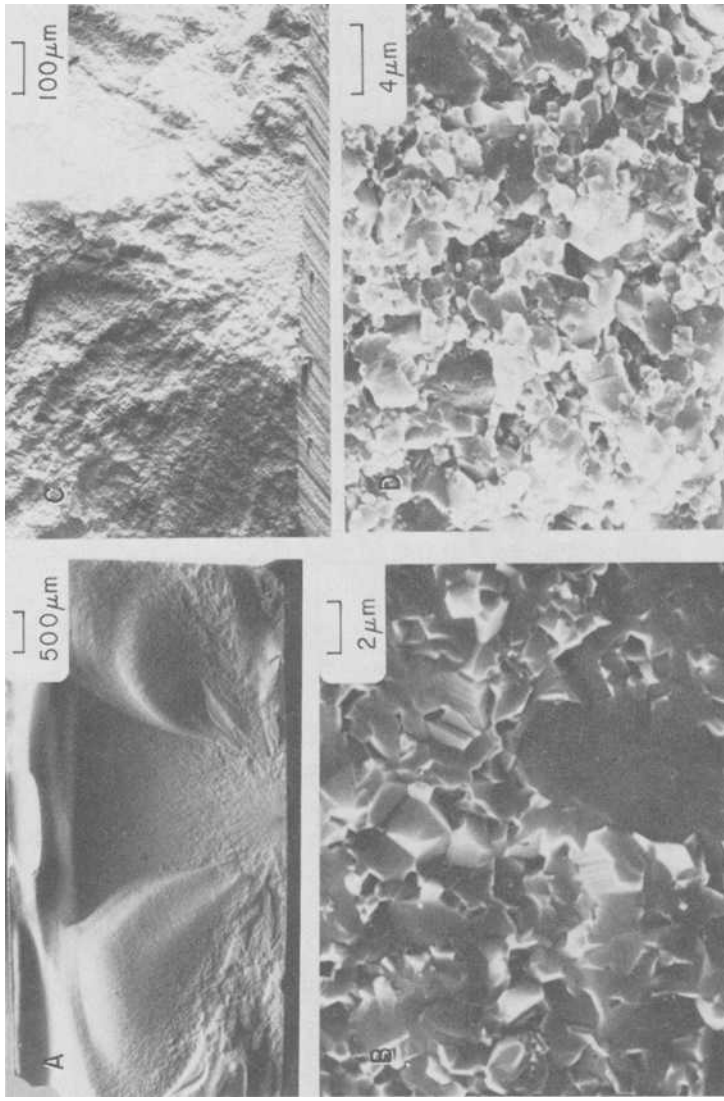

FIG. 51—*Fracture of high-strength Al_2O_3 bodies.* (a) *"Pure" hot-pressed Al_2O_3 specimen fractured at room temperature at 539 MPa (78.2 × 10^3 psi).* (b) *Higher magnification photo of mirror region, showing a substantial amount of transgranular failure and a fair amount of relatively smooth fracture. (Photos courtesy D. Lewis, NRL.)* (c) *Intermediate magnification of an Al_2O_3–30% TiC specimen fractured at room temperature at 799 MPa (116 × 10^3 psi). (Specimens courtesy M. Watanabe, NTK Ceramics.)* (d) *Higher magnification SEM photo from the mirror area. Note the substantially rougher fracture topography than in "pure" alumina* (b) *due apparently to the presence of the second phase (TiC).*

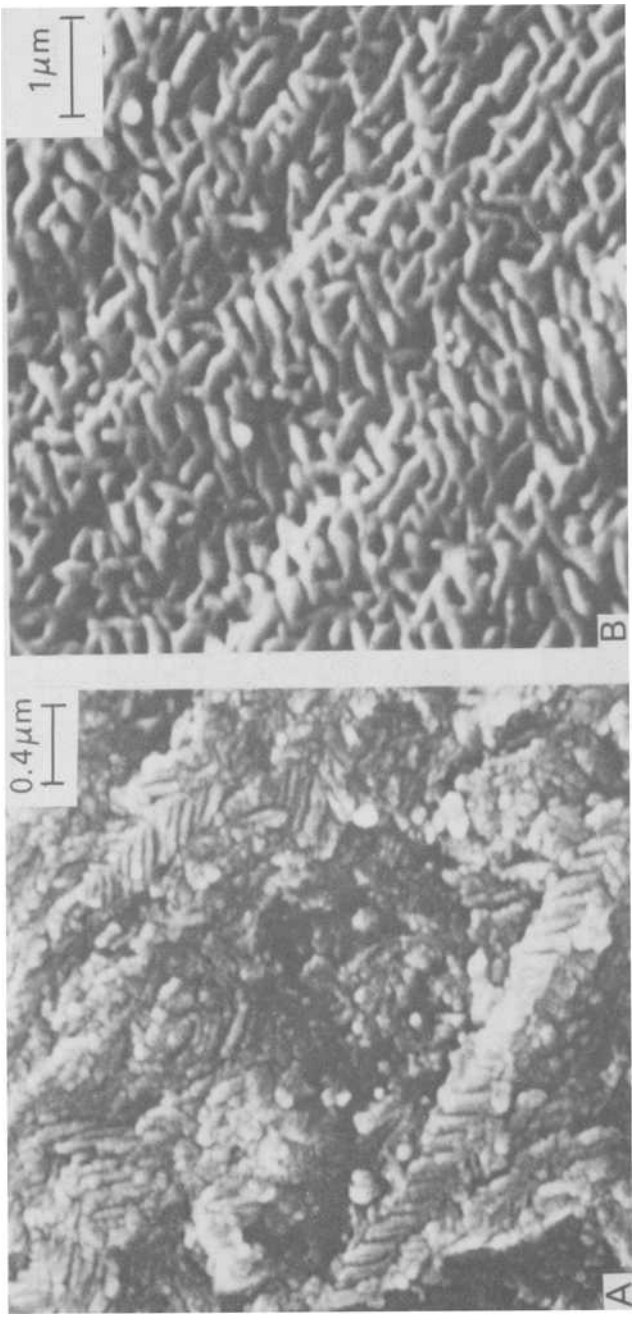

FIG. 52—*Interaction of a propagating crack with precipitates in partially stabilized* ZrO_2. (a) *SEM photo of mist-hackle region of a* ZrO_2 *crystal, partially stabilized with 6 wt%* Y_2O_3, *fractured at room temperature at 862 MPa (125* $\times$ 10^3 *psi). Note the rod-shaped features, often within Chevron-shaped features, presumably hackle. These rods are of the correct size and character to be the noncubic* ZrO_2 *precipitates formed in the* ZrO_2 *matrix.* (b) *Commercial* ZrO_2 *(Zircoa 1027), partially stabilized with 2.8 wt% MgO, fractured at 1230°C in flexure at 90 MPa (13* $\times$ 10^3 *psi). Note the even more distinct crack propagation around the elongated particles, consistent with the precipitates observed by TEM.*

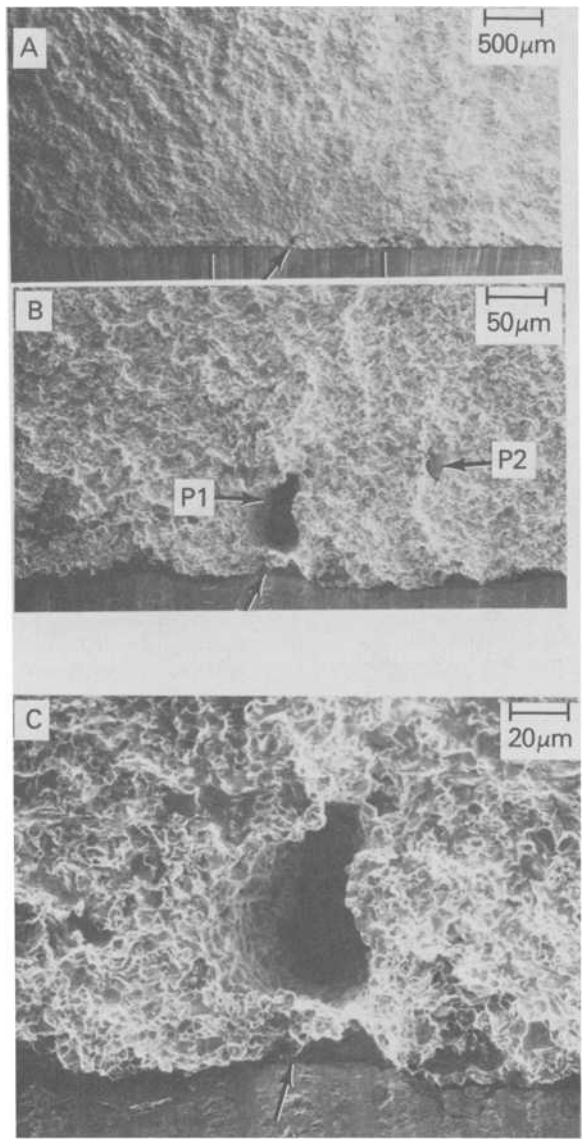

FIG. 53—*Fracture of a cermet. The 25% Inconel content of this body with 75% TaC is a major factor in the reduced clarity of the fracture features, apparently owing to plastic deformation; however, a fracture mirror can be seen in* (a). *Although the more detailed fracture markings needed to identify the specific origin are absent, the location and size of the pore* (P1) *indicate it was the origin of failure.*

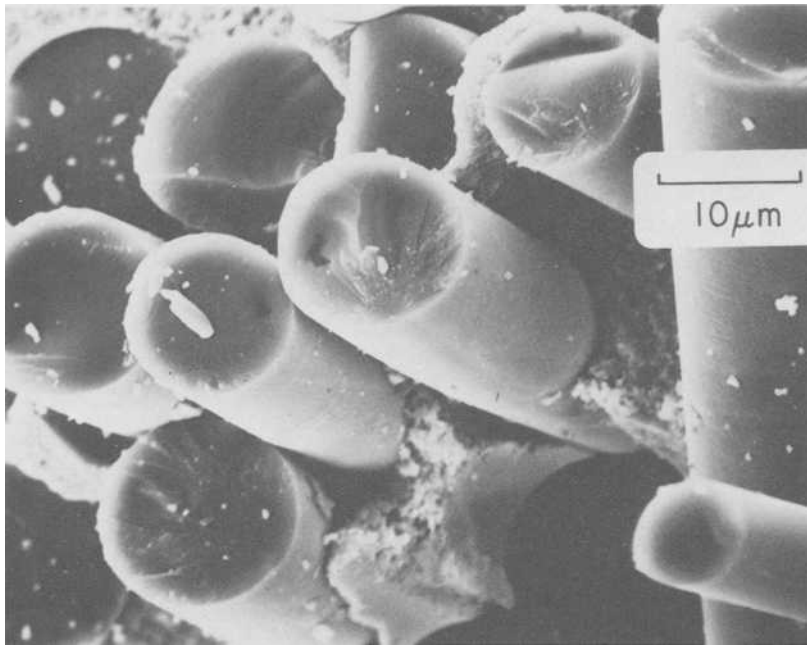

FIG. 54—*Fracture of a ceramic fiber composite tested at room temperature. Both the matrix and the fibers are ceramic. Note that one can often distinguish the fracture initiation of the individual fibers from their fracture markings. Fracture stress was ~303 (~44 × 10^3 psi).*

Effects of Other Stress Conditions

The primary focus of this paper has been on uniaxial tension, mainly in flexure. It was pointed out previously that the linear stress gradient in flexure testing leads to important alterations of the mirror fracture features, but that these are consistent with Johnson and Holloways' empirical equation (Eq 1). This distortion of the mirror patterns clearly raises the important issue of the dependence of both the character and the scale of the fracture features on the character of the stress field controlling the crack propagation.

Abdel-Latif et al [*13,70*] have claimed that the mirror constant (B_i in Eq 1) is dependent upon the state of stress, which increases in the order of three-point flexure, four-point flexure, and finally uniaxial tension. Their results, however, appear to be unique. Results of other investigators using different tests, most commonly three-point and four-point flexure, on the same material generally agree [*70*] when measured by the same standards (that is, by accounting for stress gradients); see also Ref *6*. In particular, Mecholsky et al [*71*] have shown that strength/mirror-size data for optical fibers tested in tension overlap with and appear to be a definite continuation

of the same relationship found for the same types of glasses in bulk form in flexure. More recently, Mecholsky and Rice [*72*] have shown general consistency between not only different size flexure bars but between those flexure bars and biaxially tested specimens of magnesium fluoride (MgF_2), glass, and a crystallized glass.

Besides the general consistency of results from different tests, specific evaluation of the results of Abdel-Latif et al [*13, 70*] suggests two sources of error: (1) some of their equations (for example, Eq 14 in Ref *70*) appear to be incorrect and (2) their testing procedure appears to be faulty. They used 3-mm-diameter round flame-polished glass rods tested on a span of 3 cm. This combination of small cross-sectional area, long span, high strength, and low Young's modulus may lead to significant frictional stress problems in flexure tests; see the analysis of Ritter and Wilson [*73*]. These frictional stresses would be highest in three-point flexure (because of its greater deflection), intermediate in four-point flexure, and zero in tension, hence causing a reduction of their mirror constant based only on the applied stress. Their mirror constant for tension agrees with a wide variety of other data, mostly from flexure tests; their four-point flexural data fall somewhat below this; and their three-point flexural data fall further below their tensile data and the flexural data of others. (Note that the same problem appears to exist for the sapphire tests of Abdel-Latif et al [*20*]; they used 0.25-mm-diameter fiber tested on a span of 1.9 cm.)

The R_i/R_f ratios appear to be the same for biaxial and uniaxial flexure testing, except for possible deviations caused by changes in crack character at large R_i-values [*72*]. A basic distinction readily apparent from Table 1, however, is that biaxial stressing, whether owing to thermal or mechanical stressing, generally results in a significantly larger angle of branching. Single crystals appear to be a partial exception to this. Thus biaxial tests of $MgAl_2O_4$ crystals with {100} or {111} surfaces (loaded by a small central piston and supported by three balls) tend to fail by a single fracture on {100} surface with no branching. On the other hand, the same testing of MgO crystals with {100} surfaces typically fracture on one or more {100} planes with small-to-limited {110} branching.

Whether the stress gradients in flexure testing affect branching angles is an important question. The wedge-shaped pieces commonly formed by crack branching in flexure typically show a taper from the tensile surface towards the compressive surface and may often not fully extend to the compressive surface. Nevertheless, this does not change the basic angular difference between biaxial and uniaxial flexure testing. Crack-branching angles observed in true tension testing of Al_2O_3 have essentially the same measurements as those observed in uniaxial flexure testing (Fig. 11, Table 1).

Consider next the time aspect of the stress, both the rate and duration of application. Mecholsky et al [*74*] have specifically investigated effects of slow crack growth on mirror sizes and demonstrated that R_i/R_f ratios, where R_f is

now the final flaw size due to slow crack growth, are consistent with normal flexure testing in comparison with delayed failure flexure testing. At the other extreme are high rates of loading. The basic scale and character of the mirror phenomenon in conventional impact testing seem to be consistent with normal quasi-static testing. Limited studies, such as by Kirchner et al [*75*], clearly indicate that while failure stresses may be somewhat higher in impact loading (for example, due to reduced slow crack growth from environmental effects), Eq 1 is still valid.

Greater extremes of impulse loading in glass studies, ranging from high velocity impact of water droplets or jets to solid particles or bulk bodies, have shown that basic crack-branching behavior often continues with two modifications. Firstly, the number of branches from the initial (or subsequent) branch point generally increases with the kinetic energy of the impact [*76*]. Secondly, in some of these tests, crack branching occurred without the formation of mist or hackle [*77*]. On the other hand, in some impact cases, apparently those of limited amplitude and duration of loading, none of the conventional features may occur and the only fracture features formed appear to be caused by interaction with reflected stress waves (Figs. 55 and 56). Under very high impulse loading, specimens are shattered into many pieces. Lewis and Spann [*79*] observed that such fragments of a crystallized glass (Pyroceram 9606) were covered with fracture mirrors whose size varied only a little, namely by a factor of about two (Fig. 57). Microstructural features, possibly somewhat larger than normal, were the only features at the center of these mirrors, which indicates extensive, independent nucleation of many fractures.

A related stress state that deserves fractographic attention, but has had only limited investigation, is failure under compressive loading. The difficulty here is that very extensive fracturing and crushing often occur. However, fractography may prove an important aid in understanding the specific mechanics, especially the micromechanics, of local compressive failure. An associated condition is that of high local contact stresses, especially with some motion leading to high local stresses superimposed on an overall lower applied stress. Failure from such conditions appears to be quite common and quite important for a variety of engineering applications. These conditions have been identified as a major cause of failure of some important ceramic turbine engine components [*4,80*] and as the cause of failure of piston engine components in unpublished work of the author (Fig. 58). Another very important aspect of failure associated with compressive loading is failure from hertzian loading in bearings [*81,82*] (Fig. 59).

Two stress factors remain to be considered. The first is mixed-mode failure. Besides the mirror asymmetries noted earlier, Freiman et al [*16*] observed that all the fractures quite rapidly became Mode I, forming a normal mirror from the original mixed Mode I-Mode II of the original flaw (Fig. 18). On the other hand, Sommer [*83*] has reported dramatic changes in the

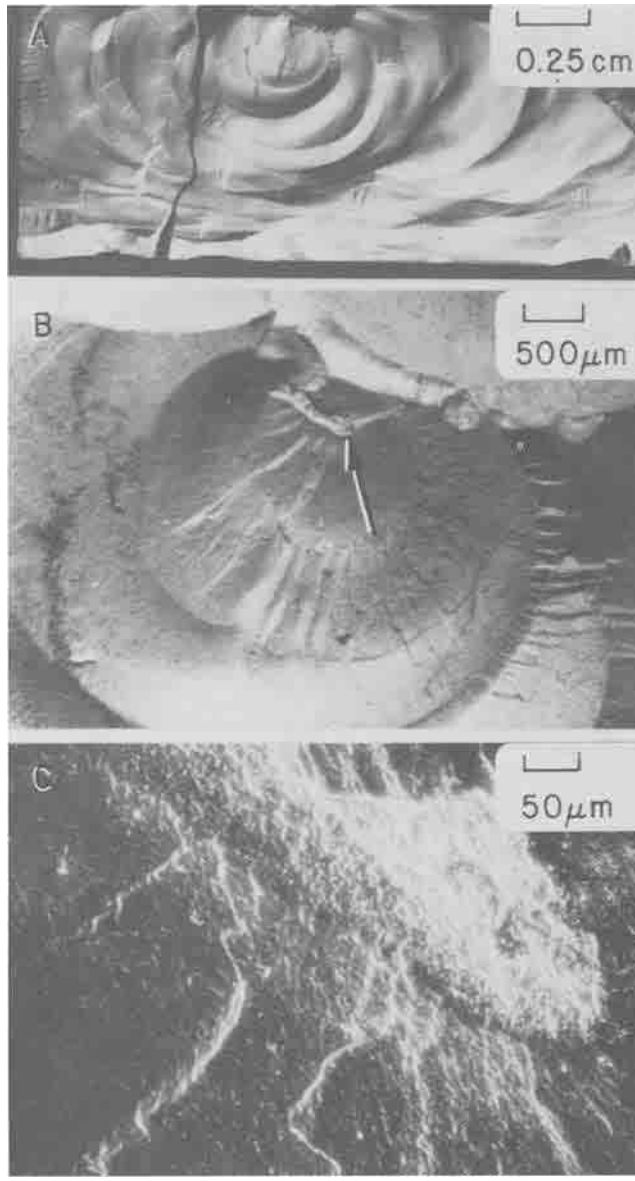

FIG. 55—*Fracture from an impacting raindrop in a β-Sialon ceramic.* (a) *Low magnification photo of spall-type fracture on part of a specimen.* (b) *and* (c) *are progressively higher magnifications showing the fracture initiating from a pore (arrow) in the material. The series of rings were attributed to the "ringing" of the shock from the impact interacting with the propagating crack. The absence of typical mirror, mist, and hackle features was attributed to the short duration of the impact stress. (Photo courtesy P. Land, AFML.)*

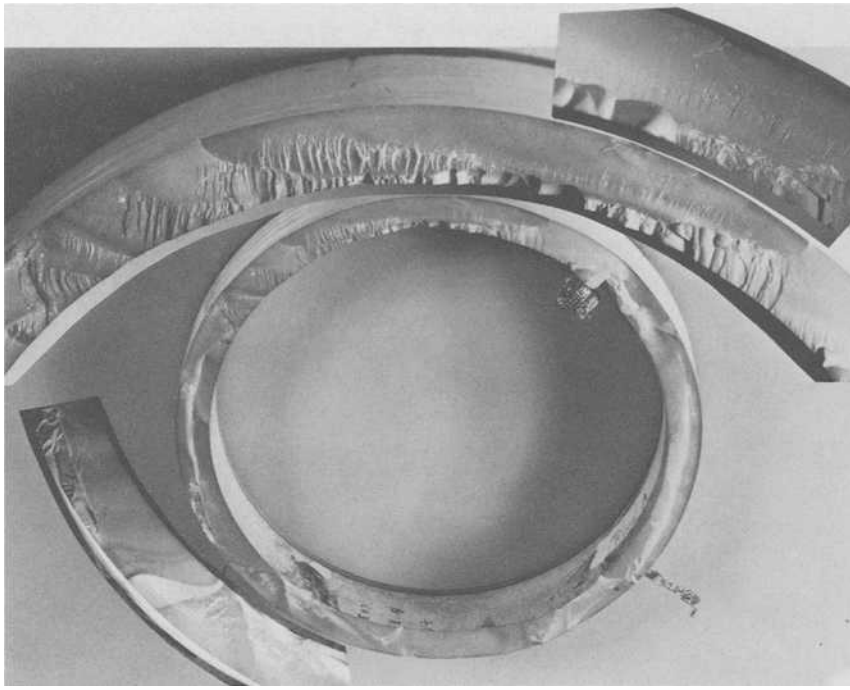

FIG. 56—*Transverse fracture of a PZT ring from a sonar transducer failed in shock loading. The complete transverse fracture of the ring is shown along with some higher magnification photos of sections of the fracture (including the fracture origin near the bottom center of the two progressively higher magnification, lower left-hand inserts). Note the absence of the typical mirror, mist, hackle, and crack-branching patterns, the presence of a variety of features attributed to the "ringing" of the specimen from the shock loading, and the resultant modulation of the crack front similar to that of Fig. 55.*

fracture features of glass rods tested under tension with some superimposed torsion. While the overall fracture mode was still Mode I, there were major changes from the normal mirror character (Fig. 60).

The remaining stress factor is that of thermal expansion anisotropy (TEA) stresses. The author and colleagues have reported that in addition to affecting fracture toughness and energy [*38,84,85*], TEA stresses can increasingly contribute directly to failure as the flaw-size-to-grain-size ratio decreases [*86*]. More recently, Lewis [*87*] has shown that the limited deviations of the Pyroceram 9606 data of Mecholsky et al [*7*] are real and related them to TEA stresses. Lewis's analysis provides a basis of estimating the strength above which and the mirror size below which such effects will have measurable effect on mirror sizes. Applying his criteria to other materials with large TEA stresses (MgF_2, Al_2O_3 and graphite (POCO)) or to related microstructural stresses in PSZ, shows that only graphite mirrors should be

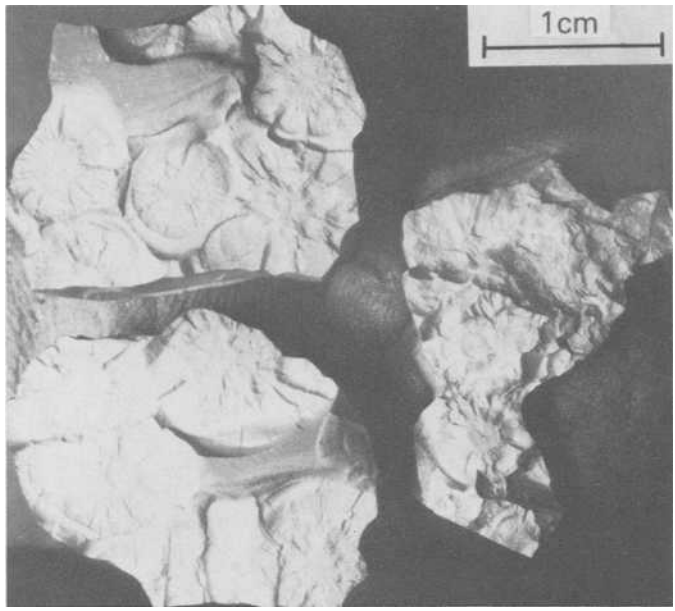

FIG. 57—*Samples of fracture mirrors on Pyroceram shattered by high-energy impulse loading. These mirrors do not vary significantly in size. Higher magnification SEM photos show no distinctive features other than possible larger microstructural features at the center of the mirror (indicating failure from intrinsic microstructural features). (Photo courtesy D. Lewis, NRL.)*

expected to show an effect of TEA on mirror size in the normally expected strength range; this is consistent with the limited graphite data (Fig. 61). Related to TEA stresses are the complex stresses that exist in the joint of two dissimilar materials, which can result in unique fracture patterns (Fig. 62).

Failure-Causing Flaws

Although a complete review of all the different failure-causing flaws cannot be undertaken here, it is particularly important to address at least some aspects of machining flaws. These are a common source of failure [*38,56,57, 63,64,88,89*], especially when processing becomes sufficiently acceptable that it limits the maximum processing defect size below the machining flaw size.

Fractography was a basic tool in demonstrating that two sets of machining flaws generally result from the typical abrasive machining operation of ceramics [*88,89*]. The first set of flaws forms along the base of, and hence parallel to, the machining grooves gouged out by the abrasive particles. The second set of flaws forms nominally perpendicular to the groove. These angular relationships relative to the groove, especially that of flaws 90 deg to

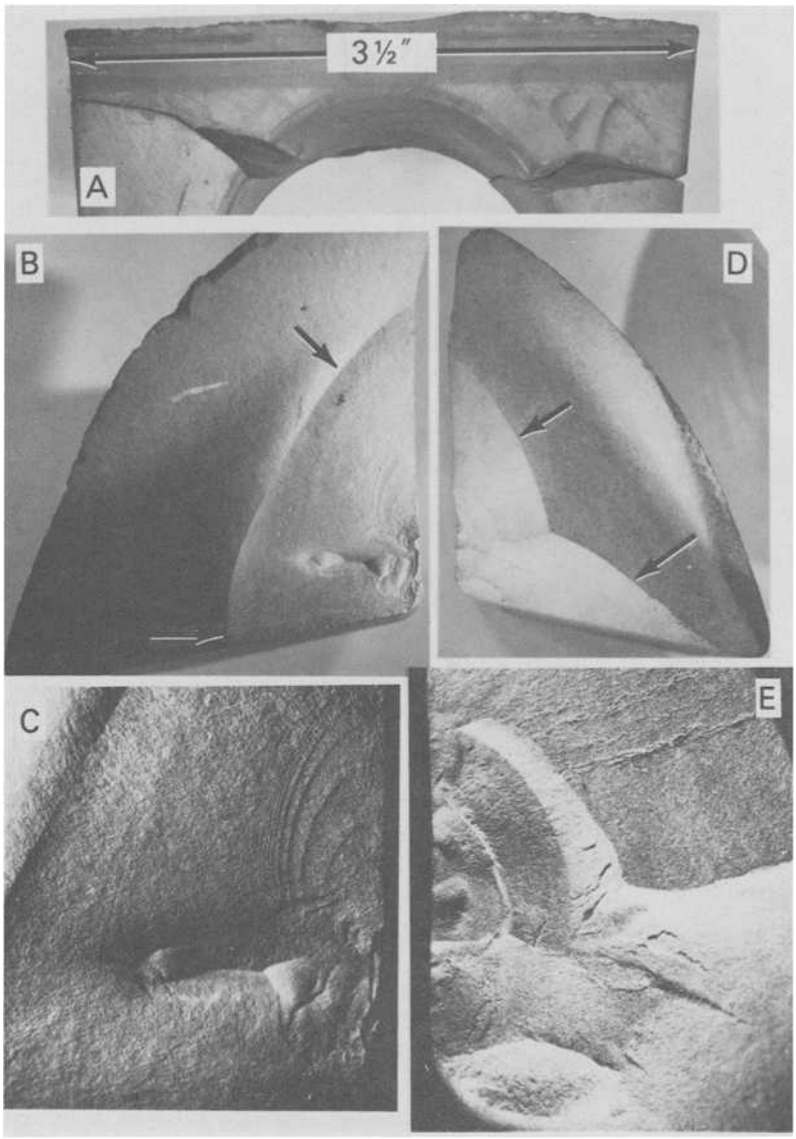

FIG. 58—*Fracture surfaces from a failed reaction sintered Si_3N_4 diesel engine piston. The top photograph shows the piston failure due to the two transverse fractures in the section surrounding the hole for the pin connecting the piston and the connecting rod. The underlying two sets of photographs show details of these two fractures; note the absence of distinct mirror, mist, hackle and crack-branching features. Also note some approximately semicircular features tentatively attributed to "ringing" of the specimen (attributed to stick-slip stresses from the rotation of the pin against the ceramic) and resultant modulation of the fracture.*

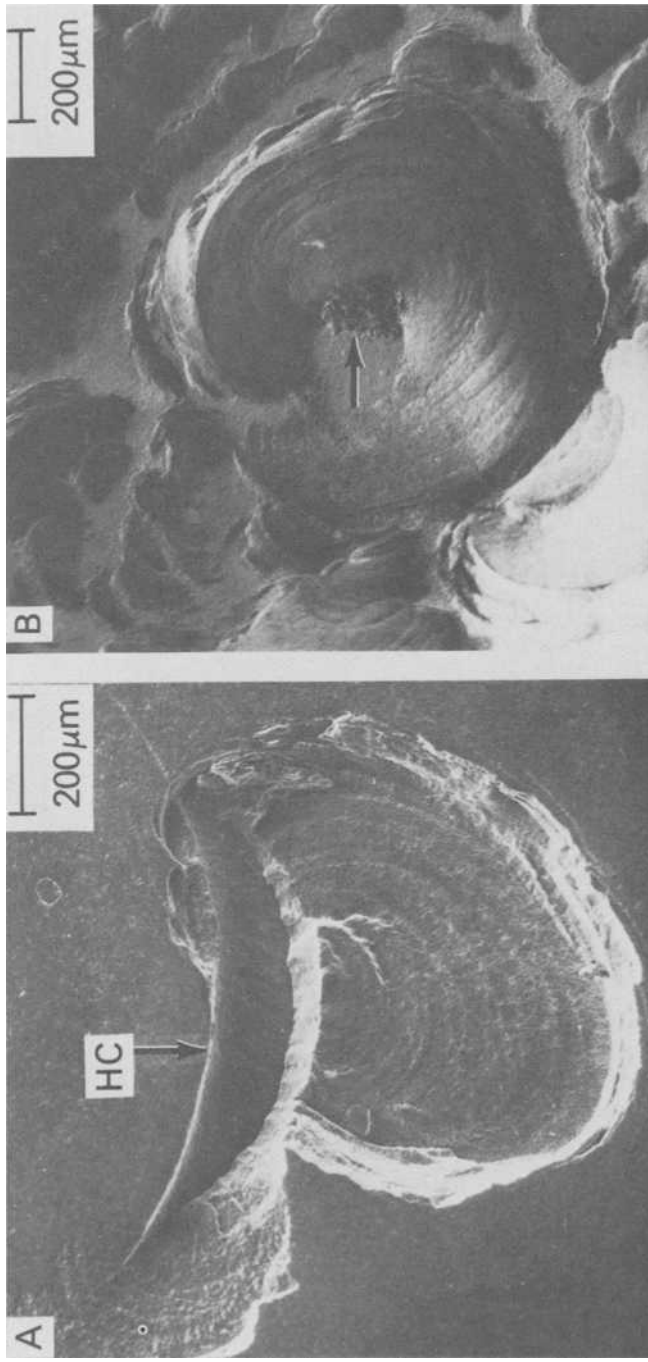

FIG. 59—*Spall failure in hot-pressed Si_3N_4 bearings.* (a) *Spall initiating from the periphery of part of a Hertzian cone crack* (HC). (b) *Large central spall from a processing defect (arrow) and subsequent surrounding secondary spalls. (Photos courtesy T. Yonushonisof, SKF.) Similar spalls from processing defects (pores) have recently been observed by the author on PSZ rolling contact fatigue test rods.*

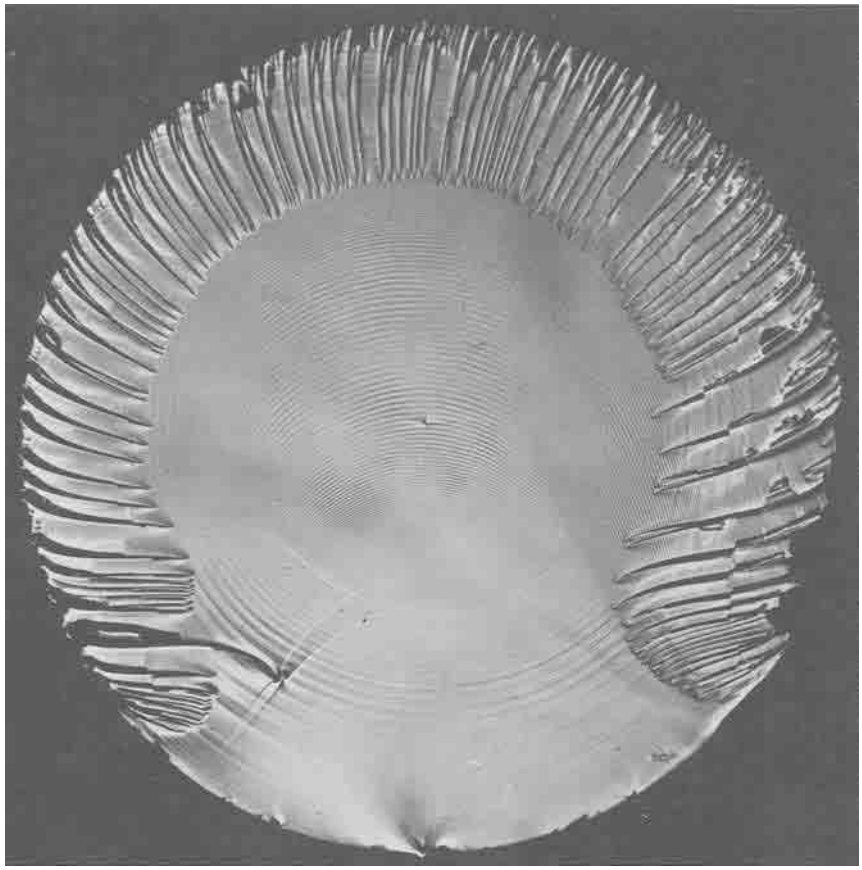

FIG. 60—*Lances formed on the fracture surface of a glass rod failed in tension with the superposition of a limited amount of torsional stress. The rod (~10 mm diameter) was ultrasonically modulated to produce timing marks on the fracture. Note the absence of the fracture lances in the bottom ~20% of the sample, which is suggestive of normal mirror behavior. Note also the nearly but not fully uniform onset of lances at a common radius, which appears to be independent of failure stress; however, the lance density appears to increase with failure stress. (Photo courtesy Dr. E. Sommer of Fraunhofer Institut für Werkstoffmechanik, who also provided additional technical input on such failure.)*

the groove, can be modified in single crystals or large-grain bodies due to preferred crack formation on certain fracture surfaces (for example, cleavage planes) [*88,89*]. Overall many flaws are simple in shape, with the periphery often fitting fairly closely the idealized pattern of semi-elliptical flaws. Even with an idealized periphery, however, there can be considerable complexity [*89*]: flaws are often not planar or show repeated boundaries and may overlap (Fig. 63). These features raise questions of possible repeated loading owing

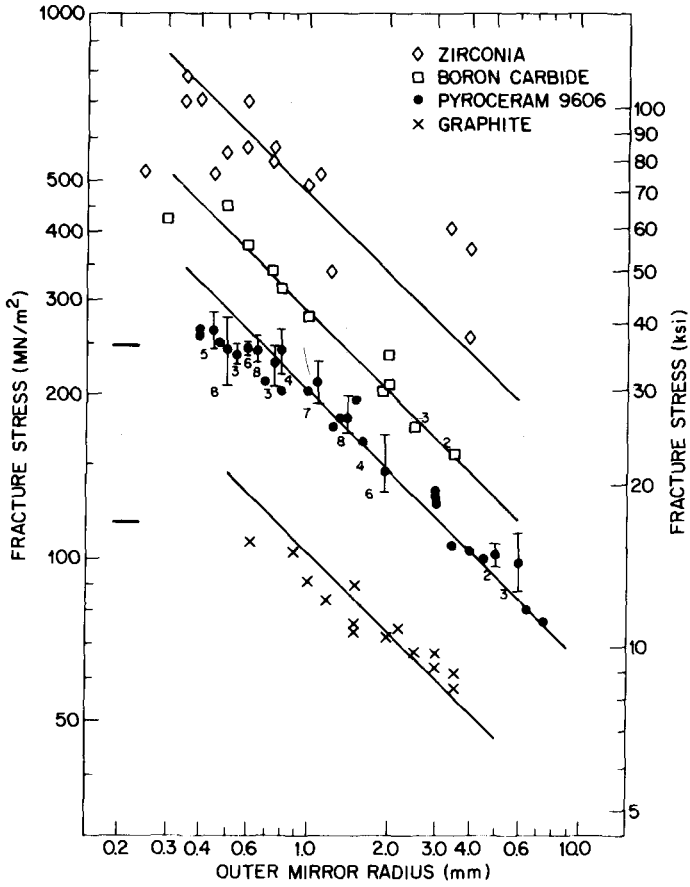

FIG. 61—*Proposed onset of the effect of stresses from TEA on mirror size. Estimates of the approximate fracture stress level at which TEA stresses would reduce the mirror size for a given applied stress are marked to the left of the graphite (POCO) and Pyroceram 9606 strength/mirror-size curves based on Lewis's* [87] *model. Both show evidence of deviations (confirmed by Lewis for Pyroceram). Zirconia would require ≥2000-MPa fracture stress. (Properties are not available to make an estimate for B_4C.)*

to repeated stick-slip phenomena or to reverberations of the stress pulse that initiated the flaws.

Another important issue recently raised concerns residual stresses that may be associated with the machining process. Marshall [*90*] has reported that an overall surface compressive stress is generated, while at the same time a deeper tensile stress may be locally present around cracks from the machining. He suggests both are factors in mechanical properties, the local tensile stress determining the aspects of local crack growth and the overall com-

FIG. 62—*Failed ceramic joint. Note the three patterns of approximately concentric rings that formed when dense hot-pressed disks of Al_2O_3 and CaO were hot pressed together and subsequently separated due to fracture during cooling. These rings may represent progressive stages of cracking as thermal stresses developed during cooling.*

pressive stress being a factor in the overall strength behavior. Marshall et al [*91*] have reported significantly lower R_i/R_f values (for example, $R_m/R_f \cong 5$) for glass failing from indent-induced flaws in various environments. They report that these reduced values are consistent with analyses of residual stresses and note that similar effects may hold for machining flaws. However, similar R_i/R_f values for failure from original machining flaws or subsequent slow crack growth, or from pores (corrected by their "bluntness" as discussed earlier), indicate much lower effects of residual stress for machining flaws, as does the generally broad agreement between K_{Ic}-values calculated from flaw sizes and failure stresses and those directly measured (for example, by double cantilever beam tests) [*17,38,55,57,85,92*]. Features are sometimes seen between the mirror boundary and the original flaw which may reflect initial crack growth due to these stresses. In general, fractography studies of the author and colleagues have taken the largest demarcation associated with the flaw as the flaw size and thus have probably generally compensated for initial growth due to these stresses. These furthest demarcations, assuming that they could be due to local stresses, are generally similar to flaws observed propagating from foreign inclusions (Fig. 48). Occasionally very large features are observed (Fig. 64), raising questions of different causes or mechanisms, and some features may not always have been observed

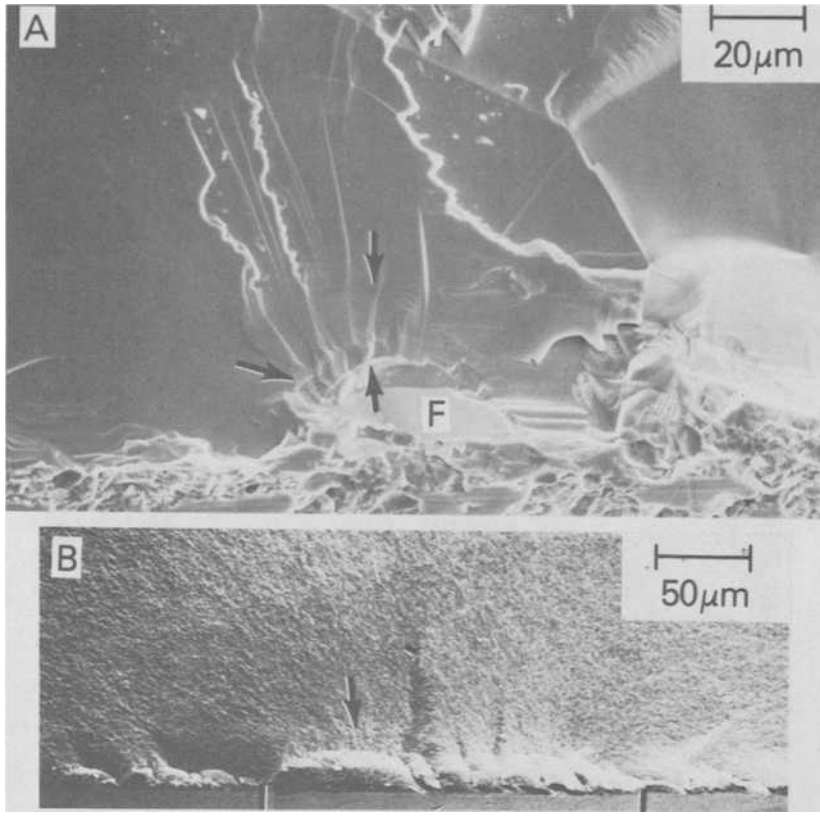

FIG. 63—*Multiple flaw boundaries.* (a) Y_2O_3 *sample fractured at 72.2 MPa (10.5* $\times$ 10^3 *psi). The machining flaw* (F) *is surrounded by three boundaries (arrows) and associate fracture steps or jogs in these steps. The flaw is much smaller than the large grain (the three lines to the right of and above the flaw are three sides of the grain in which the flaw is located).* (b) MgF_2 *disk failing biaxially at 68 MPa (9.85* $\times$ 10^3 *psi) from an elongated flaw (vertical marks) made up of a series of overlapping cracks. Note the lighter area above the left-hand side of the flaw (arrow), possibly above the right-hand portion also, which appears to be slow crack growth (see also Fig. 44). Also note the vertical fracture tails extending from irregularities of the flaw.*

or fully reflect all the effects of residual stresses. This may well have been a factor in the scatter of results calculated from fracture-initiating flaws observed by fractography.

One other aspect of the nature of the failure-causing flaws (which may also be related to test method) needs to be addressed. Tests of plates in tension typically appear to give lower B_i-values (Table 5). Further, as discussed in the next section and shown in Table 6, terminal velocity may be more rapidly approached in such plate tension tests. This might be due to failure starting from too small a crack relative to the starting notch common to most and possibly all of these plate tests, so that the flaw-notch combination behaves

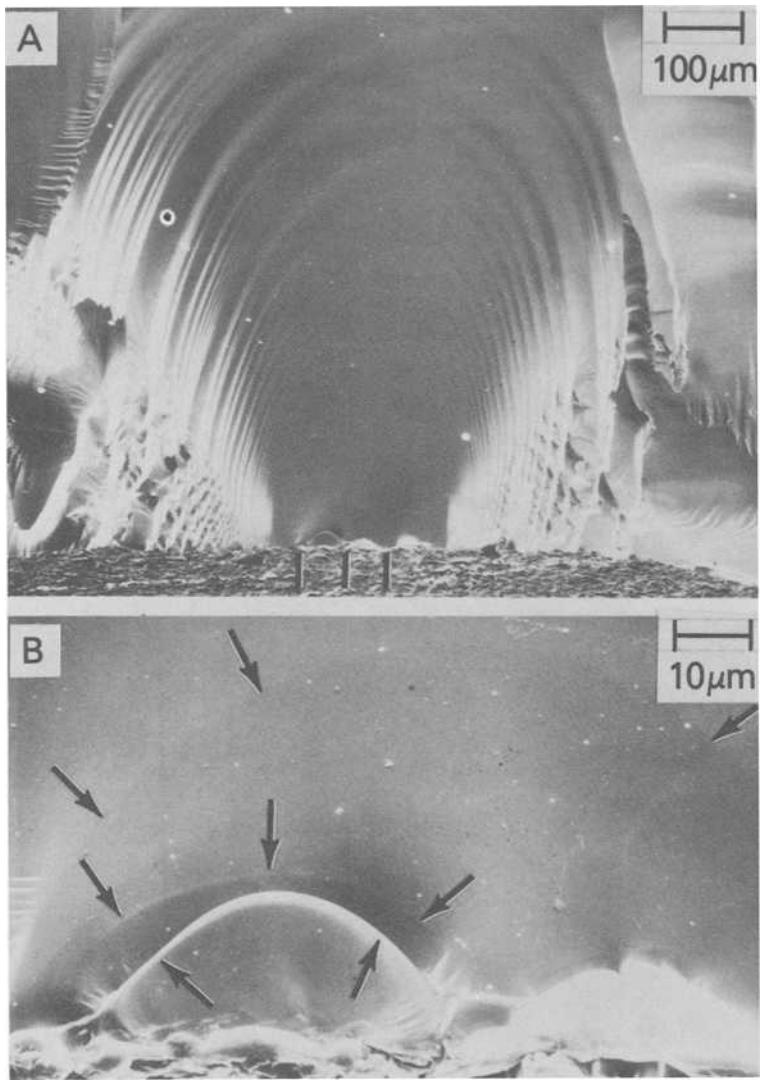

FIG. 64—*Unusually large crack boundary observed in a $MgAl_2O_4$ crystal fracture.* (a) *shows the cathedral fracture mirror, the onset of crack branching, and the original machining flaw.* (b) *Higher magnification of the flaw (vertical marks) and the much larger, not concentrically surrounding, semicircular feature (arrows) in this crystal with a {100} tensile surface and a ⟨100⟩ tensile axis fractured at 185 MPa (26.9 × 10^3 psi) at room temperature. Contrast the large size of this outer feature with the limited outer feature shown in Fig. 28.*

TABLE 5—*Comparison of* $\sigma_f\sqrt{R}$*-values (MPa·m$^{1/2}$).*

Material	Plate ($\sigma_f\sqrt{R_m} = B_m$)	Flexure ($\sigma_f\sqrt{R_h} = B_h$)		
	Anthony et al [93]	Johnson and Holloway [9]	Kirchner et al [6]	Rice
Al_2O_3	7.3	...	10	12
MgO	4.3	...	...	9.9
Glass	1.6	2.0	2.3	2.2

TABLE 6—*Ceramic crack velocity data.*

Material	Specimen	Method[a]	a/a_0 Measurement <0.9 VT[b]	Investigator	Ref
Glass[c]	plate	UM	3[d]	Field	96
SiO_2xl	plate	ERG/WL	3 to 5	Ball and Payne	97
Glass Al_2O_3xl	plate	WL	2 to 3	Anthony et al	93
Glass	plate	UM	3	Doll et al	98
Glass	plate	UM	3	Kerkhof	60
Glass	tube	WL	4 to 8	Aoki and Sakata	99

[a]UM = ultrasonic modulator; ERG = electrical resistance grid; WL = Wallner lines.
[b]a = crack length; a_0 = initial crack length; VT = terminal velocity.
[c]Field notes that this shape of curve (rapid initial rise of velocity) is typical of several other brittle solids.
[d]Obtained from Field's velocity/crack-length data by calculating a_0 (= 290 mm) from Field's data.

as a blunter flaw in direct analogy with the pore-crack situation discussed earlier. Otherwise, one must ask whether there is a basic difference between the behavior of a through-thickness and a semi-elliptical crack. Mecholsky and Rice [72] observed a deviation from a slope of $-1/2$ for σ_f-R_i data for larger bars tested in flexure and especially disks tested in biaxial flexure. Most and possibly all of the deviation appears to be due to R_i being larger than expected at lower σ_f-values, which appears to be associated with cracks going from semi-elliptical to through-thickness cracks. Correction for this change in crack character by using the fracture mechanics shape factors for semi-elliptical and through-thickness cracks in Eq 1 predicts the wrong trend. Correction for flaw shapes based on crack area appears to give the proper trend.

Mechanisms

General Mechanisms for Mirrors and Related Features

Defining the mechanisms of the formation of the various fracture features, especially in terms of quantitative theories, is fundamental to a complete

understanding of the mechanics of failure. Consider the formation of the fracture mirror and related features. It is generally agreed that the formation of mist, hackle, and crack branching represent nucleation of secondary cracks at, or possibly somewhat ahead of, the main crack front with no significant propagation for mist, limited propagation for hackle, and extensive-to-complete propagation for crack branching (depending upon whether the branching is completed to form a separate fracture piece of the material). These separate aspects of nucleation and propagation will be discussed later, along with some aspects of the generation of these features. We now consider some of the concepts of overall mechanisms involved in mirror and related feature generation.

Crack velocity has often been suggested as a basic determinant of the mirror, apparently because cracks typically reach a terminal velocity, usually about half the speed of sound. There are indeed possible correlations with velocity: it is generally observed that crack propagation from a blunt defect such as a hole or void accelerates faster, which correlates at least in a qualitative fashion with the earlier onset of mist, hackle, and branching [*60, 94, 95*]. Nevertheless, a number of observations suggest that while velocity may be a factor in formation of mirror and related features, it is not the basic determinant. Mecholsky et al [*3*] have pointed out that the approach to terminal velocity is typically asymptotic; therefore it is difficult to see how small increments of crack velocity could make such large changes in fracture character. Further, more recent measurements (Table 6) indicate that most of the acceleration of cracks occurs in shorter distances than originally thought, about three times the original flaw size in many cases. Also shown in Table 6 is some indication that the rate of acceleration of the crack may be dependent upon the nature of the tests without necessarily having a correlating shift in the location of the mist-hackle and crack branching.

Several other factors also appear to question a direct effect of crack velocity in determining these mirror-related features. Snowden's observation of significantly higher fractions of the terminal velocity under high impact loading and the absence of mist and hackle preceding branching [*77*] seriously questions a direct velocity correlation. The fact that there is not an obvious shift in macroscopic crack branching with predominately intergranular failure and the associated much higher local crack velocities (discussed in the section on Crackpath-Microstructural Interaction) also questions such a correlation. Similarly, local velocity variations (for example, along secondary cracks or along different local crack directions) question a velocity correlation.

The extensive application and validity of Eq 1 has clearly suggested stress intensity as a basic factor determining fracture mirrors and related features. This correlation is strongly reinforced by the successful normalization of flaw shape effects and the indication that this leads to universal constants (B_m, B_h, B_b). Kirchner's showing that the onset of mist as well as its termination due to stress gradients in flexure testing can be directly related to stress in-

tensities and that the toeing in of fracture mirrors at the surface can be related to a decrease in stress intensity near the surface [*100*] also adds support to this correlation.

On the other hand, recent analyses of Shetty et al [*101*] applying Eq 1 to flexure show that onset of mist—namely the mirror boundary (and hence also the onset of hackle and branching)—does not occur along lines of constant stress intensity (Fig. 65), and Lewis [*102*] has found that Eq 1 is an accurate representation of mirror, hackle, and branching boundaries. If these boundaries represent instantaneous crack front positions, then cracks do not propagate with a constant stress intensity along their periphery contrary to extensive assumption of such crack character. On the other hand, if cracks do propagate with a constant stress intensity along their periphery, then these boundaries do not represent instantaneous crack front positions; that is, points of each boundary form at different times. Recent computer analysis showing reasonable simulation of crack propagation and formation of mirror and related features along the crack periphery at different times [*103*] sup-

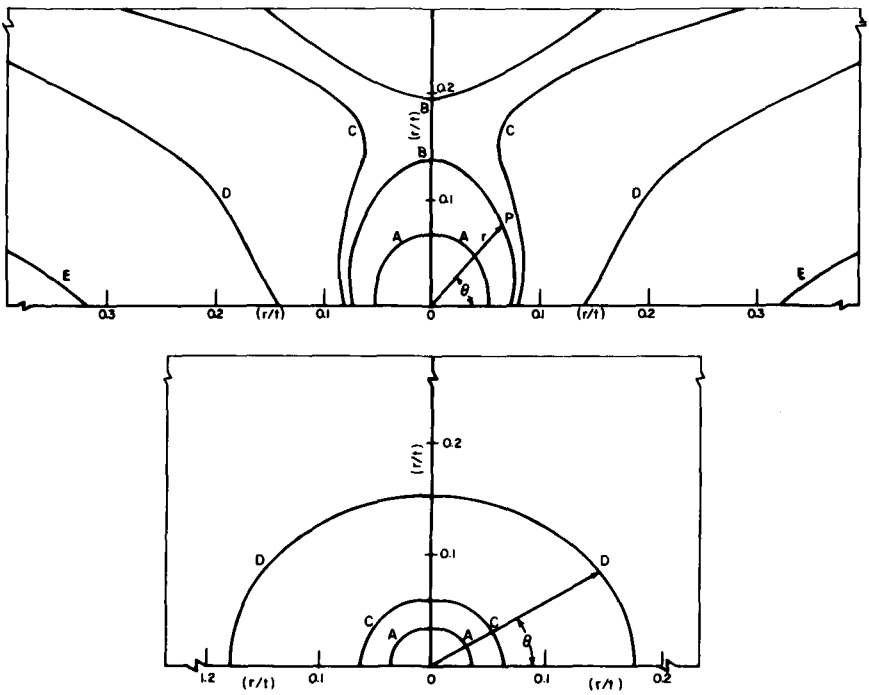

FIG. 65—*Comparison of mirror pattern models. The shape of mirrors in flexure specimens are sketched for cracks following* (top) *the empirical equation of Johnson and Holloway (Eq 1) and* (bottom) *constant stress intensity contours. These sketches (after Shetty et al* [101], *published by permission of the American Ceramic Society) show that since mirrors follow the patterns shown in the top sketch they clearly do not represent constant stress intensity contours.*

ports the concept of these features forming at constant stress intensity. Fractographic observations of branching by the author indicate that nucleation of branching occurs at different points and hence is quite consistent with different points on the branching front forming at different times (Fig. 66). The separate nature of mist and hackle is clearly consistent with their formating at different times along a crack front. Broadening of hackle so they overlap to form branches is also consistent with fracture character (Figs. 15, 66, and 67).

The occurrence of crack branching without mist or hackle and of multiple branches from a given branching point with increasing kinetic energy of impact raises the question of whether stress intensity is the fundamental or sole cause of the formation of mirrors and related features. If such is the case, this suggests a basic energy criterion, which would also be consistent with the correlations frequently seen for velocities since crack velocity can be related to mechanical energy. The earlier formation of mist and hackle with blunt flaws is also consistent with an energy criterion, since such failure typically involves more stored mechanical energy (strain energy density). Energy as a basic criterion is also consistent with stress intensity correlations, since any criterion based on stress intensity can be re-expressed in terms of strain energy density. Similarly, the larger angle of crack branching in biaxial testing can also be thought of in terms of the increased strain energy density associated with the biaxial nature of the stress; this can also be related to changes in the angle of the principal stresses associated with the crack propagation. However, common R_i/R_f values for uniaxial and biaxial testing question energy as a criterion.

A possible resolution of the energy versus stress intensity criterion is to think in terms of both nucleation and propagation as suggested by the qualitative concepts for mist-hackle and crack branching discussed previously. Thus nucleation may well be determined by stress intensity, whereas propagation may be more closely related to energy (strain energy density) criteria. Under normal crack propagation conditions the mist-hackle-branching sequence suggests that the nucleation condition is satisfied before the crack travels far enough beyond the nucleation stage to have enough energy for propagation; see Rice [*2*] for energy-distance relations. As one increases the mechanical energy input, however, such as in the case of high-velocity impact fracture, both conditions can be satisfied simultaneously. This could be the explanation of Snowden's results showing branching without mist or hackle formation. Similarly, branching in some single crystals (for example, MgO; see Fig. 10 in Ref *2*) without mist or hackle may be consistent with separate nucleation and propagation criteria. Nucleation of branch cracks on planes of lower fracture energy could also meet the energy criterion. The requirement of nucleation is reinforced by the earlier local onset of mist and hackle associated with a defect of other perturbation (Figs. 22), while the energy criterion may support the concept of different parts of a crack acting inde-

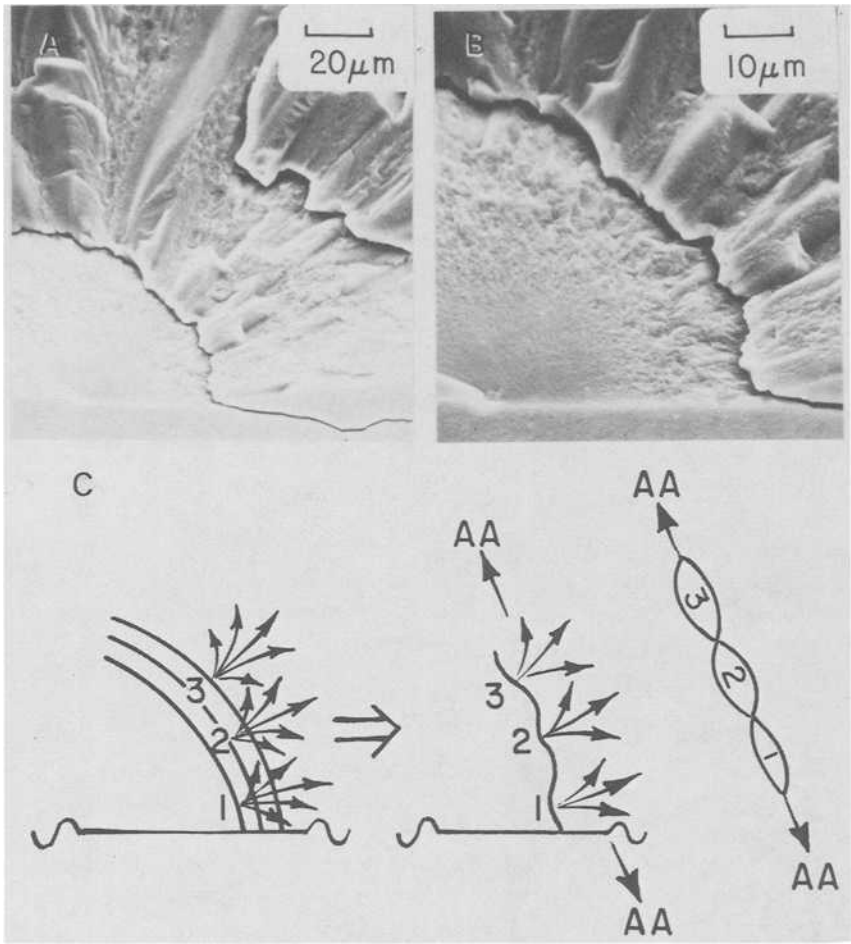

FIG. 66—*Crack branch formation.* (a) *Intermediate magnification SEM photo of part of the fracture mirror and the first and second stages of macroscopic crack branching of a CNTD SiC specimen fractured at 1250 MPa (181 × 10³ psi).* (b) *Higher magnification of part of the fracture mirror and the first stage of crack branching. The shallow angle of crack branching is consistent with earlier data and discussion (Table 1).* (c) *Schematics of a proposed mechanism whereby such crack branching occurs. Sections 1, 2, and 3 are indicative of constant stress intensity crack fronts at three different times, with separate nucleation of crack-branching areas at Points 1, 2, and 3. Their subsequent connection leads to the crack-branching profile shown in the middle sketch. Cross section* AA *(right-hand sketch) shows variations in cross section due to the lateral spreading of the larger hackle-like nuclei of this crack branching. These features are consistent with the crack branching shown in* (a) *and* (b), *especially recognizing that some of the fragile features have probably broken off. They are also consistent with the crack-branching wedges shown in Fig. 67.*

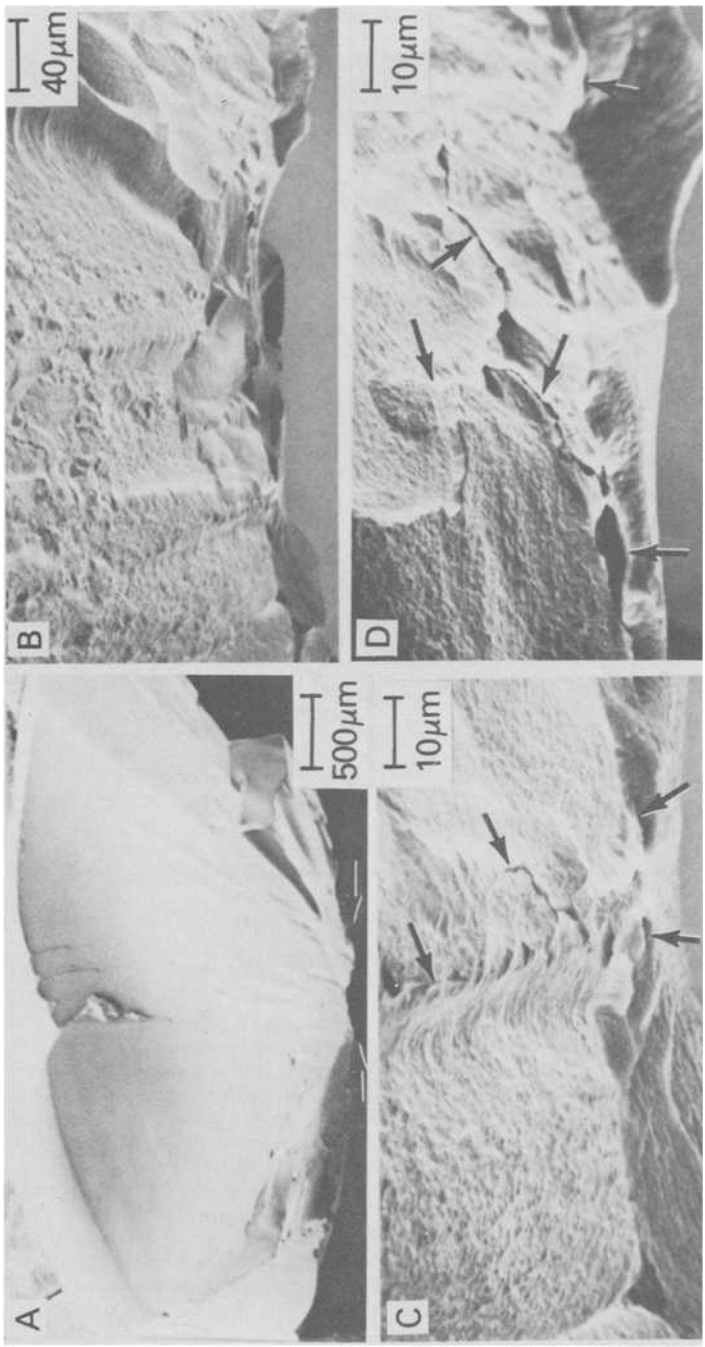

FIG. 67—*Crack-branching wedges from a crystallized glass (keatite) fracture.* (a) *Low magnification showing almost the complete wedge formed by branching. Fracture origin and mirror are on the mating pieces that fit the arc section between the arrows. Most of the arc section where branching begins is shown at intermediate magnification in* (b). (c) *and* (d) *are higher magnifications of parts of* (b). *The variation in thickness and overlapping cracks (arrows) are consistent with the model sketched in Fig. 66.*

pendently. The absence of mist and hackle on some areas of single-crystal fracture clearly shows that nucleation is a fundamental issue.

Nucleation of mist is the basis of Rice's explanation for the smaller mirror-to-flaw-size ratios in polycrystalline bodies compared with those in glasses [*53*]. He has proposed that this is due to the scale of mist nucleation being less than or equal to the size of individual grains, thus requiring grain boundary (γ_{gb}) or single crystal (γ_{sc}) fracture energies.[8] Since for glasses the fracture energies of overall crack propagation (γ) and secondary crack (mist or hackle) nucleation are the same, at first branching the requirement is 2γ. On the other hand, γ_{gb} and γ_{sc} cover the range of about $1/20$ to $1/3$ γ_{pc} where γ_{pc} is the typical (multigrain or polycrystalline) fracture energy. If one assumes that mirror sizes are linearly related to fracture energies, mirror-to-flaw-size (R_m/R_f) ratios should be proportional to the ratio of fracture energy requirements for crack propagation (γ_p) before branching to that at mist initiation (γ_m):

$$(R_m/R_f)(\gamma_p/\gamma_m) = \text{a constant} \tag{6}$$

Since for glasses $\gamma_p/\gamma_m = 1/2$ and $R_m/R_f \cong 12$, and γ_p/γ_m for polycrystals is $20/21$ to $3/4$, this gives R_m/R_f for polycrystals of ~ 6 to ~ 8, in good agreement with experimental observations. This concept implies a wide area of mist formation (due to its earlier onset) in finer grain materials where hackle is multigrain in size. It also implies that as the grain size increases to about the hackle size, its onset of formation will move toward the fracture origin due to reduced γ. Although more study is needed, limited observations support these implications (Fig. 5). Analysis of single-crystal behavior (presented below) and its agreement with experimental observations lend substantial support to these concepts.

Single-Crystal Mirror and Related Feature Formation

Consider the details of mist, hackle, and crack branching in single crystals: their varying geometrical character, partial absence, and substantially variable mirror-to-flaw-size ratios. Substantial progress has been made in this area. The previous apparent total absence of mist and hackle on some crystal fractures is now seen as being caused by specimen size and strength being too low to allow seeing mist and hackle because of much larger R_i/R_f ratios. This in turn is part of the broader correlation of whisker-lance mist-hackle and higher R_i/R_f ratios on preferred fracture planes and arc mist and hackle and lower R_i/R_f ratios on secondary fracture planes. Thus three inter-

[8]Clearly there must be a lower limit to this. As this grain size limit is reached, R_i/R_f ratios should approach those of normal glass fractures.

related factors are believed to play a major role in determining the geometry of these single-crystal mirror and related features [*104*]:

1. Orientation and fracture energies of possible alternative fracture planes (mirror surface) relative to the crack.
2. Angular relationship of the normal to the crack and possible alternative fracture planes, which determines the amount of Mode I, II, or III fracture.
3. Rotation of principal stress away from the direction of crack propagation; most analyses show this occurs as crack velocity increases.

The author had previously recognized Factors 1 and 3, but lacked a factor that depended upon direction, which is clearly required by the geometrical character of these mirrors. The absence of mist and hackle features over certain sectors of a fracture requires a factor determined by directions rather than just planes. It was clear that the planes of fracture themselves do not involve any directional factors. Factor 2 must clearly play a major role in determining on which planes micro- and macro-branching can occur. For any given possible fracture plane, however, Factor 2 by itself is independent of crack direction and hence cannot explain the observed directional dependence. Combining Factors 2 and 3 *does* provide the type of directional dependence needed: a dependence of fracture on the crack direction on a given plane which is dependent on the crystallography of that plane [*105*]. This results from Factor 3 introducing a directional dependence for the amount of Modes I, II, and III failure for the crack to deflect onto any other fracture plane.

Factor 1 provides an explanation for the different mirror-to-flaw-size ratios (R_m/R_f) with different orientations within a given crystal. Fracture initiating on a plane in a crystal having a higher fracture energy than other planes intersecting it at possible branching angles (< 90 deg) should lead to branching on a micro- or macro-scale in a shorter distance relative to the initial flaw size than in glasses, because the fracture energy controlling each secondary crack nucleation and propagation is less than that for the crack prior to branching. This is essentially the same as the situation noted previously for the earlier onset of mist in polycrystalline materials relative to glasses. On the other hand, when fracture initiates on the lowest fracture energy plane in a single crystal, it must propagate further, often substantially further, relative to the initial flaw size than a crack in glass or polycrystals in order to start generating mist or hackle, because the fracture energies for secondary crack nucleation and propagation are higher than for the main crack propagation. These ratios are one of the factors that can be used in estimating the ratios of fracture energies for different planes once one knows the secondary planes involved in mist, hackle, and crack branching.

Factors 2 and 3 provide explanations of mirror character to the extent that fracture preferences for different crystal planes are known (for example, for the fracture tongues seen on metal and ceramic crystals) [*105*]. In iron, molybdenum, tungsten, and MgO crystals the primary [100] and secondary

[110] cleavage planes do not provide a reasonable, low-enough fracture energy and a sufficiently Mode I path to allow cracks to deflect from [100] cleavage planes at or near ⟨100⟩ directions (Fig. 40). Higher stress failures, having higher stress intensities and strain energy densities, can more closely approach this forbidden, or more difficult, zone near ⟨100⟩. Similarly, {111} primary and {110} secondary cleavage in chromium are consistent with the indications of mirror tongues in ⟨110⟩.

Further understanding of crystal fracture patterns will require more study of the applicability of the foregoing criteria. For example, these criteria address the issue of which directions and on which planes propagation will or will not generate mist and hackle, but not the issue of nucleation of these features. Dislocation and possibly atomic defects will be suggested as a possible source of nucleation below. Specific evaluation will require detailed measurements of the fracture planes involved in the mist and hackle on single crystals, detailed measurements of the fracture energies of different crystal planes, and better understanding of mixed-mode failures. It may be feasible to predict the fracture patterns of some crystals by using fracture energies of different crystal planes (supplemented by estimates of fracture energies using surface energy data where fracture energies are lacking) and incorporating these with crystallography and mixed-mode failure in computer programs. Iterative evaluation of fracture energy and mixed-mode failure parameter estimates may provide a major opportunity for advancing the understanding of both mixed-mode failure and fracture energies within single crystals, thus improving our understanding of the micromechanics of failure.

A fourth factor, *dislocations* (and possibly atomic defects), may be important in single crystals. Gilman [*106*] has shown that screw dislocations are a basic source of cleavage steps on lithium fluoride (LiF). Many have questioned, however, whether dislocations (implying slip) are a factor in fracture of hard ceramics. Weiderhorn et al [*107*] believe that the absence of any mobile dislocations associated with arrested cracks in sapphire argues against any dislocation activity associated with fracture. They argued against the validity of Guard and Romo's results [*108*] showing X-ray evidence of slip associated with fracture surfaces in polycrystalline Al_2O_3. Such dismissal of Guard and Romo's results neglects two important factors that could affect dislocation activity:

1. *The polycrystalline character of Guard and Romo's specimens* means that significantly higher stresses occur due to thermal expansion mismatches between grains as well as local redistribution of applied stresses, especially near grain boundaries, due to elastic anisotropy effects not found in single crystals. The polycrystalline character may also result in greater fracture on planes of different orientations and hence be more favorable for dislocation activity than in single crystals.
2. *Crack dynamics*—the rotation of the principal stress and high strain

rate (shock) effects that may change dislocation activity over that associated with a crack arrested after relatively low velocity motion.

Three factors indicate that dislocations may be associated with fracture:

1. Rice [*2*] has shown some correlation of higher mist-hackle density with slip bands in MgO, and several orders of magnitude increase of etch pit density in mist and hackle versus mirror areas on MgO fractures. More importantly, Becher [*109*] has shown a two-to-four order of magnitude higher etch pit density in mist and hackle versus mirror regions on sapphire fractures.
2. Lankford and Davidson [*110*] have reported electron-channeling results indicating deformation of fractured Al_2O_3 grains.
3. Grown-in (sessile) dislocations may also be sources of cleavage steps.

Gilman's [*106*] observation that the screw component of dislocations caused cleavage steps (Fig. 68*a*) apparently did not consider directional effects. Changing the angle of the screw component to the cleavage plane should only change the height of the step, giving some directional aspect to fracture steps from screw dislocations. Gilman considered propagation only parallel with the plane of the dislocation loop; however, propagation at other angles on the same plane (Fig. 68) or different planes should give similar steps. Thus such interaction does not appear to have much dependence on direction (contrary to the present author's earlier feeling that slip might provide the directional dependence needed to explain single-crystal mirror character). Furthermore, the essential factor in such step creation is the stacking of a few atoms along the core of the dislocation where the cleavage plane intersects the dislocation (Fig. 68*b*). This raises the possibility that some type of atomic defects (for example, certain cluster defects) might also be sources of cleavage steps. Either this hypothesis or the concept of dislocations in glasses [*111*] would be an explanation for possible intrinsic sources of cleavage steps in glasses, supplementing possible microstructural defects such as microvoids and heterogeneities.

Dislocations (or defects) may be particularly pertinent to the generation of whisker or lance mist-hackle. Firstly, there is considerable similarity between this type of hackle and typical cleavage steps. In fact, generally little or no difference can be seen between fracture steps extending from the origin itself and whisker or lance mist-hackle (Fig. 38). Secondly, nucleation of such mist-hackle by dislocations provides a possible answer to the question of how a crack gets deflected off a preferred fracture plane. The characteristic $\sigma_f(R)^{1/2}$ relation requires that dislocations be generated at the appropriate σ-R levels or that nucleation is not feasible or effective until the appropriate σ-R levels (due to Factor 2 or 3 noted earlier). The latter requirement seems more important in view of the limited directional dependence of fracture step generation from screw dislocations.

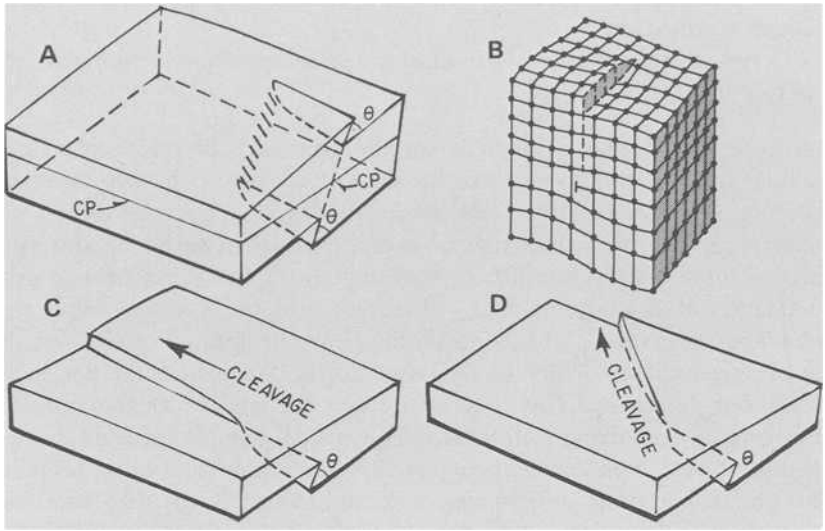

FIG. 68—*Schematics of possible formation of cleavage steps from screw dislocations.* (a) *Screw dislocation at an angle to the cleavage plane* (CP). (b) *Atomic arrangement of a screw dislocation and the related edge component; this sketch is in a different orientation than* (a) *to show the edge dislocation component. Note that cleavage on a plane at an angle (for example, perpendicular to the screw dislocation, as shown by the plane with slash marks between atoms) will lead to a step, but that cleavage on the plane of the screw or parallel to it will not give a step (hence no effect of the edge dislocation). Thus the cleavage step is due to the shift in atomic planes right near the screw dislocation, and these steps form over a wide range of crack propagation angles so long as the fracture plane intersects the screw dislocation.* (c) *Bottom half of the sample of* (a) *after cleavage along the cleavage plane from the right-hand edge of the sample. This is similar to the sketch of Gilman* [106], *except here the possibility of the screw dislocation not being normal to the plane is shown.* (d) *Bottom half of the fracture plane if the initiation of cleavage is moved around to the corner or part way along the front surface of the sample, changing the direction of cleavage step as shown.*

Mode of Polycrystalline Fracture

Consider intergranular versus transgranular failure. Basic mechanics of this phenomenon are clearly complicated by the frequent tendency for pores and impurities or second phases to occur preferentially at the grain boundaries, hence enhancing intergranular failure. The present author submits, however, that these factors have been far too casually cited as an overall explanation for the observed fracture mode trends. Lower fracture energies of grain boundaries (for example, by 50%) predicted on the basis of lower boundary surface energies are also cited as a reason for intergranular fracture. Nonetheless, two factors show that there is substantial compensation for such lower boundary fracture energies:

1. Intergranular fracture involves nearly twice the fracture area as transgranular fracture.
2. Very substantial Mode II fracture must occur with intergranular fracture (Fig. 69).

It is suggested that a rationale for the grain size dependence of intergranular fracture can be provided in terms of the following micromechanics concepts. Consider first the trend for increasing transgranular failure with increasing grain size in materials of cubic structure. The elastic anisotropy (EA) of these materials results in perturbation of the stress field at grain boundaries. It is suggested that enhancement of the stress at some grain boundaries near the tip of the crack (and generally approximately normal to the principle stress so that Mode I fracture is dominant) may fail shortly ahead of the crack tip. This commonly allows the main crack to more easily propagate by connecting with these microcracked grain boundaries ahead of the crack front, often enhancing intervening intergranular fracture (Fig. 70). This process can occur only so long as there is a sufficiently high stress over favorable grain boundaries just ahead of the crack front to cause intergranular failure. As grain size increases and this condition ceases to be met, the crack will switch more to transgranular failure.

Materials of noncubic crystal structure, on the other hand, have permanently built in stresses concentrated at the grain boundaries owing to thermal expansion anisotropy (TEA). These TEA stresses, which are independent of (and hence exist in addition to) elastic anisotropy throughout the body of anisotropic materials, lead to enhanced intergranular failure at larger grain sizes due to the superposition of TEA and the applied stress (including the effects of elastic anisotropy).

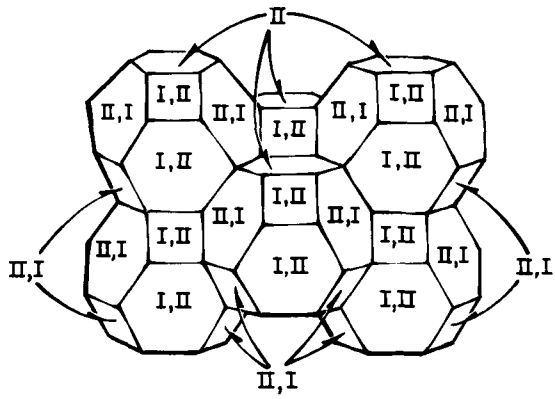

FIG. 69—*Schematic of intergranular fracture. The fracture mode for each boundary facet is marked based on the fracture stress being perpendicular to the page. Where two modes are involved, the first listed should be the dominant one.*

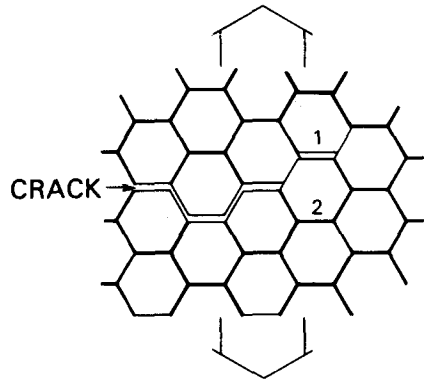

FIG. 70—*Schematic of possible intergranular fracture mechanism. The main crack from the left nucleates a secondary crack ahead of it at Boundary 1 because of the combination of elastic anisotropy, orientation (giving mainly Mode I failure), and proximity to the crack tip (closer than Boundary 2). Having nucleated this secondary crack, the main crack can now link to it by fracture of the less favorably oriented intervening boundary. This mechanism becomes less viable as grain size increases, since stresses are reduced on boundaries ahead of the crack, and thus provides an explanation for decreasing intergranular fracture in cubic materials as grain size increases.*

This effect of grain size on transgranular fracture at finer grain sizes is caused by the fact that crack nucleation along grain boundaries due to locally concentrated stress is now known to definitely increase with increasing grain size; that is, crack nucleation is of decreasing occurrence at decreasing grain sizes [*112*]. Both EA and especially TEA should enhance stress corrosion even in finer grain size bodies due to the higher local stresses, thus enhancing intergranular failure during slow crack growth as noted previously. Note also that the observations made earlier about the greater area of grain boundary fracture and hence greater local velocity for the same overall average velocity would allow intergranular failure at low crack velocity such as in slow crack growth. Where transgranular failure is feasible, however, this velocity-fracture mode effect may favor transgranular failure at higher velocities. Such transgranular fracture would initially be smooth due to the limited stress-intensity/strain-energy-density available to allow significant crack deflection or wandering.

On the other hand, at still higher velocities where crack branching can occur, the allowance of two cracks and differing crack angles along with higher stress intensities and strain energy densities can again enhance intergranular failure. This is consistent with the observations of enhanced intergranular failure further from the fracture origin, presumably outside the fracture mirror area. This interpretation appears to be inconsistent with proposals made by Kirchner [*50,51*] concerning increases in intergranular failure at and beyond certain distances from the fracture origin. Kirchner proposes that (1) the flatter transgranular fracture around the origin is a region of slow crack

growth rather than fast fracture, and (2) that the increasing fracture roughness, due in part to intergranular failure beyond this, arises from increased crack stress intensity meeting criteria for higher fracture toughness modes of failure. A basic difference between Kirchner's and the author's interpretation appears to be the question of EA and TEA stresses contributing to failure. If these stresses contribute to failure, Kirchner's calculations of the critical stress intensity neglecting these stresses are in error, occurring at substantially too large a distance from the fracture origin. Clearly this is an area for further study.

Applications and Improvements of Fractography

There are basically two classes of applications in fractography, scientific and technological. Both of these depend upon the same capability: interpreting fracture markings in terms of mechanics hypotheses or theories. The limited extent to which fractography has been utilized for this purpose is both surprising and disappointing, especially since the uncertainties of fractography are really no greater than those of most theories. On the other hand, indirect attempts to verify fracture mechanics concepts and theories (for example, by comparing predicted and observed failure stresses) are used extensively. One should not view either of these approaches as a replacement for the other but as complementary.

Several important examples were cited earlier for the scientific applications of fractography. One of the broadest is more detailed experimental study and theoretical modeling of the micromechanics of single-crystal failure to extend our knowledge of mixed-mode failure and the orientation dependence of fracture energies in single crystals. Another important example cited earlier is that of verifying whether cracks actually assume a constant stress intensity along their periphery during propagation and whether micro- and macro-branching represent a single, continuous, simultaneous event. Besides such general scientific application to typical fast fracture failure, there are important applications to fracture mechanics tests. Rice et al [*113*] showed that study of fractures of double cantilever beam specimens explained some variations of fracture energy results by microstructural factors. More recently, McKinney and Rice [*114*] have shown that fracture of glass notch beam specimens often failed to satisfy the assumed condition of a through-thickness crack at the base of the notch. Variations in results correlated with variations of the character of the crack extending from the notch. Ingel [*115*] has shown that similar variations of notch beam tests of PSZ are related to variable crack character at the base of the notch as revealed by fractography.

Technological applications of fractography are already extremely extensive and will grow with increased scientific understanding of the mechanics leading to the formation of various fracture features. Two general applica-

tions are identifying the sources or causes of failure and estimating the stress of failure where this is unknown (for example, in thermal shock, impact, and other types of applications where stress is typically not measurable). Very often, identifying the source of the failure is of most importance. However, both the origin of, and stress at, failure are usually desired if the stress is not measured. Figures 13, 55, 56, 58, and 59 illustrate several examples from studies related to practical applications. References *78, 80* to *82,* and *116* to *118* also give several applications.

There are other applications of fractography. Identifying the direction of crack propagation can be important in some cases. Failure analyses of small electronic tubes losing adequate vacuum after variable periods of time have shown that connection of some of the pores in the ceramic wall of the tube could allow the expected gas in these pores to reach the interior of the tube, hence raising the vacuum above operational levels due to the small volume of the tubes [*119,120*]. Cracks were observed in the devices, and fractography subsequently showed that the cracks did propagate from the interior of these devices into the walls of the tube, thus providing for progressive connection of more and more pores with the interior of the tube. (The presence of gasses was confirmed by other investigations in the author's laboratory by crushing the ceramic vacuum system and observing the release of gas.)

It has been useful to briefly consider some of the advances in the understanding and observation of fractographic features that will improve the application of fractography. Clearly, though, further clarification of the many areas of limited data or incompletely defined mechanisms noted in this paper is a substantial need. Several general needs can be seen. The first is more detailed study of the character of mist-hackle and crack branching to better define their mechanisms of formation. Studies of single crystals to define the character and planes of their occurrence and of the character of mist and hackle seem particularly important. Also needed is more study of fracture features within the mirror, especially of the flaws and their stages of propagation to failure.

Another need is to improve the accuracy of measurements for quantitative purposes. While it is generally true that measurements can be made quite accurately at present, there is frequently a judgment factor involved (where do mist, hackle, and crack branching actually begin?), since there is often some uncertainty in these boundaries as noted earlier. Standardization of the measurement criteria (by analysis of topography, for example, to more consistently define the onset of mist and other features) deserves serious investigation. Correction by computer techniques of fracture dimensions for the angles of the features relative to the angle of observation would be useful. Also, knowledge of whether or not computer evaluation of topography can identify mirror and related fractures or other important features on those fractures having too rough a topography due to other factors (for example, crack interaction with the microstructure such as grains, second-phase particles, or pores) could be valuable.

Summary and Conclusions

The occurrence and character of ceramic mirrors and related features (mist, hackle, and crack branching) have been reviewed in glasses, polycrystalline bodies, and single crystals. The finding that the product of the failure stress and the square root of the distance to the onset of each of these features is a constant has been shown to be widely applicable, provided that stress gradient and flaw characteristics are properly accounted for. Past work has indicated that accounting for such factors gives a universal "mirror constant." Support for this concept was provided by demonstrating that correcting for flaw "bluntness" appears to bring results for specimens failing from blunter flaws such as pores into agreement with results from failure from sharp (machining) flaws. In addition, it was suggested that asymmetrical mirrors are often associated with failure from irregular flaws or flaws having a substantial angle to the stress axis (that is, involving mixed-mode failure). The fact that portions of such flaws may initially act as independent flaws, or that only part of the flaw may cause failure with resultant different mirror sizes associated with those corresponding portions of the flaw, also appears to agree with such a universal mirror constant.

Smaller mirror-to-flaw-size ratios in many polycrystalline bodies were attributed to lower fracture energies for initiation of secondary cracks on the scale of the grains, namely involving fracture energies approaching, or equal to, those of single crystals or grain boundaries as opposed to the polycrystalline fracture energy required for overall crack propagation. This concept was substantially reinforced by the observation of a much broader range of mirror-to-flaw-size ratios observed in single crystals. Very large ratios were observed on primary fracture planes where secondary crack nucleation and propagation can occur only by deviating onto planes which have higher fracture energies. Correspondingly lower mirror-to-flaw-size ratios occur where failure initiates on secondary fracture planes so the secondary cracks can then nucleate and propagate on lower energy (primary fracture) planes.

This concept of mist representing nucleation of secondary cracks, hackle representing some propagation of these, and macroscopic crack branching representing extensive propagation of secondary cracks was further reinforced and refined. Firstly, it was demonstrated that macroscopic crack branching can commonly involve either forming two separate branches without the main crack continuing or can involve two separate branches with the crack continuing just as had been observed previously for mist and hackle. Secondly, it was shown that actual fractographic evidence as well as computer simulation supports the concept that macroscopic crack branching begins at different points along the crack front at different times and hence is a logical extension of hackle formation and in fact may often simply be formed by spreading of hackle features perpendicular to the direction of crack propagation. Such lateral spreading also raises questions about the validity of velocity

as the basic criterion for determining the formation of these fracture features. It was suggested that stress intensity may be a more fundamental factor for nucleation and that an energy (strain energy density) criterion may be more fundamental to propagation. In most circumstances, the nucleation criterion is satisfied first, with further propagation needed to meet the energy criterion for maintaining propagation of branches, hence leading to the characteristic mist-hackle-crack branching sequence. However, with greater stored mechanical energy (as from a blunter flaw) or especially from high-velocity impact, propagation and nucleation may be simultaneously satisfied, which would provide an explanation for the occurrence of crack branching in the absence of mist and hackle formation.

Intergranular versus transgranular mode of fracture was also discussed. It was noted that substantial mixed-mode failure must accompany intergranular failure. This at least in part compensates for possible lower fracture energies of grain boundaries. Elastic anisotropy and thermal expansion anisotropy effects were cited as possible causes of the grain size dependence of fracture mode, namely increasing transgranular failure with increasing grain size in cubic materials but reducing transgranular failure in larger grain size bodies of anisotropic crystal structures (for example, Al_2O_3). The importance of studying the changes in mode of failure instead of simply giving an overall characterization of intergranular or transgranular failure was stressed. The flat transgranular fracture regions often observed around fracture origins in many polycrystalline samples followed by the increased roughness and often associated increased intergranular failure have been interpreted by this author as respectively the mirror and mist-hackle areas due to secondary crack nucleation on lower energy (grain boundary) paths. This is in contrast to Kirchner's interpretation of respectively slow crack growth and higher levels of stress intensity allowing fracture on higher fracture energy surfaces. Finally, it was noted that there may be significant local velocity differences between intergranular and transgranular failure and that these should be clearly accounted for when measuring velocities and considering velocity as a criterion for formation of key features.

Extensive evidence showing a wide variety of single-crystal fracture features was presented. It was also shown, however, that some definite patterns emerge; for example, whisker or lance-like mist-hackle forms mainly on primary fracture planes, and mist-hackle consisting of arc segments is primarily, if not exclusively, associated with fracture initiation on secondary planes. The progressive increase in arc-rib mist-hackle amplitude and the resultant transition of this to crack branching also support the concept of these three sets of features being progressive stages of the same phenomenon. It was pointed out that extended observation of no dislocation activity associated with arrested cracks in hard ceramics is not necessarily grounds for assuming that dislocations cannot be involved with propagating cracks due, for example, to velocity effects. Evidence of dislocations associated with mist and

hackle in ceramic crystal fractures was also cited. Further, consideration of screw dislocations as sources of fracture steps and possibly whisker-lance mist-hackle showed that formation of such features may occur over a wide variety of angles and might also occur from some (clustered) atomic defects. Substantially more research and understanding are needed in this area. It seems, however, that crack interaction with slip does not appear to provide significant directional dependence to the formation of fracture steps and hence does not by itself explain the directional dependence of the formation of mist and hackle. It is instead now seen that the angle of the principal stress (which can change with velocity) and the resultant amount of Mode I failure this would result in on other fracture planes provide a directional factor needed to explain the mirror tongues and other absences of mist and hackle around certain directions in single-crystal fractures.

Finally, some aspects of the characteristics of flaws causing failure in ceramics have been reviewed. The issue of residual stresses associated with flaws from machining was discussed and possible evidence of limited slow crack growth from such flaws shown. Evidence for initial flaw formation around some inclusions has also been indicated. These were cited as important areas for further fractographic studies.

References

[1] Frechette, V. D., *Proceedings of the British Ceramic Society*, Vol. 5, Dec. 1965, pp. 97-106.

[2] Rice, R. W. in *Surfaces and Interfaces of Glass and Ceramics*, V. D. Frechette et al, Eds., Plenum, New York, 1974, pp. 439-472.

[3] Mecholsky, J. J., Jr., Freiman, S. W., and Rice, R. W. in *Fractography in Failure Analysis, ASTM STP 645*, American Society for Testing and Materials, 1978, pp. 363-379.

[4] Richerson, D. W., *Modern Ceramic Engineering: Properties, Processing and Use in Design*, Marcel Dekker, New York, 1982.

[5] Shand, E. B., *Journal of the American Ceramic Society*, Vol. 42, No. 10, Oct. 1959, pp. 474-477.

[6] Kirchner, H. P., Gruver, R. M., and Sotter, W. A., *Philosophical Magazine*, Vol. 33, No. 5, 1976, pp. 775-780.

[7] Mecholsky, J. J., Jr., Freiman, S. W., and Rice, R. W., *Journal of Materials Science*, Vol. 11, 1976, pp.1310-1319.

[8] Bansal, G. K., *Philosophical Magazine*, Vol. 34, No. 4, 1977, pp. 935-944.

[9] Johnson, J. W. and Holloway, D. G., *Philosophical Magazine*, Vol. 14, No. 130, Oct. 1966, pp. 731-744.

[10] Bullock, R. E. and Kaae, J. L., *Journal of Materials Science*, Vol. 14, 1979, pp. 920-930.

[11] Weimer, R. J. and Rogers, H. C., *Journal of Applied Physics*, Vol. 50, No. 12, 1980, pp. 8025-8030.

[12] Weimer, R. J., "The Fracture of Brittle Metals under Explosive Loading," Ph.D. thesis, Drexel University, Philadelphia, June 1977.

[13] Abdel-Latif, A. I. A., Bradt, R. C., and Tressler, R. E. in *Fractography and Materials Science, ASTM STP 733*, American Society for Testing and Materials, 1981, pp. 259-270.

[14] Johnson, J. W. and Holloway, D. G., *Philosophical Magazine*, Vol. 17, No. 149, May 1968, pp. 899-909.

[15] Beauchamp, E. K., "Fracture Branching and Dicing in Stressed Glass," Sandia National Laboratories Research Report SC-RR-70-766, Albuquerque, N.M., Jan. 1971.
[16] Freiman, S. W., Gonzalez, A. C., and Mecholsky, J. J., Jr. *Journal of the American Ceramic Society*, Vol. 62, No. 3-4, March-April 1979, pp. 206-208.
[17] Rice, R. W., "Pores as Fracture Origins in Ceramics," to be published in *Journal of Materials Science*.
[18] Baratta, F. I., *Communications of the American Ceramic Society*, Vol. 64, No. 1, 1981, pp. C-3-C-4.
[19] Rice, R. W. and Becher, P. F., *Journal of the American Ceramic Society*, Vol. 60, No. 3-4, March-April 1977.
[20] Abdel-Latif, A. I. A., Tressler, R. E., and Bradt, R. C. in *Proceedings*, Fourth International Congress on Fracture, Vol. 3, 1977, pp. 932-939.
[21] Ball, A. and Payne, B. W., *Journal of Materials Science*, Vol. 11, 1976, pp. 731-747.
[22] Johnson, O. W. and Gibbs, P. in *Fracture of Solids*, Vol. 20, D. C. Drucker and J. J. Gilman, Eds., Interscience, New York, 1963, pp. 315-338.
[23] Haneman, D. and Pugh, E. N., *Journal of Applied Physics*, Vol. 34, No. 8, Aug. 1963, pp. 2269-2272.
[24] McKinney, K. R., Wu, C. Cm., and Rice, R. W., "Velocity-Dependent Fracture Path in $MgAl_2O_4$ Crystals," to be published.
[25] Becher, P. F. and Freiman, S. W., *Journal of Applied Physics*, Vol. 49, No. 7, July 1978, pp. 3779-3783.
[26] McNeil, J. F., *Journal of the Institute of Metals*, Vol. 87, 1958-59, pp. 79-87.
[27] Crutchley, D. E. and Reid, C. N. in *High Temperature Materials*, F. Benesovsdy, Ed., Springer-Verlag, New York, 1969, pp. 57-66.
[28] Pilkington, R. and Hull, D. in *Fracture Toughness of High-Strength Materials: Theory and Practice*, ISI Publication 120, pp. 5-10.
[29] Gilbert, A., Warke, W. R., and Wilcox, B. A., *Journal of Less-Common Metals*, Vol. 7, 1964, pp. 222-227.
[30] Limb, H. R., *Journal of the Institute of Metals*, Vol. 92, 1963-4, pp. 423-426.
[31] Beardmore, P. and Hull, D. in *Refractory Metals and Alloys IV*, Vol. I, R. I. Jaffee et al, Eds., Gordon and Breach Science Publishers, New York, 1967, pp. 81-94.
[32] Wilcox, B. A. and Gilbert, A. in *Refractory Metals and Alloys IV*, Vol. I, R. I. Jaffee et al, Eds., Gordon and Breach Science Publishers, New York, 1967, pp. 95-113.
[33] Hull, D., Beardmore, P., and Valintine, A. P., *Philosophical Magazine*, Vol. 12, 1965, pp. 1021-1041.
[34] Hull, D. and Beardmore, P., *International Journal of Fracture Mechanics*, Vol. 2, No. 2, 1966, pp. 468-487.
[35] Cordwell, J. E. and Hull, D., *Philosophical Magazine*, Vol. 19, No. 161, May 1969, pp. 951-966.
[36] Cordwell, J. E. and Hull, D., *Philosophical Magazine*, Vol. 26, No. 1, July 1972, pp. 215-224.
[37] Rice, R. W. Hunt, J. G., Freidman, G. I., and Sliney, J. L., "Identifying Optimum Parameters of Hot Extrusions," Final Report, Boeing Company Report for NASA Contract NAS 7-276, Aug. 1968.
[38] Rice, R. W. in *Treatise on Materials Science and Technology*, Vol. II, K. K. MacCrone, Ed., Academic Press, New York, 1977, pp. 199-381.
[39] Rice, R. W., McKinney, K. R., Wu, C. Cm., Freiman, S. W., and McDonough, W. J., "Fracture Energy of Si_3N_4," submitted for publication.
[40] Rice, R. W. and Racus, R. G., *Journal of Applied Physics*, Vol. 38, No. 1, Jan. 1967, pp. 422-423.
[41] Johnson, W. C., Stein, D. F., and Rice, R. W., *Journal of the American Ceramic Society*, Vol. 57, No. 8, Aug. 1974, pp. 342-344.
[42] Congleton, J., Petch, N. J., and Shiels, S. A., *Philosophical Magazine*, Vol. 19, No. 160, April 1969, pp. 794-807.
[43] Rhodes, W. H., Cannon, R. M., Jr., and Vasilor, T. in *Fracture Mechanics of Ceramics*, R. C. Bradt et al, Eds., Plenum Press, New York, 1974.
[44] McKinney, K. R., Mecholsky, J. J., Jr., and Freiman, S. W., *Journal of the American Ceramic Society*, Vol. 62, No. 7-8, 1979, pp. 336-340.

[45] Mecholsky, J. J., Jr., *Journal of the American Ceramic Society*, Vol. 64, No. 9, 1981, pp. 563-566.
[46] Mecholsky, J. J., Jr., private communication, Sandia National Laboratories, Albuquerque, N.M., 1980.
[47] Heuer, A. H., *Journal of the American Ceramic Society*, Vol. 52, No. 9, Sept. 1969, pp. 510-511.
[48] Dorward, R. C., *Communications of the American Ceramic Society*, Vol. 65, No. 1, Jan. 1982, p. C-6.
[49] Rice, R. W., McKinney, K. R., and Ingel, R. P., *Journal of the American Ceramic Society*, Vol. 64, No. 12, Dec. 1981, pp. C175-C177.
[50] Kirchner, H. P. and Gruver, R. M., *Journal of Materials Science*, Vol. 14, 1979, pp. 2110-2118.
[51] Kirchner, H. P., Gruver, R. M., and Richard, D. M., *Journal of Materials Science*, Vol. 14, 1979, pp. 2713-2720.
[52] Kirchner, H. P. and Gruver, R. M., *Journal of the American Ceramic Society*, Vol. 63, No. 3-4, March-April 1980, pp. 169-174.
[53] Rice, R. W., *Journal of the American Ceramic Society*, Vol. 62, No. 9-10, Sept.-Oct. 1979, pp. 533-535.
[54] Rice, R. W. in *Processing of Crystalline Ceramics*, H. Palmour III et al, Eds., Plenum Press, New York, 1978, pp. 303-319.
[55] Rice, R. W. in *Fracture Mechanics of Ceramics*, Vol. 1, R. C. Bradt et al, Eds., Plenum Press, New York, 1974, pp. 323-345.
[56] Rice, R. W., Mecholsky, J. J., Jr., Freiman, S. W., and Morey, S. M., "Failure Causing Defects in Ceramics: What NDE Should Find," NRL Memorandum Report 4075, National Research Laboratory, Washington, D.C., 30 Oct. 1979.
[57] McDonough, W. J., Flinn, D. H., Stern, K. H., and Rice, R. W., *Journal of Materials Science*, Vol. 13, 1978, pp. 2403-2412.
[58] Suzuki, H. and Hayashi, K., *Planseeberichte für Pulvermetallurgie*, Vol. 23, 1975, pp. 24-36.
[59] Almond, E. A. and Roebuck, B., *Metal Science Journal*, Oct. 1977, pp. 458-461.
[60] Kerkhof, F. in *Proceedings*, International Conference on Dynamic Crack Propagation, G. C. Sih, Ed., Noordhoff, Leyden, 1973, pp. 3-33.
[61] Green, D. J., Nicholson, P. S., and Emburr, J. D., *Journal of Materials Science*, Vol. 12, 1977, pp. 987-989.
[62] Luyckx, S. B., *Metallurgica*, Vol. 23, Jan. 1975, pp. 109-115.
[63] Rice, R. W., Morey, S. M., and Fraser, F. W., "Fracture Initiation in Irdome Trade MgF_2," NRL Memorandum Report 3685, National Research Laboratory, Washington, D.C., Jan. 1972.
[64] Dutta, S., Rice, R. W., Graham, H. C., and Mendiratta, M. C., *Journal of Materials Science*, Vol. 15, 1980, pp. 2183-2191.
[65] Green, D. J., Nicholson, P. S., and Embury, J. D., *Journal of Materials Science*, Vol. 12, 1977, pp. 987-989.
[66] Khaund, A. K. and Nicholson, P. S., *Journal of Materials Science*, Vol. 15, 1980, pp. 177-187.
[67] Kuyckx, S. B. in *Proceedings*, Fourth International Congress on Fracture, Vol. 2, 1977, p. 223.
[68] Rice, R. W., Becher, P. F., Freiman, S. W., and McDonough, W. J., *Ceramic Engineering and Scientific Proceedings*, Vol. 2, No. 7-8, July-Aug. 1980, pp. 424-443.
[69] Rice, R. W., Matt, C. V., McDonough, W. J., McKinney, K. R., and Wu, C. Cm., *Ceramic Engineering and Scientific Proceedings*, Vol. 3, No. 9-10, 1982, pp. 698-713.
[70] Abdel-Latif, A. I. A., Bradt, R. C., and Tressler, R. E., *International Journal of Fracture*, Vol. 13, No. 3, June 1977, pp. 349-359.
[71] Mecholsky, J. J., Jr., Freiman, S. W., and Morey, S. M. in *Fiber Optics: Advances in Research and Development*, B. Bendow and S. S. Miitra, Eds., Plenum Press, New York, 1979, pp. 187-207.
[72] Mecholsky, J. J. Jr., and Rice, R. W., this publication, pp. 185-193.
[73] Ritter, J. E., Jr., and Wilson, W. R. D., *American Society of Lubrication Engineers Transactions*, Vol. 18, No. 2, 1974, pp. 130-134.

[74] Mecholsky, J. J., Jr., Gonzalez, A. C., and Freiman, S. W., *Journal of the American Ceramic Society*, Vol. 62, No. 11-12, 1979, p. 577.
[75] Kirchner, H. P., Gruver, R. M., and Sotter, W. A., *Journal of the American Ceramic Society*, Vol. 58, No. 5-6, 1974, p. 188.
[76] Field, J. E., Hutchings, I. M., and Gorham, D. A., "Instrumentation for Impact, Erosion and Fracture Studies at Cambridge," *ICIASF Record*, International Congress on Instrumentation in Aerospace Simulation Facilities, 1977, pp. 142-149.
[77] Snowden, W. E., "Crack Growth in Glass Subjected to Controlled Impacts," Ph.D. thesis, University of California at Berkeley, Lawrence Berkeley Laboratory Report for U.S. ERDA Contract W-7405-ENG-48, Nov. 1976.
[78] Land, P. L. and Holmquist, S., "Evaluation of β-Sialon for Radome Application," Final Report, AFML-TR-78-79, Air Force Materials Laboratory, Dayton, Ohio, 1977.
[79] Lewis, D. and Spann, J. R., *Journal of the American Ceramic Society*, Vol. 65, No. 10, 1982, pp. C173-C174.
[80] Richerson, D. W., Lindberg, L. J., Carruthers, W. D., and Dahn, J., *Ceramic Engineering and Science Proceedings*, Vol. 2, No. 7-8, 1981, pp. 578-588.
[81] Morrison, F. R. and Yonushonis, T., "Establishment of Engineering Design Data for Hybrid Steel/Ceramic Ball Bearings—Phase II (Aug. 1979-Aug. 1980)," NavAir Final Report, Contract N00019-79-C-0418, Sept. 1980.
[82] Morrison, F. R., Pirvics, J., and Yonushonis, T., "Establishment of Engineering Design Data for Hybrid Steel/Ceramic Ball Bearings (April 1978-Aug. 1979)," NavAir Final Report, Contract N00019-78-C-0304, Sept. 1979.
[83] Sommer, E., *Engineering Fracture Mechanics*, Vol. 1, Pergamon Press, Oxford, 1969, pp. 539-548.
[84] Rice, R. W., Freiman, S. W., and Becher, P. F., *Journal of the American Ceramic Society*, Vol. 64, No. 6, June 1981, pp. 345-350.
[85] Rice, R. W. and Freiman, S. W., *Journal of the American Ceramic Society*, Vol. 64, No. 6, June 1981, pp. 350-354.
[86] Rice, R. W., Pohanka, R. C., and McDonough, W. J., *Journal of the American Ceramic Society*, Vol. 63, No. 11-12, Nov.-Dec. 1980, pp. 703-710.
[87] Lewis, D., III, *Journal of the American Ceramic Society*, Vol. 64, No. 2, Feb. 1981, pp. 82-86.
[88] Rice, R. W. and Mecholsky, J. J., Jr., in *The Science of Ceramic Machining and Surface Finishing—II*, B. J. K. Hockey and R. W. Rice, Eds., National Bureau of Standards Special Publication 562, Oct. 1979, pp. 351-378.
[89] Rice, R. W., Mecholsky, J. J., Jr., and Becher, P. F., *Journal of Materials Science*, Vol. 16, 1981, pp. 853-862.
[90] Marshall, D. B., *American Ceramic Society Bulletin*, Vol. 61, No. 3, 1982, p. 412.
[91] Marshall, D. B., Lawn, B. R., and Mecholsky, J. J., Jr., *Journal of the American Ceramic Society*, Vol. 63, No. 5-6, 1980, pp. 358-360.
[92] Mecholsky, J. J., Jr., Rice, R. W., and Freiman, S. W., *Journal of the American Ceramic Society*, Vol. 57, No. 10, Oct. 1974, pp. 440-443.
[93] Anthony, S. R., Chubb, J. P., and Congleton, J., *Philosophical Magazine*, Vol. 22, Dec. 1970, pp. 1201-1216.
[94] Huang, J. L. and Virkar, A. V., *American Ceramic Society Bulletin*, Vol. 61, No. 3, 1982, p. 334.
[95] Rose, L. R. F., *International Journal of Fracture*, Vol. 12, No. 6, 1976, pp. 799-813.
[96] Field, J. E., *Contemporary Physics*, Vol. 12, No. 1, 1971, pp. 1-31.
[97] Ball, A. and Payne, B. W. in *Proceedings*, Fourth International Congress on Fracture, Vol. 3, 1977, pp. 971-978.
[98] Doll, W., Schinker, M. G., and Weidman, G. W. in *Proceedings*, Fourth International Congress on Fracture, Vol. 3, 1977, pp. 965-969.
[99] Aoki, S. and Sakata, M. in *Mechanical Behavior of Materials*, The Society of Materials Science (Japan), Vol. 5, 1972, pp. 563-570.
[100] Kirchner, H. P. and Kirchner, J. W., *Journal of the American Ceramic Society*, Vol. 62, No. 3-4, March-April 1979, pp. 198-201.
[101] Shetty, D. K., Bansal, G. K., Rosenfield, A. H., and Duckworth, W. H., *Journal of the American Ceramic Society*, Vol. 63, No. 1-2, Jan.-Feb. 1980, pp. 106-107.

[*102*] Lewis, D., private communication, 1982.
[*103*] Bahat, D., Leonard, G., and Rabinovitch, A., *International Journal of Fracture*, Vol. 18, No. 1, Jan. 1982, pp. 29-38.
[*104*] Argon, A. S., Backer, S., McClintock, F. A., Reichenbach, G. S., Orowan, E., Shaw, M. C., and Rabinowicz, E. in *Mechanical Behavior of Materials*, F. A. McClintock and A. S. Argon, Eds., Addison-Wesley, Reading, Mass., 1966, pp. 488-517.
[*105*] Rice, R. W., "Single Crystal Fracture Topography: Basic Detriments," to be published.
[*106*] Gilman, J. J., *Transactions of AIME*, Vol. 212, 1958, pp. 310-315.
[*107*] Weiderhorn, S. M., Hockey, B. J., and Roberts, D. E., *Philosophical Magazine*, Vol. 28, No. 4, Oct. 1973, pp. 783-796.
[*108*] Guard, R. W. and Romo, P. C., *Journal of the American Ceramic Society*, Vol. 48, No. 1, Jan. 1965, pp. 7-11.
[*109*] Becher, P. F., private communication, 1982.
[*110*] Lankford, J. and Davidson, D. L., *Journal of Materials Science*, Vol. 17, No. 5, May 1982, pp. 1501-1507.
[*111*] Gilman, J. J., *Journal of Applied Physics*, Vol. 44, No. 2, Feb. 1973, pp. 675-679.
[*112*] Rice, R. W. and Pohanka, R. C., *Journal of the American Ceramic Society*, Vol. 62, No. 11-12, Nov.-Dec. 1979, pp. 559-563.
[*113*] Rice, R. W., Freiman, S. W., and Mecholsky, J. J., Jr., *Journal of the American Ceramic Society*, Vol. 63, No. 3-4, March-April 1980, pp. 129-136.
[*114*] McKinney, K. R. and Rice, R. W. in *Fracture Mechanics for Ceramics, Rocks, and Concrete, ASTM STP 745*, American Society for Testing and Materials, 1981, pp. 118-126.
[*115*] Ingel, R. P., "Structure-Mechanical Property Relations for Single Crystal Y_2O_3 Stabilized ZrO_2," Ph.D. thesis, Catholic University of America, Washington, D.C., 1982.
[*116*] McKenna, J. F., *Ceramic Bulletin*, Vol. 40, No. 2, 1961, pp. 61-65.
[*117*] Vega-Boggio, J. and Vingsbo, O., *Journal of Materials Science*, Vol. 11, 1976, pp. 2242-2246.
[*118*] Vega-Boggio, J., Vingsbo, O., and Carlsson, J., *Journal of Materials Science*, Vol. 12, 1977, pp. 1750-1758.
[*119*] Rice, R. W., Freiman, S. W., Jones, R. L., and Jarvis, N. L., "NRL Engineering Materials and Chemistry Divisions Studies of the A2 Tube Failure," NRL Memorandum Report 3535, National Research Laboratory, Washington, D.C., June 1977.
[*120*] Viechnicki, D. J., *American Ceramic Society Bulletin*, Vol. 56, No. 4, 1977, pp. 412-415.

DISCUSSION

B. Cina[1] (*written discussion*)—Is it not surprising that fractographic features such as mirror, mist, and hackle are observed both in amorphous material such as glass and in crystalline materials such as alumina, magnesia, calcium fluoride, and graphite?

If there is a mode of fracture common to all these materials, does this not imply that it is one which can not be explained by one of our conventional crystallographic mechanisms and therefore we should seek a new mechanism?

Furthermore, if crystalline material can fail in a noncrystalline manner, need the phenomenon be confined to ceramic materials? Could it be that some of the problematic features sometimes associated with brittle fractures in metals are caused by such a new fracture mechanism or mechanisms?

[1]Israel Aircraft Industries Ltd., Lod, Israel.

R. W. Rice (author's closure)—I am not surprised at the common features for crystalline and noncrystalline fractures, in part because they are so prevalent on fractures of such a variety of materials. These include not only ceramics and brittle metals as discussed in the text, but many other materials. The latter include many rocks ("cleaved" plates of slate are often a good example) and many organic materials such as plastics and tar as well as some foods that are sufficiently brittle (cold enough, or loaded at high enough strain rates). Fracture mirror and related features can be seen on some crisp vegetables, fruits, and nuts broken rapidly (for example, by taking a bite out of them).

I do not feel that we need any new mechanisms to explain the similarity in fracture features between crystalline and noncrystalline materials. At the atomic level, we are still breaking the same different strengths and types of (metallic, ionic, and covalent) bonds. At the continuum level, we know that the same basic mechanics, as reflected in the Griffith-Irwin equation, holds. The key difference I attempted to show between single crystals and glass (that is, noncrystals) was the preference, or avoidance, of certain fracture planes, and the directional dependence and the crystallographic character to the fracture features on the crystal fractures versus the complete isotropy of the choice of "planes" and of the features on a fracture "plane" in noncrystalline materials. Polycrystalline materials are commonly overall isotropic, in which case they behave in an overall fashion like isotropic (noncrystalline) materials. However, as microstructure coarsens, or deviates from randomness, one sees more impact of the microstructure (for example, crystalline and hence nonisotropic behavior of grains) on the overall fracture.

V. D. Frechette[1]

Markings on Crack Surfaces of Brittle Materials: A Suggested Unified Nomenclature

REFERENCE: Frechette, V. D., **"Markings on Crack Surfaces of Brittle Materials: A Suggested Unified Nomenclature,"** *Fractography of Ceramic and Metal Failures, ASTM STP 827*, J. J. Mecholsky, Jr. and S. R. Powell, Jr., Eds., American Society for Testing and Materials, 1984, pp. 104–109.

ABSTRACT: Terms to characterize the markings on crack-generated surfaces of brittle materials have come to be used in different ways as a result of the variety of interests and backgrounds of workers in this field and the scattered nature of the literature. A single system of nomenclature which is explicit, universally applicable, and self-consistent should be helpful in aiding communication among fractographers. This paper suggests a possible unified system for discussion and refinement.

KEY WORDS: crack surfaces, Wallner lines, hackle, scarps

Terms to characterize the markings on crack-generated surfaces of brittle materials have come to be used in different ways as a result of the variety of interests and backgrounds of workers in this field and the scattered nature of the literature. A single system of nomenclature which is explicit, universally applicable, and self-consistent should be helpful in aiding communication among fractographers. It is the present purpose to suggest a possible unified system for discussion and refinement.

Underlying Philosophy

The present attempt to achieve a unified system can be illustrated by the classification of three sorts of lines, each of them the locus of intersection of an elastic pulse with a moving crack front, as Wallner lines. While Wallner him-

[1]Professor of Ceramic Science, New York State College of Ceramics at Alfred University, Alfred, N.Y. 14802.

self described and explained only two of these explicitly, calling them *primary* and *secondary*, the third type is implied by his basic concept. For the sake of unity it seems proper to classify this third type as a *tertiary* Wallner line.

Fundamental Nomenclature

Rib Mark

Definition—A curved line on the crack surface, usually convex in the general direction toward which the crack is running. The term is useful in referring to a mark of this shape until its specific nature is learned.

Wallner Lines

Definition—Rib marks with wavelike contour caused by temporary excursion of the crack front out of plane in response to a tilt in the axis of principal tension induced by an elastic pulse. The Wallner line is the locus of interception of the spreading pulse with successive points along the running crack front.

Primary Wallner Line—The elastic pulse is generated by the encounter of some portion of the crack front with a singularity in the specimen, such as a discontinuity at the free surface or within the specimen, or any localized stress field or elastic discontinuity.

Secondary Wallner Line—The elastic pulse is generated by a discontinuity in the progress of the crack front, typically mist-hackle details.

Tertiary Wallner Line—The elastic pulse, or train of pulses, is generated from outside the crack front by mechanical shock or by vibration of the specimen resulting from stress release by cracking.

Arrest Line

Definition—Rib mark defining the crack front shape of an arrested crack prior to resumption of crack spread under more-or-less altered stress configuration. The duration of arrest may be long to infinitesimal.

Intersection Scarp

Definition—A line, of any shape, which is the locus of intersection of two portions of a crack with one another. This is exemplified by intersection of a portion of a slow crack running wet with a portion not wetted.

Transition Scarp

Definition—Rib mark generated when a crack changes from one mode of growth to another, as when a wet crack accelerates abruptly from Region II (plateau) to Region III (dry) of the K-V curve.

Hackle

Definition—A line on the crack surface, running parallel to the local direction of cracking, separating parallel but noncoplanar portions of the crack surface.

Twist Hackle

Definition—Hackle separating portions of the crack surface, each of which has rotated from the original crack plane in response to a twist in the axis of principal tension.

In a single crystal, hackle separating portions of the crack surface, each of which follows the same cleavage plane, the normal to the cleavage plane being inclined to the principal tension.

In a bicrystal or a polycrystalline material, hackle initiated at a twist grain boundary.

Wake Hackle

Definition—Hackle line extending from a singularity at the crack front in the direction of cracking, as upon encounter with an inclusion.

Shear Hackle

Definition—Hackle generated by interaction of a shear component with the principal tension under which the crack is running.

Mist Hackle

Definition—Markings on the surface of a crack accelerating close to the effective terminal velocity, observable first as a mist on the surface and with increasing velocity revealing a fibrous texture elongated in the direction of cracking and coarsening up to the stage at which the crack bifurcates. (*Velocity bifurcation* or *velocity forking* is the splitting of a single crack into two mature diverging cracks at or near the effective terminal velocity of about half the transverse speed of sound in the material.)

Fabrication Traces

Definition—Fabrication traces are anomalous markings which may appear on crack surfaces where the developing crack encounters regions of unusual weakness, density, or elastic modulus, introduced—usually inadvertently—during fabrication.

Grain Growth and Etch Terraces

Intergranular fracture in polycrystalline materials may expose surfaces of grains whose markings are not the result of cracking but are intergranular growth or etch terraces. Such markings are useful in identifying the fracture mode as intergranular.

Other Markings

Certain fracture markings have not been included because they are merely special cases of the fundamental types. Thus *gull wings* are Wallner lines, sometimes primary, sometimes secondary. *River patterns* are special cases of twist hackle. *Sierra scarps* are arrays of intersection scarps. The *lambda mark* is a complex Wallner line. *Plumose markings* are families of wake hackle.

DISCUSSION

R. W. Rice[1] *(written discussion)*—I certainly sympathize with the goal of trying to get a unified nomenclature and I feel that you have made some very useful contributions. However, I feel that substantial changes and some additions are necessary to more closely approach this goal.

It is very important to have as consistent an underlying logic as possible in setting up a scheme of definitions. It seems to me that there are two basic choices of making definitions. One is to establish them based upon physical characteristics such as shape, appearance, etc., and the other is to define them based upon the mechanisms that are operational. However, we must be fairly cautious about the latter because many of the mechanisms are not yet fully understood or may be quite controversial. The two systems can be mixed, but again there should be a natural logic to the mixing. I would propose that, in general, the best approach is to make fairly broad definitions based on the physical characteristics and then develop subheadings or subdefinitions under these that can be based on either clear subsets of the physical characteristics, the mechanisms involved, or possibly both. The first part of your definitions illustrates this approach fairly well. You define rib mark as the general class of physical features consisting of curved lines, convex in the general direction towards which the crack is running. The different types of Wallner lines based upon mechanisms involved are then defined.

[1]Head, Ceramics and Glass Branch, Naval Research Laboratory, Washington, D.C. 20375.

Beyond your definition of Wallner lines, however, I begin to have problems. For example, I agree with the idea of defining an arrest line, but I am concerned as to whether we really always know whether a rib mark has been made due to true crack arrest or whether very similar if not identical rib marks might not be made by simply having a significant change in velocity. Thus it seems to me that we need a term, for which I cannot at present think of a good word or phrase, which would define a rib mark simply due to a significant change in crack velocity. Then an arrest line would be a specific subdefinition under this based on a more specific and exact mechanism.

I have further problems when I get to your definition of intersection and transition scarps. You define a transition scarp as a rib mark generated when a crack changes from one mode of growth to another (for example, from Region II to Region III). How is this different from your definition of an intersection scarp being due to a portion of a slow crack running wet with a portion not wetted? Thus I do not see a logical distinction between part of your definitions of transition scarp and intersection scarp. On the other hand, I feel that your inclusion of the intersection of two crack members (for example, in completing the ringing of a cylinder) is too diverse in physical appearance and the mechanisms involved to be lumped under intersection scarp. I strongly suggest that similar features of these two scarp definitions be logically combined under one heading and that crack intersection be left as a separate definition because of its distinctly different physical characteristics and mechanisms. In fact, I would make a specific definition of crack intersection as being one crack literally running into the other or a portion of itself generated earlier in its propagation history. Crack intersection would be distinguished from crack branching discussed below by, at the very minimum, the timing of the formation of two crack surfaces at or near the point of intersection and also very commonly by both the angle of their intersection and the crack directions at their intersection.

I also disagree with some aspects of your definition of hackle and the various subcategories under this. One of the problems is confusion between definitions based on mechanisms and definitions based on physical characteristics. Mist, hackle, and crack branching or macrocrack branching are terms widely used to refer to features generated by mechanisms associated with certain stages of crack propagation (that is, the typical mirror-mist-hackle markings around a fracture initiation site). Instead, you generalize about the term *hackle* based on physical appearance. While it is clear that a broad term is needed to describe a feature that you describe by the term *hackle*, I believe this could be very confusing because of the long use of that term relating to a specific location and mechanisms around the origin. This generalization and hence confusion of the term *hackle* is probably unfortunate and unnecessary in view of the several other terms available, such as *fracture step*, *cleavage step*, *river mark*, and *river patterns*.

I suggest an approach along the following lines. Define fracture step as any fairly abrupt change in the fracture surface such as that due to two overlap-

ping cracks connected by a short secondary crack. Several subdefinitions would follow from this broad physical feature definition. These include *cleavage step*, where the feature is formed due to cracks propagating on specific sets of cleavage planes in those materials exhibiting cleavage. It would entail a river mark which would be a fracture step forming a line on the crack's surface running parallel to the local direction of cracking, separating parallel but noncoplanar portions of the crack surface (that is, your general definition of hackle). One could thus correspondingly redefine each of your subsequent definitions of twist, wake, and shear hackle by the corresponding substitution of fracture (cleavage) step for the term *hackle*, although I am not sure that we need such fine tuning of the definition. (Another alternative to the use of the term *wake fracture step* would be the use of the term *fracture tail*, since this may be somewhat more descriptive and has been in some use.) The above approach would then leave use of the usual terms *mist*, *hackle*, and *macrocrack branching* associated with specific stages of a crack propagating to failure from a given origin for their normal and widely used purposes. Here I would make two side notes. Firstly, while you do not state that these phenomena occur upon reaching the terminal velocity (as many people previously believed), your statement might be taken as support of that idea, an idea which now seems to be rather significantly disputed by a number of velocity measurements. Secondly, we need a term to distinguish between the crack branching associated with the normal mist and hackle phenomena from branching that can occur at much lower velocities (such as Carl Wu has extensively demonstrated in DCB-type tests). I do not think this represents a basic problem but one that needs to be given thought for precise use of terminology.

I also have some problems with your definition of fabrication traces and grain growth and etch traces. I see some utility for defining some things of this sort, but I think it requires considerably more thought and organization. Thus I am not at all sure what you mean by fabrication traces. How do these differ from the fracture markings already identified? Your *wake hackle* term (or the proposed *fracture tail* term) would be one such feature presumably already encompassed in the above definitions but also fitting under fabrication traces. A basic problem is that both definitions are very vague, and in fact the one on grain growth and etch traces really is not a definition since it simply reiterates the title in the text of the definition.

A final suggestion is to accompany the definitions with sketches or illustrations. These would provide the reader with a clearer understanding of the terms.

Let me state again that you have done a useful job of getting the ball rolling and have suggested many good ideas. It is clear that a useful set of definitions will require the efforts of a number of people experienced and knowledgeable in the area of fracture surfaces.

V. D. Frechette (author's closure)—I appreciate Dr. Rice's interest and I thank him for his comments.

M. J. Ball,[1] *D. J. Landini,*[1] *and R. C. Bradt*[1]

Fracture Mist Region in a Soda-Lime-Silica Float Glass

REFERENCE: Ball, M. J., Landini, D. J., and Bradt, R. C., **"Fracture Mist Region in a Soda-Lime-Silica Float Glass,"** *Fractography of Ceramic and Metal Failures, ASTM STP 827*, J. J. Mecholsky, Jr. and S. R. Powell, Jr., Eds., American Society for Testing and Materials, 1984, pp. 110-120.

ABSTRACT: The mist region near the fracture origin was studied in a series of soda-lime-silica float glass specimens ranging in strength from about 30 to 90 MPa. Both the mirror/mist and the mist/hackle radii were measured to ascertain the dependence of the width of the mist region on the strength level. The mirror/mist constant was found to be 1.80 ± 0.15 MN/m$^{3/2}$ and the mist/hackle constant to be 2.42 ± 0.16 MN/m$^{3/2}$. Both analytically and experimentally, the width of the mist region was found to be inversely related to the square of the fracture stress; that is, (W_{mist}) is proportional to ($1/\sigma_f^2$). This suggests a dependence of the mist region width on the elastic strain energy at fracture initiation.

The surface topography of the mist region was analyzed by a scanning electron microscopy computerized contour mapping technique to determine the surface roughness within the mist region. It was observed that the average root-mean-square roughness in the mist region was proportional to the fracture stress squared. This suggests that the fracture surface roughness of the mist region, or alternatively the true surface area of the mist region, is also determined by the stored elastic strain energy in the specimen before fracture.

It is concluded that the mist region width and the mist region roughness are both determined by a strain energy criterion. It is suggested that they may be related through a generalized mist region parameter.

KEY WORDS: fractography, fracture analysis of glass, fracture surface topography, glass strength, mist region, quantitative fractography

Understanding the fracture characteristics of glass and the intriguing patterns which develop on glass fracture surfaces has long been a point of interest to glass researchers. In general, these characteristics may be classified into two groups: (1) macrofracture patterns and (2) microfracture features. The

[1]Ceramic Science and Engineering Program, Department of Materials Science and Engineering, Pennsylvania State University, University Park, Pa. 16802.

macrofracture patterns include the classical star pattern usually occurring during a large-scale impact failure and the Hertzian cone crack which develops around and under an indenter. The microfracture features are those fine-scale features which develop near the fracture origin as the critical flaw propagates into a large crack. It is in this latter group that the progressive developments of the mirror, the mist, and the hackle features occur as the crack extends from its point of origin. There has always been considerable interest in these microfracture features in the vicinity of the fracture origin in glass as evidenced by the recent review articles of Govila et al [*1*] and Mecholsky and Freiman [*2*], which complement the earlier summary of Kirchner and Gruver [*3*].

The continued study of these microfracture features has fostered some controversy as to the criteria for their formation, about which there does not exist universal agreement; this has been discussed in some detail by Abdel-Latif et al [*4*]. However, the progression of events leading to the mirror, mist, and hackle regions schematically shown in Fig. 1 is reasonably well understood.

As the critical flaw extends from the fracture origin and increases its velocity of propagation, it leaves behind a distinctive pattern that consists of surface features which are known as the mirror, the mist, and the hackle regions. In their perfect stage of development, which may be expected only for failures occurring under a state of uniform tensile stress, these regions are concentric about the fracture origin. The mirror region is an almost perfectly flat surface where the crack velocity is rapidly increasing and the crack grows in a nearly planar fashion. The mirror region gives way to the mist region at a distance from the fracture origin that is commonly known as the mirror/mist radius

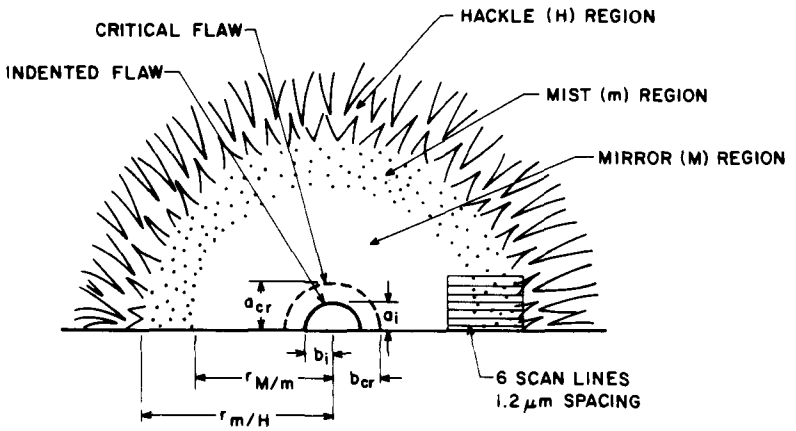

FIG. 1—*Schematic of the mirror, mist, and hackle regions surrounding a fracture origin. The indented flaw and the critical flaw are also illustrated. The positions of the topography scan lines are shown.*

($r_{M/m}$). It has been demonstrated by many researchers [*4–13*] that this mirror/mist radius is directly related to the fracture stress of the glass artifact (σ_f) through the empirical relationship

$$\sigma_f r_{M/m}^{1/2} = A_{M/m} \tag{1}$$

where $A_{M/m}$ is known as the mirror/mist constant. It is sometimes referred to as just the mirror constant. For a typical soda-lime-silica glass, this constant $A_{M/m}$ is about 2 MN/m$^{3/2}$ although a range of values between about 1.6 and 2.4 have been reported [*4–13*].

Once formation of the mist region initiates, the perfectly flat mirror surface gives way to the rougher, somewhat stippled, or pock-marked type of misty appearance of the mist region. When viewed with the naked eye, or even with a low-magnification ocular, it is readily apparent where the mist region initiates, since the total reflectance of the mirror region gives way to a more diffuse reflectance [*14*]. It is obvious that the planar nature of the crack propagation in the mirror region is beginning to degenerate into some form of local, angular deviation from the original crack plane. In essence, the overall planar stability of the complete crack becomes susceptible to very localized instabilities on the propagating crack front. These localized instabilities cause minor deviations of the fracture surface from the original plane of propagation and subsequently develop into the hackle region. The hackle region is eventually followed by the phenomenon of macroscopic crack branching, the crack bifurcation process.

The precise physical details of the localized instabilities which cause the formation of the mist region are not fundamentally understood. For example, one possibility is that the mist region results from the nucleation of microcracks in the process zone or stress field just ahead of the main crack. Alternatively, a mechanism of minibifurcation is also a possibility, where one of the branches immediately arrests due to some localized effect. Although this latter process may appear more palatable as a precursor to the hackle region and eventual macroscopic bifurcation, it is by no means universally accepted as the mechanism for the mist formation. It is fair to state that the mechanism of mist formation is not known with certainty at this time.

The breakdown of the mist region into the hackle region is also readily observed on fracture surfaces, since the gentle haziness of the mist rapidly degenerates into a series of distinct ridges radiating from the fracture origin. These ridges, if extended back through the mist and the mirror regions, directly focus on the fracture origin and can be very helpful in locating and identifying it. Similar to the mirror/mist radius, it is also possible to define and measure the mist/hackle radius ($r_{m/H}$), which also follows the same form of empirical equation:

$$\sigma_f r_{m/H}^{1/2} = A_{m/H} \tag{2}$$

where $A_{m/H}$ is known as the mist/hackle constant. Since the radius of the mirror/mist boundary is always smaller than that of the mist/hackle boundary, it follows that the mirror/mist constant must always be less than the mist/hackle constant. It is considerably beyond the mist/hackle boundary that the ever-increasing instability of the propagating crack gradually results in crack branching or bifurcation, a very interesting fracture feature in its own right [*15-17*].

Thus, in the sequence of events occurring during post-critical crack growth in glass, the mist region surrounding the fracture origin is a very interesting feature, since it heralds the initiation of crack front instability on a very localized scale. Surprisingly, with few exceptions, the mist region has not received a significant amount of proprietary research attention. It is usually addressed only as a portion of the general discussion of the mirror/mist/hackle features. However, the mist region certainly merits continuing research as a crack instability precursor; furthermore, recent analysis of the occurrence of multiple-mist regions [*18*], although only observed in very high-strength glass specimens, has lent further impetus to research efforts by creating additional interest. It is the purpose of this paper to describe research specifically addressed toward a further understanding of the mist region, its width, and its surface roughness.

Experimental Procedures

The glass used for this study of the width and the surface roughness of the mist region surrounding glass fracture origins was a commercial soda-lime-silica glass prepared by modern float technology. It was received in the form of plate, approximately 1.25 cm in thickness. Using a diamond saw blade, rectangular bars were cut to approximately 15.25 by 2.54 by 1.25 cm, after which the tin surface was identified using an ultraviolet lamp. The tin layer was removed by diamond grinding and subsequent polishing techniques.

To obtain a range of strengths for the glass specimens, flaws were introduced at the centers of the 2.54 by 15.25 cm faces of the bars by a Vicker's microhardness indenter. Loads ranged from 400 to 3600 g. The sample edges were then bevelled to ensure failure from the indent flaws. After indentation and bevelling, the residual stresses were removed by annealing. The annealing procedure consisted of heating the specimens to 550°C at a rate of about 3°C/min, then holding at 550°C for 5 min, cooling to 450°C at 1°C/min, and furnace cooling to room temperature. Examination of the flaws by polarized light microscopy revealed that all the residual stresses had been removed by this annealing schedule. Most of the specimens were then broken in 3-point loading over a 12.70-cm span by a commercial testing machine at crosshead speeds from about 0.001 to 0.5 cm/min. Testing was performed at room temperature in air. Fracture stresses were determined from the standard strength of materials formula

$$\sigma_f = \frac{3}{2}\frac{PL}{bh^2} \tag{3}$$

where L is the test span, b is the sample width, h is its thickness, and P is the load at fracture. In addition, five specimens indented at 3600 g were loaded at stress levels below the strengths of the similarly indented specimens broken in the normal strength tests, then allowed to fail through static fatigue. For these, the flaws exhibited substantial slow crack growth, yielding lower strengths and producing much larger mirror regions.

After fracture, the most planar, best preserved of the two sample halves was used for measurements of the mirror/mist and mist/hackle radii and the generation of surface topography profiles by computerized scanning electron microscopy (SEM) techniques [*19-21*]. The boundary radii were measured using an optical microscope with a calibrated eyepiece. The diameters of the respective boundaries were measured at the tensile surface of the bend specimens, then divided by two to yield the appropriate radii. The widths of the mist regions were then determined by subtracting these two radii. Thus no direct measurements of the mist width were actually made, only calculations from the differences of the boundary diameter measurements.

Since topography by SEM is an expensive, time-consuming operation, only a few specimens were analyzed by this technique. Six specimens—two each of low, medium, and higher strength levels—were chosen. After sawing to appropriate thicknesses, the fracture surfaces were gold coated and individually examined. As shown schematically in Fig. 1 and photographically in Fig. 2, six scan lines, parallel to the original tensile surface and spaced 1.2 μm apart, were taken across the mist region. Fundamentally, it would be better to take each of the scans on a direct radial trace from the fracture origin; however, the roughness and mist width scatter on a local scale does not merit the additional effort for this consideration. After the six traces were taken for each specimen, the root mean square (RMS) surface roughnesses were determined and averaged, and the 95% confidence limits for the RMS roughnesses calculated by applying the "t"-distribution.

Results and Discussion

The results of the measurements of the mirror/mist and the mist/hackle radii are illustrated on the classical strength (σ_f) versus the inverse square root of the radius plot in Fig. 3. It is evident that the individual points ascribe fairly well to Eqs 1 and 2 as expected from the studies of previous investigators [*1-13*]. The lines on Fig. 3 are the least-squares regression lines through the data points, but they are not force fit through the origin. The R^2-values of these lines are 0.98 and 0.99 respectively. The mirror/mist slope or constant is 1.80 $\pm$ 0.15 MN/m$^{3/2}$ and that of the mist/hackle radius is 2.42 $\pm$ 0.16 MN/m$^{3/2}$. Other studies reporting both of the constants for similar

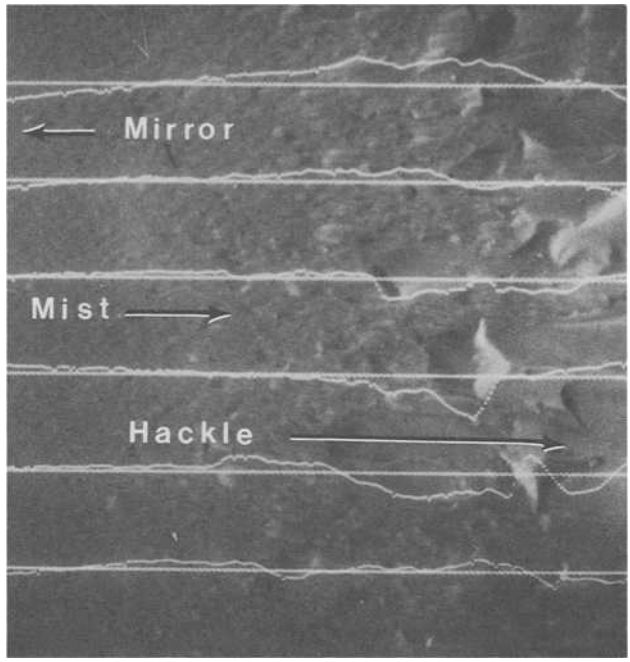

FIG. 2—*Set of surface topography scan lines through the mist region of the glass fracture surface for the 72.5 MPa specimen.*

soda-lime-silica glasses are those of Johnson and Holloway [*9*] and Mecholsky et al [*22,23*]. They report values of 1.9 and 2.0, and 1.9 and 2.1, respectively, for the two constants, as noted by Freiman [*24*] in his review article of glass fracture. Agreement exists as to the correct order of the magnitudes of these constants, but there is some disagreement as to their absolute values. These two regression lines appear to intersect for very large radii, and also appear to pass very near to the origin. According to the empirical Eqs 1 and 2, they should not intersect, but rather meet at the origin. This discrepancy probably occurs because it is difficult to precisely determine the boundaries between the different regions for the very low strength specimens. If the regression lines are force fit through the origin using appropriate techniques, then the mirror/mist constant is 1.81 ± 0.25 MN/m$^{3/2}$ and the mist/hackle constant is 2.29 ± 0.24 MN/m$^{3/2}$, practically the same because of the σ_f versus $r^{-1/2}$ functional form.

Another point is evident in Fig. 3, namely that the data and the two regression lines diverge at higher strengths or smaller radius values. The coordinates create an illusion, for it appears that the mist width increases at higher strengths, as suggested by the diversion of the two lines, when actually the reverse is true. This is because of the inverse square root coordinate of Fig. 3.

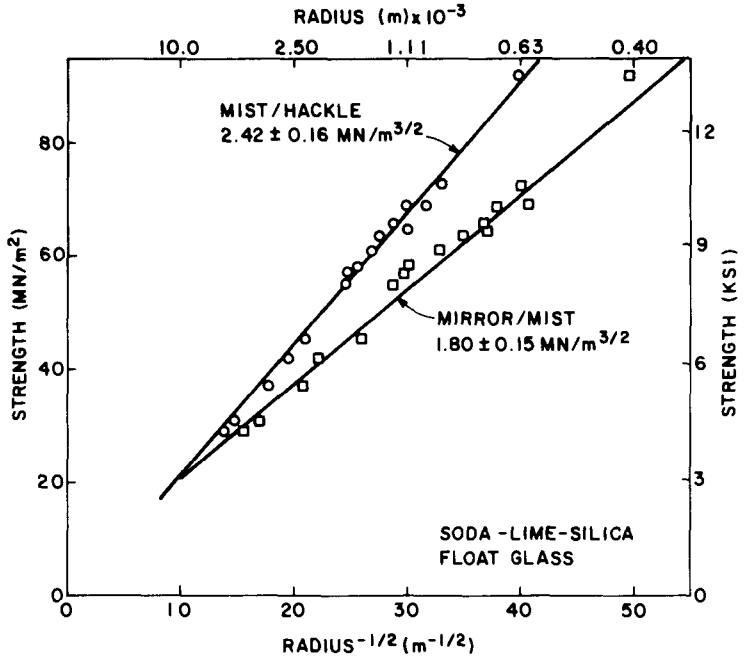

FIG. 3—*Classical fracture stress versus inverse square root radii plots for the mirror/mist and mist/hackle boundaries.*

That the mist width actually increases at lower strength levels can be readily shown by rearranging Eqs 1 and 2, then squaring both sides to yield

$$r_{M/m} = \frac{A_{M/m}^2}{\sigma_f^2} \quad \text{and} \quad r_{m/H} = \frac{A_{m/H}^2}{\sigma_f^2} \tag{4}$$

which can be subtracted to yield the mist width (W_{mist}):

$$W_{mist} = r_{m/H} - r_{M/m} = \frac{A_{m/H}^2 - A_{M/m}^2}{\sigma_f^2} \tag{5}$$

This clearly illustrates that the width of the fracture mist region is inversely related to the square of the fracture stress, a quantity which is directly related to the stored elastic strain energy in the specimen at fracture. Higher strain energies yield narrower mist regions.

Figure 4 illustrates the mist width, as the individual radii differences for each of the specimens, versus the inverse square of the specimen's fracture stress, as suggested by Eq 5. The solid line is the least-squares regression line. It has an R^2-value of 0.90 and describes the results reasonably well. The slope

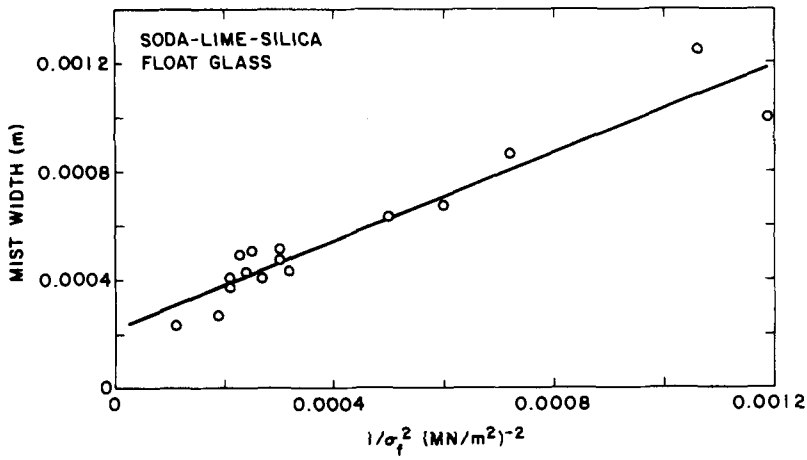

FIG. 4—*Fracture mist width versus the inverse square of the strength for the same data illustrated in Fig. 3.*

of the line is, however, 0.81 MN^2/m^3; whereas $A^2_{m/H} - A^2_{M/m}$ is 2.62 MN^2/m^3, if the lines in Fig. 3 are not force fit through the origin and 1.96 MN^2/m^3 if they are. Both are larger than the experimentally determined value, but of the same order of magnitude. A number of arguments can be proposed to explain this difference; however, perhaps the best reason for the difference is that the line's slope in Fig. 4 is dominated by the low-strength, wide mist region data, for which it is most difficult to determine the exact boundaries of the mist. If the higher strengths specimens which have more distinct, better defined mist boundaries are considered separately, then a slope of about 2 MN^2/m^3 is obtained, in excellent agreement with the calculations utilizing Eq 5.

In addition to measuring the radii for the mirror/mist and mist/hackle boundaries, the critical flaw sizes were optically estimated and the fracture toughnesses were calculated. A K_{Ic}-value of 0.74 ± 0.03 MN $m^{-3/2}$ was obtained, which is in good agreement with Wiederhorn's [*25*] value of 0.75 ± 0.01 MN $m^{-3/2}$ and the value of 0.75 ± 0.07 MN $m^{-3/2}$ reported by Shinkai et al [*26*].

The RMS surface roughnesses for the mist regions of the six strength specimens were determined from SEM scan line profiles such as those depicted in Fig. 2. If Z_i is specified as the elevation of each point on the line profile, then the RMS surface roughness can be defined as

$$\text{RMS} = \left\{ \frac{1}{N} \sum_{i=1}^{i=N} (Z_i - \bar{Z})^2 \right\}^{1/2} \tag{6}$$

where N is the number of points on the line profile and $\bar{Z}$ is their average

elevation. This convenient measure of the mist region roughness is related to the strength of the glass, for as the strengths of the specimens increase, the surface roughness of the mist region also increases. Figure 5 illustrates the correspondence of the mist region surface roughness to the fracture stress squared, a measure of the stored elastic strain energy in the specimen at fracture. The R^2-value for this line is 0.97. Again, as previously noted for the mist width, the surface roughness of the mist region also shows excellent agreement with the square of the strength. As previously noted for mist widths at lower stresses, the surface roughness of the mist region of the lowest strength specimen is also below the regression line.

It is appropriate to consider the effects of strength, or alternatively of the stored elastic strain energy, on the combination of mist width and mist roughness in a very general sense. The higher stored elastic strain energy in the stronger specimens results in a narrower mist region, but one which has a much rougher surface. A rougher surface is indicative of a greater real surface area, which suggests that more surface energy is required for its formation. In combination, these two features indicate that during the actual mist region formation process a given amount of stored elastic strain energy is available to cause this instability precursor to form, and if it is not utilized to extend the width of the mist region, it results in an increased roughness. This suggests that there may exist a mist region parameter or constant that includes in one form or another a product of the mist width and the mist region roughness. Very likely the mist region only forms over a very narrow range of strain en-

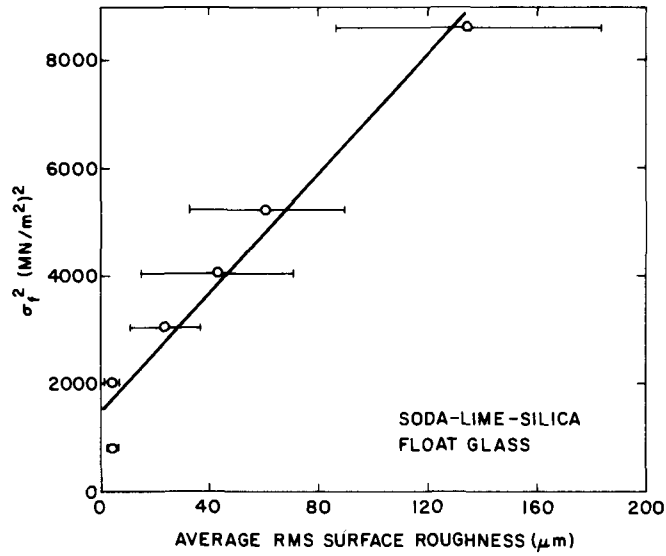

FIG. 5—*Relation between the mist region surface roughness and the square of the strength, a measure of the stored elastic strain energy.*

ergy release rates, rates which are too large for the crack to remain planar but too small for complete macroscopic bifurcation. However, to further pursue the details of a mist region parameter requires a fundamental understanding of the mechanisms of the physical process of mist region formation, and that problem is beyond the scope of this study.

Summary and Conclusions

The mist region between the mirror and the hackle near the fracture origin of a soda-lime-silica glass was studied. The mirror/mist radii and the mist/hackle radii were measured for a range of fracture stress levels, yielding constants of 1.80 ± 0.15 MN/m$^{3/2}$ and 2.42 ± 0.16 MN/m$^{3/2}$ respectively. The width of the mist region correlated with the inverse square of the fracture stress, higher strengths yielding narrower mist regions. From an SEM topographical study it was noted that the mist roughness also correlated with the strength squared, again suggesting a strain energy relationship. The combined results of the mist width and roughness trends suggest that formation of the mist may occur over a particular range of strain energy release rates, but the specific mechanism is not known with certainty at this time.

Acknowledgments

The authors gratefully acknowledge F. F. Ernsberger of PPG Industries for supplying the float glass used in this study, and the technical advice and assistance of J. Lebiedzik of Lemont Scientific Company with the surface topography. Discussions with N. Shinkai of Asahi Glass Company were instrumental in creating the initial interest in the problems addressed in this paper.

References

[1] Govila, R. K., Beardmore, P., and Kinsman, K. R. in *Fractography and Materials Science, ASTM STP 733*, American Society for Testing and Materials, 1981, pp. 225-245.
[2] Mecholsky, J. J., Jr. and Freiman, S. W. in *Fracture Mechanics Applied to Brittle Materials, ASTM STP 678*, American Society for Testing and Materials, 1979, pp. 136-150.
[3] Kirchner, H. P. and Gruver, R. M. in *Fracture Mechanics of Ceramics*, Vol. 3, Plenum Press, New York, 1978, pp. 365-378.
[4] Abdel-Latif, A. I. A., Bradt, R. C., and Tressler, R. E., *International Journal of Fracture*, Vol. 13, No. 31, 1977, pp. 349-359.
[5] Terao, N., *Journal of the Physical Society of Japan*, Vol. 8, 1953, pp. 545-549.
[6] Levengood, W. C., *Journal of Applied Physics*, Vol. 29, No. 5, 1958, pp. 820-826.
[7] Shand, E. B., *Journal of the American Ceramic Society*, Vol. 42, No. 10, 1959, pp. 747-749.
[8] Kerper, M. J. and Scuderi, T. G., *Bulletin of the American Ceramic Society*, Vol. 43, No. 9, 1964, pp. 622-625.
[9] Johnson, J. W. and Holloway, D. G., *Philosophical Magazine*, Vol. 14, No. 130, 1966, pp. 731-743.
[10] Shinkai, N. and Hara, M., *Asahi Research Reports*, Vol. 19, No. 2, 1969, pp. 73-84.
[11] Orr, L., *Materials Research and Standards*, Vol. 12, No. 1, 1972, pp. 21-23, 47.

[12] Mecholsky, J. J., Jr., Rice, R. W., and Freiman, S. W., *Journal of the American Ceramic Society*, Vol. 57, No. 10, 1974, pp. 440-443.
[13] Shinkai, N., *Japanese Journal of Applied Physics*, Vol. 14, No. 1, 1975, pp. 147-148.
[14] Johnson, J. W. and Holloway, D. G., *Philosophical Magazine*, Series 8, Vol. 17, No. 149, 1968, pp. 899-910.
[15] Congleton, J. and Petch, N. J., *Philosophical Magazine*, Vol. 16, No. 142, 1967, pp. 749-760.
[16] Kobayashi, A. S., Wade, B. G., Bradley, W. B., and Chiu, S. T., *Engineering Fracture Mechanics*, Vol. 6, No. 1, 1974, pp. 81-92.
[17] Aoki, S. and Sakata, M., *Engineering Fracture Mechanics*, Vol. 13, No. 3, 1980, pp. 491-499.
[18] Abdel-Latif, A. I. A., Bradt, R. C., and Tressler, R. E. in *Fractography and Materials Science, ASTM STP 733*, American Society for Testing and Materials, 1981, pp. 259-270.
[19] Lebiedzik, J. and White, E. W. in *Scanning Electron Microscopy/1975 (Part I)*, Proceedings of 8th SEM Symposium, IITRI, Chicago, April 1975, pp. 181-188.
[20] Lebiedzik, J., Edwards, R., and Phillips, B. in *Scanning Electron Microscopy/1979 (Part II)*, SEM Inc., AMF O'Hare, Ill., pp. 61-66.
[21] Lebiedzik, J., *Scanning*, Vol. 2, No. 4, 1979, pp. 230-237.
[22] Mecholsky, J. J., Jr., Freiman, S. W., and Rice, R. W., *Journal of Materials Science*, Vol. 11, No. 7, 1976, pp. 1310-1319.
[23] Mecholsky, J. J., Jr., Freiman, S. W., and Rice, R. W. in *Fractography in Failure Analysis, ASTM STP 645*, American Society for Testing and Materials, 1978, pp. 363-379.
[24] Freiman, S. W. in *Glass: Science and Technology*, Vol. 5, D. R. Uhlmann and N. J. Kreidl, Eds., Academic Press, New York, 1980, pp. 21-78.
[25] Wiederhorn, S. M., *Journal of the American Ceramic Society*, Vol. 52, No. 2, 1969, pp. 99-105.
[26] Shinkai, N., Bradt, R. C., and Rindone, G. E., *Journal of the American Ceramic Society*, Vol. 64, No. 7, 1981, pp. 426-430.

DISCUSSION

R. Rice[1] *(written discussion)*—You have nicely demonstrated in more detail the widely observed general inverse trend between failure stress and density of fracture features—mist in this case. You also noted a correlation with strain energy, which I feel makes much sense. Have you quantitatively tested such a relation? For example, compared the mist surface area to the strain energy density?

M. J. Ball et al (authors' closure)—We have not directly compared the mist region fracture surface area with the strain energy density. However, the graph of σ_f^2 versus RMS surface roughness (Fig. 5) does just that in an indirect fashion: the strain energy per unit volume is simply $\frac{1}{2}\sigma^2/E$ and the surface area is related to the RMS roughness.

[1]National Research Laboratory, Washington, D.C. 20375.

Terry A. Michalske[1]

Fractography of Slow Fracture in Glass

REFERENCE: Michalske, T. A., **"Fractography of Slow Fracture in Glass,"** *Fractography of Ceramic and Metal Failures, ASTM STP 827*, J. J. Mecholsky, Jr. and S. R. Powell, Jr., Eds., American Society for Testing and Materials, 1984, pp. 121-136.

ABSTRACT: Slow fracture in soda-lime silica glass produces fracture surface markings associated with (1) a limit for stress corrosion crack growth, (2) plateau crack growth in humid environments, and (3) dynamic effects of liquids. For each case, the associated fracture surface marking is described and its interpretation reviewed. Discussion of each marking demonstrates the usefulness of fractography in solving problems of failure analysis as well as understanding slow fracture in glass.

KEY WORDS: fractography, glass fracture, fracture mechanics, crack propagation

This publication contains several articles concerned with surface features generated during glass fracture. Armed with interpretations of these fracture surface markings (FSM), information concerning the failure event can be obtained by postmortem examination of a failed part. The magnitude of stress at failure, the direction and state of stress, and the origin flaw location are examples of data obtainable from FSM generated during the rapid or catastrophic stage of failure. In many cases, an incubation period may precede catastrophic failure, and processes occurring during the initial stage of fracture also leave characteristic markings on the fracture surface. This paper reviews the FSM associated with slow fracture in glass and discusses the importance of these markings in determining the cause of component failure as well as their significance to understanding slow fracture processes.

Slow Crack Growth in Glass

The incubation period prior to catastrophic failure of glass (often referred to as *delayed failure*) has been attributed to slow growth of pre-existing flaws.

[1] Sandia National Laboratories, Albuquerque, N.M. 87185.

Under applied load, small surface cracks can grow large enough to serve as sites for rapid failure. Because of this effect it is important to understand what controls crack growth rates in glass. Figure 1 demonstrates the strong effect of environment on the rate of crack growth in soda-lime silica glass. The plot of crack velocity (V) versus stress intensity (K_I) indicates that water, either as a moist gas or liquid, increases the crack growth rate. These crack growth curves have been partitioned into three basic regions of behavior by Wiederhorn [*1*]. Region I is controlled by the chemical reaction rate of water with glass at the crack tip, Region II is controlled by water transport within the crack, and Region III represents crack propagation which is independent of water in the surrounding environment. Figure 1 also shows Region IA occurring at low stress intensity, which indicates the onset of a stress corrosion limit.

The time-to-failure under constant load can be calculated from K_I versus V data when an initial flaw size and stress level are known. This calculation uses the measured K_I versus V relationship (Eq 1) along with a fracture mechanics equation (Eq 2) relating flaw length C, applied stress σ, and test geometry Y. This expression can be integrated to yield an equation describing the time-to-failure (Eq 3).

$$V = \frac{dc}{dt} = AK_I^n \tag{1}$$

$$K_I = Y\sigma_a\sqrt{c} \tag{2}$$

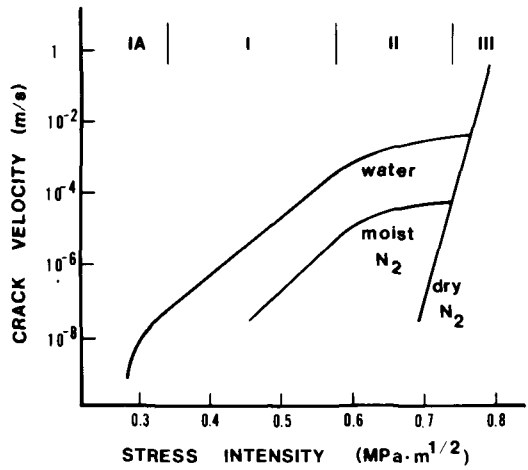

FIG. 1—*Fracture behavior of soda-lime silica glass exposed to environments of liquid water, moist air, and dry air.*

$$t_f = \frac{2[(K_{IC}/K_{Ii})^{n-2} - 1]}{(n-2)AY^2\sigma_a^2 K_{IC}^{n-2}} \tag{3}$$

where K_{Ii} and K_{IC} are the initial stress intensity and the stress intensity for catastrophic failure respectively. This calculation requires knowledge of the environment, applied stress, and initial flaw size. When this information is not known, analysis of FSM on a failed component can provide it.

Stress Corrosion Limit

As previously mentioned, K_I versus V measurements [*2*] suggest that there may be a limit in K_I below which no further crack growth occurs (Region IA of Fig. 1). This effect is seen at $K_I \approx 0.3$ MPa · $m^{1/2}$ for soda-lime-silica glass in water. Charles and Hillig [*3*] have modeled this phenomenon based on crack tip geometry changes. Figure 2 summarizes the results of their model. The dashed lines indicate the initial crack tip shape. The solid lines indicate the crack tip shape after some exposure to a corrosive environment (water). At high stress (Fig. 2*a*), corrosion at the crack tip is accelerated, yielding a sharpening of the tip radius; at low stress, uniform corrosion results in a radius increase (Fig. 2*c*); and at intermediate stress, corrosion and stress-enhanced corrosion are balanced to yield a constant radius of curvature with time (Fig. 2*b*).

Combining fracture surface analysis and fracture mechanics techniques, this model for a stress corrosion limit due to crack blunting was experimentally verified by Michalske [*4*]. Figure 3 illustrates the relationships between

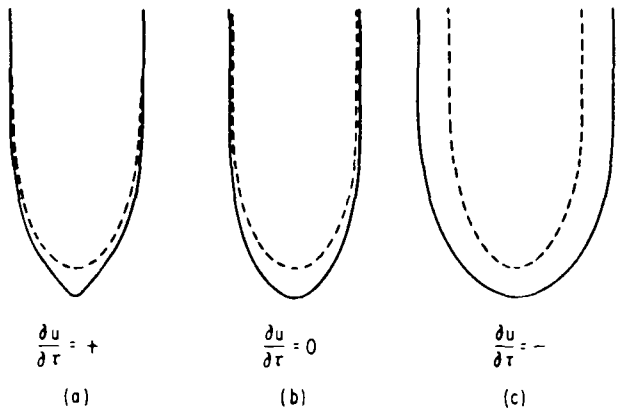

FIG. 2—*Hypothetical changes in crack tip geometry.* (a) *High stress: crack sharpening due to stress-enhanced corrosion.* (b) *Intermediate stress: stress-enhanced corrosion and corrosion balanced to yield constant tip radius.* (c) *Low stress: crack tip rounding due to corrosion (after Charles and Hillig* [3]*).*

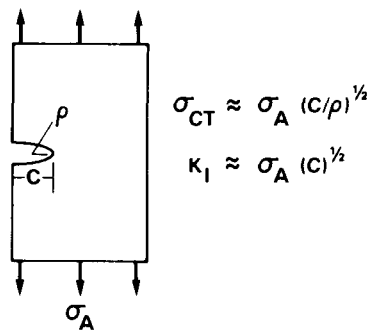

FIG. 3—*Schematic of tension specimen with elliptical notch. Equations show that stress intensity* (K_I) *depends on crack length* (c) *whereas the crack tip stress* (σ_{ct}) *is also a function of the tip radius* (ρ) *(after Michalske* [4]*).*

the stress concentrated at a crack tip and the applied stress. The relationships show that the radius of curvature is important only to the concentrated stress at the crack tip and is not reflected in the stress intensity factor. Since the rate of a chemical reaction is considered to be dependent on stress, a change in the crack tip radius will affect the local fracture process and this effect would be observed in the measured K_I versus V response. The experiment utilized a double cantilever beam specimen loaded to a stress intensity below the apparent stress corrosion limit ($K_I = 0.225$ MPa·m$^{1/2}$). After aging in water for 16 h, the stress intensity was raised above the fatigue limit. In Fig. 4, the dashed line indicates crack growth for an unaged specimen. The solid line indicates the behavior observed when the specimen was aged. The slopes indicate that the crack velocities are the same in either case; however, the aged sample required some time before crack propagation began. The hysteresis was ascribed to the time required to reform a sharp crack after blunting.

Figure 5 is a photomicrograph showing the FSM generated by aging in water. The crack propagation direction is left to right. The first vertical line (a) on the fracture surface is an arrest line which results from changing the applied load without aging. The next vertical line (b), which is much more pronounced, resulted from the 16-h aging cycle. Michalske interpreted this FSM as representing the process of resharpening a corrosion-blunted crack tip. Each of the segments (light and dark areas along the blunted crack front) represent a specific point of origin for the resharpening process. As the nuclei for the sharp crack grow, they intersect to form the hackle ridges extending parallel to the direction of crack growth. This interpretation suggested that equilibrium crack growth rates (as measured in K_I versus V studies) will not be obtained until a continuous crack front has formed. It is noteworthy that the same FSM was observed by Wiederhorn [5] on borosilicate glass exposed to acidic solution.

The evidence (fractographic and fracture mechanics) for crack blunting in

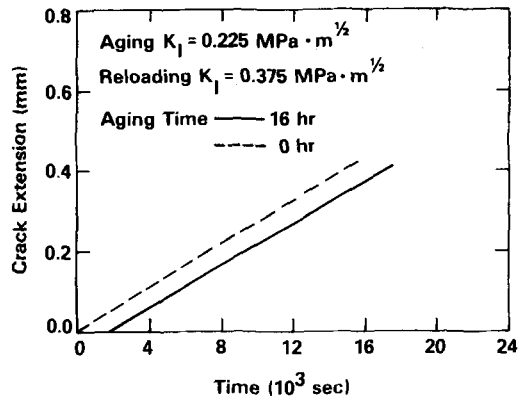

FIG. 4—*Crack extension versus time after reloading soda-line silica specimen aged in water (after Michalske* [4]*).*

soda-lime silica glass has strong implications for long-term structural reliability. Firstly, a crack which is held below the K_I for blunting ($K_I = 0.25$ MPa·m$^{1/2}$) will show no crack growth with time and never experience delayed failure. From a design point of view, this sets a limit in the stress (provided the flaw population is known) for which the material can be expected to reliably perform. Secondly, flaws which have blunted before loading (or never were sharp) will require some incubation period before the onset of slow crack growth. Figure 6 is a plot showing the calculated time to failure (t_{cal}) for a 25-μm flaw (from Eq 3) as well as experimentally measured sharpening times (t_s) for cracks blunted in water. This representation shows that blunt flaws loaded to stress intensities above the stress corrosion limit will require an order of magnitude more time to sharpen than is required to grow an equal length sharp crack to failure. The plot also suggests that if a specimen with 25-μm flaw size has not failed due to crack growth in 10^6 s ($\approx$ 11 days) crack blunting will occur and preclude any delayed failure.

Plateau Crack Growth

As shown in Fig. 1, Region II crack growth in humid environments appears as a plateau on the K_I versus V diagram. Frechette et al [*6, 7*] have studied the FSM generated during Region II crack growth in soda-lime silica glass.

Figure 7 shows the fracture surface detail generated when a through crack is propagated in Region II in a moist environment (liquid decane with approximately 1% water). The vertical lines in the sketch indicate the crack front shapes as they appeared at various times during crack extension. The wedge-like marking (intersection scarp) is the FSM associated with plateau crack growth. The crack front shape at the far left demonstrates the normal

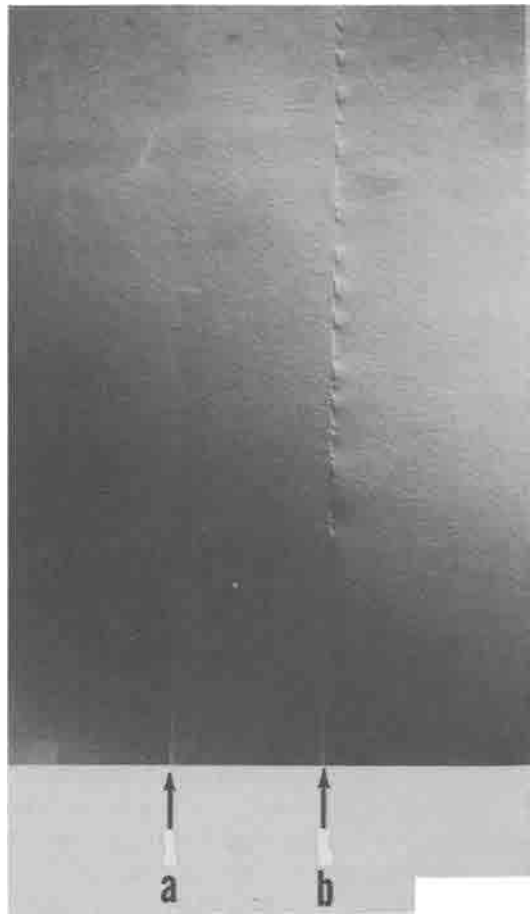

FIG. 5—*Optical photomicrograph of fracture surface showing detail resulting from* (a) *momentary crack arrest and* (b) *16-h aging period. Fracture direction from left to right: Nomarski differential contrast optics (after Michalske* [4]*).*

shape for a through-cracked plate specimen. In this part of the specimen, the crack is moving slowly enough for water to diffuse evenly along the front of the crack. As the crack velocity increases, water cannot diffuse evenly along the entire crack; the center portion of the crack represents a longer diffusion path and is first to be starved of water. The limited access causes the center portion of the crack front to lag behind the outside edge. With increased velocity, the boundary for water diffusion spreads to either free surface. At that point, the intersection scarp reaches the free surfaces of the specimen and the crack front shape returns to the normal positive curvature. The wedge-like marking is an intersection scarp. The term *intersection scarp* is used since the

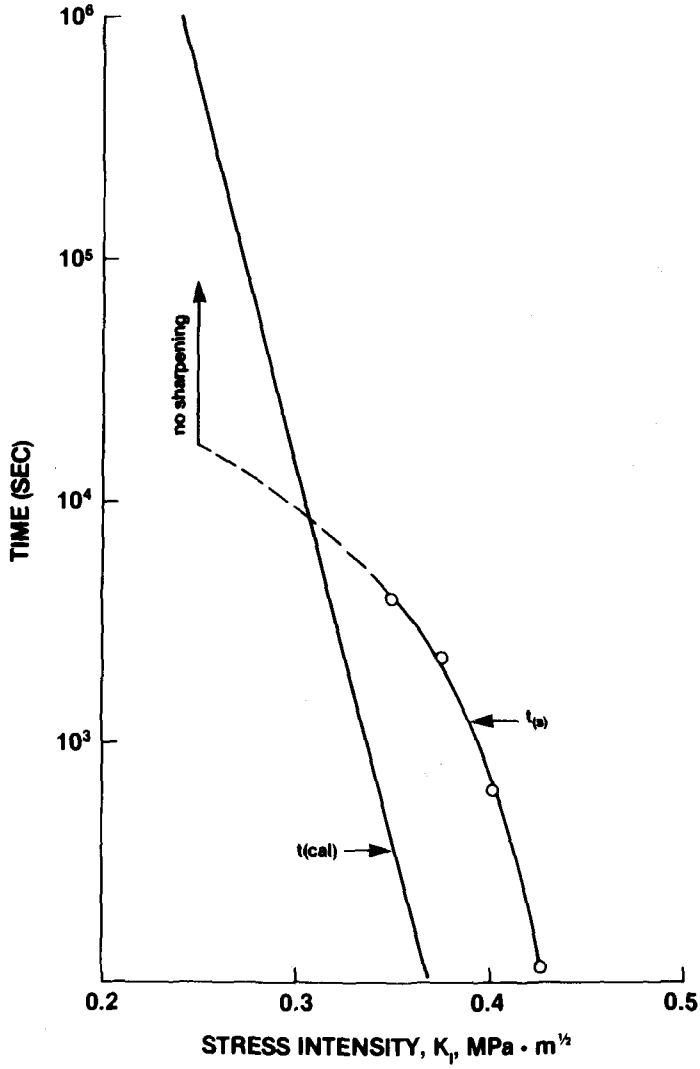

FIG. 6—*Time required to nucleate a sharp crack after blunting* ($t_{(s)}$) *and time-to-failure due to crack growth* ($t_{(cal)}$) *plotted as a function of applied* K_I *(after Michalske* [4]*).*

FSM is generated at the intersection of moist and dry environments and its surface topography resembles the geologic scarp.

The interpretation of Frechette et al [*6, 7*] shows that Region II in moist environments is not a unique region of crack growth but is composed of components from Regions I and III. Crack growth during the intersection scarp was generated such that the outside portion of the crack front is running in

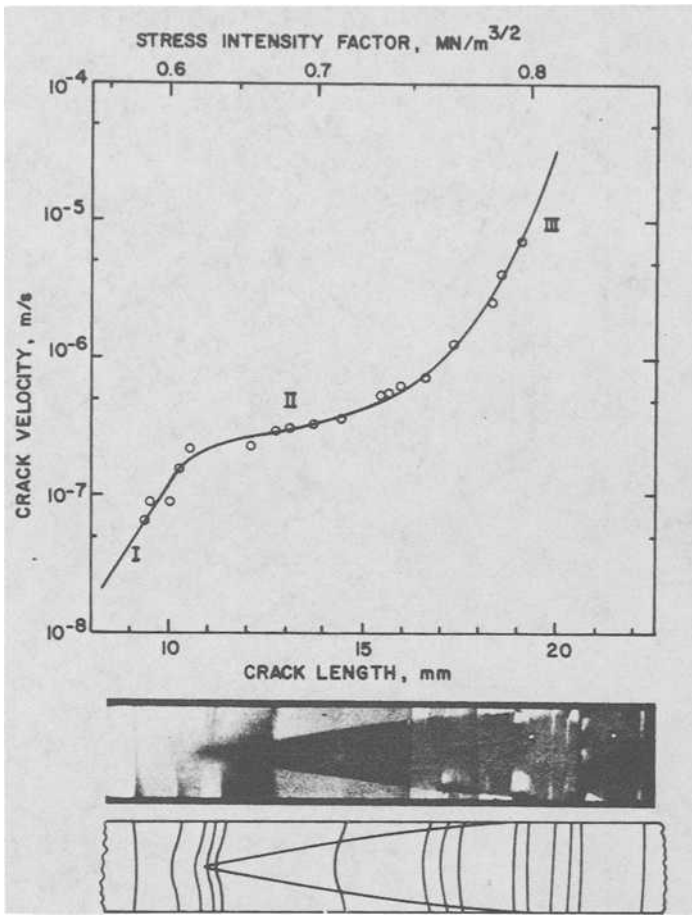

FIG. 7—*Relation between* K_I, *crack velocity, crack length, and appearance of fracture surface of glass sheet broken in liquid decane. Crack length scale is common to both plot and micrograph. Black top and bottom borders in photograph are sample surface; fracture direction from left to right (after Quackenbush and Frechette* [7]*).*

(Region I) and the inside portion of the crack front is running in a water-free mode (Region III). This interpretation suggests that Region II behavior is affected by the geometry of the crack. The crack geometry influence on Region II is expected to be strongest for surface flaws which have only one line of access to environmental water. Presently, fractography has not been used to study Region II effects for surface flaws; however, it is clear that this information is critical to the fracture mechanics evaluation of proof testing in humid environments [*8*].

Another type of intersection scarp not associated with plateau crack growth has been observed by Michalske et al [*9*]. In this case, the intersection scarp is

formed at the boundary between wet and dry portions of a crack front which is propagating in an environment with limited access to water. Figure 8*a* shows the sequence that is observed as a dry crack (free of liquid) encounters water on the specimen surface. At Position 1 the normal DCB crack front shape is observed. At Position 2 the crack front encounters water on the specimen surface. At this time two events take place: (1) capillary action draws

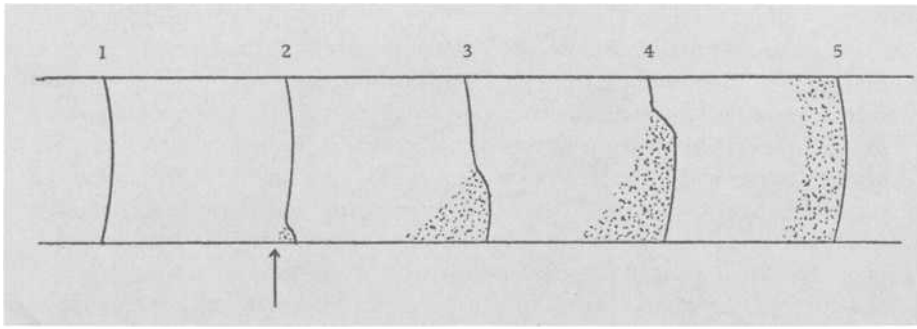

(a)

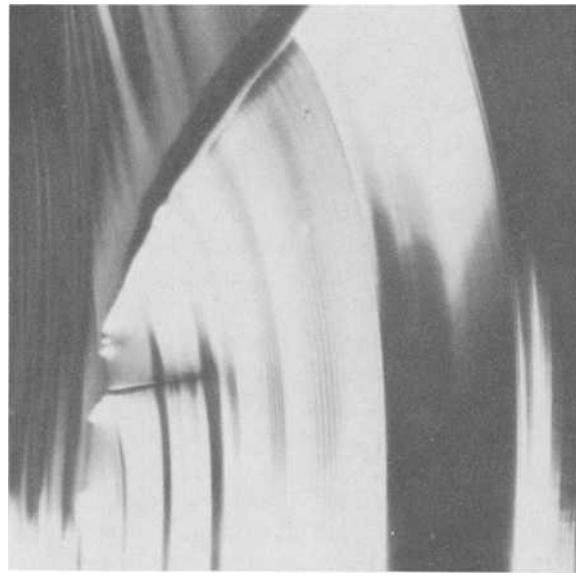

(b)

FIG. 8—(a) *Stages (1 to 5) in fracture front development from a dry starter crack in a partly wetted specimen under double cantilever beam (DCB) loading. Stippled areas indicate liquid water trailing the crack front. Arrow shows initial area of water contact.* (b) *Fracture surface showing scarp development at water boundary.* ×25 *(after Michalske et al* [9]*).*

some water into contact with the moving crack front and (2) the wetted portion of the crack front jogs slightly ahead of the dry section. Positions 4 and 5 represent the continued spread of water across the moving crack front until at Position 5 the crack front is completely wet. Figure 8*b* is a photomicrograph showing a fracture surface in soda-lime silica glass prepared in this manner. The intersection scarp forms at the boundary of liquid water penetration.

Formation of the intersection scarp was interpreted on the basis of the K_I versus V diagram (Fig. 1). At velocities below 0.1 mm/s, the wetted portion of the crack front propagates more easily than the dry. (In this case, *dry* refers to that portion of the crack front exposed to room air.) Accordingly, the wet section requires less stress to propagate and is displaced slightly ahead of the dry section. The magnitude of this displacement is limited since the advance of one section will increase the mechanical loading on the other. Since the conditions of fracture are different on the wet and dry portions of the crack front, the individual planes of fracture also differ. This difference in crack plane results in a sharp ridge or scarp at the line of intersection.

This type of intersection scarp can be useful in determining the cause of failure because it shows that water was present at the time of failure. This may be of interest in a forensic case where it is important to know if it was raining at the time of an incident or possibly in questions of thermal shock fracture where the exact nature of the thermal shock event is unknown. (What is a liquid or air quench?)

Dynamic Effects of Liquids

Michalske et al [*10*] have examined the FSM generated as a crack is accelerated to catastrophic velocities (>1 m/s) in a liquid environment.

Figure 9*a* is a schematic of the FSM generated when a through crack accelerates through the Region II/III transition range in water. At low velocity (left side of sketch) the crack surface appears mirror-like. As the velocity increases to approximately 10^{-2} m/s fine hackle ridges form. The hackle increases in density until it is sharply terminated by a distinct change in the fracture surface plane. This change in plane is termed a *cavitation scarp*. After cavitation scarp formation, the fracture surface returns to a mirror-smooth condition. Figure 9*b* is a photomicrograph of a soda-lime silica glass sample prepared in this manner.

Crack velocity effects associated with the cavitation scarp were obtained using ultrasonic fractography [*11*]. This technique involves marking the fracture surface with Wallner lines which are induced by periodic imposition of shear waves on the principal applied stress. The spacing of these lines can be used to calculate local crack velocity.

Figure 10 contains a plot of the crack velocity during cavitation scarp formation and a photomicrograph showing timing lines. A discontinuous increase in crack velocity occurs at the cavitation scarp. The complete interpretation

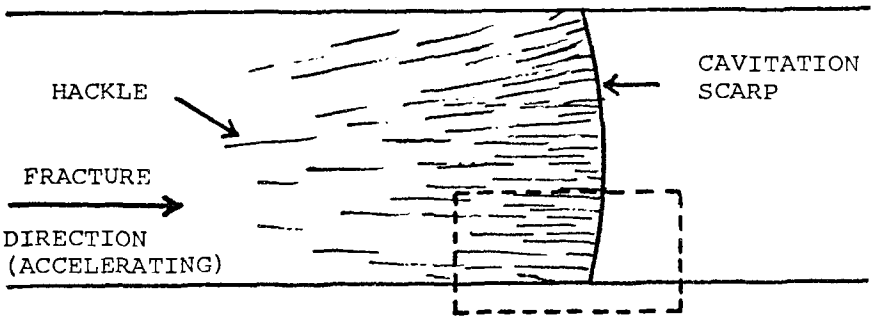

(a)

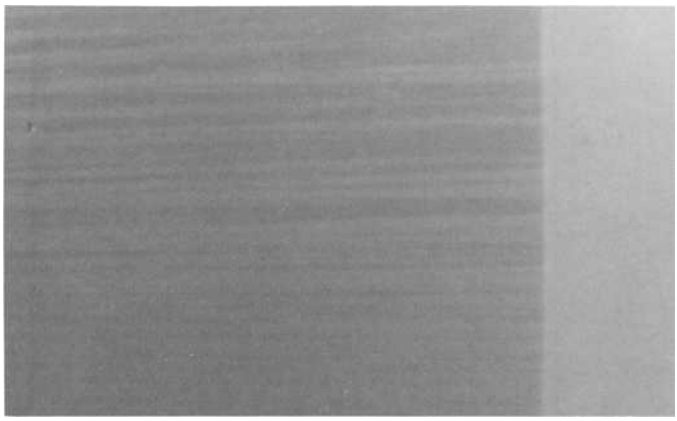

(b)

FIG. 9—(a) *Schematic of exposed surface of glass fracture accelerated through Region II/III transition in water. With increasing velocity, initially mirror smooth surface (far left) shows generation of hackle steps, followed by a cavitation scarp and return to mirror smoothness at greater velocity.* (b) *Micrograph of area within dashed lines.* ×93 *(after Michalske et al* [10]*).*

of this velocity effect will not be discussed here, but the results of that interpretation are summarized in Fig. 11. At crack velocities greater than 10^{-2} m/s viscous effects will begin to retard the crack propagation rate [*12*]. The viscous effect appears on the crack growth diagram as the onset of the plateau region in liquid water. As the crack velocity increases, the viscous effects cause the crack growth curve in the liquid to intersect and cross the crack growth curve for a dry environment. At sufficiently high velocity, the viscous forces cause the liquid environment within the crack to cavitate, leaving the crack dry. At the point of cavitation, the crack velocity jumps from the wet

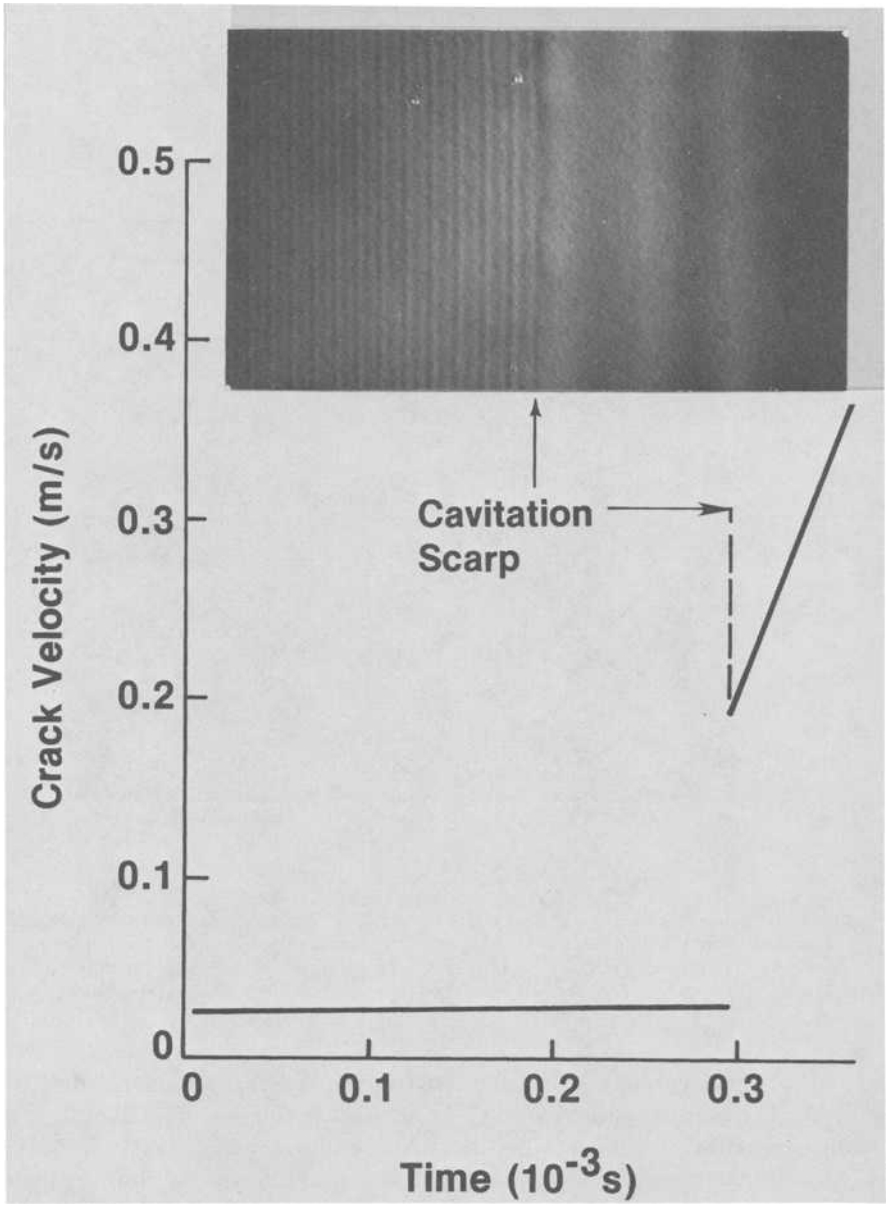

FIG. 10—*Crack velocity versus time on either side of the cavitation scarp. Insert shows fracture surface with timing marks (after Michalske et al* [13]*).*

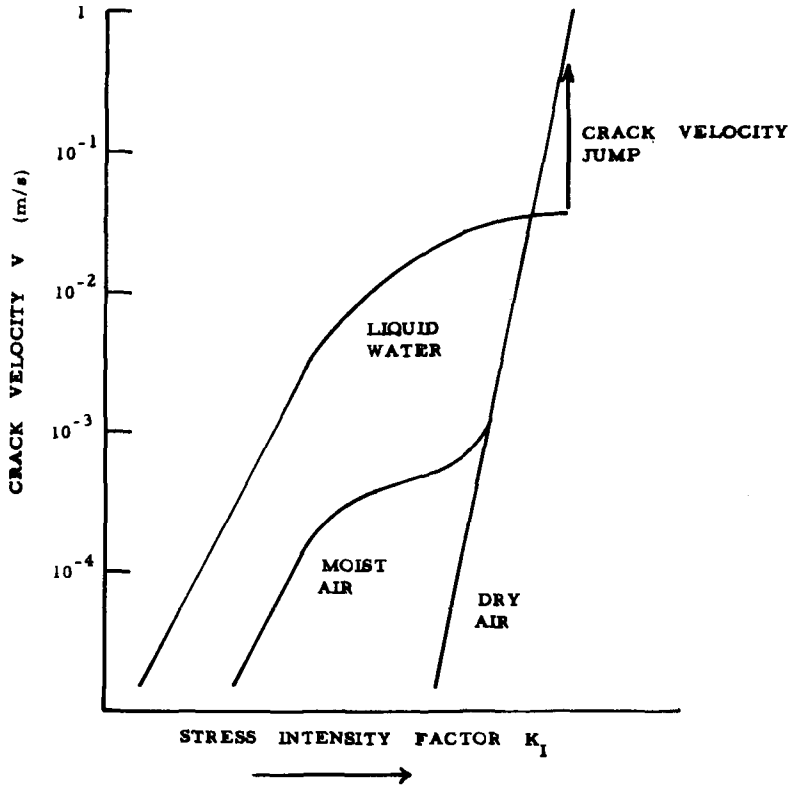

FIG. 11—*Idealized crack velocity curves in liquid water, moist air, and dry air. The crack velocity jump (indicated by arrow) occurs when an accelerating water-filled crack breaks away from its liquid environment and assumes the corresponding dry-environment velocity of that stress intensity (after Michalske et al* [10]*).*

curve, which is held back by viscous forces, to the equilibrium position on the dry curve. This instantaneous change in environment causes the order of magnitude jump in crack velocity experimentally observed. The process of cavitation in the moving crack has been modeled by Michalske and Frechette [*10*], and the calculated velocity for cavitation was in excellent agreement with the measured velocity of cavitation scarp formation.

The transition from slow to rapid failure was also investigated for the case of surface-flawed specimens broken in water [*13*]. Figure 12*a* is a schematic of the FSM observed. The sketch shows the controlled flaw which was induced by the technique described by Hudson and Frechette [*14*]. This flaw served as the origin of failure and was present in the surface before the external stresses were applied. Next, the fine hackle ridges termed *transition hackle* develop as the origin crack grows under the applied stress. This hackle is identical in appearance to that observed on the edge-cracked specimen. The surface flaw

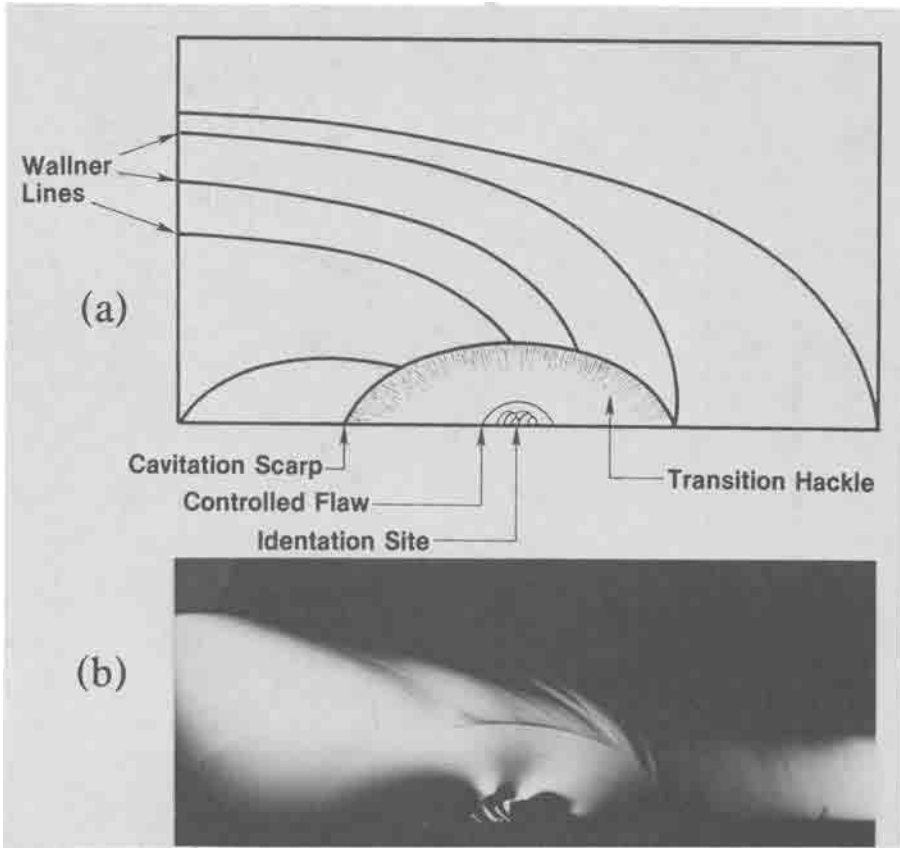

FIG. 12—(a) *Schematic of exposed surface of glass fracture resulting from bending in water. Various surface detail which were formed during crack growth are labeled.* (b) *Micrograph showing enlargement of area in sketch.* ×15 *(after Michalske et al* [13]*).*

also shows formation of a cavitation scarp which sharply terminates the transition hackle. After formation of the cavitation scarp a series of Wallner lines appeared, indicating the growth pattern during the rapid fracture regime. Figure 12*b* is a photomicrograph of a soda-lime silica glass bar broken in such a manner.

The arrows in Fig. 13 show the growth pattern observed as the origin flaw developed. Initially, the flaw grows in all directions, spreading more rapidly along the tensile surface to form a semielliptical front. Following the cavitation scarp, the crack develops from the left side of the ellipse, spreading from that area to severe the specimen. Along the tensile surface of the specimen the crack velocity is highest; thus that portion of the crack front serves as the initial site for liquid cavitation. After cavitation, the increased rate of crack propagation in the dry area causes that portion of the crack to sweep around

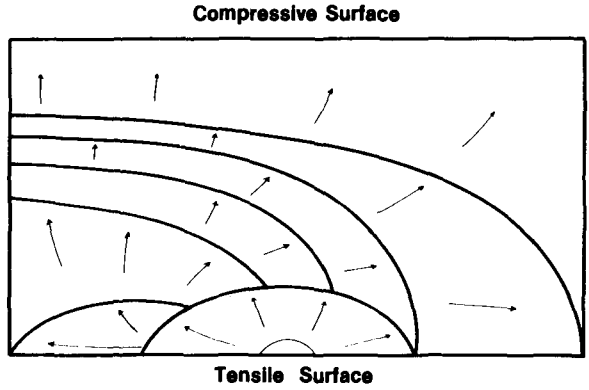

FIG. 13—*Schematic showing development of surface flaw by application of bending stresses in water environment. Arrows indicate direction of local fracture (after Michalske et al* [13]*).*

and intersect those portions still wet. (The remaining wet section of the crack is unable to cavitate since its velocity is too low.)

This interpretation has several important implications. Firstly, it provides an understanding of the mechanism responsible for the transition from slow to rapid fracture in liquid environments. Wiederhorn [*15*] has shown that this information is essential to the models used to predict the effect of proof testing on the strength. The cavitation scarp is also important in its role of defining the size flaw present at the onset of catastrophic failure. The critical flaw size is necessary to the calculation of the K_{IC}-value measured in a stress corrosion environment. It is important to note that critical flaw size taken from the cavitation scarp must be measured from the center of the origin flaw to the point on the scarp where cavitation initiated. Finally, after the K_{IC} has been measured by this technique, the stress at failure may be calculated (Eq 2) from a post-mortem measurement on the failed component.

Summary

The fracture surface markings generated during slow fracture in soda-lime silica glass are reviewed. In each case the markings can be attributed to effects of aqueous environments on the rate of crack growth. In the low applied stress regime, water corrodes the glass in the crack tip region, thereby altering the crack geometry. Crack blunting drastically reduces the fracture rate and produces a prominent fracture marking associated with the process of sharpening a corrosion-blunted crack tip. At intermediate stress levels, the crack velocity is independent of applied stress for fracture in moist air. Fracture markings generated in this regime show that plateau crack growth is caused by limited water transport to the crack tip. The surface detail suggests that water is transported from the sides of the crack; thus the plateau region will

be sensitive to crack geometry. Finally, in the high stress regime, dynamic effects of liquids can alter the crack velocity. Fracture markings formed in this region are associated with viscous drag, which tends to slow the fracture, as well as liquid cavitation, which can result in a discontinuous increase in crack velocity.

Acknowledgments

This work was performed at Sandia National Laboratories and supported by the U.S. Department of Energy under Contract DE-ACO4-76DP00789.

References

[1] Wiederhorn, S. M., *Journal of the American Ceramic Society*, Vol. 50, No. 8, 1967, pp. 407-14.

[2] Wiederhorn, S. M. and Bolz, L. H., *Journal of the American Ceramic Society*, Vol. 53, 1970, pp. 543-548.

[3] Charles, R. J. and Hillig, W. B., "The Kinetics of Glass Failure by Stress Corrosion," Symposium on Mechanical Strength of Glass and Ways of Improving It, Florence, Italy.

[4] Michalske, T. A. in *Fracture Mechanics of Ceramics*, Vol. 5, R. C. Bradt, D. P. H. Hasselman, and F. F. Lange, Eds., Plenum, New York, 1983, pp. 277-289.

[5] Wiederhorn, S. M. and Johnson, H., *Journal of the American Ceramic Society*, Vol. 56, No. 4, 1973, pp. 192-197.

[6] Varner, J. R. and Frechette, V. D. in *Amorphous Materials*, D. W. Douglas and Bryan Ellis, Eds., Wiley-Interscience, New York, 1972, pp. 507-512.

[7] Quackenbush, C. L. and Frechette, V. D., *Journal of the American Ceramic Society*, Vol. 61, No. 9, 1978, pp. 402-406.

[8] Wiederhorn, S. M., to be published in ASTM Symposium on Methods for Assessing Structural Reliability of Ceramic Materials.

[9] Michalske, T. A., Varner, J. R., and Frechette, V. D. in *Fracture Mechanics of Ceramics*, Vol. 4, R. C. Bradt, D. P. H. Hasselman, and F. F. Lange, Eds., Plenum, New York, 1978, pp. 639-649.

[10] Michalske, T. A. and Frechette, V. D., *Journal of the American Ceramic Society*, Vol. 63, No. 11-12, 1980, pp. 603-609.

[11] Michalske, T. A. and Frechette, V. D., *International Journal of Fracture*, Vol. 17, No. 3, 1981, pp. 251-256.

[12] Wiederhorn, S. M. in *Fracture Mechanics of Ceramics*, Vol. 4, R. C. Bradt, D. P. H. Hasselman, and F. F. Lange, Eds., Plenum, New York, 1978, pp. 549-580.

[13] Michalske, T. A., Frechette, V. D., and Hudson, R. in *Advances in Fracture Research*, Vol. 2, D. Francis, Ed., Pergamon, New York, 1981, pp. 1091-1097.

[14] Hudson, R. L. and Frechette, V. D., *Journal of the American Ceramic Society*, Vol. 65, No. 2, 1981, pp. 26-27.

[15] Wiederhorn, S. M., Freiman, S. W., Fuller, E. R., and Simmons, K., "Effects of Water and Other Dielectrics on Crack Growth," accepted for publication, *Journal of Materials Science*.

Ceramics

Surface Analysis Techniques

C. G. Pantano[1] *and J. F. Kelso*[1]

Chemical Analysis of Fracture Surfaces

REFERENCE: Pantano, C. G. and Kelso, J. F., **"Chemical Analysis of Fracture Surfaces,"** *Fractography of Ceramic and Metal Failures, ASTM STP 827*, J. J. Mecholsky, Jr. and S. R. Powell, Jr., Eds., American Society for Testing and Materials, 1984, pp. 139-156.

ABSTRACT: The applicability of various instrumental techniques for chemical analysis of fracture surfaces is reviewed. It is shown that methods which possess both a high spatial and a high in-depth resolution are usually required for analyzing structural heterogeneities on the fracture surface. When the features of interest have submicron dimensions, scanning Auger microanalysis (SAM) is most applicable, whereas features whose dimensions exceed 1 to 2 μm may be more easily characterized with scanning electron microscopy and energy dispersive X-ray analysis (SEM-EDXA). Chemical analysis of fracture surfaces can also be used to investigate the atomistic mechanisms of crack propagation; this is of particular benefit when chemically-assisted crack growth is involved. In this case, a method with exceptional in-depth resolution is required to measure the composition of reaction products and modified surface layers in the fracture plane. In this regard, the unique capabilities of ion-scattering spectroscopy (ISS) and ion microscopy are also discussed.

KEY WORDS: fracture surfaces, chemical analysis, scanning Auger microanalysis, scanning electron microscopy, energy dispersion X-ray analysis, ion scattering spectroscopy, ion microscopy, spatial and depth resolution

Chemical analysis of fracture surfaces is usually performed for one of two reasons. In most instances, the object is to determine the chemical composition of any structural heterogeneities observed at the fracture surface. These inhomogeneities are typically particulate contamination, precipitates, pores, glassy phase, or grain boundaries. Very often, these inhomogeneities facilitate the initiation or propagation of the crack. For example, unexpected reductions in the fracture strength of polycrystalline ceramics are most often caused by grain boundary segregants or precipitates. Here, a chemical analy-

[1]Department of Materials Science and Engineering, Pennsylvania State University, University Park, Pa. 16802.

sis of the intergranular fracture surface can be used to identify the segregant or precipitate [*1*]; usually, these segregants or precipitates originate from impurities in the raw materials or sintering aids used to process the materials. Similarly, chemical analysis has been used to understand the spontaneous failure of tempered sheet glass. In this case, nickel sulfide inclusions were found within the fracture surfaces [*2*]; although the sulfur was an expected constituent of the commercial glass, the nickel was identified as an impurity introduced during the glass melting.

The other rationale for performing chemical analysis of fracture surfaces concerns the atomistic mechanisms of crack propagation in glasses, single crystals, or polycrystalline materials. Of particular interest are the chemically-assisted crack propagation phenomena responsible for slow crack growth and static fatigue. Thus, although there are no techniques that will allow the direct chemical analysis of a crack tip under stress, a variety of surface analysis techniques are available for characterizing the chemical nature of the fracture surface which results from crack tip propagation under particular conditions. Of course, these analyses are very difficult because an atomistic interpretation of fracture phenomena will require the ultimate in surface sensitivity and extreme care during the preparation and preservation of the fracture surface for analysis.

In this paper the applicability of various instrumental techniques for chemical analysis of fracture surfaces is reviewed.

Techniques for Chemical Analysis of Fracture Surfaces

Numerous instrumental methods are available for chemical analysis of surfaces. In the case of fracture surfaces, however, the size, geometry, and surface roughness of the specimen, as well as the type of information required, limit the applicability of the techniques. It has already been pointed out that the chemical analysis of fracture surfaces is usually aimed at measuring the elemental composition of a structural heterogeneity, or chemical inhomogeneity, on or within the fracture surface (for example, precipitates, pores, glassy phase, grain-boundaries, contamination), or the surface composition of a fractured glass, grain, or grain boundary and the reaction products resulting from chemically-assisted crack growth phenomena. Some of these atomic and microstructural features are schematically shown in Fig. 1 along with a schematic representation of the sampling volumes of X-ray analysis and Auger analysis. In the case of structural heterogeneities, the spatial resolution of the technique is of utmost importance, whereas the surface sensitivity, or in-depth resolution, of the technique is of most concern when the atomistic mechanisms of fracture are of interest. In many instances, one may require a high spatial and in-depth resolution simultaneously. For example, the grain boundary precipitates decorating an intergranular fracture surface may be extremely small. Or, one may want to compare the surface composi-

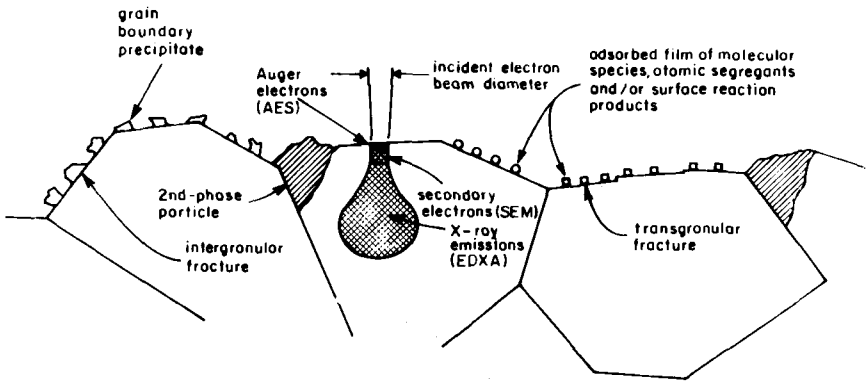

FIG. 1—*Schematic representation of various atomic and microstructural features of potential interest at fracture surfaces. The relative sampling volumes associated with AES, SEM, and EDXA analyses are shown for a particular incident electron beam diameter. In practice, the electron beam diameter is on the order of 50 to 200 nm for AES, 2.0 to 6.0 nm for SEM, and 0.5 to 1.0 μm for EDXA. The Auger electrons originate from 0.5 to 5.0 nm beneath the surface, the secondary electrons from 10 to 20 nm beneath the surface, and the X-ray emissions from 1 to 2 μm beneath the surface.*

tion at the fracture origin of a glass—where chemically-assisted crack growth may have occurred—with the surface composition in the hackle region where the high crack velocity might preclude any chemical interactions at the crack tip. In either case, the analysis technique must be surface sensitive, and at the same time must have sufficient spatial resolution to permit an analysis at particular microscopic regions of the fracture surface.

The most applicable techniques available for these fracture surface analyses are given in Table 1 according to their relative capability for microanalysis and surface analysis. It should be noted that Auger electron spectroscopy is the only technique which, at least in principle, offers high spatial and in-depth resolution simultaneously. The principles and practical applicability of each of these methods for chemical analysis of fracture surfaces are reviewed

TABLE 1—*Techniques available for fracture surface analyses.*

Technique	Spatial Resolution	In-Depth Resolution	Detection Sensitivity
Energy dispersive X-ray analysis (EDXA)	1 μm	1 to 2 μm	0.5 to 1% atomic
Scanning Auger microanalysis (SAM)	50.0 to 200.0 nm	0.5 to 5.0 nm	0.1 to 1% atomic
Ion microscopy	<1 μm	5.0 to 10.0 nm	0.01 to 100 ppm
Ion scattering spectrometry (ISS)	100 μm	1 monolayer	0.01 monolayer

in the following sections. For more detailed presentations of the theory, instrumentation, and application of these methods, the reader is referred to a number of excellent sources [*3–9*].

Scanning Electron Microscopy with Energy-Dispersive X-ray Analysis (SEM-EDXA)

Scanning electron microscopy with energy-dispersive X-ray analysis (SEM-EDXA) is perhaps the most widely applied method for fracture surface analysis. Here, the specimen surface is excited, or probed, with a finely focussed beam of electrons. The secondary and backscattered electrons emitted from this excited surface can be used to generate a high-resolution, three-dimensional image of the fracture surface topography. In addition, the characteristic X-rays emitted from the excited surface can be detected by an energy dispersive X-ray analyzer. This can provide a qualitative or quantitative measure of the elemental composition of particular features on the surface and their distribution.

The SEM-EDXA combines three analytical features with general applicability for fracture surface analysis:

1. Exceptional image resolution (typically 2.0 to 6.0 nm) *and* depth of focus for morphological and microstructural evaluation of the fracture surface.
2. The ability to perform a semiquantitative microchemical analysis.
3. Widespread availability of SEM-EDXA instrumentation capable of routine operation with little or no special sample preparation.

It should be emphasized that the SEM-EDXA is best used to establish the relationship between various microstructural features of the material and the morphology of the fracture surface, and not to examine the macromorphology, or fractography, of the fracture surface. This latter objective is more successfully accomplished with phase sensitive, and other, light optical techniques.

Thus the SEM-EDXA instrument can be used in the secondary electron emission mode to examine the morphology of the fracture surface and to determine precisely the microstructural nature and origin of the fracture. Subsequently, the energy dispersive X-ray analyzer can be used to obtain an X-ray spectrum from the grains, precipitates, or other microstructural defects associated with the fracture surface. In addition, an X-ray image may be obtained to illustrate the relationship, if any, between the microstructure of the fracture surface and the distribution of particular elements.

There are, of course, a number of limitations associated with chemical analysis of fracture surfaces by SEM-EDXA. Firstly, the depth resolution, or surface sensitivity, of EDXA in the SEM is limited to 1 to 2 μm in thickness. Hence, soluble grain-boundary segregants exposed along an intergranular

fracture surface may go undetected because they are often confined to the outer 1.0 to 10.0 nm of the grain. Even in cases where the segregant produces a measurable X-ray signal, it is impossible to obtain any quantitative information because the in-depth distribution of the species cannot be measured. Similarly, the precipitates and other microstructural inhomogeneities often associated with fracture can be, and often are, less than 1 μm in thickness. Here again, a determination of the precipitate composition is complicated by the X-ray signal emitted from the material underneath the precipitates (Fig. 1).

Secondly, the spatial resolution of the X-ray analysis or X-ray image is limited to about 1 μm due to electron beam spreading effects within the specimen. Therefore the composition of structural heterogeneities and chemical inhomogeneities whose dimensions within the plane of fracture are less than 1 μm cannot be accurately determined because of X-ray signal contributions from their surroundings. It should also be noted that any attempt to perform a chemical analysis of linear features in the fracture surface (for example, grain boundaries, slip bands, phase boundaries, and triple points) is difficult when the spatial resolution is limited to >1 μm.

The third point of concern regarding chemical analysis of fracture surfaces by SEM-EDXA is the inability to detect the low atomic number elements. In most cases, elements whose atomic number is less than sodium ($Z = 11$) cannot be detected. This is a severe limitation in the case of ceramics, and even in metals where boride, carbide, hydride, hydrate, nitride, oxide, and sulfide precipitates are often associated with fracture initiation or propagation. Of course, many SEMs are now equipped with wavelength dispersive X-ray analyzers which can detect elements down to boron ($Z = 5$). However, the wavelength dispersive analyzer requires an extremely smooth and flat surface in order to perform a meaningful analysis. Nonetheless, the wavelength dispersive X-ray analyzer offers distinct advantages over EDXA where a qualitative microchemical analysis of fracture surfaces containing low atomic species is desired.

Since many papers in this volume involve the use of SEM-EDXA for fracture surface analysis of brittle materials, examples of applications of SEM-EDXA will not be presented here.

Scanning Auger Microscopy (SAM)

Scanning Auger microscopy (SAM), or Auger microanalysis, has undergone major advances in the last five years. In this method, more generally known as Auger electron spectroscopy (AES), the specimen surface is excited with a beam of electrons. The so-called Auger electrons emitted from the excited region of the surface are detected by an electrostatic energy analyzer. The energy spectrum of the emitted Auger electrons provides for the qualitative and quantitative determination of surface composition. Unlike the

X-rays detected in SEM-EDXA, these Auger electrons have limited escape depths (Fig. 1). Thus AES has exceedingly high surface sensitivity, typically 0.5 to 5.0 nm in depth. All elements with atomic number $Z=3$ or greater will emit Auger electrons. In fact, the sensitivity of AES to low atomic species, in particular, is excellent and offers an important advantage over X-ray techniques. The exciting electron beam used in AES can be focussed to a small spot to permit a microanalysis. In SAM the beam is rastered over the surface for acquisition of Auger electron images.

It is especially significant that an Auger microanalysis or an SAM image can have exceptional spatial resolution. Since the detected Auger electrons arise from only the upper 0.5 to 5.0 nm of the surface, there is little effect of beam spreading within the specimen surface. Thus, whereas the spatial resolution in the SEM-EDXA is limited to 1 μm by beam spreading effects, the spatial resolution in AES/SAM is limited only by the incident electron beam size (Fig. 1). The minimum electron beam size varies depending upon the instrument but is available as small as 500 nm in commercially available SAM systems. In this regard it can be noted that some SEM instruments—where the electron beam can be focussed to less than 10.0 nm—have the capability to perform SAM. One must recognize, though, that the signal-to-noise ratio required to obtain a meaningful spectrum imposes a practical limit upon the minimum spot size which can be used for AES or SAM. Unless one can justify and tolerate exceedingly long data acquisition times, the electron beam size must be on the order of 10 to 200 nm for AES and SAM. Nonetheless, the capability to perform Auger microanalysis or SAM in an SEM is of special benefit in fracture surface studies because the high resolution secondary electron topographical images and the higher resolution Auger chemical analyses can be obtained in the same instrument. Unfortunately, these SEM-SAM instruments are currently very expensive because the Auger option necessitates an ultra-high vacuum system.

It is noted finally that the in-depth distribution of reaction products or solute species at the fracture surface can be determined by AES or SAM. An auxiliary inert ion beam can be used to remove the outermost 0.5 to 5.0 nm of the fracture surface and permit a compositional analysis of the underlying 0.5 to 5.0 nm. The sequential measurement of surface composition provides for the generation of in-depth chemical concentration profiles.

The capabilities of AES for chemical analysis of fracture surfaces can best be demonstrated with some examples. The AES spectra in Fig. 2*a* was obtained from the intergranular fracture surface of a hot-pressed MgO ceramic by Johnson [*10*]. Although the bulk impurity level of calcium is known to be about 100 ppm, the intergranular fracture surface analysis indicated about 8 to 10% calcium. The in-depth distribution of calcium was obtained via inert ion sputtering and is shown in Fig. 2*b*. Johnson concluded that the calcium had segregated to the MgO grain boundaries during a slow cool after the high-temperature processing. The calcium-enrichment in the grain bounda-

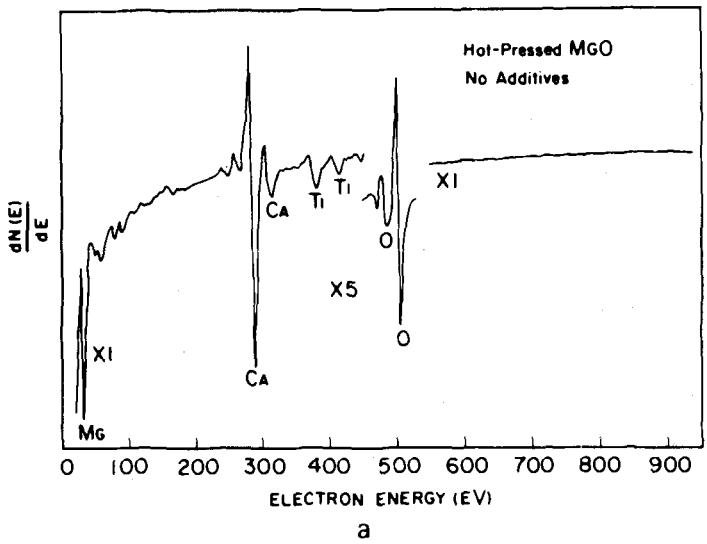

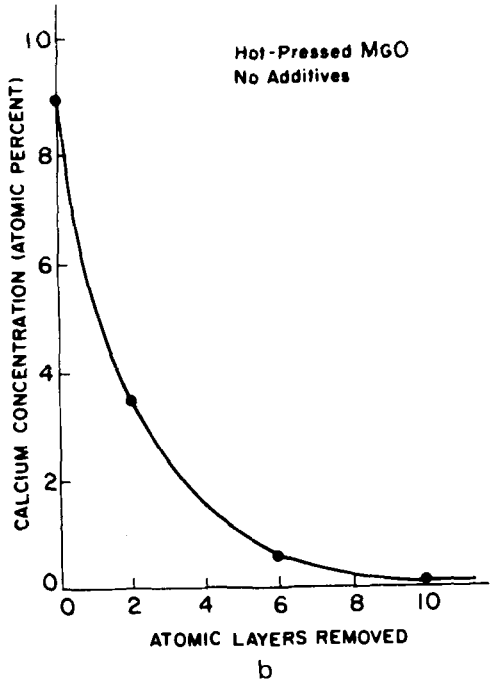

FIG. 2—(a) *AES spectrum for the intergranular fracture surface of hot-pressed MgO.* (b) *Depth-concentration profile for calcium at the intergranular fracture surface of hot-pressed MgO* [10].

ries, by a factor of 100 over the bulk calcium level, had a significant influence upon the mechanical properties of the MgO ceramic.

The mechanical failure of β''-alumina has also been investigated through chemical analysis of the fracture surfaces [*11*]. The combined use of AES and SEM-EDXA showed fine-grained regions—rich in sodium—along the fracture surface. It was suggested that these regions initiated the observed transgranular fractures. Similarly, high concentrations of calcium were detected by AES at the intergranular fracture surfaces of calcium-doped sodium-alumina [*12*]. A detrimental increase in the ionic resistivity of this material was attributed to the observed enrichment of CaO within a 20.0 nm region of the grain boundary. Finally, AES analyses of intergranular fracture surfaces in iron, copper, and steels have been reported and provide direct evidence for solute segregation of species such as chromium, molybdenum, phosphorus, boron, bismuth, sulfur, antimony, tin, or tellurium [*13*].

The particular advantages of a high spatial resolution fracture surface analysis using SAM have also been shown by Johnson [*14*]. Although conventional AES can detect the presence of segregated species along an intergranular fracture surface, SAM can measure the spatial distribution of the surface species. The SAM data in Fig. 3 are for magnesium in Al_2O_3. It shows that the magnesium observed at this intergranular fracture surface is confined to particular regions. The conventional AES analyses of the Al_2O_3 fracture surfaces averaged this magnesium concentration over the area circled in Fig. 3

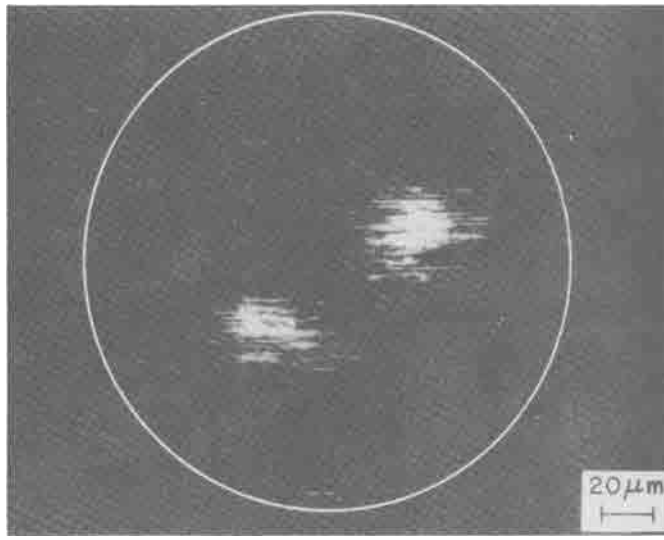

FIG. 3—*Scanning Auger micrograph for magnesium at the intergranular fracture surface of* Al_2O_3 [14].

and thereby underestimated the local concentration. The high-resolution SAM analysis, however, has led to the conclusion that the magnesium detected at the fracture surface by conventional AES (and XPS) [*15*] was not due entirely to soluble magnesium segregated at the grain surface. Rather, the bulk solubility limit for magnesium has been exceeded, resulting in precipitation of a second-phase $MgAl_2O_4$ spinel along the grain boundaries. The topographical micrographs for this fracture surface showed that these magnesium-rich regions were, in fact, intergranular second-phase precipitates. These observations could be related to both the processing of the polycrystalline Al_2O_3 and to its mechanical properties.

All instrumental techniques have limitations and AES/SAM is no exception. Firstly, the extreme surface sensitivity of AES itself imposes some limitations. Since the technique is sensitive to only a 0.5 to 5.0 nm surface layer, the exposure and handling of the specimen, after the fracture surface has been generated, is especially important. Any post-contamination or ambient reaction of the fracture surface can be inadvertently attributed to the original fracture event. This is an especially difficult problem for reactive materials such as metals and other nonoxides. Thus the chemical nature of the fracture surface may change between the time the surface was created and the time the analysis is performed. For this reason, many AES/SAM systems have *in situ* fracture attachments to permit propagation of fractures within the vacuum system of the AES/SAM spectrometer. Of course, this has tremendous value in those instances where a fracture event can be reproduced for study. However, more often than not, one may be interested in a failure analysis on a specific fracture surface produced under a unique set of conditions. Here it is critical that the specimen be properly handled, and most importantly, that the possibility of contamination or reaction of the surface, *post fracture*, be kept in mind during the data interpretation.

Secondly, the analysis of insulating materials with AES/SAM can be limited by charging of the surface. In SEM-EDXA analysis, the insulating material can be coated with a thin layer of metal or carbon to alleviate charging of the surface because the X-ray signal is obtained from a volume of the specimen considerably greater than the corresponding volume of the coating. Obviously, the surface sensitivity of AES/SAM precludes the use of coatings. While there are no all-encompassing rules for the analysis of insulators by AES/SAM, it is observed in practice that careful adjustment of the electron beam energy and current density, glancing angle electron bombardment, specimen heating, or simultaneous ion-bombardment can be beneficial in the alleviation of charging during AES/SAM.

Thirdly, the potential for electron beam induced desorption, decomposition, and diffusion at the surface under study must also be considered. These are particularly aggravating problems in the case of nonmetallic materials. Each one of these problems can limit the capability, and thereby the applicability, of the AES/SAM technique. Nonetheless, one may be forced to cope

with these complications in order to obtain at least a qualitative surface compositional analysis.

The last point about AES/SAM analysis of fracture surfaces concerns the practicalities of the analysis. Although AES/SAM instruments have experienced widespread proliferation in recent years, they are still somewhat specialized and expensive instruments. Moreover, the specimen sizes and geometries which can be tolerated are not as flexible as those accepted in an SEM-EDXA instrument. Thus it may be necessary to section the fractured specimen and thereby subject the specimen to additional contamination.

Ion Microscopy

Ion microscopy has not been applied to any significant extent for chemical analysis of fracture surfaces. Nonetheless, it does have capabilities, at least for a qualitative chemical analysis of fracture surfaces, which warrant its inclusion in this review. Ion microscopy is based upon a more general surface analysis technique called secondary ion mass spectroscopy (SIMS). Here, the solid surface is bombarded with a beam of primary ions. The sputtered secondary ions enter a mass spectrometer to provide a mass analysis of the atomic and molecular species sputtered from the surface. Since the solid is continually sputter etched, any changes in the flux of a particular mass fragment can be related to the in-depth chemical or compositional distribution of that species.

Ion microscopy is distinguished from SIMS because it produces a spatially resolved mass analysis of the surface [*16*]. That is, the ion optics—termed *direct imaging*—are designed so that the original spatial distribution of the sputtered secondary ions (at the sample surface) is retained throughout the mass filtering. The mass spectrometer is tuned to the element or secondary ion mass of interest so that only the sputtered secondary ions of interest exit the spectrometer. Thus a magnified image of the sample surface is generated by using the secondary ions selected at the mass spectrometer. The ion image typically has a spatial resolution less than 1 μm and encompasses an area at the specimen approximately 250 μm in diameter. In addition to high spatial resolution, the method has exceptional detection sensitivity, is surface sensitive, and can detect hydrogen, isotopes, and molecular fragments.

The high detection sensitivity, typically in the sub-ppm range, and the ability to detect hydrogen, are important advantages of ion microscopy for chemical analysis of fracture surfaces. Unfortunately, the method is not especially quantitative and requires a rather specialized and expensive instrument. However, its most important limitation with regard to chemical analysis of fracture surfaces concerns surface roughness. The ion optics in these instruments are designed for a flat, smooth surface, and in current practice the method is applied almost exclusively to smooth films or polished surfaces. For this reason, one can expect a loss of spatial resolution in the examination of

fracture surfaces. This will be especially true in the case of insulating glass and ceramic materials where nonuniform surface charging may contribute to a further loss of resolution. Nonetheless, the special advantages of ion microscopy can warrant its use for chemical analysis of fracture surfaces. It is the authors' belief that the range of applicability of the ion microscope for chemical analysis of fracture surfaces has not yet been evaluated.

Figure 4 presents the oxygen secondary ion image from a Cu-1.7Be alloy which has undergone internal oxidation [*17*]. Although this is not a fracture surface, it does demonstrate the inherent capabilities of ion microscopy. The micrograph indicates a preferential oxidation along the grain boundaries, as well as within particular regions of the grains themselves. Similar secondary ion micrographs were obtained for BeO^+, Be_2O^+, BeO^- and BeO_2^- showing that beryllium and oxygen are associated in the oxidized regions. High-resolution electron microscopy revealed that these oxidized regions were composed of precipitates approximately 5 nm in size.

Ion Scattering Spectroscopy (ISS)

Ion scattering spectroscopy (ISS) is based upon the elastic scattering of a primary beam of low-energy ions from a solid surface. The energy analysis of the scattered ions, whose mass and initial energy are known, allows one to determine the masses of atomic species at the solid surface. Because the elastic scattering is confined exclusively to the outermost monolayer of the solid,

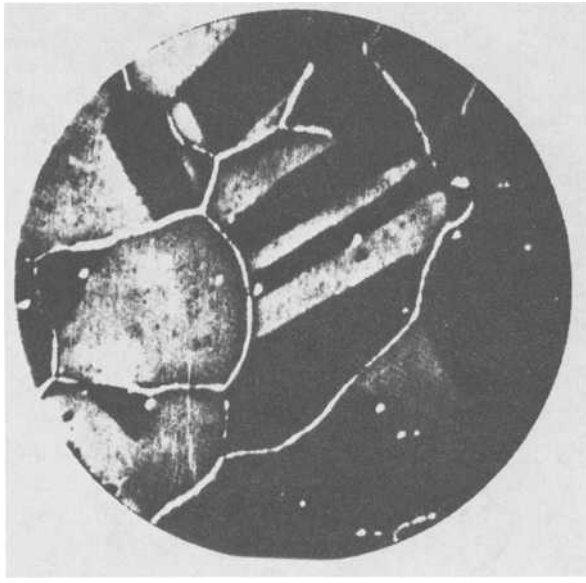

FIG. 4—*Ion micrograph for* $^{16}O^-$ *in a Cu-1.7Be alloy* [16].

this method provides the ultimate in surface sensitivity, usually one monolayer. Moreover, the in-depth distribution may be probed because the low-energy ions sputter-etch the surface, albeit very slowly. Unfortunately the spatial resolution of this method is limited to about 100 μm. Thus the ISS technique has limited applicability for chemical analysis of fracture surfaces. Nonetheless, the use of ISS and its inherent high surface sensitivity, in combination with SEM-EDXA or SAM and their high spatial resolution, can be of benefit in many cases. For example, the fracture of a particular steel composition was found to be intergranular using SEM analysis; however, the EDXA was insensitive to the antimony segregant found on the fracture surface with ISS. The ISS data in Fig. 5 suggest that the antimony, present at a level of only 600 ppm in the bulk of the alloy, was segregated within the outermost monolayer of the grain [*18*]. This nearly pure antimony grain boundary was presumably responsible for failure in the steel. In this instance, then, the SEM analysis showed that the fracture surface was intergranular and free of precipitates etc., while the ISS showed that the composition of the exposed grain boundary was enriched in the antimony solute species.

Another situation where ISS can be of great value for fracture surface analysis is in microstructure-free materials (for example, glasses and single crystals), particularly where chemically assisted crack growth phenomena are of interest. In these applications, spatial resolution is not required; rather, a

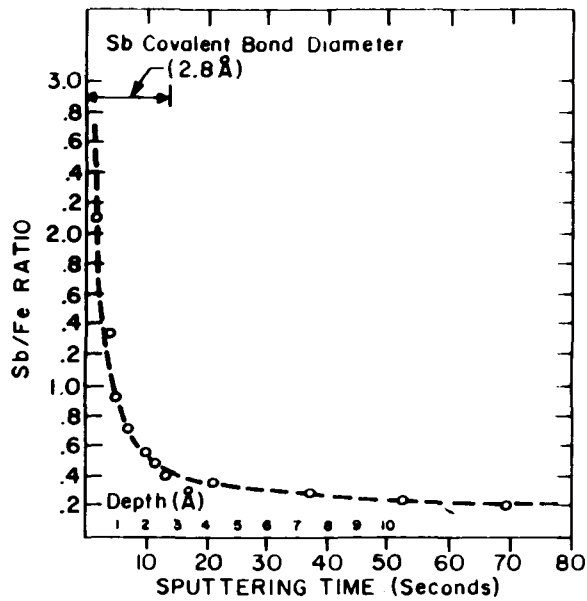

FIG. 5—*A depth-concentration profile for antimony at the intergranular fracture surface of steel. The measurements were made with the monolayer-sensitive technique ISS* [18].

high in-depth resolution is needed to measure the composition of the outermost monolayer where reconstruction processes, stress-induced diffusion, or chemical reactions may have occurred. Perhaps the extreme surface sensitivity of ISS is best demonstrated by the analyses in Fig. 6 for the cleavage faces of a cadmium sulfide (CdS) single crystal [*19*]. Under the conditions of this experiment, only sulfur atoms are detected on one of the fracture surfaces and primarily cadmium atoms on the opposing face.

It is in this regard that ISS has been used to study the atomistic mechanisms of crack propagation in multicomponent silicate glasses. Figure 7 shows the ISS spectra obtained from fracture surfaces of SiO_2 and $K_2O \cdot 3SiO_2$. These fracture surfaces were created *in situ* by fracturing glass rods within the ISS ultra high vacuum system. The surfaces were analyzed within 5 min, and therefore they should not have been modified by gaseous adsorption processes. Utilizing the SiO_2 spectra for reference, one concludes that the $K_2O \cdot 3SiO_2$ fracture surface monolayer is not representative of the "bulk" composition. ISS spectra have also been obtained for a systematic compositional series of sodium-silicate and potassium-silicate glasses, and these further verified that fracture surfaces of alkali-silicate glasses do not exhibit the "bulk" composition [*20*]. It has been suggested by LaCharme et al [*21*] that composition differences between the sur-

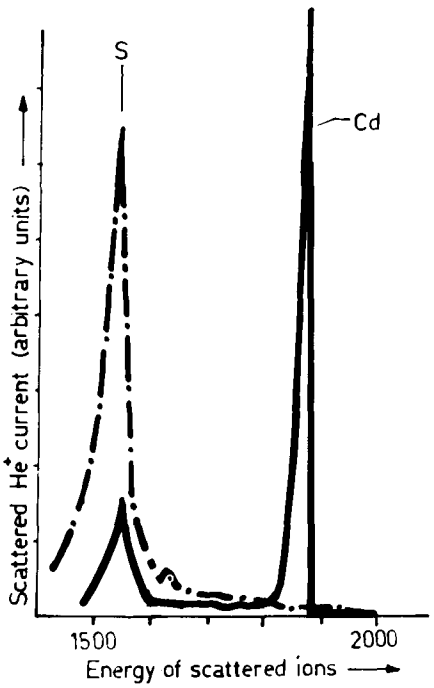

FIG. 6—*ISS spectra for the opposing cleavage fracture surfaces of cadmium sulfide* [19].

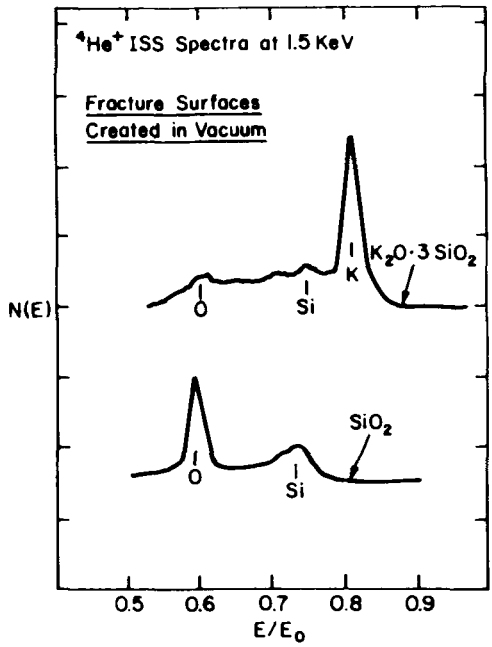

FIG. 7—*ISS spectra for the fracture surfaces of silica glass and potassium-trisilicate glass. The surfaces were prepared in vacuum by fracturing glass rods.*

face and bulk of alkali silicate glasses fractured in vacuum indicate a confinement of crack propagation to regions of alkali enrichment within the bulk glass. We are suggesting, alternatively, that crack propagation is random through the glass and that an atomic rearrangement at the surface is responsible for the composition differences. It is not yet known whether the rearrangement is an intrinsic phenomena associated with clean surfaces of alkali-silicate glasses or whether it occurs under the influence of stress at the advancing crack tip. In either case, the spectra in Fig. 7 indicate a shielding of oxygen by potassium in the outermost monolayer of the fracture surface. The surface atomic arrangement at these glass fracture surfaces is being further characterized by examining the angle and energy dependence of the ISS spectra.

Other Techniques

Other techniques for surface analysis do exist but are not especially suited to fracture surface studies. This is not meant to imply that they cannot be used for chemical analysis of fracture surfaces, but only that the analysis will be less than routine. For example, Taylor et al [*15*] have used X-ray photoelectron spectroscopy (XPS) to examine the fracture surfaces of MgO-doped

Al_2O_3. This method was chosen in spite of the lack of any spatial resolution in XPS analysis because it is more sensitive to magnesium than AES.

In some instances, it is possible to use transmission electron microscopy (TEM) for chemical analysis of microstructural features within the fracture surface. In most modern instruments, the very high spatial resolution (<1.0 nm) of TEM is combined with analytical capabilities such as EDXA, electron energy loss spectroscopy (EELS), and electron diffraction [*6*]. Unfortunately these approaches are successful only when the microstructural features to be analyzed can be extracted from the fracture surface by using the extraction replica technique. Nonetheless, it is the only means for obtaining crystallographic and phase analysis of microstructural features within the fracture surface; SAM and EDXA provide only an elemental chemical analysis.

Another technique which may be especially useful for studying the atomistic mechanism of chemically assisted crack growth is based upon the phenomena termed *electron stimulated desorption* (ESD) or *photon stimulated desorption* (PSD). Here, electron or photon irradiation is used to "desorb" atomic and molecular species from the surface; these species are detected by using a mass spectrometer. Thus the method is not only monolayer sensitive, but is capable of detecting the presence of hydrogen, water, and organic species. The method is so extremely surface sensitive, however, that the preparation and handling of specimens is most critical. For this reason, ESD and PSD may not be applicable to the chemical analysis of "in-service" fractures, but may be more suited to fundamental studies of crack propagation in well-controlled environments. Although ESD and PSD have been used extensively to study surfaces [*22*], their application to fracture surface analysis has not yet been reported.

Summary

Although many instrumental methods exist for microanalysis and surface analysis of materials, only a limited number of these are applicable to the chemical analysis of fracture surfaces. Many common analytical techniques such as infrared reflection spectroscopy (IRRS), X-ray fluorescence spectroscopy (XRF), Rutherford back-scattering (RBS), and others are ruled out for chemical analysis of fracture surfaces because they lack the required in-depth or spatial resolution. Ideally, a technique which possesses both a high spatial and a high in-depth resolution is desired.

It has been shown that scanning Auger microscopy exhibits the best combination of these features; namely, the spatial resolution can be on the order of 50 nm, and at the same time, the depth resolution is about 0.5 to 5.0 nm. Unfortunately, the majority of commercially available SAM systems cannot produce high-resolution (<10.0 nm) topographical secondary electron images. Unless the morphological characteristics of the fracture surface are already known, it is difficult to perform a meaningful SAM analysis of the frac-

ture surface. Thus it may be necessary to precede the SAM analysis with an SEM examination. The ability to perform these complementary analyses is not a problem when the fracture surface studies are part of a research program where multiple samples are often available. However, it may be difficult to achieve this in a failure analysis where the amount of material available for study is limited. Under these conditions, it is extremely important that the specimens be handled and prepared with forethought.

Of course, not all fracture surface analyses require the ultimate in spatial and depth resolution. If the microstructural features of interest have dimensions on the order of 1 to 2 μm or greater, the scanning electron microscope with energy dispersive X-ray analysis is by far the instrument of choice, unless the analysis of low atomic species is required.

Finally, it has been pointed out that although ion microscopy and ion scattering spectroscopy are not especially suitable for fracture surface analyses, they possess unique capabilities which may justify their use nonetheless. The ion microscope has exceptional detection sensitivity, usually in the ppm range. Most importantly, it can detect hydrogen, isotopes, and molecular species. Ion scattering spectroscopy, on the other hand, exhibits the ultimate in depth resolution: one monolayer. This method is applicable to the study of soluble grain boundary segregants, and may be particularly suited to fundamental mechanisms of crack propagation, especially in microstructure-free solids (for example, glasses and single crystals).

In general, it can be stated that the chemical characterization of fracture surfaces requires more than a routine analysis. The instrumental methods applicable to fracture surface studies are limited. Thus a complete characterization of the fracture surface requires careful forethought, and very often, a complementary set of analyses.

Acknowledgments

The authors' ion-scattering studies of glass surfaces are supported by the National Science Foundation under DMR-8018473.

References

[1] Johnson, W. C., *Metallurgical Transactions*, Vol. 8A, No. 1, 1977, p. 1413.
[2] Swain, M. V., *Journal of Non-Crystalline Solids*, Vol. 38-39, 1980, p. 451.
[3] Kane, P. F. and Larrabee, G. B., Eds., *Characterization of Solid Surfaces*, Plenum Press, New York, 1974.
[4] Czanderna, A. W., *Methods of Surface Analysis*, Elsevier, Amsterdam, 1975.
[5] Goldstein, J. I. and Yakowitz, H., Eds., *Practical Scanning Electron Microscopy, Electron and Ion Microprobe Analysis*, Plenum Press, New York, 1977.
[6] Hren, J. J., Goldstein, J. I., and Joy, D. C., *Introduction to Analytical Electron Microscopy*, Plenum Press, New York, 1979.
[7] Van Oostrom, A., *Surface Science*, Vol. 89, 1979, p. 614.

[8] Carbonara, R. S. and Cuthill, J. R., Eds., *Surface Analysis Techniques for Metallurgical Applications, ASTM STP 596*, American Society for Testing and Materials, 1976.
[9] Barr, T. L. and Davis, L. E., Eds., *Applied Surface Analysis, ASTM STP 699*, American Society for Testing and Materials, 1980.
[10] Johnson, W. C., Stein, D. F., and Rice, R. W., *Journal of the American Ceramic Society*, Vol. 57, 1974, p. 342.
[11] Stoddards, C. T. H. and Hondros, E. D., *Journal of the British Ceramic Society*, Vol. 73, No. 2, 1974, p. 61.
[12] Unertl, W. N., de Jonghe, L. C., and Tu, Y. Y., *Journal of Materials Science*, Vol. 12, 1977, p. 739.
[13] Joshi, A. and Stein, D. F. in *Temper Embrittlement of Alloy Steels, ASTM STP 499*, American Society for Testing and Materials, 1972, pp. 59-89.
[14] Johnson, W. C. and Stein, D. F., *Journal of the American Ceramic Society*, Vol. 58, 1975, p. 485.
[15] Taylor, R. I., Coad, J. P., and Hughes, A. E., *Journal of the American Ceramic Society*, Vol. 59, No. 7-8, 1976, p. 374.
[16] Morrison, G. H. and Slodzian, G., *Analytical Chemistry*, Vol. 47, No. 11, 1975, p. 932 A-43A.
[17] Roques-Carmes, C., Slodzian, G., and Lacombe, P., *Canadian Metallurgical Quarterly*, Vol. 13, No. 1, 1974, p. 99.
[18] Sparrow, G. R. and Feng, H. C., unpublished data.
[19] Brongersma, H. H. and Mul, P. M., *Chemical Physics Letters*, Vol. 19, 1973, p. 217.
[20] Pantano, C. G. Kelso, J. R., and Suscavage, M. J. in *Advances in Materials Characterization*, Vol. 15, D. R. Rossington et al, Eds., Plenum Press, New York, 1982.
[21] LaCharme, J. P., Champion, P., and Leger, D., *Scanning Electron Microscopy*, Vol. 1, 1981, p. 237.
[22] Madey, T. E. and Yates, J. T., *Surface Science*, Vol. 63, 1977, p. 203.

DISCUSSION

R. Rice[1] *(written discussion)*—Electron probe or SEM-EDAX methods can often identify grain boundary phases in a number of ceramics. For example, I have found calcium concentrations at the boundaries of the same or similar MgO bodies as those examined by William Johnson, but at larger grain sizes, presumably where there was more concentration associated with the heat treatment to obtain the larger grain size. Such treatment to enhance concentration can extend substantially the utility of probe-type observations. I have also found impurities on grain boundaries of fused MgO by electron probe.

The foregoing probe analysis raises an important question that relates to many, if not all, of the techniques you have discussed—namely the effect of fracture surface topography on any quantitative data, not only of amount of a given constituent, but also of depth profiling. Can you discuss, hopefully quantitatively, effects of fracture topography on results?

With regard to the issue of analysis of a crack under stress (for example, to study stress corrosion), have you considered the possibility of using Raman

[1]National Research Laboratory, Washington D.C. 20375.

techniques? I have wondered if it is possible to multiply-pass a laser beam back and forth through the crack tip region in a transparent material with a crack under load and in corrosive environment.

C. G. Pantano and J. F. Kelso (authors' closure)—We agree that X-ray analysis using an electron microbeam probe can be used to perform many of these analyses, particularly when the grain boundary phases are distinct or when their dimensions are enhanced by heat treatment. However, it is not always possible to enhance the size of the grain boundary phase with heat treatment without introducing other changes in the microstructure. Moreover, the grain boundary phases, or adsorbates, are not always distinct. While the electron probe may show the presence of an impurity or contaminant at the boundary, for example, it is difficult to determine whether it is distributed uniformly over the 1 μm sampling depth of the probe or is truly segregated in the boundary. Nonetheless, we do recommend, in general, that the SEM-EDXA be used to examine fracture surfaces of polycrystalline materials before any surface-sensitive analyses.

The topography on a fracture surface can "shadow" some regions of the surface either from the incident exciting beam probe or from the detector. The extent of the shadowing will depend upon the relative angles between the beam probe, the sample surface, and the detection system, as well as upon the magnitude of the surface roughness. In most AES systems, for example, the exciting electron beam probe and detector are coaxial. Thus, if the sample surface is perpendicular to the probe and detector, there is little or no shadowing. Unfortunately, the examination of ceramics usually requires a glancing angle between the sample surface and probe; this can lead to shadowing. In the SEM-EDXA, the probe and detector are usually 90 deg apart; here also, shadowing can be a problem.

In depth profiling of a rough surface, one must be concerned with nonuniform sputter-etching. That is, different regions of the surface may be eroded at different rates due to variations in their orientation relative to the incident ion beam and also due to shadowing by adjacent asperities on the surface. Nonuniform etching tends to broaden the true concentration profile.

In general, these effects do not preclude qualitative elemental spatial analysis or depth profile analysis. However, they may introduce severe artifacts in any image analysis, and at the very least, will degrade the image resolution. Of course, any quantitative analysis of a rough fracture surface will require that careful attention be paid to each of these factors.

In principle, at least, *in situ* Raman spectroscopy at crack tips is possible, although the sample design and experimental arrangement may be complex. The question is whether or not the effects of the stress can be observed. The laser excitation must be confined to the stressed regions in order to avoid a large background from unstressed regions of the material. Also, glasses have broadened Raman spectra. Thus it may or may not be possible to sense any line shape changes or peak shifts due to the stress effect.

J. T. Healey[1] *and J. J. Mecholsky, Jr.*[2]

Scanning Electron Microscopy Techniques and Their Application to Failure Analysis of Brittle Materials

REFERENCE: Healey, J. T. and Mecholsky, J. J., Jr., **"Scanning Electron Microscopy Techniques and Their Application to Failure Analysis of Brittle Materials,"** *Fractography of Ceramic and Metal Failures, ASTM STP 827*, J. J. Mecholsky, Jr. and S. R. Powell, Jr., Eds., American Society for Testing and Materials, 1984, pp. 157-181.

ABSTRACT: The applicability of scanning electron microscopy (SEM) to failure analysis of glasses, glass ceramics, and polycrystalline ceramic materials is presented. The principle electron operational modes include the secondary electron mode and the backscattered electron mode, where the traditional backscattered electron image obtained from a negatively biased Everhart-Thornley detector is compared with the topographical and compositional backscattered electron images obtained from the newer solid-state backscattered electron detectors. Both the energy-dispersive and wavelength-dispersive X-ray analysis modes and their relation to failure analysis are presented.

The principles of fracture mechanics are combined with the fracture surface analysis to illustrate the correlation between the fracture surface features and fracture mechanics. Examples of phase-separated glasses will show the ability to determine the propagation path with respect to the phase-separated regions. Glass ceramic fracture toughness samples will be used to illustrate the ability to observe the microstructure and fracture features independently using backscattered electron imaging techniques. Ceramic samples will be used to show the applicability of determining failure mode (transgranular versus intergranular) as well as interaction with twinning and second phases.

KEY WORDS: glass, glass ceramic, ceramic, fracture, scanning electron microscopy

The scanning electron microscope (SEM) is widely used as an analytical tool in the field of failure analysis, primarily because of its combination of good depth of field and high-resolution. The enhanced depth of field allows the edge-to-edge in-focus viewing of largely irregular fracture surfaces. The high resolution is necessary to observe very small fracture origins, microfractures, and microstructure. The electron beam can be restricted to small

[1]Sperry Gyroscope, Clearwater, Fla. 33518.
[2]Sandia National Laboratories, Albuquerque, N.M. 87185.

areas, enabling chemical analysis on the micron scale. This aids in the interpretation of failure origins when inclusions are present or when examining multiphase materials. The combination of these features are extremely important in brittle materials since the dimensions of small origin sites and fracture features on individual grains are often pertinent information to the failure analysis.

This paper presents the application of scanning electron microscopy to failure analysis and the relationship between the fracture features observed to fracture mechanics. This is not meant to neglect the importance of optical examination of fracture surfaces, which is always the first step in failure analysis of brittle materials. Sample preparation techniques are presented with respect to improvements in the means of obtaining information. A second section presents the various electron-imaging and X-ray techniques as they are related to fracture analysis. Finally, the relationship between the information obtained by these techniques is correlated to fracture mechanics utilizing actual failure analysis.

Sample Preparation Techniques

Glasses, glass ceramics, and ceramic fracture surfaces usually require some sample preparation before SEM analysis. After the initial optical examination it is usually necessary to clean the fracture surface; this is often accomplished by cleaning in trichlorotrifluoroethane - 35% alcohol or in alcohol, so long as none of the sample components is soluble in either of these solvents. If particulate contamination is present on the surface, many times in the form of fine chips or grains of the materials, trichlorotrifluoroethane is an effective cleaning agent. The low surface tension of the trichlorotrifluoroethane removes the particles from the surface when the fracture surface is held face down and ultrasonically cleaned.

Most glass, glass ceramic, and ceramic samples lack sufficient conductivity for analysis in the SEM. Some ceramic features can be analyzed uncoated by using low accelerating voltages (1 to 2 kV); however, much of the depth of field for which the electron microscope is being used is sacrificed. Figure 1 shows this effect. To eliminate the problem of surface charging, the sample is coated with a thin conductive layer (10 to 40 nm). To produce this conductive layer, carbon, chromium, or gold is evaporated onto the fracture surface; alternatively, gold or gold-paladium can be sputtered onto the fracture surface. Carbon is generally used whenever X-ray spectrographic information is required. The heavy metal layers produce a higher quality secondary electron micrograph with enhanced spacial resolution as a result of a higher secondary electron yield, and consequentially, a higher signal-to-noise ratio. These one-step techniques, whose main function is to provide a conductive coating, produce a uniform layer which does not enhance contrast.

There are several two-step coating procedures whereby contrast or resolu-

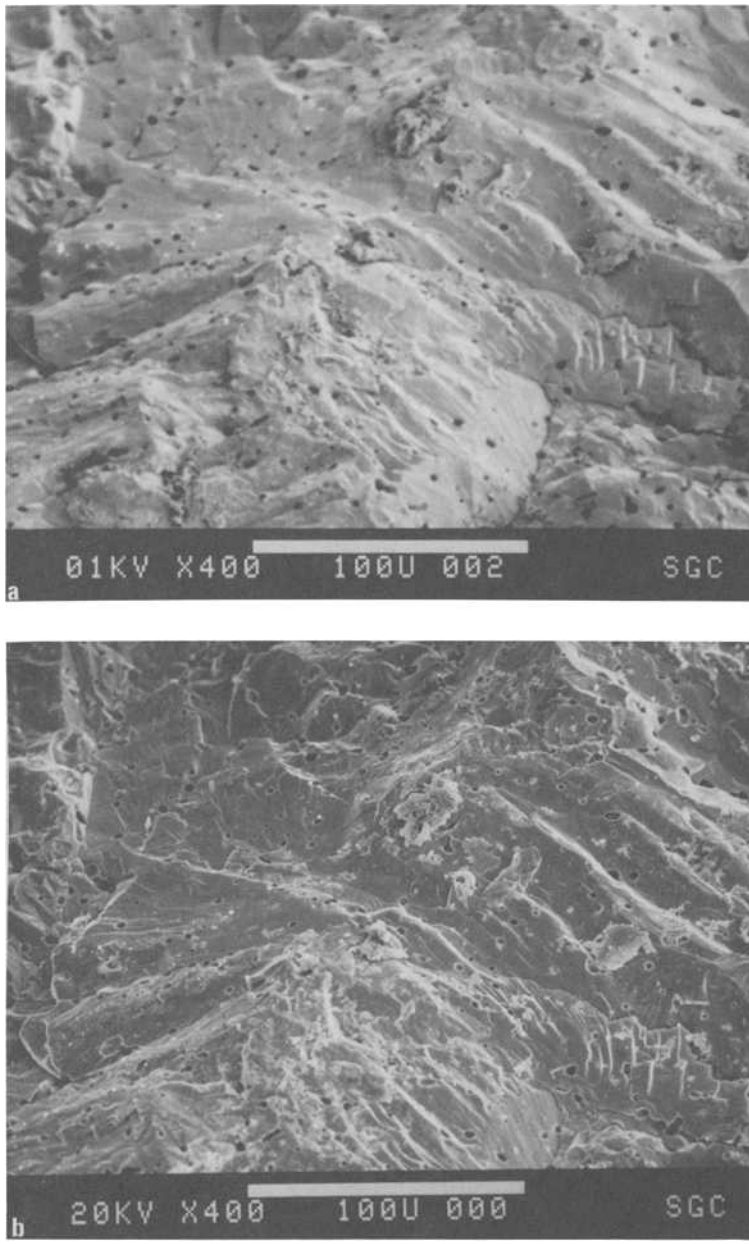

FIG. 1—*Accelerating voltage effects on resolution of a fracture surface at* (a) *1 kV and* (b) *20 kV.*

tion or both can be enhanced. The first of these is used on samples with minimal topographical differences, as is often found with glass failures. This technique is known as low-angle gold shadowing. The procedure involves first evaporating approximately 10 nm of carbon on the fracture surface by utilizing electrodes positioned at a high angle with respect to the sample, and rotating the samples in a planatary holder. The second step involves evaporating a gold layer from an electrode held at a low angle with respect to a fixed sample. The sample is fixed with the evaporation direction nearly perpendicular to the fracture initiation surface.

This two-step process will coat the entire surface with carbon for conductivity, then the gold evaporation step accomplished at a low angle will coat only those topographical features with a direct line of sight to the gold electrode. The higher secondary and backscattered electron yield of the gold enhances the contrast of the gold-coated side and thereby enhances the topographical features.

The second two-step coating process is generally used on surfaces displaying extreme relief. The first step involves a standard carbon evaporation as presented in the previous method. The second step is accomplished by sputtering a gold or gold-paladium layer over the carbon. The carbon layer provides a continuous conductive layer around sharp or re-entrant corners, while the gold layer provides enhanced resolution and slightly diminishes the edge effect problems present at sharp edges.

A second type of problem encountered with sample preparation involves large or nonmobile part failures. In this case, samples can be prepared by replication. For scanning electron microscopy, one-step replicating processes are generally used. For field failures, the common replication technique is thick plastic tape replication. To prepare the replica, a strip of cellulose acetate tape (approximately 0.1 to 0.25 mm thick) is wet on one side with acetone until it softens. The cleaned fracture surface is then wet with acetone and the tape is pressed down onto the surface, care being taken to eliminate all trapped gas. The tape is allowed to dry and then is mechanically stripped from the fracture surface. The replica is coated by any of the aforementioned techniques and examined directly in the SEM. Caution must be taken not to produce artifacts during the replication process, especially those produced by entrapped gas bubbles. Several other one-step and two-step replication processes exist for fracture surfaces; these processes have been reviewed elsewhere [*1*]. Many of these other replication techniques are used primarily for transmission electron microscopy examination of fracture surfaces and are not frequently used for SEM analysis.

Replication of fracture surfaces presents several additional problems. Inherently, the spacial resolution of replicas is poorer than that obtained by direct observation of the fracture surfaces. Artifacts can be introduced by tearing or pulling the tape during stripping from the fracture surface, or by a failure to remove all the entrapped gas bubbles during the surface replication

procedure. In addition, backscattered electron imaging is greatly diminished as a result of the low atomic number of replicating tape, and all X-ray compositional information is lost.

Sample preparation should never be done before a plan for the failure analysis is complete. If Auger electron spectroscopy (AES) or ion microscopy is to be performed, no surface coatings should be applied to the sample since they will influence the results.

SEM Fractographic Techniques

The most common electron imaging techniques used for fractography are the secondary electron imaging mode collected with a positively biased Everhart-Thornley (ET) detector, and the backscattered electron imaging mode collected with a negatively biased ET detector [*2-7*]. The secondary electron mode processes the best spacial resolution (approximately 4.0 nm) and provides a surface topographical image. Edge effects and localized surface charging are problems encountered when utilizing the secondary electron mode, especially on extremely rough fracture surfaces. Figure 2 shows the edge effect present on a three-point bend test sample, and the same area viewed in a backscattered electron mode. The edge effect is somewhat reduced by utilizing either gamma imaging processing or homomorphic imaging processing; however, some of the fracture surface detail is sacrificed by utilizing either of these image processing techniques. Techniques such as charge neutralization eliminate some of the localized surface charging but do nothing to eliminate the edge effects and result in a diminished spacial resolution. The secondary image often contains a significant portion of line-of-sight backscattered electrons, and is, therefore, not a pure secondary image.

One of the problems with secondary electron imaging is determining what angle the fracture surface should be examined with respect to the incident electron beam. In the early days of SEM, the sample was generally tilted at 45 deg to enhance the secondary electron signal. This can result in foreshortening and the loss of certain fracture features. Advances in electronics have made 45-deg examination unnecessary, and the sample can usually be examined perpendicular to the incident electron beam. At times it is necessary to tilt the fracture surface to enhance some specific fracture feature, but large ($>$15-deg tilt) angles should not be used arbitrarily, and should only be used when the tilt angle is being used as a contrast enhancement mechanism for specific fracture features, and when corrections for foreshortening are utilized.

The backscattered electron image detected by a negatively biased ET detector is really a combination of a topographical contribution and an atomic number contrast contribution [*8*]. The solid angle subtended by the ET detector for backscattered electron is very low and, as a consequence, usually results in a low signal-to-noise ratio when examining light-element glasses

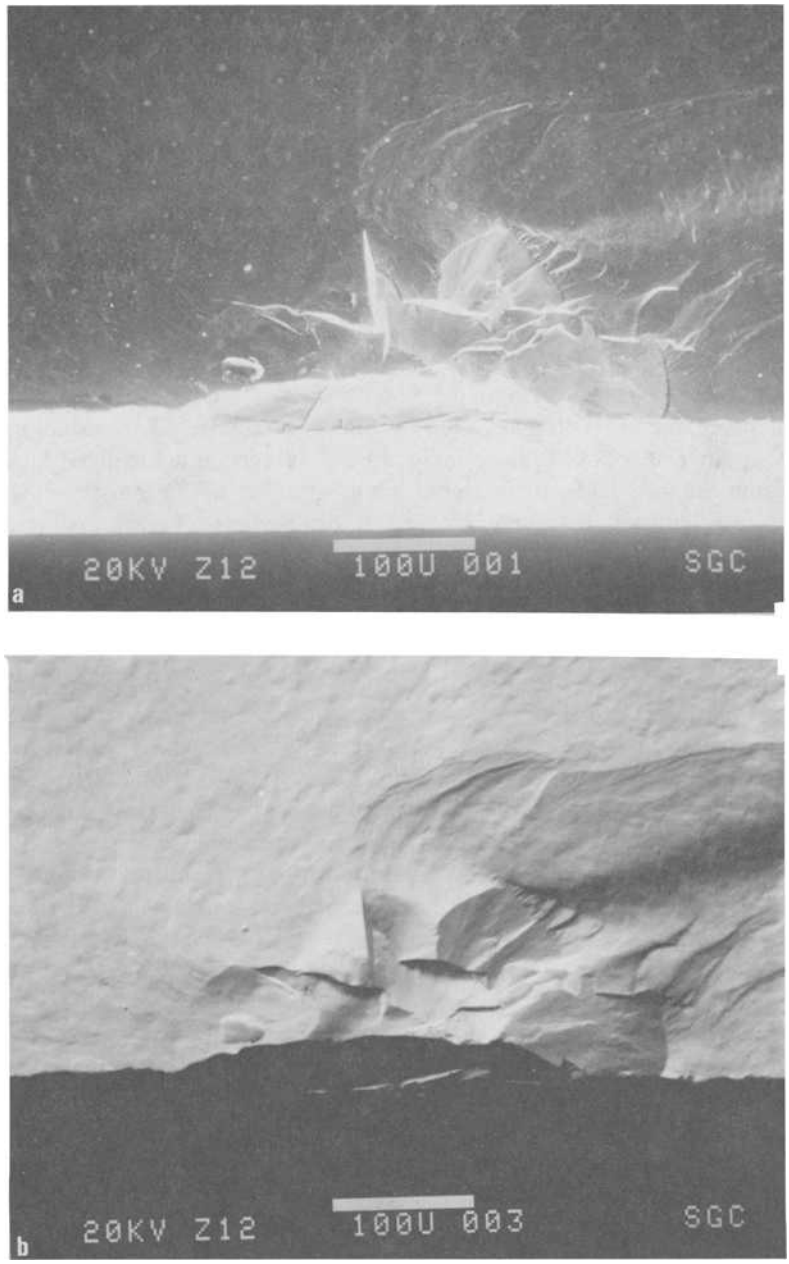

FIG. 2—*Edge-charging effects present in secondary image* (a) *are eliminated with backscattered electron imaging* (b).

and ceramics at beam currents generally compatible with secondary electron operation (10^{-10} A). Figure 3 shows a comparison between the secondary electron image and the ET backscattered electron image collected at the same beam current as the secondary image, and also at a beam current one order of magnitude higher. The particular sample examined here is $PbO\text{-}ZrO_2\text{-}TiO_2$ (PZT) material and has a high backscattered electron cross section. The difference in the two images will be more dramatic for lighter element materials such as alkali-borosilicate glasses. The advent of high sensitivity annular backscattered electron detectors has added a new dimension to the study of fracture surfaces of glasses, glass ceramics, and ceramics [*8, 9*]. Both the split ring and the four-quadrant annular backscattered electron signal can be separated into a topographical component and a compositional component (atomic number contrast). With a four-quadrant detector, the topographical image is obtained by subtracting the signal from one side of the detector from the signal of the other ((1 + 2) − (3 + 4)), while the compositional image is obtained by adding the signal from all four quadrants together (1 + 2 + 3 + 4). Figure 4 shows the arrangement of a four-quadrant backscattered electron detector. This detector subtends a far greater solid angle than the negatively biased ET type of detector as a result of being attached to the pole piece, directly above the sample. The solid-state backscattered electron detector produces more than adequate signal-to-noise ratios at normal secondary electron operating currents (10^{-10} A). However, the solid-state detector must be aligned with respect to the sample in order to produce the proper sense of the topographical micrographs.

Several large scintillator type of backscattered electron detectors exist that encompass a large solid angle for backscattered electrons. These detectors produce a good signal-to-noise ratio, but are not capable of being ganged and deganged, and eliminate the possibility of presenting separate topographical and compositional images.

The backscattered electron image eliminates the problem of edge effects present in the secondary electron image. By being able to separate the two components of the backscattered electron signal, the pure topography of a fracture surface can be observed without the influence of atomic number contrast by utilizing the topographical backscattered mode. The compositional backscattered electron image allows observation of the microstructure of the material directly on the fracture surface of glass ceramics and ceramics, without altering the fracture surface by etching. Figure 5 shows a series of micrographs taken of the fracture surface of a lead-zirconium-titanate (PZT) ceramic. Figure 5*a* shows the secondary electron image displaying predominantly topography, which is somewhat confused with the presence of edge effects and some microstructural features. Figure 5*b* is the ET backscattered image taken with a beam current approximately 10 times that used for Fig. 5*a*. The higher beam current was necessary to produce a sufficient signal-to-noise ratio; even higher beam currents would be necessary for samples of low atomic

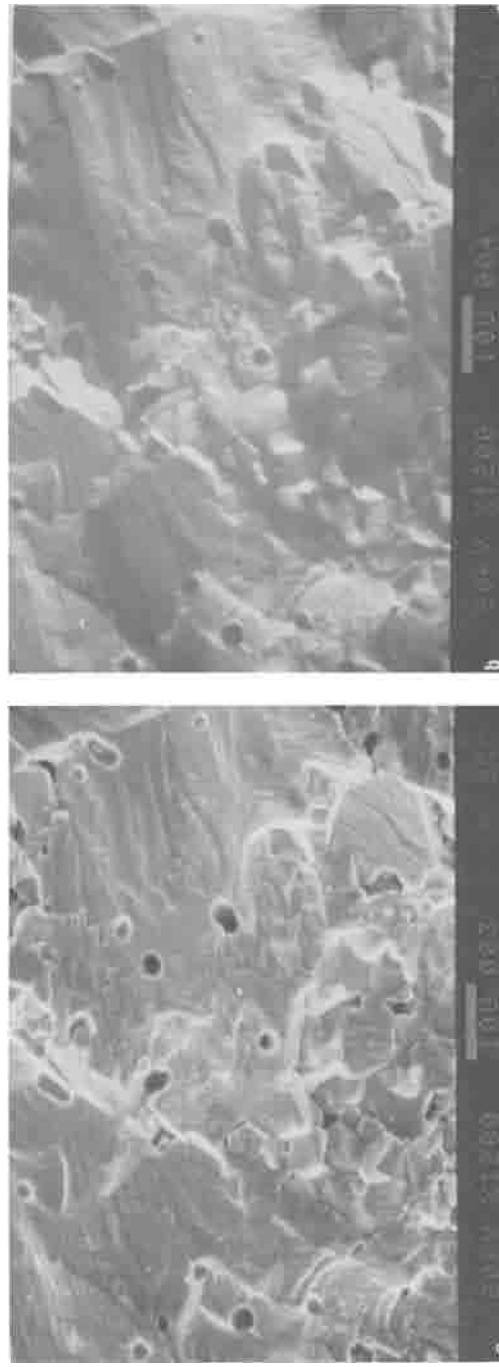

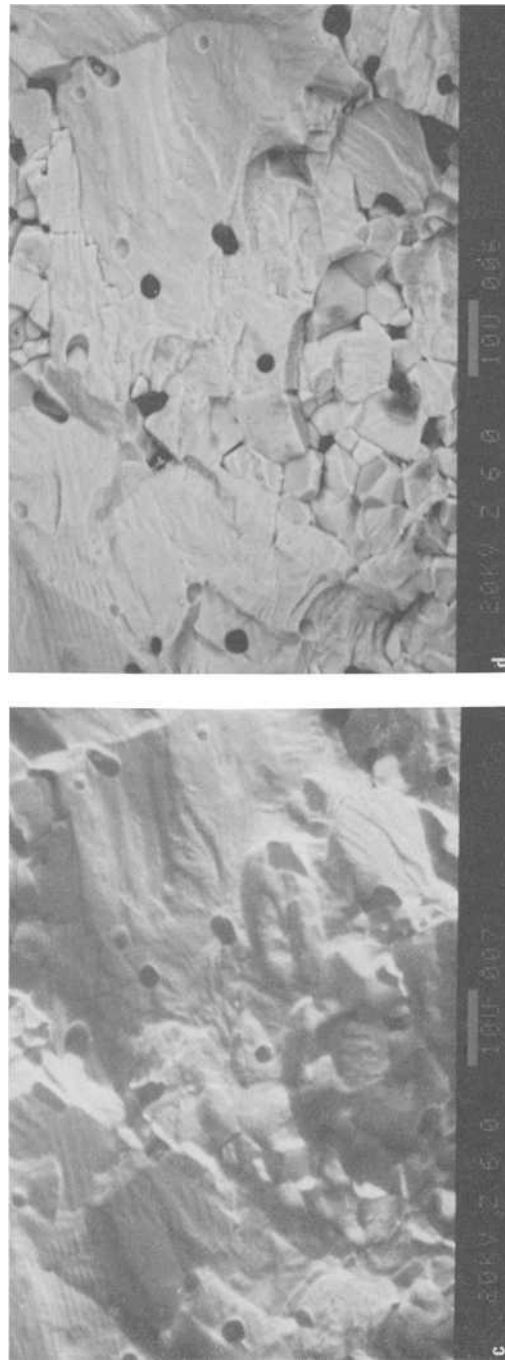

FIG. 3—*Secondary electron image* (a), *Everhart-Thornley (ET) backscattered electron image* (b), *ET backscattered electron image* (c) *taken at* ×*10 the beam current as* (b), *and a solid-state backscattered image* (d) *taken with the same beam current as* (b).

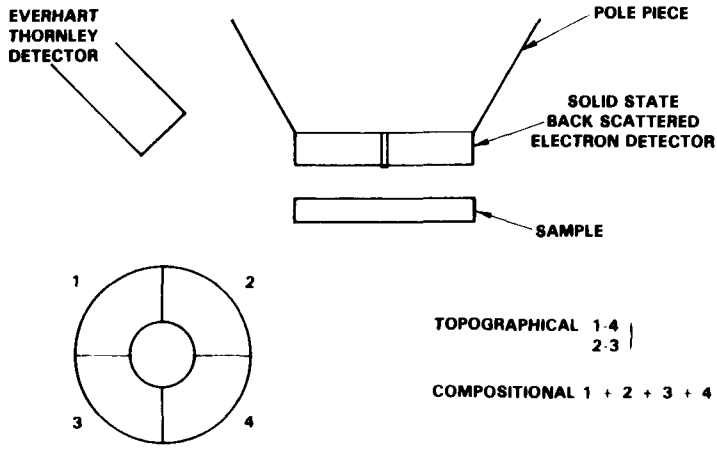

FIG. 4—*Configuration of a four-quadrant backscattered electron detector system.*

number such as alumina-silicate ceramics. The ET backscatter image displays a predominantly topographical image. However, samples displaying extreme relief may result in excessing shadowing at the base of tall features. Figure 5*c* is the topographical backscattered image obtained with the solid-state annular backscattered detector taken at the same beam current as Fig. 5*a*. Even at the lower beam current, the signal-to-noise ratio and hence the contrast is far superior to that of Fig. 5*b*. Figure 5*d* is the compositional backscattered image also taken at the same beam current as Fig. 5*a*. Clearly visible is the microstructure of the material, including the grains, twinning, porosity, and a glassy region (shown at the arrow).

The compositional backscattered electron mode can also detect the presence of second phases, inclusions, and voids in ceramics and glasses. Figure 6 shows the presence of ZrO_2 grains in an Al_2O_3-ZrO_2 material. A multiphase phosphate ceramic shows the contrast differences between a series of Ba-P-O phases with minor variations in Ba-P ratio in Fig. 7. This analysis is important for fracture toughness calculations where the fracture toughness of the various phases are significantly different.[3] Figure 8 shows a series of micrographs of a fractured alumina silicate ceramic. The secondary image (Fig. 8*a*) supplies very little information concerning the failure. The critical flaw is clearly visible in the topographical backscattered image (Fig. 8*b*). The compositional backscattered image (Fig. 8*c*) determines that the critical flaw surrounds a particular grain of higher average atomic number. The X-ray map (Fig. 8*d*) shows this grain to be high in iron. From this series of micrographs, it is apparent that the second phase acted as the initiation site, something that

[3]Fracture toughness is a measure of the resistance to crack propagation of a material.

would have been missed if only a standard secondary electron analysis had been performed.

Another technique that enhances the topographical features is the use of stereographic pairs. Stereo pairs are produced by taking two pictures of the same area, with the second picture tilted or rotated with respect to the first picture. The tilt angle is usually from 5 to 10 deg, while the rotation angle is determined according to Lane [*10*] as

$$\sin R = (\sin P)/\sin \theta$$

where R is the rotation, P is the parallax angle, and θ is the tilt angle. The stereo image is observed by viewing the two micrographs in an appropriate stereo viewer. The three-dimensional image is really an optical illusion, the depth being generated by the perception of the viewer. Quantitative information concerning depth can be obtained from stereopairs [*11*].

Characteristic X-rays, detected by both energy-dispersive and wavelength-dispersive systems, are used primarily to identify second phases, inclusions, and inhomogeneities contributing to fracture. Identification of second phases is important since inhomogeneities can act as fracture origins when they process a lower fracture toughness than the bulk ceramic [*12,13*], when the thermal expansion properties between the two phases differ such that localized cracking can occur, or when second phases are hydroscopic and result in volume changes during environmental exposure.

For example, a wavelength-dispersive X-ray system was used to identify a foreign particle in the surface of a silica optical fiber shown in Fig. 9. The particle was identified as an iron-magnesium silicate. The fiber failed by a crack initiated at the particle fiber interface as a result of thermal expansion differences between the fiber and the particle. The origin of the particle was probably "dust" from the furnace used to heat the glass preform before drawing.

Microstructural Effects

Fracture mechanics equations have successfully been applied to fracture in glasses and fine-grained polycrystalline ceramic bodies [*14,15*]. Work has been done to extend this methodology to fracture in single- and large-grained polycrystalline ceramics [*16*]. This extension is typically conducted by measuring the strength and the fracture energy γ (where $\gamma = K_{Ic}^2/2E$ and E is the elastic modulus) and using this information along with the elastic modulus of the material to calculate flaw sizes. However, applying fracture mechanics to polycrystalline materials assumes that perturbations to crack advance due to microstructural interactions are negligible. This is not always a valid assumption. For example, as the ratio of the flaw size (c) to the grain size (G) decreases, the pertinent fracture mechanics equations must be modified to account for the effects of internal stresses, phase transformations, and thermal


20KV Z14 100U 003 SGC
b

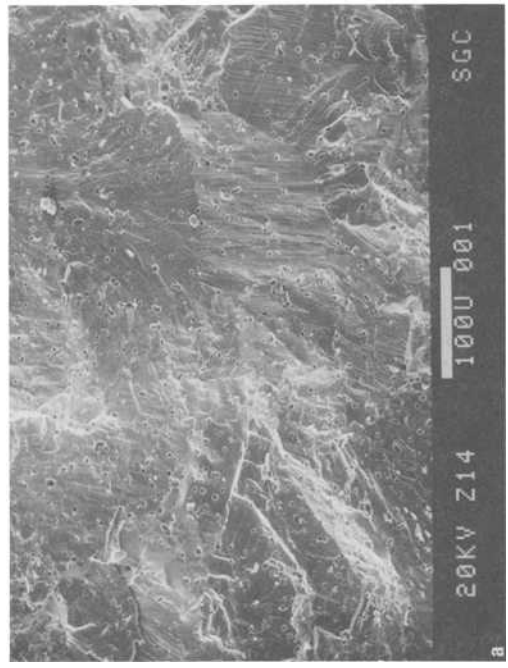
20KV Z14 100U 001 SGC
a

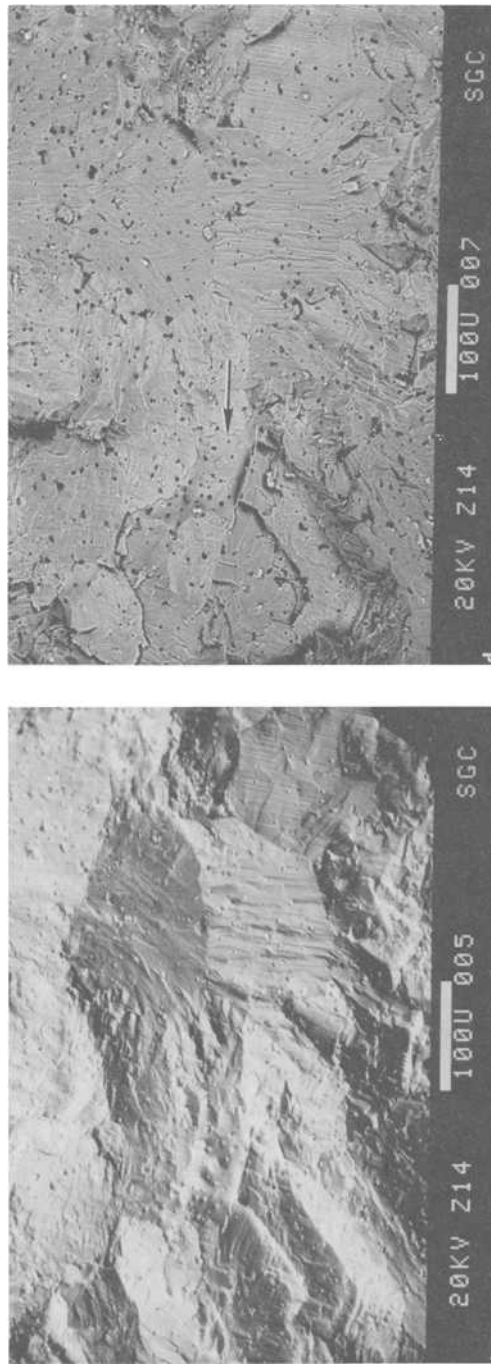

FIG. 5—*Comparison of secondary electron* (a), *ET backscattered electron* (b), *compositional backscattered electron* (c), *and topographical backscattered electron* (d) *images of a fracture surface of a PZT ceramic.*

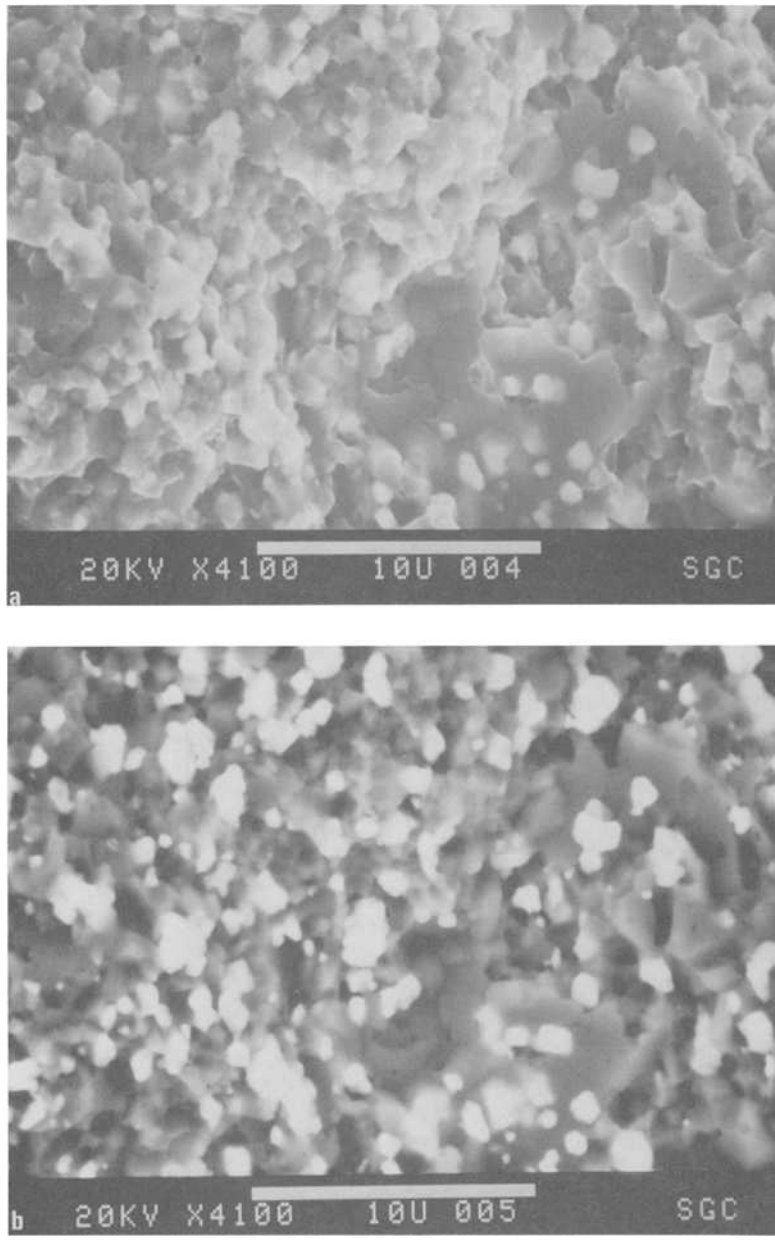

FIG. 6—*Fracture surface of an Al_2O_3-ZrO_2 ceramic.*

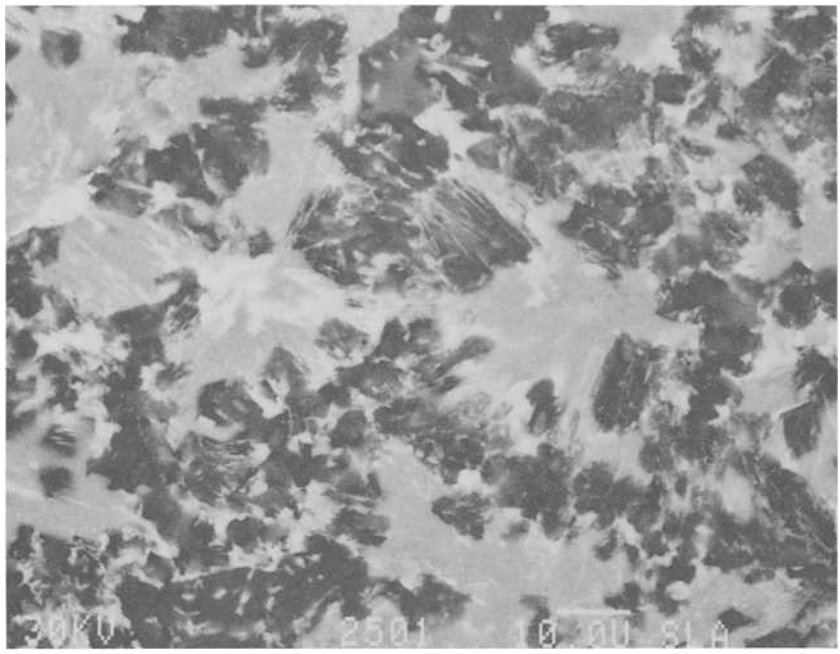

FIG. 7—*Multiphase phosphate glass ceramic showing barium variation in the various crystalline phases.*

expansion anisotropy (which can be present in anisotropic noncubic materials or in two-phase materials). As the ratio c/G decreases, a point is ultimately reached where the flaw boundary encounters just enough grains to average out these nonuniform effects and therefore exhibits the normally accepted polycrystalline fracture energy. Further decreases in the ratio c/G leads to a decreasing resistance to crack propagation, with the lower limit being determined by either the energy for grain boundary fracture, or the energy necessary for fracture to occur along an easy cleavage plane within one grain, which would be equivalent to cleavage in a single crystal of the material. Therefore the fracture toughness, K_{Ic}, which is typically measured using large flaws compared with the grain size, is not applicable to samples with lower c/G ratios, even though K_{Ic} is generally regarded as a material parameter independent of test conditions. There is a transition from the single-crystal fracture energy to the polycrystalline fracture energy at some c/G ratio for a given material [*16–18*]. Thus it is extremely important to be able to observe the relationship of the fracture initiating flaw to the local microstructure in order to determine the ratio c/G. For example, failure in dense, medium-to-large-grained zinc selenide occurs primarily from flaws contained within one or two large grains, and is, therefore, controlled by the single-crystal fracture energy

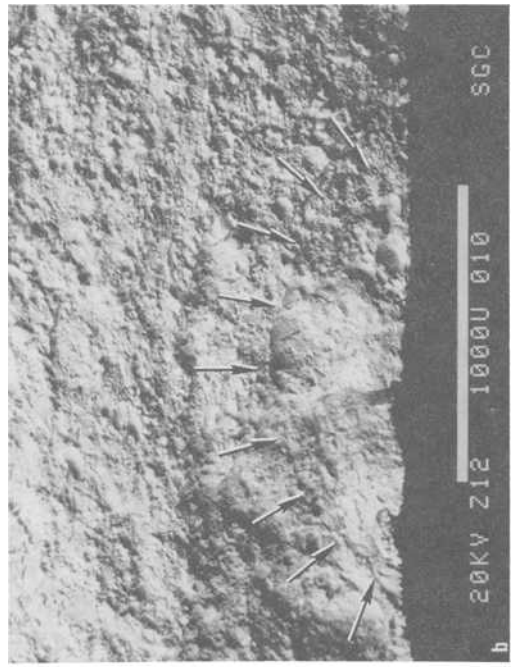
20KV Z12 1000U 010 SGC
b

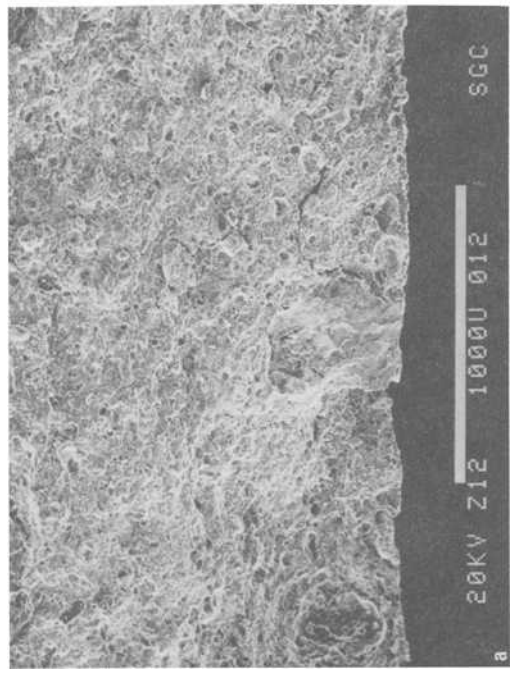
20KV Z12 1000U 012 SGC
a

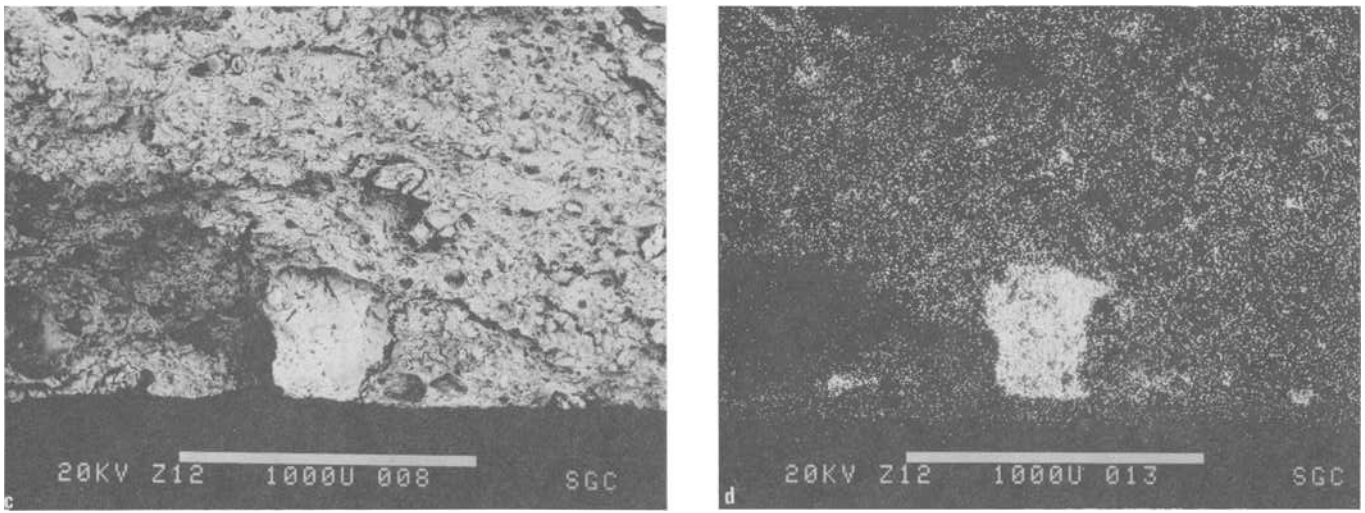

FIG. 8—*Secondary electron image* (a), *topographical backscatter image* (b) *showing critical flaw, compositional backscatter image* (c) *showing inclusion, and iron X-ray map of an alumina silicate ceramic* (d).

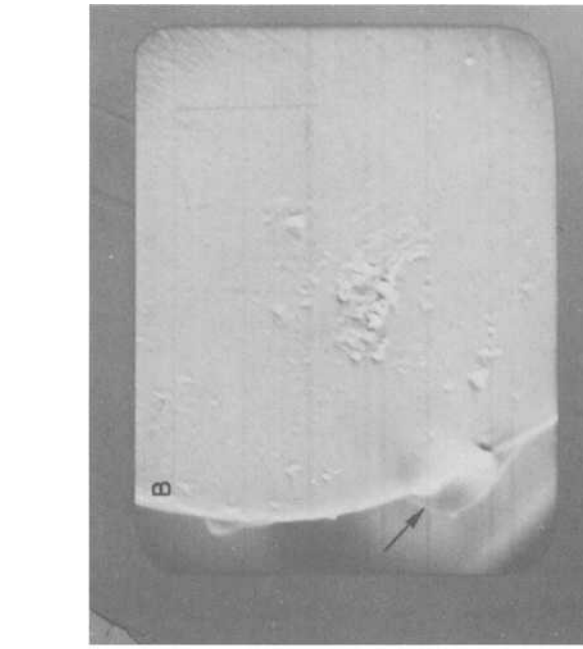
B

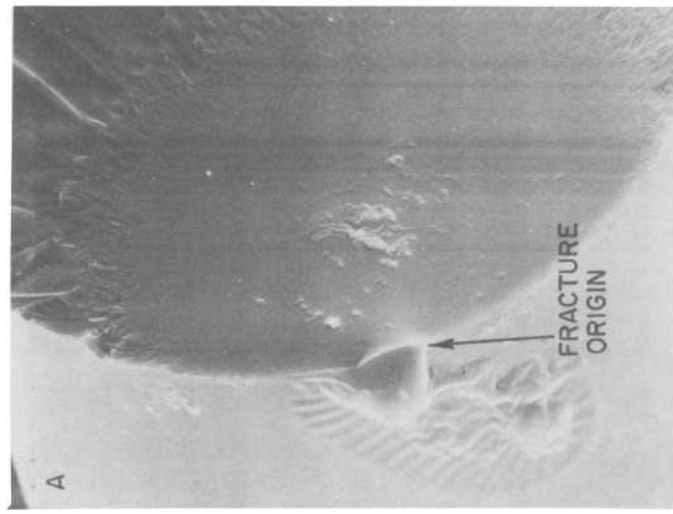
A
FRACTURE ORIGIN

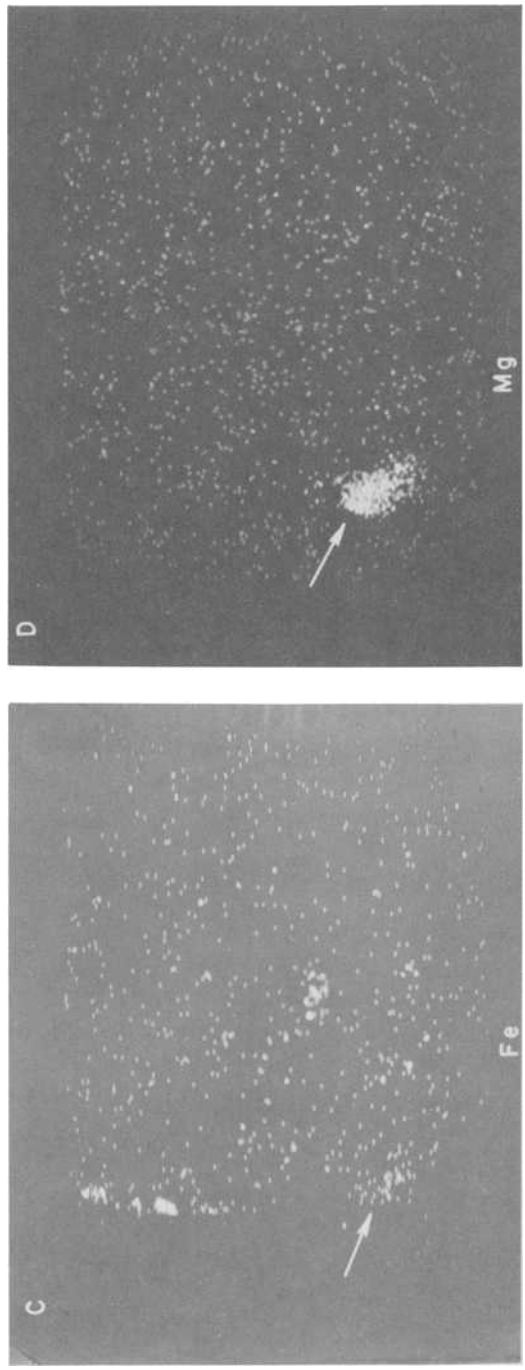

FIG. 9—*Fracture origin* (a), *particle on surface of glass optical fiber* (b), *and X-ray map of same area, iron* (c) *and magnesium* (d).

(approximately 0.3 MPa $M^{1/2}$) rather than the polycrystalline fracture energy (0.9 MPa $M^{1/2}$). This has many implications, the most important being that the proof test ratio based on polycrystalline fracture mechanics data is approximately 1.1 times too low. This difference in proof stress results in a 25 to 1 difference in time-to-failure for delayed failure [*18*].

Healey and Mecholsky [*9*] have used the new backscattered electron annular detector discussed previously to observe the relationship of the critical flaw to the local microstructure, most notably to observe the ratio c/G and deviations of the critical flaw boundary from a smooth elliptical front as a result of interaction with local microstructure. Three different zinc silicate glass ceramics (used for molybdenum sealing) were investigated; the microstructures varied in size from 10 to 500 μm. Figure 10*a* shows a topographical backscattered electron image with a marked deviation from a smooth elliptical critical flaw boundary. The compositional backscattered electron image (Fig. 10*b*) was used to determine the microstructure of the glass ceramic in and around the critical flaw directly on the unetched fracture surface. The deviation of the crack front was the result of an interaction with a large grain at the critical flaw boundary. Previously, this information has been obtained from polished and etched surfaces, the preparation of which destroys the one-to-one relation between the fracture features and microstructure.

In Ref *9* a series of photomicrographs of the fracture surfaces using the new backscattered electron techniques enabled the discrepancies between the values of fracture toughness calculated from the fracture surface features and measured on the fracture mechanics samples to be resolved. It was shown that the critical flaw in the large grained glass ceramics was present within only one or two microstructural units. The fracture in the large-grained samples was dependent on the ratio c/G in a manner similar to that observed in large-grained polycrystalline ceramic materials [*19*].

Microstructural effects can also be observed in phase-separated glasses. The crack propagation path with respect to the phase separate regions can be observed at high magnification. Figure 11 shows crack propagation through the phase-separate regions in the critical flaw region and propagation around the phase-separate regions in the rapid growth region. Such analyses can be used to explain an increase in fracture toughness in phase-separated glasses by determining the relationship of crack propagation with respect to the phase-separated regions.

Stress Corrosion Cracking

Scanning electron microscopy is extremely useful in observing delayed failure due to stress corrosion cracking in brittle materials [*15*]. An excellent example of delayed failure in a polycrystalline ceramic is shown in Fig. 12. It is the fracture surface of a MgF_2 infrared transmitting dome. Clearly visible are three regions, two initial flaws which grew into one critical flaw.

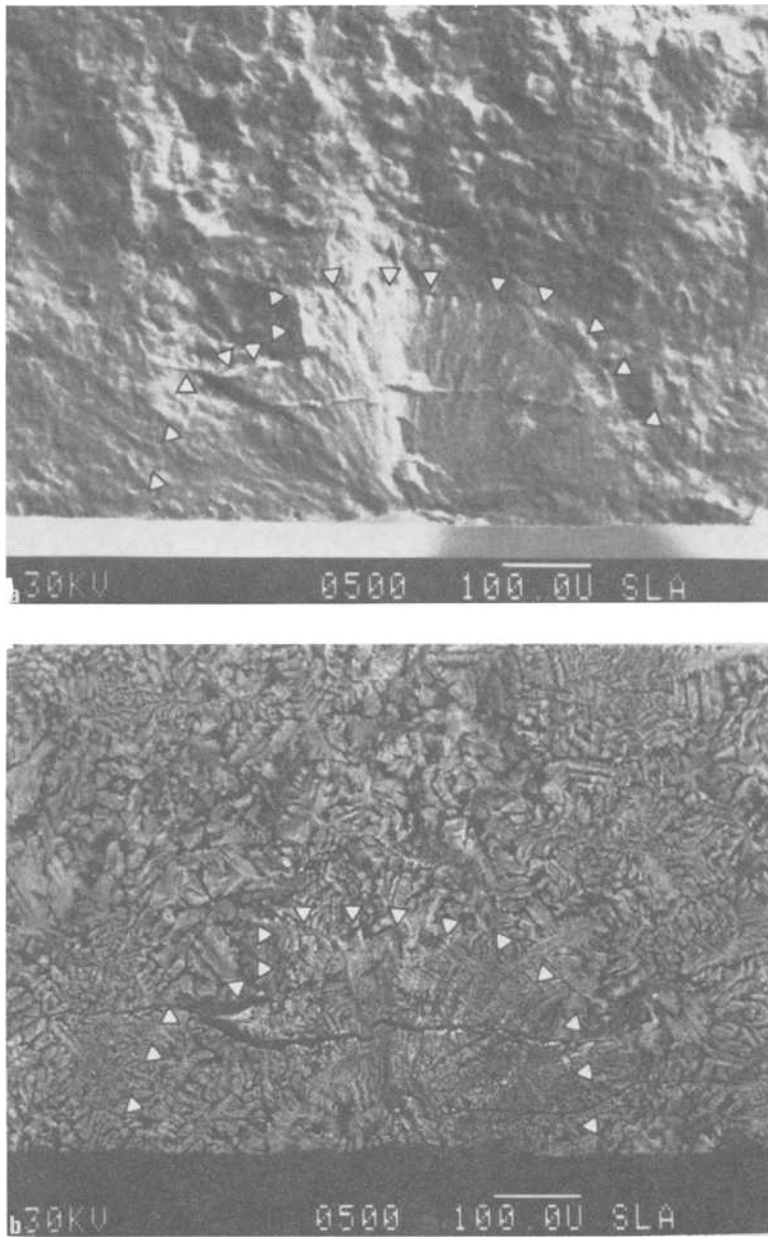

FIG. 10—*Fracture surface of glass ceramic showing the deviation from a smooth flaw in the topographical backscattered image, and the corresponding local microstructure in the compositional backscattered image.*

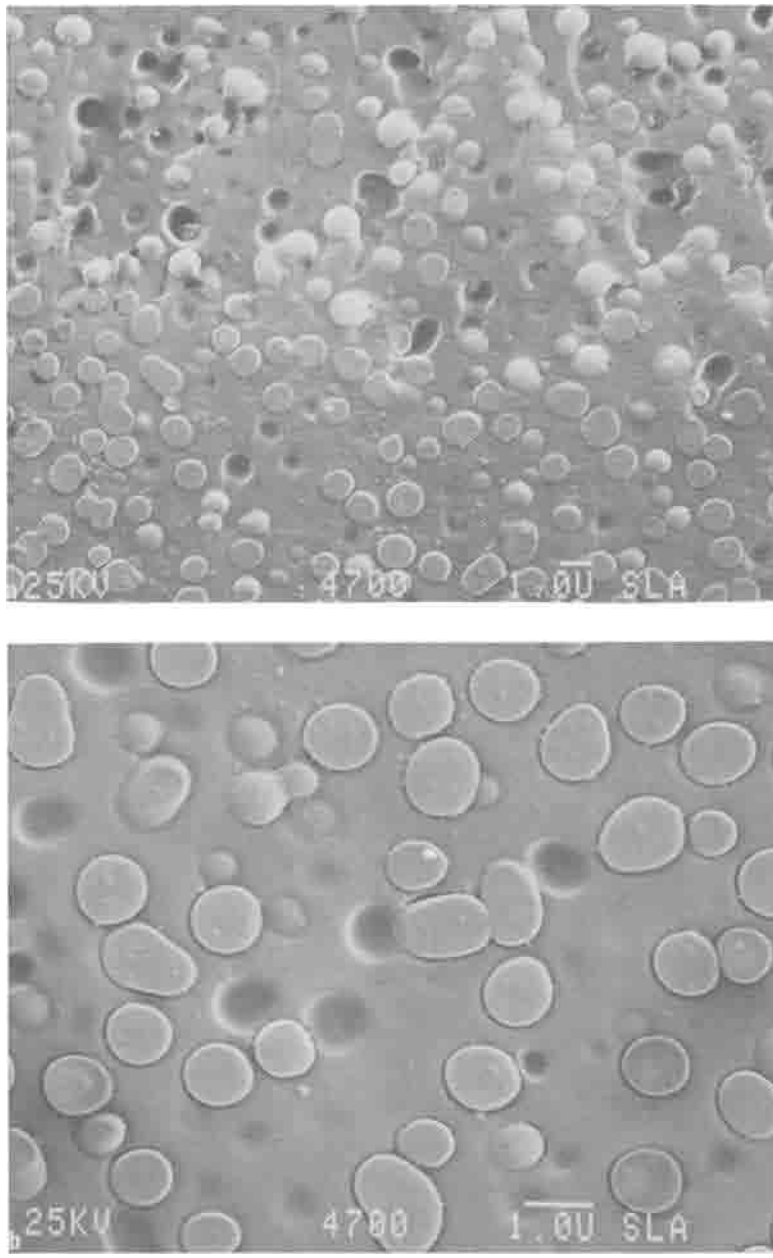

FIG. 11—*Crack path propagation through a phase-separated glass,* (a) *in the vicinity of the flaw-mirror interface showing the transition from propagation through the phase-separate regions to around the phase-separate regions, and* (b) *in the critical flaw where through-propagation persists.*

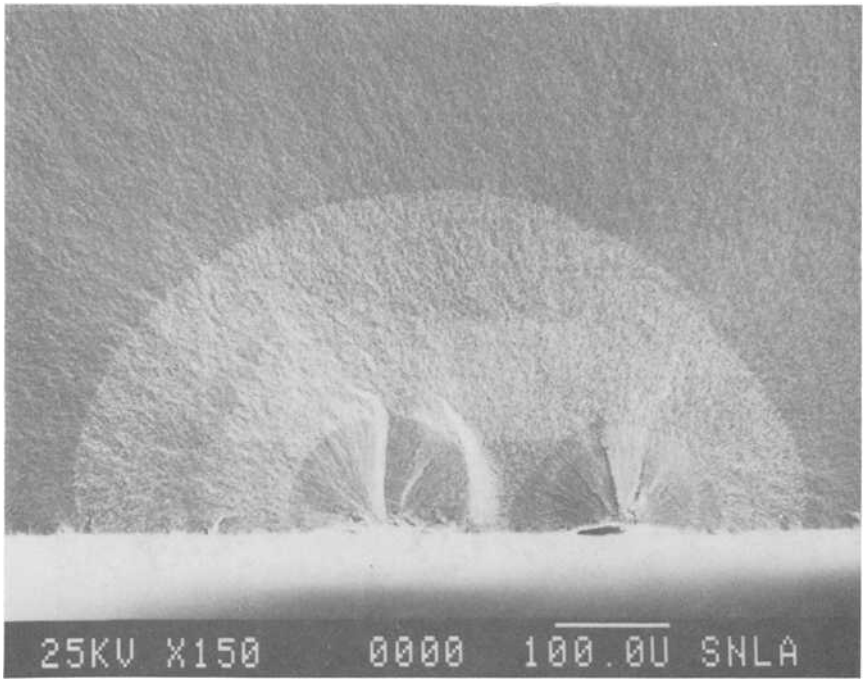

FIG. 12—*Stress corrosion cracking of MgF_2 growing from two initial flaws.*

Both initial flaws occurred rapidly and are transgranular in nature, the slow crack growth region is intergranular, and the fast fracture region is again transgranular.

The same type of transition from intergranular slow crack growth to transgranular rapid crack growth occurs in a number of other ceramic materials [*20–22*]. Silicon carbide exhibits almost no slow crack growth at room temperature; however, the same intergranular subcritical crack growth and transgranular rapid crack growth occur at elevated temperature [*20*]. Hot-pressed silicon nitride [*21*] and a glass ceramic [*22*] both show similar high-temperature stress corrosion cracking. It is generally accepted that impurities present at grain boundaries weaken the grain boundaries; thus it is not surprising that stress corrosion cracking usually occurs intergranularly in brittle materials.

Other Materials

The use of the topographical and compositional backscattered modes is not restricted to ceramic-type materials. Failure analysis of metal fracture surfaces by these techniques provides information that would generally have to

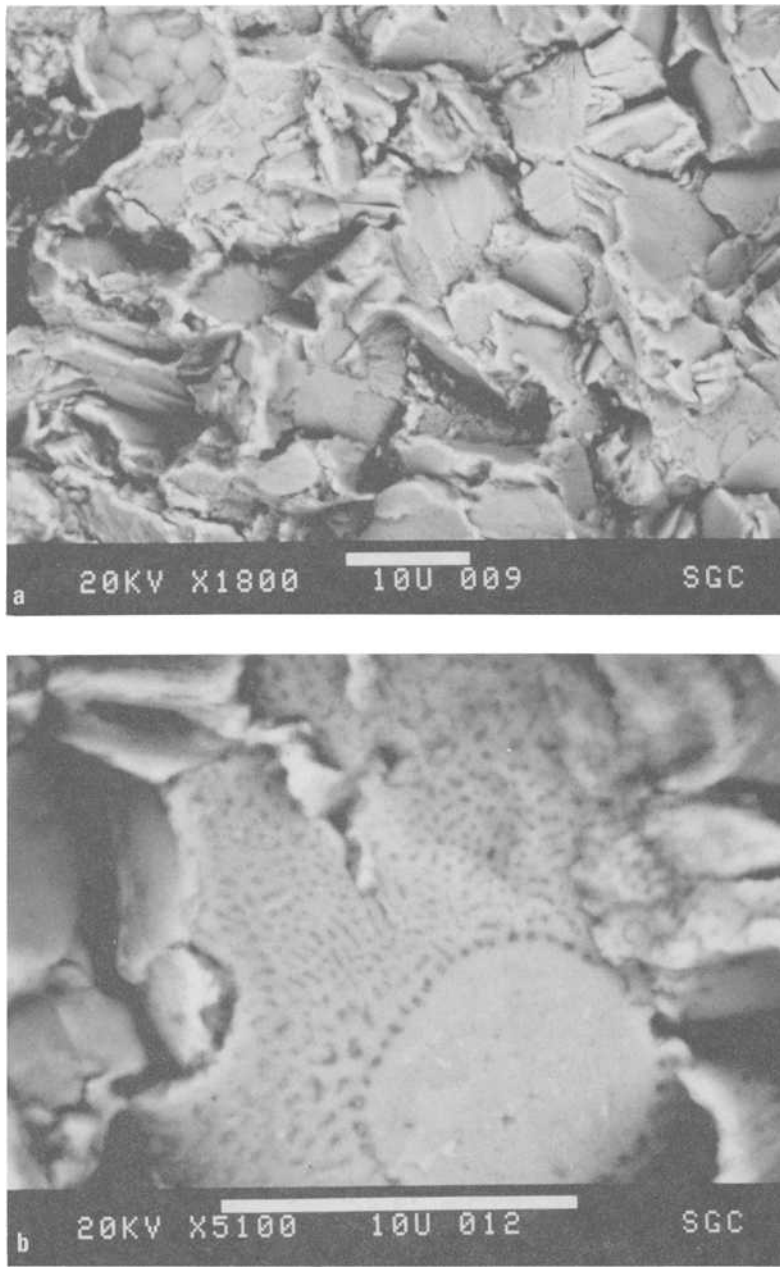

FIG. 13—*Microstructure of a Zn-Al alloy directly from the fracture surface of a metal failure utilizing the solid-state backscatter electron detector.*

be obtained by metallography. Figure 13 shows the fracture surface of a Zn-Al alloy. The light areas are the regions of the high-zinc phase, and the two-phased region is the Zn-Al eutectic structure.

Summary

Scanning electron microscopy is applicable to the study of fracture in brittle materials in a number of ways. The depth of field and resolution enable easy observation of extremely fine fracture origins and other fracture features. The ability to select different signals allows the direct observation of microstructure on the fracture surface, pure topography, interaction of fracture with inclusions and second phases, and X-ray identification of these phases.

References

[1] Fellows, J. A., Ed., *Fractography and Atlas of Fractographs*, Vol. 9 of *Metals Handbook*, 8th ed., American Society for Metals, Metals Park, Ohio, 1974.
[2] Wells, O. C., *Scanning Electron Microscopy*, McGraw-Hill, New York, 1974.
[3] Well, O. C., *Applied Physics Letters*, Vol. 16, 1970, pp. 151-153.
[4] Robinson, V. N. E., "Backscattered Electron Imaging," in *Scanning Electron Microscopy 1975*, IITRI, Chicago, 1975, pp. 51-60.
[5] Robinson, V. N. E., *Scanning*, Vol. 3, No. 1, 1980, pp. 15-25.
[6] Lin, P. S. D. and Becker, R. P., "Detection of Backscattered Electrons with High Resolution," in *Scanning Electron Microscopy 1975*, IITRI, Chicago, 1975, pp. 61-70.
[7] Goldstein, J. I. and Yakowitz, H., Eds., *Practical Scanning Electron Microscopy*, Plenum Press, New York, 1975.
[8] Kimoto, S., Hashimoto, H., and Suganuma, T., "Stereographic Observation in Scanning Microscopy Using Multiples Detectors," in *Proceedings*, Electron Microprobe Symposium, Washington, D.C., 1964, Wiley, New York, 1966, pp. 480-489.
[9] Healey, J. T. and Mecholsky, J. J., Jr., *Scanning*, Vol. 4, 1981, pp. 62-68.
[10] Lane, W. C. in *Proceedings*, 3rd Annual Stereoscan Colloquium, Morton Grove, Ill., Kent Cambridge Scientific, 1970, p. 83.
[11] Wells, O. C., *British Journal of Applied Physics*, Vol. 11, 1960, p. 199.
[12] Freiman, S. W., Williams, A., Mecholsky, J. J., Jr., and Rice, R. W. in *Ceramic Microstructures 1976*, R. A. Fullrath and J. A. Pask, Eds., Westview Press, Boulder, Colo., 1977.
[13] Lange, F. F., *Abstracts of the American Ceramic Society 1982*.
[14] Mecholsky, J. J., Jr. and Freiman, S. W. in *Fracture Mechanics Applied to Brittle Materials, ASTM STP 678*, American Society for Testing and Materials, 1979, pp. 136-150.
[15] Mecholsky, J. J., Jr. and Freiman, S. W. in *Fractography and Materials Science, ASTM STP 733*, American Society for Testing and Materials, 1981, pp. 246-258.
[16] Rice, R. W., Freiman, S. W., and Mecholsky, J. J., Jr., *Journal of the American Ceramic Society*, Vol. 63, No. 3-4, 1980, pp. 129-136.
[17] Rice, R. W., *Proceedings of the British Ceramic Society*, Vol. 20, 1972, pp. 205-257.
[18] Singh, J. P., Vickar, A. V., Shetty, D. K., and Gordon, R. S., *Journal of the American Ceramic Society*, Vol. 62, No. 3-4, 1979, pp. 179-183.
[19] Mecholsky, J. J., Jr. and Lappin, S. M., *Bulletin of the American Ceramic Society*, Vol. 59, No. 3, 1980, p. 352.
[20] Govila, R. K., Kinsman, K. R., and Beardmore, P., *Journal of Materials Science*, Vol. 14, No. 5, 1979, p. 1095.
[21] Govila, R. K., Beardmore, P., and Kinsman, K. R. in *Fractography and Materials Science, ASTM STP 733*, American Society for Testing and Materials, 1981, pp. 225-245.
[22] Coppola, J. A., "Investigation of Fracture Surface Energy, Fracture Stress in Thermal Shock of Ceramic Materials," Ph.D. thesis, Pennsylvania State University, University Park, Pa., Dec. 1971.

Ceramics

Applied Fractography

J. J. Mecholsky, Jr.,[1] *and R. W. Rice*[2]

Fractographic Analysis of Biaxial Failure in Ceramics

REFERENCE: Mecholsky, J. J., Jr. and Rice, R. W., **"Fractographic Analysis of Biaxial Failure in Ceramics,"** *Fractography of Ceramic and Metal Failures, ASTM STP 827*, J. J. Mecholsky, Jr. and S. R. Powell, Jr., Eds., American Society for Testing and Materials, 1984, pp. 185–193.

ABSTRACT: Borosilicate and silica glass, Pyroceram 9606 glass ceramic, and polycrystalline magnesium fluoride ceramic disks were biaxially stressed and the fracture surfaces examined to determine the size of the fracture surface features. The fracture stress (σ) - fracture mirror radii (r_j) relationship

$$\sigma r_j^m = M_j$$

where M_j are the mirror constants ($j = 1, 2, 3$) and m is constant, usually 0.5, is shown to hold for uniaxial, flexural, and biaxial loading conditions. This implies that any local differences of the stress state at the fracture-initiating site are dissipated by the time the crack-front forms mist, hackle, and crack branching, making measurement of the boundaries of these features a general fracture characteristic.

KEY WORDS: fractography, brittle materials, biaxial failure, fracture (materials), ceramics, mechanical properties, fracture mechanics

A number of investigators [*1-6*] have shown that stress state alters the fracture criterion of brittle materials. Thus there is considerable interest in the relationship between the stress state and the orientation of the fracture initiating crack. Petrovic and Mendiratta [*1*], Jortner [*2*], and Freiman et al [*5*] show that mixed mode loading affects the failure criterion. Freiman et al also show, however, that the stress (σ) - fracture mirror radii (r_j) relationship

$$\sigma r_j^{1/2} = \text{constant}$$

[1]Member Technical Staff, Sandia National Laboratories, Albuquerque, N.M. 87185.
[2]Head, Ceramics and Glass Materials Branch, Naval Research Laboratory, Washington, D.C. 20375.

where r_j is the radius from the origin to either the mirror-mist ($j = 1$), mist-hackle ($j = 2$), or crack branching ($j = 3$) boundary, is valid regardless of the angle of the initial crack to the (uniaxial) stress direction.

The present investigation was initiated to study the relationship of biaxial stress state to the fracture surface features of mirror, mist, and hackle. We measured the mirror radii ($j = 1, 2, 3$) and the fracture stress of biaxial disks of silica and borosilicate glass, Pyroceram glass ceramic, and polycrystalline magnesium fluoride, and compared these measurements with those in tension and flexure. We presented these comparisons for one representative radius for each material. We found that the relationship

$$\sigma r_j^m = \text{constant}$$

where m is usually 0.5, is valid regardless of the loading conditions examined.

Experimental Procedure

The glass and small glass ceramic disks (2.5 mm thick) were fractured in an Instron testing machine at a head travel speed of 3×10^{-5} m/s with a piston-3 ball biaxial loading apparatus described in ASTM Test for Biaxial Flexure Strength (Modulus of Rupture) of Ceramic Substrates (F 394). The fracture stress (maximum stress at failure) was calculated from the load and geometry of the specimens. The magnesium fluoride (2.0 mm thick) and large Pyroceram disks (2.5 mm thick) were fractured in a ring-on-ring test at a head travel rate of ~1 mm/min. Magnesium fluoride bars of 10.0 and 5.0 mm thickness were fractured in three-point flexure, with a span-to-thickness ratio of ≈5:1 loaded at ≈13 mm/min. Fracture of the optical fibers and flexural bars is described elsewhere [*8,9*]. The fracture surfaces were analyzed by the techniques described by Rice [*10,11*].

Analytical Background

Many investigators [*12-16*] have shown that the empirical relationship between fracture stress (σ) and the radius (r_j) between the origin and the mirror-mist ($j = 1$), mist-hackle ($j = 2$), and crack bifurcation ($j = 3$) boundaries is generally valid for flexure failures:

$$\sigma r_j^m = M_j \tag{1}$$

[3]For nonmetallic brittle materials, this has not yet been defined. ASTM Subcommittee E24.07 on Fracture Toughness of Brittle Nonmetallic Materials is presently developing a definition. In the ceramics literature, K_{Ic} is considered a measure of the resistance to rapid crack propagation and is generally measured at ~1 m/s.

where M_j is the "mirror" constant corresponding to r_j and m is a constant, usually 0.5. Abdel-Latif et al [*17*] found different M_j for tension and three- and four-point flexure. Most investigators, however, find the same constant for the same material regardless of the type of flexural or tensile loading [*12,13,18*]. Frechette and Michalske [*19*] and Bahat et al [*20*] found this relationship to hold for bottles loaded by internal pressure.

Equation 1 is thought to be related to the strain energy associated with fracture and has been related to the Mode I critical stress intensity factor (K_{Ic}).[3] Thus Kirchner and Kirchner [*21*] have related the mirror-mist, mist-hackle, and crack branching boundaries to stress intensity factors in a set of equations analogous to Eq 1 with $m = 0.5$:

$$K_j = Q\frac{2}{\pi^{1/2}}\sigma r_j^{1/2} \tag{2}$$

where $j = 0, 1, 2, 3$ and $j = 0$ corresponds to $K_0 = K_{Ic}$, and r_0 is the critical flaw size (in Mode I loading). Q is the value of K_I/K_{Ic} necessary to correct K_{Ic} for an internal penny-shaped crack to obtain the stress-intensity factor (K_I) for a semicircular surface crack. Although there is some question of the total validity of this approach [*16*], it has appeal because it can be used in failure analysis and gives some analytical validity to fractography.

Results and Discussion

Fracture surface analysis of silica glass fractured in tension (optical fibers), three-point flexure, and biaxial flexure (Fig. 1) shows that Eq 1 (solid line in Fig. 1) is a good representation of the relationship between stress and the mirror-mist boundary. The calculated values of $M_j (j = 1)$ for tension, flexure, and biaxial tension data are 2.2 ± 0.5, 2.3 ± 0.5, and 2.4 ± 0.3 MPa $m^{1/2}$, respectively. Statistical comparison shows that we are 95% confident that these averages are the same. The solid line represents data previously reported [*8,9*]. This implies that there would be no difference in "mirror" constants expected in three- or four-point flexure and tension; this is in contrast to the findings of Abdel-Latif et al [*17*]. Ritter [*22*] has shown analytically and experimentally that thin beams in bending can lead to anomalously high (factor of 2 to 3 higher than true) stresses due to large deflections and frictional forces. Abdel Latif et al [*17*] used the same diameter rods as Ritter [*22*] but with smaller spans. If we assume the effect of large deflections is only one tenth that which Ritter calculated, the mirror constants for three- and four-point flexure in Ref *17* would be reduced (by ~30%) to 2.0 and 1.9 MPa $m^{1/2}$, respectively. These values are very close to that observed in the literature for tensile and other flexural experiments. The agreement of the mirror

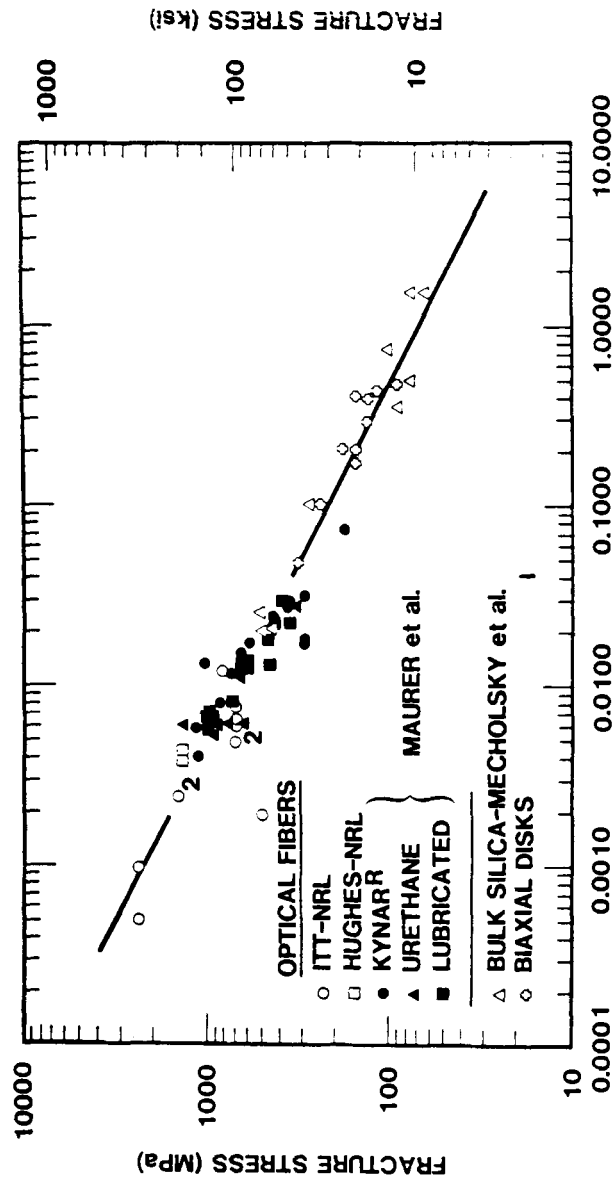

FIG. 1—*Fracture stress as a function of "mirror-mist" radius for tensile, (three-point) (bulk) flexural, and biaxial loading of silica glass. The solid line represents Eq 1 with* $m = 0.5$ *and agrees with much flexural data* [9]. *The information on fiber fracture is included in Ref* 8.

constant for pressurized bottles [*19,20*] and other flexural data [*18*] tends to reinforce the present findings.

Comparison of fracture features of borosilicate (Pyrex 7740) glass disks and three-point flexure bars in Fig. 2 shows that Eq 1 with $m = 0.5$ can describe behavior for both cases in agreement with that found for silica glass. The M_j-values ($j = 1$) calculated from the flexural bar and biaxial tension data are both 1.9 ± 0.3.

The relationship between fracture-stress and fracture surface features in the magnesia-alumina-silicate (Pyroceram 9606) glass ceramic is more complicated than glass fracture and is shown in Fig. 3. The solid straight line represents Eq 1 with $m = 0.5$. Flexure bar data of Mecholsky et al [*14*] and Lewis [*23*] obey Eq 1 (solid straight line) for low stresses and deviate with the curved line for higher stresses. The biaxial data for two different size disks and two types of tests [one the analog of three-point flexure (piston - 3 ball) and the other four-point flexure (ring on ring)] agree with one another. The disk data show a clear deviation from the usual $\sigma r_j^{1/2} = M_j$ relation at high σ, low r_j. However, this deviation is the same as that found for extensive flexure bar [*23*] and other biaxial disk tests [*24*]. Thus the deviation is not caused by the type of loading but by the material itself. Lewis has presented analysis showing that this deviation may be due to internal stress from expansion differences between the grains of the glass ceramic [*23*].

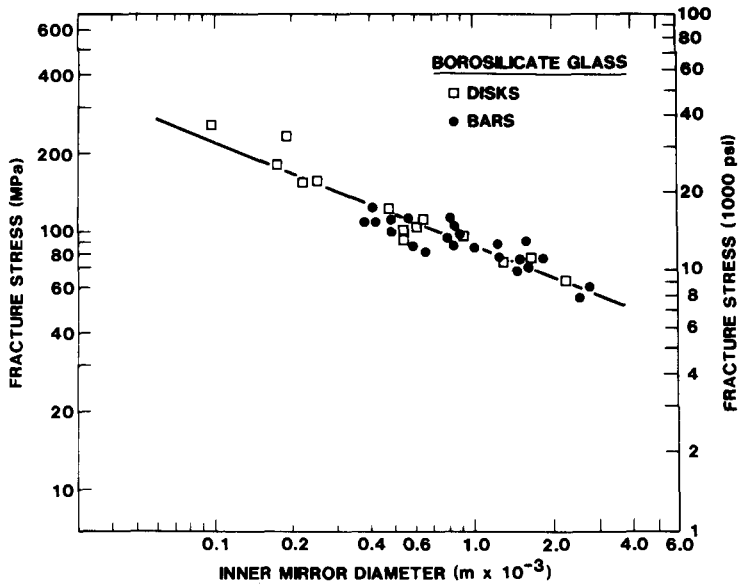

FIG. 2—*Fracture stress as a function of "mirror-mist" radius for biaxial disks of borosilicate (Pyrex 7740) glass. The solid line represents Eq 1 with* m = *0.5 and agrees with three-point flexural data* [9].

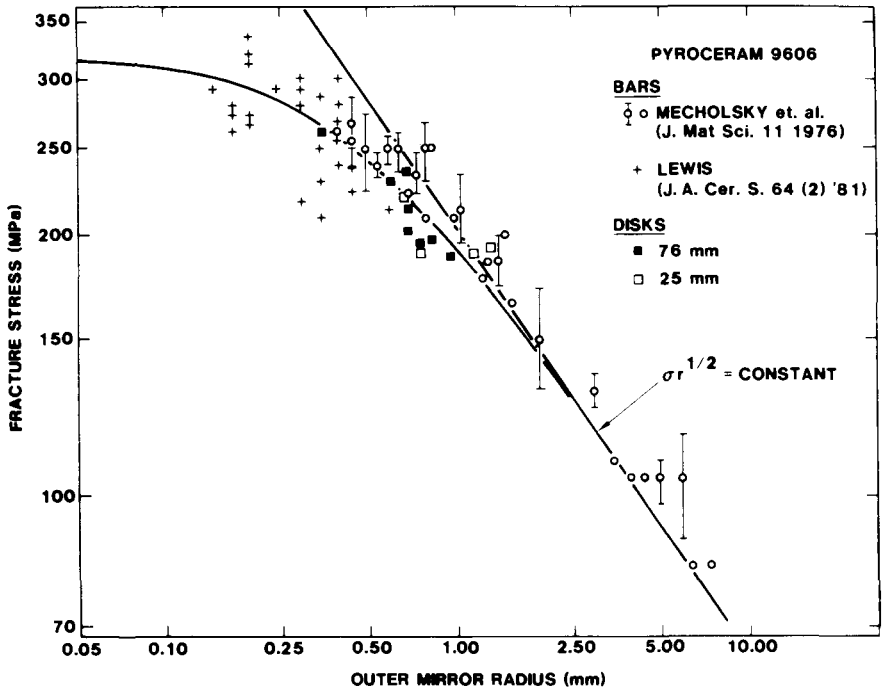

FIG. 3—*Fracture stress as a function of "mist-hackle" radius on fracture surfaces of biaxial disks of Pyroceram 9606. The solid straight line represents Eq 1 with* m = *0.5; three-point flexural data* [14] *agrees with this line at lower stresses (and larger mirror radii) up to the point of deviation at the curved line. The flexural* [23] *and biaxial data* [24] *both deviate at this point. Thus the deviation is a function of the material and not the test procedures.*

Fracture stress - mirror diameter measurements were obtained for mist, hackle, and crack branching demarcations on the fracture surface of magnesium fluoride (MgF_2) bars and disks. All measurements showed agreement between flexural and biaxial (tensile) loading, but more than usual scatter, and deviations from Eq 1 with $m = 0.5$ were observed. As an example, we show in Fig. 4 the fracture stress and crack branching diameter for MgF_2 biaxially loaded disks and for two sizes of flexurally loaded bars. The slope of a straight-line fit to the biaxial disk data is -0.26 ± 0.13 and to the flexural bar data is -0.31 ± 0.19. Statistical analysis shows that there is no difference between these slopes at a 99% confidence level. Note that the deviation and scatter from the solid line in Fig. 4 is approximately the same for bar and disk data, which indicates that the scatter is caused by the material and not by the biaxial loading. There is a significant difference between the data and the solid line (Eq 1 with $m = 0.5$) at the 0.01 level of significance. At least some of the deviation is caused by the difficulty of clearly defining the radii r_j owing to increasing diffusiveness of fracture features at lower σ, and hence

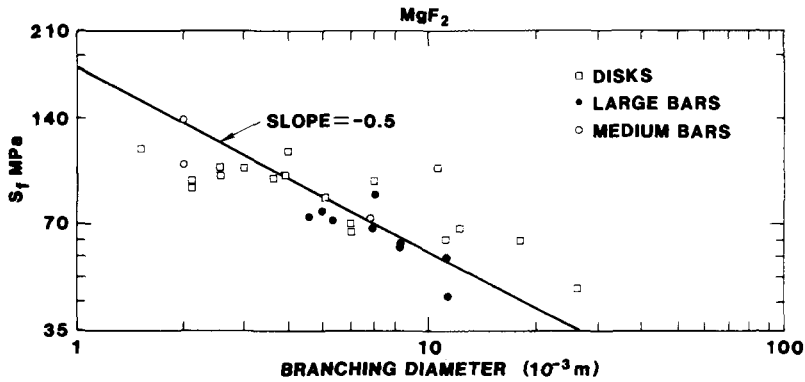

FIG. 4—*Fracture stress as a function of crack branching diameter for (three-point) flexural bars and biaxial disks of polycrystalline magnesium fluoride (Kodak IRTRAN 1). The solid line represents Eq 1 with* m = *0.5. The best-fit straight line has a slope of* m ≈ *0.3.*

larger r_j. Changes in the character of the crack relative to the specimen size—that is, cracks small relative to the specimen, and cracks penetrating through the thickness of the specimen—may also be a factor as noted by Rice [*11*].

In all cases, we assumed Eq 1 was valid (except for the deviations shown by Lewis [*23*] described previously); the biaxial data presented were compared with uniaxial data. The solid lines are not best-fit lines, but represent Eq. 1. The agreement of the uniaxial and biaxial (tension-tension) data implies that initial stress state will not greatly influence the fracture stress—mirror relationship. This statement and the following statements are made for the case of biaxial tension stress states, since the cases of tension-compression and torsion have not been examined. The stress direction is expected to greatly influence onset of the fracture as shown in many mixed-mode loading experiments [*1*,*5*,*6*]. But once the crack starts propagating, the crack tends to propagate at right angles to the stress. Any small deviations from the normal stress direction caused by shear components at the onset of crack propagation are not detected in the measurements of the formation of mist, hackle, or crack branching. Since the mirror radii are not influenced by the local stress state, the effect of Mode II or Mode III loading on the crack can be studied by observing the size and shape of the fracture-initiating crack with the influence of mixed-mode loading and the size of the mirror boundaries without the influence of mixed-mode loading.

Since there is more strain energy stored in a biaxial than a uniaxial specimen at the same fracture stress level,[4] and since mist, hackle, and crack branching occur at the same stress level, then an energy criterion alone (for

[4]The reader will be convinced of this if he calculates the stored energy [1/2 (stress)(strain)] in both and compares them. The biaxial stored energy will be larger.

example, crack branching occurring at some constant energy level) cannot explain the formation of mist, hackle, and crack branching. Thus the achievement of a certain level of energy or energy density may be a necessary but not sufficient condition for the formation of mist, hackle, and crack branching.

Conclusions

The fracture stress (σ) - fracture mirror radius (r_j) relationship

$$\sigma r_j^m = M_j$$

where M_j is the "fracture mirror" constant and m is another constant, usually 0.5, is valid for tensile, flexural, and biaxial (tension) loading. Since local stress states at the initial crack do not influence the distance to the formation of mirror, mist, and hackle, fractography can be useful in the study of biaxial [*6*] and mixed mode [*5*] loading. These two facts also suggest that fractography can be applied to shaped articles with complicated stress states [*19,20*] (large stress gradients may influence the formation of the fracture features).

There can be some deviations from the fracture stress - fracture mirror radius relationship, at least in some materials, at quite high or low fracture stress (hence, low and high r_j, respectively) relative to typical values for a given material. However, these deviations are attributed to material, crack-specimen relations, and to reduced accuracy of r_j-values caused by increased diffuseness of fracture features. The deviations clearly are not caused by different tests nor are they basic to different forms of these tests (for example, three- and four-point flexure or their biaxial counterparts).

The agreement between biaxial and uniaxial results means that an energy criterion alone (for example, strain energy density alone) cannot explain mist, hackle, and crack branching. This agreement also means that thermal stress failures which are typically biaxial can be directly related to uniaxial and flexural data.

Acknowledgments

The authors thank K. R. McKinney of the Naval Research Laboratory for providing the large Pyroceram disks for analysis, J. R. Hellmann and T. A. Michalske of Sandia National Laboratories for reading the manuscript and providing useful suggestions, and J. M. Mata of SNL for reducing much of the data.

References

[*1*] Petrovic, J. J. and Mendiratta, M. G., *Journal of the American Ceramic Society*, Vol. 59, No. 3-4, 1976, pp. 163-167; correction: *Journal of the American Ceramic Society*, Vol. 60, No. 9-10, 1977, p. 463.

[2] Jortner, J., "Biaxial Tensile Fracture of 994 Graphite," Air Force Materials Laboratory Technical Report, AFML-TR-76-150, Wright-Patterson Air Force Base, Ohio, Aug. 1978.
[3] Batdorf, S. B., *International Journal of Fracture*, Vol. 13, No. 1, 1977, pp. 5-11.
[4] Petrovic, J. J., "Controlled Surface Flaw Fracture in Tension and Torsion," in *Fracture Mechanics of Ceramics*, R. C. Bradt, D. P. H. Hasselman, F. F. Lange, and A. G. Evans, Eds., Vol. 5 & 6, Plenum Press, New York, 1982.
[5] Freiman, S. W., Gonzalez, A. C., and Mecholsky, J. J., Jr., *Journal of the American Ceramic Society*, Vol. 62, No. 3-4, 1979, pp. 206-208.
[6] Tappin, G., Davidge, R. W., and McLaren, J. R., "The Strength of Ceramics under Biaxial Stresses," in *Fracture Mechanics of Ceramics*, R. C. Bradt, D. P. H. Hasselman, and F. F. Lange, Eds., Vol. 3, Plenum Press, New York, 1978, pp. 435-449.
[7] Vitman, F. F. and Pukh, V. P., *Aavodskaya Laboratoriya*, Vol. 29, 1963, pp. 863-867.
[8] Mecholsky, J. J., Jr., Freiman, S. W., and Morey, S. M., "Fracture Surface Analysis of Optical Fibers," in *Fiber Optics*, B. Bendow and S. S. Mitra, Eds., Plenum Press, New York, 1979.
[9] Mecholsky, J. J., Rice, R. W., and Freiman, S. W., *Journal of the American Ceramic Society*, Vol. 57, No. 10, 1974, pp. 440-443.
[10] Rice, R. W., *Surface of Interfaces of Glass and Ceramics*, Plenum Press, New York, 1979, pp. 439-472.
[11] Rice, R. W., this publication, pp. 5-103.
[12] Shand, E. G., "Breaking Stresses of Glass Determined from Fracture Surfaces," The Glass Industry, New York, April 1967, p.190ff.
[13] Orr, L., *Materials Research and Standards*, Vol. 12, No. 1, 1972, pp. 21-23 and 47.
[14] Mecholsky, J. J., Jr., Freiman, S. W., and Rice, R. W., *Journal of Materials Science*, Vol. 11, 1976, pp. 1310-1319.
[15] Kirchner, H. P. and Gruver, R. M. in *Fracture Mechanics of Ceramics*, R. C. Bradt, D. P. H. Hasselman, and F. F. Lange, Eds., Vol. 1, Plenum Press, New York, 1974, pp. 309-321.
[16] Shetty, D. K., Bansal, G. K. Rosenfield, A. R., and Duckworth, W. H., *Journal of the American Ceramic Society*, Vol. 63, No. 1, 1980, pp. 106-108.
[17] Abdel-Latif, A. I. A., Tressler, R. E., and Bradt, R. C., *International Journal of Fracture Mechanics*, Vol. 13, 1977, pp. 349-359.
[18] Mecholsky, J. J., Jr. and Freiman, W. S. in *Fracture Mechanics Applied to Brittle Materials, ASTM STP 678*, American Society for Testing and Materials, 1979, pp. 136-150.
[19] Frechette, V. D. and Michalske, T. A., *Bulletin of the American Ceramic Society*, Vol. 57, No. 4, 1978, pp. 427-429.
[20] Bahat, D., Leonard, G., and Rabinovitch, A., *International Journal of Fracture*, Vol. 18, No. 1, Jan. 1982, pp. 29-38.
[21] Kirchner, H. P. and Kirchner, J. W., *Journal of the American Ceramic Society*, Vol. 62, No. 3-4, 1979, pp. 198-202.
[22] Ritter, J. E., "Effect of Polymeric Coatings on Strength of Soda-Lime Glass," in *Fracture Mechanics of Ceramics*, R. C. Bradt, D. P. H. Hasselman, and F. F. Lange, Vol. 2., Plenum Press, New York, 1974, pp. 735-747.
[23] Lewis, D., III, *Journal of the American Ceramic Society*, Vol. 64, No. 2, 1981, pp. 82-86.
[24] Shetty, D. K., Rosenfield, A. R., Bansal, G. K., and Duckworth, W. H., *Journal of the American Ceramic Society*, Vol. 64, No. 1, Jan. 1981, pp. 1-4.

George C. Phillips[1]

Fractography of Metalized Ceramic Substrates

REFERENCE: Phillips, G. C., **"Fractography of Metalized Ceramic Substrates,"** *Fractography of Ceramic and Metal Failures, ASTM STP 827*, J. J. Mecholsky, Jr., and S. R. Powell, Jr., Eds., American Society for Testing and Materials, 1984, pp. 194-205.

ABSTRACT: The purpose of this paper is to expand the understanding of 96% alumina ceramic breakage in metalized ceramic (MC) processing. By observing the location of cracks and studying the fractured surfaces, it is possible to determine the origin of the fracture, the type of fracture, and the relative stresses that caused the fracture. Cracks were observed by the use of dye penetrants, and fracture surface details were enhanced by spraying with collodial graphite. Scanning electron microscopy (SEM) photomicrographs were used to distinguish between intergranular and transgranular fractures.

Breakage that occurs during MC processing includes impact from substrate handling, bending during the pinning operation, and thermal effects from tinning. These cracks and fractured surfaces were compared with substrate damage caused by known types of applied stresses. Samples from impact testing, flexural strength measurements, pinning, and thermal shock studies were used. Impact breakage occurs primarily in corner cracks and chips. Breakage from bending occurs during pinning and flexure testing. The fractured surfaces show concave crack front profiles originating from the tensile surface. Thermal shock fractures caused by tinning produce smooth and wavy fractured surfaces.

KEY WORDS: ceramic breakage, cracks, fractured surfaces, impact shock, bending breakage, thermal shock, ceramic substrate, graphite coating, pinning, tinning

IBM thin film packaging technology involves the blanket evaporation of chromium and copper films onto alumina ceramic substrates that are approximately 24-mm square, 1.5-mm thick, with 0.5-mm hole diameters, on a 2.5-mm grid. The circuitry is developed from the blankets by photolithography; a resist protects the unetched circuit lines. Input/output connections are made through the holes by mechanically swagging copper pins into the holes. Soldering of the exposed copper ensures electrical continuity and is the basis for chip connections and connection of the pins into printed circuit boards.

[1] IBM Corporation, General Technology Division, Endicott, N.Y. 13760.

The use of 96% alumina for substrates is dictated by its properties. Alumina ceramics have excellent dielectric properties combined with high mechanical strength, thermal stability, conductivity and low expansion, and chemical inertness. A limiting feature of ceramic materials is their brittleness and under applied stresses they may exhibit catastrophic failures. At IBM the substrates are subjected to a variety of stresses during processing. The need for relatively large volumes of ceramic parts makes automatic handling necessary. Our ceramic substrate handling technique requires traypack carriers to store the substrates between processes. The traypacks are unloaded into a process station and reloaded, after processing by gravity feed. The sliding action in and out of these traypacks causes impact shock stresses to the substrates. Bending stresses occur during the pinning operation where soft copper pins are mechanically swagged around the holes. Thermal shock stresses can result from rapid quenching during the tinning operation.

The fracture surfaces of glassy materials have been studied [*1–3*]. The features on the fracture surfaces can be related to the applied stresses. Fractured surfaces on 96% alumina are not as revealing as glass surfaces [*4–7*].

Procedure

Impact Fractures

Substrates that were cracked or chipped from impact forces were obtained from the process line. This breakage, primarily from handling, occurs during the loading and unloading of the substances into the traypacks at the various process stations. Substrates that were damaged from the impact test were also studied. The impact tester, which simulates line handling, uses two traypacks mounted end-to-end at a 70-deg angle. Substrates are loaded into the top half and dropped into the bottom half against a nylon stopper. The dropping is repeated ten times to simulate repeated line handling. The cracks were observed after use of a dye penetrant. The fracture surfaces were studied after spraying with collodial graphite to improve the contrast. Scanning electron microscopy (SEM) photomicrographs were taken at various magnifications (×50 to ×2500).

Bending Fractures

Two distinctly different sources for bending fractures were studied. One was the standard flexure test where bending was caused by three-point loading. The substrate was placed on two knife edges, and a load was applied along a knife edge between the two on the top surface. The loads-to-failure were recorded and the modulus of rupture calculated using a three-point beam flexure formula. Fracture surfaces were observed after graphite coat-

ing, and comparisons were made of the surface features to the applied load-to-failure. SEM photomicrographs were taken for high and low flexural strength samples at various magnifications.

The second source of bending fractures occurred during the pinning operation. Soft copper pins were inserted into the ceramic holes so as to project slightly above the substrate. A ram presses against these projecting pins and deforms the soft copper to fill the holes; the excess remains above the hole to form the head. The bulge on the bottom side was formed by raising the substrate slightly off the die block and again pressing the ram deforming the copper in the space between the substrate and the die block. Broken substrates resulted from increased camber and hole location tolerances. Substrates were checked for cracks by use of dye penetrant, and fracture surfaces were observed after spraying with graphite. SEM photomicrographs were taken of typical fractures at various magnifications.

Thermal Shock

Ceramic substrates were subjected to thermal shock by rapid cooling from a solder bath at 350°C into an unheated tank of perchlorate and isopropanol. This shock can occur during the tinning operation. Variations in thermal shock were accomplished by varying the delay times from the solder bath to an unheated quench tank. Cracks were observed with ultraviolet lighting, and fracture surfaces were studied after graphite spraying. SEM photomicrographs were taken for fractured surfaces at various magnifications.

Results

Impact Fractures

Impact-type cracks develop primarily from the corners of the substrate. They usually occur at a 45-deg angle. Impact fractures are usually corner chips. A typical corner chip is shown in Fig. 1. An SEM photograph at a magnification of ×50 shows considerable hackle (Fig. 2) around the fracture origin. Higher magnification of the fracture origin (Fig. 3) shows the fracture mode to be primarily transgranular. Observations on many corner chips that had been coated with graphite show large variations of the fractured surfaces. Some were very smooth with the absence of hackle; others showed very pronounced hackle, the amount of which was a function of the applied stress.

Bending Fractures

The fractured surface of a substrate that exhibited a high flexural strength [276 000 kPa (40 000 psi)] is shown in Fig. 4. The origin of fracture is the bottom surface, as shown by the concave crack front profiles on the right- and

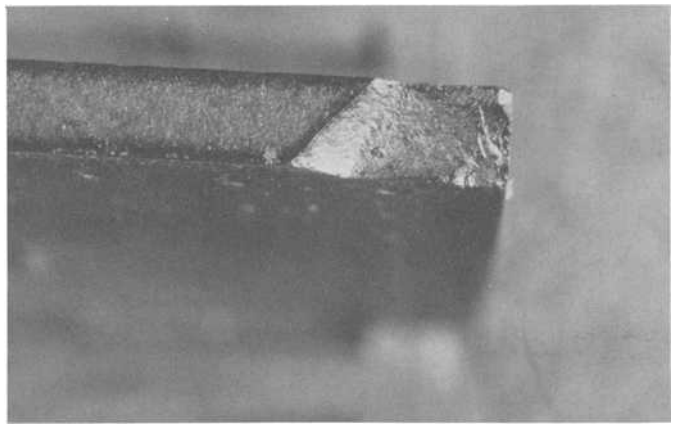

FIG. 1—*Typical corner chip (×5).*

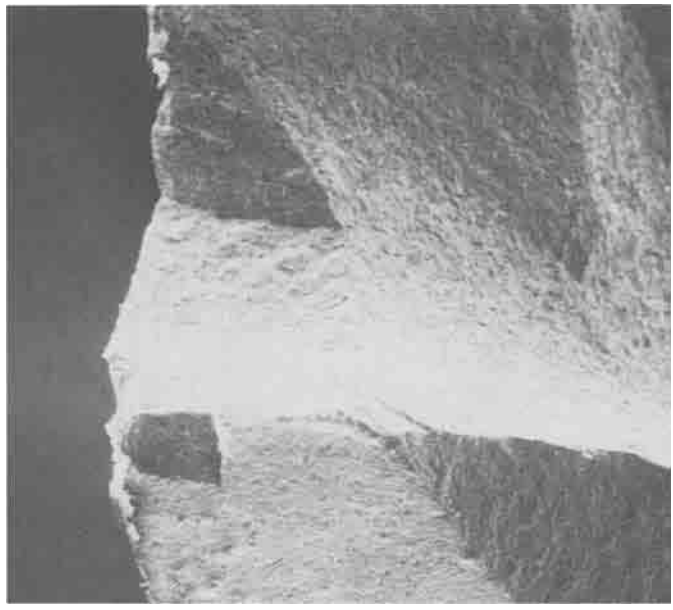

FIG. 2—*SEM photomicrograph of corner chip (×50).*

left-hand sides towards the top surface. These markings are equivalent of Wallner lines on glass surfaces. In contrast, a fractured surface of a substrate that had a low flexural strength [138 000 kPa (20 000 psi)] is shown in Fig. 5. The concave crack front profiles are barely visible on the extreme sides that again indicate the origin on the bottom surface. The origins of the fractures, as observed by the SEM for the high-and-low flexural values, are shown in

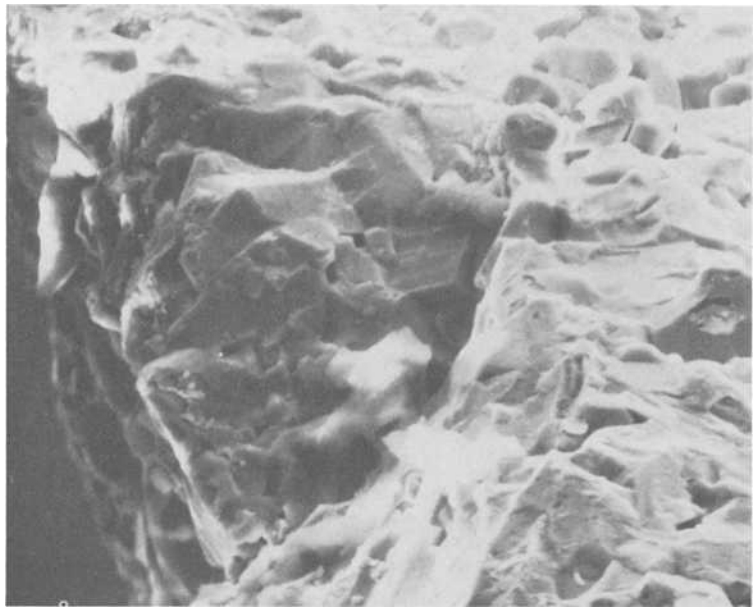

FIG. 3—*SEM photomicrograph at corner crack (×1000).*

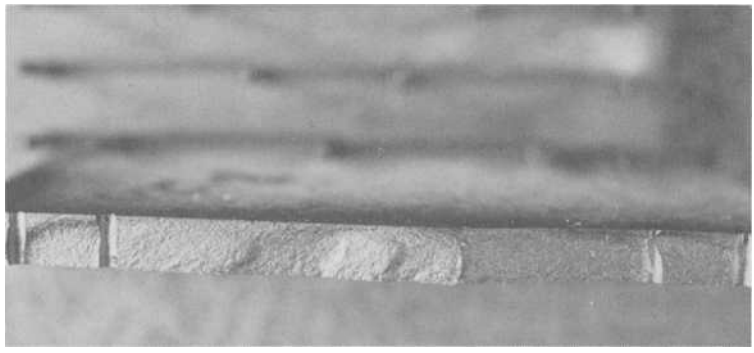

FIG. 4—*Fractured surface for high flexural strength sample (×5).*

Figs. 6 and 7. The high-value sample shows a considerable amount of ridges and additional cracks around the origin. The low-value sample shows only faint markings. At higher magnifications (Figs. 8 and 9) the fracture mode for both samples appears to be transgranular.

Cracks that develop from the pinning operation from flexural loading originate primarily on the sides of the substrates, not from the corners. Fractured surfaces caused by pinning will typically show the marking illustrated in Fig. 10. The origin of the fracture is the bottom of the third hole from the left.

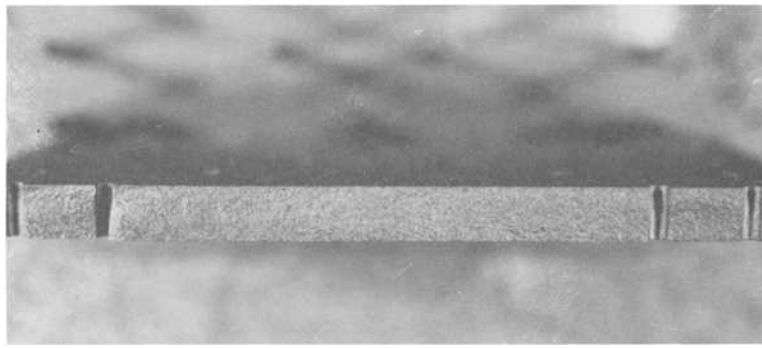

FIG. 5—*Fractured surface for low flexural strength sample (×5).*

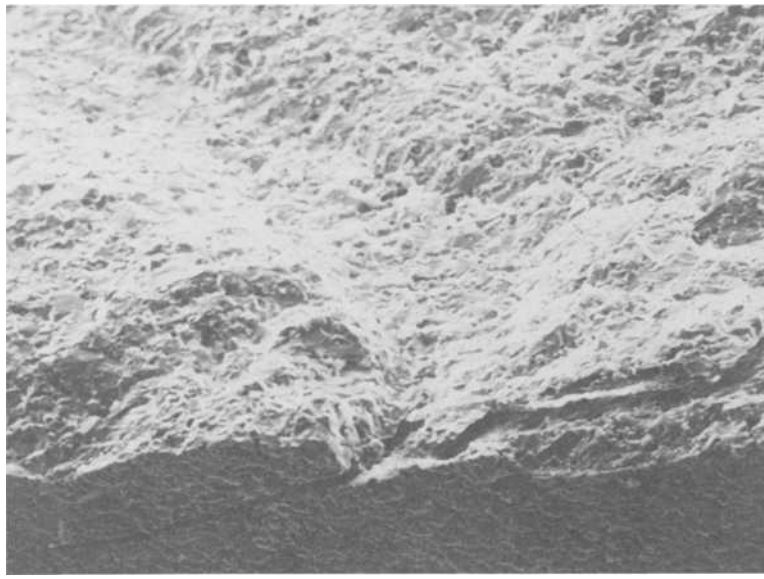

FIG. 6—*SEM photomicrograph near fracture origin of high flexural strength sample (×200).*

From this origin, the concave wave fronts propagate to the top surface, which is in compression. Sometimes the wave fronts will be concave towards the top side. For this condition, the compressive surface is at the bottom and the origin is from the tension or top surface. Observations on many pinning fractures after graphite spraying have shown that sometimes the wave fronts are very pronounced and that other times they are barely visible. The origin of the fractures are mostly from the bottom surface in the automatic pinners and mainly from the top surfaces in the semi-automatic pinners. This information

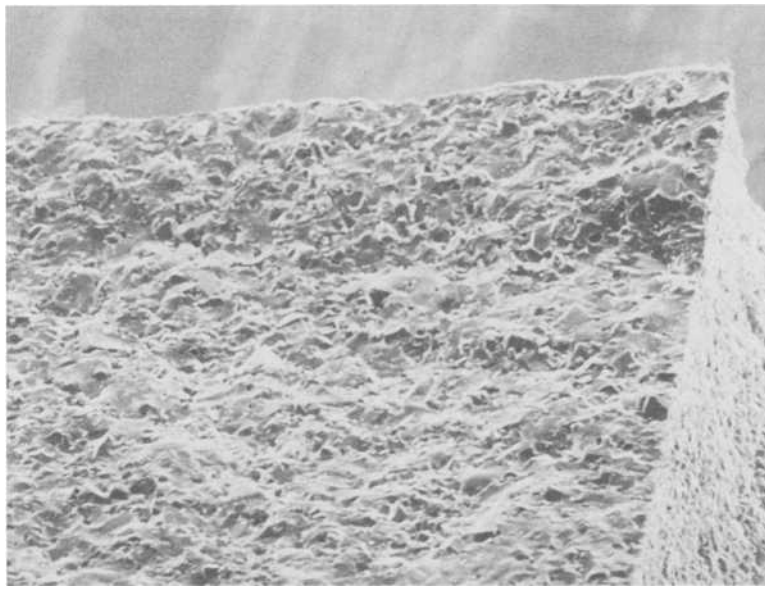

FIG. 7—*SEM photomicrograph near fracture origin of low flexural strength sample (×200).*

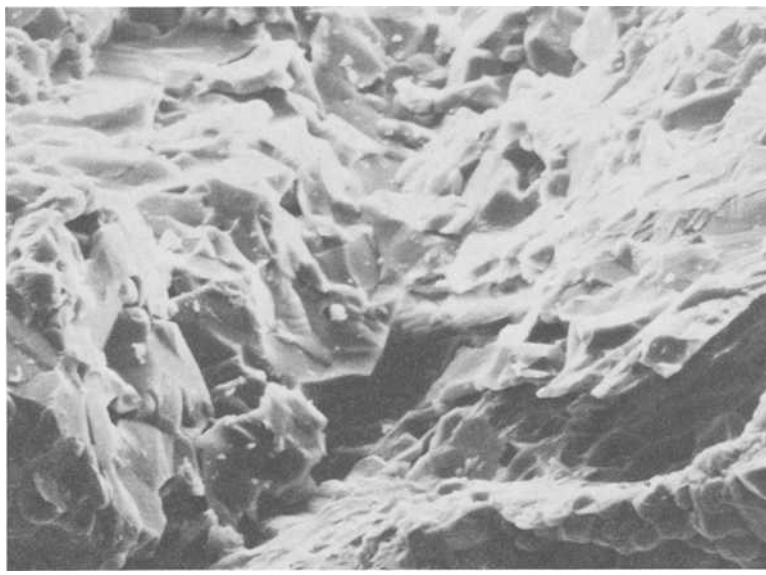

FIG. 8—*SEM photomicrograph near fracture origin of high flexural strength sample (×1000).*

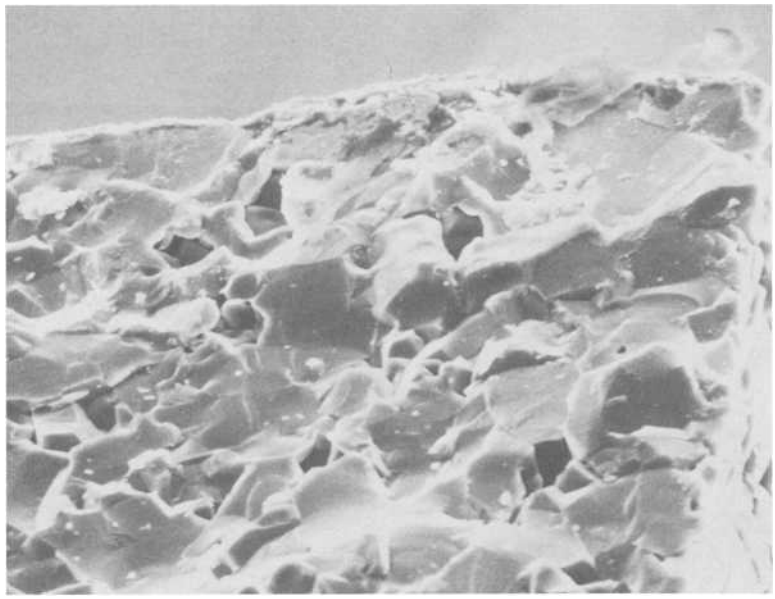

FIG. 9—*SEM photomicrograph near fracture origin of low flexural strength sample (×1000).*

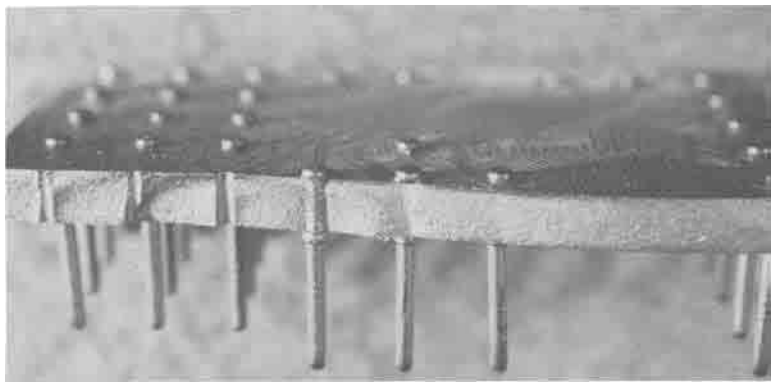

FIG. 10—*Typical pinning fracture (×5).*

is an observation; modeling of the pinning stresses has not been completed. The location of the origin is normally from a hole position. Generally the larger the substrate size, the further the fracture origin is from the edge. Figure 11 shows the origin of a pinning fracture around the hole on the bottom side. As evident in this SEM photomicrograph, a series of ridges or hackle are radiating from the corner. At high magnification, the fracture mode around the origin appears to be transgranular (Fig. 12).

FIG. 11—*SEM photomicrograph at fracture origin of pinning failure (×100).*

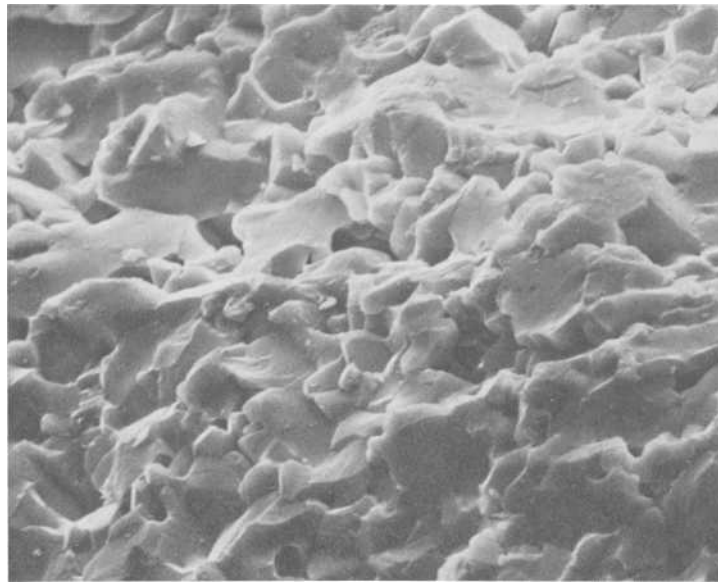

FIG. 12—*SEM photomicrograph at fracture origin of pinning failure (×1000).*

Thermal Fractures

Cracks that develop from the thermal shock will show either a wavy path or branching of the crack. The cracks primarily develop from the side, not the corners. The fracture from thermal shock will have a wavy feature, though the fractured surface will be very smooth (Fig. 13). SEM photomicrographs of the fractured surfaces at high magnification (Fig. 14) do not show any markings, and the fracture mode (Fig. 15) appears to be primarily intergranular from the origin. As the wave fronts go towards the compressive loading, the fracture origin will be on the opposite or tensile side.

The observations of these fracture surfaces were made at visual or very low magnification ($\times 10$). High magnification does not appear to improve the distinguishable features of the various types of fractures. The collodial graphite spray on the fracture surfaces significantly improves the contrast and allows rapid identification.

Discussion

Observation of cracks from known sources of stresses (impact, bending, and thermal) shows definite trends. Corner cracks are seen almost exclusively from impact testing. Side cracks from impact tests will typically show the 45-deg entrance angle. The impact test, which simulates the worst case of automatic substrate handling used for processing, results in such corner cracks. Those corner cracks observed by ultraviolet inspection of the specimen at the end of the line are most likely caused by impact stresses induced by the automatic handling mechanism. Corner cracking is reduced by minimizing the forces from the gravity-fed traypack transfer—for example, by allowing only

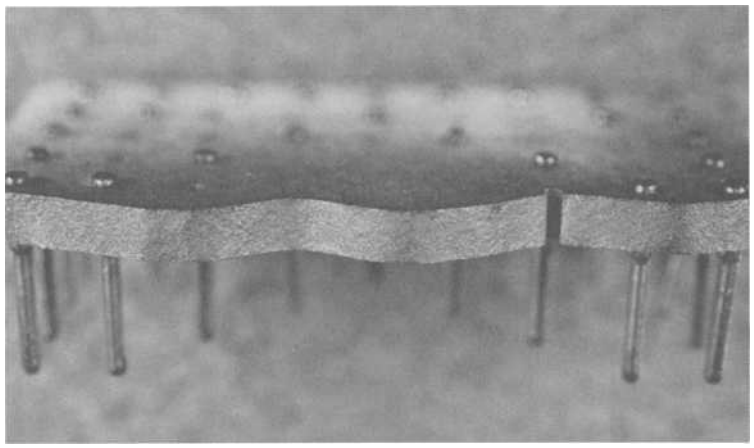

FIG. 13—*Typical tinning fracture* ($\times 5$).

FIG. 14—*SEM photomicrograph of fracture surface of tinning failure (×50).*

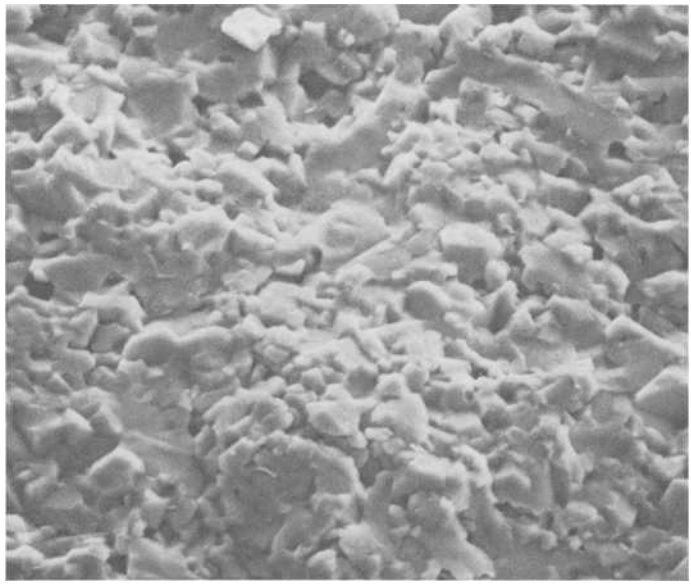

FIG. 15—*SEM photomicrograph of fracture surface of tinning failure (×500).*

one traypack to drop at a time and using a lower angle for traypack mounting. The current observations show that straight cracks along the sides of the substrates are almost always due to pinning. Cracks originating from the corners have not been observed after pinning. In fact, maximum stresses have to occur away from the corners, the substrate flatness being the most significant factor in the location of the origin. The pure thermal cracks will usually show a wavy or branching effect and normally occur from the side crack. Propagation of pinning fractures can occur in the tinning operation.

Conclusions

Fractography can be used to distinguish the type of loading stresses that cause alumina ceramic breakage. The location and shape of cracks indicate the type of applied stress: corner cracks coming from impact, side cracks resulting from bending, and wavy cracks produced by thermal shock. The investigations of the fracture surfaces reveal the origin of the fracture and the type and relative amount of the applied stresses. In addition, with these data one can implement corrective actions to minimize breakage. Observations at visual or low magnifications ($\times 10$) on graphite-coated surfaces showed the most contrast for identifying features.

Acknowledgments

The author wishes to extend his appreciation to J. J. Turner and K. Huebner for their assistance in taking the photographs and SEM photomicrographs.

References

[1] Orr, L., *Materials Research and Standards*, Vol. 12, No. 1, 1972, pp. 21-23 and 47.
[2] Kerper, M. J. and Scuderi, T. G., *American Ceramic Society Bulletin*, Vol. 43, No. 9, 1964, pp. 622-625.
[3] Bansal, G. K. and Duckworth, W. H., *Journal of the American Ceramic Society*, Vol. 60, No. 7-8, 1977, pp. 304-310.
[4] Kirchner, H. P. and Gruver, R. M., *Philosophical Magazine*, Vol. 27, No. 8, 1973, pp. 1433-1446.
[5] Rice, R. W., *Journal of the American Ceramic Society*, Vol. 62, No. 9-10, 1979, pp. 533-535.
[6] Frechette, V. D. and Cline, C. F., *American Ceramic Society Bulletin*, Vol. 49, No. 11, 1970, pp. 994-997.
[7] Kirchner, H. P., Gruver, R. M., and Sotter, W. A., *Journal of the American Ceramic Society*, Vol. 58, No. 5-6, 1975, pp. 188-191.

Metals

Failure Analysis Techniques

J. V. Pellegrino[1] *and R. F. McCartney*[1]

Analysis of Failures Associated with Intergranular Fracture

REFERENCE: Pellegrino, J. V. and McCartney, R. F., **"Analysis of Failures Associated with Intergranular Fracture,"** *Fractography of Ceramic and Metal Failures, ASTM STP 827*, J. J. Mecholsky, Jr. and S. R. Powell, Jr., Eds., American Society for Testing and Materials, 1984, pp. 209–233.

ABSTRACT: Intergranular fracture is usually the most easily recognizable mode of fracture, but determining the cause may be quite difficult. Although fractography identifies the presence of intergranular fracture, a correlation of both fractographic and metallographic features should be obtained to aid in identifying the mechanism responsible.

Case histories of failure analyses in which intergranular fractures were observed and were attributed to a variety of mechanisms are presented and include (1) liquid-metal embrittlement of an AISI 1070 rod caused by copper pickup during processing, (2) liquid-metal embrittlement of a low-carbon steel caused by lithium in service, (3) liquid-metal embrittlement of a platinum and platinum-rhodium thermocouple caused by a low-melting platinum-silicon eutectic that formed in service, (4) fracture of a steel-strand wire-rope caused by an area of untempered martensite, (5) "rock candy" brittle fracture of a steel casting caused by the presence of aluminum nitride at the solidification grain boundaries, and (6) brittle fracture of heat-treated bolts manufactured from columbium-treated fine-grain AISI 1541 steel caused by the presence of a columbium film at prior-austenite grain boundaries.

The investigative techniques used included light microscopy, scanning electron microscopy, energy-dispersive spectroscopy, electron diffraction, and secondary-ion mass spectroscopy.

KEY WORDS: intergranular fracture, liquid-metal embrittlement, brittle fracture, fractography, grain-boundary films

[1] Associate Research Specialist and Associate Research Consultant, respectively, United States Steel Corporation Research Laboratory, Monroeville, Pa. 15146.

Fractography is an important tool in failure analysis. It reveals information about the structural features of the material, state of stress, chemical environment, origin of the fracture, and mode of crack progression to the terminal stage. The principal types of fractures are cleavage, quasicleavage, dimples from microvoid coalescence, fatigue striations, and intergranular fracture. Intergranular fracture is usually the most easily recognizable mode of failure, but determining the cause may be quite difficult. Liquid-metal penetration, hydrogen embrittlement, stress-corrosion cracking, and grain-boundary segregation may all result in intergranular fracture. Therefore a correlation of both fractographic and metallographic features should be obtained to aid in identifying the mechanism responsible.

This paper describes six case histories involving intergranular fracture: liquid-metal embrittlement of an AISI 1070 rod, a low-carbon steel drum, and a platinum and platinum-rhodium thermocouple; environmentally assisted cracking of a steel-strand wire rope; and grain-boundary segregation of aluminum nitride in a steel casting and of columbium in a SAE Grade 8 bolt.

The investigative techniques used in the analysis of these fractures included light microscopy, scanning electron microscopy (SEM), energy-dispersive spectroscopy (EDS), electron-diffraction, and secondary-ion mass spectroscopy.

Case 1: AISI 1070 Rod Failure

Repeated complaints of localized embrittlement causing an AISI 1070 steel rod to fracture during wire drawing prompted an investigation to determine the failure mechanism.

Fractographic examination in the scanning-electron microscope (SEM) showed three transverse cracks in the rod surface, one of which propagated across the rod to cause the failure (Figs. 1*a*, 1*c*, and 1*d*). In the higher magnification fractographs (Fig. 1*b*) it is apparent that the small transverse crack is intergranular in nature and that the terminal fracture propagated in a cleavage mode. To determine the cause of the intergranular crack, a longitudinal cross section was prepared for metallographic examination (Fig. 2*a*). A photomicrograph of the cross section of the preexisting crack, which is the fracture-initiation site (Fig. 2*b*), showed that the crack surface was heavily oxidized, indicating that the crack was present while the rod was at hot-rolling temperatures. Also, the prior-austenite grain boundaries are outlined by a copper-colored phase, which is shown at higher magnification in Fig. 2*c*. Energy-dispersive spectroscopy revealed that copper was the main element present in the boundary phase, but a minor concentration of tin was also identified. Pools of copper were observed in the oxide layer on the rod surface. Liquid-copper penetration of austenite grain boundaries at hot-rolling temperatures may be caused by pickup of copper from the strand-casting molds, selective oxidation during heating operations concentrating copper at a scaling surface, or contamination of the hot-steel surface by any copper-rich substance.

The first possibility was ruled out because the rod was ingot-cast. The second possibility was ruled out because it is extremely unlikely that the low copper content of the steel (0.02%) would cause such contamination. Therefore the possibility of contamination of the rod surface by a copper-tin external source was pursued.

Subsequent investigation revealed that the rod rolling mill guides were made of copper alloy No. 905, a bronze with a nominal composition (88Cu-10Sn-2Zn). Thus the most probable source of copper/tin contamination was the pickup of material from the rod-mill guides during hot rolling. Insomuch as this copper alloy solidifies over the temperature range from 1038 to 871°C (1900 to 1600°F), there would be ample opportunity for liquid-metal penetration of the grain boundaries during the hot-rolling operation. The absence of zinc in the energy-dispersive spectra of the grain-boundary phase may be because of depletion of zinc by high-temperature oxidation to a concentration level beyond the detection limit in the SEM.

Case 2: Failure of a Low-Carbon-Steel Drum in Lithium Service

Circumferential cracks developed along the apex of rolling hoops swaged in the drum shell of low-carbon-steel drums used for the packaging of lithium metal. Exposure to liquid lithium occurred when the drums were filled and when the lithium was melted for removal.

Examination of the fracture surface in the SEM revealed that the fracture was intergranular (Fig. 3*a*). Metallographic examination of cross sections of the drum showed that numerous other intergranular cracks were present in the formed rolling hoop. All cracks initiated on the inside surface and were presumably the result of liquid-lithium metal penetration. The extreme susceptibility of low-carbon steels to the embrittling effect of lithium at its melting point (180.5°C or 356.9°F) is well documented in the literature [*1*].

Case 3: Platinum/Platinum-Rhodium Thermocouple Failure

The hot end of the thermocouple assembly consisted of a closed-end outer pipe of UMCo50 (28% chromium, 50% cobalt) alloy containing a closed-end mullite tube within which a four-hole alumina sleeve was inserted. The sleeve contained two support and two thermocouple wires, one Pt-6Rh and one Pt-30Rh wire. Repeated thermocouple failure prompted an investigation to ascertain the failure mechanism.

The wire that fractured near the thermocouple junction (Fig. 4*a*) was the Pt-6Rh wire. Metallographic examination of a longitudinal cross section (Fig. 4*b*) showed that the surface of the wire near the fracture was severely degraded and that an intergranular phase was present throughout the wire at this point. EDS analysis in the SEM revealed that the intergranular phase was rich in silicon and that the degraded surface contained many particles rich in

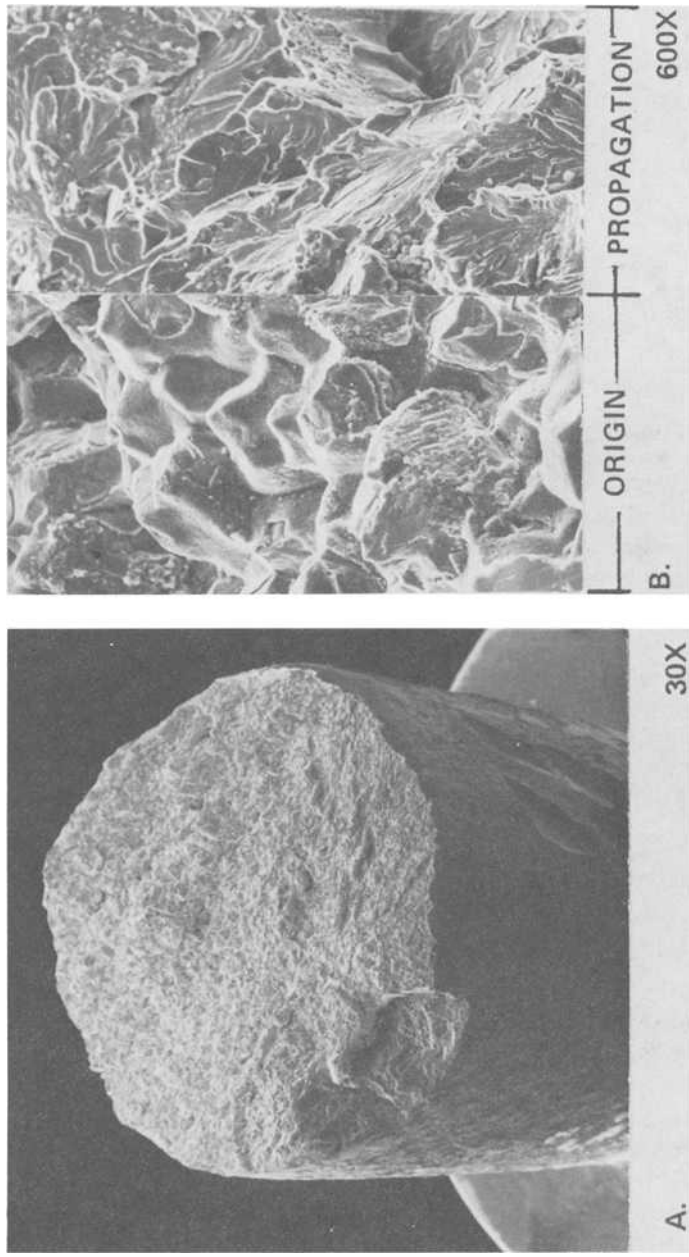
ORIGIN
PROPAGATION
B.
600X
A.
30X

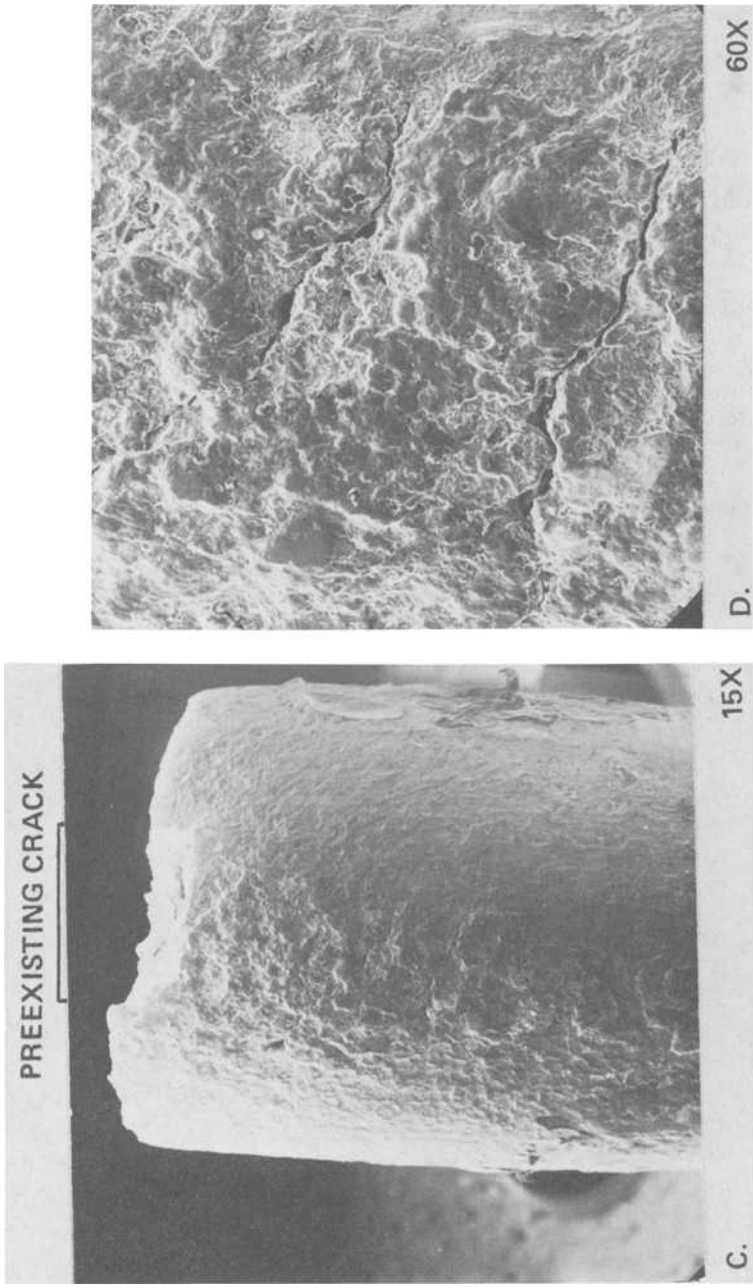

FIG. 1—*Failed AISI 1070 rod showing* (a) *oxidized-fracture origin,* (b) *intergranular-fracture origin and cleavage propagation, and* (c and d) *transverse cracks parallel to fracture surface.*

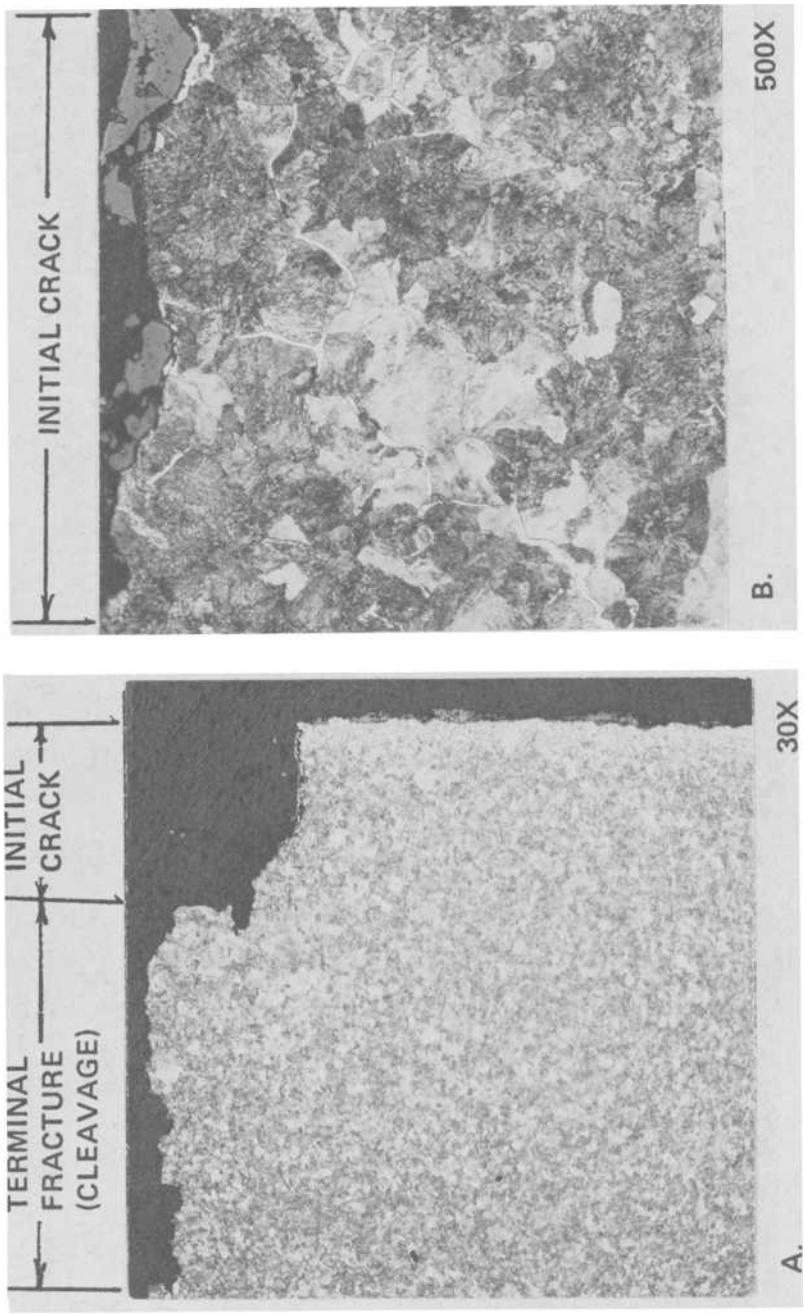
INITIAL CRACK
B.
500X
TERMINAL FRACTURE (CLEAVAGE)
INITIAL CRACK
A.
30X

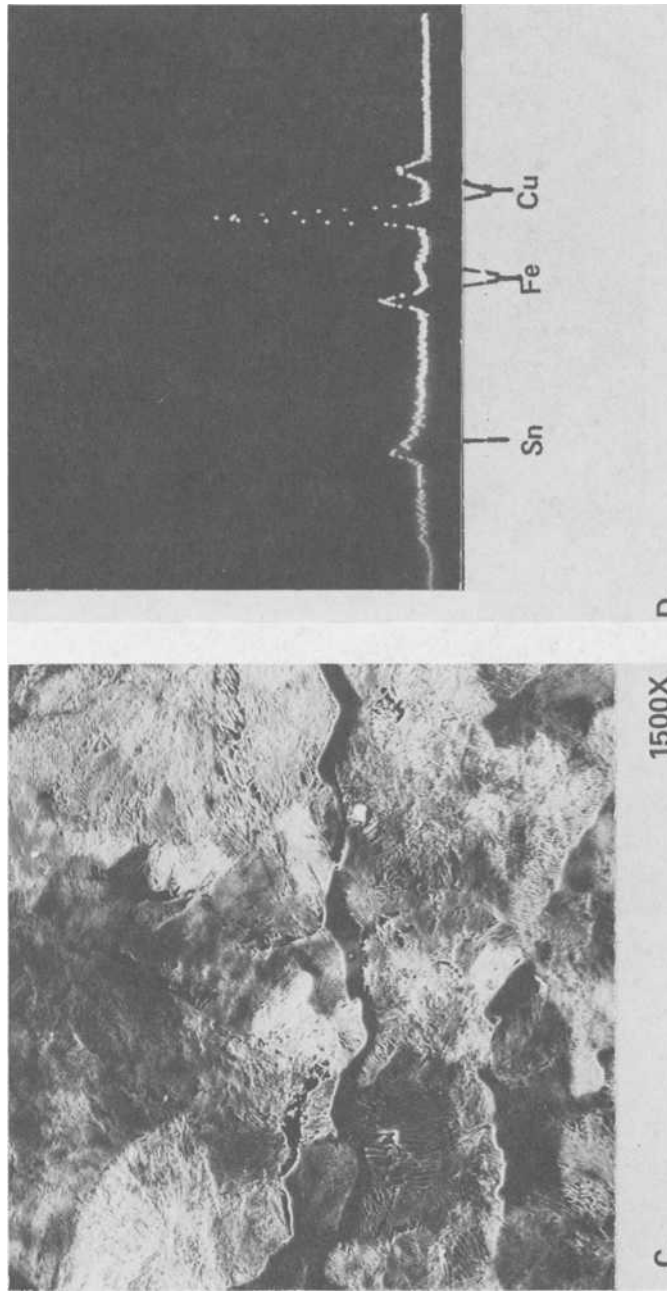

FIG. 2—*Failed AISI 1070 rod showing* (a) *longitudinal cross section through fracture origin,* (b) *extent of liquid-metal penetration,* (c) *grain-boundary phase, and* (d) *EDS spectra of grain-boundary phase showing presence of copper and tin.*

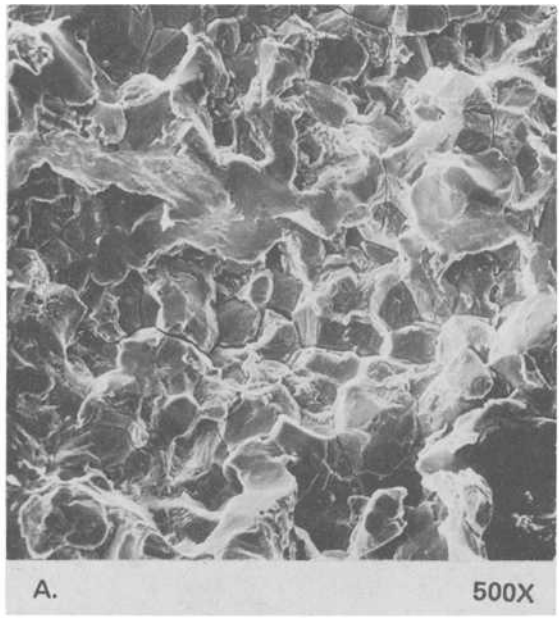

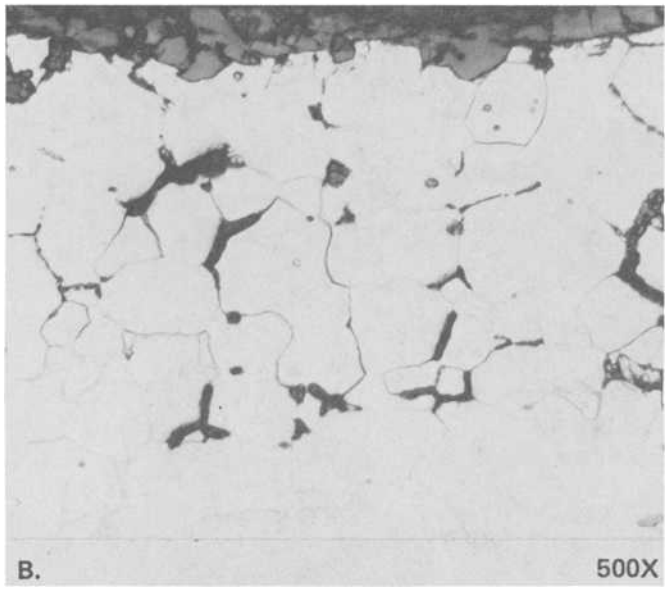

FIG. 3—*Failed low-carbon-steel drum in lithium service showing* (a) *intergranular fracture surface, and* (b) *longitudinal cross section of inside surface and presence of numerous intergranular cracks.*

iron and chromium (Figs. 4*c* and 4d). It appeared, therefore, that the failure of the Pt-6Rh thermocouple wire was caused by liquid-metal penetration of the grain boundaries. Contamination by silicon at elevated temperature led to the formation of a low-melting platinum-silicon eutectic, which penetrated and separated the grain boundaries. The concentration of silicon necessary for formation of the low-melting eutectic is very low (about 0.2%) [*2*].

EDS analysis of the support wires in the thermocouple assembly revealed that they were a nickel-base alloy containing chromium and iron (probably Inconel 601), and could have contributed the iron and chromium contamination found in the thermocouple wire. Insomuch as Inconel 601 contains 0.2% silicon, it is also possible that the support wires contributed the silicon contamination.

The interior of the mullite ($3Al_2O_3 \cdot 2SiO_2$) tube exhibited a green deposit that, when analyzed in the SEM, was found to contain primarily chromium and a lesser concentration of iron. Aluminum and silicon from the mullite substrate were also detected.

It is not known whether the source of the silicon contamination, which was primarily responsible for the failure, was the mullite protection tube or the Inconel 601 support wires. In either case, the remedial measure for failures of this type is to embed the end of the platinum-rhodium thermocouple in a closed-end alumina tube packed with alumina or magnesia powder.

Case 4: Steel-Strand-Wire-Rope Failure

Fractographic examination of a strand-wire break from a coal-boom support revealed that the fatigue failure (Fig. 5*a*) had initiated at an 0.25-mm-deep (0.01-in.) intergranular crack (Figs. 5*b* and 5*c*). The expected fatigue-initiation site would be a surface imperfection associated with a wear point. Metallographic examination of a longitudinal cross section (Fig. 6*a*) through the intergranular crack (fatigue-crack origin) revealed that this crack and others parallel to it were associated with a region of untempered martensite (Fig. 6*b*), which had a hardness of $HV_{100}830$ (64.5 HRC) versus HV_{100} 425 (43 HRC) for the unaffected wire.[2] The strand wire was electrogalvanized, and it is surmised that an electric arc that occurred during the electrogalvanizing process caused the untempered martensite to form where the fatigue crack then initiated.

Case 5: Lemniscate-Link Failures

Lemniscate links are eyebars that position the roof shields of longwall coal-mining machines. Four links are used in each shield, two in tension and two in compression (Fig. 7). Seven identical brittle (rock candy, see Fig. 8) frac-

[2]HRC = Rockwell C Hardness.

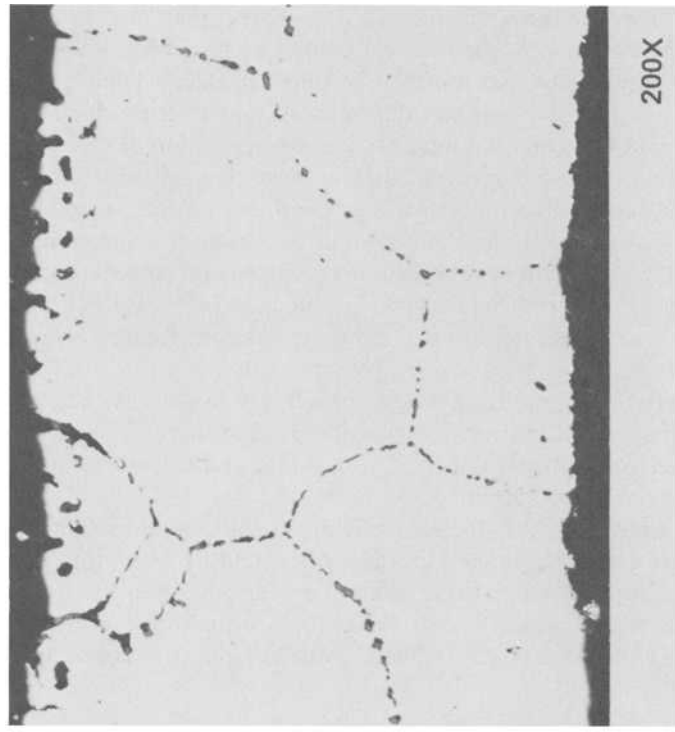
200X

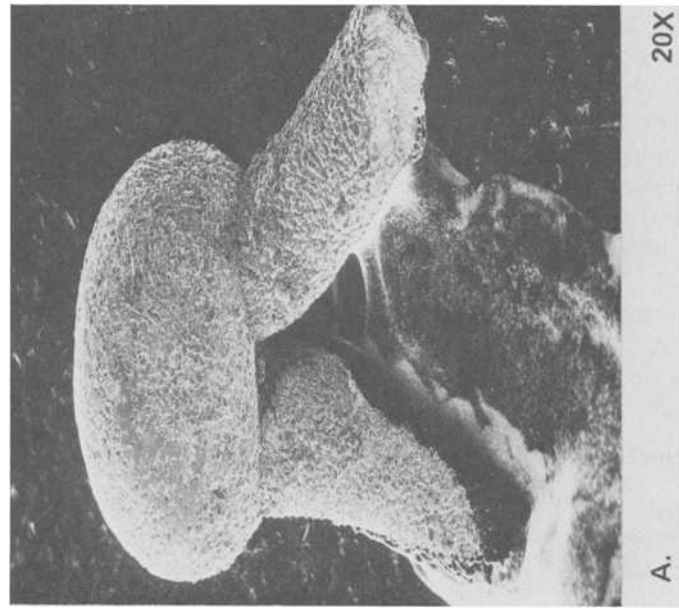
A.
20X

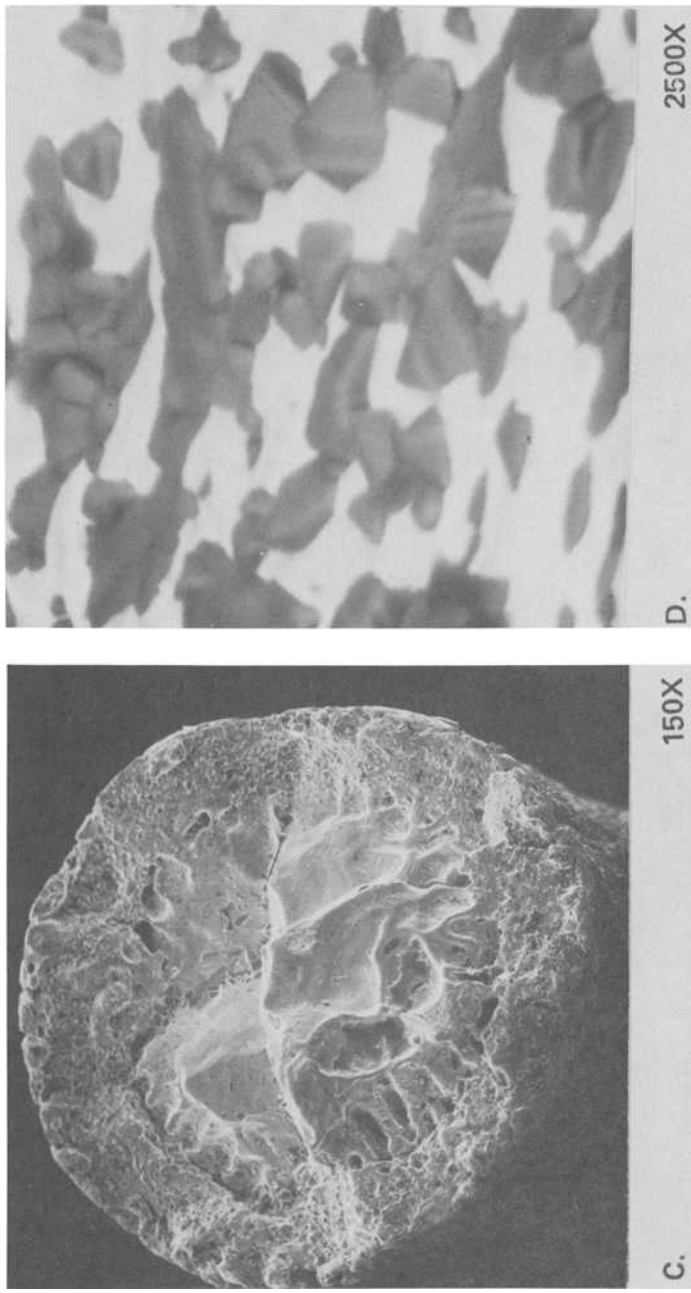

FIG. 4—*Failed platinum/platinum-rhodium thermocouple showing* (a) *failed thermocouple with severely degraded surface,* (b) *intergranular platinum-silicon phase present,* (c) *intergranular fracture surface, and* (d) *iron-chromium particles on surface of thermocouple.*

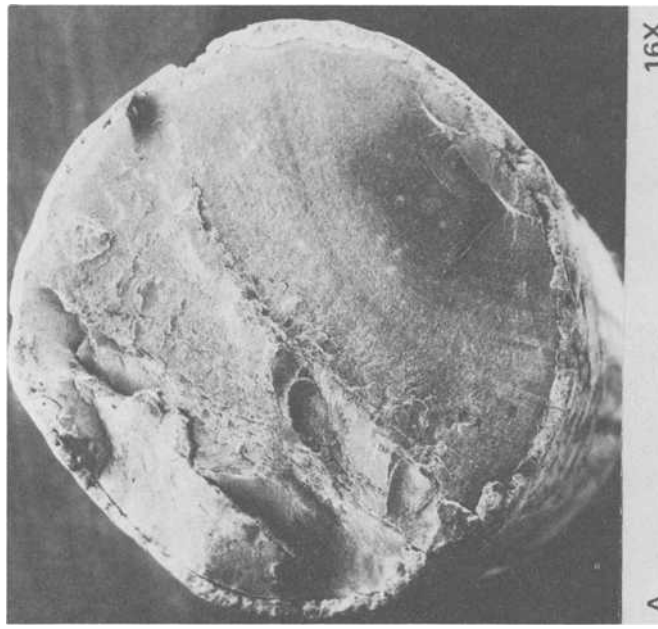
16X
A.

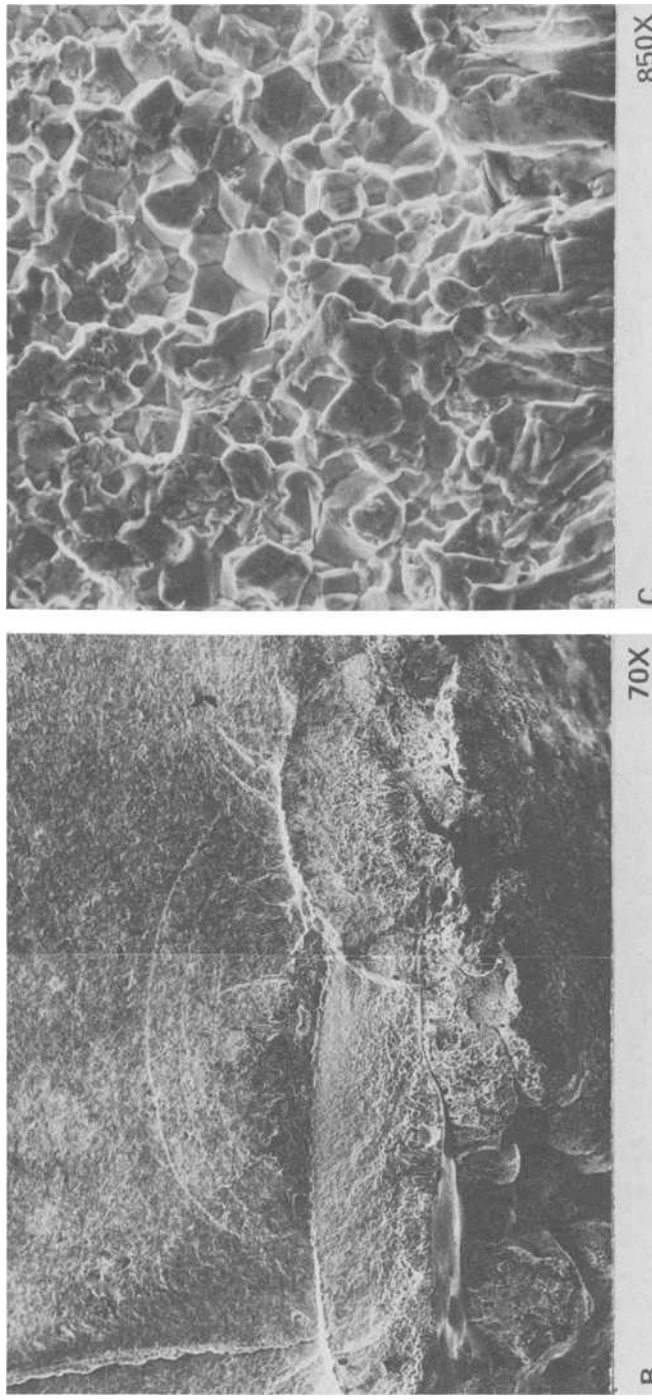

FIG. 5—*Steel-strand-wire-rope failure showing* (a) *fatigue-cracked wire,* (b) *origin of fatigue crack, and* (c) *intergranular fatigue crack origin.*

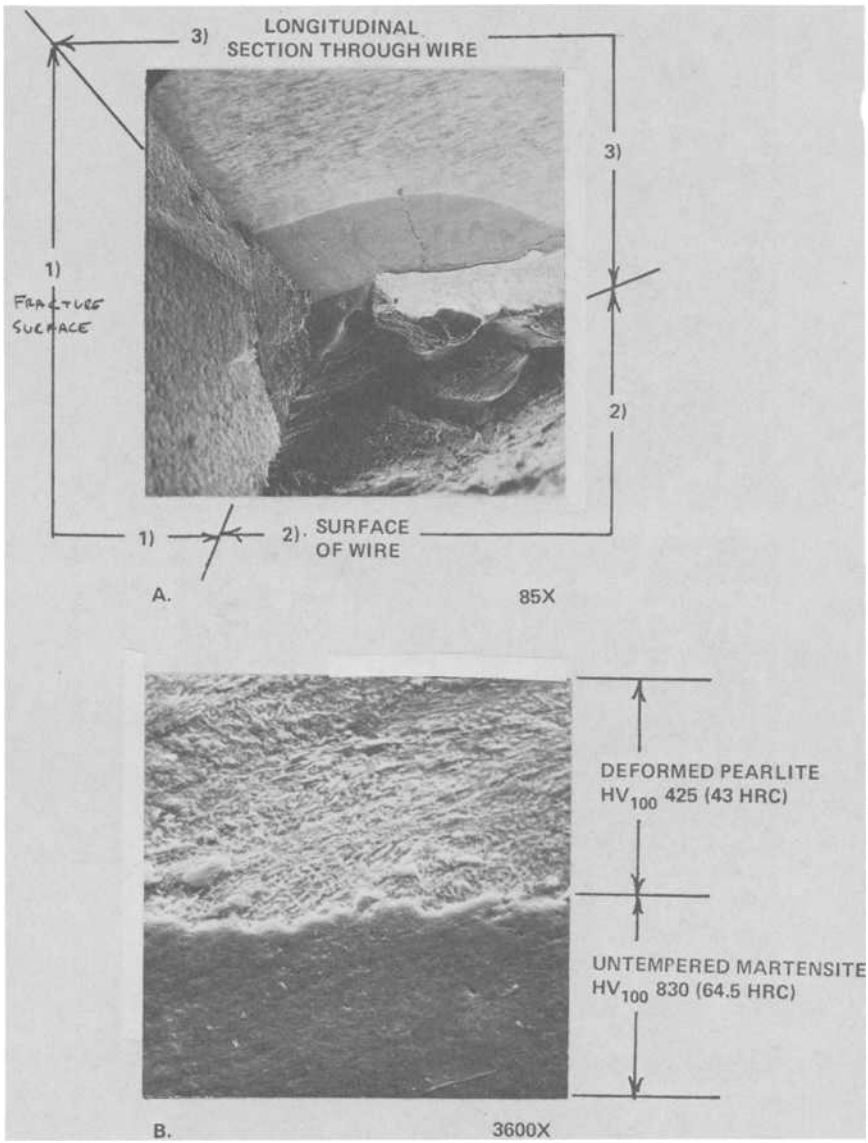

FIG. 6—*Steel-strand-wire-rope failure showing* (a) *relationship between* (1) *fracture surface,* (2) *surface of wire, and* (3) *longitudinal section through origin of fatigue crack, and* (b) *longitudinal section showing deformed pearlite and untempered martensite.*

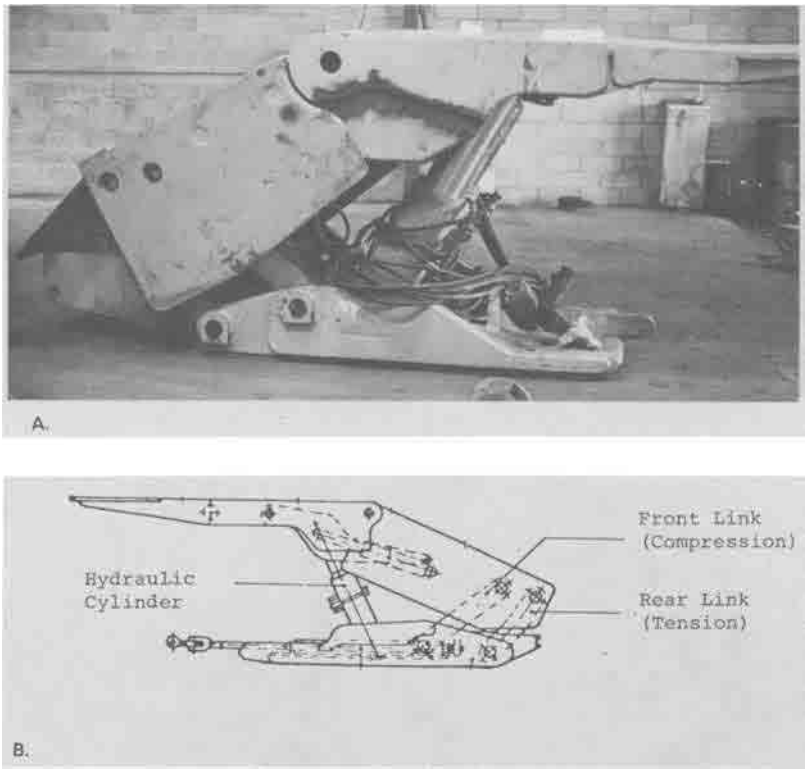

FIG. 7—*Longwall shield.* (a) *General view.* (b) *Sketch showing location of lemniscate links.*

tures that occurred through the eyes of the rear-tension-loaded links shortly after the shields were put into service were investigated to determine the cause of failure.

The links were heat-treated castings produced to a modified ASTM A148 Grade 105-85-17 specification (chemical composition similar to an AISI 8630 steel) and a requirement of an average Charpy V-notch energy of 27.2 J (20 ft · lb), with none less than 20.4 J (15 ft · lb) at room temperature.

The chemical composition, yield strength (0.2% offset) of 606.7 MPa (88 ksi), and tensile strength of 786 MPa (114 ksi) were within specification, but the elongation of 11% and reduction of area of 14% were below the values specified in ASTM A148 Grade 105-85-17, which are 17% and 35% respectively. Charpy V-notch impact specimens located adjacent to the inner surface of the eye (to simulate service fracture) absorbed energies of 9.5, 13.6, 20.4, and 34 J (7, 10, 15, and 25 ft · lb) for an average of 19 J (14 ft · lb) at 21°C (70°F); these are values below those specified. All fractures (tension

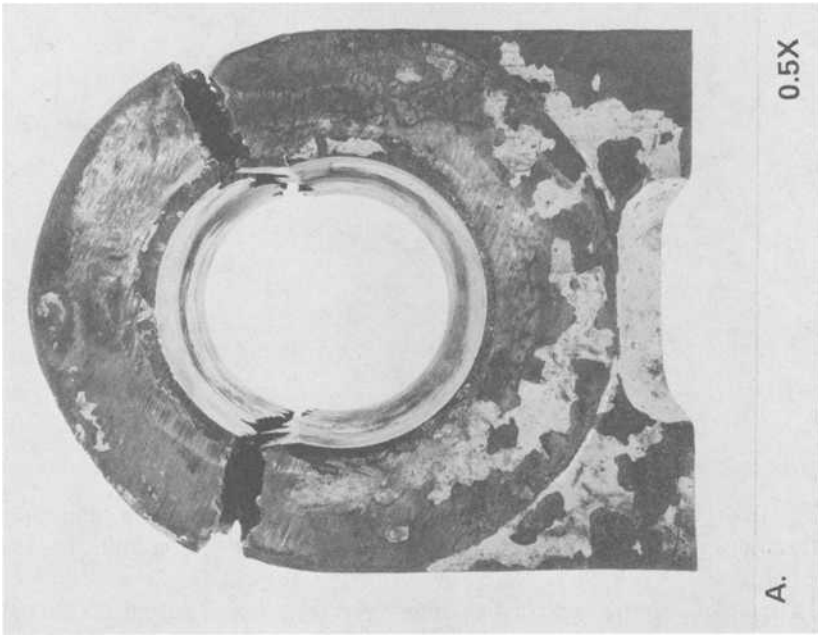
0.5X
A.

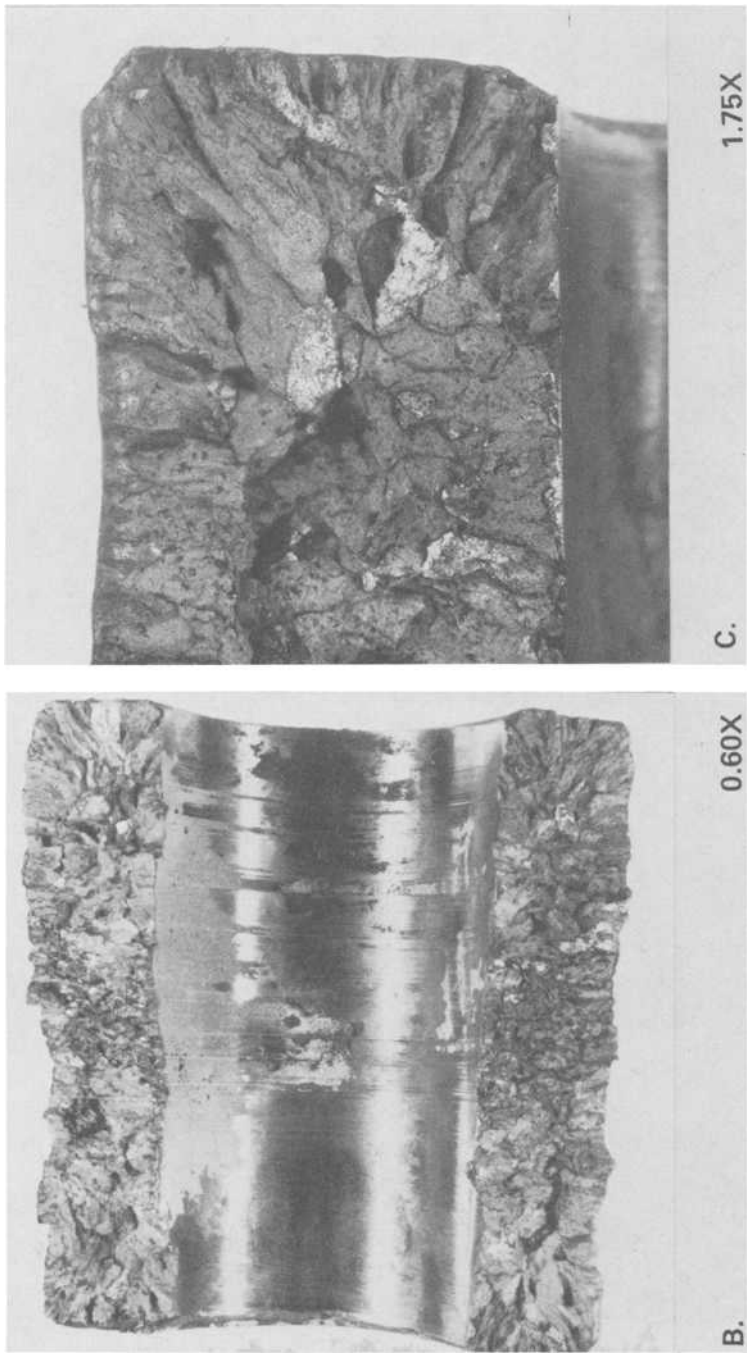

FIG. 8—*End of failed lemniscate link showing* (a) *location of fracture and* (b and c) *brittle rock-candy intergranular-fracture surfaces and very coarse grain size.*

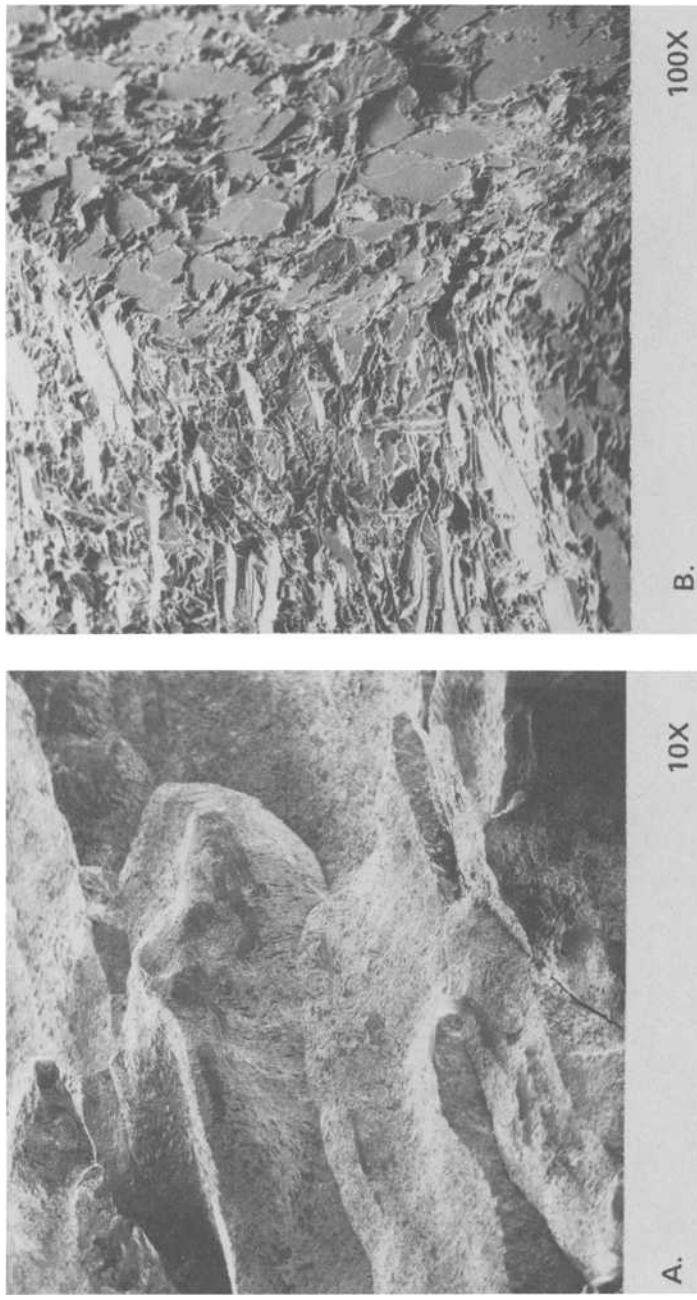
A.
10X
B.
100X

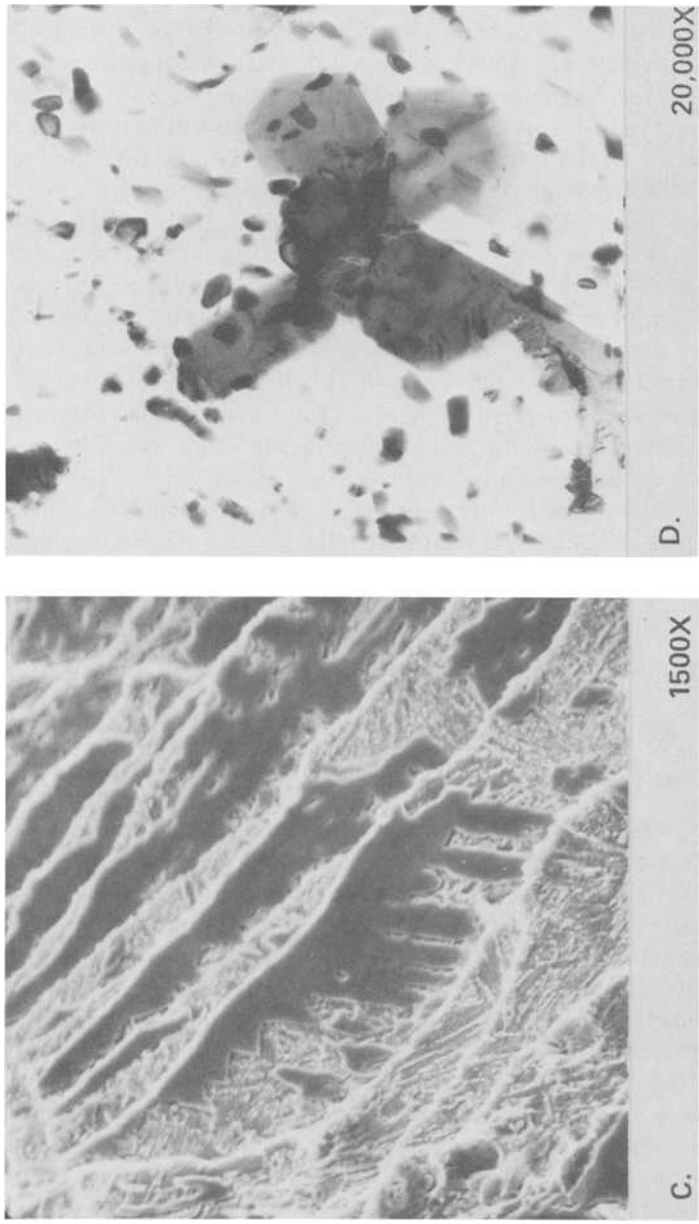

FIG. 9—*Failed lemniscate link showing* (a) *rock-candy intergranular fracture,* (b) *flat facets that decorate the rock-candy intergranular fracture,* (c) *etched fracture surface showing the AlN film associated with the facets, and* (d) *carbon-extraction replica of intergranular fracture surface.*

tests and impact tests) were similar to the service fracture, which had a brittle rock-candy appearance.

Macroscopic examination showed no evidence of plastic deformation, crack initiation sites, or casting imperfections. A radial macrosection through the eyebar eye adjacent to the fracture and the appearance of the service fracture (Fig. 9*a*) showed that the as-cast grain size was very coarse and that no grain refinement occurred during the subsequent heat treatment. SEM examination of the fracture surface (Fig. 9*b*) showed that the rock-candy fracture was decorated with relatively featureless facets. Etching of the fracture surface revealed the presence of an aluminum-rich film (Fig. 9*c*). Selected area diffraction on a carbon-extraction replica of the fracture surface identified the aluminum-rich film as AlN (aluminum nitride), and foundry casting practice was suspected as being responsible for the aluminum segregation at the solidification boundaries. The aluminum-nitride film probably prevented any grain refinement during heat treatment.

An elastic-stress analysis [*3*] of a link under the maximum load that would be applied in service by the hydraulic piston that positions the shield indicated that the tensile stress on the inside surface of the eye was 710.2 MPa (103 ksi), a level that exceeded the measured yield strength of 606.7 MPa (88 ksi). The absence of any plastic deformation before fracture and the elastic-stress analysis suggest that over-stressing of a brittle steel casting was the probable cause of the service failures. If the steel in the inner surface of the eye had been ductile, harmless localized plastic deformation would have occurred, and the links would not have fractured.

Case 6: Failure of High-Hardness Engine-Head Bolts Manufactured from Columbium Fine-Grain AISI 1541 Steel

Engine-head bolts manufactured from columbium fine-grain AISI 1541 steel (Table 1) that failed in engine heads shortly after assembly initiated a laboratory investigation to ascertain the cause of failure. SAE Grade 8 bolts (hardness range of 32 to 38 HRC) are frequently specified for engine heads, but the engine manufacturer purchased cold-formed bolts from several suppliers and heat-treated them to a higher hardness level (38 to 43 HRC).

Examination of two fractured bolts revealed that the fractures had initiated at the fillet between the shank and the head and had propagated through the shank in a brittle manner. The presence of brittle fracture in a bolt is unexpected because bolts should be intrinsically ductile enough to tolerate localized plastic deformation in the shank-head fillet and in the first threads when they are torqued during installation. The hardness of the bolt was 43 HRC, and it appeared that the toughness at the high-strength level corresponding to 43 HRC might have been low enough that a usually harmless surface imperfection could initiate a brittle fracture. However, fractographic examination in the SEM showed the fracture to be intergranular (Fig. 10).

TABLE 1—*Chemical composition (weight percent) of failed high-hardness engine-head bolts.*

C	0.42
Mn	1.58
P	0.023
S	0.013
Si	0.20
Cu	0.04
Ni	0.02
Cr	0.06
Mo	<0.004
V	<0.003
Ti	0.003
Al	<0.002
N	0.005
Cb	0.040
As	<0.01
Sb	<0.01
Sn	<0.01

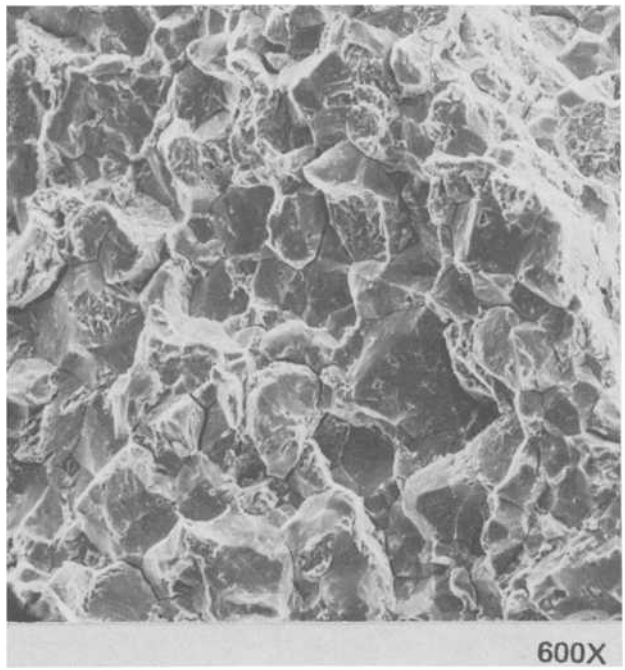

FIG. 10—*Failed high-hardness engine-head bolt showing brittle intergranular crack path.*

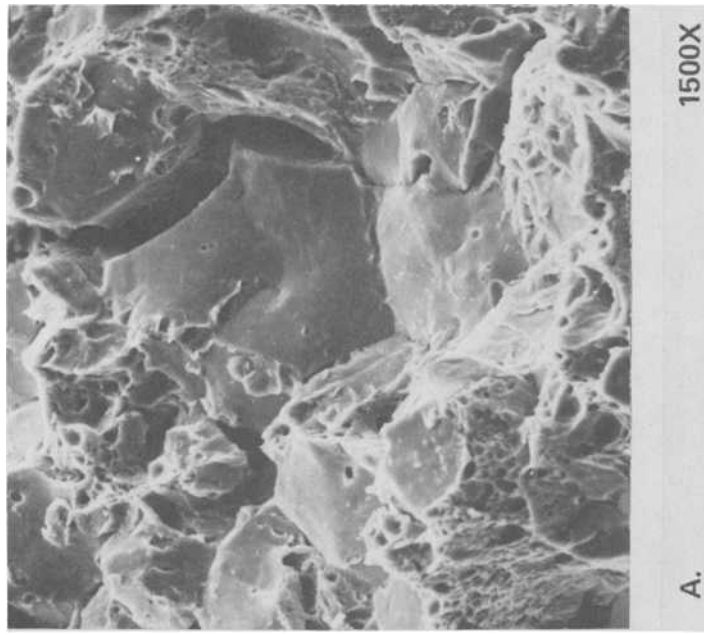
A.
1500X

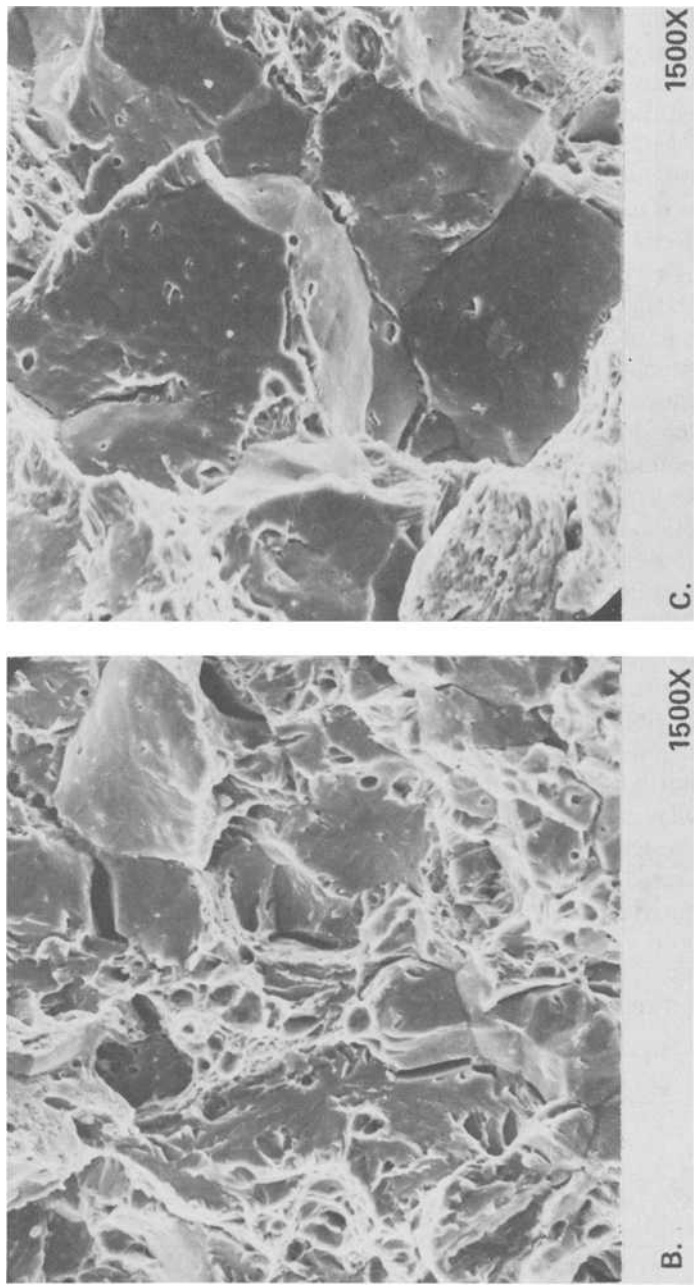

FIG. 11—*Failed high-hardness engine-head bolt round-bar-impact test fracture surface of* (a) *broken at* $+75°F$, *20 ft · lb absorbed energy.* (b) *broken at* $+32°F$, *23 ft · lb absorbed energy, and* (c) *broken at* $-20°F$, *15 ft · lb absorbed energy.*

In order to determine whether the service fractures were related to stress-corrosion cracking, hydrogen embrittlement, or grain-boundary films, impact tests of nonstandard notched round-bar specimens were conducted. The full diameter of the bolt shank was used, 11.4 mm (0.45 in.). The notch was of standard Charpy geometry, and its depth was 20% of the specimen diameter. A flat surface, 3.8 mm wide (0.150 in.), was machined axially on the specimen $\pi/2$ rad (90 deg) away from the notch to keep the specimen from rolling away from the anvil during impact testing. The hardness (HRC) at midradius of the bolt shank was measured on wafers machined with flat parallel surfaces.

The results of the hardness and impact tests are shown in Table 2. The fracture toughness (energy absorbed) was the same at 23.9 and 0°C (75 and 32°F), but the lower toughness at −28.9°C (−20°F) indicates that this temperature lies in the ductile-to-brittle transition range of this material. Fractographic examination in the SEM of the impact-test specimens showed that the intergranular fracture that occurred at prior-austenite grain boundaries was present on all three specimens (Fig. 11). It is likely that the ductile dimpled fracture surrounding the intergranular facets contributed the bulk of the energy absorption observed. The presence of intergranular fracture in impact-test specimens indicated that the brittle fracture of the bolts in service occurred because of low-energy grain-boundary fracture and was not related to stress corrosion cracking or hydrogen embrittlement.

Metallographic examination of polished and etched cross sections and EDS analysis in the SEM of the fracture surfaces were unsuccessful in revealing the existence of grain-boundary films. Carbon-extraction replicas for transmission electron microscopy were made of the intergranular fracture surfaces, but these also failed to yield any new information. However, the secondary-ion mass-spectrometry (SIMS) technique did result in positive identification of columbium on intergranular fracture surfaces of newly broken impact-test specimens of columbium-treated AISI 1541 bolts that had been heat-treated by the engine manufacturer. A comparative SIMS analysis of a planar cross section through one of the aforementioned three specimens

TABLE 2—*Results of hardness and round-bar-impact tests of failed bolts.*[a]

Test Temperature	Energy Absorbed, ft · lb[b]
75	20
32	23
−20	15
Hardness (HRC)[c] = 43.9	

[a] 1.36 J = 1 ft · lb; °C = 5/9(°F − 32).
[b] Average of duplicate determinations.
[c] Average of four determinations at midradius.

showed that the concentration of columbium in the polished plane was below the limit of detection of the method. Therefore the only clue to the nature of the intergranular constituent was that the intergranular fracture surface was columbium-rich.

It should be emphasized that the intergranular fracture was observed only on bolts heat-treated to the high-hardness (43 HRC) level. Tempering to a slightly lower hardness level (40 HRC) eliminated the intergranular fracture.

Summary

Of the six failure analyses described, three are examples of liquid-metal embrittlement that led to intergranular fracture. These include the bronze intrusion of the AISI 1070 steel rod, the lithium penetration of a low-carbon-steel drum, and the platinum-silicon eutectic that attacked a platinum-rhodium thermocouple. All are examples of environmentally assisted intergranular fracture. The fourth case history involving a steel-strand-wire-rope fracture is probably another example of environmentally assisted fracture.

Two of the failures described (that of the cast-steel eyebar and the AISI 1541 steel bolts) involved fast fracture along prior-austenite grain boundaries that contained segregated metallurgical constituents. It is not widely appreciated that fast fracture along grain boundaries is as valid a mechanism as cleavage in describing a mode of brittle fracture in steels.

References

[1] Rostoker, W., McCaughey, J. M., and Marcus, H., *Embrittlement by Liquid Metals*, Reinhold, New York, 1960, pp. 22-23.

[2] *Metals Handbook*, Vol. 10, 8th ed., American Society for Metals, Metals Park, Ohio, 1975, pp. 283-284.

[3] Timoshenko, S., *Strength of Materials*, 3rd ed., Van Nostrand, Princeton, N.J., 1960, pp. 383-384.

T. Kobayashi,[1] *G. R. Irwin,*[2] *and X. J. Zhang*[2]

Topographic Examination of Fracture Surfaces in Fibrous-Cleavage Transition Behavior

REFERENCE: Kobayashi, T., Irwin, G. R., and Zhang, X. J., **"Topographic Examination of Fracture Surfaces in Fibrous-Cleavage Transition Behavior,"** *Fractography of Ceramic and Metal Failures, ASTM STP 827,* J. J. Mecholsky, Jr., and S. R. Powell, Jr., Eds., American Society for Testing and Materials, 1984, pp. 234-251.

ABSTRACT: In order to increase understanding of the fibrous-to-cleavage fracture transition phenomenon, an examination of the fracture surfaces of A36 and A533B steel was made with a scanning electron microscope and stereoscopic photographs.

By topographical characterization of matching sites of conjugate fracture surfaces, the crack tip opening stretch (δ), the fracture process zone size (through the measurement of fracture surface height variation), and the deformation of grains (such as the lifting of unbroken ligaments from the fracture surfaces) were determined. Topographical characterization of two sides of some fracture surfaces also revealed local fracture processes such as formation of voids ahead of a crack tip and crack extension from the voids. Finally, fractographic estimates of crack tip opening displacement were correlated to the fracture toughness measurement.

KEY WORDS: fractography, stereography, topographic measurement, parallax bar, scanning electron microscope, fibrous fracture, cleavage fracture

Tearing instability fracture analysis applied to steels in the fibrous-cleavage transition temperature range is complicated by the possibility that rapid cleavage fracturing may occur before fibrous instability. A second aspect, which may be of greater interest, is the increase of average values and scatter with reduction of specimen size when estimates of K_{Ic} are determined by initiation of cleavage fracturing. Additional understanding from microscopic analysis of conditions for cleavage fracturing is needed. Useful information can be obtained from thorough examination of fracture surfaces of steel samples which exhibited fibrous-cleavage transition.

[1]SRI International, Menlo Park, Calif. 94025.
[2]Department of Mechanical Engineering, University of Maryland, College Park, Md. 20742.

Examination of fracture surfaces with a scanning electron microscope has provided useful information on such aspects as local fracture mechanisms and fracture propagation directions [*1,2*]; however, with the use of stereophotography and fracture surface height measurements of conjugate fracture surfaces much more information on fracture processes can be obtained. This paper describes the method and some results from A36 and A533B steels. Furthermore, the results indicate that the analysis of fracture surface contour measurements from conjugate fracture surfaces may provide the bridge between microscopic information such as local deformation and macroscopic parameters such as J-integral values.

Stereography and Topographical Analysis

For stereography, two photographs of a fracture surface are produced by rotating a specimen by $\pm\theta$ deg, as shown schematically in Fig. 1. The height (h) of the point P can then be computed by measuring the relative displacement of the same point P on two photographs and by substituting in the equation [*1*]

$$h = \frac{\Delta d}{2M \sin \theta}$$

where

Δd = relative displacement of the corresponding point,
M = magnification of the photograph, and
2θ = rotational angle of the specimen between a pair of stereographs.

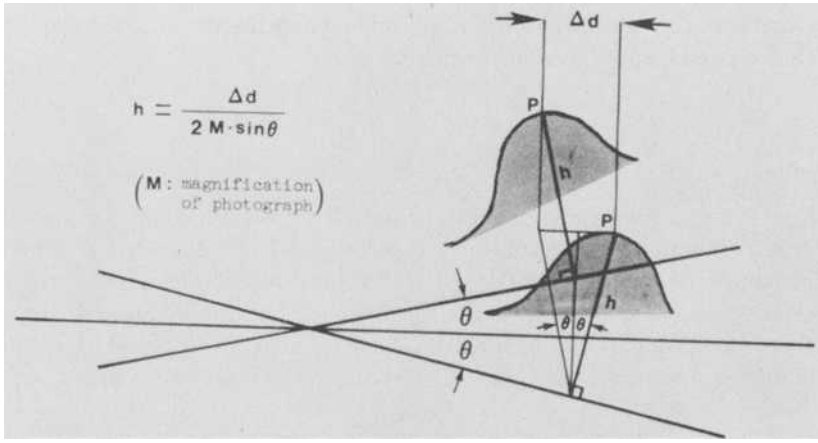

FIG. 1—*Schematic representation of fracture surface contours after* $\pm\theta$*-deg rotations.*

For application of stereography and topographical measurement to the fracture surface analysis in this study, the following procedures were used:

1. The specimen surface was initially placed perpendicular to the incident electron beam.
2. The specimen rotational axis for stereophotography was made parallel to the crack propagation direction in the fracture plane by adjusting the specimen mounting stage of the scanning electron microscope. The specimen was then rotated 4-deg-right from the normal to the surface. No rotation of the specimen about the axis normal to the fracture surface was introduced after the initial setting of the specimen in the scanning electron microscope stage. After photographing the surface, the specimen was rotated 4-deg-left from the normal to the surface. The specimen mounting stage of the microscope was adjusted by parallel translational movement (no rotation about the axis perpendicular to the fracture surface) so that the same area could be photographed.
3. Magnification of the photographs was adjusted to be the same for both angles.
4. For measurement of relative displacement of the corresponding points on the stereophotographs, each pair of photographs was carefully placed parallel along the axis of rotation. Furthermore, the photographs were placed so that corresponding points appeared on a line perpendicular to the axis of rotation.
5. Measurement points were selected along a straight line drawn on one side of the fracture surface photograph, and the corresponding points were located on the other photograph. The distances between corresponding points were measured with a parallax bar and without using a stereoviewer.
6. Relative displacements of the corresponding points on the photographs were computed by selecting a reference point such as one on the fatigue fracture surface of the initial crack and by subtracting the distance between the reference points from other measurements.

Results

Figures 2 and 3 represent the pairs of stereographs from conjugate fracture surfaces of A36 steel tested at room temperature.[3] The specimen was a three-point bend type (beam height $W = 75$ mm and beam thickness $B = 38.1$ mm). A spring plate adjacent to the specimen was used to increase the speed of fibrous extension when this form of separation extended beyond maximum load. In the A36 fractures discussed here, cleavage fracture occurred at the

[3]These fracture tests were conducted at Del Research Division, Hellertown, Pennsylvania, in a project funded by Piccatinny Arsenal.

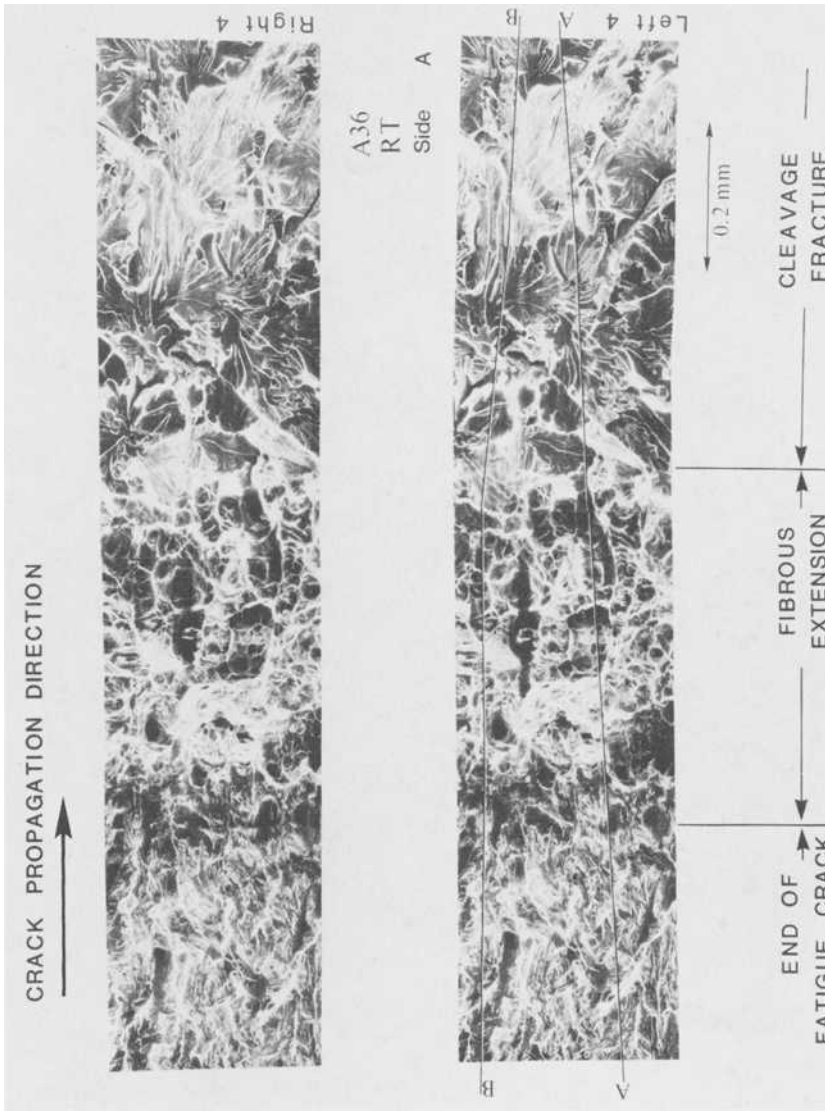

FIG. 2—*A pair of stereographs from top fracture surface (Side A) of A36 steel tested at room temperature.*

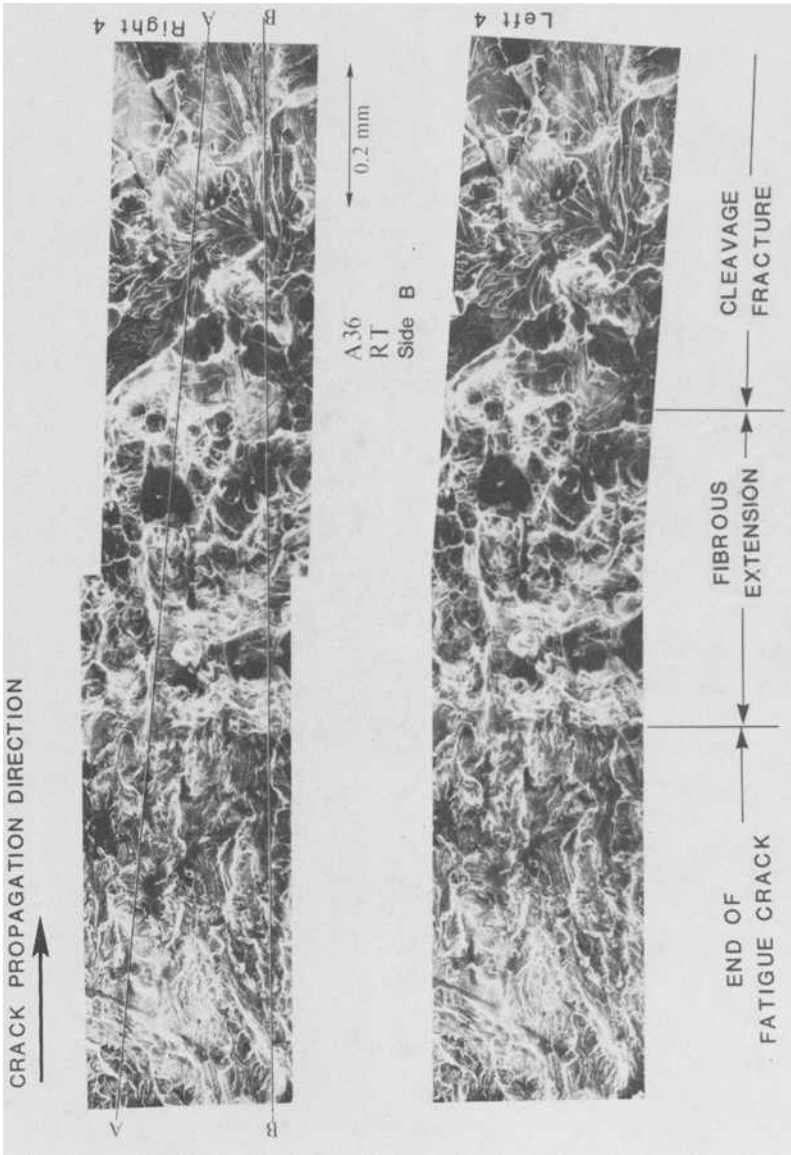

FIG. 3—*A pair of stereographs from bottom fracture surface (Side B) of A36 steel tested at room temperature.*

maximum load with negligible stable fibrous crack extension. Fracture surfaces in Figs. 2 and 3 show a portion of the initial fatigue fractured surface and a narrow band of fibrous fracture followed by cleavage.

Fracture surface contour measurements were performed along the two lines, *A-A* and *B-B*, shown in the figures. The results are plotted in Figs. 4 and 5. These fracture surface contour plots indicate an elevation of surface starting from the end of the fatigue crack tip into the stretch zone and fibrous extension zone. In the stretch zone and fibrous extension zone several mountains and valleys are seen. Cross-examination with fracture surface photographs indicates that the valleys correspond to holes formed in fibrous regions and that the mountains consist of highly stretched material.

In the cleavage fracture regions, the surface contour appeared to have sharp ridges and flat surfaces, and the top and bottom surface features appear to match well. In the next section a detailed analysis of contour plots will be presented.

Figures 6 and 7 are pairs of stereographs from conjugate fracture surfaces of A533B steel tested at 54°C. The specimen was of a compact tension type ($W = 50$ mm and $B = 25.4$ mm). Loading was done with a spring-in-series mode. In these tests the specimen was connected to the spring plate by an

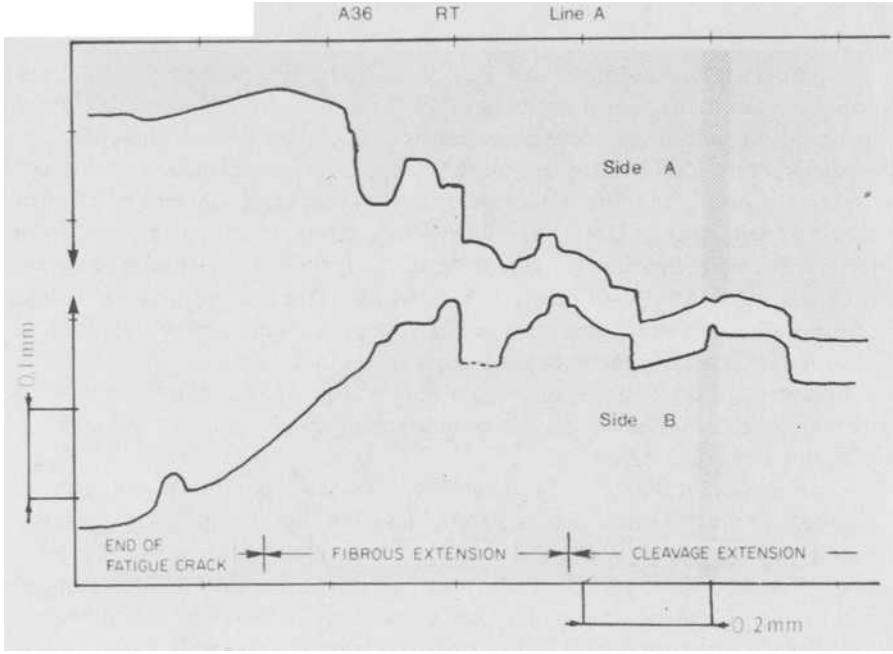

FIG. 4—*Fracture surface contours of Side A and Side B along Line A-A.*

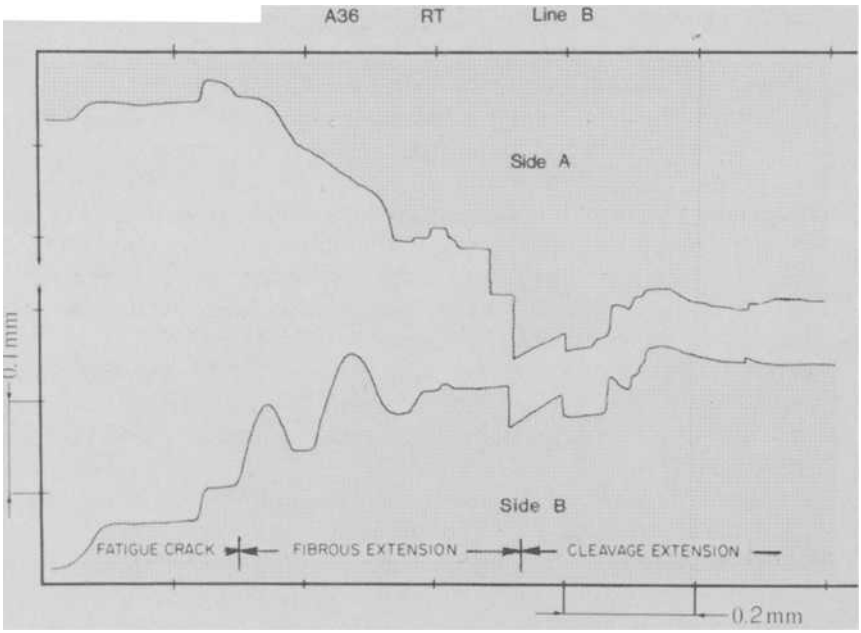

FIG. 5—*Fracture surface contours of Side A and Side B along Line B-B.*

approximately 1.2-m-long bar.[4] Examination of the load versus loading-point-displacement record indicated that the specimen underwent a tearing instability. From the fracture appearance and loading record, the character of the fracture changed from mainly fibrous to largely cleavage during the "tearing instability". Due to inertia and the rather long connection between specimen and spring plate, the rapid crack extension in which a change from fibrous to largely cleavage fracture occurred (approximately 9 mm) must have caused a substantial load drop. This would explain the pronounced crack-arrest marking (a sharp step seen in Figs. 6 and 7). Rapid reloading initiated cleavage fracturing directly beyond the line of crack arrest.

Fracture surfaces shown in Figs. 6 and 7 also indicate the trend toward increase of cleavage across the fracture segment which preceded the position of temporary crack arrest.

Figures 8 and 9 show the results of fracture surface contour measurements made along the two lines, *C-C* and *D-D*, shown in Figs. 6 and 7. Cross-examination of the contour plots with fracture surfaces shows that clusters of cleavage fracture correspond to the valleys and that fibrous regions correspond to mountains. It is of interest to note that a sharp step in elevation can be seen in the cleavage fracture region at the position of temporary crack arrest.

[4]These tests were conducted at the NSRDC Laboratory, Annapolis, Maryland.

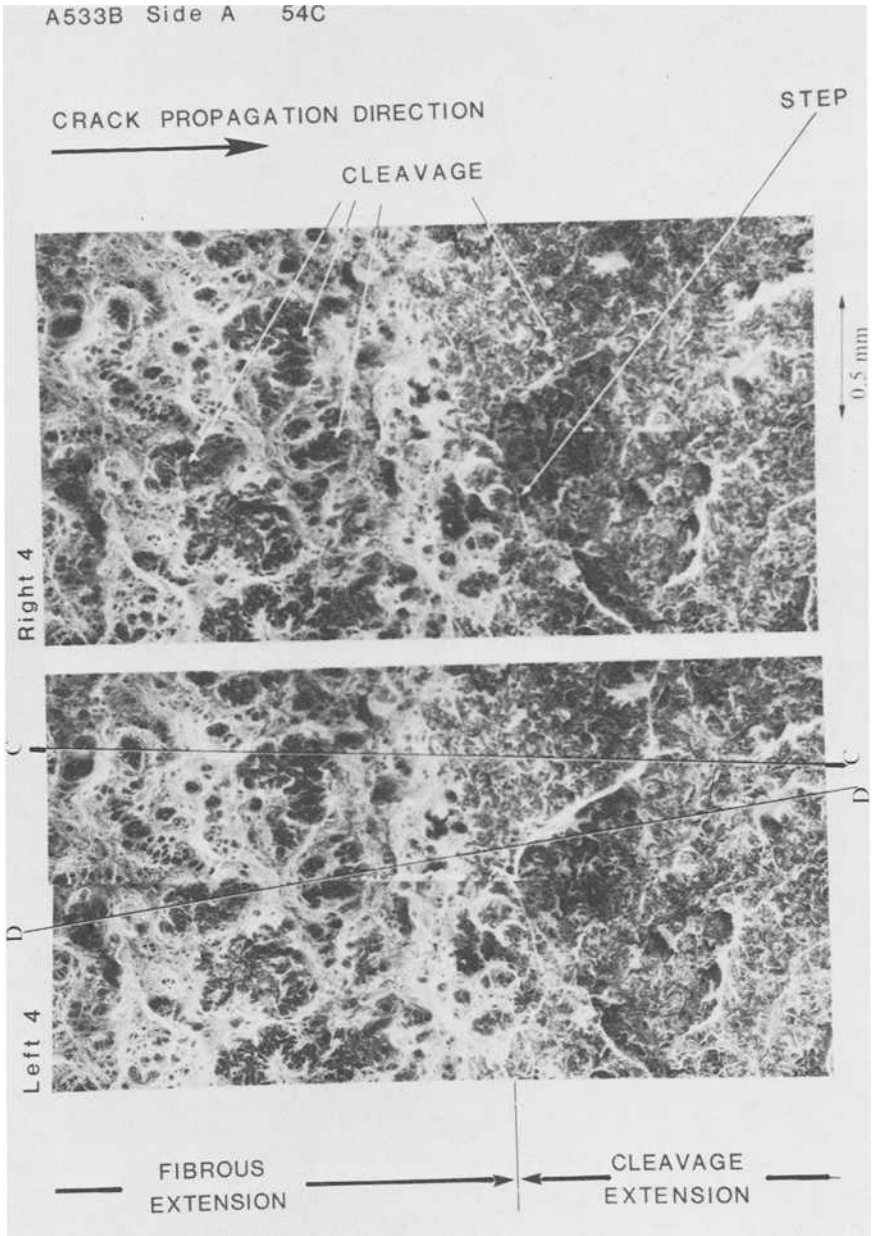

FIG. 6—A pair of stereographs of top fracture surface (Side A) of A533B steel tested at 54°C.

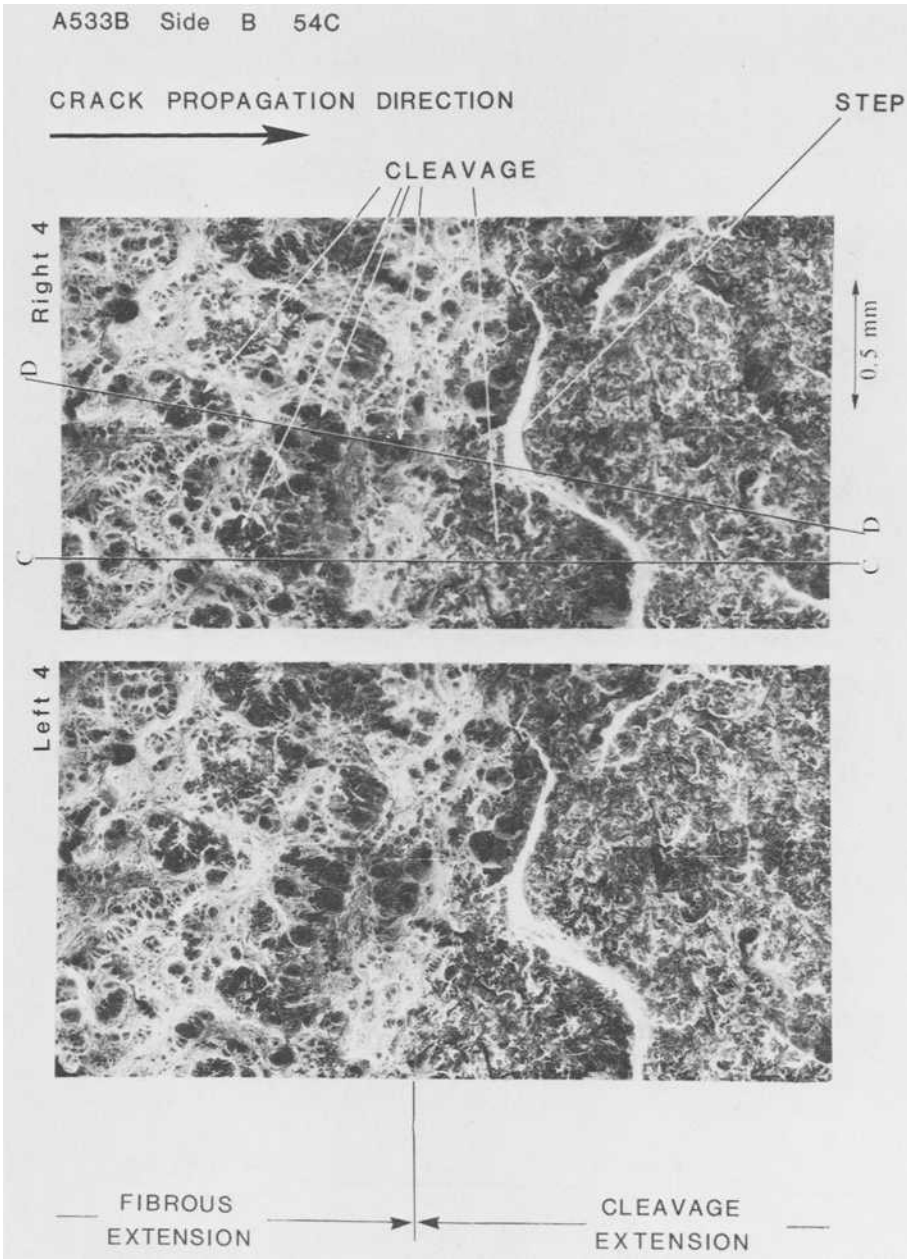

FIG. 7—*A pair of stereographs of bottom fracture surface (Side B) of A533B steel tested at 54°C.*

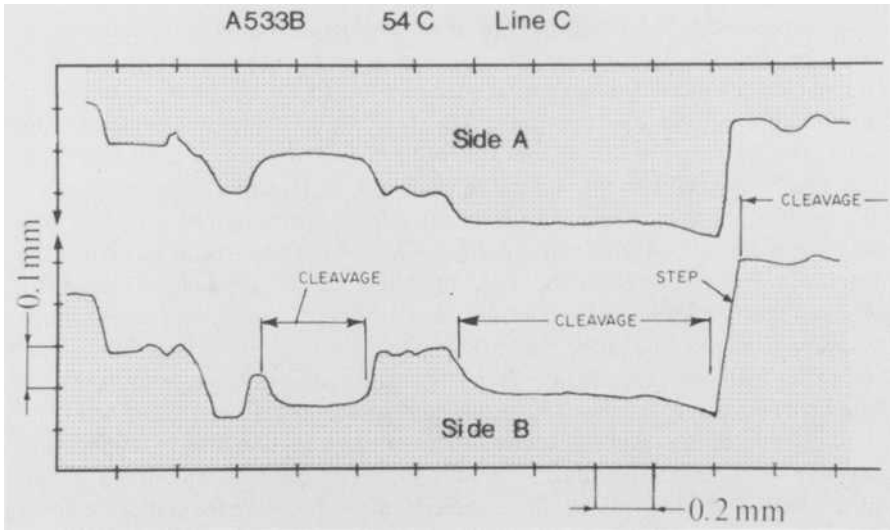

FIG. 8—*Fracture surface contours of Side A and Side B along Line C-C.*

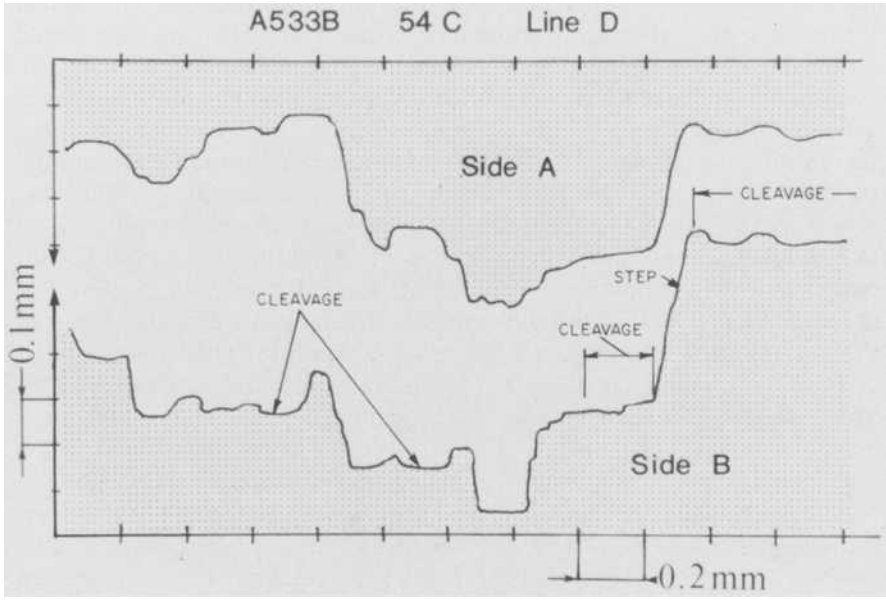

FIG. 9—*Fracture surface contours of Side A and Side B along Line D-D.*

Analysis of Results and Discussion

We are seeking information from fracture surface analysis on the general fracture processes leading to fibrous-cleavage transition and on quantitative assessment of fracture parameters (such as K and J values) at crack initiation and at fibrous-cleavage transition. This information may be obtained from fracture surface contours of top and bottom fracture surfaces in matching regions. However, it should be made clear that, although the relative uncertainty of height measurement with the current system would be less than 5%, other uncertainties in the analysis exist. One of the uncertainties is that the fracture surfaces may be further deformed by the strain field of the advancing crack tip; thus it may not represent the surface morphology present when fracture occurred. Secondly, the surface contours along the selected lines may not be typical or average for the fracture surfaces. Thirdly, in order to calculate J and K values, the crack tip opening displacements are determined from the two sides of the fracture surfaces. Due to the irregularities of the fracture surfaces, it is difficult to define where the opening displacement should be measured. In order to clarify these uncertainties, much more elaborate studies are necessary. With these qualifying remarks, the topographical analysis of fracture surfaces is presented.

If the gap in the fracture surface contour plots for the top and bottom surfaces along the line A-A shown in Fig. 4 is closed until the two surfaces contact, then Fig. 10 is obtained. It is apparent that cleavage regions show a reasonable match. This figure indicates that opening displacement existed at the moment when cleavage fracture took place. A similar figure constructed for the line B-B is shown in Fig. 11. From these figures the opening displacement in the fatigue crack region at the time of about 0.4 mm of fibrous crack extension was determined to be 0.39 mm and, at a near-crack-tip position, the opening displacement at the start of cleavage fracturing was approximately 0.08 mm. The locations where these measurements are taken are shown in Figs. 10 and 11. Substituting the opening displacement value of 0.39 mm and flow stress of 359 MPa (yield strength and ultimate strength for this material at room temperature were 228 MPa and 490 MPa respectively)[5] in the equation $J = \delta \times \sigma_0$ and converting the J-value into a K-value with $K = \sqrt{E \times J}$, the stress intensity factor for cleavage fracture initiation was computed to be 170 MPa$\sqrt{\text{m}}$. On the other hand, the stress intensity factor of 77 MPa$\sqrt{\text{m}}$ can be obtained if the crack tip opening displacement of 0.08 mm is used.

It should be noted that the macroscopic determinations of J-value are not easily related to the actual opening near the crack tip after some fibrous tearing has occurred. This is due to deformation and stress relaxation in the bypassed plastic zone. However, if we picture the crack tip strains associated

[5]Carman, C., U.S. Army Armament R&D Command, Dover, N.J., private communication.

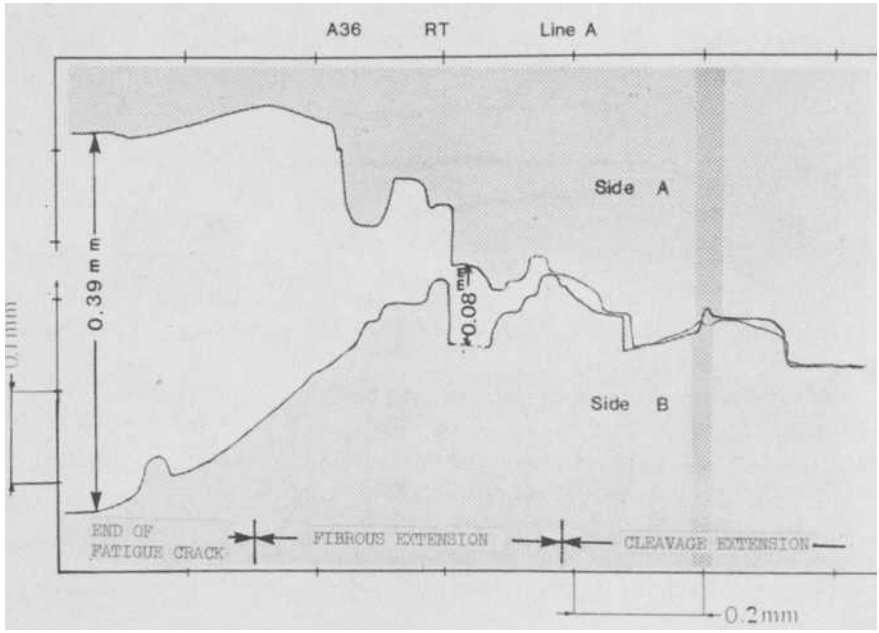

FIG. 10—*Closing of fracture surface contours shown in Fig. 4 until cleavage surfaces contact along Line A-A.*

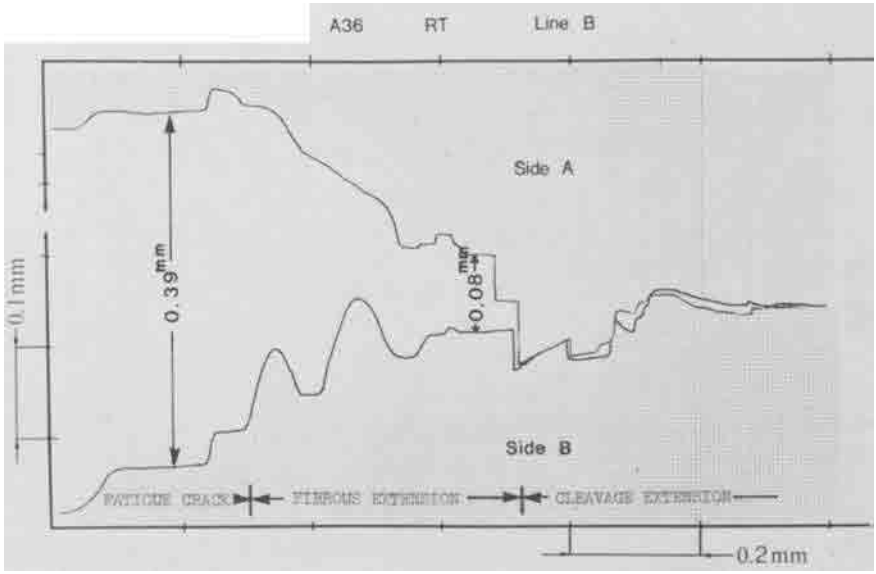

FIG. 11—*Closing of fracture surface contours shown in Fig. 5 until cleavage surfaces contact along Line B-B.*

with the 0.08 mm opening measurement as a condition for start of cleavage directly from the fatigue pre-crack, the initiation event would have been governed by a larger degree of plane-strain. As a crude check, the $K_c = 170$ MPa$\sqrt{m}$ value was converted to a corresponding K_{Ic} (plane-strain) estimate using the equation [*3*]

$$K_c^2 = (K_{Ic})^2 (1 + 1.4\beta_{Ic}^2)$$

where $\beta_{Ic} = (1/B)(K_{Ic}/\sigma_0)^2$. The result was 76 MPa$\sqrt{m}$. These values can be regarded as plausible for a coarse-grained 38.1-mm-thick plate of A36 steel at room temperature.

Further closure of the top surface and the bottom surface was effected; the results are shown in Fig. 12 for the line *A-A* and Fig. 13 for the line *B-B*. Figure 12 shows that a hole was formed ahead of the crack tip and that the material between the main crack tip and the hole stretched.

Finally, Figs. 14 and 15 show the crack opening displacement at the time of fatigue crack extension. The crack opening displacement measured was approximately 0.14 mm. The stress intensity factor for initiation of the fatigue crack was 102 MPa$\sqrt{m}$.

Similar analysis was made with the fracture surface contour plots of A533B steel. Figures 16 and 17 show the closure of conjugate surfaces until contact of the surfaces was made. These figures indicate that cleavage fracture between the end of the fibrous region and the step was formed before the cleavage fracture which follows the step. Furthermore, the opening displacement ex-

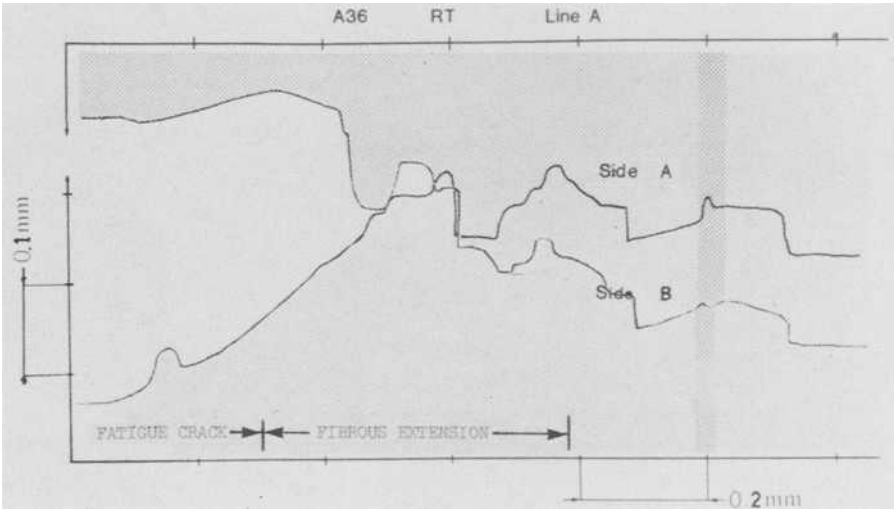

FIG. 12—*Further closing of fracture surface contours along Line A-A shown in Fig. 10.*

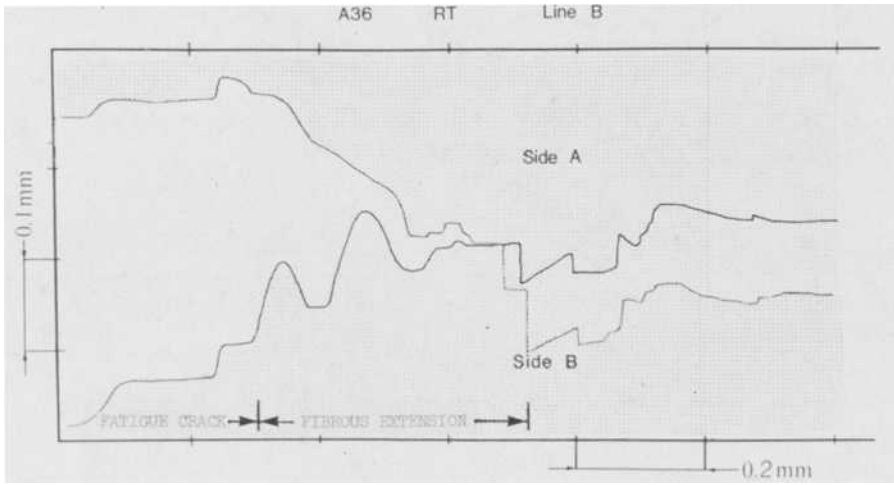

FIG. 13—*Further closing of fracture surface contours along Line B-B shown in Fig. 11.*

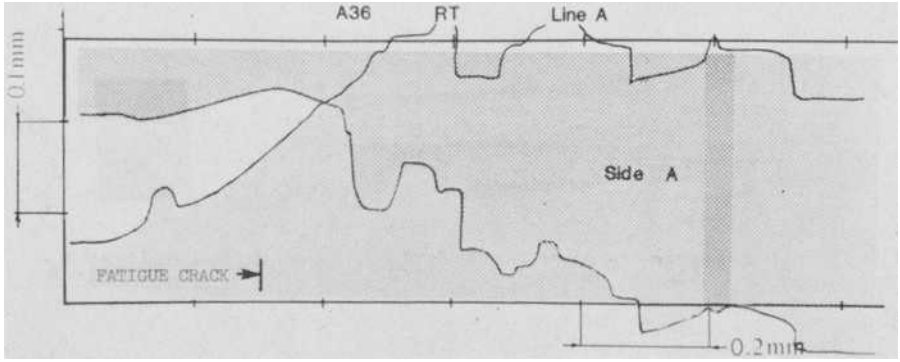

FIG. 14—*Further closing of fracture surface contours along Line A-A up to the end of fatigue crack.*

isting at the time of final cleavage fracture was 0.1 mm. This observation suggests that after tearing instability the fracture mode converted from fibrous to cleavage; however, this cleavage fracture appeared to be arrested quickly, possibly because of load relaxation. With the use of an opening displacement of 0.1 mm and a flow stress of 560 MPa, the stress intensity factor necessary to cause final cleavage fracture was computed to be 108 MPa$\sqrt{\text{m}}$. This value appears to be low compared with the reported K_{Ic}-values around 54°C; however, the rate of loading for the re-initiation of crack must be extremely high. It is, therefore, quite conceivable that the value of flow stress of

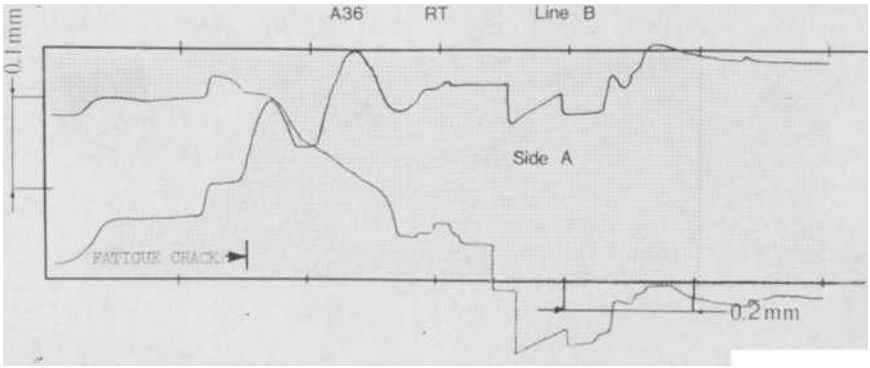

FIG. 15—*Further closing of fracture surface contours along Line B-B up to the end of fatigue crack.*

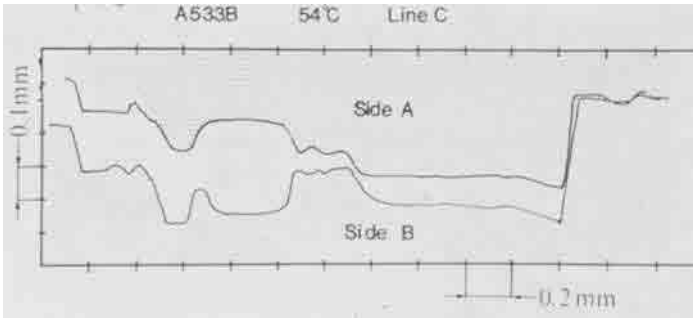

FIG. 16—*Closing of fracture surface contours along Line C-C shown in Fig. 8 until cleavage surfaces contact.*

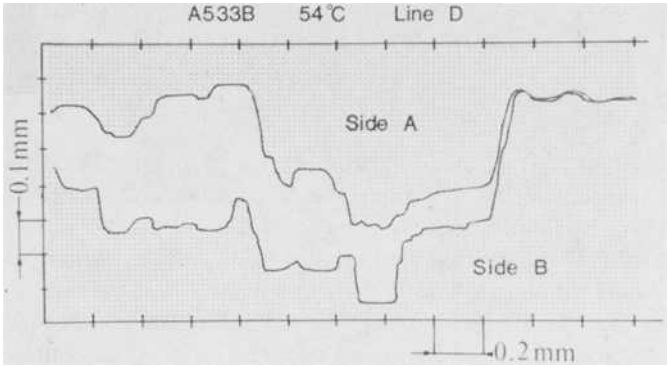

FIG. 17—*Closing of fracture surface contours along Line D-D shown in Fig. 9 until cleavage surfaces contact.*

560 MPa is too low to represent this re-initiation state. Further study to correlate the local opening displacements to macroscopic fracture parameters is necessary.

Figures 18 and 19 show the results of further closing of conjugate fracture surfaces until the cleavage surfaces before the step were contacted. These figures indicate the amount of opening displacement that existed at the cleavage surfaces of several adjacent grains.

Further closure of these surfaces was effected; the results are shown in Figs. 20 and 21. These figures suggest that the clusters of cleavage fracture observed in the fibrous region shown in Figs. 6 and 7 were formed well ahead of a main crack tip. It is apparent that the manipulation of conjugate fracture surface contour plots provides information on which cleavage fracture or holes formed first and how the subsequent fracture processes took place.

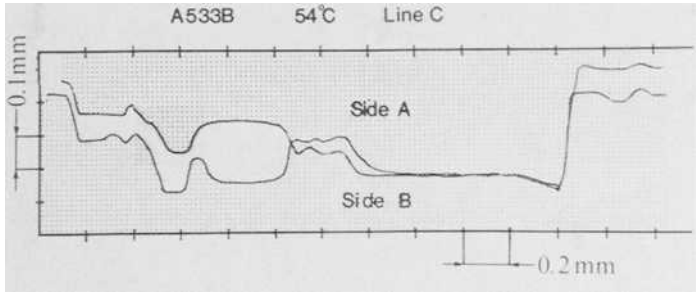

FIG. 18—*Further closing of fracture surface contours along Line C-C until the end of fibrous crack surfaces contact.*

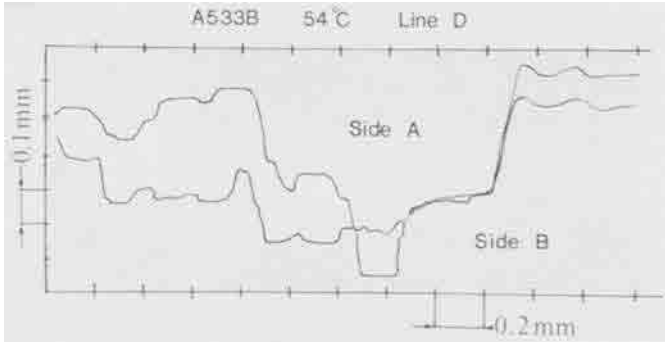

FIG. 19—*Further closing of fracture surface contours along Line D-D until the end of fibrous crack surfaces contact.*

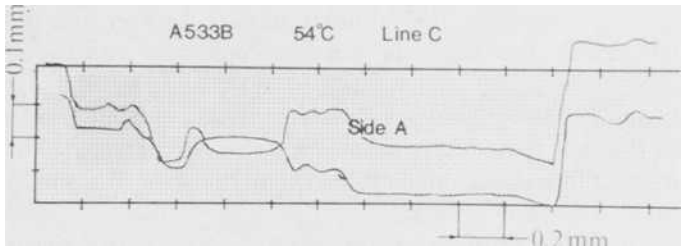

FIG. 20—*Further closing of fracture surface contours along Line C-C demonstrating formation of advance cracking.*

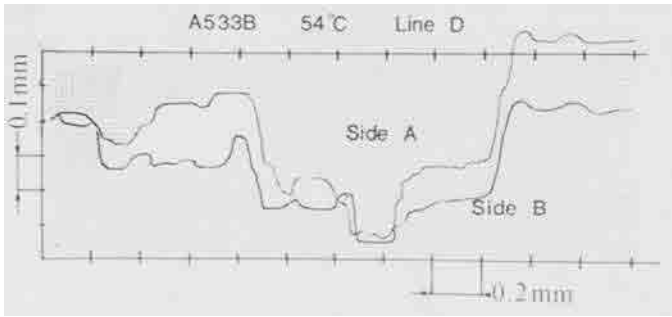

FIG. 21—*Further closing of fracture surface contours along Line D-D demonstrating formation of advance cracking.*

Conclusions

With the use of stereography and topographical analysis of matching pairs of fracture surfaces, information on fracture processes such as cleavage formation in dominantly fibrous fracture regions can be obtained. Quantitative information of crack opening displacements can also be obtained. It is hoped that this information can improve the understanding of fibrous-cleavage transition behavior of steels and make it possible to construct a mechanistic model which describes the fracture behavior of steel in the transition temperature range.

Acknowledgments

The authors would like to acknowledge the cooperation provided by C. Carman, U.S. Army Armament Research and Development Command, Dover, New Jersey, and by J. P. Gudas and D. A. Davis of David W. Taylor Naval Ship Research and Development Center, Annapolis, Maryland, in generously providing fractured specimens and sharing their test results.

References

[1] Beachem, C. D., *Fracture*, Vol. 1, 1968, pp. 243-349.
[2] Beachem, C. D. and Pelloux, R. M. N. in *Fracture Toughness Testing and Its Applications, ASTM STP 381*, American Society for Testing and Materials, 1965, pp. 210-245.
[3] Irwin, G. R., *Journal of Engineering for Power, Transactions of ASME*, Series A, Vol. 86, 1964, p. 444.

B. Cina,[1] *I. Eldror,*[1] *and T. Kaatz*[1]

Some New Fractographic Features in the Fatigue of High-Strength Aerospace Alloys

REFERENCE: Cina, B., Eldror, I., and Kaatz, T., **"Some New Fractographic Features in the Fatigue of High-Strength Aerospace Alloys,"** *Fractography of Ceramic and Metal Failures, ASTM STP 827*, J. J. Mecholsky, Jr. and S. R. Powell, Jr., Eds., American Society for Testing and Materials, 1984, pp. 252-266.

ABSTRACT: The object of this research was to further a systematic fractographic study of fatigue in aerospace materials to facilitate failure investigations of actual components. Smooth and notched laboratory specimens were fatigue tested in pulsating tension and in alternating stress at a frequency of 1 to 2 Hz and at stresses that gave failure in 10^3 to 10^5 cycles. Fractures were examined by stereoscopic and scanning electron microscopes.

A ridge structure that had been previously observed in aluminum alloys that emanates from fatigue origins but precedes the formation of striations was observed in ultra-high-strength steels. The implications of such ridges in the mechanism of fatigue cracking are discussed. Not all the steels studied showed fatigue striations, and failure mechanisms not specific to fatigue were frequently observed.

Such nonconformity of fractographic features increased with the tensile strength of the steels. Secondary cracking was sometimes found to be a more reliable method of identifying fatigue failure in some of these steels. Intergranular cracking at prior austenite grain boundaries was also frequently observed, although its formation appeared, on occasion, to be related to the attainment of a minimum level of stress intensity. Hydrogen from the environment also probably played a role in such intergranular cracking, as indicated by distinct hairlines on the fracture surface. Intergranular crack surfaces also sometimes showed unexpected crystallographic features.

For the aluminum alloys, further quantitative relationships have been established between the total number of striations in the development of the crack and the number of fatigue cycles in the entire fatigue test. This enables the fatigue stress to be estimated where unknown.

Counting striations in the steels was found to be very difficult and unreliable. However, trends in 4340 steel were found to be akin to those in aluminum alloys. Ridge formation in the aluminum alloys did not appear to be related to specimen geometry.

KEY WORDS: fractography, fatigue, high-strength low-alloy steels, aluminum alloys, aerospace

[1] Chief Metallurgist, Senior Metallurgist, and Senior Physicist, respectively, Materials and Process Engineering, Engineering Division, Israel Aircraft Industries Ltd., Lod, Israel.

A systematic study of the fractography of fatigue failures in high-strength alloys for constructional use in flight vehicles serves at least two purposes. It aids our understanding of the fundamentals of the fatigue mechanism and it facilitates a more precise interpretation of service failures. Little such systematic work has been carried out. A previous report [*1*] attempted to rectify this situation for high-strength aluminum alloys. The present work details results obtained on several high-strength low-alloy (HSLA) steels and also reports some further progress obtained with the aforementioned aluminum alloys. The work on the steels is concerned with fractographic features observed after systematic variation of the load required to cause failure. The progress with the aluminum alloys is in extending the relationships between the number of fatigue striations (N_s) observed on the fracture surface and the total number of applied stress cycles (N_f).

Experimental Procedure

Materials

Three low-alloy steels of significantly different chemical composition were selected for study: 35NCD16, SAE 4340, and SAE 4130. Their compositions are given in Table 1.

The compositions of the 2024 and 7075 aluminum alloy bar and plate respectively were the same as in Ref *1*. Fatigue tests were also carried out on 2024-T3 clad sheet stock conforming to Federal Specification QQ-A-250/5; its chemical composition is shown in Table 2.

Form of Raw Stock

The 4340, 4130, and 35NCD16 steels were in the form of 14.3, 12.7, and 12.2 mm diameter bars respectively. The aluminum clad sheet was 2 mm thick; its cladding was removed mechanically. The specimens from all the alloys were taken from the rolling direction.

Details of Heat Treatment

The steels were obtained in the annealed condition. The 4340 and 4130 steels conformed to U.S. Specifications MIL-S-5000 and MIL-S-6758 respec-

TABLE 1—*Chemical analyses (weight percent) of the low-alloy steels.*

Alloy	C	Si	Mn	S	P	Cr	Ni	Mo
SAE 4340	0.40	0.27	0.78	0.025	0.010	0.90	1.80	0.26
SAE 4130	0.33	0.27	0.53	0.016	0.010	1.10	0.20	0.25
35NCD16	0.36	0.32	0.45	0.010	0.013	1.70	3.80	0.38

tively. The 35NCD16 steel conformed to French Specification AIR 9160. The specimens for fatigue testing were machined from the bars in the annealed condition to within +0.5 mm of their final diameter, austenitized in a neutral salt bath, and tempered in air furnaces as required by the following in-house process specifications (PS) for the several levels of tensile strength desired: SAE 4340 per Israel Aircraft Industries (IAI) PS 019050, SAE 4130 per IAI PS 019030, and 35NCD16 per IAI PS 019053.

Details of heat treatment, hardness results, and equivalent ultimate tensile strength (UTS) values are given in Table 3.

The aluminum bar and plate have been described previously. The sheet material was supplied in the standard T3 temper. Typical yield strength (YS) and UTS values for such material stripped of its cladding are 345 and 483 MPa respectively.

Details of Fatigue Testing

For the steels, fractures were obtained under conditions of pulsating tension in the range of about 10^3 to 10^5 cycles at a test frequency of 1 Hz. Solid cylindrical button-head specimens were employed with a test section diameter of 5 mm [2]. Notched samples had K_t-values of 2.4 to 3.1. The equipment used is described in Ref *1*. For reversed stressing of the steels and the aluminum plate and bar, hourglass-type specimens were used whose hourglass section had a radius of 40 mm and a minimum diameter of 5 mm. Some specimens were notched in the center of the hourglass section, the notch having the following nominal dimensions: radius 0.35 mm, depth 0.45 mm, and an angle of 60 deg. The actual K_t-values of the notches were 2.5 to 2.6. The test

TABLE 2—*Chemical composition (weight percent) of 2024-T3 clad sheet stock.*

Cu	Mg	Fe	Si	Mn	Cr	Ti	Zn
4.3	1.35	0.36	0.08	0.63	<0.10	0.01	<0.10

TABLE 3—*Heat treatment and mechanical properties of the low-alloy steels.*

	4340 Steel	4130 Steel	35NCD16 Steel
Austenitizing temperature, °C	860	830	875
Tempering temperature, °C	205, 230, 500, 540	560	205
Average hardness, VHN	621, 540, 457, 365	291	606
UTS, MPa, equivalent to hardness value	2139, 1863, 1518, 1158	966	2105

frequency was 1 to 2 Hz. The fatigue specimens made from the aluminum sheet were of simple tensile type with a gage length and width of 50 and 11 mm respectively. Some were notched on both edges at the center of the gage length, the notch radius and depth being 0.25 and 0.15 mm respectively. These gave K_t-values of 2.5. The test frequency in pulsating tension was 1 Hz. The test temperature was 24 ± 4°C.

Fractographic Observations of HSLA Steels Stressed in Pulsating Tension

For all the HSLA steels stressed in pulsating tension, the fatigue fracture became less easily identifiable as the tensile strength increased. This applied to examination at low and high magnification. Classical fatigue striations were sometimes almost entirely missing from fractures of some of the steels at very high strength levels. The following descriptions will therefore focus on some of the abnormal features observed.

35NCD16 Steel

There was no major difference in the fractures from unnotched and notched specimens in 35NCD16 steel at a tensile level of about 2105 MPa. All fracture origins, as for those of the 4340 steel at comparable tensile levels, were identified by ridges radiating from them (Fig. 1). These were sometimes free of striations and extended for a distance of about 60 μm from the origin. Striations are visible however in the center of the field in Fig. 1. Their highly truncated character and possibly damaged appearance are seen at much higher magnification in Fig. 2. A striking feature in this photomicrograph is the strong association of the striations with secondary cracking. The latter feature was very characteristic of all the high-strength steels, and in fact it was sometimes the sole feature which enabled a fatigue fracture to be identified unambiguously.

It should be noted that what is here meant by *secondary cracking* is parallel arrays of very many and relatively fine transgranular cracks lying normal to the direction of growth of the main crack, and whose density approaches that of striations. These features would therefore allow secondary cracks to be distinguished from those caused by single overload failure of high-strength steels. In the latter case, intergranular failure might be observed, and if bending stresses were present the density of the secondary cracks would be very much less than that associated with fatigue.

Commencing at a distance of about one quarter of the final crack length from the fracture origin in both smooth and notched samples, isolated zones of intergranular fracture at prior austenite grain boundaries were observed. (Crack length is measured as the distance from the crack origin in any direction of crack propagation.) This is shown in Fig. 3 for a notched specimen of $N_f = 10\ 055$. It was of extreme interest to examine the intergranular facets at

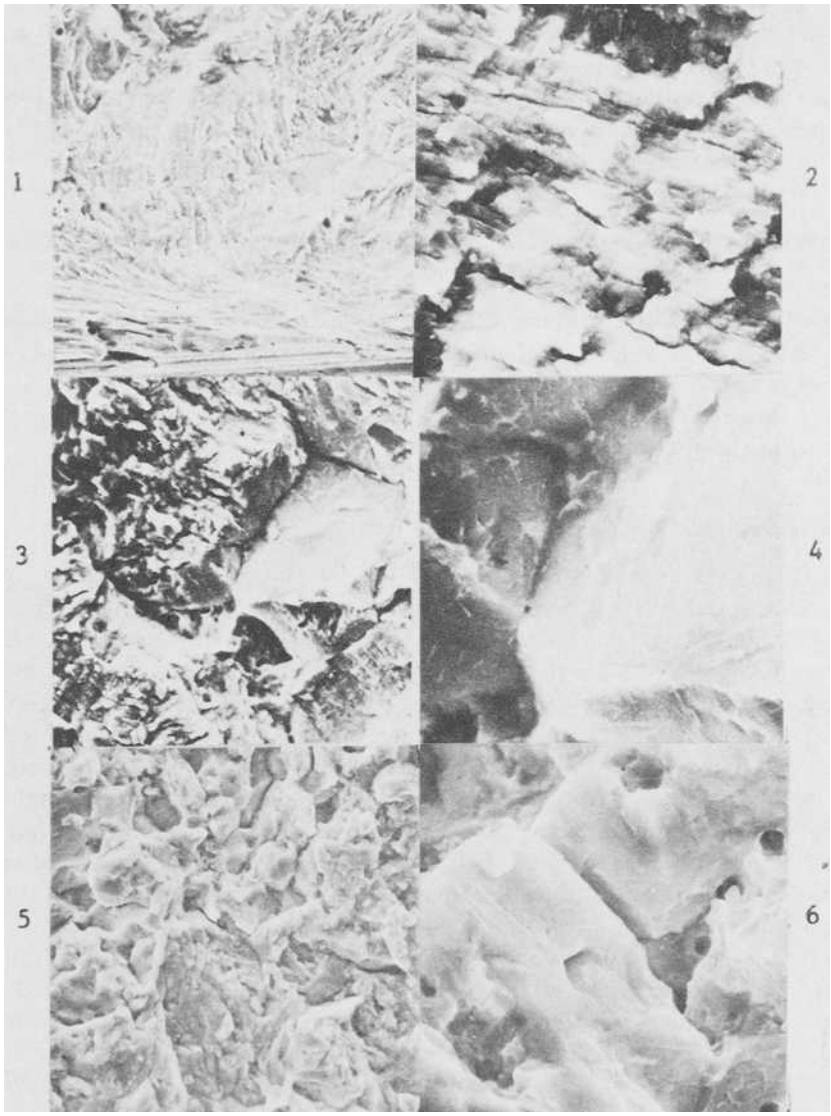

FIGS. 1 to 6—(1) *Notched 35NCD16;* $N_f = 2850$*; 0 to 1587 MPa stress; ridges at varied angles to notched surface (×1300).* (2) *Same as Fig. 1; truncated but possibly damaged striations (×13 000).* (3) *Notched 35NCD16;* $N_f = 10\ 055$*; 0 to 966 MPa stress; isolated zone of intergranular fracture (×1000).* (4) *Same as Fig. 3; features suggestive of quasi-cleavage on prior austenite grain boundaries (×4000).* (5) *Notched 4340; 2139-MPa UTS;* $N_f = 1130$*; 0 to 1145 MPa stress; zone of transition from transgranular to intergranular fracture (×1350).* (6) *Unnotched 4340; 2139-MPa UTS;* $N_f = 3950$*; 0 to 1415 MPa stress; quasi-cleavage and intergranular fracture (×6300). The direction of crack propagation in each photomicrograph is from bottom to top.*

higher magnification. Figure 4 shows hairline marks seemingly crystallographic in nature (note the three primary directions) and suggestive of quasi-cleavage on the prior austenite grain boundaries. Such intergranular fracture persisted to the point of onset of ductile transgranular failure, as indicated by dimples, where both fracture mechanisms were present.

4340 Steel (2139-MPa UTS)

At a very high level of tensile strength (2139 MPa) classical fatigue striations in 4340 steel were almost entirely absent from notched and unnotched specimens fractured in the range of 391 to 10 670 cycles. The fatigue zone in each case was in the form of a crescent over a small portion of the periphery of the fracture. As with results for the 35NCD16 steel at a similar level of tensile strength, ridges emanated from the fracture origins. These ridges, however, did not contain any striations. Beyond a distance of about 20 μm from the origin, the predominant modes of fracture in the crescent zone were intergranular at the prior austenite grain boundaries and quasi-cleavage (Figs. 5 and 6 respectively). Figure 5 shows the transition from somewhat indefinite transgranular fracture in the lower half of the photomicrograph to predominantly intergranular in the upper half. The occasional dimples in Fig. 5 are probably associated with undissolved particles. In Fig. 6 the hairline facets are possibly due to quasi-cleavage and the major cracks are probably intergranular. The presence of secondary cracking was sometimes one of the main means of identifying the fatigue fracture as such in these specimens.

4340 Steel (1518-MPa UTS)

The fractures of unnotched specimens of 4340 steel (1518-MPa UTS) were characterized by shallow flow lines radiating from a single origin, often an inclusion just beneath the surface. Notched specimens showed the classical multiple origins with indefinite ridges emanating from them (Fig. 7). Although striations were visible in these specimens, the secondary cracking associated with them was the more pronounced feature and therefore the more positive evidence of fatigue. A typical structure is shown in Fig. 8. The highly fragmented nature of these mixed structures observed at much higher magnification was akin to that shown in Fig. 2. There was a hint of even finer striations in some of the fragmented blocks. It is interesting to observe how such a mixed structure gives way to one of fine dimples at the border of the zone of final ductile failure (Fig. 9). The fatigue zone is in the lower half of the figure.

4340 Steel (1863-MPa UTS)

The fractographic features observed in 1863-MPa UTS specimens were between those observed in specimens of tensile strengths 1518 and 2139 MPa for

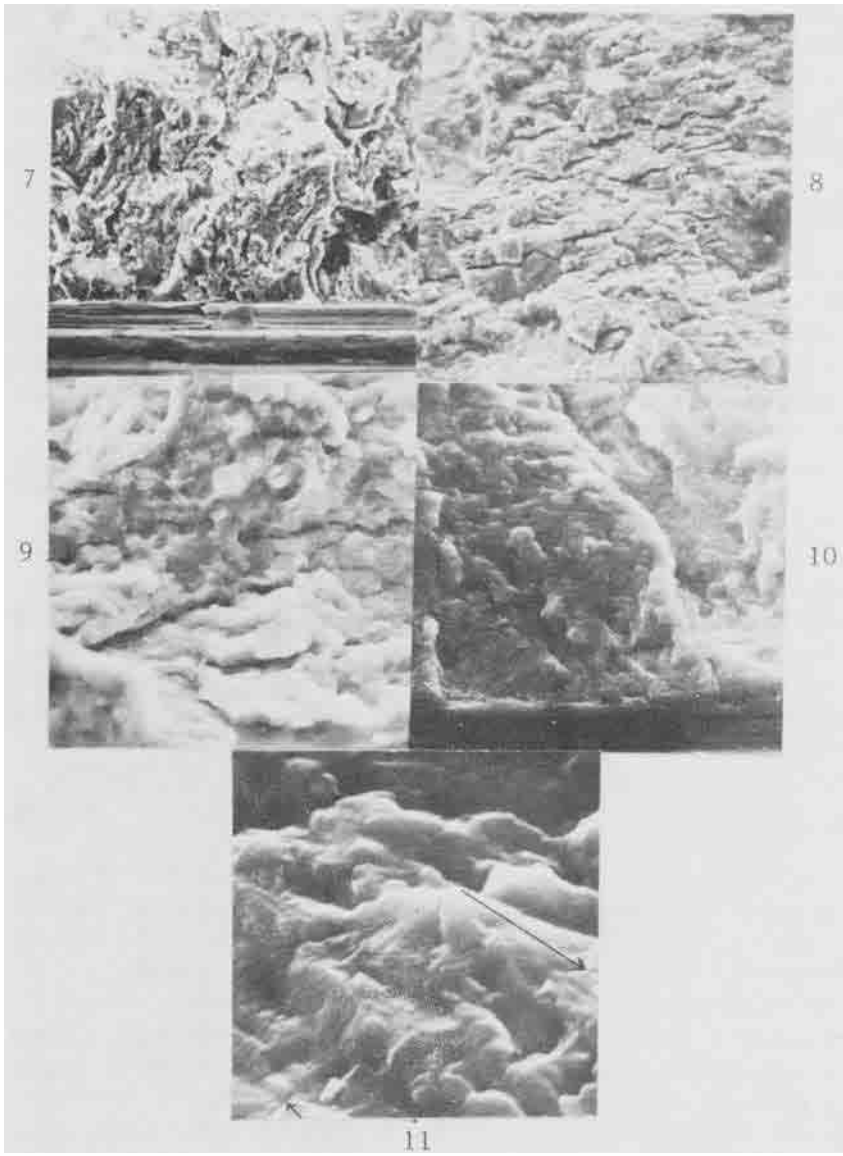

FIGS. 7 to 11—(7) *Notched 4340; 1518-MPa UTS;* $N_f = 4500$*; 0 to 1173 MPa stress; indefinite ridges emanating from fatigue origins (×1320).* (8) *Unnotched 4340; 1518-MPa UTS;* $N_f = 4925$*; 0 to 1346 MPa stress; striations and secondary cracking (×720).* (9) *Same as Fig. 8; merging of fatigue and ductile fractures (×2900).* (10) *Notched 4340; 1173-MPa UTS;* $N_f = 2240$*; 0 to 1035 MPa stress; striations on broad ridges at commencement of fracture (×3000).* (11) *Unnotched 35NCD16; 1932-MPa UTS;* $N_f = 5407$*; ±1070 MPa stress; ridges with fine striations 150 μm from crack origin (×10 000). The direction of crack propagation in each photomicrograph is from bottom to top, except in Fig. 11 where it is as indicated by the large arrow.*

both the notched and unnotched conditions. Striations, secondary cracking, and intergranular fracture were observed.

4340 Steel (1158-MPa UTS)

Fractographic features observed in 1158-MPa UTS specimens were largely akin to those observed in 1518-MPa UTS specimens, except that ridges emanating from the origin, and striations, were more continuous and clear. There was no significant difference between the fractures from unnotched and notched specimens.

In contrast to the fractures from specimens at higher levels of strength, striations were observed on the ridges from their commencement at the origin. This is shown in Fig. 10.

4130 Steel (966-MPa UTS)

It was difficult to obtain a fatigue fracture in less then about 10 000 cycles in unnotched specimens. Instead, continuous necking and ductile fractures were obtained. Even for notched specimens, the fracture contour became increasingly elliptical with increasing the number of cycles from 4000 to about 14 000, again presumably because of the great ductility of the material.

Where fatigue fractures were obtained, fine ridges were observed emanating from the origins; these ridges showed fine striations. Eventually, as the density of the striations decreased, secondary cracking was observed.

Fractographic Observations of HSLA Steels after Reversed Stressing

No fractographic features were observed after reversed stressing which had not previously been observed after stressing in pulsating tension. The difference which was observed was in the extent of the several modes of fractures. Thus for the same numbers of cycles-to-fracture, the overall size of the fatigue zone was larger for reversed stress than for pulsating tension. This is presumably due to the lower maximum tensile stress in the former. Similarly the extent of intergranular fracture at the prior austenite grain boundaries and the extent of quasi-cleavage were greater nearer the fracture origins in reversed stress than in pulsating tension. Less of both fracture mechanisms was observed near and beyond the middle of the fatigue zone in reversed stress than in pulsating tension.

Fine ridges which, when present, seemed to constitute the main topographical feature determining the direction and plane of the fatigue crack, were observed as much in fractures of reversed stress as in pulsating tension. Figure 11 is an unnotched sample of 35NCD16 steel of 1932-MPa UTS. The ridges here display fine fatigue striations. There is a striking similarity between this photomicrograph and that of a notched 2024 aluminum alloy spec-

imen fractured in 100 870 cycles in pulsating tension (Fig. 5(f) in Ref *1*) despite the totally different crystallographic and metallographic structures of the two alloys.

Relation Between Striations and Cycles

In previous work on aluminum alloys [*1*], clear relations had been found between the total number of striations (N_s) on the fracture surface and the total number of applied cycles (N_f) for conditions of pulsating tension. It was important to establish whether such relations also existed for HSLA steels. It was also important to know for the aluminum alloys the relations for conditions of reversed stress for the bar and plate material examined previously and the relations for sheet material tested in pulsating tension.

HSLA Steels

Only for the lower levels of tensile strength was it possible to obtain accurate counts of the total number of fatigue striations, though this was also dependent to some extent on the specific steel examined. Thus striations could be counted in the 35NCD16 steel at a tensile strength of 2105 MPa, an operation which was impossible in the 4340 steel at a similar level of strength. A plot of N_s/N_f versus N_s for all the steels showed too much scatter to allow a clear relationship to be determined. However, as Fig. 12 shows, a somewhat better relationship was obtained when plotting log N_s versus log N_f for unnotched specimens of 4340 and 35NCD16 steels, and for notched specimens of 4130 and 4340 steels for UTS up to 1518 MPa. Further data are required to establish whether there is a significant difference between unnotched and notched specimens.

Aluminum Alloys

Bar and Plate—The relationships between striations and cycles were plotted as N_s/N_f versus N_s for 7075 plate stock and 2024 bar stock. The curves for notched specimens showed higher N_s/N_f ratios for a given total number of fatigue striations than those for smooth ones; the same result was noted in Ref *1*. A comparison of the results for reversed stress and pulsating tension for each of the two alloys and for smooth and notched specimens is shown in Fig. 13. The very high ratios of N_s/N_f for notched specimens of both alloys, especially for shorter lives to failure, can be explained by the very high effective stresses operating in these specimens, which resulted in rapid nucleation of cracks and the formation of striations very soon thereafter.

Sheet—Figure 14 shows the experimental results obtained for the 2024-T3 sheet specimens and, for comparison, the results for the 2024 bar material from Ref *1*. Again the unnotched specimens have lower N_s/N_f ratios than

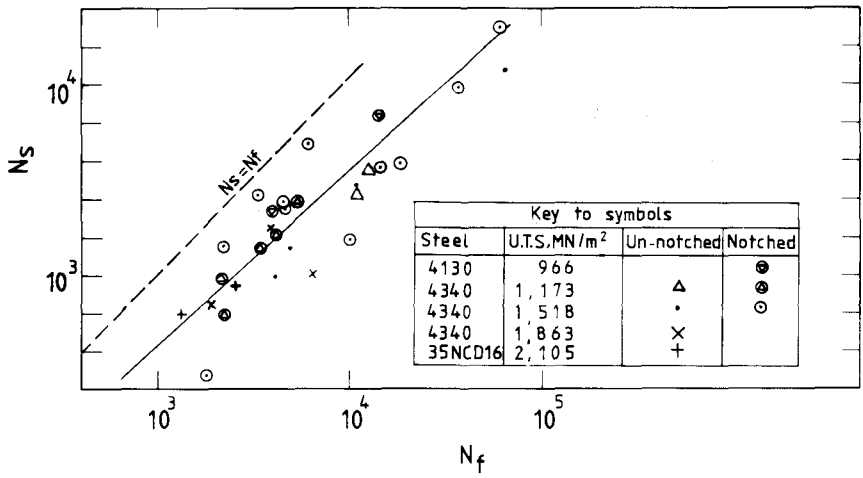

FIG. 12—*Relation between number of striations* (N_s) *and number of cycles* (N_f) *for the HSLA steels.*

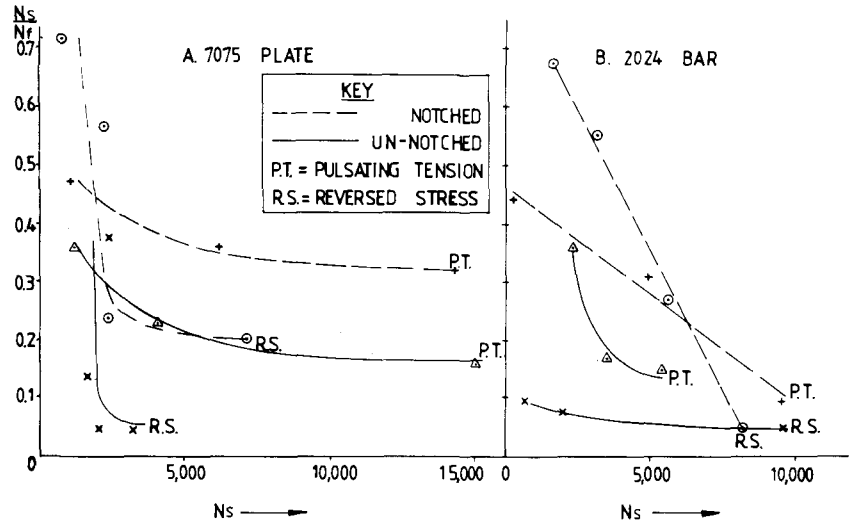

FIG. 13—*Relation between number of striations* (N_s) *and cycles* (N_f) *for the aluminum alloys. (The results for pulsating tension are reproduced by kind permission of Pergamon Press, Oxford.)*

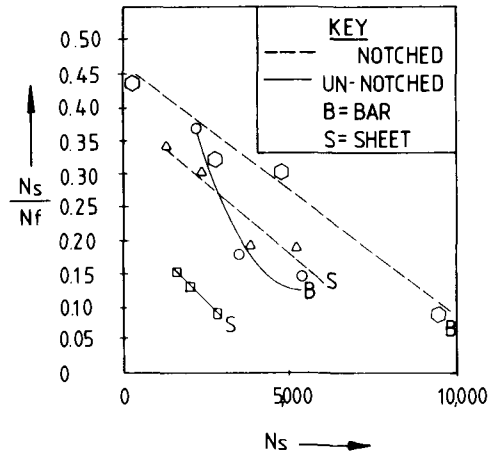

FIG. 14—*Relation between number of striations* (N_s) *and cycles* (N_f) *for 2024 bar and sheet tested in pulsating tension.*

notched ones. All sheet specimens have lower N_s/N_f ratios than bar specimens for the same surface condition.

Effect of Specimen Geometry on Ridge Formation

The possibility was investigated that ridge formation emanating from the fracture origin was related to the geometry of the fatigue specimens. The latter were circular in section and about 5 mm in diameter. Employing the same stress range (0 to 511 MPa) as used in Ref *1*, and the same 7075 aluminum alloy plate, fatigue tests to fracture were carried out on specimens of 2.5, 5.0 and 10.0 mm diameter. A similar fatigue test at 0 to 469 MPa was carried out on specimens of square cross sections (4 by 4 mm). Ridges with and without striations were observed in all these specimens.

Examination of the fatigue fractures in the sheet specimens tested in pulsating tension also revealed the presence of ridges emanating from the fracture origins, initially without and eventually with striations.

The geometry of the fatigue specimens does not appear to be a factor in ridge formation.

Discussion

Intergranular Failure in HSLA Steels

Although the phenomenon of intergranular fracture at prior austenite grain boundaries in the fatigue failure of HSLA steels has been known for

over a decade, Phillips and co-workers [3] give only one example of it: an AISI 52100 steel of 2208-MPa UTS that failed after only 100 cycles of pulsating tension applied at a frequency of 1000 cpm. The phenomenon was observed by Dahlberg [4] in precracked specimens of 4340 steel of 2001-MPa UTS. He found its formation to be favored by a humid atmosphere and in fact suggested that it was a superposition of atmospheric corrosion cracking on mechanical fatigue.

The role of the atmosphere in intergranular cracking would appear to be confirmed by the work of Thompson et al [5] on a 4340 steel of 1918-MPa UTS. Two unnotched specimens were tested identically: one whose failure initiated at the surface gave mixed intergranular and transgranular fracture, while that which initiated subsurface showed only transgranular failure. Miller [6] and Broek and Van der Vet [7] also observed intergranular fatigue fracture in 4340 steel of very high tensile strength, namely 1421 and 2070 MPa in the Dutch work. The latter specimens were notched. Miller's specimens were quenched and then tempered at 93°C (200°F) and were probably over 2070-MPa UTS. It is not stated whether they were notched. Miller observed a mixture of intergranular fracture, quasi-cleavage, and dimpled rupture in his fatigue fractures and concluded that the absence of striations prevented a positive identification of fatigue failure. Broek and Van der Vet found larger areas of intergranular fracture in steel specimens of 1421-MPa UTS than in those of 2070-MPa UTS.

Thielen and Fine [8] and Kim et al [9] studied the fatigue fractures in notched specimens of 4140 steel. Intergranular fractures were observed to the extent of 70% in specimens of untempered martensite [9]. In the earlier work [8] the extent of intergranular fracture increased with ΔK. These earlier tests were carried out in dry argon under sinusoidal loading at 30 Hz [8]. This would seem to disprove the suggestion of Dahlberg [4] for the necessity for moisture in the atmosphere. Kim et al [9] also found secondary cracking along prior austenite grain boundaries and occurring transgranularly.

More recently, Hirano et al [10] have measured fatigue crack growth rate in steels similar in composition to the SAE 4130 steel used in the present work, but under conditions of electrolytic charging. It was found that hydrogen had little effect in the near-threshold region. However, at intermediate growth rates and therefore at larger values of ΔK, predominantly prior austenite intergranular fracture was observed. At still higher ΔK-values, quasi-cleavage was also observed. The intergranular fractures of Hirano et al are in keeping with the present results. The latter, however, suggest that the intergranular fracture was itself associated with quasi-cleavage. This would imply that a prior austenite grain boundary is a more crystallographically ordered region than has hitherto been considered.

No attempt has been made in the present work to control atmospheric humidity; thus its effect can not be assessed. The fact that intergranular fracture was never found immediately adjacent to a fracture origin, however, suggests

that the role of humidity was not dominant. The precise location of zones of intergranular fracture was not studied systematically by most of the aforementioned workers.

Since intergranular fracture in fatigue tests of HSLA steel can be obtained in the absence of moisture but can also be favored by the presence of moisture, the following possibilities exist: (1) stress corrosion can play a role in the fatigue tests, (2) the intrinsic hydrogen content of the steel can result in hydrogen embrittlement at a critical level of stress intensity at the crack tip, and (3) the prior austenite grain boundary can be intrinsically weak and will fail at a critical stress intensity; this has been suggested elsewhere [*11*]. These points can not be resolved at the present time.

From the practical point of view, the present work shows that, in contrast to the conclusions of Miller [*6*], if intergranular failure in an engineering component is observed other than at the origin, it can be taken as positive evidence of fatigue failure, provided that (1) the fracture origin or origins can be identified as being at the surface, and (2) the initial fracture is transgranular and not ductile (dimpled) nor due to cleavage. Supporting evidence for the identification of fatigue may also be found in the presence of secondary transgranular cracking lying perpendicular to the suspected direction of crack propagation. It is interesting that intergranular fracture and secondary cracking were observed in a notched specimen which failed after only 391 cycles.

Multiplicity of Fracture Mechanisms in the Fatigue of HSLA Steels

The HSLA steel specimens, especially those of very high tensile strength, had fatigue fracture surfaces that sometimes displayed regions of striations, intergranular fracture, quasi-cleavage, and ductile rupture. This suggests that although cyclic stressing was being applied, the failure mechanism was not unique to fatigue but was a possible combination of fatigue, stress corrosion, hydrogen embrittlement, brittle intergranular and transgranular failure, and ductile rupture. The precise combination seems to be dependent on alloy composition (especially hydrogen and other impurity content), environmental conditions, and local stress intensity. The term *high-stress low-cycle fatigue* applied to HSLA steels can be strictly applied only to the mode of stressing. It can be misleading when applied to the subsequent failure mechanism. A more appropriate term might be *fatigue-accelerated failure*.

The present work again draws attention to the phenomenon of ridges on the fracture surface emanating from the fracture origins; a phenomenon as observed previously in aluminum alloys [*1*]. Since these ridges were observed before the formation of striations, and since striations were eventually observed on the surface of the ridges as the latter progressed away from the origin, the ridges would again appear to be a topographic feature defining the plane or planes of the crack surface. If such planes are crystallographic, a

factor of commonality must exist between the face-centered-cubic matrix of the aluminum alloys and the body-centered-cubic (actually modified tetragonal) matrix of the steels. The identification of such planes remains to be established. It would be of interest to investigate whether such fine fatigue ridges are also observed in alloys of hexagonal close packed (HCP) structure.

Ability to Identify Fatigue Striations

It is realized that the relations obtained between the number of fatigue striations and fatigue cycles are dependent on the resolution of the SEM employed. For the steels, the striations, where visible, were generally fairly coarse, so that it is felt that most of them were detected. For the aluminum alloys, where striations were more preponderant than in the steels, some very fine striations may have gone undetected at the commencement of the fractures. Their relative number, however, would have been small because under the high-stress low-cycle fatigue conditions employed, the striations, very soon from the formation of the crack, were of size within the resolution of the SEM.

Summary and Conclusions

1. High-strength low-alloy steels subjected to high-stress low-cycle fatigue can show a multitude of fracture mechanisms, not all of which are uniquely associated with fatigue (for example, prior austenite grain intergranular fracture and quasi-cleavage).

2. Despite the absence of classical fatigue fractographic features, fatigue can still be recognized—for example, by the presence of secondary cracking (parallel arrays of very many fine transgranular cracks lying normal to the direction of growth of the main crack), or by fine ridges emanating from the fracture origin, or by regions of cracking at prior austenite grain boundaries, provided (1) the latter phenomenon is not present at the fracture origin, (2) the fracture origin or origins can be identified as being at the surface, and (3) the initial fracture is transgranular and not ductile (dimpled) nor due to cleavage.

3. Ridge formation determining the plane or planes of the fatigue crack origin is common to HSLA steels and to high-strength aluminum alloys. It is not related to specimen geometry. The crystallographic commonality between these two totally different materials has now to be determined.

4. Further relationships have been determined between the number of striations on a fracture surface and the total number of fatigue cycles, especially for high-strength aluminum alloys. This should be of practical use in failure investigations. Less certain relationships were obtained for very high strength steels.

5. The term *high-stress low-cycle fatigue* for HSLA steels can be fairly applied to the mode of stressing but not to the failure mechanism. A more appropriate term might be *fatigue-accelerated failure*.

References

[1] Cina, B. and Kaatz, T., *Fatigue of Engineering Materials and Structures*, Vol. 2, No. 1, 1979, pp. 85-95.
[2] Hirschberg, M. H. in *Manual on Low-Cycle Fatigue Testing, ASTM STP 465*, American Society for Testing and Materials, 1970, pp. 67-86.
[3] Phillips, A., Kerlins, V., Rawe, R. A., and Whiteson, B. V., "Electron Fractography Handbook," MCIC-HB-08, Battelle Columbus Laboratories, Columbus, Ohio, 1976.
[4] Dahlberg, E. P., *Transactions of ASM*, Vol. 58, 1965, pp. 46-53.
[5] Thompson, K. R. L., Araki, T., and Uchiyama, I., *Journal of the Iron and Steel Institute*, Vol. 207, Dec. 1969, pp. 1624-1627.
[6] Miller, G. A., *Transactions of ASM*, Vol. 62, 1969, pp. 651-658.
[7] Broek, D. and Van der Vet, W. J., TR 69043, National Aerospace Laboratory, The Netherlands, 1969.
[8] Thielen, P. N. and Fine, M. E., *Metallurgical Transactions A*, Vol. 6A, 1975, pp. 2133-2141.
[9] Kim, Y. H., Mura, T., and Fine, M. E., *Metallurgical Transactions A*, Vol. 9A, 1978, pp. 1679-1683.
[10] Hirano, K., Kobayashi, Y., Kobayashi, H., and Nakazawa, H. in *Proceedings*, Fatigue '81, Warwick, England, 1981, published by Westbury House, U.K., 1981, pp. 87-96.
[11] Cina, B. in *Proceedings*, Conference on Environmental Degradation of Engineering Materials, Virginia Polytechnic Institute and State University, Blacksburg, Va., 1977, pp. 533-542.

R. S. Vecchio[1] *and R. W. Hertzberg*[1]

An Examination of Cleaning Techniques for Post-Failure Analysis

REFERENCE: Vecchio, R. S. and Hertzberg, R. W., **"An Examination of Cleaning Techniques for Post-Failure Analysis,"** *Fractography of Ceramic and Metal Failures, ASTM STP 827*, J. J. Mecholsky, Jr. and S. R. Powell, Jr., Eds., American Society for Testing and Materials, 1984, pp. 267-281.

ABSTRACT: A study has been made of the effectiveness of cleaning techniques for post-failure analysis. Air blast, organic solvents, and repeated stripping of cellulose acetate replicas (benign techniques) are useful in removing loosely adhering particles, grease, and oils. More aggressive removal techniques, however, are required for tightly bonded oxidation and corrosion products. A solution containing Alconox cleaning detergent was examined and found to remove most corrosion debris from fracture surface regions associated with cleavage and intergranular and microvoid coalescence fracture micromechanisms. In some instances, however, indications of surface degradation and etching were apparent which resulted from excessive exposure time in the cleaning solution. Degradation and etching led to complications in the interpretation of these fracture surface markings. Fatigue fracture surfaces exhibited the poorest response to the benign cleaning techniques of all fracture modes examined. Thus it was not possible to reveal typical fatigue markings (for example, striations) after specimen exposure to the Alconox solution.

KEY WORDS: failure analysis, fractography, cleaning techniques, corrosion, cleaning agents, replication, fracture, steel

The metallurgist has found fractographic examination of fracture surfaces to be a valuable tool in failure analysis. A meaningful examination, however, may not be possible if the fracture surfaces become contaminated with grease, oil, debris, oxidation, and corrosion products. Typical cleaning practices include the use of a dry air blast, organic solvents (such as acetone, toluene, and alcohol), and repeated stripping of cellulose-acetate replicas. These procedures are useful in the removal of loosely adhering particles, grease, and oils, whereas more tightly bonded oxidation and corrosion products require more aggressive removal methods. Several previous studies [*1,2*]

[1]Swiss Aluminium Ltd. Co. Fellow, and New Jersey Zinc Professor of Metallurgy, respectively, Lehigh University, Bethlehem, Pa. 18015.

have demonstrated the effectiveness of acid-based corrosion removal techniques. For example, Kayafas [*2*] has shown that cleaning with an inhibited hydrochloric acid pickling solution yields adequate fractographic results on the internal surface of hydrogen blisters in pipe line steel. Lohberg et al [*3*] have reported success in removing oxidation products from ferritic materials using a deoxidizing agent known as Endox. In addition, Zipp [*4*] has recommended that if the benign cleaning methods (air blast, organic solvents, and repeated replica stripping) are unsuccessful in the removal of tightly bonded oxidation and corrosion products, then the fracture surface could be cleaned in the following manner: submerge the sample in a water-based detergent (15-g Alconox powder[2] + 350 cm^3 water) heated to 90°C and agitated in an ultrasonic cleaner for 30 min.

The object of this study is to evaluate the effectiveness of the cleaning procedure recommended by Zipp. To this end, a comparison is made of fracture markings from surfaces of as-fractured samples and corroded samples which were subsequently cleaned with the benign techniques and with the Alconox solution.

Experimental Procedures

The material chosen for this study was ASTM A36 bridge steel because of its wide commercial use in structures and its tendency for fracture surface deterioration in the presence of aggressive environments. Three different fracture mechanisms were generated and examined in an ETEC Autoscan scanning electron microscope (SEM) at an accelerating voltage of 20 keV. None of the surfaces was coated before viewing. Cleavage fracture was generated in simple tension at liquid nitrogen temperature. A fatigue fracture surface was generated by load-cycling a compact tension specimen at an R-ratio of 0.7 over a stress intensity factor range of 13 to 28 MPa $m^{1/2}$. Unstable crack growth in the remaining ligament of the fatigue sample led to the formation of microvoid coalescence.

The as-fractured samples were exposed to a corrosive environment of 5% salt water at 100°C for 2 h and then left exposed in room air (60% humidity) for 48 h. This resulted in the formation of corrosion products on the fracture surfaces. An energy dispersive X-ray analysis using a Tracor Northern 1710 system was performed to examine the nature of corrosion products resulting from the salt water exposure and reaction products which might have resulted from the Alconox cleaning treatment. In addition to the laboratory-generated fracture surfaces a polished metallographic section was treated in the Alconox solution for different lengths of time (15 and 30 min) and examined in the SEM.

[2]Alconox powder is a detergent made by Alconox Inc., New York, N.Y. 10003; ingredients are not available.

Results and Discussion

The typical appearance of the as-fractured samples is shown in Figs. 1*a* to 1*c*, which reveal examples of microvoid coalescence, cleavage, and fatigue striations, respectively, as developed in this material. Isolated regions of fracture through pearlite packets, as evidenced by the observed carbide and ferrite lamellae, were also noted on all fracture surfaces. A photomicrograph typical of all fracture regimes in the corroded condition is shown in Fig. 1*d*. This photograph clearly illustrates how difficult it is to examine a corroded fracture surface for evidence of specific micromechanisms of failure. After use of the benign cleaning techniques some oxidation and corrosion product remained on the surface, though the microvoid coalescence and cleavage regions (Figs. 2*a* and 2*b*) could be identified. The fatigue-damaged region did not lend itself to easy analysis owing to the persistent corrosion products found on the fracture surface (Figs. 2*c* and 2*d*).

Figure 3 shows the appearance of the fracture surfaces after being cleaned with Alconox solution; much of the corrosion debris remaining after the standard cleaning procedure was removed, though there is evidence that the fracture surfaces were etched by the Alconox. Note the considerable presence of pearlite colonies on the fracture surfaces (see especially Figs. 3*b* and 3*c*). As a result, the interpretation of fatigue fracture markings is greatly complicated by the simultaneous presence of parallel lamellae within the etched pearlite regions and parallel fatigue striation markings. Some parallel fracture surface markings were verified as fatigue striations by matching their spacings with the striation spacings predicted from the prevailing stress intensity factor conditions associated with the fatigue test [*5*]. Fatigue striations were also differentiated from most pearlite lamellae, since the striations were generally parallel to the advancing crack front whereas pearlite lamellae assumed a random orientation relative to the crack front. Overall, however, it was difficult to make a reliable determination of striations on the fatigue fracture surfaces; while much of the corrosion products were removed, the etching introduced complicating surface artifacts.

In general, it was found that the fatigue surfaces exhibited the poorest response to corrosion removal techniques. Other experiences in our laboratory have shown similar results with failed turbine disks.[3] Here, intergranular failure was easily identified, while evidence for fatigue damage remained obscured after both fracture zones were cleaned with the benign techniques. It appears that these cleaning techniques are most effective in removing corrosion products from morphological features that exhibit long-range flatness (that is, 20 to 40 μm). The (100) cleavage facets in body-centered-cubic materials, the side walls of the larger microvoids, and the intergranular facets all exhibit such long-range flatness and appear to clean more easily than the fa-

[3]Unpublished research, Lehigh University, Bethlehem, Pa. 18015.

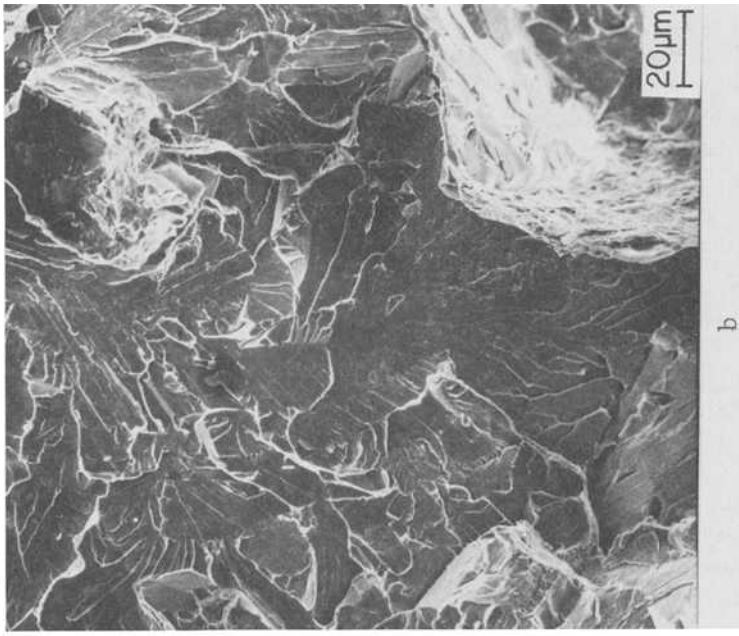
20μm
b

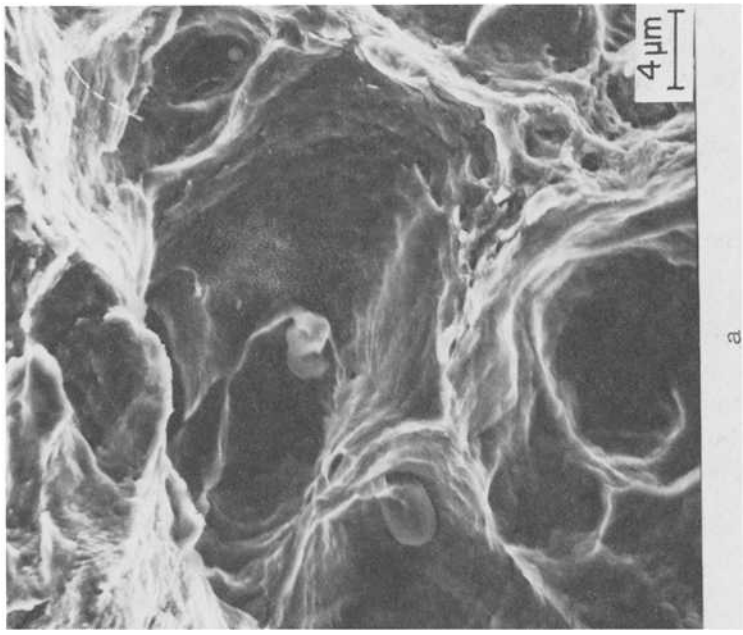
4μm
a

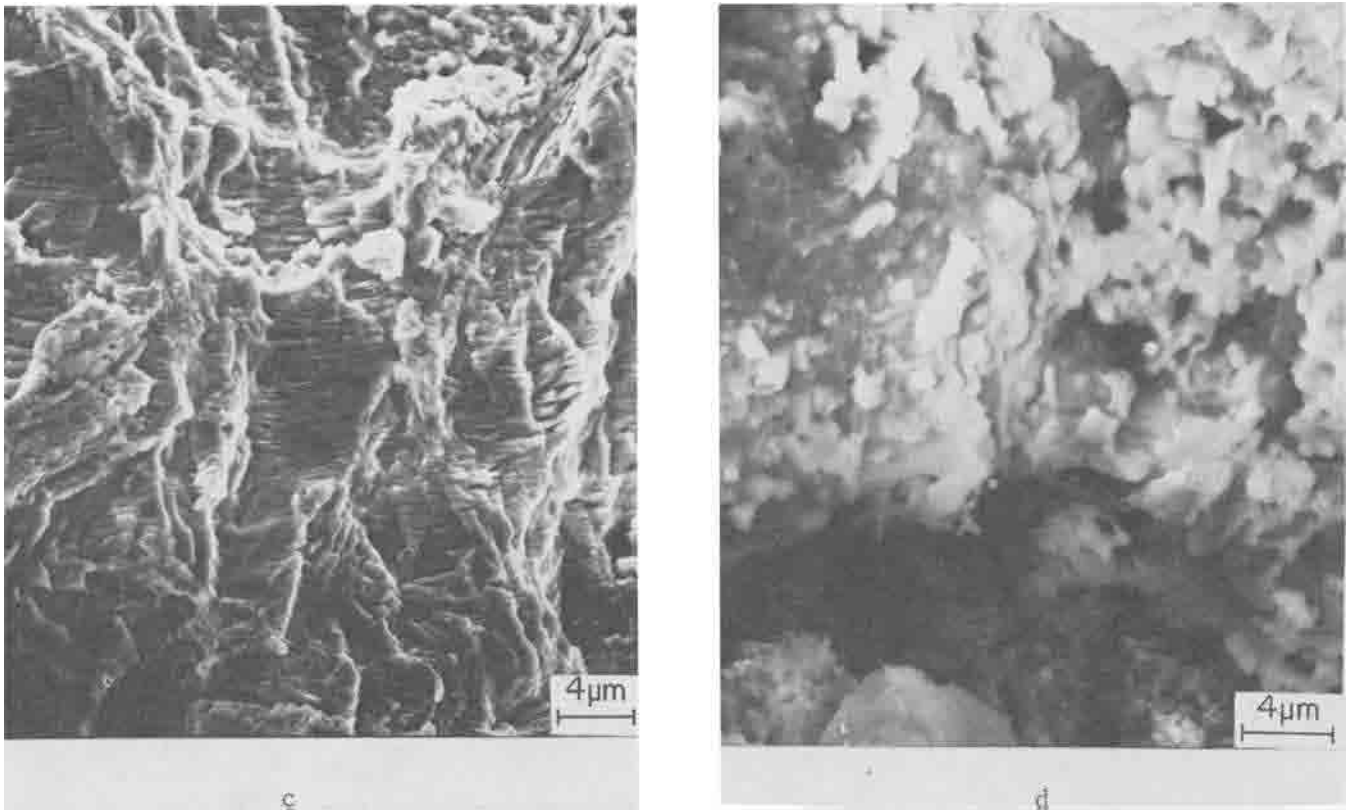

FIG. 1—*Photomicrographs of the as-fractured and as-corroded surfaces*: (a) *microvoid coalescence*, (b) *cleavage*, (c) *fatigue striations, and* (d) *typical appearance of fracture surfaces after salt water exposure.*

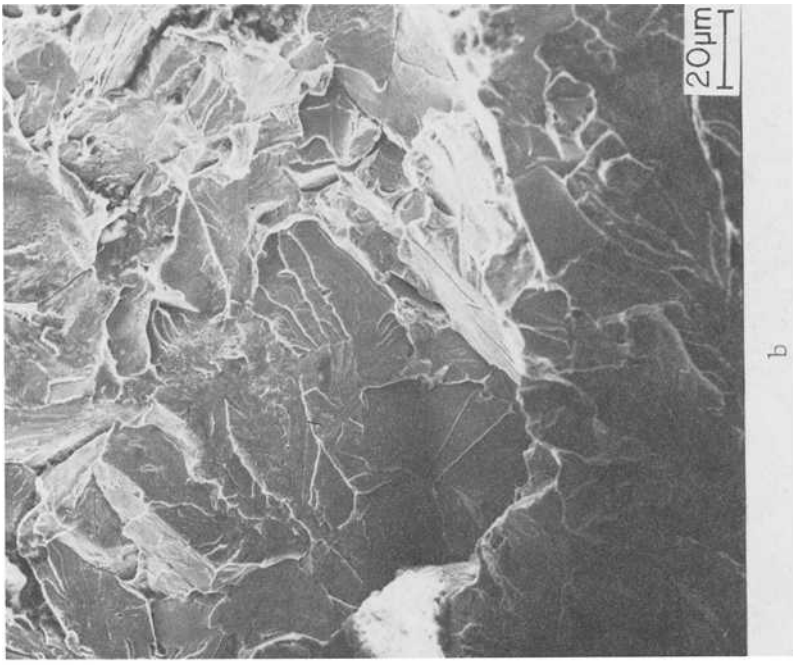
20μm
b

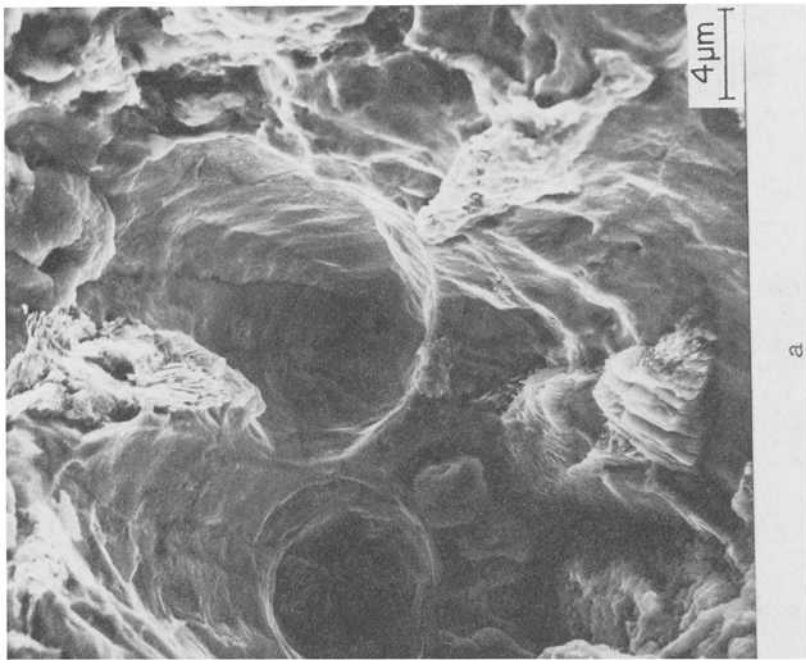
4μm
a

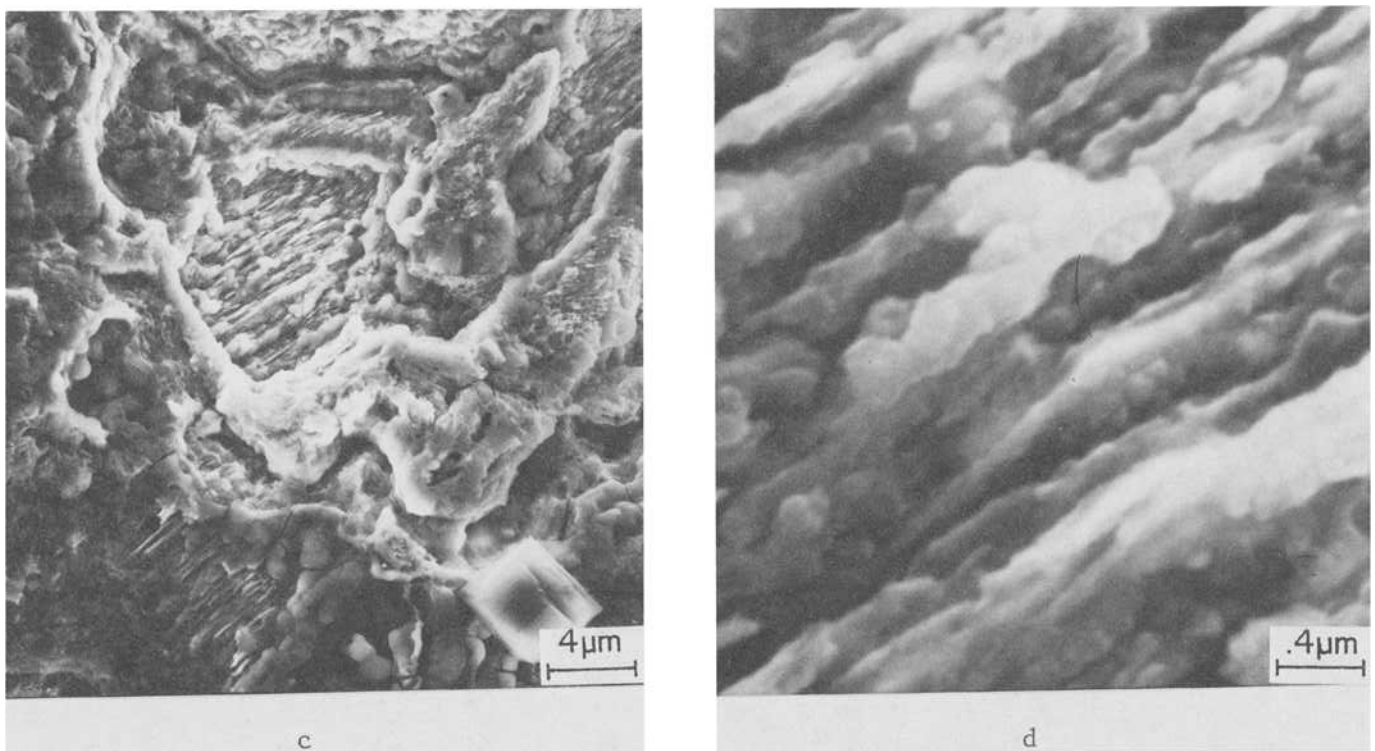

FIG. 2—*Fracture surface appearance after cleaning by benign techniques.* (a) *Microvoid coalescence.* (b) *Cleavage.* (c) *and* (d) *Fatigue striations.*

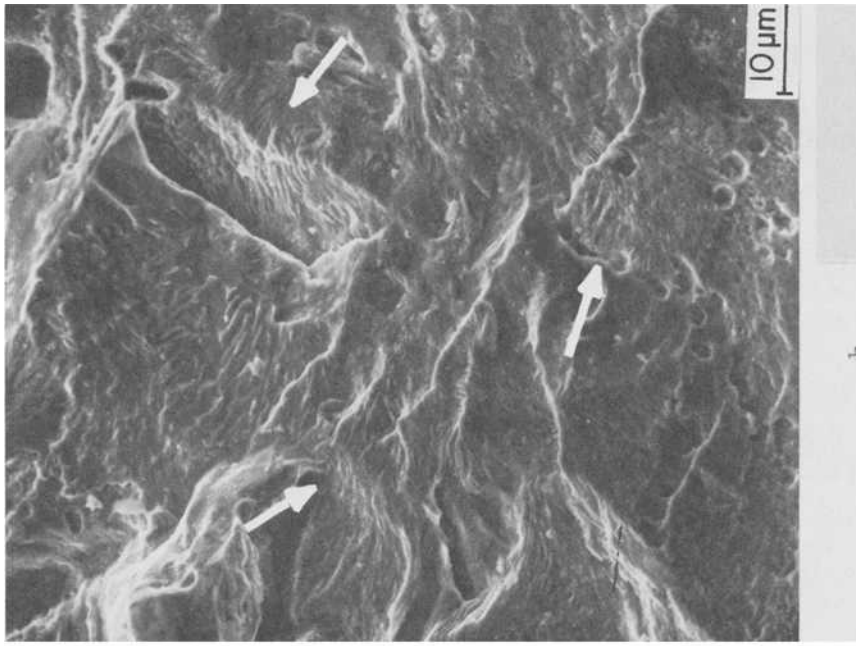
10 μm
b

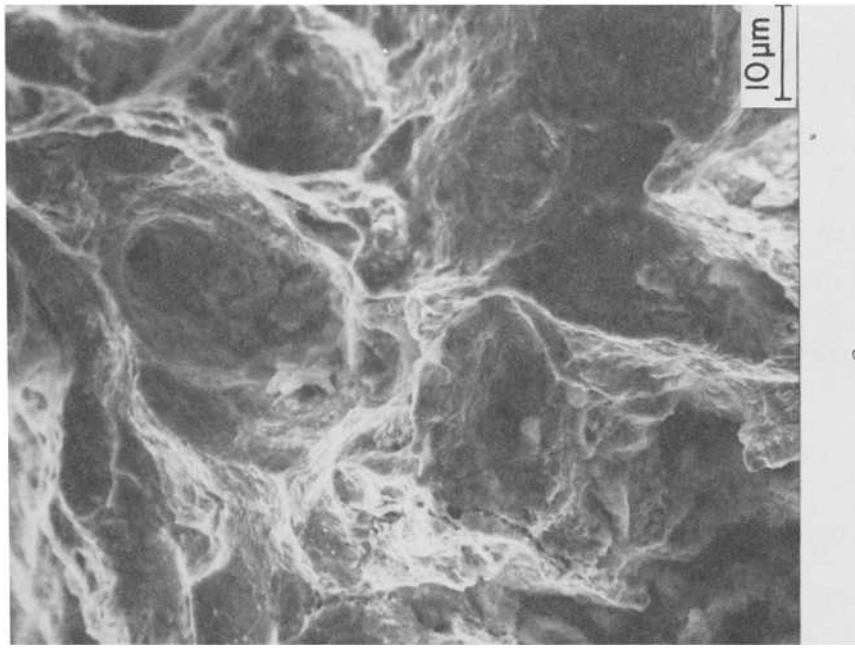
10 μm
a

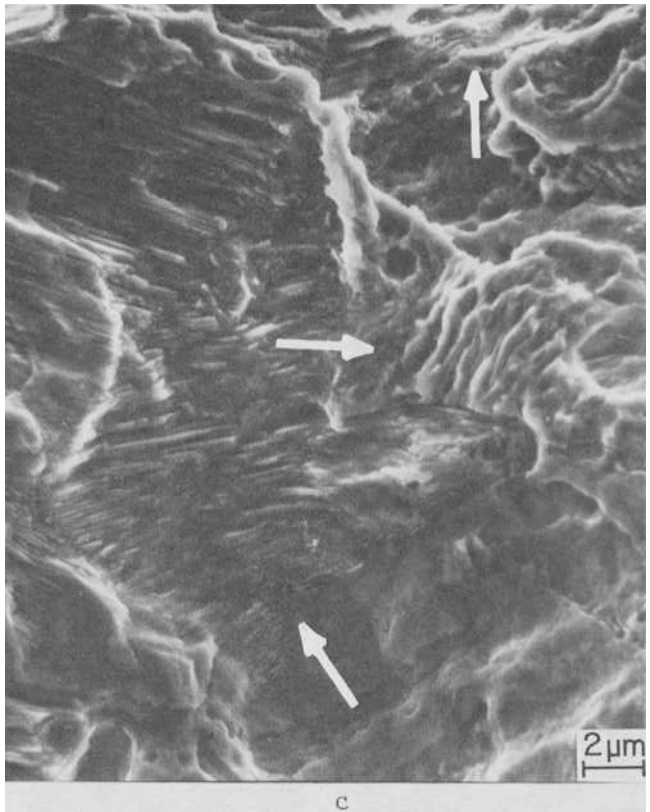

FIG. 3—*Typical fracture surface appearance following cleaning in Alconox solution.* (a) *Microvoid coalescence.* (b) *Cleavage.* (c) *Fatigue fracture region. Note considerable cleavage and evidence of pearlite on fatigue fracture surfaces (see arrows).*

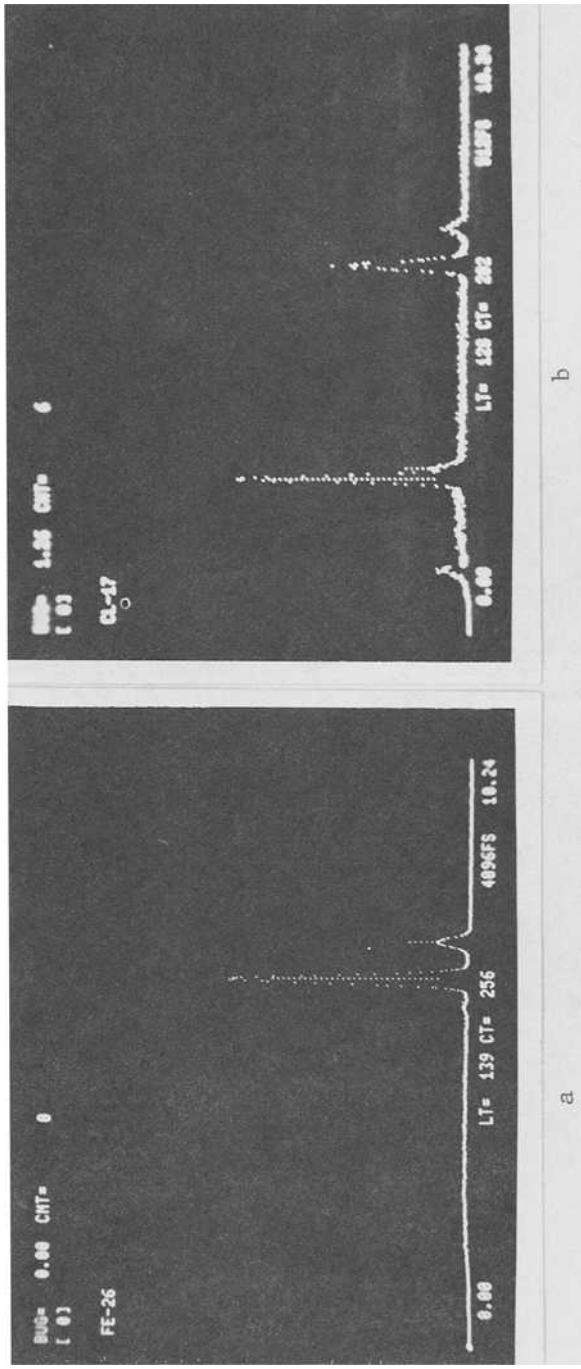
BUG= 0.00 CNT= 0
[0]
FE-26
0.00
LT= 139 CT= 256
4096FS 10.24
a
[0]
Cu-Kα
0.00
LT= 139 CT= 288
b

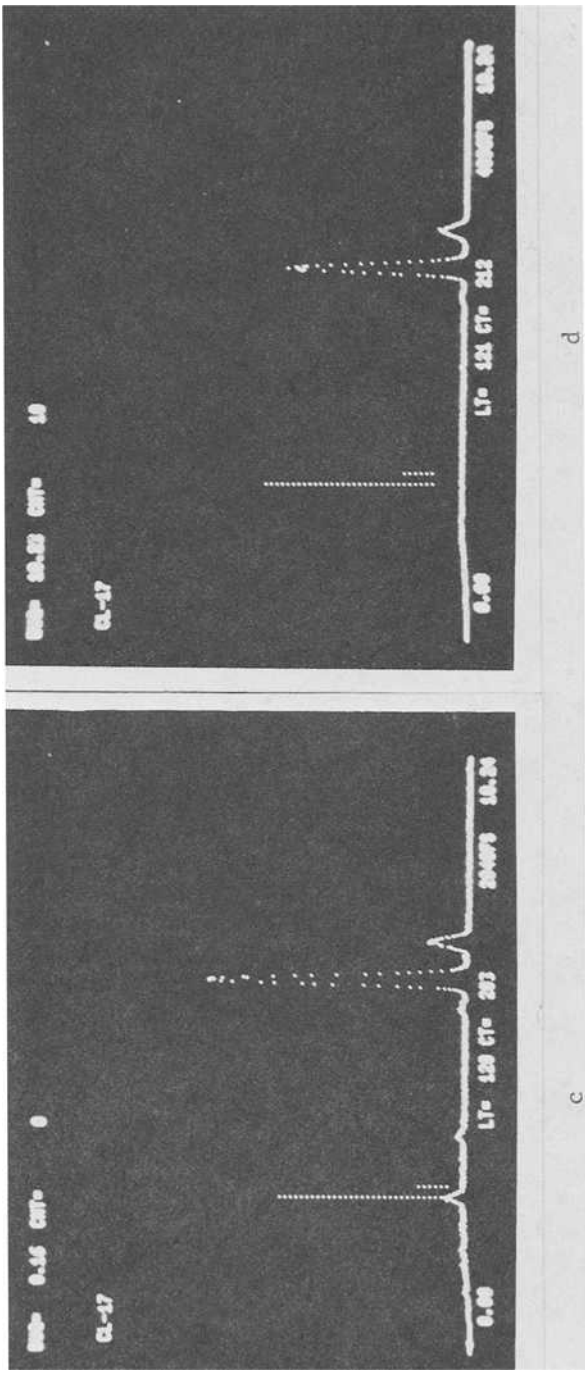

FIG. 4—*Photospectragraphs of* (a) *as-fractured surface,* (b) *as-corroded surface,* (c) *after being cleaned with benign techniques, and* (d) *after being cleaned in Alconox solution. Note the chlorine peak after cleaning by benign procedures and the absence of the peak following the cleaning in Alconox.*

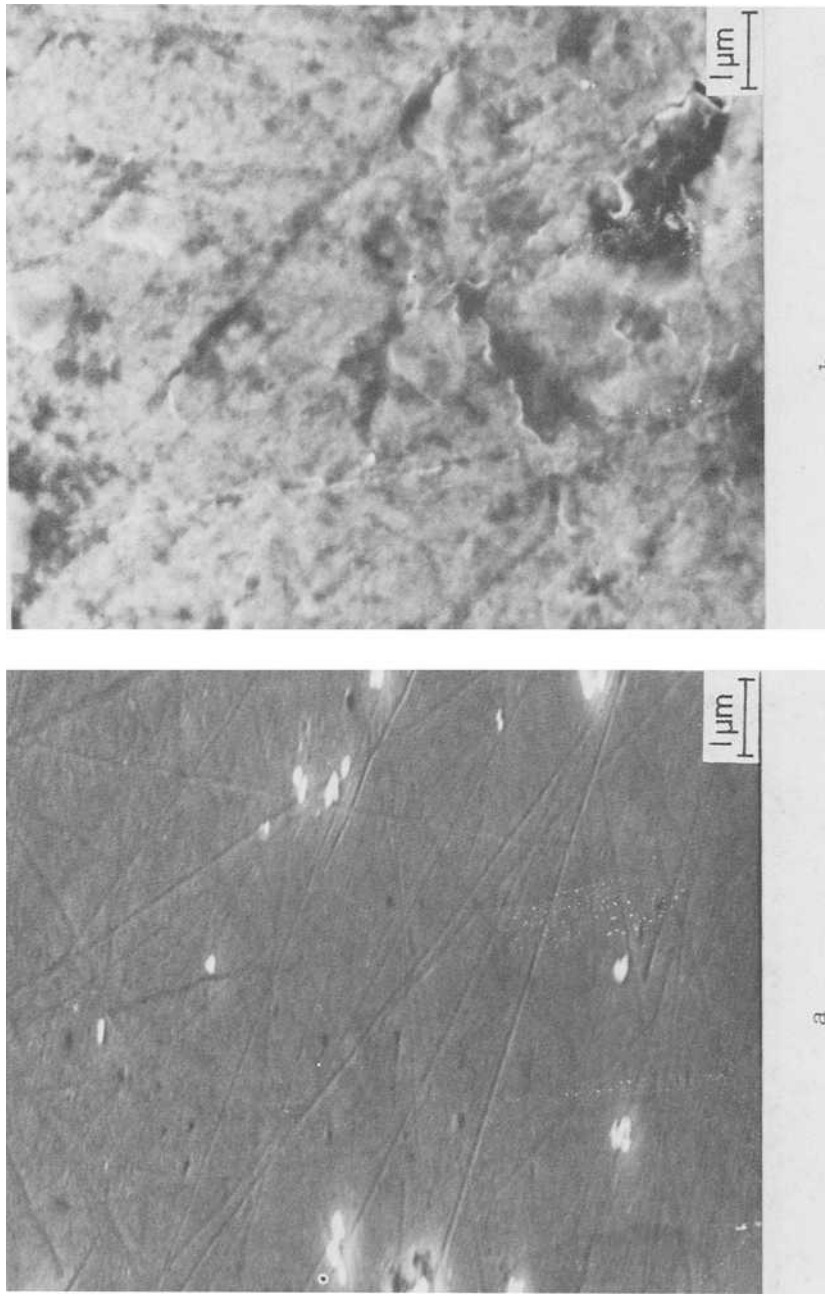
1 μm
1 μm
a
b

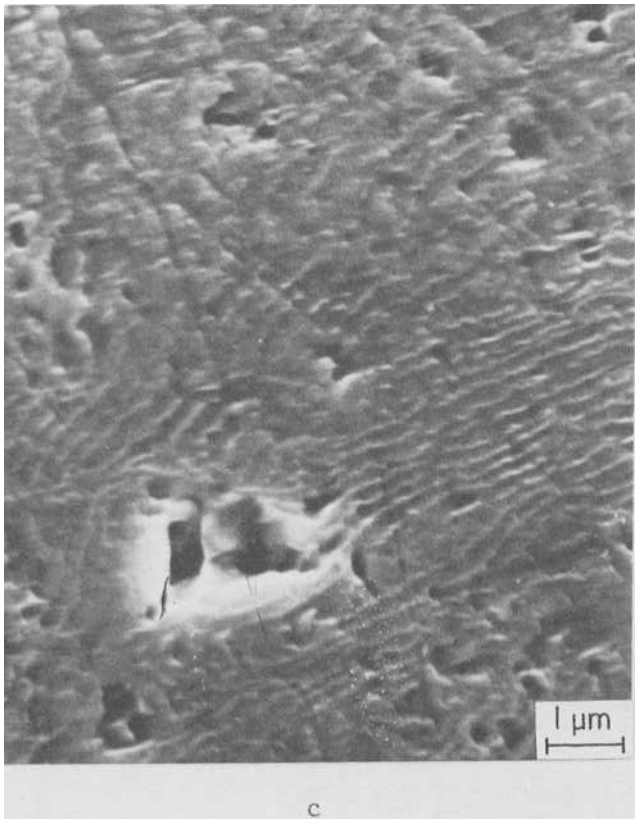

FIG. 5—*Photomicrographs of metallographically prepared section exposed to Alconox solution for different lengths of time.* (a) *As-polished.* (b) *After 15-min exposure.* (c) *After 30-min exposure. Note the extensive amount of pearlite revealed after the 30-min exposure.*

tigue fracture surfaces. By comparison, the size of fatigue striations are on the average one to two orders of magnitude smaller than these other fracture markings, and thus are more likely to be obscured by corrosion debris. If the benign cleaning techniques leave numerous corrosion-free regions on cleavage, microvoid coalescence, and intergranular fracture surfaces, then the absence of large corrosion-free regions may serve as an indication of the existence of fatigue damage. If this is the case, then these observations may aid in failure analysis. More studies are needed to clarify this point.

In many failure investigations an X-ray analysis is essential in determining the nature of fracture surface contaminants. Figure 4*b* indicates the presence of large amounts of chlorine on the fracture surfaces of the as-corroded samples. If this were an actual service failure, the chlorine peak would serve as a clue in determining the nature and possible source of the corrosive medium [*6*]. The presence of the corrosive environment may have contributed to the failure (that is, stress corrosion cracking or corrosion-assisted fatigue). After cleaning the surface by the benign techniques, small amounts of chlorine were still detectable (Fig. 4*c*). After use of the Alconox detergent, however, no indications remained of surface contaminants. Therefore it is suggested that if an X-ray analysis is indicated with failure examination, then use of the Alconox detergent should be avoided or deferred until after the analysis is completed.

To further study the nature of cleaning-induced damage, a metallographic section was examined after a 15-min detergent exposure. No pearlite colonies were revealed (Fig. 5*b*), though the surface exhibited a moderate degree of degradation. After a 30-min exposure in Alconox, pearlite colonies were clearly evident. Figure 5*c* shows dramatically how the surface of the metallographic section has been etched. We conclude that if cleaning in this detergent is necessary for the purpose of a fractographic examination, the exposure time should be limited to 15 min.

Conclusions

Based on the results of this investigation, the following conclusions have been reached:

1. Benign cleaning techniques are effective in the removal of loosely adhering particles, grease, and oils.
2. Fatigue-damaged surfaces exhibited the poorest response to the benign cleaning techniques. Based on this observation, identification of mechanisms responsible for fatigue damage may be difficult and unreliable when the fracture surface is obscured by corrosion debris.
3. Cleaning in Alconox detergent removes most tightly adhering oxidation and corrosion debris, though there is evidence that this procedure results in etching the surface. This degradation complicates the interpretation of fatigue-damaged regions.

4. If cleaning in Alconox detergent is necessary for the purpose of a fractographic examination, the exposure should be limited to 15 min.

5. Insomuch as Alconox detergent removes most surface contaminants, dispersive X-ray analysis should be completed before such cleaning.

Acknowledgments

This work was supported in part by the Materials Research Center and the Department of Metallurgy and Materials Engineering, Lehigh University, Bethlehem, Pennsylvania, and Swiss Aluminium Ltd. Co., Zurich, Switzerland. The authors wish to acknowledge the help of Steve Paterson and Raymond Stofanak for their valuable discussions and assistance.

References

[1] DeLeiris, H. et al, *Mem. Scient. Rev. de Met.*, Vol. 63, May 1966, pp. 463-472.
[2] Kayafas, I., *Corrosion NACE*, Vol. 36, No. 8, Aug. 1980, pp. 443-445.
[3] Lohberg, R. et al in *Microstructural Science*, Vol. 9, Elsevier-North Holland, New York, 1981, pp. 421-427.
[4] Zipp, R. D. in *Scanning Electron Microscopy I*, SEM Inc., AMF O'Hare, Ill., 1979, pp. 355-362.
[5] Bates, R. C. and Clark, W. G., Jr., *Transactions of the American Society for Metals*, Vol. 62, No. 2, 1969, p. 380.
[6] Ballard, D. B. and Yakowitz, H. in *Scanning Electron Microscopy 1970*, IITRI, Chicago, Ill., April 1970, p. 32.

Metals

Applied Fractography

Ray V. Dainty[1]

Use of "Marker Blocks" As An Aid in Quantitative Fractography in Full-Scale Aircraft Fatigue Testing: A Case Study

REFERENCE: Dainty, R. V., **"Use of "Marker Blocks" As An Aid in Quantitative Fractography in Full-Scale Aircraft Fatigue Testing: A Case Study,"** *Fractography of Ceramics and Metal Failures, ASTM STP 827*, J. J. Mecholsky, Jr. and S. R. Powell, Jr., Eds., American Society for Testing and Materials, 1984, pp. 285-308.

ABSTRACT: Damage tolerant design criteria and the current use of random or flight-by-flight loading methods in the full-scale testing of aircraft structures have necessitated the development of new techniques for acquiring accurate fatigue crack growth information from fracture surface analysis. This paper describes a technique that utilized a 64-cycle constant-amplitude "marker block", in an otherwise random load spectrum of 4469 cycles, to derive fatigue crack growth data from an aluminum alloy spar cap and two wing skin rivets. The presence of an undetected incipient crack in the spar cap, from a previous full-scale test, provided an opportunity of accounting for the entire random loading crack growth history in terms of the "marker band" spacings. It was possible to identify the marker bands in the scanning electron microscope at relatively short crack lengths of 2.6 mm for the spar cap and 0.5 mm for the rivets. A total of 89 of the 90 marker blocks applied in the test were accounted for on the spar cap fracture surface. Examination of the rivet fracture surfaces revealed 12 and 8 marker bands, respectively, over crack lengths of some 3 mm.

KEY WORDS: quantitative fractography, full-scale aircraft fatigue testing, random, spectrum, flight-by-flight loading, marker blocks, marker loads, marker bands, fatigue crack propagation, aluminum alloys, scanning electron microscopy

Although a considerable amount of research has been carried out in recent years to explain many of the fundamental aspects of fatigue crack propagation (FCP) and striation formation [*1-6*], one of the major challenges that still confronts engineers and researchers is the procurement of accurate fatigue

[1]Senior Technical Officer, Structures and Materials Laboratory, National Aeronautical Establishment, National Research Council of Canada, Ottawa, Ontario.

crack growth information from fracture surface analysis. The fractographic derivation of FCP rates is entirely dependent upon the fractographer's ability to correlate accurately the striated fracture surface topography with the test or service loads. In order to satisfy current damage tolerant design criteria that require the experimental determination of crack growth rates for various aircraft components, specialized techniques may have to be developed. The desirability of this type of FCP data in the aircraft industry is reflected in a United States Air Force (USAF) military specification [*7*] that states "At the end of the full-scale durability test.... This inspection shall include disassembly and laboratory-type inspection of critical structural areas.... Fractographic examinations shall be conducted to obtain crack growth data and to assist in the assessment of the quality of the airframe...."

The Structures and Materials Laboratory of the National Aeronautical Establishment (NAE) has been involved in several full-scale aircraft fatigue tests and has been called upon to derive fatigue crack growth data by fractographic means [*8,9*]. In addition, numerous failed components have been submitted to the laboratory from both test and service loading environments by several aircraft and industrial manufacturing, operational, and maintenance organizations for quantitative fatigue fracture analysis [*10,11*]. Several of the analyses have involved components that have been tested under constant-amplitude or programmed block loading conditions. Figure 1 is an example of a programmed block spectrum where the fatigue loads are applied in a repetitive sequence with a discrete number of cycles at each of the individual load levels. As in the case of constant-amplitude fatigue tests, numerical analysis of this type of fracture surface is relatively straightforward, since the load cycles at the various load levels can be identified in the electron microscope by their respective fatigue striation spacings. By measuring the load block spacings along the length of the fatigue crack it is possible to relate crack growth rates to crack length and to estimate the time of crack initiation.

With the development of computer-controlled fatigue loading equipment, recent tests have utilized what are termed "random", "spectrum" or " flight by flight" loading techniques to simulate service loading conditions. This randomization of the application of load cycles has, however, created new problems similar to those generally encountered in the quantitative analysis of fracture surfaces from service fatigue failures. These problems include identifying and correlating the randomly spaced striations on the fracture surface with the specific loads that were applied during the test. This identification and correlation can be extremely difficult particularly when a complex load spectrum, consisting of a large number of cycles at various levels and amplitudes, is involved. Generally with this type of load spectrum not all load cycles will create an increment of crack growth that can be readily distinguished and accounted for even at the relatively high magnifications of an electron microscope. In addition, load interaction effects may cause "retardation" that may significantly arrest crack growth for several subsequent load cycles.

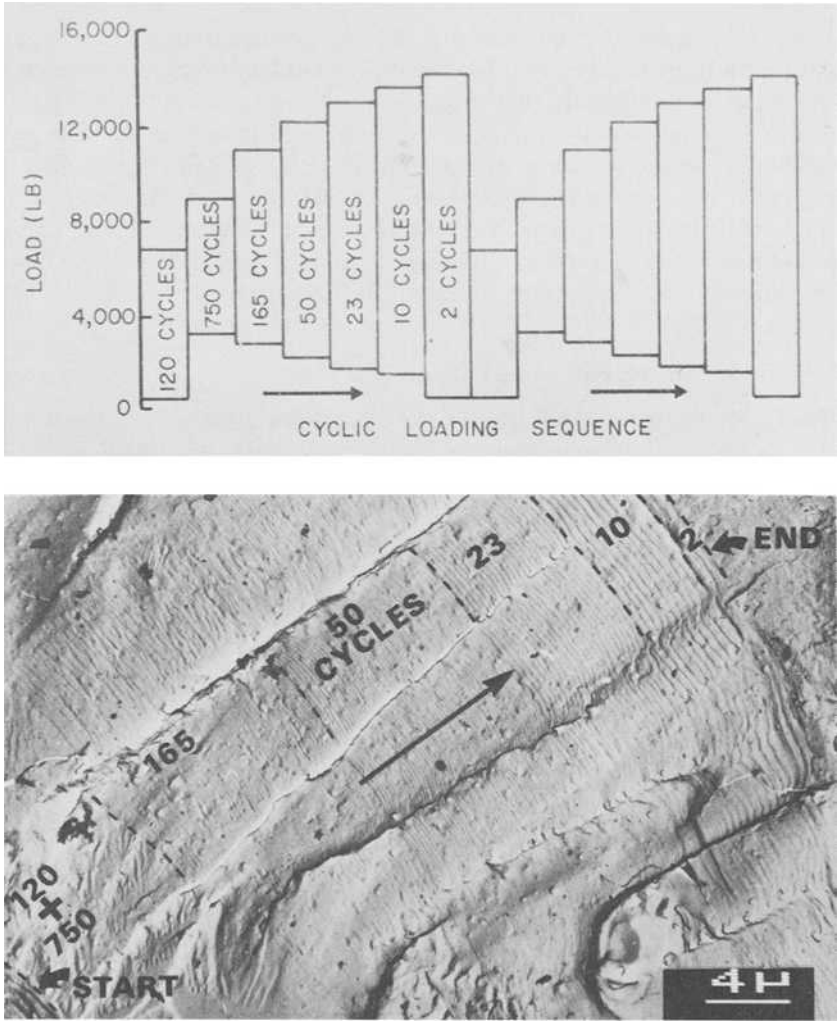

FIG. 1—*Programmed block fatigue load spectrum.*

One solution to these problems in a full-scale aircraft fatigue test conducted at NAE in 1976 was to use a "marker block". This marker block consisted of a specific number of constant-amplitude load cycles, at an intermediate level, that were applied periodically in an otherwise random load spectrum. The purpose of the marker block was to provide, after crack initiation, an identifiable region of crack growth (marker band) that would appear periodically across the fracture surfaces. It was recognized that the sequential application of the marker block load cycles would be a distortion of the random program that might affect overall FCP rates and crack initiation times.

However, it was felt that the potential benefits of acquiring accurate crack growth data from a fracture surface analysis would outweigh the estimated relatively small discrepancy that might occur. These data would be particularly useful in the case of an unobserved component failure or if it were not possible or practical to measure accurately the crack growth visually. By using the scanning electron microscope (SEM) to identify the marker bands and to measure their successive spacings it was possible to determine fatigue crack growth rates and to estimate crack initiation times that otherwise might have been difficult, if not impossible, to establish.

CL-41 Tutor Aircraft Full-Scale Fatigue Test

The CL-41 Tutor aircraft is used by the Canadian Forces in a "trainer" role and in an aerobatic display referred to as the "Snowbird" role. Although it is not the intent of this paper to elaborate on all the fatigue test parameters, some explanation of the test load spectra is necessary so that the entire crack growth history of the failed components may be fully explained by the fractographic observations [*12*].

The entire fatigue test consisted of two tests involving two separate load spectra both derived from flight accelerometer data. During the first phase of the test, fatigue loads equivalent to 30 000 "trainer" flying hours were applied to the aircraft structure. At the conclusion of 30 000 h,visual and dye penetrant inspection of the rear half lower spar cap area of the port wing did not indicate the presence of a crack although subsequent fractographic examination revealed that a crack did exist at this time. The second phase of the test involved a load spectrum derived from the same aircraft type flown in the "Snowbird" role. Table 1 lists some of the Snowbird load spectrum details, with the 20 intervals of 4469 cycles representing 100 equivalent Snowbird flight hours. A major difference between the first and second phase of the fatigue test, and of paramount importance with respect to the fractographic analysis, was the load application format. While the first phase used a repetitive lo-hi-lo load application block form, the second phase utilized a spectrum in which 4405 cycles in each 100 equivalent flight hour load block were computer generated in a random sequence. The remaining 64 load cycles (Interval 10, Table 1) were utilized as a constant-amplitude "marker block" that was applied as the concluding segment of each 100-h load block. The 64 cycles of Interval 10 were selected for the marker block sequence as a result of previous fatigue investigations. These investigations established that even at relatively small crack lengths of some 2 mm, the marker bands were discernible in the electron microscope. Figure 2 shows the command signal for a portion of the Snowbird test spectrum, including the 64-cycle marker block sequence, and a portion of a typical well-defined "marker band" as observed in the SEM. It is clear from this series of fractographs that at the lower magnifications the marker band appeared as a relatively flat, featureless increment of

TABLE 1—*Snowbird test load spectrum.*

TOTAL CYCLES PER BLOCK	4469
EQUIVALENT FLIGHT HOURS PER BLOCK	100
ESTIMATED SPAR CAP STRESS	18.8 MPa (2.727 KSI) PER G

Interval	G Load Max.	G Load Min.	Cycles Per Block	Miner's Rule Estimate of Fatigue Damage (% Per Block)
1	8.231	-2.000	1	0.8
2	7.798	-2.000	2	1.3
3	7.461	-2.000	5	2.8
4	7.123	-2.000	10	4.8
5	6.802	-2.000	16	6.5
6	6.491	-1.963	25	8.7
7	6.182	-1.602	34	9.1
8	5.873	-1.296	45	9.1
9	5.561	-1.034	55	8.4
10	5.252	-0.810	64	7.3
11	4.943	-0.615	76	6.4
12	4.632	-0.437	89	5.4
13	4.323	-0.269	109	4.8
14	4.013	-0.102	142	4.4
15	3.703	0.074	194	4.0
16	3.394	0.267	287	3.9
17	3.084	0.488	447	3.8
18	2.774	0.734	653	3.3
19	2.465	0.981	920	2.7
20	2.155	1.000	1295	2.5

crack growth. At the higher magnifications the presence of some 64 uniformly spaced striations unequivocally established that this band was formed during the application of the "marker block" interval of 64 constant-amplitude load cycles.

Fractographic Analysis

Spar Cap Failure: Specimen Preparation and SEM Examination Technique

Through periodic visual inspections a crack in the rear half lower main spar cap of the port wing was first observed at the conclusion of Block 21 (that is, after 2100 equivalent Snowbird flight hours). The crack length was reported to be between 3 and 6 mm in length at that time. The spar cap failed after 91 completed 100-h Snowbird load blocks plus approximately 1000 cycles of Block 92. It should be noted that from Block 73 to the conclusion of the test, the 2215 load cycles indicated in Intervals 19 and 20 in Table 1 were eliminated from the test spectrum in order to expedite the fatigue test. It was esti-

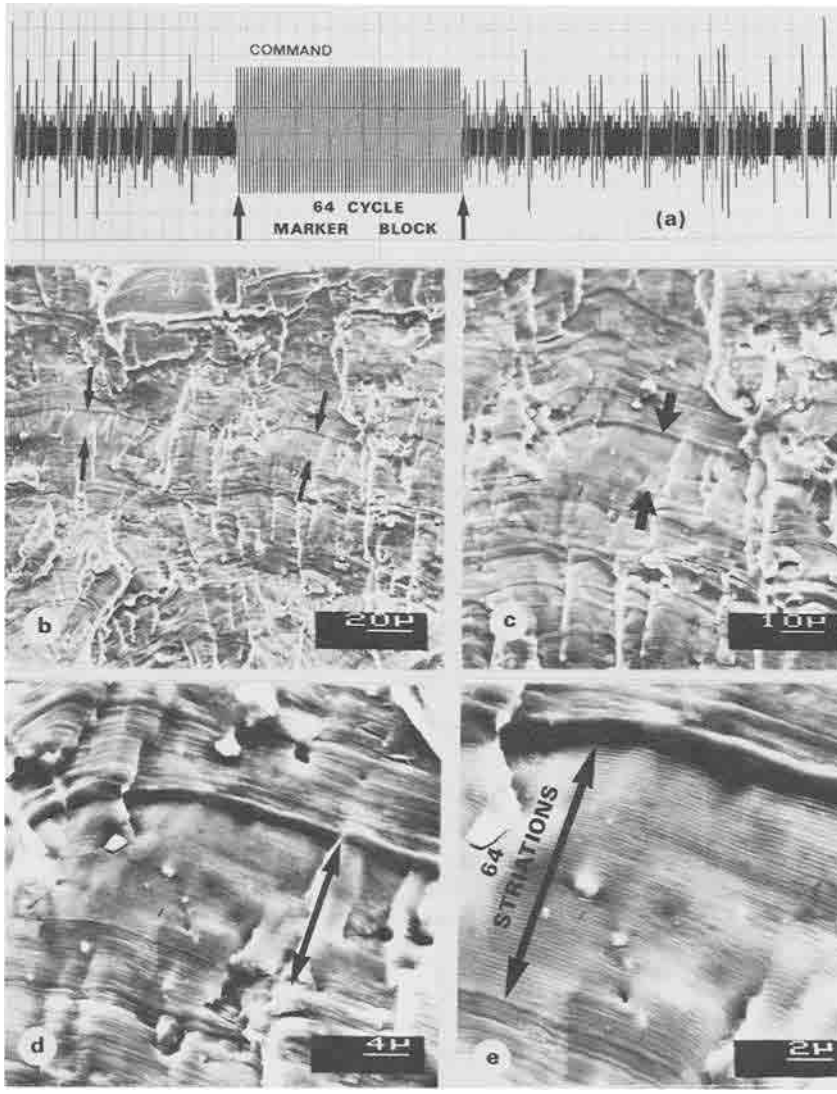

FIG. 2—(a) *Snowbird load spectrum with marker block.* (b) to (e) *Marker band as viewed on fracture surface A1, rivet 1 (arrows indicate marker band).*

mated that this truncation would result in a reduction of less than 5% of the accumulated fatigue damage from Block 73 to the end of the test. It should also be noted that for equipment calibration purposes the fatigue loads of the first 100-h block of the Snowbird spectrum were not applied in a random sequence but were applied in a block-type format similar to the interval groupings indicated in Table 1.

The failed 2024-T4 aluminum alloy extrusion spar cap section is shown in Fig. 3. To facilitate examination of the fracture surface in the SEM, the spar cap was sectioned into the three segments shown in Fig. 4. The striated surface was fractured, rather than cut, into the three lengths to preserve as much of the original fracture surface as possible for microscopic examination. The punch marks and scriber line evident on the fracture surface in Fig. 4 were used as reference marks so that the maximum crack length could be accurately recorded as the successive marker bands were observed in the SEM. This path generally coincided with maximum crack penetration as indicated by the curved macroscopic crack growth lines. The specimens were examined in a plane approximately normal to the electron beam and were periodically rotated in the horizontal plane so that specimen translation was generally along the path of maximum crack growth.

Since it was anticipated that the final marker bands formed on the fracture surface would be most easily identified, the location of the final marker band was established first. The distances between successive marker bands were then measured in the direction towards the crack initiation site.

Crack Initiation Area—As indicated by Arrows A in Figs. 3 to 5, crack initiation occurred in the region where the flange faired into the main body of

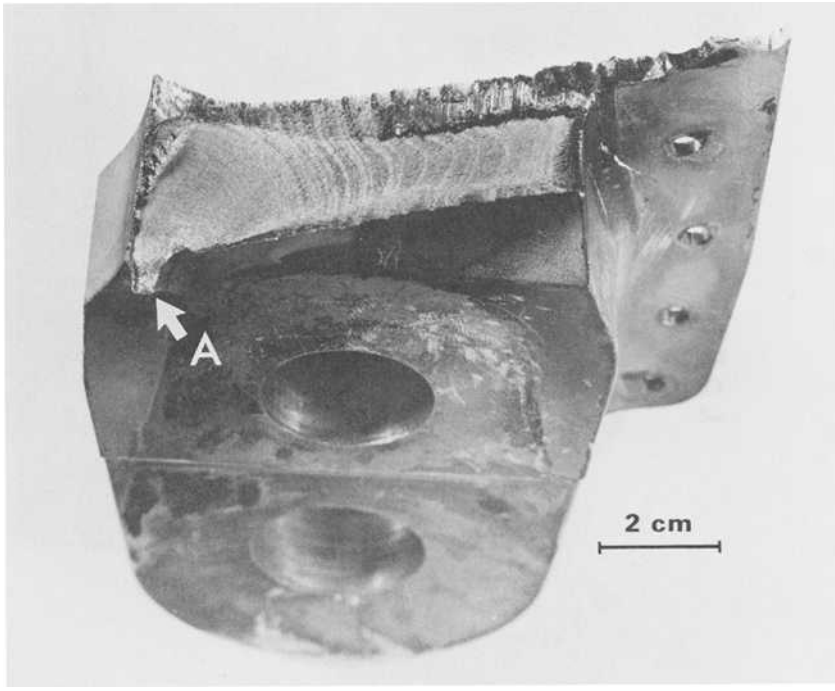

FIG. 3—*Failed spar cap section of 2024-T4 aluminum extrusion (Arrow A indicates crack initiation site).*

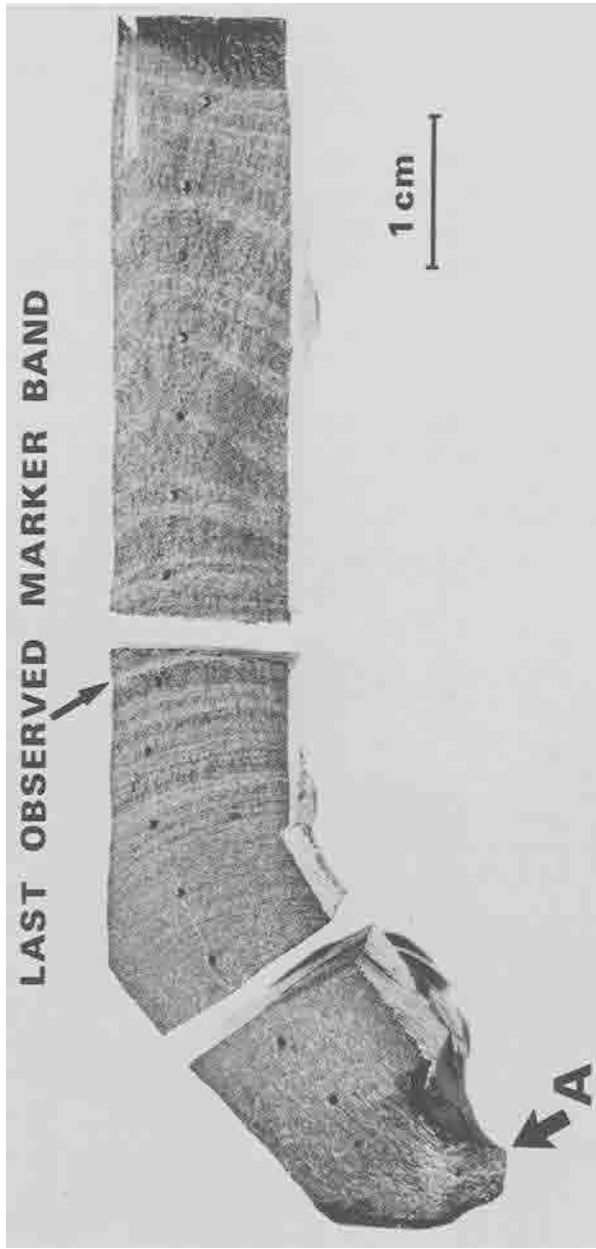

FIG. 4—*Fracture surface prepared for SEM examination.*

the spar cap. The first evidence of fatigue striations was observed in the SEM 0.3 mm from the crack initiation site. Further examination of the initiation area, up to approximately 2.5 mm from the crack nucleation site (Fig. 5), revealed well-defined fatigue fracture topography (Fig. 6). The regularity of these fatigue striations was somewhat unexpected, since it had been presumed that crack initiation had occurred during the second phase of the fatigue test (that is, in the Snowbird load spectrum) and therefore the spacings of the striations should have been of a random nature. Detailed examination of several of these regular repetitive bands of striations indicated that crack initiation occurred during the initial "trainer" phase of the fatigue test.

Figure 7 clearly illustrates an area of crack growth involving the transition from the trainer to the Snowbird phase of the fatigue test. Arrows A indicate the position of the crack front at the conclusion of the trainer phase of the test. The distance from A to B (Fig. 7*b*) represents the crack growth that occurred during the first 100-h Snowbird load block which as previously indicated, was applied in a block-type format. The distance from B to C represents the crack growth that occurred during the second Snowbird load block,

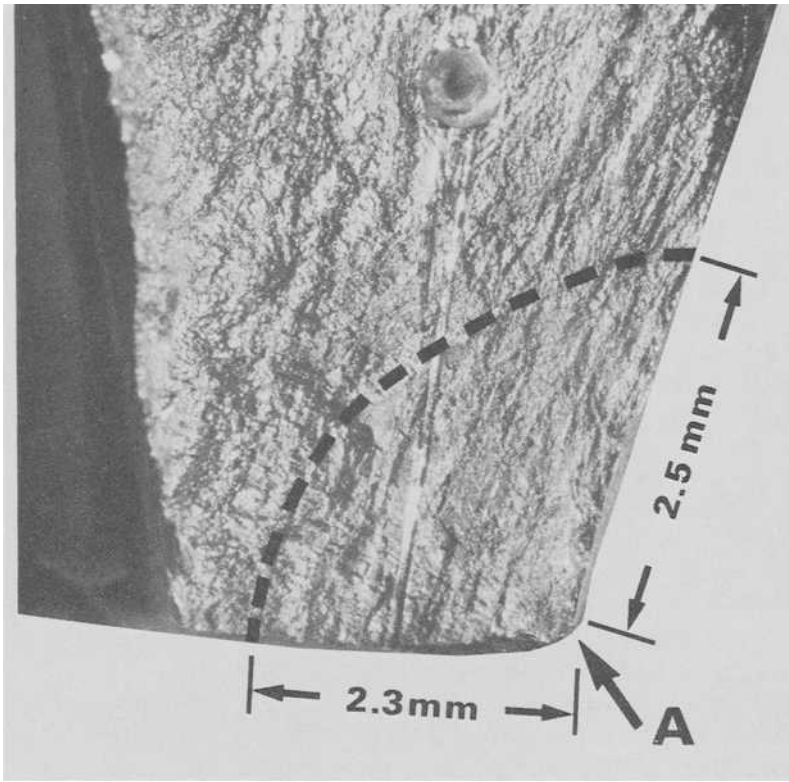

FIG. 5—*Fatigue crack initiation area of Trainer load spectrum.*

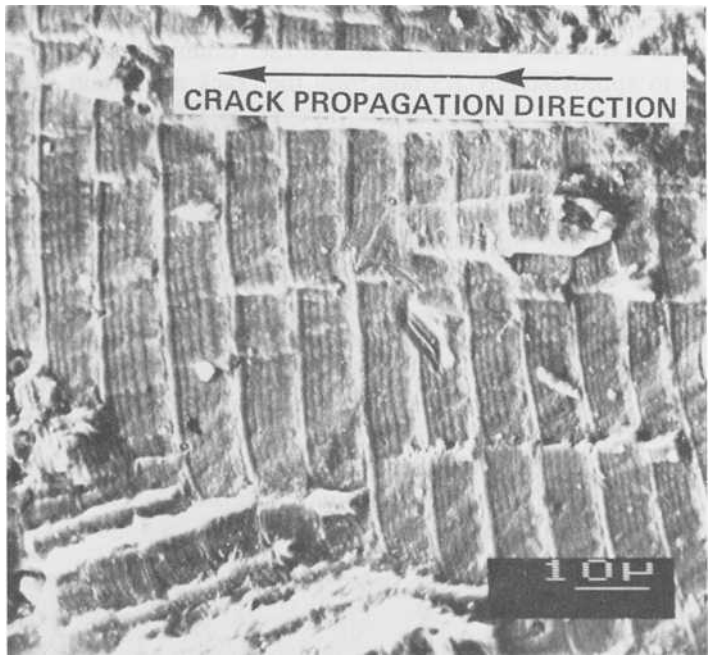

FIG. 6—*Fatigue striations of Trainer spectrum (2.4 mm from crack initiation site).*

which was the first block applied in the random format. Arrow C also indicates the location of the first observed "marker band" of 64 striations.

Marker Block Identification and Crack Propagation Rate Determination—Since it had been established that crack initiation and 2.5 mm of crack growth occurred during the "trainer" phase of the fatigue test, it followed that the 91 complete blocks plus approximately 1000 cycles of Block 92 of the Snowbird load spectrum were involved in crack growth from 2.5 mm to failure of the spar cap, some 83 mm from the crack initiation site. Thus 90 marker blocks were applied during this 80.5 mm of crack growth, since the first load block cycles were not applied in a random sequence. With these parameters established, the identification and location of the successive marker blocks were attempted to determine the crack propagation rate for the Snowbird portion of the fatigue test, and to establish how many of the 90 marker bands could be positively identified within a region of crack growth in which the entire load history was known.

The initial marker bands, located approximately 2.6 mm from the crack initiation site, appeared at lower magnifications as relatively flat, featureless regions (Fig. 8*a*). However, as indicated in Fig. 8*b*, an enlarged view of this marker band, 10.3 μm in width, revealed the presence of some 64 regularly spaced striations, with an average spacing of 0.16 μm. As expected, the aver-

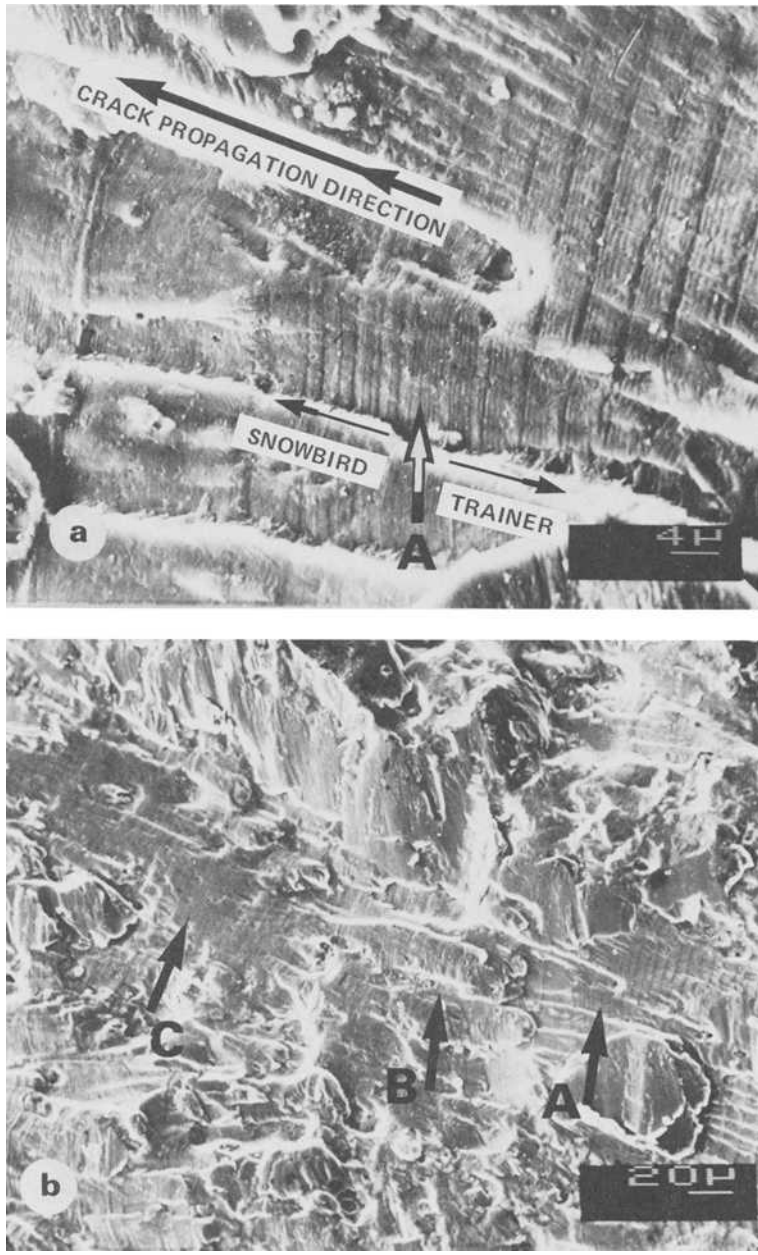

FIG. 7—*Trainer-Snowbird fatigue transition area (2.5 mm from crack initiation site).*

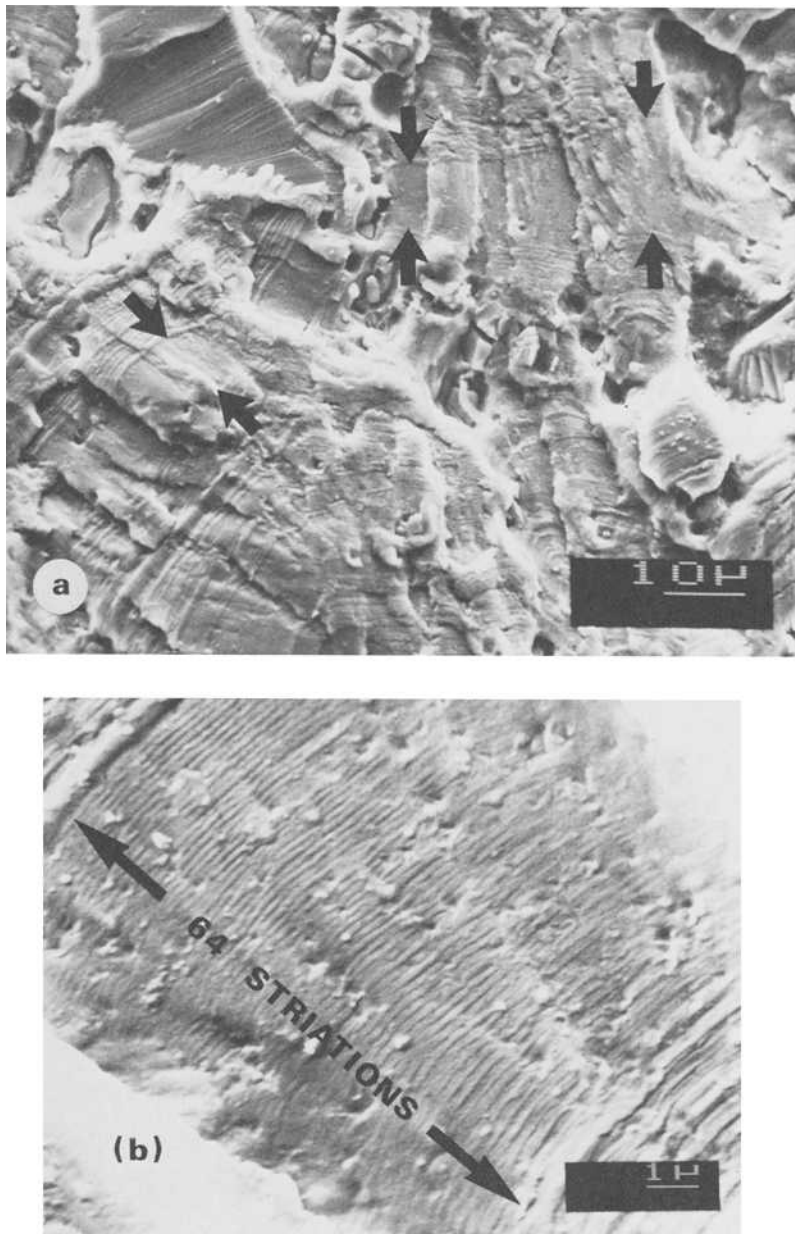

FIG. 8—(a) *First observed marker band of Snowbird spectrum (2.6 mm from crack initiation site).* (b) *Marker band width = 10.3 μm; average striation spacing = 0.16 μm.*

age width or increment of crack growth of successive marker bands increased with crack length. As the width increased, the overall clarity generally improved facilitating the identification of the 64 uniformly spaced striations within the marker band. It should also be noted that, as with constant-amplitude cycle striations, the width of an individual 64-cycle marker band across the fracture surface could vary by a factor of 2 or 3. These variations were probably associated with localized microstructural effects and crack front geometries. Figure 9 shows the last observed marker band, located approximately 42 mm from the crack initiation site (see Fig. 4). Some 64 striations are clearly resolved and extend over a crack length of approximately 76 μm, yielding an average spacing of 1.2 μm. For comparison purposes Fig. 10 shows a marker band located some 9 mm (formed during approximately load block 46) from the crack initiation site. This band is approximately 19 μm in width, with an average striation spacing of 0.3 μm. As indicated in Table 2, a total of 89 of the 90 marker blocks applied were sequentially identified during the traverse of the fracture surface.

In the general area of the last marker band it was observed that a relatively large portion of the fracture surface consisted of ductile dimples. These dimples would have been formed during periods of relatively rapid, unstable crack growth caused by the application of the higher level loads. Following the last marker band the fracture surface exhibited several lightly shaded macroscopic crack growth bands (Figs. 3 and 4). Examination showed that they contained well-defined fatigue striations, while the darker areas on either side of these regions consisted of ductile dimples. If it is assumed that the final observed marker band was formed during the application of load block 91, then it may be concluded that the striations in the lightly shaded regions following this marker band were formed during periods of relatively slow crack growth. Therefore it follows that these lightly shaded bands were formed during the application of the less severe loads in the 1000 cycles that were applied in Block 92 (truncated) immediately before final fracture of the spar cap. Based on this assumption, these final 1000 load cycles (approximately 50 equivalent flight hours) accounted for approximately half of the total crack length. Test log records tend to substantiate this conclusion, since they state that the crack had propagated approximately halfway through the spar cap at the conclusion of load block 91. From the successive marker band spacings, summarized in Table 2, and based on a final fracture time of 9150 equivalent flight hours, it was possible to derive a crack growth curve for the Snowbird portion of the fatigue test (Fig. 11). It should be noted that the 89th observed marker band listed in Table 2 was in fact formed during the application of the marker loads in Block 91.

Wing Skin Rivets

During the "Snowbird" phase of the test, two failed 2024-T31 aluminum alloy rivets (Fig. 12) from the starboard lower wing skin surface were exam-

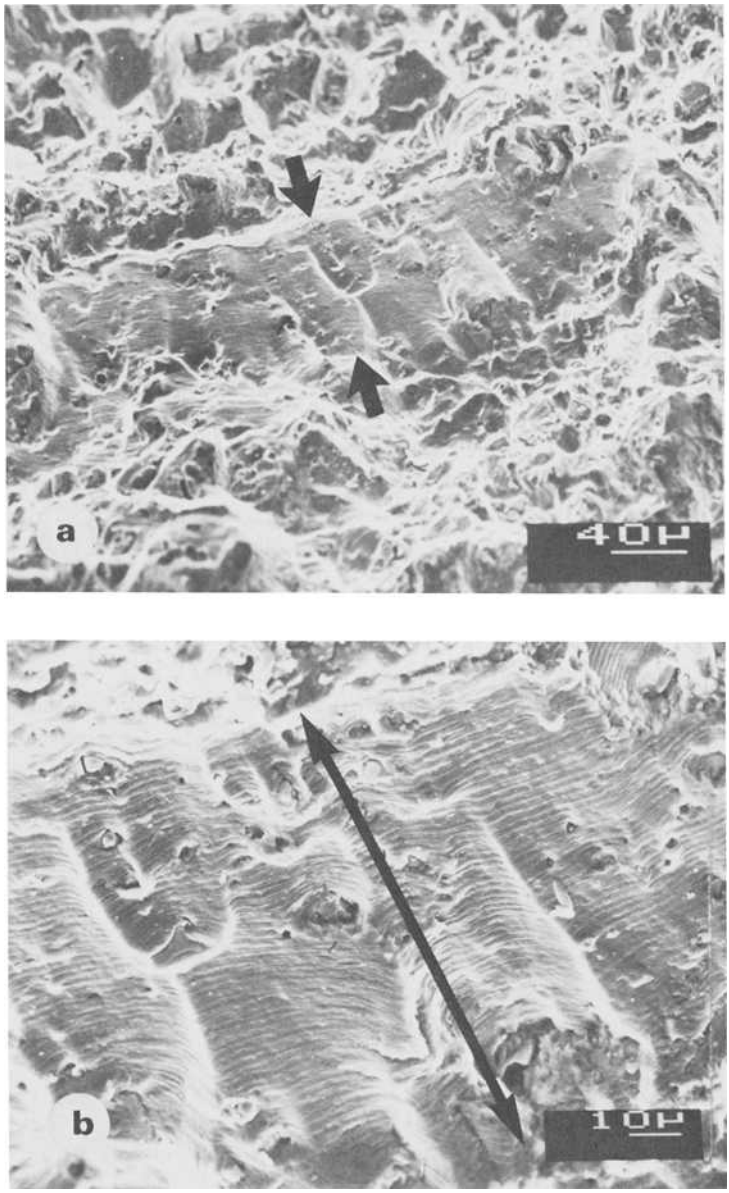

FIG. 9—(a) *Last observed marker band of Snowbird spectrum (42 mm from crack initiation site).* (b) *Marker band width = 76 μm; average striation spacing = 1.2 μm.*

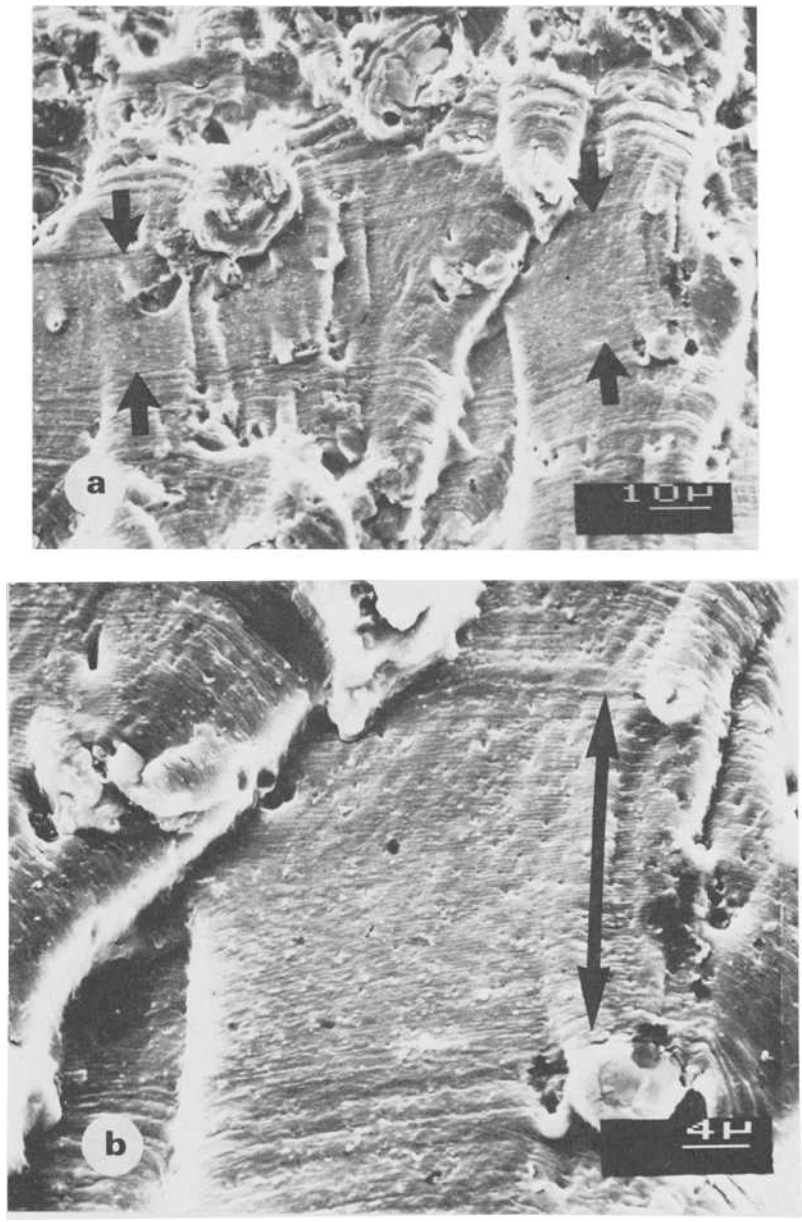

FIG. 10—(a) *Marker band of Snowbird load block 46 (9 mm from crack initiation site).* (b) *Marker band width = 19 μm; average striation spacing = 0.3 μm.*

TABLE 2—*Spar cap marker band locations.*

Marker Band	Distance From Crack Initiation Site (mm)	Marker Band	Distance From Crack Initiation Site (mm)
		62	12.9
*	2.5	64	13.5
5	3.3	66	14.2
10	4.0	68	14.9
15	4.6	70	15.7
20	5.1	72	16.6
25	5.6	74	17.6
30	6.2	76	18.7
35	7.0	78	20.1
40	7.8	80	21.8
42	8.2	81	22.7
44	8.6	82	23.5
46	9.0	83	24.6
48	9.4	84	25.8
50	9.9	85	27.0
52	10.3	86	28.4
54	10.8	87	30.2
56	11.2	88	33.0
58	11.8	89	42.0
60	12.3	**	83.0

* CRACK LENGTH AFTER 30,000 EQUIVALENT 'TRAINER' FLIGHT HOURS

** TOTAL FATIGUE CRACK LENGTH

ined. Apparently one of the 4.8-mm ($3/16$-in.) diameter rivets had failed during the application of load block 82 and the other was found during the subsequent inspection. Optical and SEM examinations established that both rivets had failed as a result of reverse bending fatigue. As indicated in Table 3, the SEM fractographic analysis of Rivet 1 revealed the presence of 12 marker bands along the 3.0 mm length of fracture surface A1, and 2 marker bands along the 1.2 mm length of fracture surface B1. A relatively narrow (0.4 mm) band of ductile dimples separated the two fatigue crack regions. Owing to reverse bending, the final marker band that formed immediately adjacent to the overload region on each fracture surface A1 and B1 (Bands 12 and 2 respectively, Table 3) would have formed simultaneously during the application of the last marker block load sequence prior to final rapid fracture. Simultaneous formation of the second last marker bands also would have occurred (that is, Band 11, Surface A1; and Band 1, Surface B1). Examination of Rivet 2 indicated similar results, with the identification of 8 marker bands along the 3.8 mm length of fracture surface A2 (Fig. 12*b*). Although no positive identification of a marker band could be made on the 0.8 mm length of fracture surface B2, this might have been owing to the severe damage that had been incurred on this portion of the fracture surface.

Although identification of the initial marker bands on the spar cap fracture surface was relatively straightforward, this generally was not the case for the rivets. Identification of several rivet marker bands, particularly those within

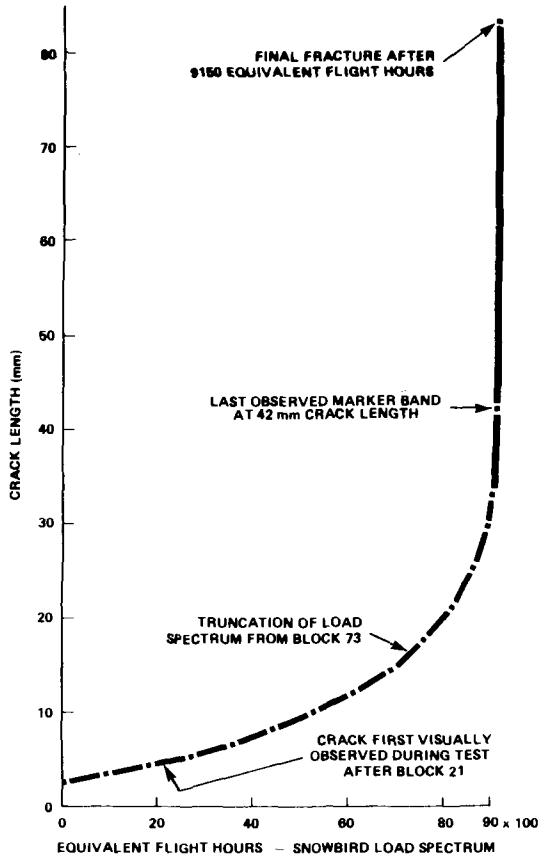

FIG. 11—*Spar cap crack growth history derived from marker band spacings.*

1 mm of the crack initiation sites, required meticulous examination at various specimen tilt angles and rotations. The examination did, however, reveal at least one or two reasonably well-defined segments of each marker band that contained approximately 64 uniformly spaced striations. In contrast, some marker bands in these same areas exhibited large regions of well-defined uniform striations that enabled them to be quickly identified and accounted for. Figure 13 shows a region of marker band 2 located 0.63 mm from the crack initiation site, Surface A1. The largest increment of rivet crack growth attributed to a 64-cycle marker block was located 3.6 mm from the crack initiation site, Surface A2. The concluding portion of this marker band (Fig. 14) was located approximately 0.2 mm from the rapid fracture zone, indicating that final fracture of this rivet probably occurred after application of relatively few cycles of the following load block. Figure 2 is a well-defined area of marker band 9 located 1.7 mm from the crack initiation site, Surface A1.

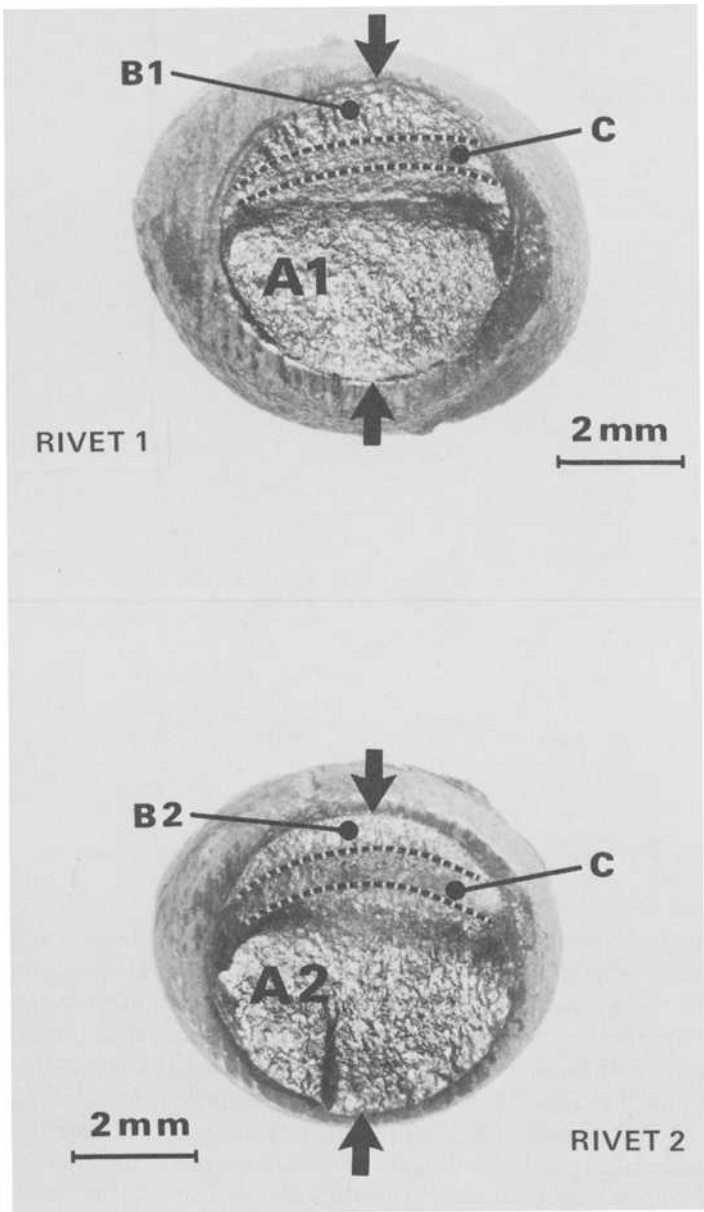

FIG. 12—Wing skin rivet fracture surfaces (2024-T31 aluminum). Arrows indicate crack initiation sites; Areas C indicate overload regions.

TABLE 3—*Rivet marker band locations.*

Marker Band			Distance From Crack Initiation Site (mm)												Rapid Fracture Location
			1	2	3	4	5	6	7	8	9	10	11	12	
Rivet 1	Fracture Surface	A1	0.52	0.63	0.75	0.89	1.0	1.2	1.4	1.5	1.7	1.9	2.2	2.6	3.0
		B1	0.22	0.50											1.2
Rivet 2	Fracture Surface	A2	0.49	0.62	0.89	1.1	1.2	1.5	2.2	3.6					3.8
		B2	Fracture Surface Severely Damaged No Marker Bands Identified												0.8

From the successive marker band spacings indicated in Table 3 it was possible to derive a crack growth curve relating equivalent flight hours to crack length (Fig. 15). Based on the assumption that final fracture of both rivets occurred midway through the application of load block 82—that is, before the application of the 64-cycle "marker block" load sequence—, extrapolation of the curves indicates that crack initiation occurred at approximately 6550 equivalent flight hours for Rivet 1 and 7000 hours for Rivet 2.

Results and Conclusions

The results of these analyses have shown that the use of a "marker block" in an otherwise random load spectrum provided an effective method of acquiring accurate crack growth data from components that had failed during a full-scale aircraft fatigue test. In retrospect, the well-defined nature of the marker bands suggests that fewer cycles or perhaps cycles from a less severe load level may have produced equally effective marker bands. Ultimately, selection of the load level and number of cycles to be used in a marker block would be based on a compromise. On the one hand, the marker block loading conditions would have to be severe enough to produce recognizable marker bands at relatively early stages of crack growth, and on the other hand, the conditions should not be too severe, so that the random or flight-by-flight loading effects would essentially be retained.

It was also recognized that the Snowbird spectrum, based on an aerobatic load profile, inherently lent itself to the use of a marker block. This load spectrum did not contain a distinct high load level flight or ground-air-ground (G-A-G) cycles that might have served as an inherent marker that would be applied on a periodic basis. A full-scale fatigue test, using random loading techniques, of a Canadian Forces CP-121 Tracker aircraft is currently in progress at the Structures and Materials Laboratory. The Tracker is used as a low-altitude maritime "patrol" aircraft. The load spectrum contains distinct G-A-G cycles, and based on the fractographic results of the Snowbird test, it also contains a "marker block". The marker block consists of 51 constant-

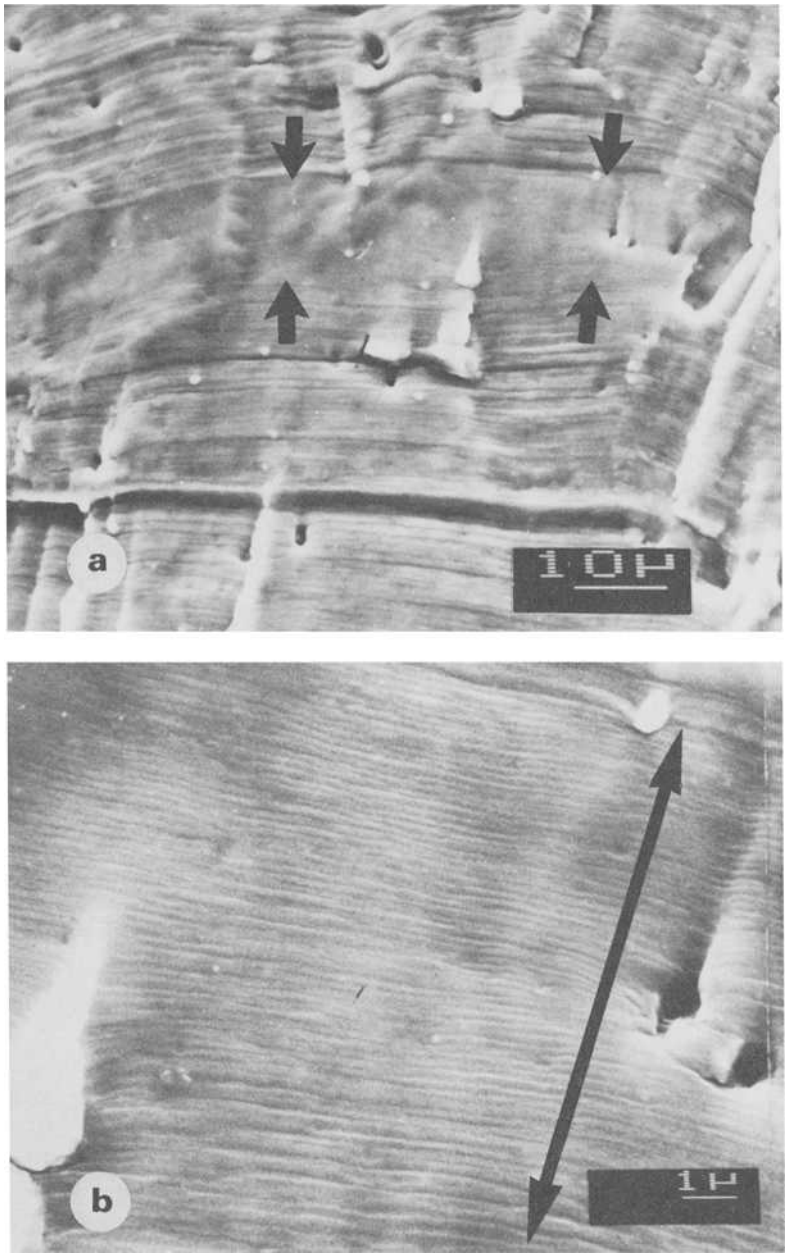

FIG. 13—(a) *Marker band 2; Surface A1, Rivet 1 (0.63 mm from crack initiation site).* (b) *Marker band width = 9.2 μm; average striation spacing = 0.14 μm.*

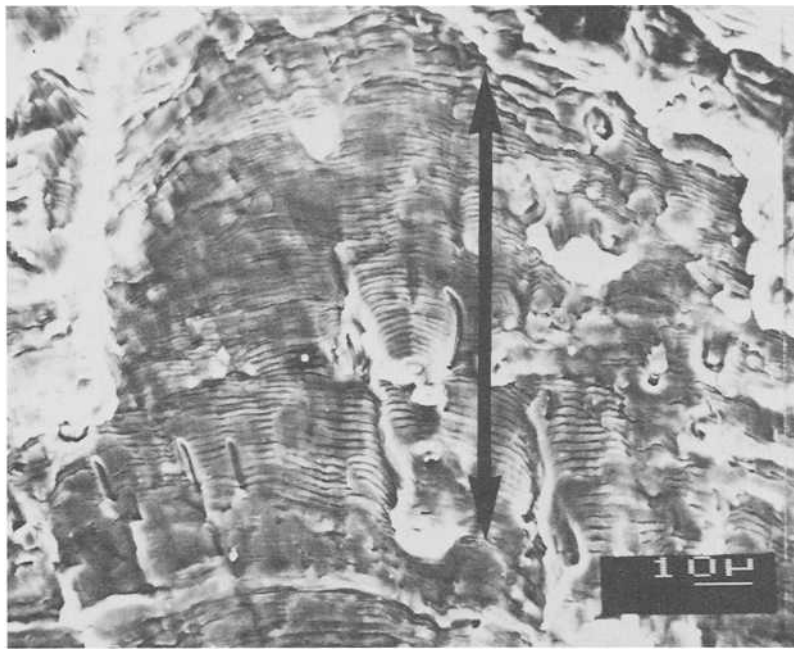

FIG. 14—(a) *Marker band 8; Surface A2, Rivet 2 (3.6 mm from crack initiation site). Marker band width = 76 μm; average striation spacing = 1.2 μm.*

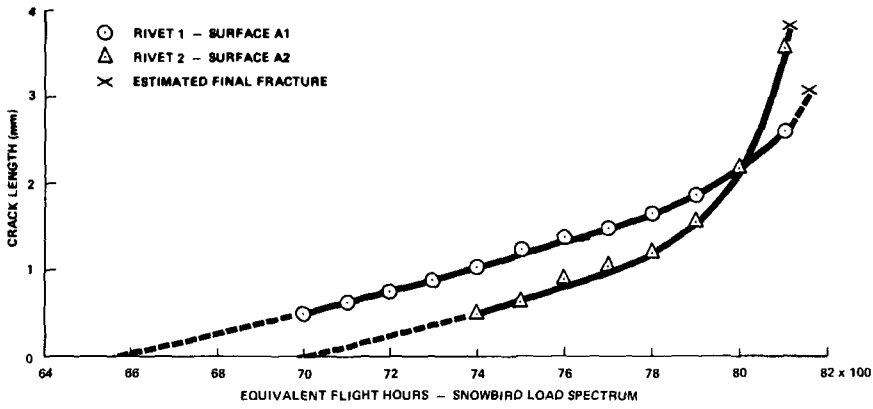

FIG. 15—*Rivet crack growth history derived from marker band spacings.*

amplitude cycles selected from an intermediate maneuver load level and is applied as the concluding portion of a 100 flight load block (Fig. 16). Each complete flight consists of 51 flight loads plus 6 ground loads that are selected from 35 intervals of gust and maneuver loads and 10 intervals of ground loads respectively. To date, only one 4 mm length of fatigue fracture of a 2014-T6 aluminum alloy "spacer strap" has been examined in the SEM. The 1-mm-thick failed section was removed from a wing search light cut-out area. Initial fractographic results indicate the presence of two marker bands located approximately 3.0 and 3.7 mm from the crack initiation site that was located at the sharp edge of a countersunk fastener hole.

Damage tolerant design criteria and the current use of random loading techniques in full-scale testing, along with the proposed use of standard randomized aircraft fatigue load spectra, have generated increased interest in "marker loads" or "marker blocks" as an effective and convenient method of acquiring accurate crack growth information by fracture surface analysis. Interest has been indicated by aircraft manufacturing companies and research and test facilities, as well as organizations involved in fatigue design and the assessment of fatigue damage related to aircraft structures and materials [*13-15*]. If the use of marker blocks is to be considered as a practical method of acquiring this information, future research should be directed towards establishing the parameters necessary for optimizing the clarity of the "marker bands" at acceptable crack lengths, while retaining as much as possible the integrity of the random loading effects.

Current studies at NAE involve the use of the USAF CRACKS IV crack propagation program to study the effects of marker loads analytically. This project will involve testing of standard specimens to determine the effects of various marker block parameters on FCP rates and crack initiation times, and to establish the limits of marker band detectability in the SEM.

As a result of the successful application of marker blocks in the full-scale tests carried out at NAE, a Canadian aircraft manufacturer has used marker blocks in a recent full-scale fatigue test and is planning to use them in a second test in the near future. It is anticipated that analysis of failed components from these tests and from the Tracker test will provide additional information on the use of marker blocks as a fractographic aid in full-scale aircraft fatigue testing utilizing random loading techniques.

Acknowledgments

The author wishes to express his sincere appreciation to Mr. W. Wiebe of this laboratory for his invaluable support and ideas associated with the fractographic analysis and the preparation of this paper. Appreciation is also extended to the fatigue testing and analysis staff, who provided essential information contained in the paper and contributed useful discussions.

FIG. 16—*Tracker load spectrum with marker block.*

References

[1] Fuchs, H. O. and Stephens, R. I., *Metal Fatigue in Engineering*, Wiley, New York, 1980.
[2] Albertin, L. and Hudak, S. J., Jr., in *Fractography and Material Science, ASTM STP 733*, L. N. Gilbertson and R. D. Zipp, Eds., American Society for Testing and Materials, 1981, pp. 187-201.
[3] Abelkis, P. R. in *Fractography in Failure Analysis, ASTM STP 645*, B. M. Strauss and W. H. Cullen, Jr., Eds., American Society for Testing and Materials, 1978, pp. 213-234.
[4] Pelloux, R. M., Faral, M., and McGee, W. M., *Fatigue of Engineering Materials and Structures*, Vol. 1, 1979, pp. 21-35.
[5] Hertzberg, R. W. and Mills, W. J. in *Fractography-Microscopic Cracking Processes, ASTM STP 600*, C. D. Beachem and W. R. Warke, Eds., American Society for Testing and Materials, 1976, pp. 220-234.
[6] *Fatigue Crack Growth under Spectrum Loads, ASTM STP 595*, American Society for Testing and Materials, 1976.
[7] MIL-A-008867B (USAF) 22 August 1975, "Military Specification: Airplane Strength and Rigidity Ground Tests," 3.2.3.4.3 Teardown Inspection, p. 10.
[8] Wiebe, W. and Dainty, R. V., *Canadian Aeronautics and Space Journal*, Vol. 27, No. 2, 1981, pp. 107-117.
[9] Wiebe, W., *Canadian Aeronautics and Space Journal*, Vol. 13, No. 3, March 1967, pp. 135-140.
[10] Wiebe, W., "A Fractographic Study of the Fatigue Failure of Aircraft Wheels," NRC NAE LR-541, National Research Council of Canada, National Aeronautical Establishment, Ottawa, Ontario, Nov. 1970.
[11] Wiebe, W. and Dainty, R. V., "Notes on the Value of Fractography in Failure Analysis," NRC NAE LTR-ST-591, National Research Council of Canada, National Aeronautical Establishment, Ottawa, Ontario, Jan. 1973.
[12] Dainty, R. V., "Fractographic Analysis of a CL-41 Main Spar Cap Subjected to a Random Load Spectrum with 'Marker Blocks' During a Full-Scale Fatigue Test," NRC NAE LTR-ST-1335, National Research Council of Canada, National Aeronautical Establishment, Ottawa, Ontario, 3 Feb. 1982.
[13] Levy, M., Kuo, A. S., and Grube, K., "Practical Method of Fatigue Crack Growth Analysis for Damage Tolerance Assessment of Aluminum Structure in Fighter Type Aircraft," Paper A1AA-80-0405, American Institute of Aeronautics and Astronautics, 18th Aerospace Science Meeting, Pasadena, Calif., Jan. 1980, p. 5.
[14] Goldsmith, N. T., "Fractographic Examinations Relevant to the F & W Mirage Fatigue Test," ARL-Mat-Tech-Memo-371, AR-001-295, Defence Science and Technology Organisation, Aeronautical Research Laboratories, Melbourne, Victoria, Australia, Aug. 1978.
[15] Darts, J., "Determination of Crack Growth Rates under Flight-by-Flight Loading from Fracture Surface Markings," RAE Technical Report 78023, Royal Aircraft Establishment, Farnborough, Hampshire, England, 1978.

N. S. Cheruvu[1]

Fractographic Observations of Fatigue Crack Growth in a High-Strength Steel

REFERENCE: Cheruvu, N. S., **"Fractographic Observations of Fatigue Crack Growth in a High-Strength Steel,"** *Fractography of Ceramic and Metal Failures, ASTM STP 827*, J. J. Mecholsky, Jr. and S. R. Powell, Jr., Eds., American Society for Testing and Materials, 1984, pp. 309-327.

ABSTRACT: The effects of high-temperature austenitizing treatments (prior austenite grain size) and internal hydrogen on the fracture mode during fatigue crack growth studies in AISI 4340 steel have been investigated. The results show no correlation between the prior austenite grain size and reverse plastic zone at the maximum incidence of intergranular fracture in specimens without hydrogen. Fatigue striations were more often observed in the coarse-grained specimens austenitized at 1200°C. The presence of internal hydrogen resulted in predominantly intergranular fracture in the fine-grained specimens at low stress intensity ranges. However, the amount of intergranular fracture was inversely related to the prior austenite grain size. The fracture mode was predominantly intergranular at intermediate stress intensity ranges for all grain sizes. The results were discussed in terms of variations in plane strain fracture toughness with austenitizing temperature and hydrogen diffusion to the prior austenite grain boundaries.

KEY WORDS: austenitizing temperature, grain size, plane strain fracture toughness, internal hydrogen, stress intensity range, crack growth, intergranular-transgranular fracture, fatigue striations

Several investigators have made fractographic observations of fatigue crack growth in ultra-high-strength steels [*1-5*]. These investigators have reported three fatigue failure modes: (1) intergranular, (2) transgranular (ductile striation), and (3) cleavage, depending upon the stress intensity range (ΔK). At low ΔK-values, the fatigue failure consists of a flat ductile striation mode with a small amount of intergranular separation. The amount of intergranular fracture increases to a peak with increasing ΔK and then gradually decreases

[1]Advanced Engineer, Materials Engineering, Westinghouse Electric Corporation, Alafaya Trail, Orlando, Fla. 32817.

at higher stress intensities. Cooke et al [*1*] and Irving and Kurzfeld [*3*] have postulated that the maximum amount of intergranular fracture occurred when the reverse plastic zone size at the crack tip became equal to the prior austenite grain size. However, in their investigations the prior austenite grain size was not varied to confirm their hypothesis. At intermediate ΔK-values, the mechanism of fatigue crack growth is primarily by transgranular ductile striation mode. The distinct fatigue striations which characterize fatigue failures were observed only in isolated packets in ultra-high-strength steels [*2,5–7*]. At higher stress intensities when maximum stress intensity (K_{max}) approaches the fracture toughness of the material (K_{Ic}), the crack propagation has been reported to occur by intergranular and cleavage mechanisms [*4*].

Very limited research has been done on the influence of high-temperature austenitization treatments on failure modes during fatigue crack growth in high-strength steels [*4*]. The present work investigates the effect of high-temperature austenization treatments and internal hydrogen on the fatigue crack growth fracture characteristics of an ultra-high-strength steel.

Experimental Procedure

The material used in the present investigation was AISI 4340 steel. The chemical composition of the steel in weight percent is shown in Table 1.

The material was austenitized at 870, 1100, and 1200°C for 1 h and quenched into agitated oil to vary the prior austenite grain size from 20 to 200 μm. All specimens were tempered at 180°C for 1 h.

Following the heat treatment, 50% of the total specimens were cathodically charged in 4% H_2SO_4 electrolyte with phosphorus as a poison for 24 h at a current density of 0.005 A/cm^2. Immediately after charging, the specimens were slightly polished, and they were cadmium plated before baking to homogenize hydrogen distribution.

Fatigue crack growth testing was performed on 15.9-mm-thick standard compact tension specimens. The tests were conducted under sinusoidal tension-tension with a load control at a load ratio of 0.25 and at a testing frequency of 10 Hz in a closed-loop Instron testing machine. Crack length measurements were periodically taken using a crack-opening displacement (COD) gage. Crack growth rates were computed by numerical differentiation of crack length versus number of cycles data using an incremental-step polynomial procedure [*8*]. The detailed experimental procedure is given elsewhere [*9*].

TABLE 1—*Chemical composition (weight percent) of AISI 4340 steel.*

C	Mn	Si	Cr	Ni	Mo	Cu	S	P	Fe
0.40	0.60	0.32	0.69	1.87	0.20	0.16	0.015	0.015	balance

All fracture surfaces were examined in a JEOL scanning electron microscope operated at 25-kV secondary electron voltage.

Results and Discussion

The variation of monotonic mechanical properties, plane strain fracture toughness of AISI 4340 steel, and prior austenite grain size with austenitizing temperature is shown in Table 2. It can be seen that plane strain fracture toughness of 4340 steel significantly increases without affecting the yield strength by austenitizing the steel at 1200°C instead of 870°C. The percentage of elongation dropped from 13.6 to 4.2 as austenitizing temperature was increased.

Fatigue Crack Growth

The fatigue crack growth rates in specimens with and without hydrogen as a function of stress intensity range (ΔK) are shown in Fig. 1. The original data points are not included in this graph for clarity. It is evident from the figure that the crack growth rates in specimens without hydrogen are almost independent of grain size at low and intermediate stress intensity ranges. However, the linear crack growth region extended to higher stress intensity ranges as grain size was increased from 20 to 200 μm. As K_{max} approaches K_{Ic}, an acceleration in crack growth was observed in all cases.

It is also evident from Fig. 1 that the presence of internal hydrogen enhanced crack growth rates in all specimens regardless of grain size. The maximum enhancement in crack growth rates was observed at intermediate stress intensity ranges.

At low stress intensity ranges ($\Delta K < 10$ MPa$\sqrt{\text{m}}$) the crack growth rates were strongly dependent upon the prior austenite grain size. As the grain size increased from 20 to 200 μm, the crack growth rate decreased from 2×10^{-5} to 9×10^{-7} mm/cycle at $\Delta K \sim 3.5$ MPa$\sqrt{\text{m}}$ (Fig. 1). At intermediate stress intensity ranges ($\Delta K > 10$ MPa$\sqrt{\text{m}}$) slightly higher crack growth rates were

TABLE 2—*Variation of mechanical properties and grain size with austenitizing temperature.*

Austenitizing Temperature °C	Grain Size, μm	Yield Strength, MPa (ksi)	Tensile Strength, MPa (ksi)	Elongation, %	Plane Strain Fracture Toughness, MPa $\sqrt{\text{m}}$ (ksi $\sqrt{\text{in.}}$)
870	20	1626 (236)	1970 (286)	13.6	60 (54.5)
1100	100	1515 (220)	1667 (242)	9.0	64 (58)
1200	200	1515 (220)	1847 (268)	4.2	94 (86)

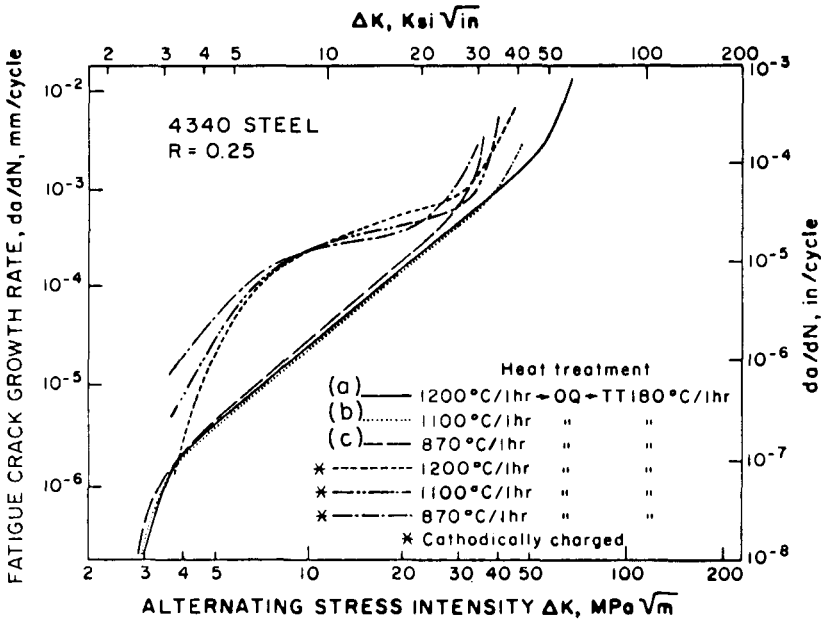

FIG. 1—*Variation of fatigue crack growth rate in specimens with and without hydrogen with austenitizing temperature or grain size.* (a) *200 μm grain size.* (b) *100 μm grain size.* (c) *20 μm grain size.*

observed in coarse-grained specimens. The extension of this region was dependent on the fracture toughness of the material.

Fractography

Following the crack growth testing, the fracture surfaces of all specimens were examined in a scanning electron microscope to determine the mechanism of crack growth at various stress intensity ranges. The fracture characteristics with and without hydrogen are next described.

Without Hydrogen—Figure 2 shows typical fracture morphology in specimens without hydrogen at $\Delta K \simeq 3.5$ MPa$\sqrt{\text{m}}$. It is clear from the figure that the fracture mode is transgranular irrespective of grain size. The percentage of intergranular separation was less than 1 at low stress intensity levels. The amount of intergranular separation increased with increasing stress intensity and reached a maximum for all grain sizes at around $\Delta K = 9$ to 16 MPa$\sqrt{\text{m}}$ ($K_{max} = 12$ to 22 MPa$\sqrt{\text{m}}$). Further increase in ΔK gradually decreased the amount of intergranular separation (Fig. 3). Similar observations were reported by Ritchie in 300M steel [*4*].

The calculated forward and cyclic plastic zone sizes at the peak incidence of

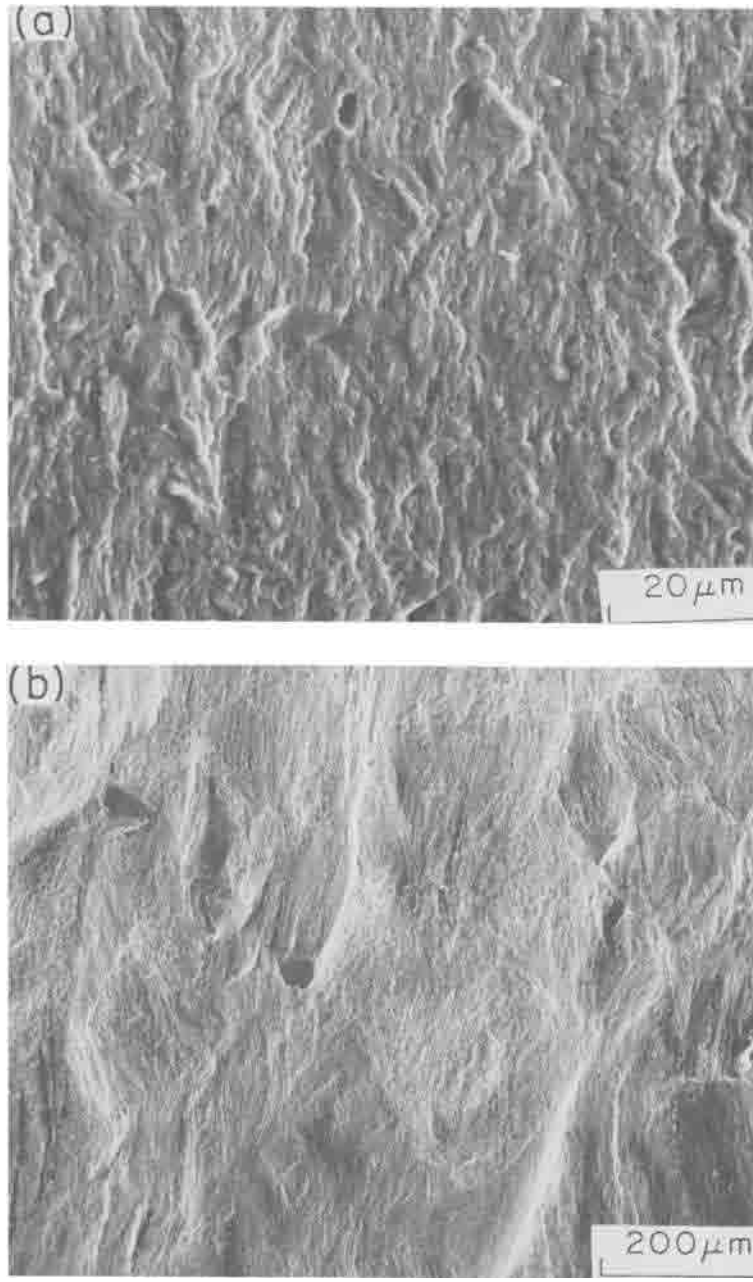

FIG. 2—*Fracture features in specimens without hydrogen at* $\Delta K \simeq 3.5\ MPa\sqrt{m}$. (a) *20 μm grain size.* (b) *200 μm grain size.*

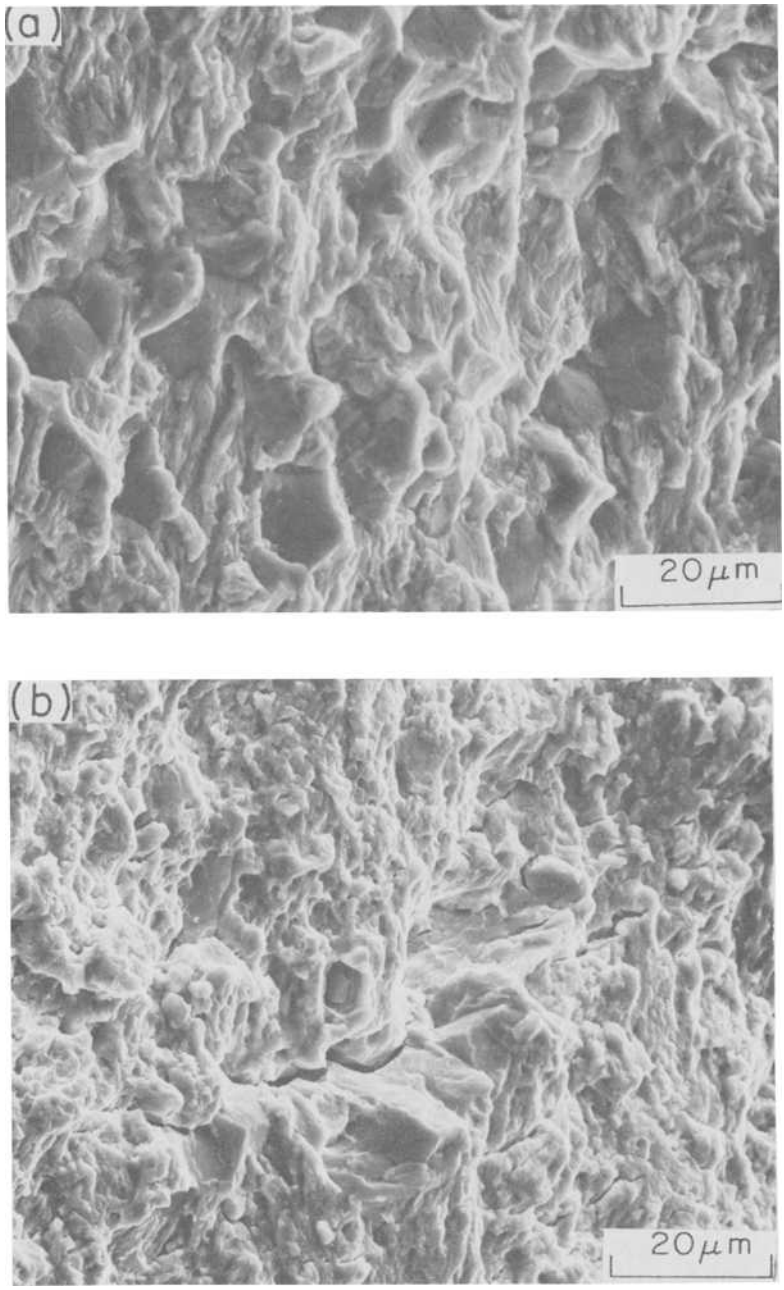

FIG. 3—*Variation in amount of intergranular fracture in fine-grained specimens (20 μm) without hydrogen with applied stress intensity.* (a) $\Delta K \simeq 9\ MPa\sqrt{m}$. (b) $\Delta K \simeq 19\ MPa\sqrt{m}$.

intergranular fracture ($\Delta K \approx 16$ MPa$\sqrt{\text{m}}$) were approximately 20.6 μm and 2.9 μm respectively [*10*]. The cyclic plastic zone size of 2.9 μm was much smaller than the prior austenite grain sizes that were investigated. Furthermore, the calculated forward plastic zone was approximately equal to the prior austenite grain size of fine-grained steel (20 μm) but smaller than the other two grain sizes. These results suggest that there was no correlation between the prior austenite grain size and the cyclic plastic zone size (or the forward plastic zone size) at the maximum incidence of intergranular fracture as reported by earlier investigators [*1,3*]. However, Gerberich and Moody [*11*] have proposed an alternative explanation that the peak incidence of intergranular fracture occurs when the applied K_{max} is equal to K_{Iscc} of the material. The K_{Iscc} for these grain sizes were reported to vary from 11 to 20 MPa$\sqrt{\text{m}}$ [*12*]. Hence it is believed that the peak incidence of intergranular fracture occurred when K_{max} was approximately equal to K_{Iscc}.

Typical intergranular fracture produced in fine- and coarse-grained specimens is shown in Fig. 4. In fine-grained specimens the intergranular facets were almost featureless and no evidence of fatigue striations was observed (Fig. 4*a*). On the other hand, localized ductile tearing on intergranular facets was often observed in coarse-grained specimens. Careful examination of these tear regions occasionally revealed fatigue striations (Figs. 4*c* and 4*d*). The calculated crack growth rate from the average spacing of striations (1.7×10^{-4} mm/cycle) was approximately equal to the measured macroscopic crack growth rate (2.5×10^{-4} mm/cycle).

In agreement with the earlier reports on similar steels [*5–7*], the distinct fatigue striations in transgranular fracture regions were observed only as isolated packets. Figure 5 shows typical such regions for three grain sizes. The calculated crack growth rates from the striations were in good agreement with measured crack growth rates. It is evident from the figure that the ductile fatigue striations cover a larger area in specimens of 200 μm grain size than the others. Furthermore, fatigue striations were more often observed in these specimens.

Miller [*5*] and Thompson et al [*7*] have observed fatigue striations as isolated packets in quenched-and-tempered AISI 4340 steel. They report that the striations were more often observed with increasing tempering temperature. Increasing the tempering temperature increases the fracture toughness/ductility at the expense of yield strength. However, austenizing the steel at 1200°C instead of at 870°C increased plane strain fracture toughness without affecting yield strength. Although uniaxial ductility decreased significantly with increasing austenitizing temperature, the drop in plane strain ductility was insignificant [*13*]. Furthermore, it has been pointed out by many investigators that the high-temperature austenitization treatment increases the dissolution of sulfide inclusions and reduces the amount of segregation on the prior austenite grain boundaries in low-alloy steels [*13–16*]. The reduction of inclusions may enhance the localized ductility ahead of the crack tip, result-

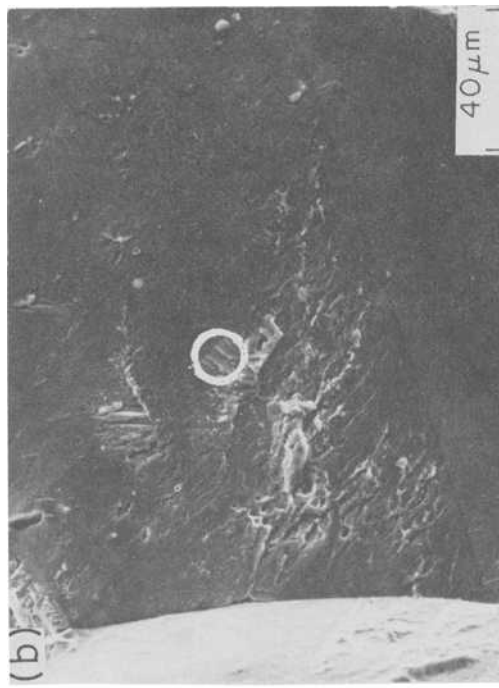
40μm
(b)

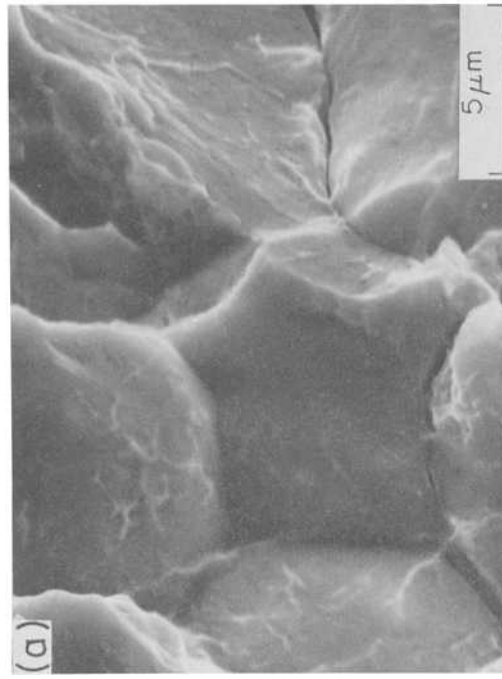
5μm
(a)

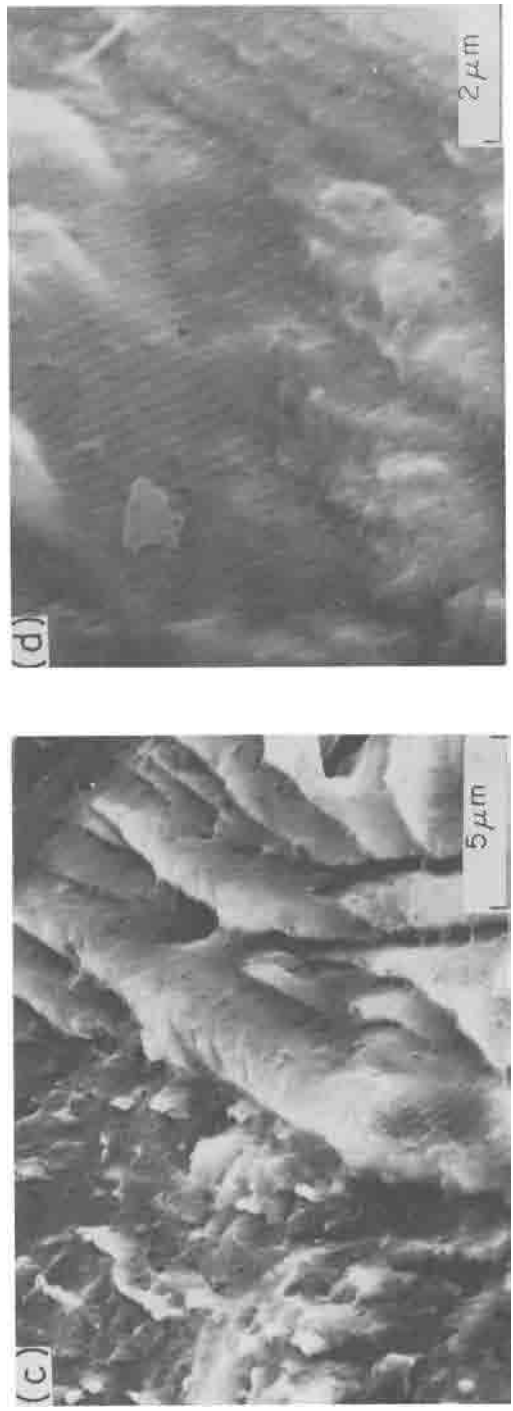

FIG. 4—*Intergranular fracture features in specimens without hydrogen at* $\Delta K \simeq 19\ MPa\sqrt{m}$. (a) *20 μm grain size.* (b) *200 μm grain size.* (c) *Enlargement of circled region in* (b), *showing fatigue striations.* (d) *Fatigue striations on intergranular facet (200 μm grain size).*

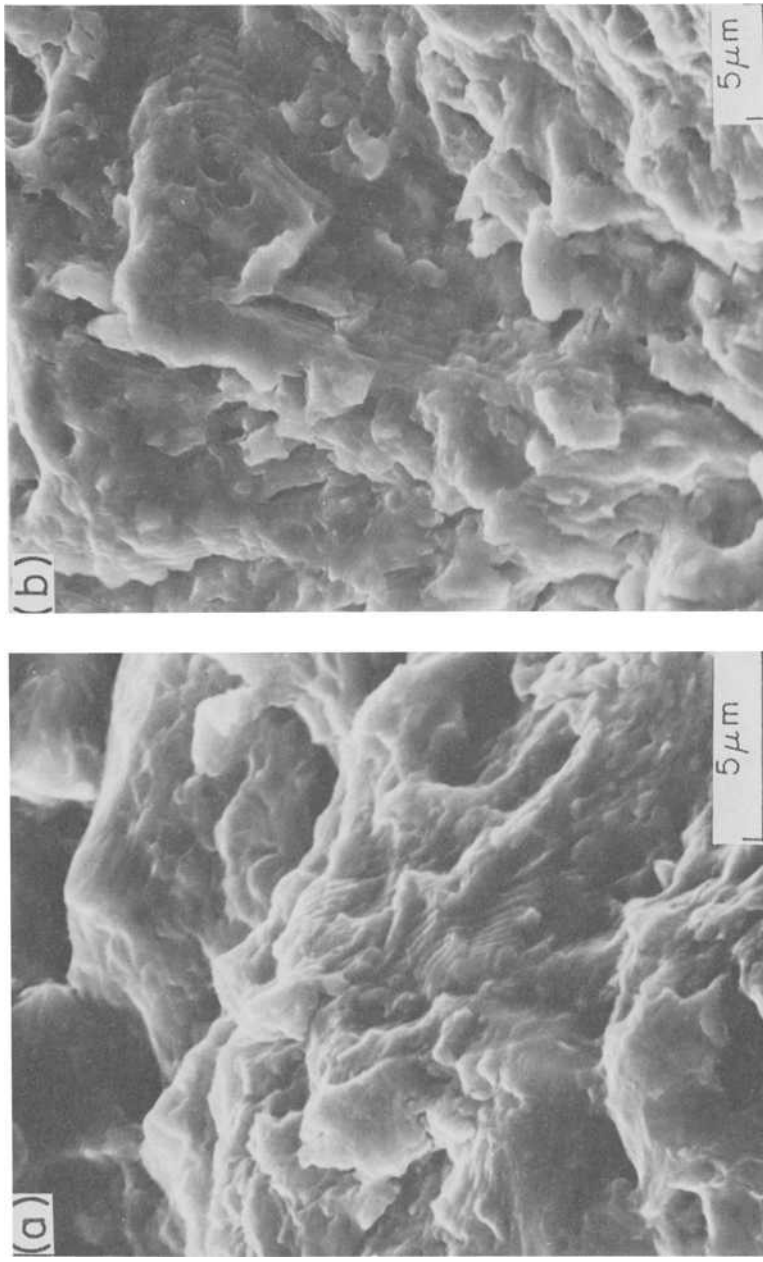
(a)
5μm
(b)
5μm

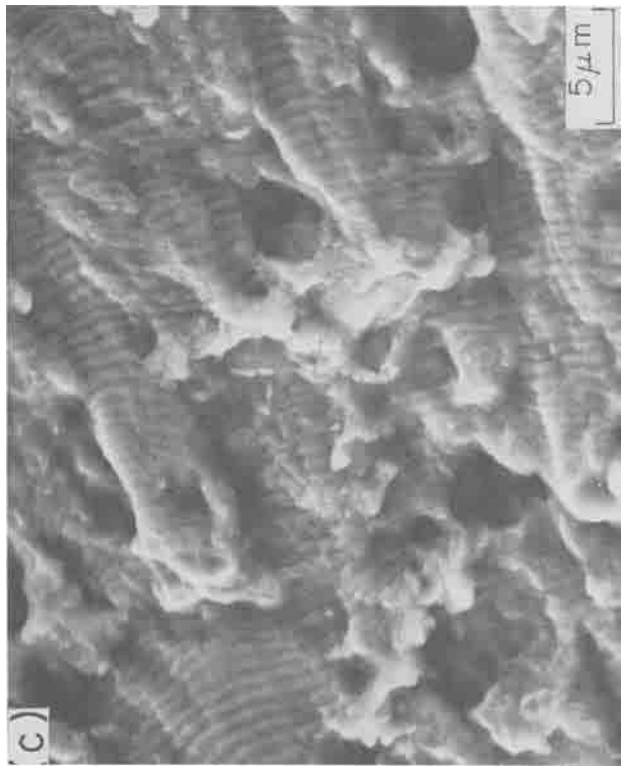

FIG. 5—*Variation of fatigue striations with grain size in specimens without hydrogen.* (a) *20 μm grain size* ($\Delta K \simeq 19\ MPa\sqrt{m}$). (b) *100 μm grain size* ($\Delta K \simeq 29\ MPa\sqrt{m}$). (c) *200 μm grain size* ($\Delta K \simeq 29\ MPa\sqrt{m}$).

ing in greater crack tip deformation. The reduction of segregated impurities on prior austenite grain boundaries also permits greater crack tip deformation which probably increases the occurrence of ductile tearing on intergranular facets. It is well known that the probability of formation of distinct striations increases with increasing crack tip deformation. These arguments support the observations of fatigue striations more often in the coarse-grained specimens austenitized at 1200°C.

At higher stress intensity ranges, as K_{max} approaches K_{Ic}, the fracture mode consisted of fibrous, quasi-cleavage, and intergranular cracking in all grain sizes. Similar results were reported by Ritchie in 300M steel [*4*].

With Hydrogen—Figure 6 shows the fracture mode in cathodically charged specimens at $\Delta K \simeq 3.5$ MPa$\sqrt{m}$ as a function of grain size. The fracture mode is predominantly intergranular in the fine-grained specimens austenitized at 870°C, whereas the fracture mode was mostly transgranular in the coarse-grained specimens austenitized at 1200°C. The variation in the amount of intergranular fracture in specimens with and without hydrogen as a function of grain size is shown in Table 3. As the prior austenite grain size increased from 20 to 200 μm the percentage of intergranular fracture in specimens with hydrogen decreased from 85 to 20. These results indicate that in specimens without hydrogen the grain boundaries are stronger than the grains, while in specimens with hydrogen the grain boundaries are weakened because of hydrogen diffusion to the grain boundaries. In the coarse-grained specimens, the hydrogen has to diffuse over a large region ahead of the crack tip to weaken the grain boundaries, which results in a reduced environmental influence.[2] The reduced environmental influence is consistent with the ob-

TABLE 3—*Variations in percentage of intergranular fracture at* $\Delta K \simeq 3.5$ *MPa*$\sqrt{m}$.

Grain Size, μm	Intergranular Fracture, %	
	Without Hydrogen	With Hydrogen
20	<1	80 to 85
100	<1	30 to 40
200	<1	10 to 20

[2]The high-temperature austenitization treatments not only coarsen the prior austenite grain size but also increase the amount of mechanically unstable retained austenite ($\simeq$ 3 to 5% estimated from TEM studies) [*9,17-18*]. The retained austenite decomposes into ferrite and cementite upon tempering at 280°C [*9*]. For a given austenitizing treatment, the fatigue crack growth rates at low stress intensity ranges ($\Delta K \leq 11$ MPa $\sqrt{m}$) in cathodically charged specimens were found to be independent of tempering treatment at 180 or 280°C [*9*]. Hence the crack growth rates at low stress intensity ranges were considered to depend essentially on the prior austenite grain size.

served lower crack growth rates in the coarse-grained specimens (Fig. 1). The amount of intergranular fracture was found to increase with stress intensity range. Figure 7 shows the variation of intergranular fracture with the applied stress intensity range in the coarse-grained specimens austenitized at 1200°C. The maximum amount of intergranular fracture was observed at around $\Delta K = 16$ MPa$\sqrt{\text{m}}$. The maximum incidence of intergranular fracture in cathodically charged specimens also found to occur when K_{max} was approximately equal to K_{Iscc}.

Although the fracture mode was predominantly intergranular at intermediate stress intensity ranges ($\Delta K > 16$ MPa$\sqrt{\text{m}}$), a few transgranular failure regions were present in all cases. Figures 7*c* and 8*a* show regions of intergranular and transgranular fracture modes at $\Delta K \simeq 24$ MPa$\sqrt{\text{m}}$ respectively. In the regions of transgranular failure, fatigue striations were occasionally observed only in the coarse-grained specimens austenitized at 1200°C (Fig. 8). No fatigue striations were observed on intergranular facets. Figure 8 also shows ductile rupture mode in addition to fatigue striations. The fracture mode at higher stress intensity ranges (as K_{max} approaches K_{Ic}) was found to be ductile rupture and intergranular separation in all cases.

Conclusions

Based on the results of this investigation the following conclusions can be drawn:

Without Hydrogen

1. The fatigue crack growth rate was almost independent of grain size in specimens at low and intermediate stress intensity ranges.
2. No correlation was observed between the cyclic plastic zone size and the prior austenite grain size at the maximum occurrence of intergranular fracture.
3. Fatigue striations on intergranular facets were observed only in the specimens austenitized at 1200°C. In transgranular failure regions, fatigue striations were more often observed in the coarse-grained specimens austenitized at 1200°C.

With Hydrogen

1. The presence of internal hydrogen enhanced the crack growth rates for all grain sizes.
2. The prior austenite grain size was found to have significant influence on fatigue crack growth at low stress intensity ranges. The crack growth rates at low stress intensity ranges decreased with increasing grain size.
3. At low ΔK, the fracture mode was predominantly intergranular in the

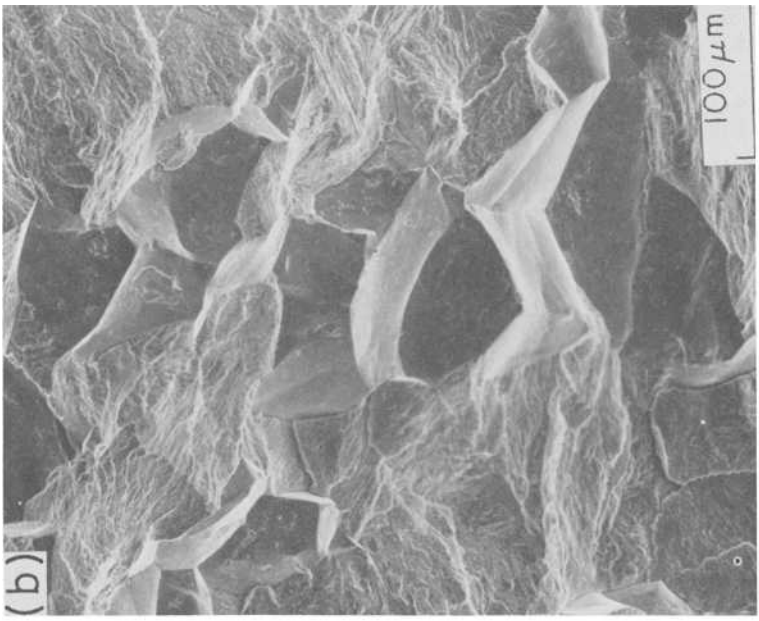
100μm
(b)

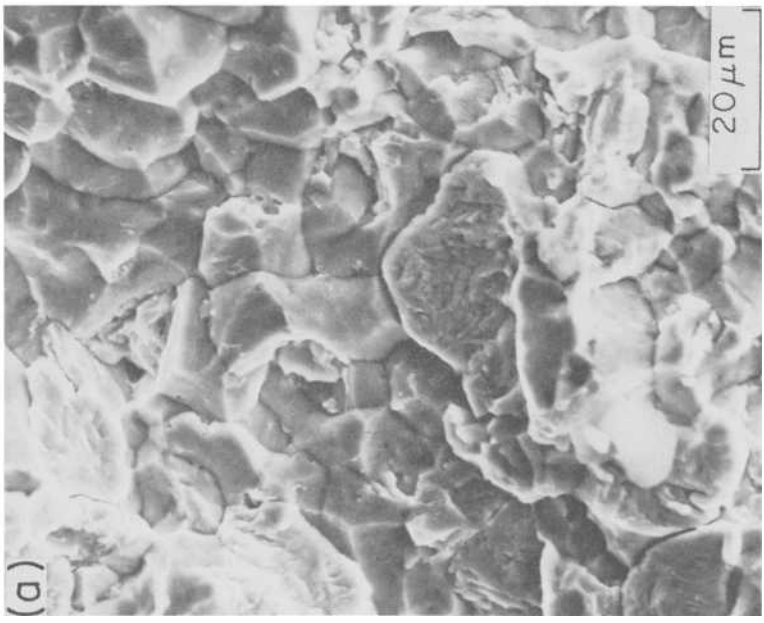
20μm
(a)

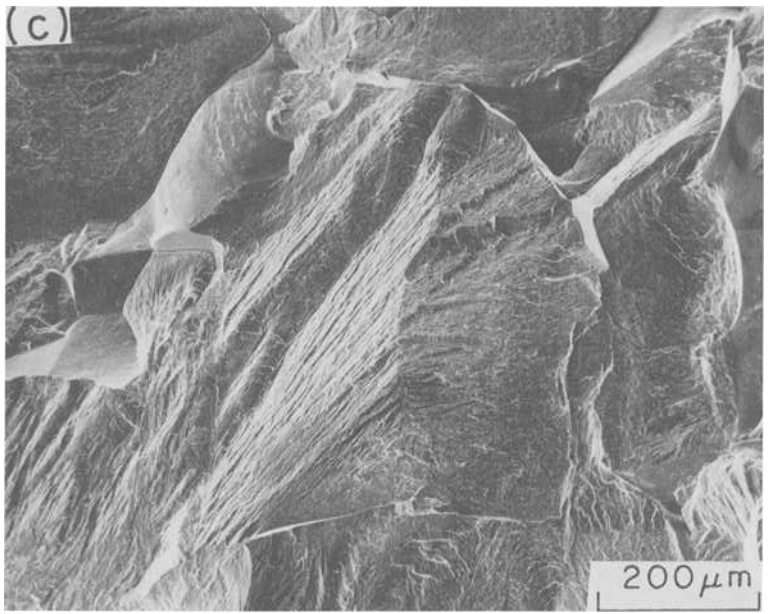

FIG. 6—*Variation of intergranular fracture at* $\Delta K \simeq 3.5\ MPa\sqrt{m}$ *with grain size in cathodically charged specimens.* (a) *20 μm grain size.* (b) *100 μm grain size.* (c) *200 μm grain size.*

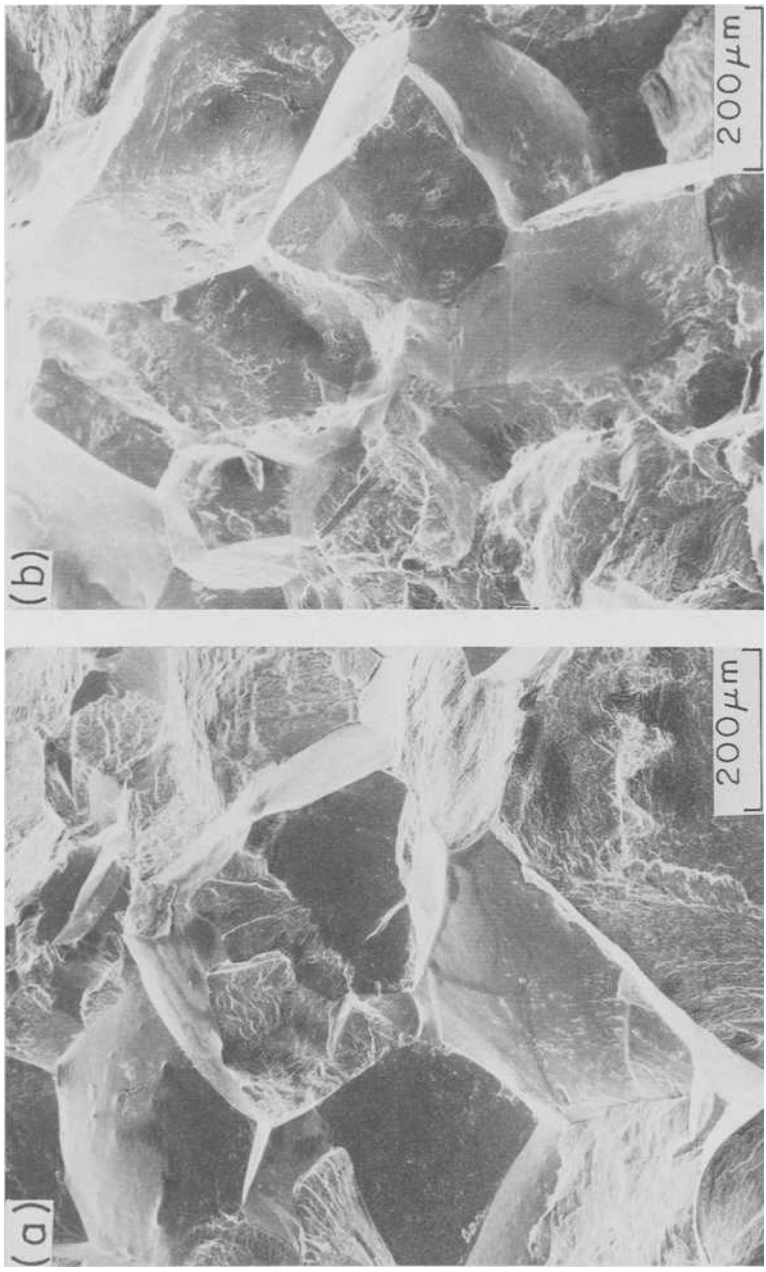
(a)
200μm
(b)
200μm

FIG. 7—*Variation of intergranular fracture in cathodically charged specimens (200 μm grain size) with stress intensity.* (a) $\Delta K \simeq 5.5$ *MPa*$\sqrt{m}$. (b) $\Delta K \simeq 14$ *MPa*$\sqrt{m}$. (c) $\Delta K \simeq 24$ *MPa*$\sqrt{m}$.

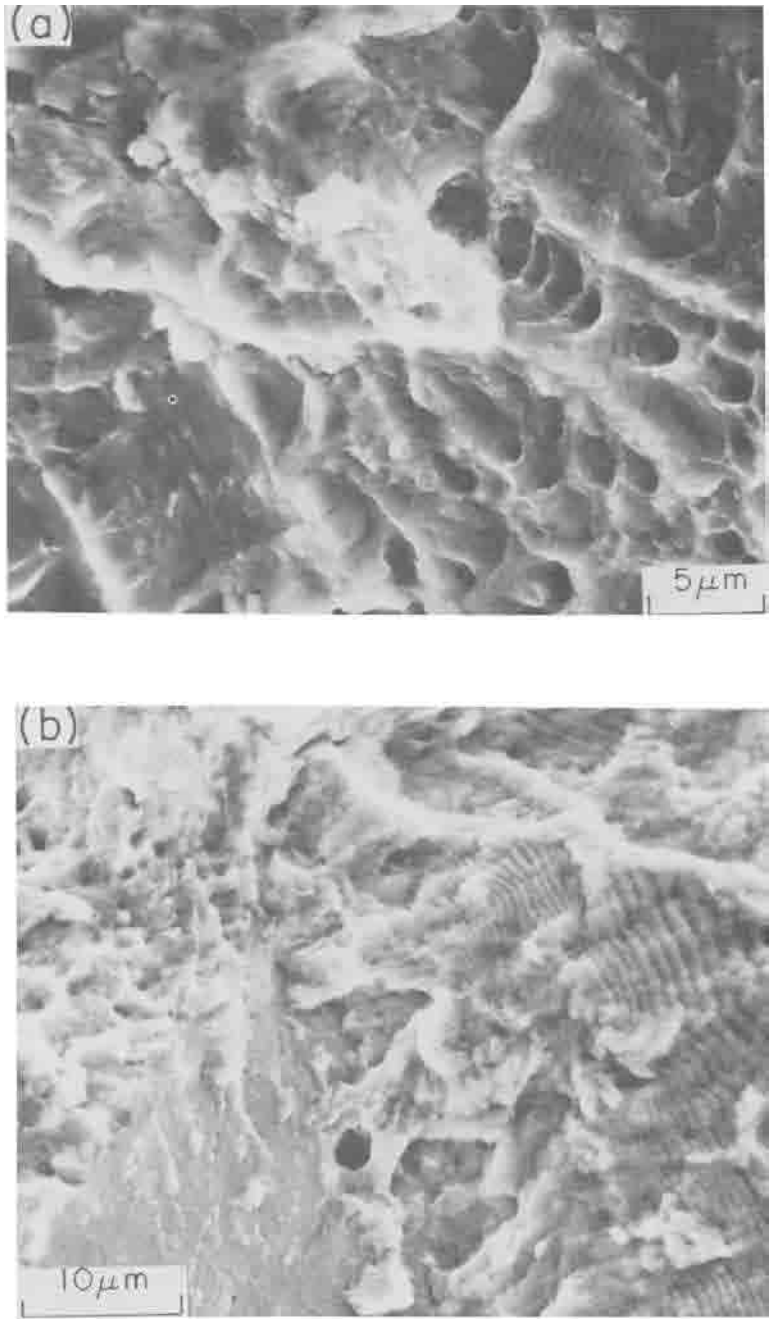

FIG. 8—*Fatigue striations and ductile rupture in cathodically charged specimens (200 μm grain size).* (a) $\Delta K \simeq 24\ MPa\sqrt{m}$. (b) $\Delta K \simeq 34\ MPa\sqrt{m}$.

fine-grained specimens austenitized at 870°C. The amount of intergranular fracture significantly decreased as the grain size increased.

4. At intermediate stress intensity ranges the fracture mode was intergranular regardless of prior austenite grain size. Fatigue striations were occasionally observed only in specimens austenitized at 1200°C.

Acknowledgments

The author wishes to express his gratitude to Dr. W. E. Wood, Professor, Oregon Graduate Center, Beaverton, for providing facilities to carry out this work and for his support throughout this investigation.

References

[1] Cooke, R. J., Irving, P. E., Booth, G. S., and Beevers, C. J., *Engineering Fracture Mechanics*, Vol. 7, 1975, pp. 69-77.
[2] Carman, C. M. and Schuler, M. F., *Journal of the Iron and Steel Institute*, Vol. 208, 1970, pp. 463-468.
[3] Irving, P. E. and Kurzfeld, A., *Metal Science*, Vol. 12, 1978, pp. 495-500.
[4] Ritchie, R. O., *Journal of Engineering Materials and Technology, Transactions of ASME*, Series H, Vol. 99, 1977, pp. 195-204.
[5] Miller, G. A., *Transactions of ASM*, Vol. 62, 1969, pp. 651-657.
[6] LeMay, I. and Lui, M. W., *Metallography*, Vol. 8, 1975, pp. 249-252.
[7] Thompson, K. R. L., Araki, T., and Chiyama, I., *Journal of the Iron and Steel Institute*, Vol. 207, 1969, pp. 1624-1627.
[8] Ritchie, R. O. and Knott, J. F., *Acta Metallurgica*, Vol. 21, 1973, pp. 639-648.
[9] Cheruvu, N. S., Ph.D. thesis, "Effect of Microstructure and Internal Hydrogen on Fatigue Crack Propagation of Ultra High Strength Steels," Oregon Graduate Center, Beaverton, Ore., 1980.
[10] Rice, J. R. in *Fatigue Crack Propagation, ASTM STP 415*, American Society for Testing and Materials, 1967, pp. 247-267.
[11] Gerberich, W. W. and Moody, N. R. in *Fatigue Mechanisms, ASTM STP 675*, American Society for Testing and Materials, 1979, pp. 292-341.
[12] Dilipkumar, D., Ph.D. thesis, "Effect of Microstructure on Internal and External Hydrogen Embrittlement of Ultra High Strength Steel," Oregon Graduate Center, Beaverton, Ore., 1980.
[13] Ritchie, R. O. and Horn, R. M., *Metallurgical Transactions A*, Vol. 9, 1978, pp. 331-341.
[14] Schulz, B. J. and McMahon, C. J., *Metallurgical Transactions*, Vol. 4, 1973, pp. 2485-2489.
[15] Ogura, T., McMahon, C. J., Feng, H. C., and Vitek, V., *Acta Metallurgica*, Vol. 6, 1978, pp. 1317-1345.
[16] Ritchie, R. O., Cedeno, M. H. C., Zacky, V. F., and Parker, E. R., *Metallurgical Transactions A*, Vol. 9A, 1978, pp. 34-40.
[17] Parker, E. R., *Metallurgical Transactions A*, Vol. 8, 1977, pp. 1025-1042.
[18] Sastry, C. N., Khan, K. H., and Wood, W. E., *Metallurgical Transactions A*, Vol. 13, 1982, pp. 676-680.

V. P. Swaminathan[1]

Fractographic Analysis of the Primary Oil Pump Shaft Fracture from a Steam Turbine

REFERENCE: Swaminathan, V. P., **"Fractographic Analysis of the Primary Oil Pump Shaft Fracture from a Steam Turbine,"** *Fractography of Ceramic and Metal Failures, ASTM STP 827*, J. J. Mecholsky, Jr., and S. R. Powell, Jr., Eds., American Society for Testing and Materials, 1984, pp. 328-345.

ABSTRACT: An extension shaft is connected to the governor end of a high-pressure steam turbine. This shaft, which drives the primary oil pump impeller in a tubine-generator unit, fractured while in service. Metallurgical analysis included extensive fractographic study using optical, scanning, and transmission electron microscopes. Fatigue striations and beach marks were observed on the fracture surface. Striation spacing measurements were made on carbon replicas taken at various crack depths. The approximate magnitude of the cyclic stresses causing these striations was calculated from data available from scale-model test specimens. Peeling-type cracks initiating from the bottom of the keyway indicative of torsional oscillations were also found. The fracture initiated at the keyway fillet and propagated in high-cycle fatigue mode under combined torsional and bending loads.

KEY WORDS: fracture (materials), steel, shaft, striations, fatigue (materials), stresses, fractography

Our knowledge and understanding of the fracture process of any component depends on the amount of information we can obtain from investigation of the fractured pieces. Both the macroscopic and the microscopic examination of the fracture surface are important steps in the failure analysis procedures. Since metal components can crack by many mechanisms, identifying the primary fracture mode and locating the fracture origin are main concerns. These objectives fall within the scope of fractography, the most powerful diagnostic technique in such an investigation. Through a detailed study of the fractographic features and careful interpretation one can determine the type of loading, the level of the applied stress, the mechanism of crack initiation and propagation, and the relative ductility or brittleness of the material. It is possible that, in the case of fatigue failure, cyclic stress range can be estimated

[1]Senior Engineer, Westinghouse Electric Corporation, Orlando, Fla. 32817.

if fatigue striation spacing can be measured [*1,2*]. In this investigation estimation of cyclic stress was made using data from model specimen testing from an earlier study.

Background

Steam turbines in power plants run on bearings that are lubricated by oil. Oil is supplied to the bearings from a main oil pump driven by an extension shaft connected to the turbine rotor. The oil pump has a large impeller keyed to the shaft. The diameter of the shaft under the oil pump impeller is about 73 mm (2.88 in.). When the oil pump ceases to function, it may lead to the loss of oil pressure in the bearings and consequently may result in their damage. Under normal operating conditions the speed is 3600 rpm. The fracture of the subject shaft occurred after eleven years of service. Figure 1 shows schematically the location of the shaft fracture. The shaft fractured completely under the oil pump-spacer ring location (Fig. 2). The metallurgical analysis consisted of the following procedures:

1. Visual assessment and macrodocumentation of the fracture.
2. Extensive fractographic study using optical microscope, scanning electron microscope (SEM), and transmission electron microscope (TEM).

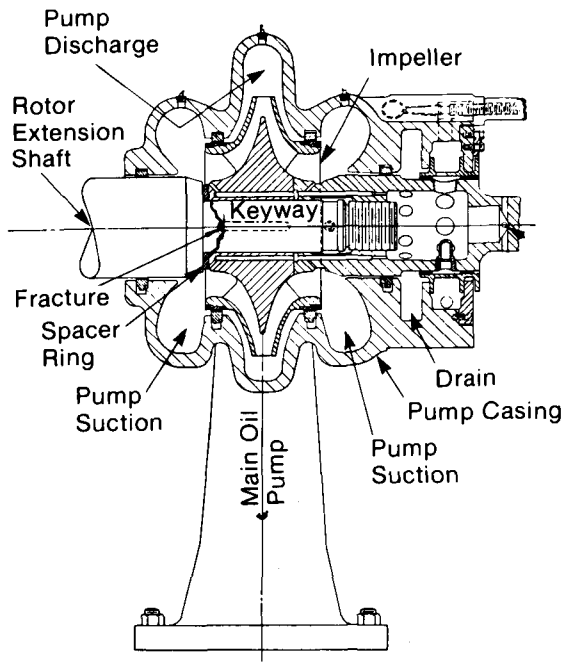

FIG. 1—*Main oil pump and shaft fracture location.*

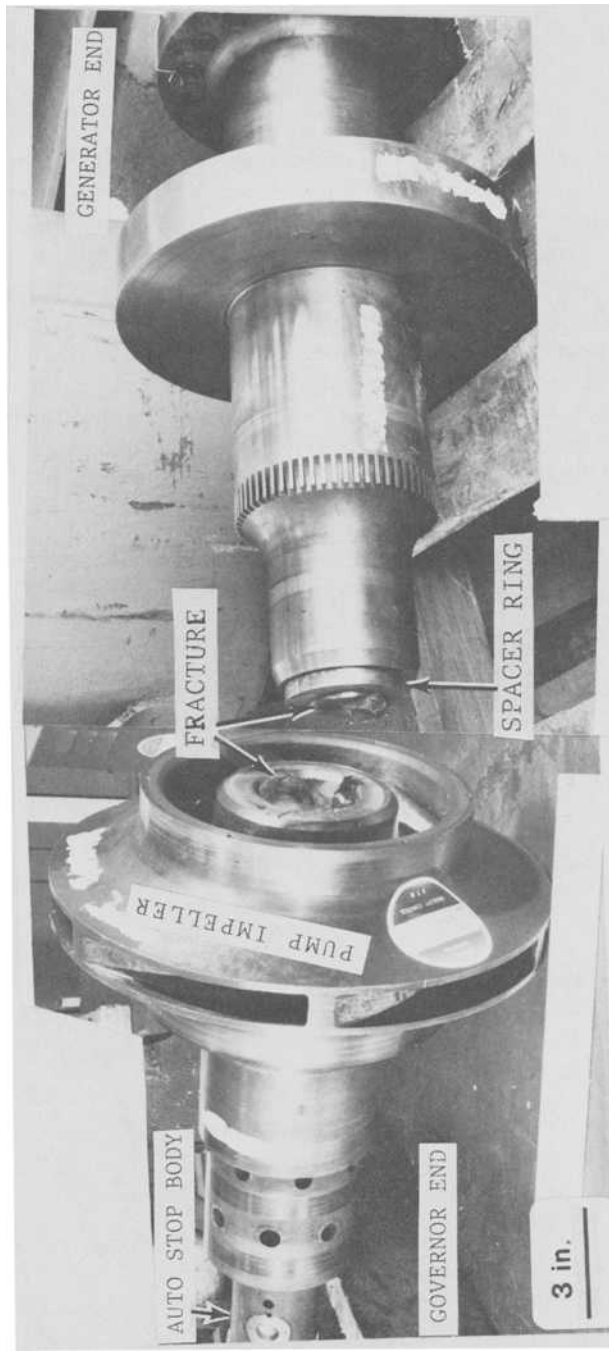

FIG. 2—*Shaft segments with oil pump impeller.*

3. Tensile and high-cycle fatigue property determination.
4. Study of the microstructure.
5. Chemical analysis of the shaft material.

Macroscopic Examination

The portion of the shaft with the pump impeller and the key assembly will be referred to as the governor side, since the speed sensor and control mechanisms are located at this end of the shaft. The mating fracture is on the generator side of the extension shaft (Fig. 2). Figure 3 shows the macrodocumentation of the governor end fracture surface with the key still in place. Areas 1 to 5 are damaged, probably because of rubbing, fretting, and oxidation. The appearance of the shaft and the key and keyway damage after the removal of the impeller is shown in Fig. 4. By the macroscopic examination two fracture initiation sites at two different planes are discernable. One is at the keyway fillet and the other is at the junction of the spacer ring and the shaft (Fig. 5). Evidence of fretting was also found on the ring and the shaft.

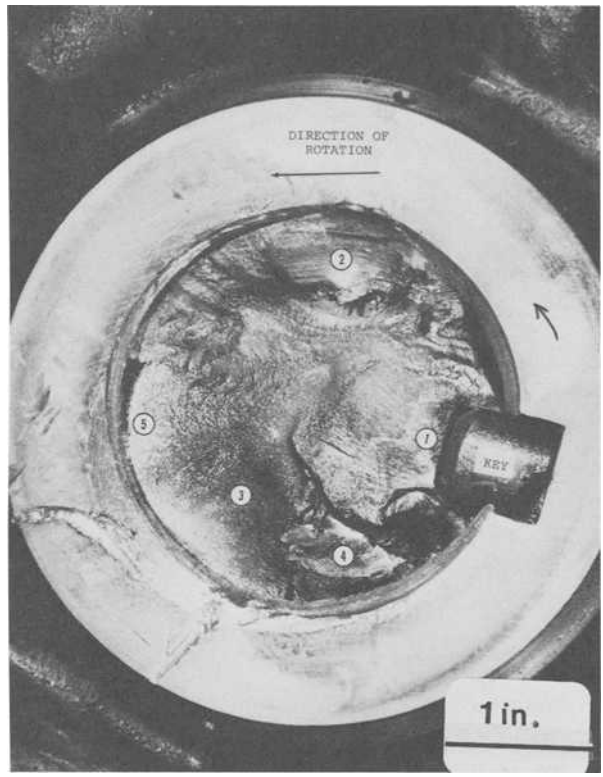

FIG. 3—*Appearance of the governor side fracture surface. Areas 1 to 5 were damaged.*

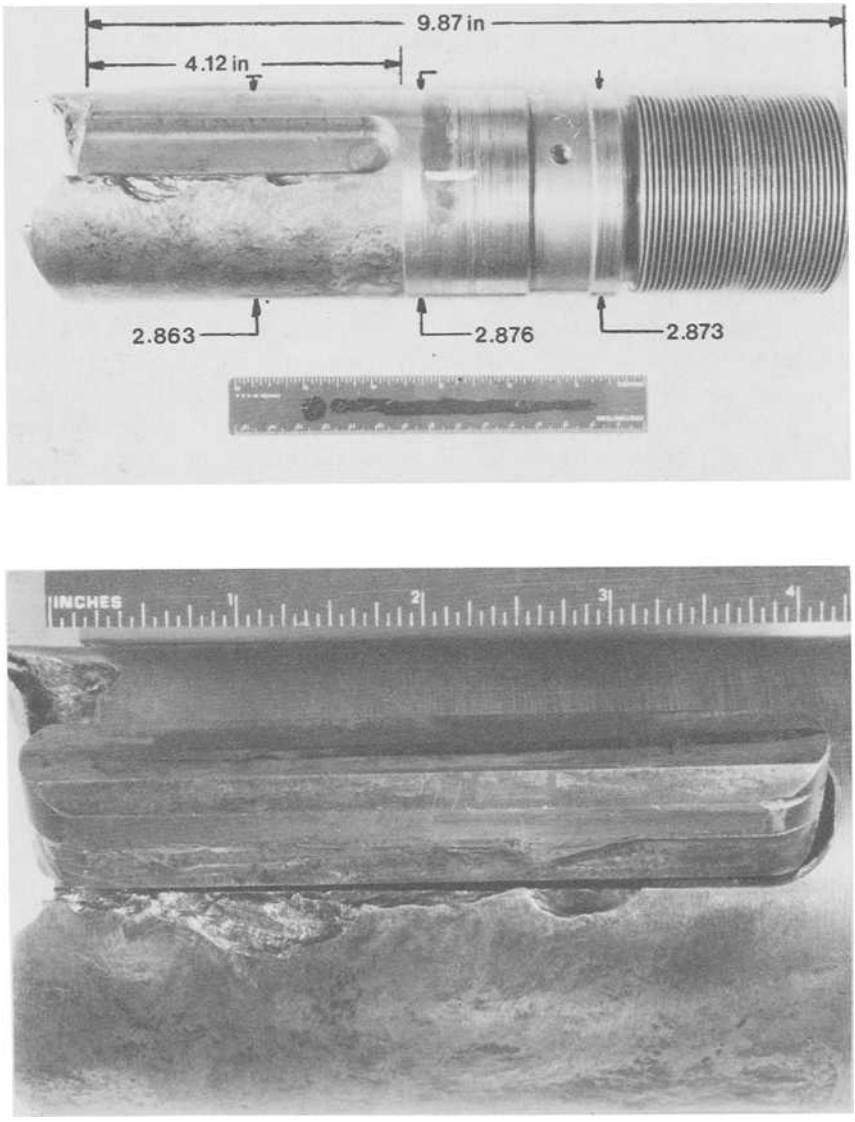

FIG. 4—*Damage to shaft, keyway, and key.*

Important features of the damage are as follows:

1. Shaft fracture surface with more than one fracture plane.
2. Fretting damage to the spacer ring and the shaft.
3. Damage to the keyway on the load carrying side, in the form of fretting and lost fragments.
4. Damage to the bore of the impeller by fretting.

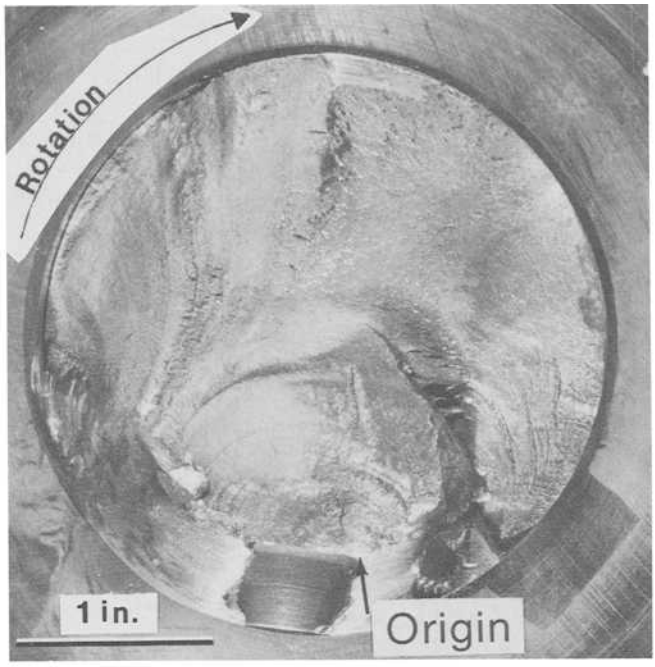

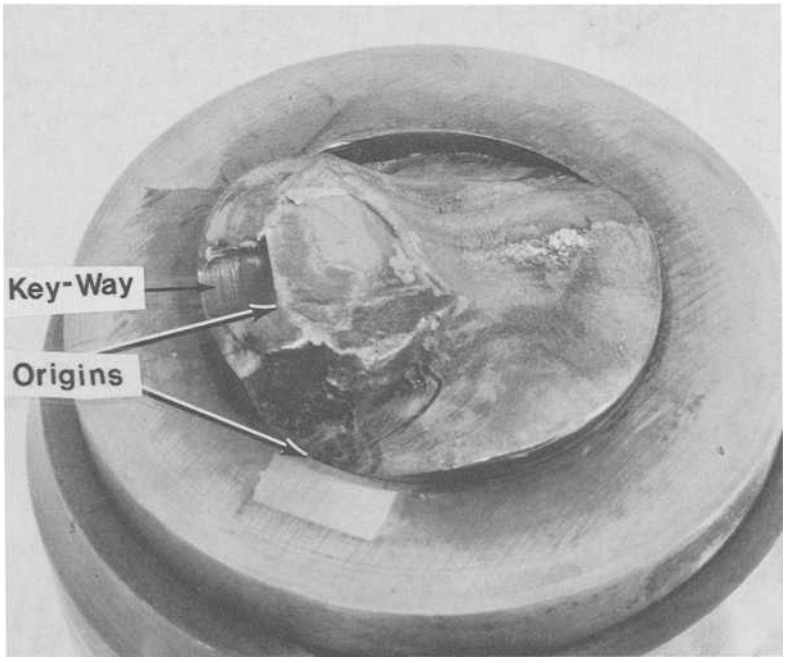

FIG. 5—*Appearance of generator end fracture surface. Note the crack is not planar.*

The primary origin of the fracture is located at the keyway fillet. This was determined by studying the beach marks, which are characteristic of a fatigue fracture surface [*3*]. A secondary crack initiating under the spacer ring also propagated and joined the primary crack and propagated until overload failures occurred. Initiation of the crack at the keyway occurred probably under rotating bending fatigue loading and propagated part-way through. Then the propagation of the crack seems to have been influenced by a combination of bending and torsional loads. About 80% of the fracture area was estimated to be associated with the fatigue-type loading.

SEM and TEM Fractography

Except for the beach marks, the areas immediately adjacent to the keyway did not contain any distinct fractographic features. This area and many other areas were probably damaged by rubbing or fretting or both. The fractographic features of primary interest were fatigue striations and dimple rupture areas. Typical appearance of the fatigue striations is shown in Fig. 6. Isolated dimples were also found in some areas, and the final overload fracture was predominantly by dimple rupture (Fig. 7).

After an extensive study of the fracture surface by SEM, some areas were selected for replication for TEM study. These areas were judged to be free of rubbing or corrosion damage. Double-stage plastic carbon replicas were taken from locations marked 1 to 13 in Fig. 8. Most of the replicas indicated that striated fatigue was the primary mode of crack propagation (Fig. 9). Striation spacing measurements were made from many TEM fractographs at various crack lengths. The results are summarized in Table 1. Application of these results for estimating the cyclic stresses that caused the fracture will be discussed later.

Chemistry and Mechanical Properties

The results of the chemical analysis of the shaft material are summarized in Table 2. The material is plain carbon steel similar to SAE 1040. Tensile properties along the longitudinal and the transverse directions were determined (Table 3). Fatigue strength of the material at room temperature was determined using a rotating beam smooth bar; these results are also included in Table 3. All these properties met the requirements of the corresponding design specifications for this material.

Stress Estimation Using Fractography

The great practical importance of knowing the stress amplitude that causes the fracture of any component is obvious. Fatigue striation spacing measurements aid in the estimation of these stresses. Sufficient data are found in the literature [*4*] to show that each striation is formed by one cycle of applied

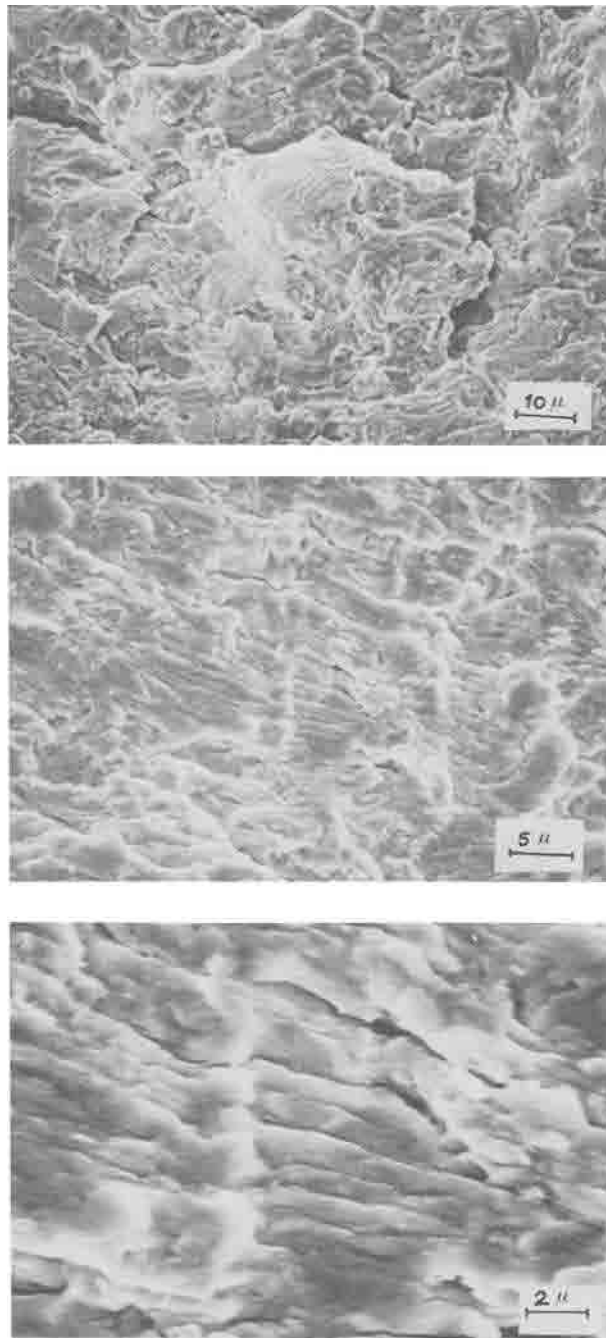

FIG. 6—*SEM fractographs showing typical appearance of fatigue striations.*

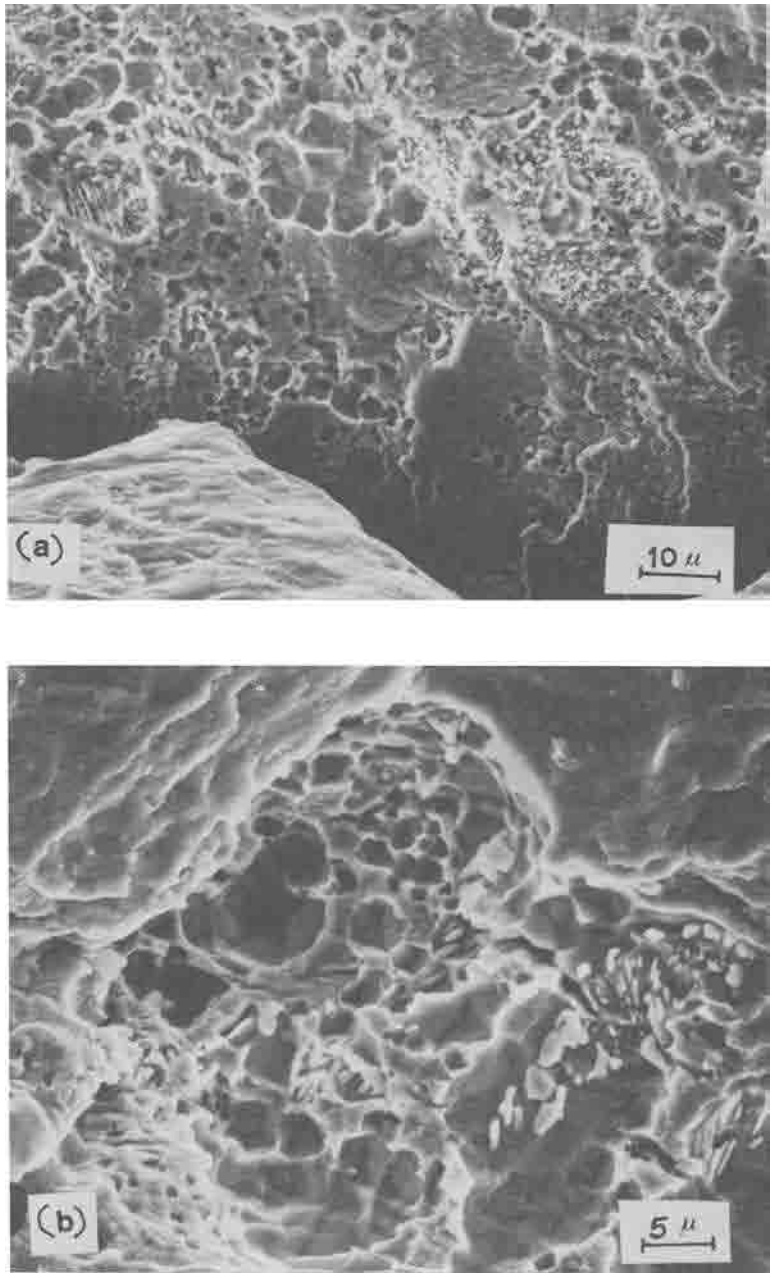

FIG. 7—*Example of dimples in fatigue area* (a) *and in overload fracture area* (b) *(SEM fractographs).*

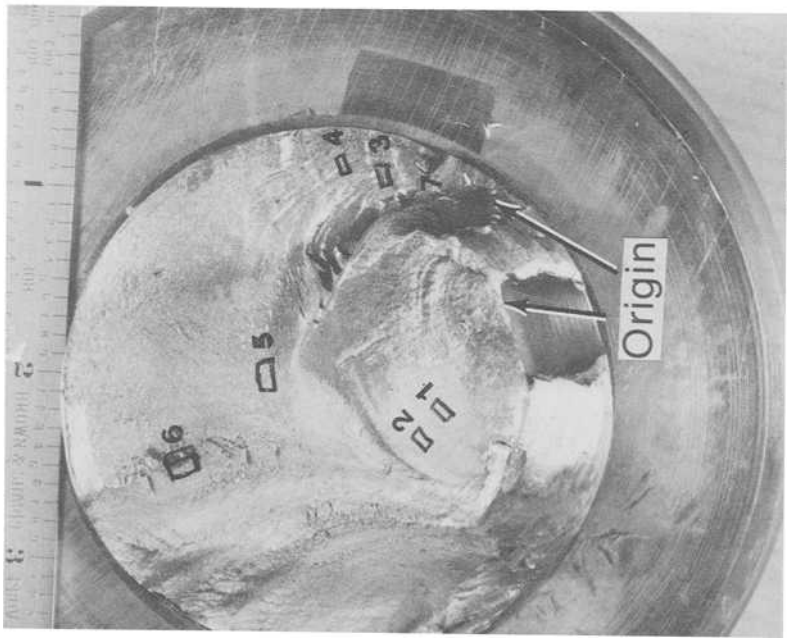

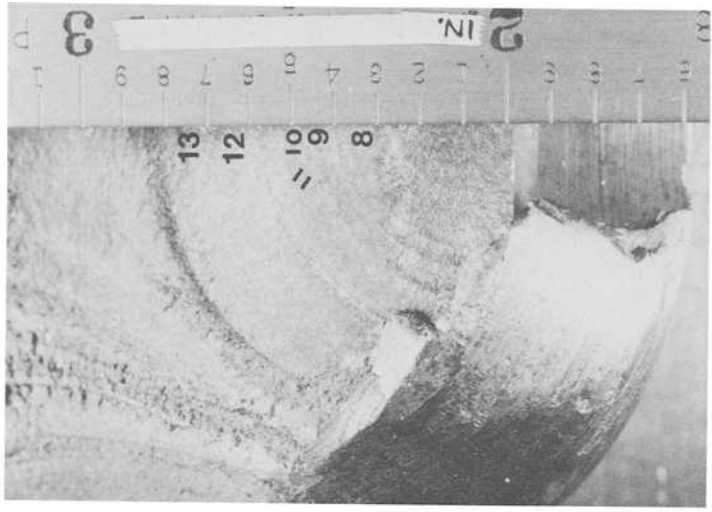

FIG. 8—*Replica locations for TEM study.*

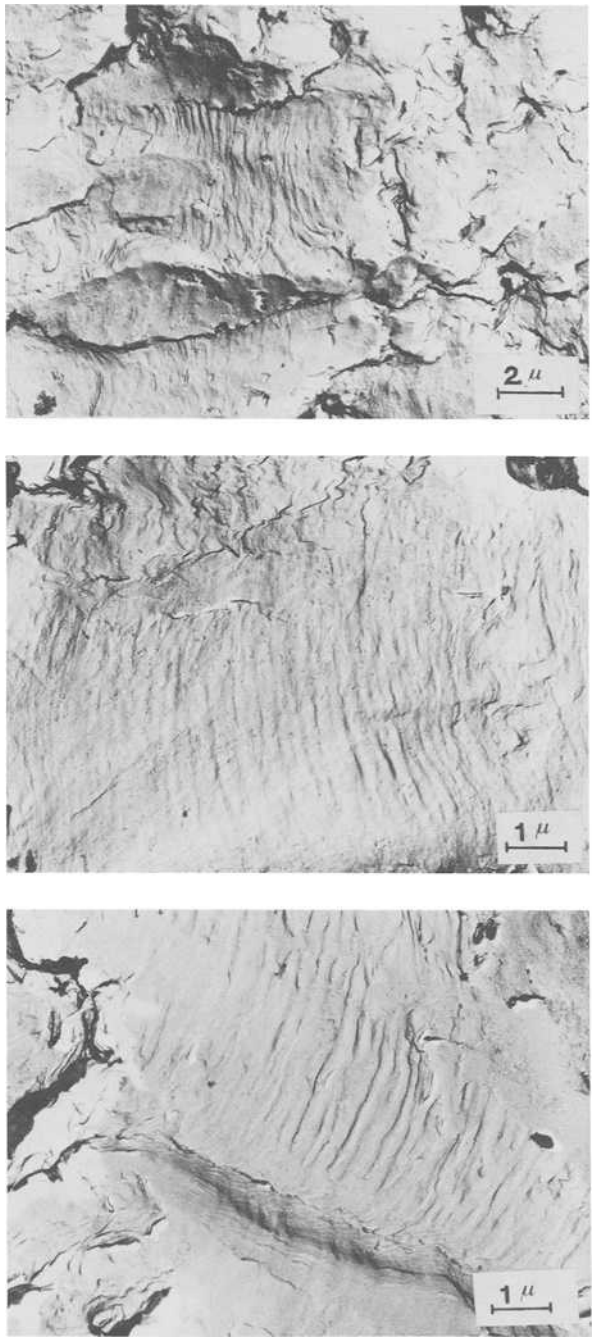

FIG. 9—*TEM replicas showing areas with fatigue striations.*

TABLE 1—*Summary of striation spacing measurements from the shaft fracture surface.*

Replica Location in Fig. 8	Crack Depth, in.[a]	a/R	Striation Spacing, μin.	Number of Striations
8	0.715	0.49	33	16
3	0.735	0.51	16.3	11
9	0.835	0.58	24.1	11
1, 10, 11	0.865	0.59	32.2	19
2	1.035	0.72	18	18
12	1.055	0.73	20	9
13	1.135	0.79	15.3	10
5	1.195	0.82	12.5	14
6	0.595	0.41	28	9

[a]1 in. = 25.4 mm.

TABLE 2—*Chemistry (weight percent) of shaft material.*

C	Mn	P	S	Si	Ni	Cr	Mo	V	Fe
0.44	0.90	0.029	0.026	0.30	0.32	0.1	0.05	0.004	balance

TABLE 3—*Tensile and high-cycle fatigue properties.*

Property	Longitudinal	Radial
Yield strength, MPa (ksi)	276 (40)	262 (38)
Tensile strength, MPa (ksi)	531 (77)	510 (74)
Elongation in 51 mm (2 in.), %	33.1	31
Reduction of area, %	58	49.4
Brinnell hardness	150	145
Fatigue strength (10^7 cycles, rotating beam) = 248 MPa (36 ksi)		

stress, although the total crack extension per cycle may be the sum of striation growth and dimple rupture that may occur during any given stress cycle. Empirical relationships between the striation spacing (S) and the stress intensity factor range (ΔK) are of the form [*1,2,4*]

$$S = A\,(\Delta K)^n \tag{1}$$

where A and n are constants. The typical value of n is 2 for a wide variety of material and specimen geometries [*1,5*]. The relationship between ΔK, crack depth a, and nominal alternating stress $\Delta\sigma$ may be given as

$$\Delta K = C \cdot \Delta\sigma \cdot \sqrt{a} \tag{2}$$

where C is a calibration factor dependent upon the ratio of crack depth to radius (a/R). Combining Eqs 1 and 2 yields

$$S = AC^2 \cdot \Delta\sigma^2 \cdot a \tag{3}$$

Equation 3 can be rearranged to give

$$\Delta\sigma = \sqrt{(S/B^2 \cdot a)} \tag{4}$$

where $B^2 = AC^2$.

By knowing several values of the striation spacing S and the corresponding values of a, Eq 4 can be used to calculate $\Delta\sigma$, provided the values of the constant B are known. The direct approach for getting values of B is by conducting similar tests at known stresses to obtain suitable fracture surfaces from similarly shaped (but not necessarily the same size) specimens. By obtaining average striation spacing measurements at various crack depths from these model specimens it is possible to calculate the constant B by rearranging Eq 4 as follows:

$$B = \sqrt{(S/a)}\ /\Delta\sigma \tag{5}$$

Values of B thus obtained are not dependent on the radius of the shaft but are dependent on a/R ratio. Therefore once the constant B is determined by scale-model tests it can be applied to any shaft size, provided the shaft geometry is similar. Data from such tests using 1/5 scale and 1/2 scale-model specimens were available from an earlier work [*6*]. The relationship between calibration factor B and a/R ratio is shown in graphical form in Fig. 10. This is essentially a master curve that can be used to generate the fatigue striation spacing for any crack depth for a given stress level. The section size dependency is not discernable in Fig. 10, since the data points from the two scale-model specimens fall in the same scatter band. The curve reaches a minimum at an a/R value of approximately 0.1. This is a consequence of the stress concentration of the keyway fillet that influences the crack growth rate and hence the striation spacing. By using the data extracted from Fig. 10, plots of fatigue striation spacing for a full-scale model (R = 36.5 mm) can be developed for various stresses (Fig. 11). A family of curves is drawn for stresses of 69, 103, 138, and 207 MPa (10, 15, 20, and 30 ksi). Note that these curves are not linear and the drop in the vicinity of a/R = 0.1 is a consequence of the minimum in the curve in Fig. 10.

The values of striation spacing measured from the current shaft fracture surface are also plotted in Fig. 11. These points fall between the curves corresponding to 103 and 207 MPa (15 and 30 ksi); that is, the striations were caused by nominal stress amplitude of about 138 MPa (20 ksi). The striation spacing does not increase with crack length (Table 1). This could be due to retardation of crack growth by sporadic overloading [*7*] and also changes in the macroscopic and microscopic crack growth directions. Such conditions may change the local stress levels, causing the variations in the fatigue striation spacing.

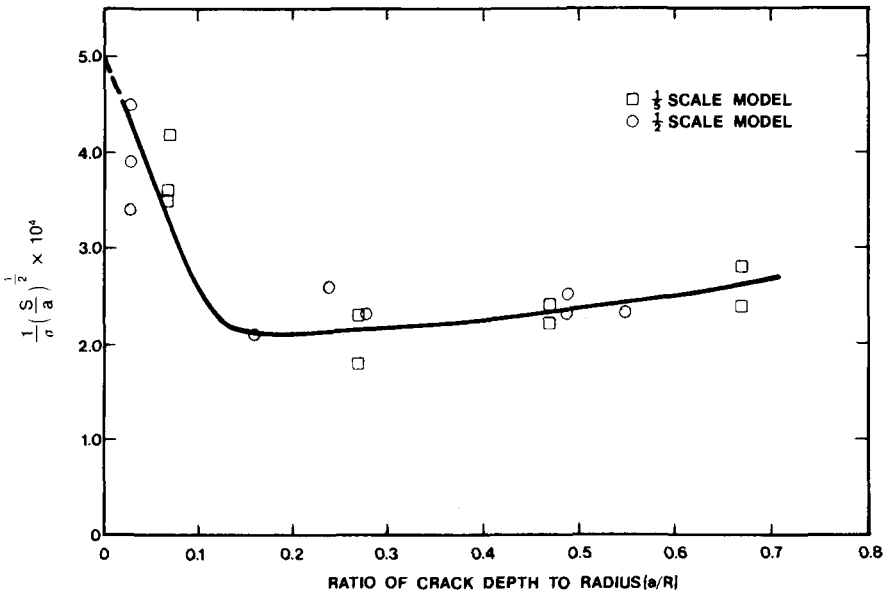

FIG. 10—*Relationship between calibration factor and ratio of crack depth to radius from scale-model tests.*

Discussion

We conclude from the macroscopic and fractographic observations that the fracture of the shaft initiated from the keyway fillet and propagated along with another crack initiated due to fretting. One important difference between the fracture of the shaft and that of the model test specimens is that the model specimens had the multiple origins indicative of typical rotating beam fracture mechanism. Multiple origins around the circumference were not found in the current failure. The origins and the direction of crack propagation are schematically shown in Fig. 12. Since heavy fretting damage was present on the shaft and the impeller bore due to loose fit, the fatigue strength of the shaft could be reduced [*8, 9*].

This fracture mechanism can not be completely classified either as rotating bending or reversed bending type. From the appearance of the fracture plane in Fig. 5 the presence of torsional loading was also suspected. The proof for such loading was found in the form of peeling-type fracture [*10*] initiating from the bottom of the keyway (Fig. 13). Under normal operating conditions the reverse bending and torsional stresses are very low, on the order of less than one tenth of the fatigue strength of the material. However, under abnormal operating conditions higher stresses may be encountered. Such conditions seem to have been present before initiation of the crack. The auto-stop body (Fig. 2) was loose when the crack was discovered on the shaft. This

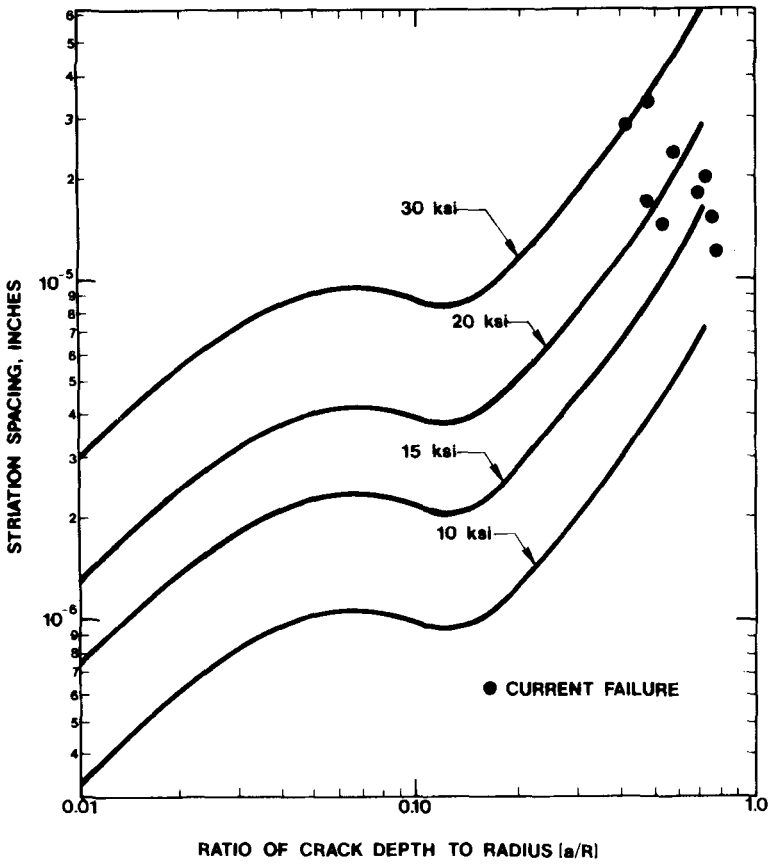

FIG. 11—*Comparison of measured fatigue striation spacing from the shaft fracture with calculated values for various stress levels.*

would cause loosening of the pump impeller and also would apply large bending loads to the shaft by eccentric rotation. Since the pump impeller was loose, nearly all the torque would be transmitted through the key. In the presence of torsional oscillations such a condition would lead to the initiation of cracks at the bottom edge of keyway parallel to the longitudinal axis of the shaft (Fig. 13).

An important observation was that the key, the keyways on the shaft and on the impeller suffered severe damage. A long imprint of the key at the bottom of the bronze impeller keyway was found (Fig. 14). This was probably caused by a sudden torque overload by abnormal operating conditions (such as sudden changes in loads or out-of-phase synchronization of the unit when switched to the power distribution line). Such an incident probably initiated the crack, and the combination of bending and torsional loading conditions propagated the crack to failure under high-cycle fatigue mode. The stresses that led to the

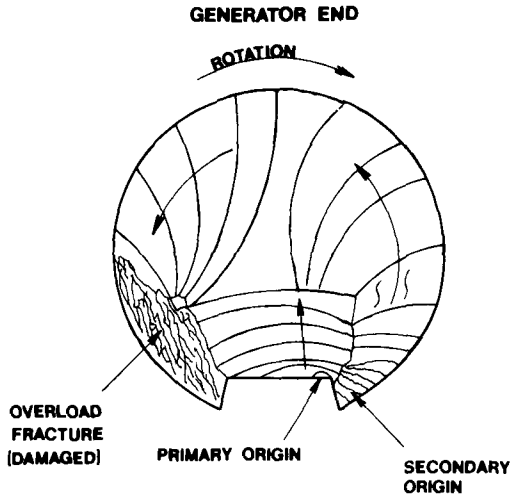

FIG. 12—*Fracture origins and crack propagation direction. About 80% of the fracture is by fatigue.*

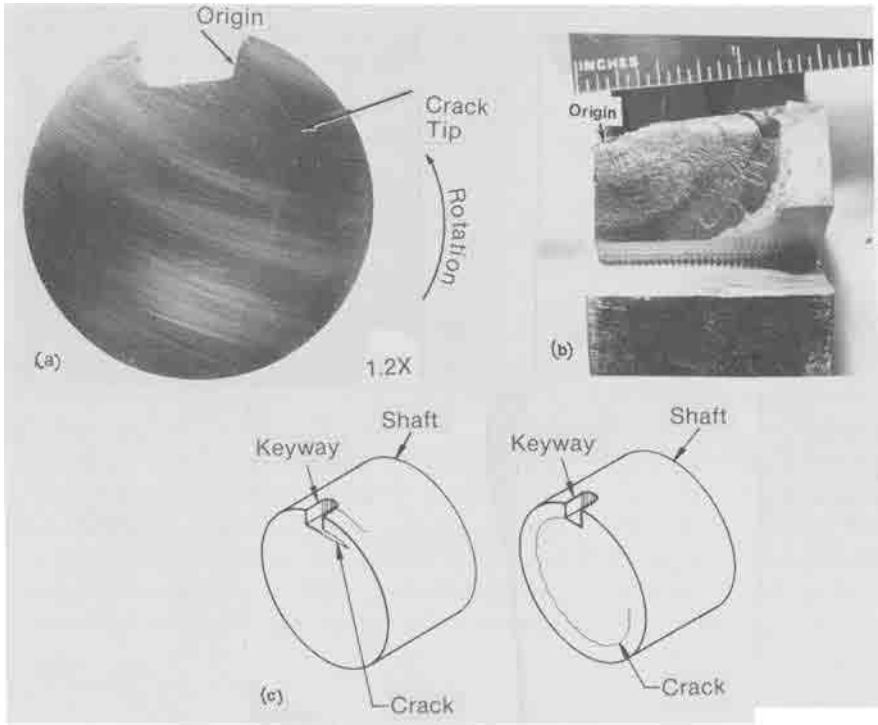

FIG. 13—*Peeling-type crack as seen under black light* (a), *after opening the fracture surface* (b), *and sketches from Ref* 10 (c).

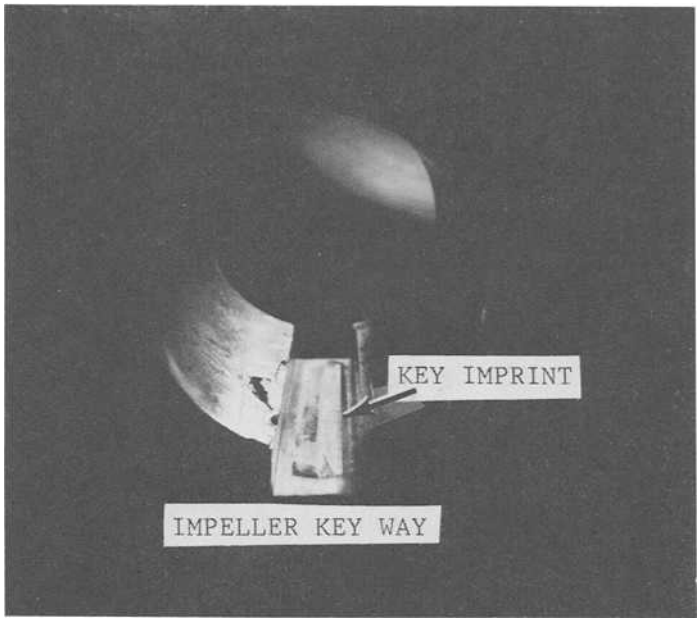

FIG. 14—*Keyway damage in bronze impeller bore. The damage caused by fretting and the long impression at the bottom of keyway imprinted by the key are visible.*

propagation of the crack would have occurred either during the last few days or sporadically during the life of the shaft.

The microstructural study of the shaft material was conducted on specimens taken near the keyway origin and other locations. The microstructure consisted of ferrite and pearlite (Fig. 15), which is typical for this grade of steel.

Conclusions

Macrofractography and microfractography were successfully applied in the analysis of the main oil pump shaft fracture. Fatigue striation spacing measurements were used to estimate the nominal stresses. The stresses that caused the propagation of the crack were in the range of 103 to 207 MPa (15 to 30 ksi). The fracture of the shaft was by low-stress, high-cycle fatigue loading. Fracture initiated at the keyway fillet and at the fretted surface, and propagated under combined torsional and bending loads. The mechanical properties and chemistry of the shaft met the material specification requirements.

Acknowledgments

R. C. Bates of the Westinghouse Research and Development Center is thanked for informative discussions. Review of the manuscript and comments

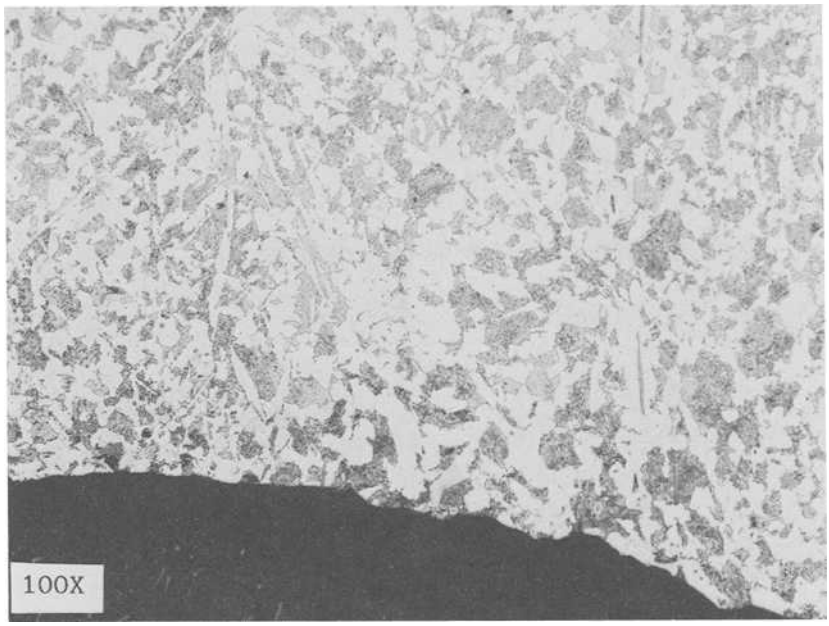

FIG. 15—*Microstructure of the shaft material near the keyway origin, showing ferrite and pearlite.*

by L. D. Kramer are also acknowledged. B. Pilla and G. Cotellesse are thanked for assistance in fractography work.

References

[1] Bates, R. C. and Clark, W. G., *ASM Transactions*, Vol. 62, June 1969, p. 380.
[2] Madeyski, A. and Albertin, A. in *Fractography in Failure Analysis, ASTM STP 645*, B. M. Strauss and W. H. Cullen, Jr., Eds., American Society for Testing and Materials, 1978, pp. 73-83.
[3] "Interpretation of Light Microscope Fractographs," in *ASM Metals Handbook: Vol. 9—Fractography and Atlas of Fractographs*, American Society for Metals, 1975, p. 43.
[4] McMillan, J. C. and Pelloux, R. M. in *Fatigue Crack Propagation, ASTM STP 415*, American Society for Testing and Materials, 1967, p. 505.
[5] Ritchie, R. O. and Knott, J. F., *Acta Metallurgica*, Vol. 21, May 1973, pp. 639-648.
[6] Bates, R. C., unpublished work, Westinghouse Research Laboratories, Pittsburgh, 1973.
[7] Jones, R. E., *Engineering Fracture Mechanics*, Vol. 5, 1973, p. 585.
[8] Sachs, A., "Fretting Corrosion and Fatigue," in *Metals Engineering Design, ASME Handbook*, O. J. Horgen, Ed., American Society of Mechanical Engineers, 1953, p. 230.
[9] Waterhouse, R. B., *Fretting Corrosion*, Pergamon Press, Elmsford, N.Y., 1972, pp. 130-162.
[10] "Failure of Shafts," in *ASM Metals Handbook: Vol. 10—Failure Analysis and Prevention*, American Society for Metals, 1975, p. 385.

H. C. Burghard[1] *and D. R. McCann*[2]

Fractographic Analysis of a Steam Turbine Disk Failure

REFERENCE: Burghard, H. C. and McCann, D. R., **"Fractographic Analysis of a Steam Turbine Disk Failure,"** *Fractography of Ceramic and Metal Failures, ASTM STP 827*, J. J. Mecholsky, Jr. and S. R. Powell, Jr., Eds., American Society for Testing and Materials, 1984, pp. 346-367.

ABSTRACT: A metallurgical evaluation of a failed steam turbine disk was performed. The disk in question had failed in service and was one of eleven shrunk-on disks comprising the LP turbine rotor of an electric generating unit. The investigation included detailed fractographic examinations of the initiation area of the primary fracture and metallographic and fractographic examination of subcritical defects. A critical magnetic particle inspection of all blade grooves was performed, and mechanical properties tests and chemical analyses were conducted to characterize the disk material. Slow-strain-rate tests were also performed to investigate the cracking susceptibility of the disk material in selected environments. The observations made and the data obtained indicate that subcritical crack growth occurred in certain blade attachment grooves by some form of stress corrosion cracking. On the basis of the results of this investigation, the failure of the disk is attributed to the combined effects of high operating stresses at the blade grooves, low fracture toughness of the disk material, and environment.

KEY WORDS: steam turbines, turbine disks, stress corrosion, NiCrMoV steels, fractography

A catastrophic turbine disk failure occurred in a low-pressure turbine at an electric generating station. The turbrine is a cross-compound 3600/1800-rpm unit that had been in service for approximately 21 years. The 1800-rpm, low-pressure turbine is a double-flow machine with eight stages at each end and a total of eleven shrunk-on disks.

The unit had been restarted after a short outage when the last-stage disk on the governor end burst without warning. The 5742-kg (12 660-lb) disk fractured into two major segments, approximately equal in size, and a number of

[1]Staff Engineer, Southwest Research Institute, San Antonio, Tex. 78284.
[2]Manager, Materials Engineering, Allis-Chalmers Corporation, Milwaukee, Wisc. 53201.

smaller fragments (Fig. 1). The primary fracture occurred in an essentially radial plane. Photographs of the primary fracture are shown in Figs. 2 and 3.

The disk contained axial fir tree blade grooves that supported 160 blades. It was forged in 1954 from a proprietary NiCrMoV steel similar to A 294-C1.6. The forging was normalized and tempered. The temperature of the rim at the time of failure was estimated to be about 43°C (110°F).

A major investigation was initiated by the utility and manufacturer with the object of identifying the principal factors involved in the failure. This paper presents only the results of an extensive fractographic and metallographic examination and supporting data from a few of the metallurgical tests. It should be noted that finite-element stress analyses, fracture mechanics analysis, and corrosion tests were also performed. The complete investigation showed that the disk failure occurred due to the combined effects of high operating blade groove stress, low material fracture toughness, and environment.

Procedures

The investigation was organized to provide a complete characterization of the disk material, establish the extent of any subcritical cracking, and identify the fracture mechanism(s) involved in the failure. All the parts of the disk were recovered, fitted together to identify the relative position of the various segments, and visually examined to establish the overall macroscopic features of the failure. After initial identification of all the segments, magnetic particle inspections of the blade grooves in all segments were performed.

Chemical analyses of the disk material were performed to determine the bulk composition, and selected metallographic sections were examined to establish the microstructure.

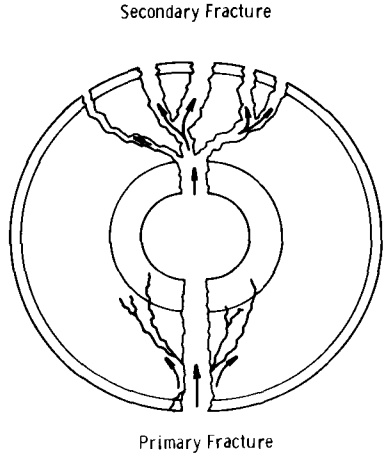

FIG. 1—*Schematic diagram of failed disk.*

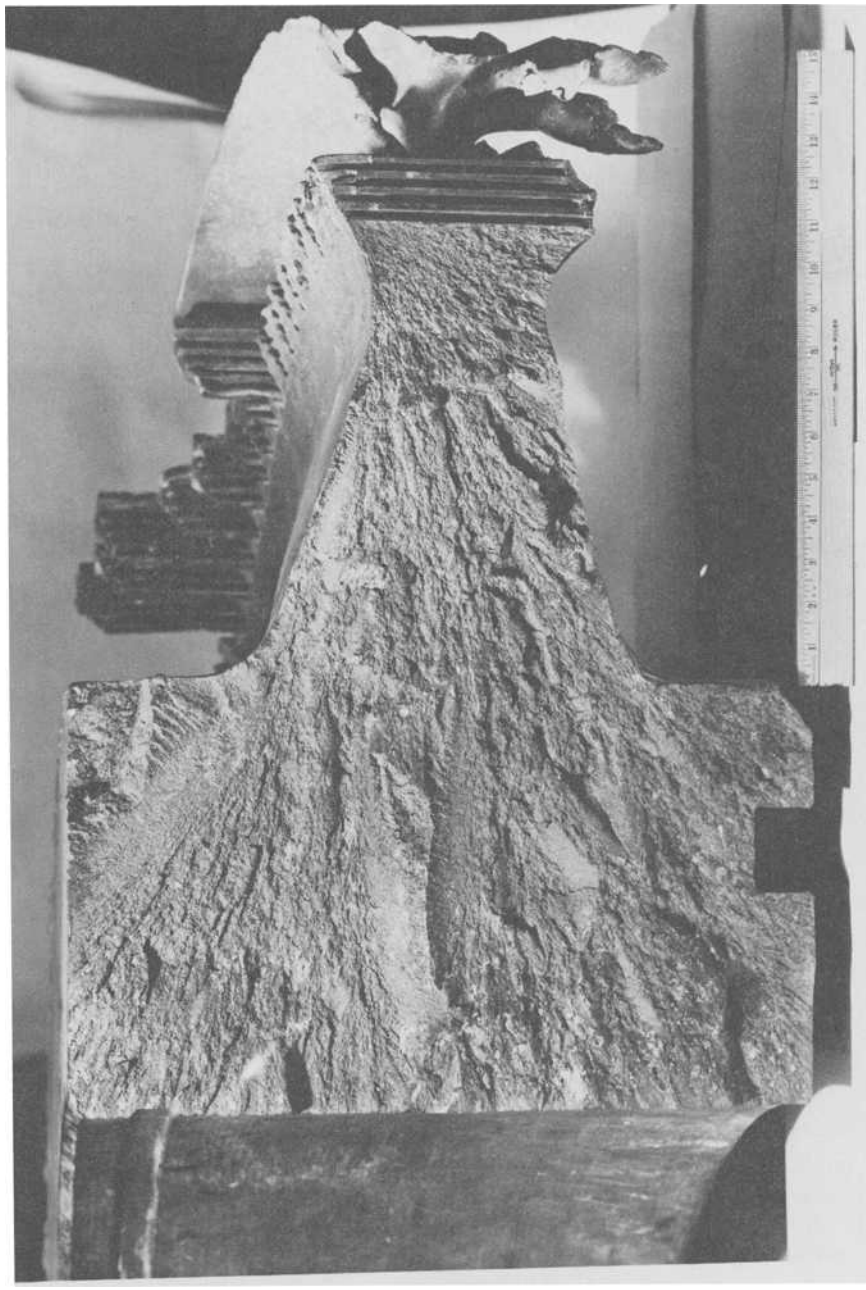

FIG. 2—*Surface of primary fracture.*

FIG. 3—*Fracture surface at base of blade attachment groove. Inlet side is at left.*

A section containing the primary fracture surface was cut from one of the major disk segments. Four specimens representing an area approximately 89 by 89 mm (3½ by 3½ in.) at the base of the blade groove on the inlet side were removed from this section for fractographic examination. These specimens were electrolytically cleaned to remove surface films and deposits, and a detailed fractographic examination was performed utilizing the scanning electron microscope (SEM). Sections containing representative subcritical cracks, as revealed by the magnetic particle inspection, were also cut from the disk sample. These specimens were then sectioned or broken open, or both, to provide for metallographic and fractographic examinations. Energy dispersive spectrographic techniques were employed to provide a qualitative analysis of the deposits within the subcritical cracks.

After completion of the metallographic and fractographic examinations, a series of slow-strain-rate tests were performed on specimens of the disk material. The slow-strain-rate test is a well-recognized procedure for the qualitative assessment of cracking susceptibility [*1*]. In these tests, specimens

are loaded in uniaxial tension at a very slow strain rate in an environment of interest, then the tests are continued to fracture. Cracking susceptibility is judged by the relative reduction in area as compared to results in a nonaggressive environment and by the extent of cracking in the test section.

Results

Macroscopic Features of Main Fracture

The overall macroscopic features of the primary fracture indicate a generally brittle fracture (Fig. 2). That portion of the fracture surface adjacent to the blade groove was flat and relatively smooth. The surface features become coarser toward the bore of the disk, forming distinct directional markings. These features clearly establish that the fracture initiated at the base of the blade attachment groove on the inlet side of the disk and propagated in a generally radial direction from the rim toward the bore. Although the fracture origin and direction of fracture were clearly defined, there was no macroscopic evidence to identify the zone of subcritical crack growth (Fig. 3).

Nondestructive Examinations

Wet magnetic particle and eddy-current methods were used to examine all the 160 blade grooves for cracks. The initial magnetic particle inspections did not reveal any crack indications, and the results of the initial eddy-current tests were indefinite. The inspection procedures for both methods were improved and refined during the course of the investigation. As a result, new crack indications were continually discovered over a period of time. Eventually, both methods provided correlating crack indications at the base of certain blade grooves.

In the final analysis, distinct crack indications were observed in 15 of the 160 blade grooves. These indications ranged in length from 1 to 15.2 mm (0.040 to 0.60 in.) and were concentrated within 20 blade grooves in the immediate vicinity of the groove which contained the origin of the primary fracture. A sketch of the blade groove configuration and a typical magnetic particle indication are shown in Fig. 4. All indications were on the inlet side of the disk and all were adjacent to the 0.64-mm (0.025-in.) blade groove radius. Several of the indications, such as the one shown in Fig. 4, included short disconnected segments. This feature is an indication of multiple crack initiation along the blade groove. Subsequent microscopic examination confirmed that the indications were subcritical cracks.

Magnetic particle inspections of the two intact keyways were also performed (secondary fracture occurred through one keyway). No crack indications were observed in either keyway.

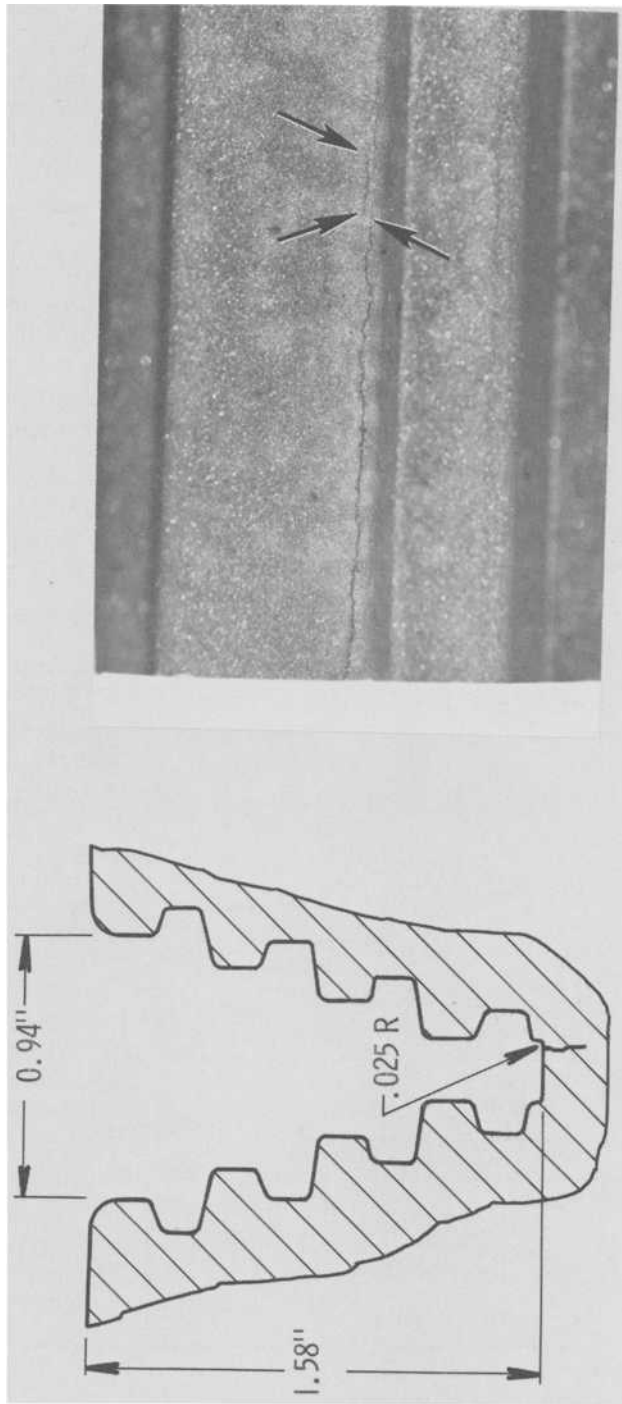

FIG. 4—*Blade attachment groove details.* (left) *Schematic drawing of groove.* (right) *Magnetic particle crack indication at base of groove.*

Composition, Mechanical Properties, and Microstructure

Chemical analyses of representative specimens of the disk material were analyzed at two independent laboratories. The maximum variation in the results from the two laboratories was 0.06% for nickel. All other concentration values varied by 0.03% or less. The average values of the results from the two analyses are presented in Table 1, together with the Mill Test Report and the specified composition. These results show that the chemical composition of the disk material conformed to the specification.

Tangential tension specimens were removed from the disk at various locations around the perimeter. These specimens were stress relieved at 593°C (1100°F) to minimize any effect of deformation produced by the rupture and then tested in uniaxial tension. The data listed in Table 2 show that the tensile properties conformed to the specification, and that the tensile and yield strengths are about 70 MPa (10 ksi) greater at the primary fracture than at the

TABLE 1—*Chemical composition of failed disk.*

	Composition, wt%		
Element	Present Analysis	Mill Test Report Ht. B 5816	Specification
Carbon	0.29	0.30	0.40 maximum
Manganese	0.71	0.70	0.90 maximum
Silicon	0.24	0.25	0.15 to 0.35
Nickel	2.74	2.70	2.50 minimum
Chromium	0.78	0.78	0.40 minimum
Molybdenum	0.48	0.54	1.50 maximum
Vanadium	0.16	0.16	0.25 maximum
Sulfur	0.006	0.015	0.050 maximum
Phosphorus	0.01	0.008	0.050 maximum

TABLE 2—*Tensile properties.*

	Tensile Strength		Tensile Strength			
Location	MPa	(ksi)	MPa	(ksi)	Elongation, %	Reduction of Area %
0 deg[a]	1010.8	(146)	803.9	(125.3)	16.5	46.0
90 deg	959.8	(139.2)	806.0	(116.9)	16.5	44.0
180 deg[a]	952.9	(138.2)	817.8	(118.6)	15.0	46.0
270 deg	1006.0	(149.9)	859.8	(124.7)	17.0	46.0
Specification (minimum)	827.4	(120)	724.0	(105)	14.0	35.0

[a]0 deg is primary fracture location; 180 deg is secondary fracture location.

secondary fracture. Brinell hardness measurements also confirmed the variation of tensile strength around the disk. Hence all cracks detected by the nondestructive inspection were confined to the hardest region of the disk.

Tangential Charpy V-notch (CVN) impact specimens were removed near the primary fracture and were tested over a temperature range of 24 to 204°C (75 to 400°F). The results are listed in Table 3. These data indicate a CVN energy of 20 J (15 ft · lb) at 24°C (75°F). The 50% fracture-appearance-transition-temperature (FATT) was 149°C (300°F). Additional CVN specimens were given a deembrittlement treatment [593°C (1100°F), 2 h, water quenched] and tested; the FATT was 118.3°C (245°F). This shift of the FATT indicates a slight degree of temper embrittlement.

Plane-strain fracture toughness specimens were removed near the primary fracture and were tested in accordance with ASTM E 399. These data, also shown in Table 3, demonstrated that the disk had relatively low fracture toughness.

General microstructure examinations were made at the failure origin, at cracked and uncracked blade groove radii, at the interior of the forging, and at the bore. No differences in microstructure could be detected among the several locations. The microstructure consisted of upper bainite (Fig. 5). The McQuaid-Ehn grain size was 5 to 6. A very small amount of cold work, presumably from the broaching operation, was observed in the dovetail radii. The maximum depth was 0.015 mm (0.0006 in.).

TABLE 3—*Fracture toughness data.*

Charpy V-Notch Impact Energy Data

Temperature		Energy	
°C	(°F)	J	(ft · lb)
24.0	(75)	20.3	(15)
65.5	(150)	20.3	(15)
121.1	(250)	25.7	(19)
148.9	(300)	33.9	(25)
176.7	(350)	46.1	(34)
204.4	(400)	62.4	(46)

FATT (50%) = 148.9°C (300°F)

K_{Ic} Data

Temperature		K_{Ic}	
°C	(°F)	MPa$\sqrt{m}$	(ksi$\sqrt{in.}$)
21.1	(70)	47.9	(43.6)
21.1	(70)	50.9	(46.3)
21.1	(70)	56.5	(51.4)

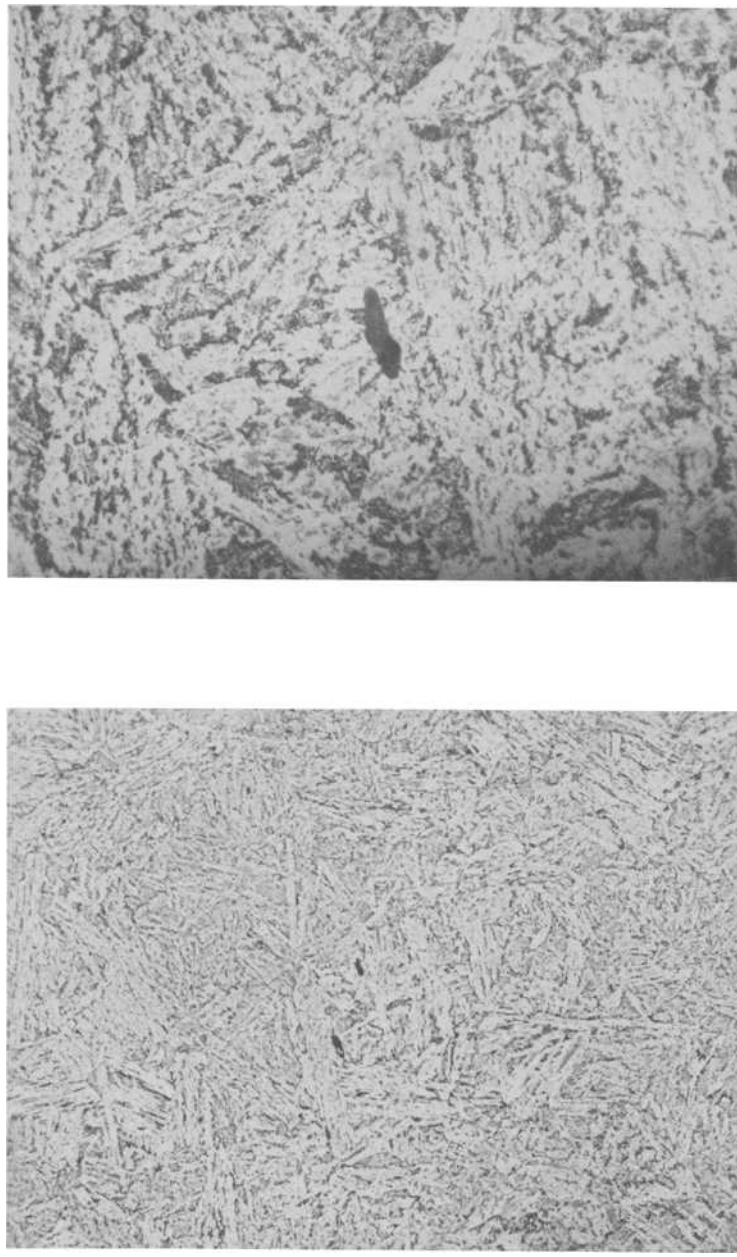

FIG. 5—*Microstructure of disk. Etchant: Picral. Reduced approximately 7% in reproduction.* (left) *Original magnification:* ×*100.* (right) *Original magnification:* ×*500.*

Metallographic and Fractographic Examinations

Initial fractographic examinations of the four primary fracture specimens revealed a substantial amount of post-fracture mechanical damage in the two specimens adjacent to the blade groove. The zone in the immediate vicinity of the corner at the inlet face was severely burnished, and some degree of burnishing or melted and resolidified metal was evident for the full length of the blade groove. A general scan of these specimens also established that all locations outside an arc of 25 mm (1.0 in.) radius about the inlet face corner were characterized by distinct cleavage facets. The undamaged portions of the fracture surface near the inlet-side corner exhibited several features which served to distinguish that zone from the major portion of the fracture surface. The corner area included a few isolated zones of intergranular facets and zones with limited, intergranular, secondary cracking. These zones were intermixed with transgranular fracture characterized by flat facets with "cleavage-like" features. In addition, a substantial portion of the inlet-side corner zone exhibited ill-defined features atypical of any specific fracture mechanism and showed evidence of corrosion of fracture surface.

The fine-scale topographic features observed at the inlet-side corner served to indicate a cracking mechanism other than mechanical cleavage and provided some evidence of slow crack growth prior to failure. No discrete fracture transition boundary was evident in the initial fractographic evaluation, and definite identification of a pre-existing crack or defect could not be made on the basis of fractographic features of the primary fracture alone. The extent of post-fracture damage also hindered the characterization of the fracture origin area.

A metallographic section through one of the subcritical cracks is shown in Fig. 6. At this location, the crack measured 1.1 mm (0.04 in.) deep. The fracture path consisted of limited intergranular features near the origin and at the midpoint of the fracture path and several straight, transgranular segments. These features are representative of the several subcritical cracks examined.

In each of the several subcritical cracks opened for fractographic examination, the crack surface was readily distinguishable from the fresh laboratory fracture. Each subcritical crack exhibited a distinct curved boundary and the crack surfaces were discolored. The exposed surfaces of two subcritical cracks, representing the largest and one of the smallest magnetic particle indications, are shown in Fig. 7.

In general, the fine-scale topographic features of all the subcritical cracks examined were very similar. Representative SEM fractographs from these crack surfaces are shown in Fig. 8, and the characteristic features are itemized as follows:

- Limited zones of intergranular facets and evidence of post-cracking corrosive attack were evident in zones corresponding to early stages of crack growth (Fig. 8*a*).

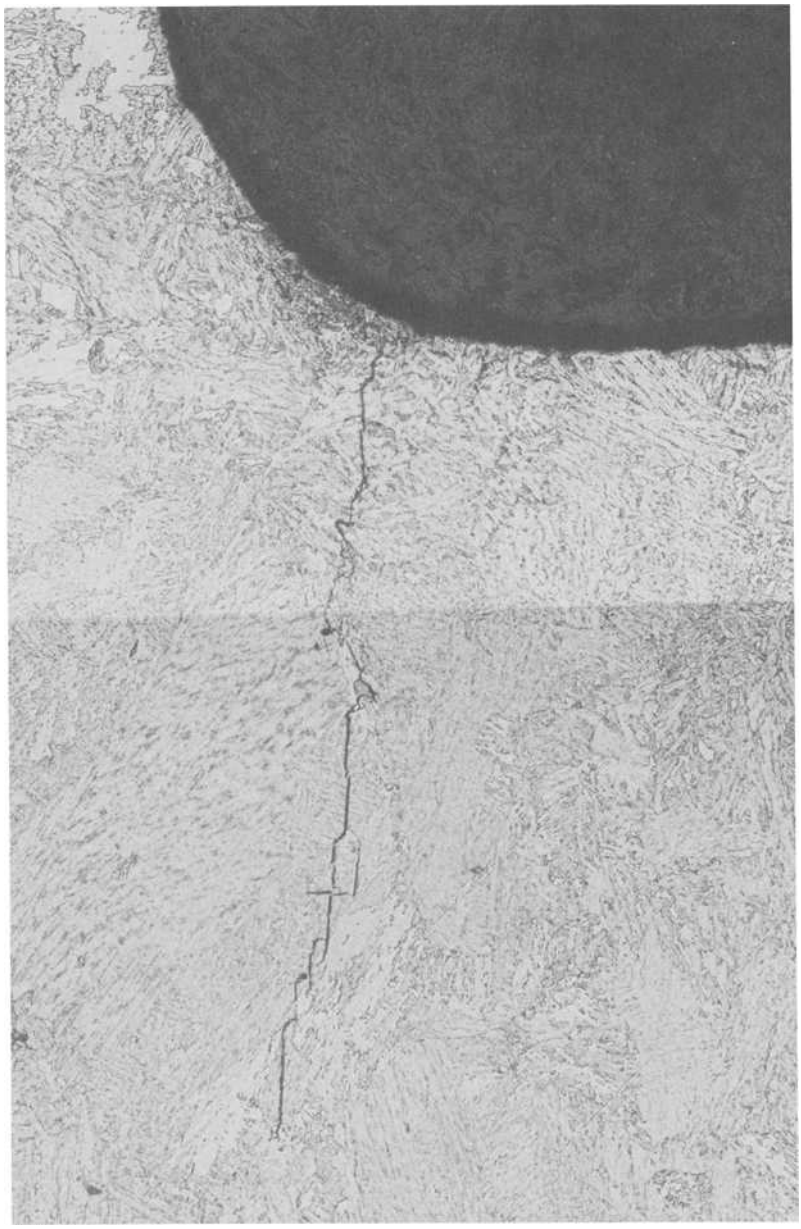

FIG. 6—*Section through a subcritical crack. Etchant: Nital.*

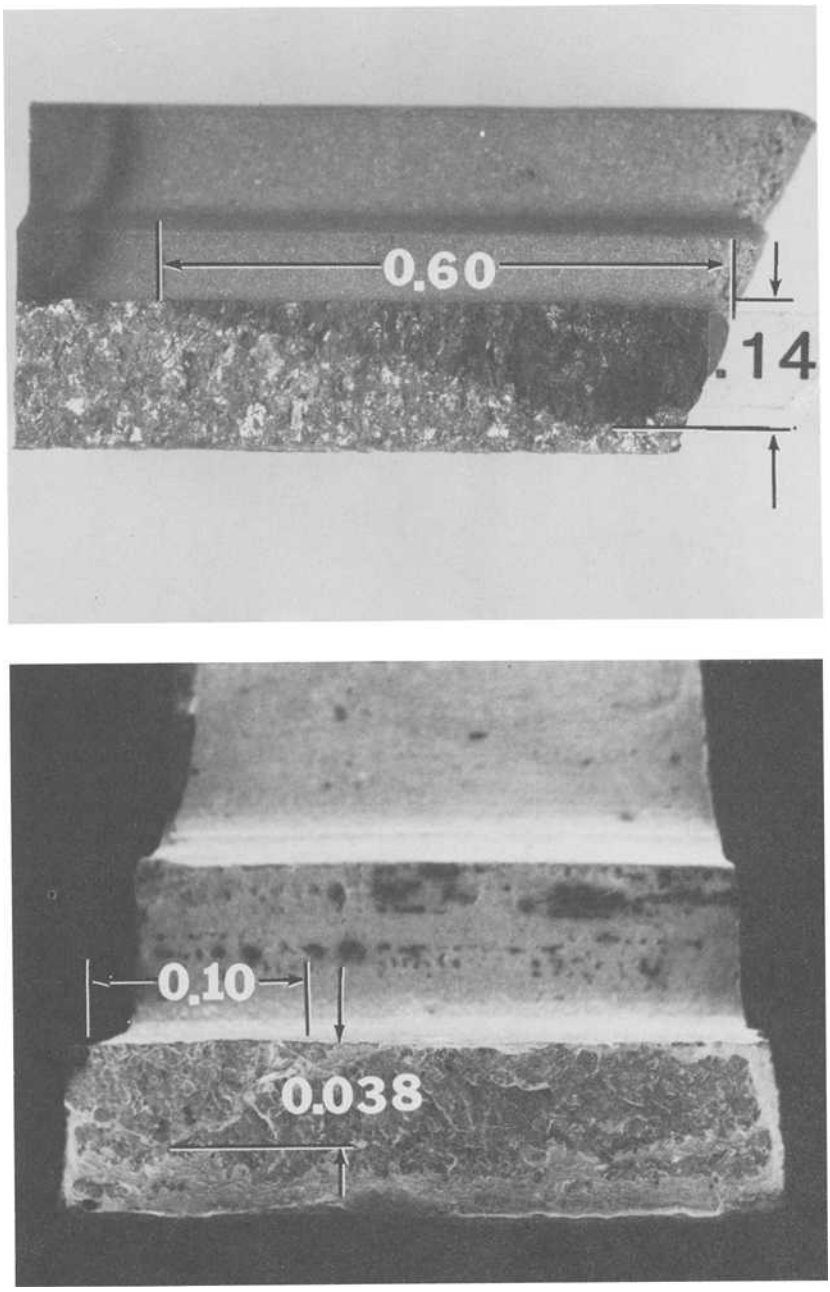

FIG. 7—*Exposed surfaces of subcritical cracks.*

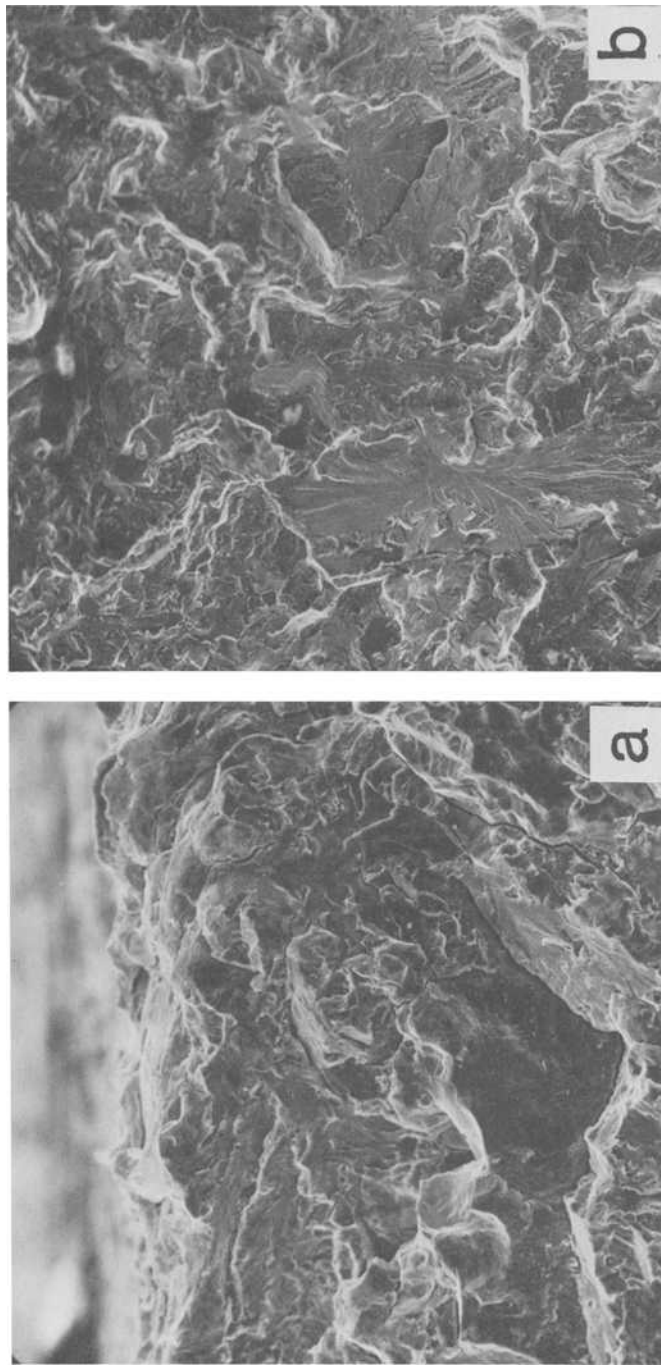
b
a

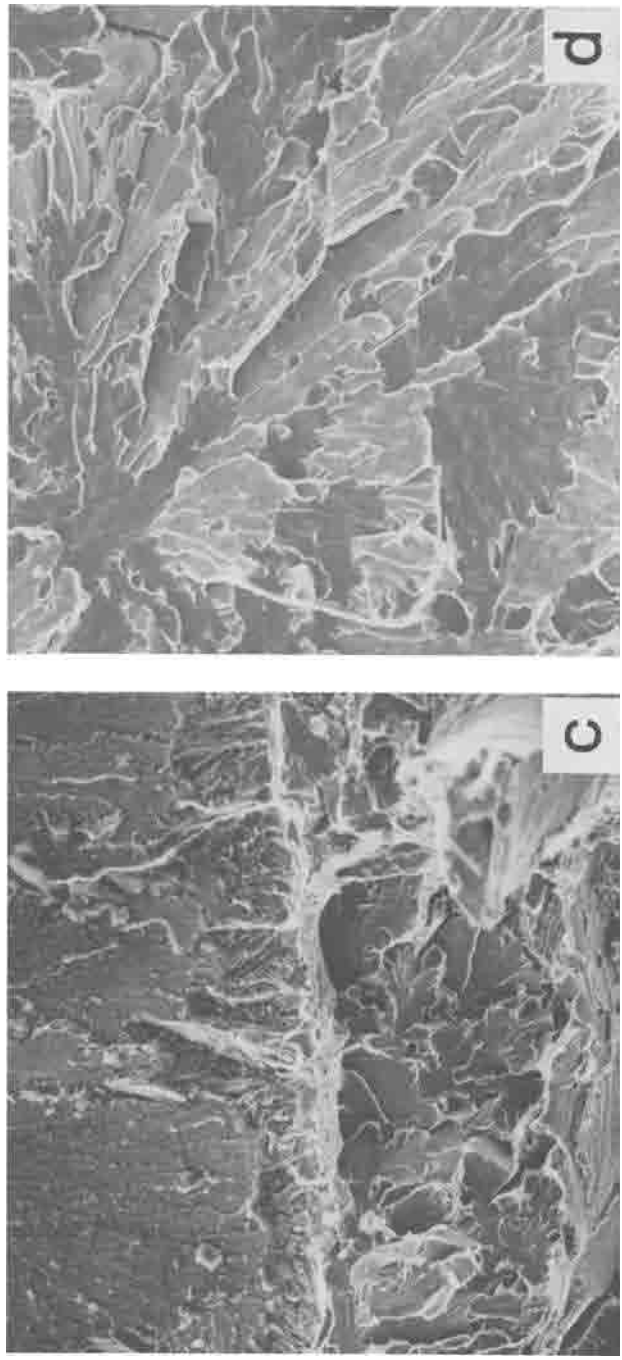

FIG. 8—*SEM fractographs from subcritical crack specimen.* (a) *At blade groove;* ×*300.* (b) *Central zone;* ×*300.* (c) *At boundary;* ×*500.* (d) *Fresh fracture;* ×*600.*

- In the as-exposed condition, a corrosion product or deposit was present on the subcritical crack surface.
- The major portion of each subcritical crack surface exhibited flat transgranular facets with small steps forming river patterns or fan markings. The typical transgranular zones were readily distinguishable from the distinct cleavage facets associated with the fresh laboratory fracture (Fig. 8*b*).
- The boundaries of the slow growth zones were readily identified as a distinct step in the surface and a narrow zone of dimples. Distinctly different fine-scale features were evident on each side of the subcritical crack boundary (Figs. 8*c* and 8*d*).

The fine-scale features of the inlet-side corner of the primary fracture surface were generally similar to those observed in the examination of the several subcritical cracks. In light of this similarity, the results of the initial fractographic examination of the primary fracture were reviewed and further critical examinations were made. Representative SEM fractographs from the initiation zone and from the unstable, fast-fracture zone of the primary fracture surface are shown in Fig. 9. Locations near the corner exhibited isolated intergranular features and evidence of corrosive attack (Fig. 9*a*). The transgranular features near the corner were characterized by relatively large flat facets with faint "river-markings" or "fan-markings" comparable with the transgranular fracture features within the several subcritical crack specimens (Figs. 9*b* and 9*c*). In contrast, locations remote from the corner exhibited distinct cleavage facets with sharply-defined steps and tear ridges (Fig. 9*d*). Small isolated patches of dimples were intermixed among these cleavage facets, serving as a second feature distinguishing cleavage zones from the transgranular portion of the slow crack growth areas. In addition, it was noted that any intergranular features, the unidentified, nonclassic fractographic features, and the evidence of corrosive attack were confined to an area in the immediate vicinity of the inlet-face corner. The fractographic features of the known subcritical defects and the fact that certain features of the primary fracture surface were unique to a relatively small zone near the inlet-face corner served to distinguish a slow crack growth region from the region of unstable fast fracture. In addition, a distinct fracture transition boundary was noted at four particular locations in the vicinity of the inlet face corner.

Point-to-point comparison of the fractographic features of the primary fracture provided for identification of a stable crack growth region at least 12.7 by 3.3 mm (0.5 by 0.13 in.) at the inlet-face corner. The limits of this region are indicated in the diagram shown in Fig. 10. It should be noted that the critical crack size is very small relative to the disk dimensions. The diagram of Fig. 10 also illustrates the extent of the post-fracture mechanical damage in the vicinity of the origin and illustrates the particular locations where the various fine-scale topographic features were observed. The fractographic character of the subcritical cracks and the stable crack growth zone of the

primary fracture were indicative of stress corrosion cracking (SCC) but did not serve to identify the specific cracking mechanism.

Crack Deposit Analyses

Energy dispersive spectroscopy was employed to provide a qualitative analysis of the deposits within the subcritical cracks. These analyses were performed *in situ* on metallographic sections and on exposed surfaces of the subcritical cracks. Analyses of five different subcritical cracks revealed significant quantities of lead and sulfur in the surface deposits. Lead was observed only at locations near the groove surface, while sulfur was consistently observed at several points within the subcritical crack, including points at the crack tip. A typical X-ray energy spectrum obtained from the crack surfaces is shown in Fig. 11. The presence of lead near the groove surfaces is attributed to the fact that white lead [$2PbCO_3 \cdot Pb(OH)_2$] was employed as a lubricant in the installation of the blades. The presence of sulfur within the subcritical cracks, particularly at points near the crack tip, is evidence of sulfur contamination in the operating environment. Such contamination is consistent with the fact that the operating history of the unit included a period during which sodium sulfite was employed as a deoxidizer in the water treatment. The exact form of the sulfur was not identified so that no conclusion could be drawn as to whether it was present as a corrosion product or as an accumulated, extraneous deposit.

Deposit material was collected from the blade grooves before any cleaning or cutting operations. Atomic absorption analysis of the nonmagnetic portion of the deposit identified lead as the principal constituent. Small but significant amounts of sodium (0.42 to 1.35 wt%) and sulfur (0.2 to 0.3 wt%) were also detected.

Slow-Strain-Rate Tests

In view of the observations made in the metallographic and fractographic examinations, a series of slow-strain-rate (SSR) tests were performed to evaluate the cracking susceptibility of the disk material in environments likely to be encountered in service. Caustic environments are frequently encountered in steam turbine operation, and caustic stress corrosion cracking of low-alloy steels is a well-documented phenomena [*2,3*]. The slow-strain-rate test matrix was organized on the basis of these factors together with the results of the deposit analysis and exploratory polarization tests.

Tests were performed in a 28% caustic solution doped with selected contaminant species. In general, the disk material exhibited a low-to-moderate susceptibility to cracking in the pure caustic and in solutions containing lead carbonate. Additions of sodium sulfide to the caustic solution resulted in a marked increase in stress corrosion cracking susceptibility. The stress corrosion cracking which occurred in the sulfide-doped solutions was predomi-

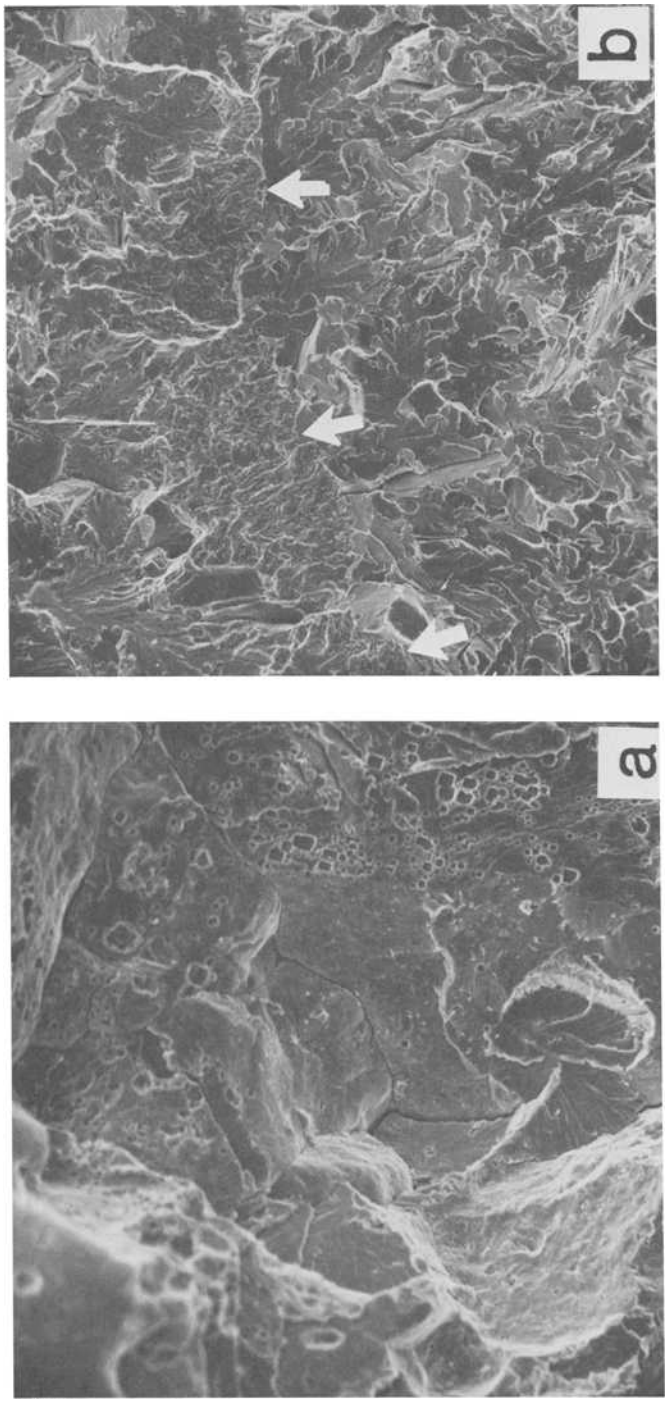
b
a

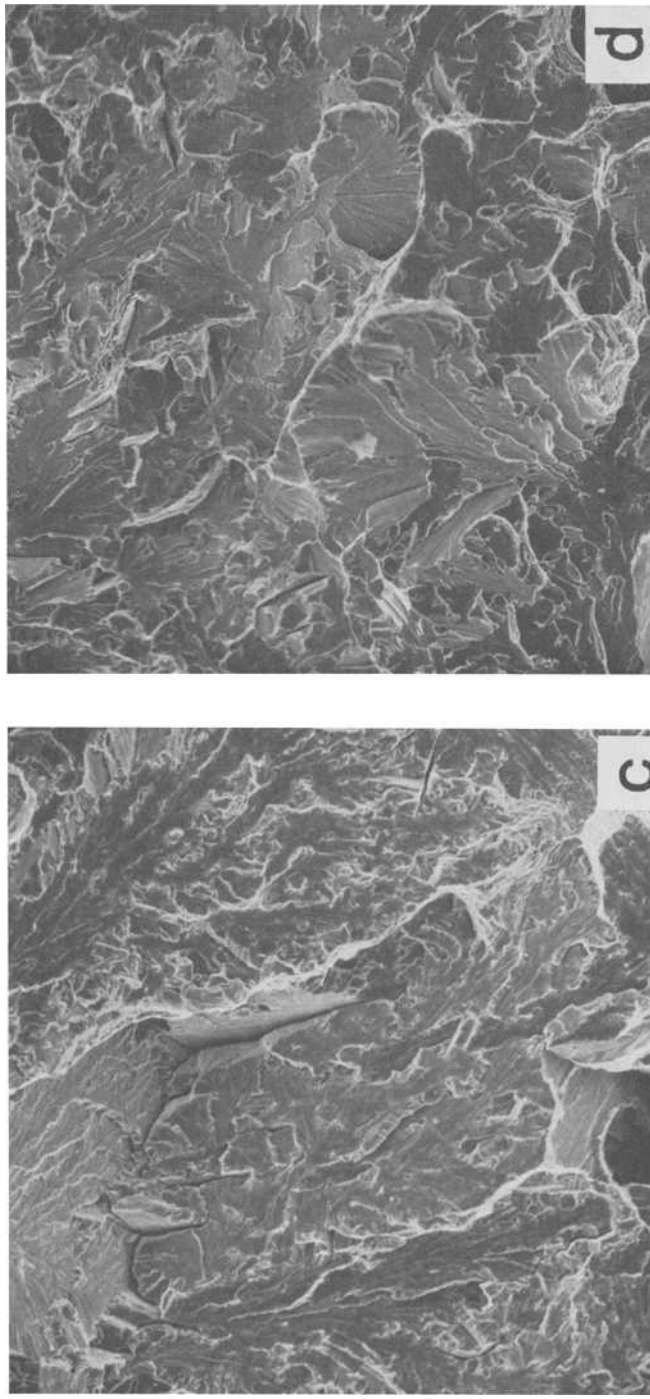

FIG. 9—*SEM fractographs from primary fracture.* (a) *At blade groove;* ×*600.* (b) *Fracture transition;* ×*300.* (c) *Central zone;* ×*400.* (d) *Fast fracture;* ×*300.*

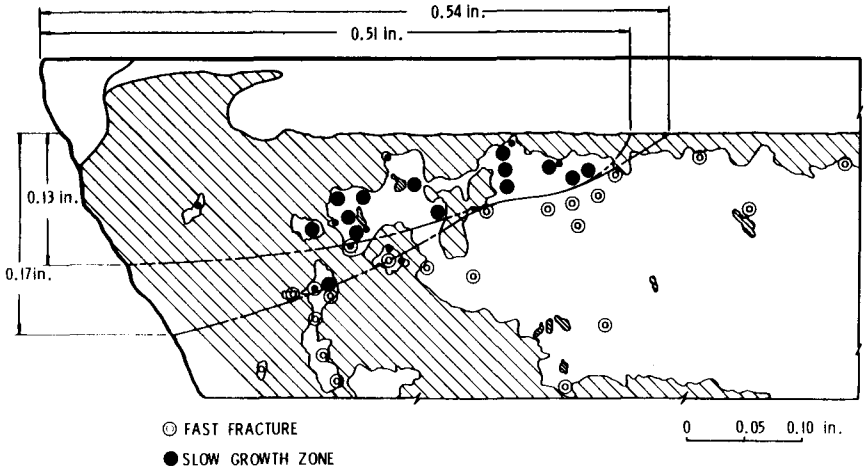

FIG. 10—*Diagram of inlet face corner of primary fracture.*

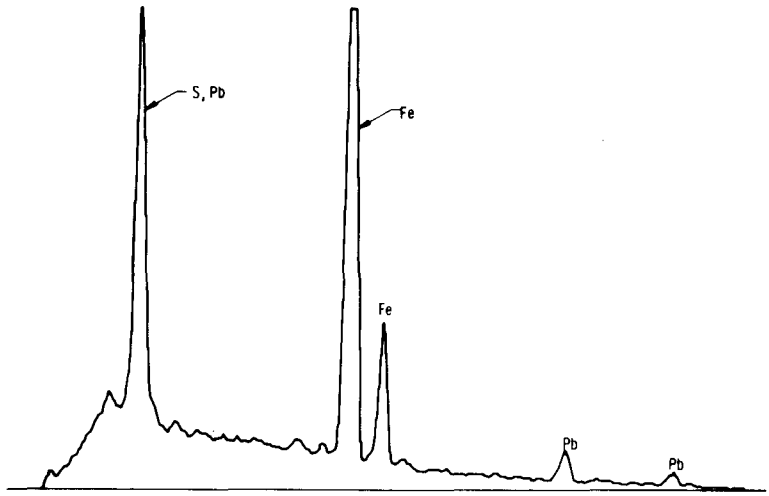

FIG. 11—*X-ray energy spectrum from subcritical defect.*

nantly transgranular, and the fractographic features were comparable to those observed for the in-service cracking (Fig. 12).

Discussion and Conclusions

The fractographic aspects of the subcritical crack zone in the primary fracture surface and of the other subcritical defects serve to identify the

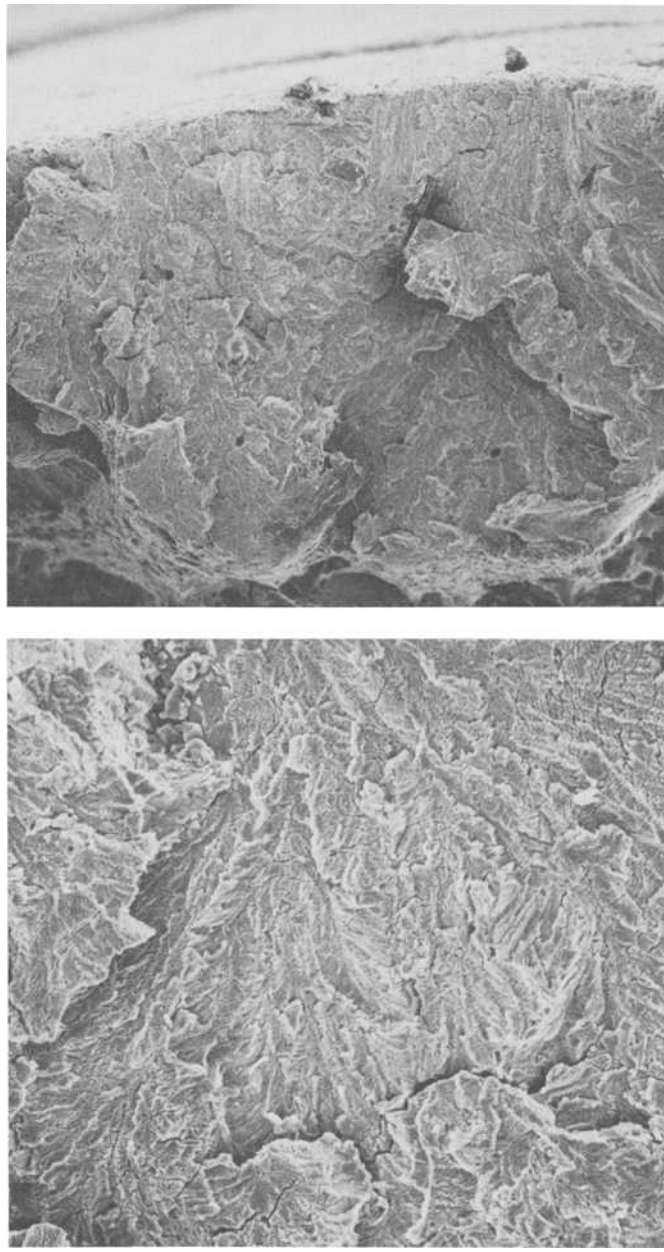

FIG. 12—*SEM fractographs from slow-strain-rate test specimen. Test performed in 28% NaOH solution with* Na_2S *additions.* (top) ×*270.* (bottom) ×*1350.*

mechanism of in-service, slow crack growth as a form of stress-corrosion cracking. This conclusion is supported by the fact that the fine-scale topographic features of the transgranular portions of the slow-crack-growth zones are distinguishable from the cleavage features of the fast fracture zones and of laboratory overload fractures, and by the absence of any evidence of fatigue crack propagation. Transgranular stress corrosion cracking is known to occur in low-alloy, high-strength steels in various environmental conditions [*2,3*]. The occurrence of multiple cracks in several adjacent grooves and multiple crack initiation within particular grooves constitute evidence of environmentally-induced cracking. The limited intergranular fracture observed within the subcritical cracking zone is also consistent with SCC.

The association of the intergranular features with the early stages of crack growth suggests that the initial stage of cracking may have occurred in a different manner from the later stage of crack propagation. Certain metallographic features of the subcritical defects also suggest more than one cracking process. It is possible, although not conclusive, that the subcritical cracking occurred in two stages under different environmental conditions prevailing during different periods of operation. In any case, it is evident that all the subcritical crack growth occurred by some form of stress corrosion cracking, with the transgranular cracking mode predominating.

A marked increase in cracking susceptibility was demonstrated in all SSR tests conducted in caustic-plus-sulfide solutions or at controlled potentials below the free corrosion potential of pure caustic. Also, the fractographic features of the laboratory-induced cracking are comparable to those of the slow-growth cracking zones of the failed disk. These factors, together with the fact that sodium and sulfur were present in blade groove deposits and that sulfur was identified as a constituent of the deposit within defects, lead to the conclusion that the subcritical cracks most likely developed by hydrogen-induced stress corrosion cracking in a caustic environment, promoted by the presence of a sulfur-bearing contaminant. In view of the results of the SSR tests, it appears that the presence of sulfur in the environment was a necessary condition for crack initiation. The clearance provided between the blade root and the disk groove at the bottom of the groove also may have contributed to the cracking process. It is important to note that the environment was only one factor involved in the occurrence of SCC. The high stress levels encountered in normal operation, the low fracture toughness, and the high strength of the disk material were also principal contributors to the failure incident.

Summary

The conclusions concerning the mechanism of the subcritical cracking and the cause of the failure of the LP turbine disk, drawn from the information obtained in this investigation, are as follows:

1. The primary fracture initiated from a critical crack, approximately 13.7 mm (0.54 in.) long by 4.3 mm (0.17 in.) deep, located at the inlet face and within the dovetail slot of a blade attachment groove.

2. The critical crack which initiated the primary fracture, and all subcritical cracks examined, developed in service by a form of stress corrosion cracking.

3. The moderate-to-low caustic cracking susceptibility of the material, together with the predominantly transgranular nature of the slow-crack-growth zones, indicates that subcritical crack growth did not occur by the usual caustic-cracking mechanism.

4. The most likely mechanism of subcritical crack growth is hydrogen-induced cracking in a caustic environment promoted by the presence of sulfides within the dovetail slot under the blade root.

5. The failure of the disk is attributed to the combined effects of environment, high operating blade groove surface stress, and low material fracture toughness.

Acknowledgments

The work described in this paper was supported by the Allis-Chalmers Corporation. The authors are grateful to Allis-Chalmers and Wisconsin Electric Power Company for their permission to publish this work.

References

[1] Payer, J. H., Berry, W. E., and Boyd, W. K. in *Stress Corrosion—New Approaches, ASTM STP 610*, H. L. Craig, Jr., Ed., American Society for Testing and Materials, 1976, pp. 82–93.

[2] McCord, T. G., Bussert, R. W., Curran, R. M., and Gould, G. G., *Materials Performance*, Vol. 15, Feb. 1976.

[3] Roberts, B. W. and Greenfield, P., *Corrosion*, Vol. 35, Sept. 1979, p. 402.

Phuc Nguyên-Duy[1]

Failure Analysis of a Hydraulic Turbine Shaft

REFERENCE: Nguyên-Duy, P., **"Failure Analysis of a Hydraulic Turbine Shaft,"** *Fractography of Ceramic and Metal Failures, ASTM STP 827*, J. J. Mecholsky, Jr. and S. R. Powell, Jr., Eds., American Society for Testing and Materials, 1984, pp. 368-386.

ABSTRACT: A complete analysis was carried out on a hydraulic turbine shaft in order to determine the origin and causes of existing cracks. A chronological scenario of crack system creation was advanced and was confirmed by macroscopic and microscopic observations of fracture surfaces and material structure. Friction welding, occurring between shaft and sleeve, was found to be the origin of the first crack system, which in turn was responsible for the creation of others.

KEY WORDS: failure, fracture, friction weld

A system of cracks was detected in a hydraulic turbine shaft 1.2 m (4 ft) in diameter in the region of the bearing guide. In this region, the shaft is composed of two independent parts (Fig. 1): (1) the shaft and (2) two cylindrical halves enveloping the shaft over approximately 1.2 m (4 ft) of its length. These two cylindrical halves, which constitute the sleeve, are fixed together by pins but are not fixed to the shaft either mechanically or metallurgically. The sleeve protects the shaft and provides lubrication. Welds were used to seal the space between the two halves; at the higher extremity of the sleeve (alternator side) the welds touched the surface of the shaft (Fig. 1).

The purpose of this paper is to detail the chronological scenario of crack formation. At an early stage of the study, the preliminary observations enabled us to obtain a global view of existing crack systems and to advance a crack-creation hypothesis that can subsequently be confirmed or disproved by microscopic observations of the different crack systems: radial-longitudinal and spiral-transverse. Finally, the chronology of crack formation was established.

[1]Chercheur, Institut de recherche d'Hydro-Quebec (IREQ), Varennes, Quebec, Canada.

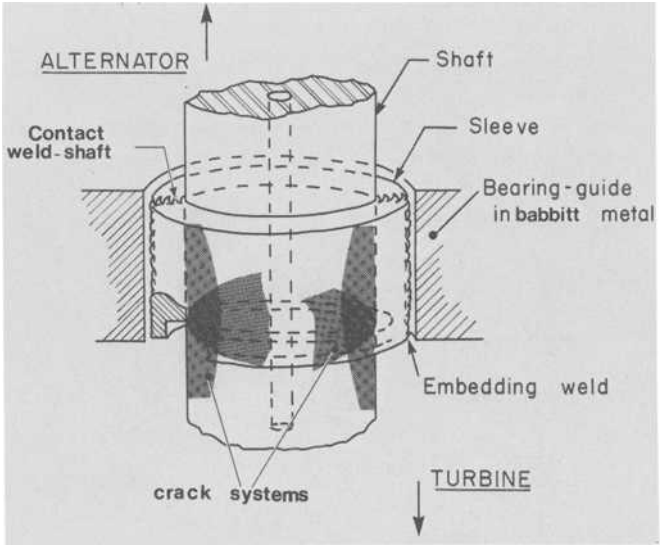

FIG. 1—*Global view of shaft, sleeve, and bearing guide.*

Preliminary Observations

In a preliminary examination, two distinct systems of cracks were found; they are shown schematically in Fig. 2. At the section corresponding to the lower extremity of the sleeve (turbine side), two traces of cracks (15 and 18 cm long) were observed diametrically opposite each other. The origins of these cracks are on the outer surface of the shaft at locations corresponding to the spaces between the two cylindrical halves. On this same section, traces of spiral crack systems were also detected, and in addition, two traces were found on the inner surface of the shaft.

After these observations, a working scheme was established that consisted of:

1. Inventorying all cracks existing in the structure.
2. Establishing the relationships between different crack subsystems, with the objective of localizing crack origins.
3. Formulating the causes and exact origin of cracks and a chronological scenario of this creation.

As mentioned earlier, two systems of cracks were detected:

1. *Radial and Longitudinal Systems*—These two cracks have different lengths in the radial direction. In the section cut at the lower end of the sleeve (turbine side), the cracks are respectively 15 and 18 cm; they are 12 and 16 cm in the higher cutting section (Fig. 3).

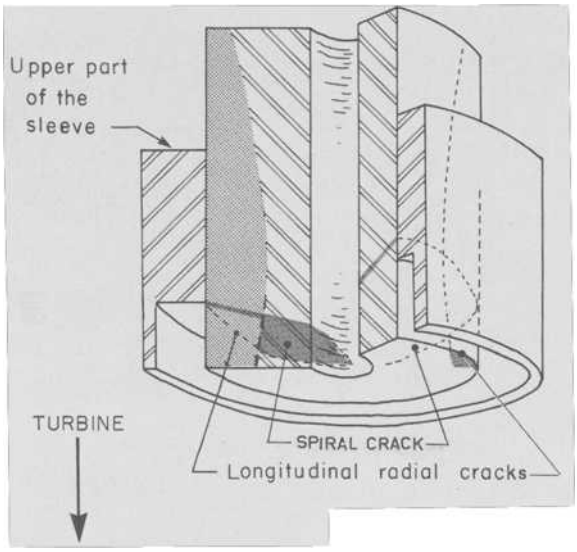

FIG. 2—*Crack systems.*

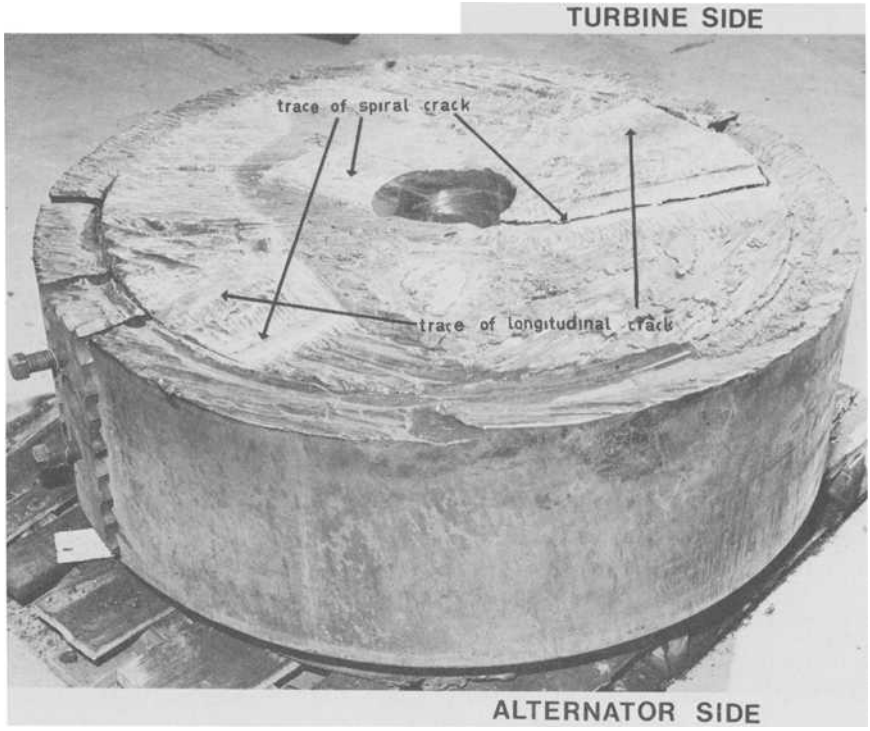

FIG. 3—*Section of the shaft cut at the lower end (turbine side).*

2. *Transverse and Spiral Systems*—In the region surrounding the radial and longitudinal systems, there developed two systems of transverse and spiral cracks of which the magnitude depends on the depth of radial cracks (Fig. 4).

In Fig. 5, in the neighborhood of the radial-longitudinal cracks, it is interesting to note the presence of many onset points resulting in two very marked zones of fatigue propagation, change in plane of propagation of spiral-transversal crack at the intersection with radial crack, and change in the morphology of fracture surfaces (rough regions and smooth regions).

Also at the inner surface of the shaft, the presence of two cracks confirms the existence of a spiral crack around each of radial-longitudinal cracks. These two spiral cracks propagate in two different planes from the outer shelf of the shaft to its inner surface (Fig. 6).

From these preliminary and macroscopic observations, the following hypotheses evolved for the formation of the cracks:

1. The radial-longitudinal cracks were not caused by the contact of the sealing welds with the sleeve.
2. The radial-longitudinal cracks of different length were not caused by fatigue loading.

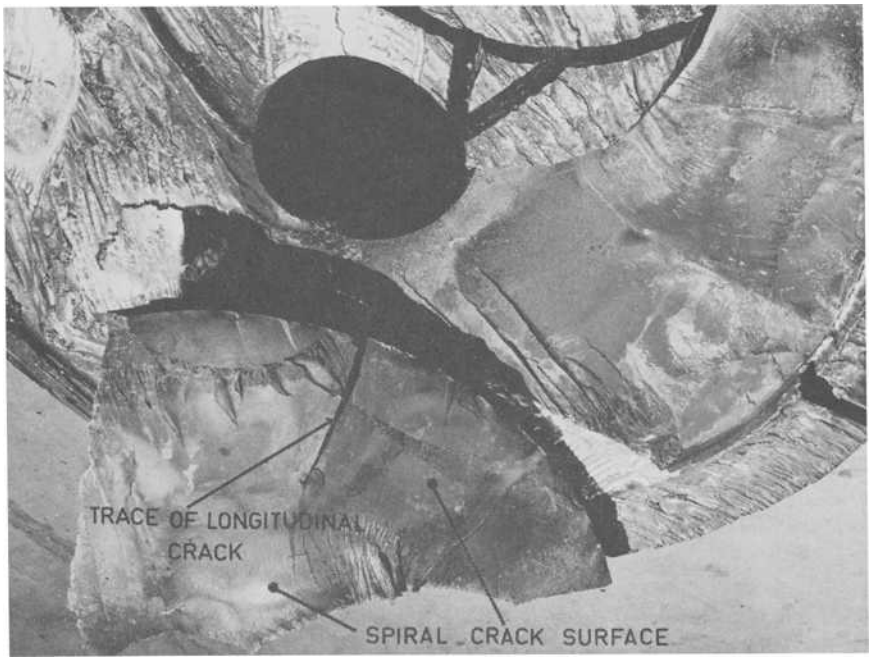

FIG. 4—*Spiral cracks.*

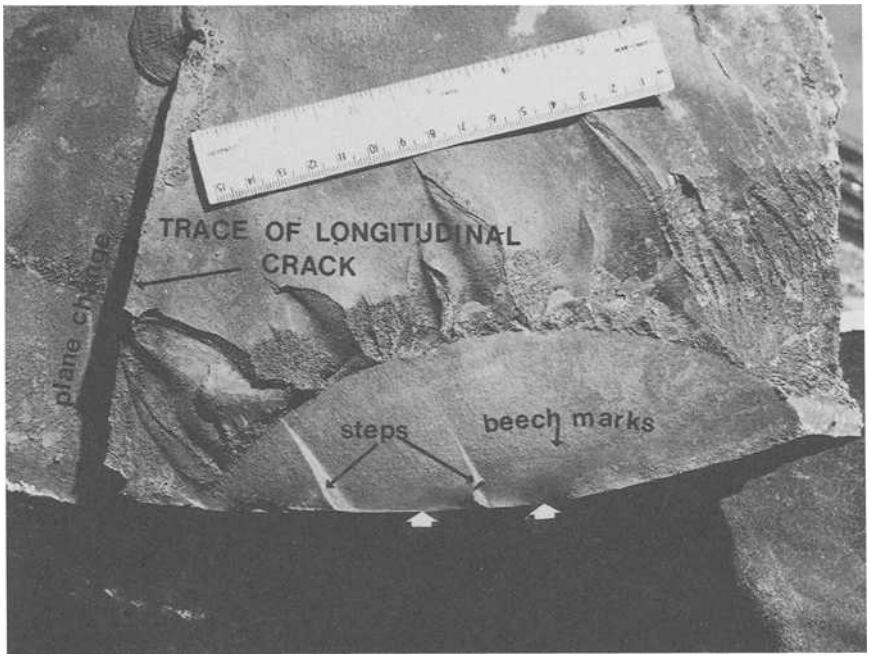

FIG. 5—*Fracture surface of spiral crack in the neighborhood of radial-longitudinal crack.*

3. The radial-longitudinal cracks occurred previous to the spiral-transversal cracks (from change of plane of propagation of the latter) (Fig. 5).

4. The spiral-transversal cracks were initiated by fatigue loading in the neighborhood of radial cracks.

Origin of Radial-Longitudinal Cracks

It was confirmed by microscopic observations that the radial-longitudinal cracks were not created by fatigue (Fig. 7); fracture surfaces were brittle and intergranular decohesion was observed. Consequently the investigation next sought the causes that would create cracks after a fast or slow monotonic loading.

At the level of the bearing guide, the shaft is enveloped by the sleeve formed of two cylindrical halves fixed together by pins. The sleeve is integral with the shaft only through tightening of the pins. There is normally no relative movement between sleeve and shaft.

Bearing in mind the narrow spacing between the bearing guide and the shaft, we note that a very slight misalignment (from several causes) can cause friction at the interface of bearing guide and sleeve. This friction creates a

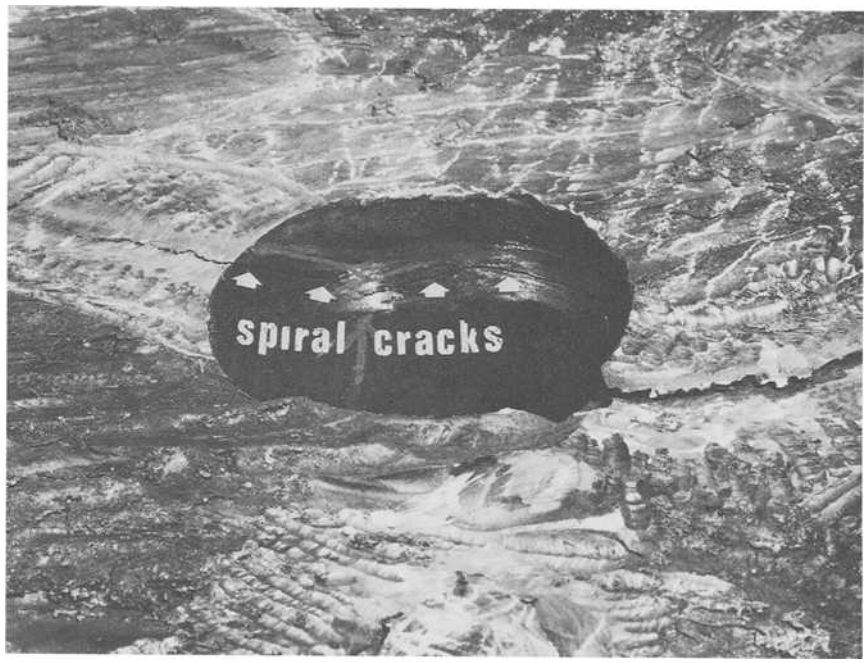

FIG. 6—*Traces of spiral cracks on inner surface of shaft.*

relative movement between sleeve and shaft. The shaft rotates at 75 rpm, while the sleeve rotates slower due to contact with the bearing guide.

Since the diameter at the sleeve-shaft interface is large, a difference of several revolutions per minute in rotative speeds results in a relatively important difference in linear speeds. The friction between sleeve and shaft causes the metal to overheat and results in friction welding at the sleeve-shaft interface. The overheating and the welding may cause the radial-longitudinal cracks.

At the sleeve-shaft interface (Fig. 8) metal has flowed and formed two wings at the interface; these two wings are nearly symmetrical relative to the interface, indicating that the two steels are of approximately the same forgeability [*1*].

In order to confirm the action of friction welding, a section of the sleeve-shaft interface was used to illustrate the weld and the heat-affected zone (HAZ) (Fig. 9).

Microstructural observations made in the region of interface indicate clearly that friction welding occurred at a temperature higher than the temperature of austenization of SAE 1020 steel sleeve, approximately 800°C. The microstructures (Fig. 10) on both sides of the interface allows the detection of the difference of the cooling rate. Carbon diffuses from the shaft (SAE 1045) to the sleeve (SAE 1020) (Table 1). This carbon diffusion can be observed

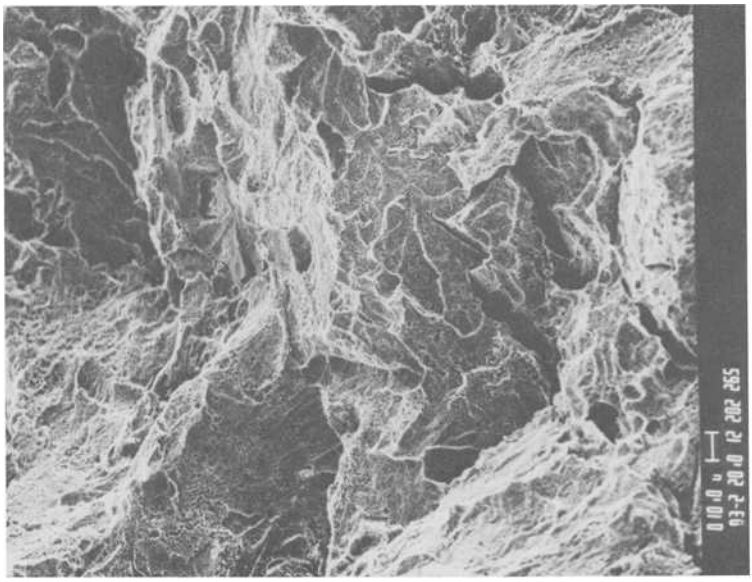

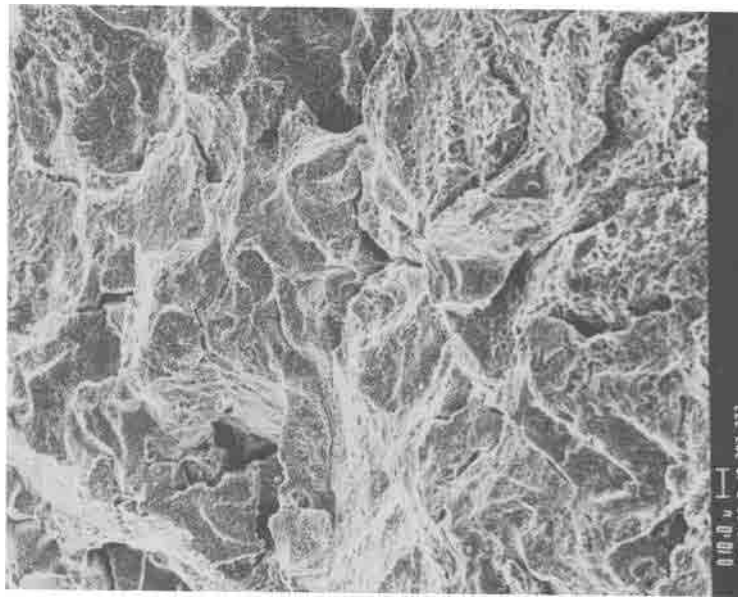

FIG. 7—*Microscopic fracture surface of radial-longitudinal cracks.*

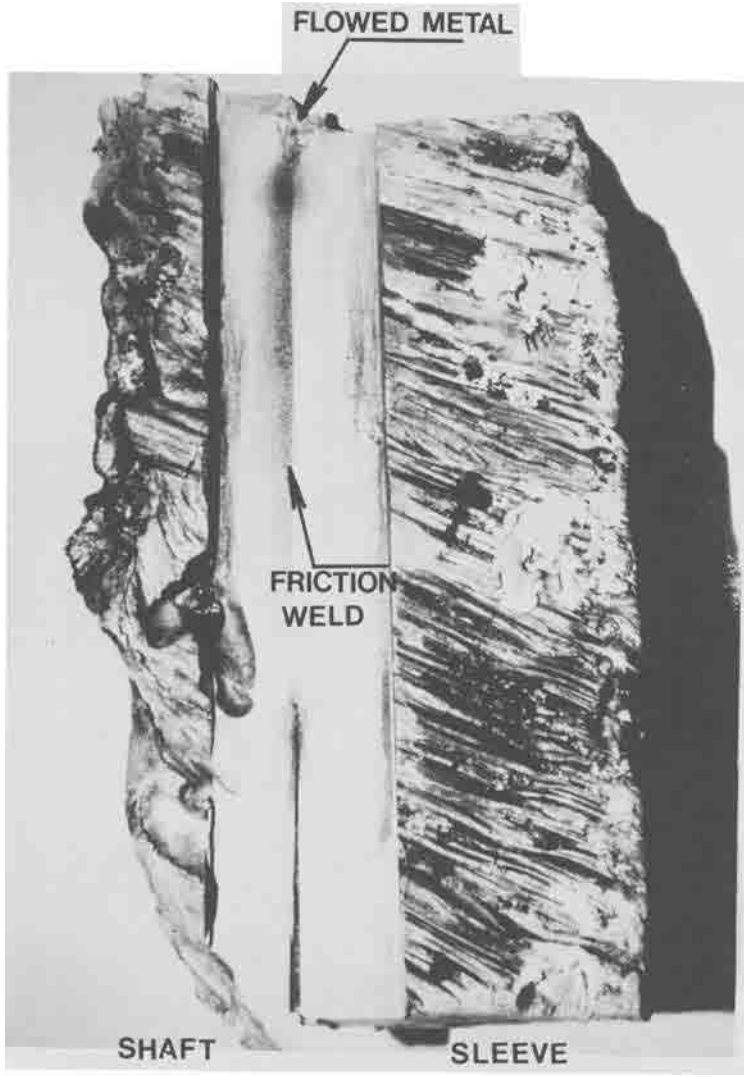

FIG. 8—*Friction weld between sleeve and shaft.*

from the coloration of different zones across the weld. The microstructure varies as a function of the distance from the weld, the temperature at which the metal was heated, and the length of time at this temperature.

The overheating, resulting in friction welding, and the subsequent cooling caused the radial-longitudinal cracks, which started at the outside of the shaft and propagated radially inwards. The onset points were located on the

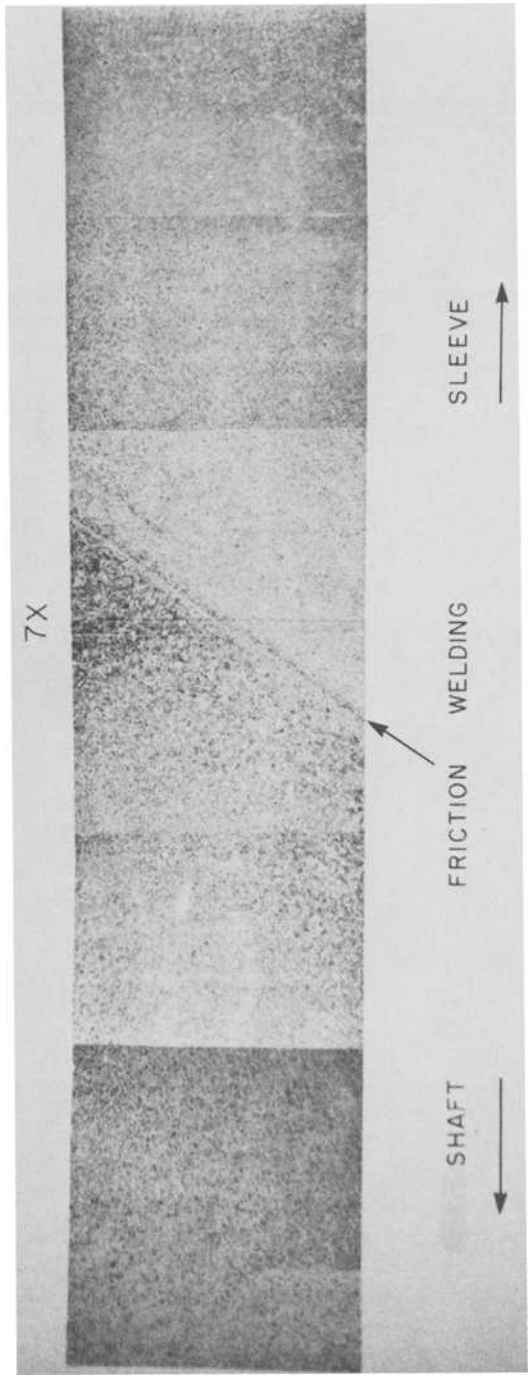

FIG. 9—*Structure across the friction weld.*

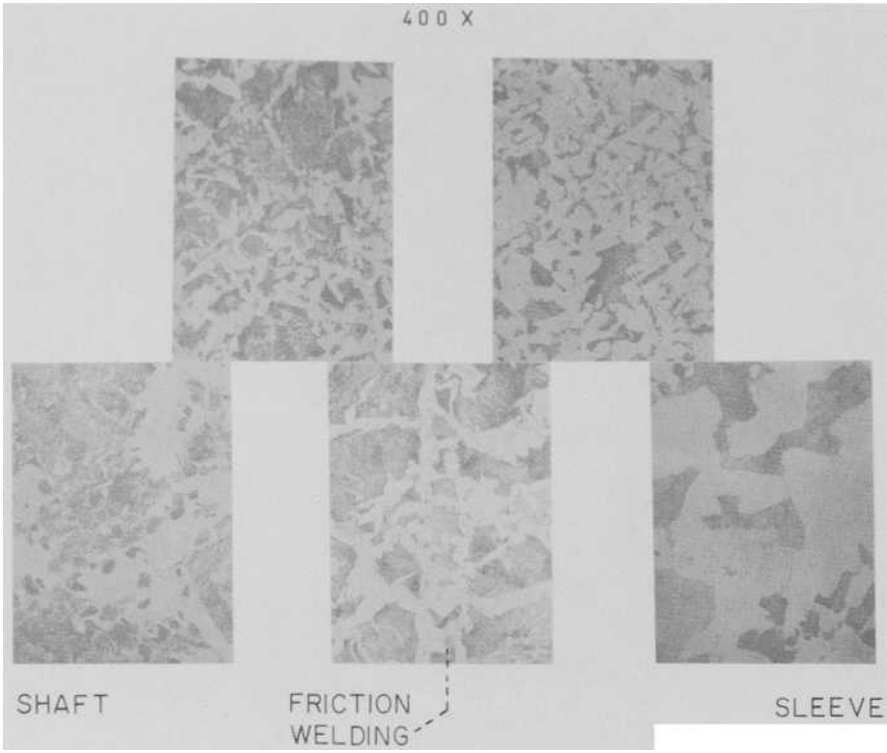

FIG. 10—*Microstructure in the neighborhood of the weld.*

TABLE 1—*Chemical analysis (weight percent) of steel of sleeve and shaft.*

	C	Mn	P	S	Si	Cu	Ni	Cr	Mo	V	Nb	Al
Sleeve	0.22	0.75	0.022	0.025	0.37	0.12	0.09	0.11	0.019	0.002	0.001	0.056
Shaft	0.38	0.62	0.026	0.029	0.15	0.31	0.31	0.01	0.015	0.003	0	0

shaft against the spaces where the two cylindrical halves were joined. It is important to note that at these onset points, metal of the shaft is free of retention by the sleeve (resulting from the friction welding). This is illustrated in Fig. 11. The thermal contraction is the principal but not the sole cause of longitudinal crack creation which is promoted by defects (metallurgical, design, mechanical) and metallurgical changes during heating and cooling.

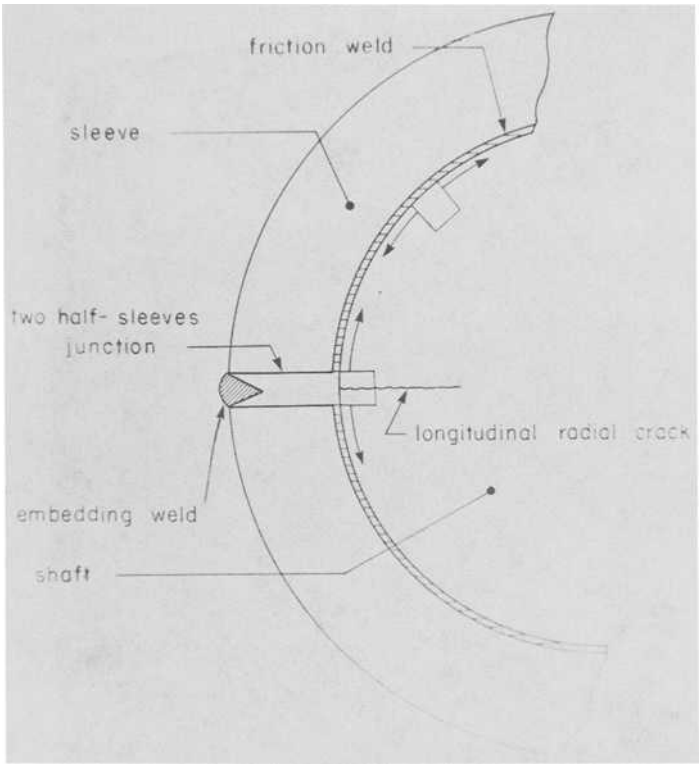

FIG. 11—*Radial-longitudinal crack creation.*

Origin of Spiral-Transversal Cracks

The two radial-longitudinal cracks caused distortion and vibrations in the structure. Added to the misalignment of the shaft, it provoked many crack onset points located on both sides of the radial-longitudinal cracks. Fatigue cracks grow towards the central hole and a stepped rupture is formed (Fig. 5). This indicates the predominance of rotative bending forces. The presence of many crack onset points confirms that the loading was severe.

Progressive propagations by rotative bending from the two sets of onset points were 6 and 8 cm (Fig. 12). Beach marks are very obvious. Progressive propagation is followed by two zones of brittle propagation caused by impact. The radial lines observed in Fig. 12 generally originate at onset points or appear after a modification of the loading mode (variation in the bending : torsion ratio of the two components).

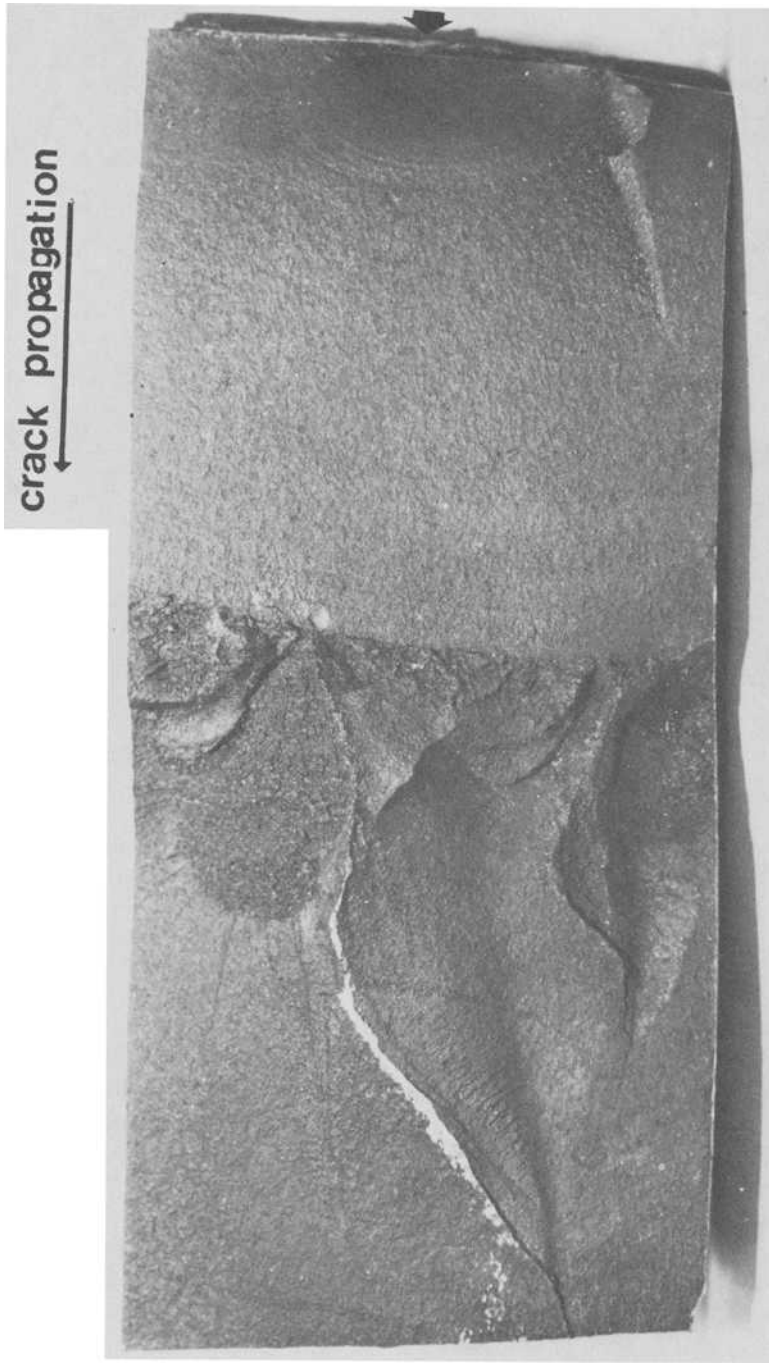

FIG. 12—*A portion of fracture surface with beach marks.*

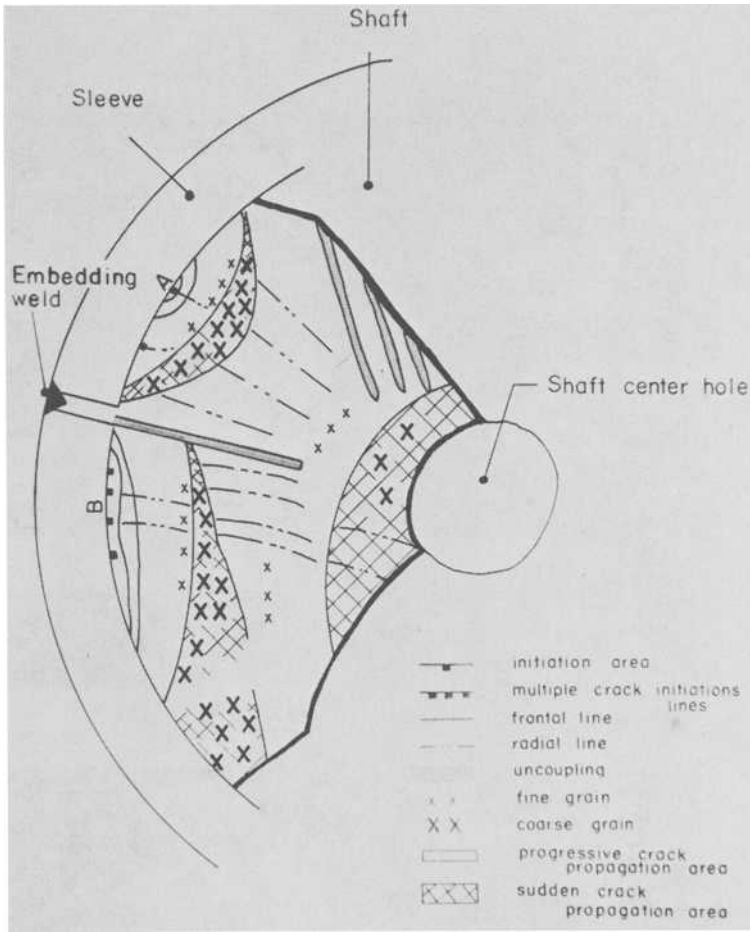

FIG. 13—*Mapping of fracture surface of spiral crack.*

Figure 13 shows schematically the characteristics of the fracture surface of spiral cracks in the region surrounding radial-longitudinal cracks [*2*].

The two sets of crack onset points were examined by a scanning electron microscope (SEM). Results are shown in Figs. 14 and 15. Striations were not in evidence. However, the general aspect of the fracture surface indicates that crack initiation and propagation are caused by fatigue loading.

Chronological Scenario of Crack System Creation

The following chronological scenario of crack system creation is proposed:

1. Mechanical misalignment originating from the installation and/or the

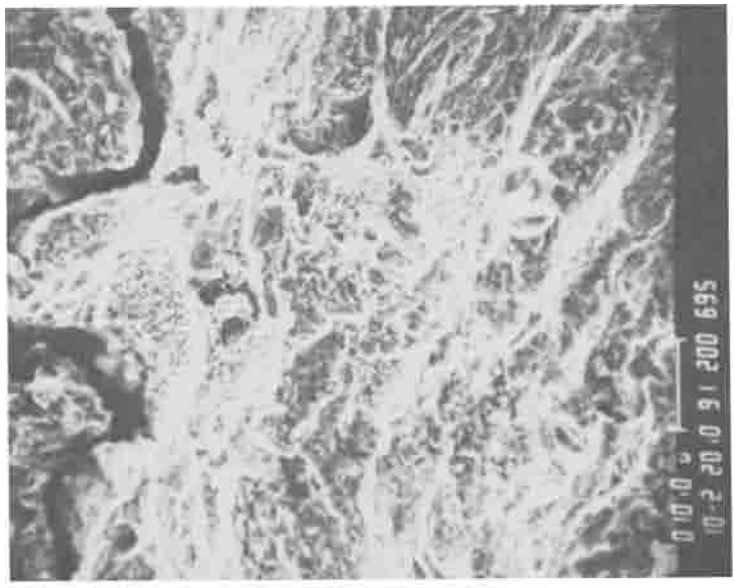
10-2 20.0 9 1 200 695
0.010

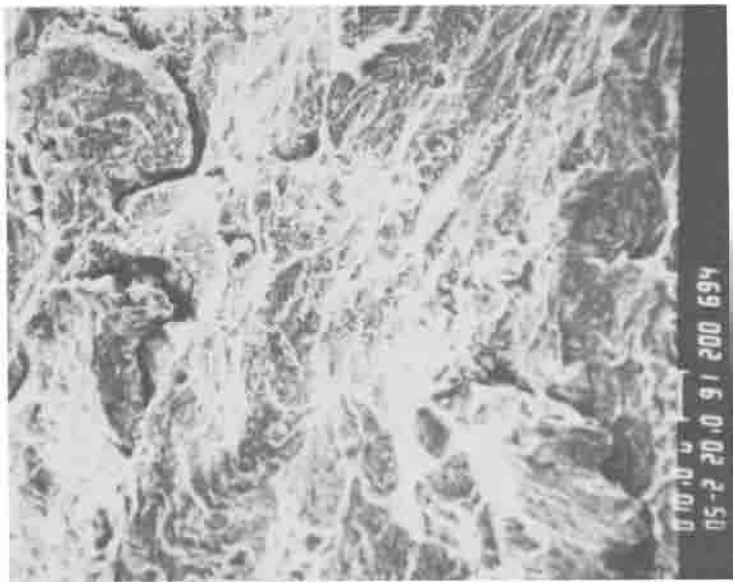
05-2 30.0 9 1 200 694
0.010

FIG. 14—*Microscopic fracture surface of spiral-longitudinal cracks.*

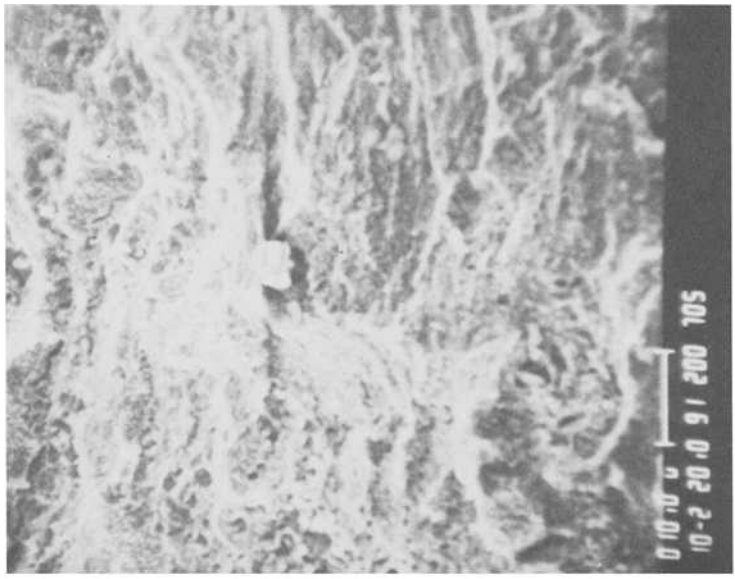

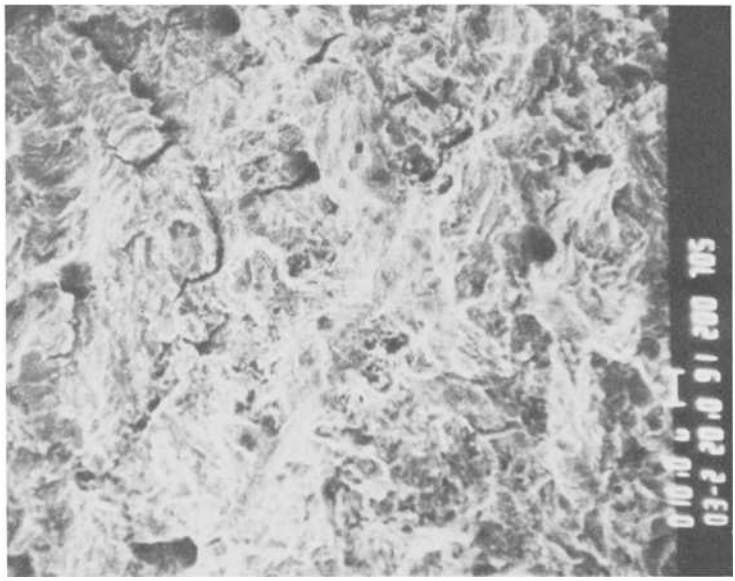

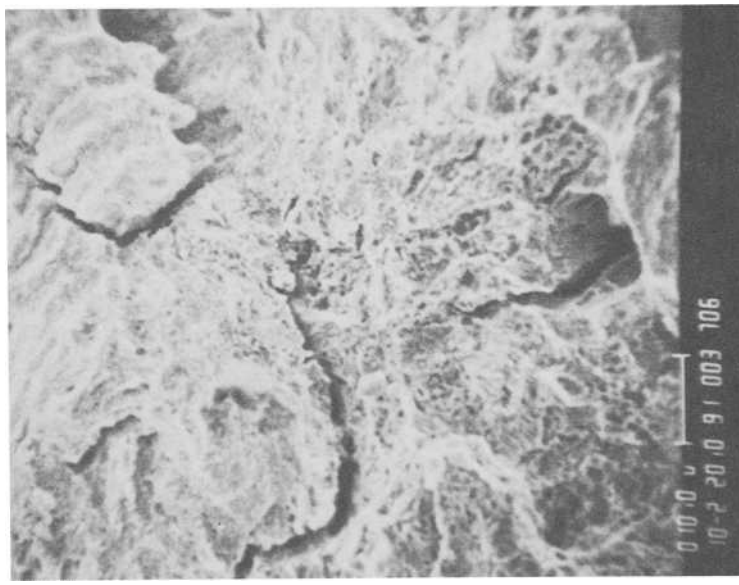

FIG. 15—*Microscopic fracture surface of spiral-longitudinal cracks.*

operation, causes friction between the sleeve and the wall of the bearing guide that slows the sleeve, thus producing a relative movement between sleeve and shaft.

2. This relative movement creates friction at the sleeve-shaft interface; excessive overheating brings the metal to a temperature superior to the temperature of austenization, and friction welding occurs.

3. Heating-cooling cycling results in thermal contraction, imposing a significant thermal stress on the shaft, especially tangentially, and opening the shaft radially at weak points. These weak points correspond to places where shaft and sleeve are not welded together by friction.

4. These two radial-longitudinal cracks increase misalignment. This cause distortion and vibration that create multiple onset points.

5. These onset points act as stress raisers for subsequent crack initiation.

6. Spiral-transversal cracks propagate progressively (smooth fracture surface) or rapidly (rough fracture surface).

To prevent this kind of failure on our actual turbine groups in this station, a special program of maintenance was recommended for detecting the presence of friction weld and longitudinal-radial crack systems. If they are observed, repairs can be carried out before irreversible damage occurs.

Acknowledgments

The author is pleased to thank Dr. R. Simoneau for helpful discussions in all stages of this study; Dr. E. A. Dancy for critically reading the manuscript; Mr. A. DiVincenzo for very efficient cutting out and welding works; Mr. C. Lanouette for his application on macrophotographic and microphotographic works.

References

[*1*] Fassnacht, W. G., "Friction Welding," in *Metals Handbook*, Vol. 6: Welding and Brazing, 8th ed., American Society for Metals, Metals Park, Ohio, pp. 507-518.

[*2*] DeLeiris, H., *L'analyse morphologique des cassures*, 2nd ed., Masson, Paris, France, p. 66.

D. Finello,[1] *Y. H. Park,* [2] *M. Schmerling,*[3] *and H. L. Marcus*[3]

Fractography of Metal Matrix Composites

REFERENCE: Finello, D., Park, Y. H., Schmerling, M., and Marcus, H. L., **"Fractography of Metal Matrix Composites,"** *Fractography of Ceramic and Metal Failures, ASTM STP 827*, J. J. Mecholsky, Jr. and S. R. Powell, Jr., Eds., American Society for Testing and Materials, 1984, pp. 387-396.

ABSTRACT: Unidirectional continuous-fiber metal matrix composites are known for high strength in the fiber direction but are weak in the transverse direction, due often to weak fiber-matrix bonds. The effects of environment (vacuum, air, etc.) and of thermal treatment (isothermal and cyclic) on the fracture behavior and occasional fiber splitting were investigated in several such materials. Fractography was done using a scanning electron microscope, and fiber-matrix interface chemistry was determined using a scanning Auger microscope. The extent of fiber pullout is often an indication of the strength of longitudinally fractured composites. When there is excessive thermal oxidation of the fiber-matrix interface in the Al matrix composites with graphite fibers, pullout and weakening occur. A second cause of significant strength loss was excessive carbide formation and frequent fiber notching, so that longitudinal failures exhibited close-cropped fiber breakage. In Ti matrix composites with SiC and B_4C/B fibers, cracks along the interface were observed for thermally fatigued specimens. Large amounts of oxygen were found on both sides of the fractured fiber interface when thermal fatigued in air. Similar effects were noted in a sulfur environment.

KEY WORDS: metal matrix composites, continuous fiber composites, titanium, aluminum, thermal fatigue, environment effect, Auger electron spectroscopy, interface chemistry, fracture mode

Metal matrix continuous fiber composites (MMC) are a class of materials that have the potential for extending the areas of applicability of resin continuous-fiber composites. The properties that characterize these materials have been discussed in detail elsewhere [*1-6*]. This paper will be aimed at showing the applicability of fractography in understanding the mechanical properties of the metal matrix composites. Of particular interest are the modes of failure in transverse fracture and under mixed-mode loading condi-

[1]Elgin Air Force Base, Fla.
[2]Materials Research Corporation, Pearl River, N.Y.
[3]Department of Mechanical Engineering/Materials Science and Engineering, University of Texas, Austin, Tex. 78712.

tions. The fractography described includes scanning electron microscopy (SEM), optical microscopy, and scanning Auger electron microscopy (AES). The mechanical tests associated with the fractographic analysis include fatigue crack growth and tensile failure. The modes of failure were influenced by thermal fatigue, test environment, and prior thermal treatment of both notched and smooth section samples.

Materials Studied

Fractography on Al and Ti metal matrix materials will be described. The Al MMCs are made of continuous graphite fibers in a 6061 Al matrix. The main type of graphite fiber investigated was pitch base. The fibers are 7 to 10 μm in diameter. The Al MMCs are prepared by liquid infiltration of graphite fibers after chemical deposition of a wetting agent [*7*] which produces wires. The wires are then consolidated into unidirectional plates by diffusion bonding. Fracture surfaces from the plate material were investigated after various heat treatments in different environments to study the aluminum carbide (AL_4C_3) and oxide formation and its influence on mechanical properties.

The Ti MMCs are made using Ti-6Al-4V for the metal matrix with continuous B_4C/B, Borsic, SCS, and SiC fibers. The fibers are nominally 150 μm in diameter. The material is formed by a diffusion bonding process. Most of the material is a four-ply unidirectional composite. All specimens (Al and Ti) and notches are cut using electrodischarge machining (EDM) techniques.

Details of the thermal, environmental, and mechanical history of the MMCs are given in the next section.

Results

Aluminum Composites

The Al MMCs were tested for changes in tensile properties with temperature at different gaseous environments as the variable. Pitch fibers have a preferred orientation for the graphite basal plane perpendicular to both the fiber surface and fiber axis normal. These fibers (VSB-32) formed plates designated as G4371 and G4411. G4371 differs from G4411 only by an enhanced oxide at the fiber interface.

Figure 1 illustrates the change in longitudinal strength of G4371 aged at 550°C at different atmospheric pressures. "Rough vacuum" is $\sim 1.3 \times 10^{-1}$ Pa obtained using an oil mechanical vacuum pump. "High vacuum" is $\sim 1.3 \times 10^{-5}$ Pa in an ion-pumped sealed capsule. Aging at 550°C in air causes severe debonding and fiber pullout at low stress (Fig. 2). The effect of aging at 550°C for 10 days in rough vacuum is shown in Fig. 3; compare with the as-received composite in Fig. 4. These figures show that aging has in-

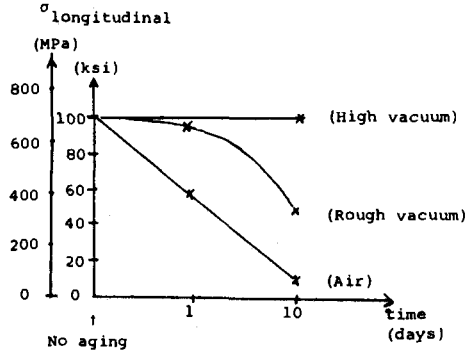

FIG. 1—*Fracture strength versus aging time as influenced by environment (G4371 VSB-32/oxide/6061 Al).*

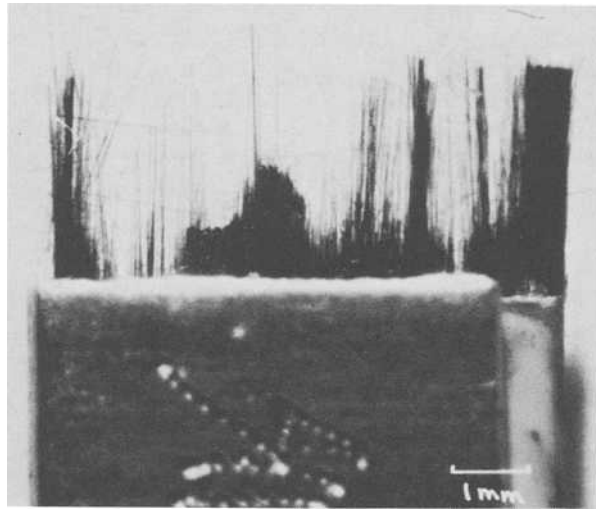

FIG. 2—*Longitudinal failure of G4371 Al MMC aged at 550°C for 1 day in air.*

duced visible effects of degradation upon fibers and caused a close-cropped longitudinal fracture compared with that of the as-received specimen. The matrix in the aged sample has deformed filling notches where the brittle fibers have been severed cleanly. These fiber flaws have resulted from chemical attack, are finely distributed, and are responsible for the large reduction in ultimate tensile stress for the longitudinal fiber orientation. The flaws are likely to form along surface pores [*8*] and other surface defects during aging.

Figure 5 shows that high-vacuum encapsulation does not degrade the ultimate tensile stress even after 10 days at 550°C. The 10-day aging in rough

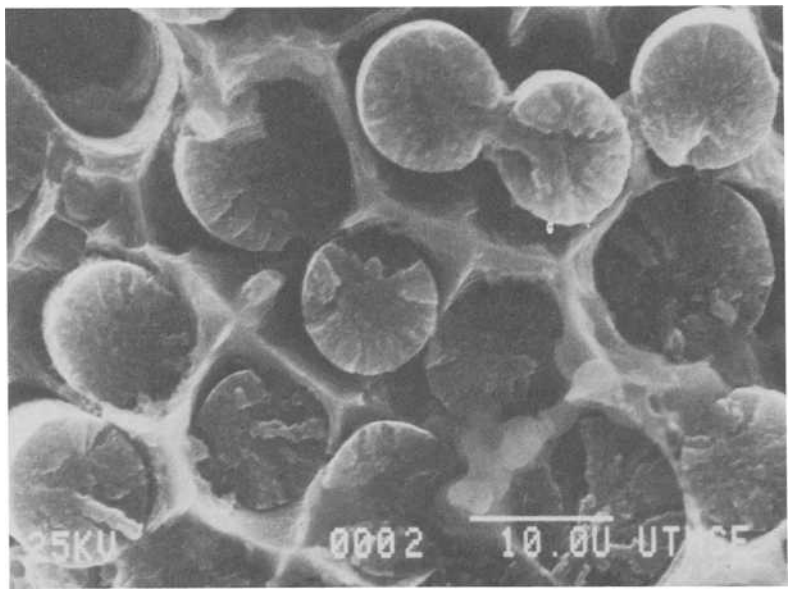

FIG. 3—*Scanning electron micrograph of longitudinal fracture surface of G4371 Al MMC aged at 550°C for 10 days in a rough vacuum.*

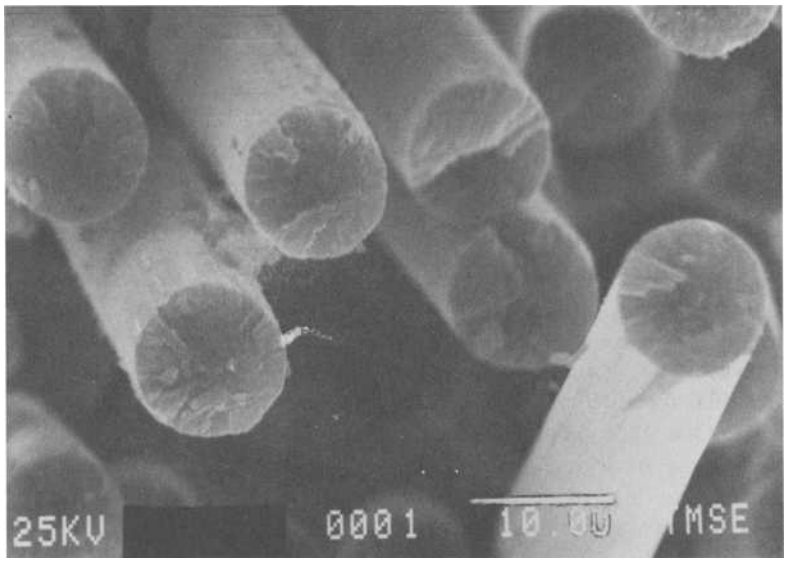

FIG. 4—*Scanning electron micrograph of longitudinal fracture surface of as-received G4371 Al MMC.*

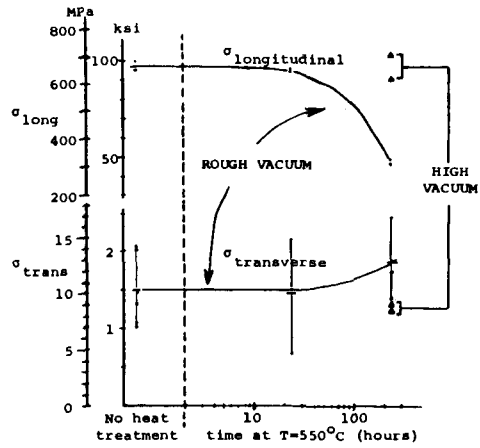

FIG. 5—*Fracture strength versus aging time at 550°C in a rough vacuum and high vacuum (G4371 VSB-32/oxide/6061 Al).*

vacuum has little effect on the ultimate transverse stress (that is, when the fibers are perpendicular to the tensile stress).

These results indicate that atoms must be transported down the interface during elevated temperature exposure to gaseous environments. Using AES combined with inert ion sputtering the distribution of reaction products can be investigated. Al_4C_3 at the interface is enhanced in the rough vacuum 550°C aging for 10 days, but is not enhanced in either the high-vacuum or atmospheric pressure aged samples [*9*]. Figure 6 shows a sputter profile into the matrix of a fiber-matrix interface exposed during high vacuum ($\sim 1 \times 10^{-7}$ Pa) *in situ* fracture. The presence of carbide as opposed to carbon is confirmed by the peak shape of the Auger derivative peak (Fig. 7). The bulk

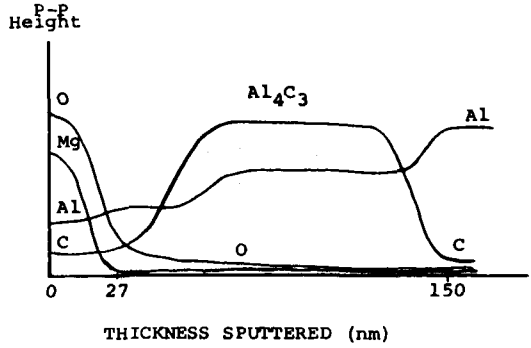

FIG. 6—*AES sputter depth profile into matrix side of fiber-matrix fracture interface (estimated layer thickness) (G4411 Pitch Gr/6061 Al aged at 550°C for 240 h).*

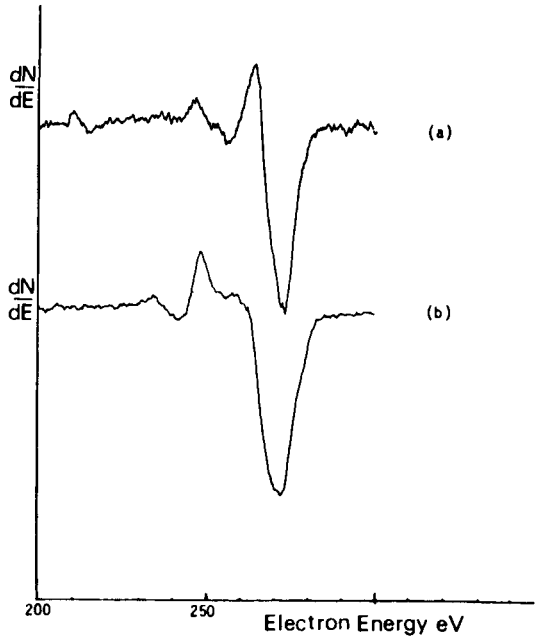

FIG. 7—*KVV carbon valence Auger features* (a) *from* Al_4C_3 *and* (b) *from graphite fiber.*

Al_4C_3 volume fraction was determined by a gas chromatographic chemical analysis technique [*10*] and is seen to be between the interfacial oxide and the bulk matrix. Thus the previously mentioned degradation of the graphite fibers appears to be by transport of carbon through the oxide toward the matrix. The mechanism for carbide formation is likely catalyzed by a hydrocarbon gas in the oil-pumped vacuum [*9*]. The thicker oxide due to aging in air inhibits carbide formation as does the lack of any significant amount of active gas in a high vacuum.

Titanium Matrix Composites

Thermal cycling can lead to enhanced degradation of MMCs primarily due to differences in thermal expansion between the matrix and fibers. Ti matrix composites were examined in order to relate thermal fatigue in several environments to interface chemistry and mechanical fracture behavior. The sample sizes ranged from 0.32 to 0.63 cm wide and were 0.08 cm thick. The thermal cycle was between room temperature and 550°C when lowered into a heated alumina fluidized bath for 1 day (144 cycles). The thermal cycle was approximately 10 min. 550°C was chosen to avoid α and β phase grain growth and the formation of an α-case around the fibers which occurred

when samples were cycled to higher temperatures and because 550°C is an upper limit to practical engineering applications.

Fractographs of transverse fractures in the as-received Ti MMCs show fracture occurs at the fiber-matrix interface. AES analysis shows only a small amount of oxygen contamination on the matrix side of the interface. The SiC and B_4C/B fibers have separated cleanly from the matrix, as would be expected from a weak fiber-matrix bond. Carbon-rich areas are found on the matrix side of the interface for SCS fibers, which indicates a stronger bond.

Thermal cycling in an air environment resulted in cracked and split fibers for transverse fractures. AES shows extensive amounts of oxygen at the interface. When cycling was done with the sample encapsulated in Pyrex with a sulfur atmosphere, the fibers were similarly broken and the interface had branch-cracks near the notch. (The notches were made before heat treatment so that the effect of diffusion from the outside surface into the sample could be seen on the fracture surface.) Branch cracks on the matrix side of the interface were also seen in longitudinally fractured specimens cycled in sulfur but were more difficult to detect due to the close-cropped nature of the fracture. The branch cracks occurred during the fracture in the sulfur embrittled region of the interface (Fig. 8). Large amounts of sulfur were found in the regions with branch cracks. By examining the relative amounts of sulfur along the interface a sulfur diffusion coefficient on the order of 10^{-8} cm^2/s was determined [*11*].

On some of the MMC samples mixed-mode fracture was examined (Fig. 9*a*). The fiber axis was at some angle from the tension axis. In a specimen with a 45-deg fiber-to-tension axis angle the following crack path was observed for a specimen whose interface was weakened by thermal cycling in a sulfur environment. The initial notch was perpendicular to the load axis. Fiber matrix interface debonding occurred near the notch and extended for the sulfur-diffusion distance. A change in mode to fiber pull-out was then observed. A slight drop in load was associated with this change (Fig. 9*b*). Subsequent growth was then along the fiber interface.

Thermally cycled Ti composites had oxygen distributed throughout the interface. In the air-cycled specimens the oxide layer was thick and appeared on both the matrix and fiber side of the interface as well as in some matrix areas. The vacuum-cycled specimens had thinner layers of oxygen at the interface. Specimens isothermally heated at 550°C for an equivalent time in vacuum show a still lower amount of oxygen observed at the interface consistent with oxygen going into solution in the alpha-rich matrix.

When Ti composites with B_4C/B and Borsic fibers were tested to determine the fatigue crack behavior, the fracture surface appearance and crack propagation rate was a function of load ratio (R) and environment. If the minimum tension load was kept at half of the maximum load ($R = 0.5$), the fractured transverse samples showed very little fiber damage; when $R = 0.1$ in a dry N_2 environment, the fibers are again also cleanly split from the

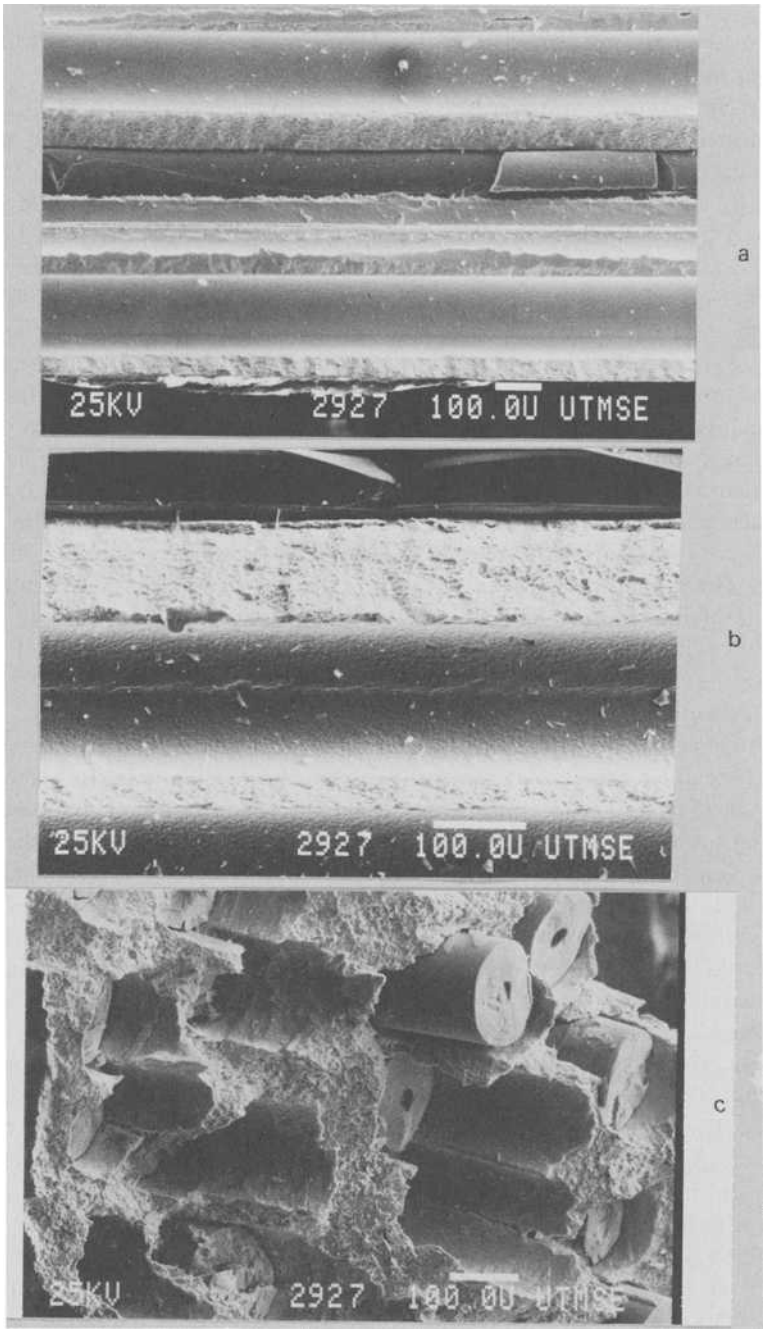

FIG. 8—*Scanning electron micrographs of Ti MMC with SCS fibers thermally cycled in sulfur atmosphere for 1 day between room temperature and 550°C.* (a) *Transverse load failure.* (b) *Magnified view of matrix interface of transverse failure.* (c) *Matrix interfaces from longitudinal load failure.*

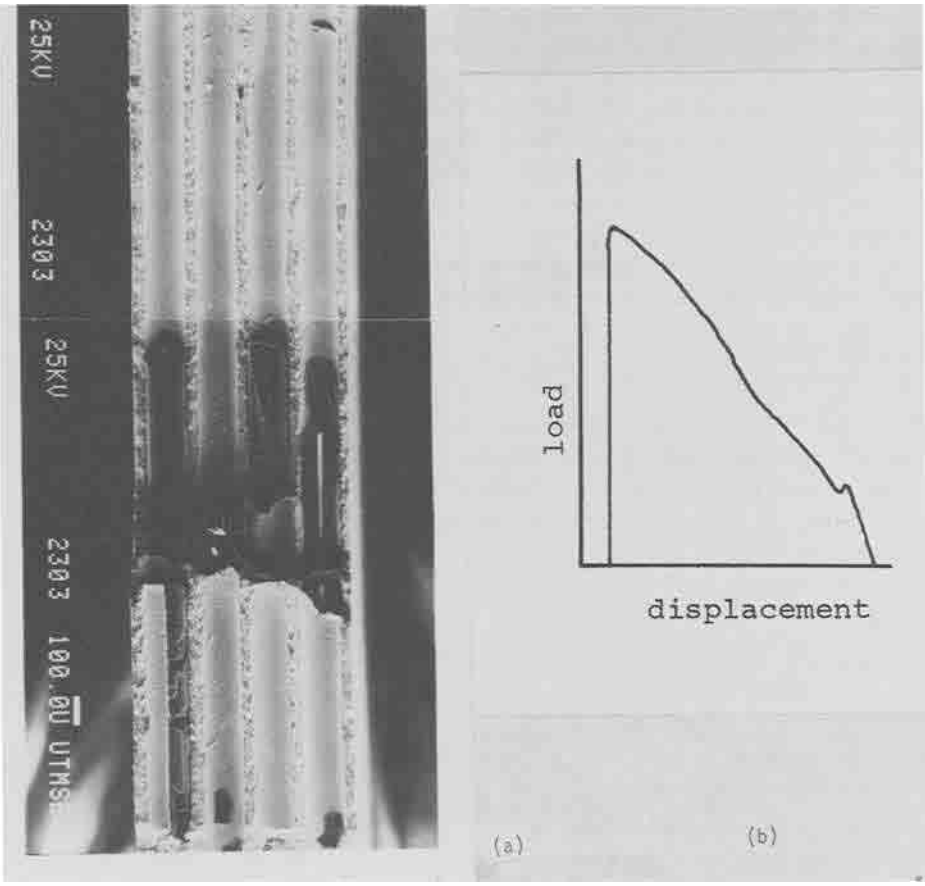

FIG. 9—(a) *Scanning electron micrograph of 45-deg fiber-to-tension axis fracture surface from thermally cycled in sulfur atmosphere Ti MMC.* (b) *Load-displacement curve.*

matrix without themselves fracturing. However, when humid air is the environment during fatigue cracking at $R = 0.1$, the fibers are broken and split and appear similar to those in Fig. 8*a*. It was concluded based on crack closure measurements that crack closure effects due to oxide buildup on the fractured matrix caused shear stresses which fractured the fibers [*12*].

Summary

The effects of environment (vacuum, air, sulfur) and of thermal treatment (isothermal and cyclic) on the fracture behavior of Al and Ti metal matrix composites were investigated. Fractography was done using a scanning electron microscope, and fiber-matrix interface chemistry was determined using

a scanning Auger microscope. The extent of fiber pullout is often an indication of the strength of longitudinally fractured composites. When there is excessive thermal oxidation of the fiber-matrix interface in the Al matrix composites with graphite fibers, pullout and weakening occur. A second cause of significant strength loss was excessive carbide formation and frequent fiber notching, so that longitudinal failures exhibited close-cropped fiber breakage. In Ti matrix composites with SiC and B_4C/B fibers, cracks along the interface were observed for thermally fatigued specimens. Large amounts of oxygen were found on both sides of the fractured fiber interface when thermal fatigued in air. Similar effects were noted in a sulfur environment.

Acknowledgments

The Al MMC research in this paper was supported by Office of Naval Research Contract N00014-78-C-0094; the Ti MMC research was supported by Air Force Office of Scientific Research Grant AFOSR 80-0052. The Air Force Materials Laboratory supplied the Ti MMC materials; the Aerospace Corporation supplied the Al MMC materials and performed the bulk Al_4C_3 chemical analysis.

References

[1] Marcus, H. L., Dull, D. L., and Amateau, M. F., "Scanning Auger Analysis of Fracture Surfaces in Graphite-Aluminum Composites," in *Failure Modes in Composites IV*, J. A. Cornie and F. W. Crossman, Eds., The Metallurgical Society of AIME, New York, 1979, pp. 308–318.

[2] Dull, D. L. and Amateau, M. F., "Transverse Strength Properties of Graphite-Aluminum Composites," TDR-0077 (2726-03)-1, The Aerospace Corp., El Segundo, Calif., 1977.

[3] Harrigan, W. C. and Goddard, D. M., *Journal of Metals*, Vol. 27, No. 5, 1975, p. 20.

[4] Steckel, G. L., Katzman, H. A., and Amateau, M. F., "Transverse Strength Properties of Graphite-Aluminum Composites," TDR-0080 (5726-03)-2, The Aerospace Corp., El Segundo, Calif., 1979.

[5] Thompson, E. R. and Lemkey, F. D. in *Composite Materials: Vol. 4—Metallic Matrix Composites*, K. G. Kreider, Ed., Academic Press, New York, 1974, pp. 101–157.

[6] Metcalfe, A. G. in *Composite Materials: Vol. 4—Metallic Matrix Composites*, K. G. Kreider, Ed., Academic Press, New York, 1974, pp. 269–318.

[7] Amateau, M. F., *Journal of Composite Materials*, Vol. 10, 1976, p. 279.

[8] Rand, B. and Robinson, R., *Carbon*, Vol. 15, 1977, p. 257.

[9] Finello, D., "Interfacial Behavior of Graphite-Aluminum Composites," Ph.D. dissertation, The University of Texas at Austin, 1982.

[10] Padilla, F., Harrigan, W. C., and Amateau, M. F., "Handbook of Test Methods for Evaluation and Qualification of Aluminum Graphite Composite Materials," TR-0075 (5621)-3, The Aerospace Corp., El Segundo, Calif., 1975.

[11] Park, Y. H. and Marcus, H. L., "Influence of Interface Degradation and Environment on the Fracture and Fatigue Properties of Titanium Metal Matrix Continuous Fiber Composites" in *Mechanical Behavior of Metal-Matrix Composites*, J. E. Hack and M. F. Amateau, Eds., TMS-AIME, New York, 1983, pp. 65–75.

[12] Mahulikar, D. S. and Marcus, H. L., "Environmentally Influenced Mixed Mode Fatigue Crack Propagation of Titanium Metal Matrix Composites," *Metallurgical Transactions*, to be published.

Panel Reports

Panel Reports

Ceramic Fractography Research Needs

One area of fractography that warrants additional research effort involves the features generated in unstable crack growth ($K_I > K_{Ic}$). At the higher velocities obtained in these conditions energy goes into the generation of the surface features known as "mist" and "hackle" and eventually into secondary crack development. Mist and hackle occur at specific values of the stress intensity factor for a given material. If the applied stress remains constant as the crack grows, the dimensions of the crack at the onset of mist or hackle bear a specific relationship to the dimensions of the crack at the point of criticality. Mecholsky and other researchers have used this fact to determine failure stress from measurements of dimensions of the "mirror" (the smooth region bounded by the mist region) and have compared it with values obtained from measurement of the initial flaw dimensions. They showed that the "mirror constant" relating the mirror size to applied stress at failure was proportional to the elastic modulus.

The fact that the onset of mist and of hackle occurs at specific values of the stress intensity factor suggests that the process (or processes) involved in their production is a fundamental one. Examination of the mist region of a glass fracture surface with the electron microscope reveals that the surface features are ridges elongated in the fracture direction. They are produced by deviation of portions of the crack front out of the primary crack plane. Apparently, the onset of mist heralds an instability of the crack tip, that is, a tendency to deviate from the original fracture plane. This tendency is consistent with stress analyses for the moving crack; these show that the maximum tensile stress moves out of the midplane as velocity increases. However, we do not understand any of the details of how the ridges are generated or what governs their size and shape, and we remain ignorant of what governs the transition from mist to hackle.

We also do not know why mirror constants are different for different materials. Presumably, the generation of mist and hackle is related to the work of fracture of a material; thus an understanding of what governs the onset of these features might provide insight into improving fracture toughness.

Eventually, as K_I increases above the values for the onset of severe hackle, fracture branching occurs. Congleton and Petch have suggested that the secondary fracture which characterizes branching is caused in some materials by the activation of microcracks by the stress field of the primary crack front.

They pointed out, however, that secondary fracture also occurs in materials which apparently contain no microcracks. The mechanism for generating secondary cracks in such materials appears to be an extension of that which produces hackle, that is, a deviation of a segment of the crack front out of the primary plane and the growth of that segment to critical size. In apparent contradiction is the observation by Snowden that in high-velocity impact, secondary fractures may occur without any prior appearance of mist or hackle. Bifurcation occurs in the mirror region.

Ed Beauchamp

Sandia National Laboratories, Albuquerque, New Mexico

Suggestions for Research in Fractography and Failure Analysis of Ceramics

In the past, failure analysis has been used mainly to determine the causes of failure of parts in service. The response to any knowledge gained has been to reduce the applied stresses, modify the environment, or alter the application in some other way to improve the survivability of the parts. In these cases the material was usually taken as a "given." Over the last few years emphasis has shifted to some extent towards the use of failure analysis to obtain improved understanding of the role of the defects in failure of the materials, and the response has been to use the improved understanding to develop improved materials with fewer or less severe defects. This trend is likely to continue. However, this approach can be broadened considerably to include investigation of micromechanisms of subcritical crack growth and investigations of the contributions of various micromechanisms to the fracture toughness. Suggestions for research in these areas are listed in the following outline. The suggestions emphasize fracture of fine-grain polycrystalline ceramics where the flaw sizes are usually several times the grain sizes.

A. New information needed for investigation of micromechanisms of fracture.
   1. Determination of the orientations of individual grains in fracture surfaces (selected area electron channeling).
   2. Determination of the fracture energies of grain boundaries.
   3. Increased use of available methods of determining fracture energies for various lattice planes in single crystals.
   4. Determination of the characteristics of microcracked zones at crack tips.
   5. Development of computerized methods of analysis of fracture surface topography.
   6. Determination of the magnitudes and distributions of localized residual stress (X-ray diffraction microanalysis).

B. Applications of the new information to investigation of micromechanisms of fracture.
   1. To characterize the variations in fracture mode (relative proportions of intergranular and transgranular fracture) observed along radii from fracture origins.
   2. To use the results of the above characterization to locate the subcritical crack growth region and the boundary at which the transition from subcritical to critical crack growth occurs.
   3. To obtain an understanding of the micromechanisms responsible for crack growth resistance and to improve the fracture toughness by interfering with the mechanisms responsible for the subcritical to critical transition.
   4. To understand the effect of failure of a particular element (grain boundary or crystal plane) on the failure of succeeding elements.
   5. To understand the systematic variations in fracture mode as functions of K_I, crack velocity, temperature, and environment.
   6. To determine local variations in resistance to subcritical crack growth and to relate these variations to variations in specimen characteristics.
   7. To understand flaw linking.
   8. To characterize crack front shapes at various stages of crack growth.

C. Other areas of fractographic investigation.
   1. Investigate flaw severity as distinguished from flaw size. (Include effects of residual stresses.)
   2. Investigate the mechanics of crack branching.
   3. Investigate the fractography of single crystals.

Henry P. Kirchner

Ceramic Finishing Company, State College, Pennsylvania

Future Research Needs in Ceramic Fractography and Failure Analysis

Future research needs in ceramic fractography and failure analysis may be divided into three broad categories: (1) the mist-hackle-crack branching sequence and resultant mirror size and shape, (2) a broader range of loading conditions, and (3) features within the mirror region or in the absence of any mirror patterns.

The following sections discuss these three categories and some points made by other speakers at this symposium.

Mirror Features

One of the first areas needing improvement in the study of mirror features is the accuracy of measurements. Though we have fairly general agreement between measurements for a given investigator at different times as well as between different investigators, there is considerable room for improvement in agreement and accuracy. A considerable amount of judgment is involved in placing the boundary of the mist, hackle, or crack branching, because of either their irregularities or their diffuseness, especially for many mist boundaries and to some extent for hackle boundaries. An example of the problem is the question of definition of the boundary and the magnification at which it is defined. Higher magnification often allows us to see mist ridges further in towards the fracture origin than we might see at lower magnifications; however, the boundaries also become more diffuse at higher magnifications. This problem becomes even more acute as we go to lower strengths and hence larger mirror sizes and lower mist and hackle densities.

The second aspect of mirror features that needs more study is the nucleation of secondary cracks and the resultant formation of mist, hackle, and ultimately crack branching. Whether we think of nucleation of secondary cracks ahead of the main crack front or right at the crack tip there remains a nucleation issue. We should also recognize that there may be really two issues, nucleation and propagation, and that these may be controlled by different factors; for example, nucleation may be more controlled by stress intensity and propagation more by energy. I believe that secondary cracks are probably nucleated quite near the main crack tip, not significantly ahead of it. We have not yet seen any clear evidence of what appear to be secondary cracks propagating back towards the main crack. If secondary cracks are nucleated fairly close to the original crack tip such that upon nucleation there may no longer be a high stress between them and the main crack front, then there is no significant driving force to propagate them back into the main crack. Furthermore, ceramic crack velocities are two to five times those of materials such as polymethyl methacrylate (PMMA), where such propagation of secondary cracks back towards the main crack is seen. Thus the main crack in a ceramic should have much more opportunity to grow towards a secondary crack ahead of it during the nucleation and early growth stages of the secondary crack than in plastics such as PMMA.

There could be serious dangers in drawing too close an analogy between the known crack nucleation ahead of the main crack in plastics such as PMMA and the subsequent propagation of the secondary cracks back towards the main crack front. The primary reason this analogy may not be strictly applicable to ceramics is that there are fundamental differences in the behavior of ceramics and PMMA. The mechanism of nucleating secondary cracks ahead of the main crack found in PMMA is by plastic flow, a phenomenon that is far more restricted if not totally absent in all or nearly all of the ceramic fracture

cases that we consider. This plastic flow ahead of the crack changes the stress distribution ahead of the crack and may also blunt cracks.

Velocity measurement is the next topic associated with mirror features that could use further work. Firstly, as I noted in my paper,[1] there appears to be a potentially significant discrepancy of where terminal velocity occurs in relation to the mirror boundary. Also, increased sophistication of velocity measurements is necessary to address the issue of secondary crack nucleation discussed previously. I have been interested in the possibility of using more sophisticated ultrasonic timing of cracks—for example, with a known pattern of pulse lengths—in order to clear up the questions of whether secondary cracks initiate ahead of the main crack front (and if so how much) and whether some parts of the crack front jump or run ahead of other parts. Another possibility may be to attempt frequency modulation of the ultrasonic signal used for timing. Such techniques, as well as detailed study, are needed to resolve the issues of how extensive multiple sources of failure are and their interaction in fracture of many large-grain bodies.

Loading Conditions

Almost all work on loading conditions is focused on uniaxial tension or flexure, usually at normal loading rates, predominately with Mode I failure. We have begun to obtain some data on biaxial flexure conditions. We do have evidence, however, that other loading conditions can make substantial changes in fracture character, for example, from the superposition of torsion and tension stresses. Although we do have a fair sampling of effects of loading rate, there is substantial opportunity and need for further development here.

Features within the Mirror Region or in the Absence of Mirror Patterns

The third major area for further work is the study of features within the mirror region or in the absence of mirror patterns. Work such as that of Michalske[2] and Frechette shows that a variety of markings can be brought out by sensitive techniques. These markings can provide substantial information. This area is worthy of study since the issue of slow crack growth is quite important in ceramics. Also, there are a variety of failures in which one does not get the normal mirror pattern. A particularly important example of this is failure of ceramics under large local stress but low body stress, such that when the crack has propagated to the normal distances where one would expect normal mist etc. features the long range stress is now so low that they do not form. Important examples of these are failures from contact stresses.

[1]Pages 5-103.
[2]Pages 121-136.

Points Made by Other Speakers

I would like to briefly address some points made by other speakers. I endorse essentially all the points that Henry Kirchner made; in particular, his call for further data on single crystals as a function of orientation. In this regard I would also note that gaining further understanding of the fracture topography of single crystals as a function of orientation can be an important aid to one of his other requests, namely how to determine the orientation of individual grains on a fracture surface. We can do this in some cases now, and certainly with further study could do substantially better.

With regard to the issue of associating velocity as a basic correlation with, or cause of, crack branching associated with mist etc., I would express caution. Firstly, as I noted in my paper, there appears to be substantial differences in the times for cracks to approach terminal velocity. This point and the fact that many of the measurements show a close approach to terminal velocity well before mist starts forming lead us to question velocity as a fundamental or direct causative factor of branching. There are also possibly important correlations with energy; this is suggested by glass fractures from impinging water jets.

Again, I would stress that there may be both stress intensity and energy type requirements in which velocity plays a role. The very interesting work of Bill Snowden bears on this issue, since he observed that a crack could propagate a characteristic distance and then branch, often multiply, without any formation of mist or hackle. This should not be surprising. It has been observed previously that there is a higher density of features with higher stresses and that there appears to be a fairly definite tendency for the microscopic crack branching boundary to move in closer to the hackle boundary and the hackle boundary closer into the mist boundary with higher stresses. Also, one can look upon this trend of higher stresses as a trend with increasing strain energy density. Thus Snowden's experiments in which a very large amount of impulse energy is dumped into the specimen imply the collapse of the mist, hackle, and branching boundaries to a single branching boundary. This also is not surprising, since the general view of mist and hackle formation is that they represent nucleation but only limited growth of secondary cracks.

The need for a crack to propagate further in order to have the capability to fully branch can be associated with gaining enough excess energy to propagate two sets of cracks. In a situation where a large excess of mechanical strain energy is provided in the system, however, the extra distance of propagation before macrocrack branching after initial secondary crack nucleation may not be required. This is not to suggest that we have the final answer, but merely to provide a hypothesis or framework within which to construct possible experiments for clearly identifying what has been done.

Finally, I support the point that Steve Freiman has made about uncertainty in the failure-originating flaws themselves. We have, I think, identified the

major types of flaws that cause failure initiation in most high-strength ceramic materials. Further, we have obtained general agreement between the observed and predicted flaw sizes in many cases. This is clearly not adequate for many situations, however, especially those involving specific design and reliability issues, and there are a number of cases in which our knowledge is rather weak. This is another example where more detailed fractographic studies within the mirror region can be quite important. The areas of residual stresses, irregular flaw shape, multiple flaws, etc., require substantially more study.

Roy W. Rice

Naval Research Laboratory, Washington, D.C.

Summary

Summary

This volume was organized into two major sections: Ceramics and Metals. The Ceramics section is further subdivided into three subsections: Fracture Analysis Techniques, Surface Analysis Techniques, and Applied Fractography. The Metals section is subdivided into Failure Analysis Techniques and Applied Fractography.

The two Fracture Analysis Techniques subsections present the basic principles and approach to utilizing fractography in the failure analysis of ceramics and metals. Both Applied Fractography subsections provide case histories and applications of the principles presented in the Fracture Analysis Techniques subsections. The Ceramics section has a Surface Analysis Techniques subsection which presents new approaches to chemical and topographical analysis of brittle materials.

The following sections summarize the papers from each of the groups.

Ceramics

Fracture Analysis Techniques

Rice summarizes our current knowledge of fracture surfaces and presents state-of-the-art techniques. This comprehensive paper can be used as a ready reference to the subject of fracture surface appearance of glass and single crystal and polycrystalline ceramics. A nomenclature for fractography is suggested by *Frechette.* Though there may be some disagreements on the proposed usage, this is the first written comprehensive suggestion for a common nomenclature and will serve as a basis for future debate.

Ball et al describe the relationship between fracture strength and topography, particularly addressing the rate of fracture on surface roughness and mist spacing. The techniques presented in this paper will serve as a basis for future quantitative fractography. *Michalske* identifies the cavitation scarp and transition hackle and demonstrates the usefulness of observing fracture features on surfaces formed because of stress corrosion processes. This paper is a summary of the most recent work performed in this field.

Surface Analysis Techniques

Pantano and Kelso summarize the chemical analysis techniques available for fracture surfaces, such as Auger electron spectroscopy and ion scattering

spectroscopy, and identify the rationale for selecting the appropriate method. While many of the techniques have been available for some time, they have generally not been used for fracture surface analysis. A new scanning electron microscope backscatter image technique is presented by *Healey and Mecholsky*. This technique enables the worker to interpret the interaction of microstructure with fracture-initiating cracks by separating the topography and composition images. Fracture mechanics principles are combined with surface analysis to demonstrate how small cracks (~ 50 μm) behave differently than large cracks (~ 500 μm) because of the size of the microstructure (~ 500 μm) in large-"grained" glass ceramics.

Applied Fractography

Mecholsky and Rice apply the principles of fracture surface analysis to biaxial flexure and show that the same principles apply to tension, flexure, and (tension-tension) biaxial flexure. This analysis suggests that many complex shapes observed in service can be analyzed and compared with laboratory specimens. *Phillips* extends this assumption by directly applying failure analysis techniques to alumina substrates used in production. He shows the different fracture surface characteristics obtained by impact, thermal shock, and pin placement.

Metals

Failure Analysis Techniques

Pellegrino and McCartney illustrate case histories of failure analysis where intergranular fracture were observed and attributed to a variety of mechanisms. These histories include liquid-metal embrittlement of an AISI 1070 steel rod caused by copper pickup during processing, a low-carbon steel embrittled by lithium in service, a platinum and platinum-rhodium thermocouple embrittled by a low-melting platinum silicon eutectic that formed in service, the stress-corrosion failure of an XM-15 (18-18-2) stainless heat exchanger, the "rock-candy" brittle fracture of a steel casting caused by the presence of aluminum nitride at the solidification grain boundaries, the brittle fracture of heat-treated bolts manufactured from columbium-treated fine-grain AISI 1541 steel, and the intergranular fatigue fracture of a bar overheated during forging.

The fibrous-to-cleavage fracture transition phenomenon is discussed by *Kobayashi et al.* An examination of fracture surfaces of A36 steel and A5333 steel was made with a scanning electron microscope (SEM) and stereoscopic photographs. Pertinent information was obtained through topographical characterization of fracture surfaces. This characterization was made with a parallax bar in conjunction with SEM stereo-photographs. The height mea-

surement was made relative to a reference plane such as initial fatigue crack surface in the photograph. Through topographical characterization of matching sites of top and bottom fracture surfaces, crack tip opening stretch, fracture process zone size, and deformation of grains were determined. Fracture surface measurements such as crack tip opening displacement were correlated to the fracture toughness measurement.

Cina et al describe a systematic fractographic study of fatigue in aerospace materials to facilitate failure investigations of actual components. For aluminum alloys, quantitative relationships have been established between the total number of striations in the development of the crack and the total number of fatigue cycles in the entire fatigue test. This enables an estimate of fatigue stress where unknown. Striation counting in steels was found to be very difficult and unreliable. For 4340 steel, however, trends akin to those in aluminum alloys were observed.

Cleaning techniques for post-failure analysis are compared by *Vecchio and Hertzberg*. They determined that benign techniques such as air blasting and replica stripping are effective in removing loosely adhered particles, grease, and oils, and will not affect surface topography. The authors warn about the use of active techniques such as cleaning detergents; these can alter surface topography and thus alter interpretation. This very instructive paper can be used as a guide for the preparation of surfaces for fractographic examination.

Applied Fractography

Dainty describes a technique that can aid in the fractographic determination of fatigue crack propagation rates of aluminum alloy components which have failed during full-scale aircraft fatigue tests where spectrum loading has been used. This technique was successfully utilized to determine the crack growth rate of a failed 2024 aluminum alloy extrusion spar cap that was subjected to both block and spectrum loading in a two-phase full-scale aircraft fatigue test.

The effects of high-temperature austenitizing treatments and internal hydrogen on the fracture mode during fatigue crack growth studies in AISI 4340 steel have been investigated by *Cheruvu*. The observed variations in the occurrence of fatigue striations among the specimens austenitized at different temperatures are discussed in terms of variations in plane strain fracture toughness in these specimens. Variations in the amount of intergranular fracture at low ΔK in charged specimens are discussed in terms of hydrogen diffusion to the prior austenite grain boundaries.

Swaminathan uses SEM examination of the fracture surface to reveal many areas containing striations formed by the propagating crack under fatigue loading conditions. The fracture topography was also studied under the transmission electron microscope (TEM) using the carbon replica technique. Fatigue striation spacing measurements were made at many locations using a

fracture mechanics model in order to calculate the magnitude of probable stresses that caused crack propagation. From the results of this analysis a failure scenario was developed that could explain the failure of the shaft.

Burghard and McCann discuss how the macroscopic features of a fracture established that the primary fracture initiated at one of the blade attachment grooves in the disk rim, even though there was no macroscopic evidence of preexisting defects or of subcritical crack growth in the initiation area. Preliminary magnetic particle inspection of the failed disk did not reveal any defects or cracks at other blade grooves. Test results, together with the fact that caustic and sulfur were present in the blade groove deposits, suggested that the in-service subcritical cracks were developed by hydrogen-induced cracking in a caustic environment, promoted by the presence of a sulfur-bearing contaminant.

A complete analysis performed on a hydraulic turbine shaft in order to determine the origins and causes of its cracks is presented by *Nguyên-Duy.* The origins of the first crack were responsible for the initiation of other cracks.

Finello et al explain that unidirectional continuous-fiber metal matrix composites have high strength in the fiber direction but are weak in the transverse direction often because of weak fiber-matrix bonds. The effects of environment and thermal treatment on decohesive behavior and occasional fiber splitting were investigated in several such materials. Fractography was done using a scanning electron microscope, and fiber-matrix interface chemistry was determined using a scanning Auger microscope. In titanium matrix composites with SiC and B_4C/B fibers, cracks along the interface were observed for thermally fatigued specimens. Large amounts of oxygen were found on the surface of the broken fibers and on some of the matrix sides of the failed interface, but no oxygen was present on the matrix side for isothermally treated specimens.

A panel discussion was held on the direction of future research needs in ceramic fractography and failure analysis. The panel consisted of Ed Beauchamp, Sandia National Laboratories; Van Derek Frechette, State University of New York at Alfred; Henry P. Kirchner, Ceramic Finishing Company; and Roy W. Rice, Naval Research Laboratory. Messrs. Beauchamp, Kirchner, and Rice have provided summaries of their remarks.

J. J. Mecholsky, Jr.

Sandia National Laboratories, Albuquerque, New Mexico; symposium chairman and editor

S. R. Powell, Jr.

Bell Helicopter Company, Ft. Worth, Texas; symposium chairman and editor

Index